

DISS. ETH No. 25591

# Dendronized Polymers: Pushing Synthetic & Analytical Limits

A thesis submitted to attain the degree of  
DOCTOR OF SCIENCES of ETH ZURICH  
(Dr. Sc. ETH Zurich)

presented by

*DANIEL MESSMER*

*MSc Chemistry, ETH Zurich*

born on 08.05. 1991

citizen of Dörflingen, SH

Accepted on the recommendation of

*Prof. Dr. A. Dieter Schlüter (examiner)*

*Prof. Dr. Jan Vermant (co-examiner)*

*Prof. Dr. Christoph Weder (co-examiner)*

2018

*"I know that there are people who work on problems to which they know the answer. They know it can be done. I am convinced that it's more interesting to work on challenges where you don't know the answer. In chemistry, you should enter into an adventure with molecules"*

- Ben L. Feringa<sup>1</sup>

## Abstract

Thickness and steric congestion are not usually considered when studying the behavior of conventional linear polymers, where chain length, polydispersity, and intrinsic chain stiffness are the primary determinants. In a dendronized polymer, the control of thickness and steric congestion is possible. A dendronized polymer consists of a linear polymeric backbone with multiply, regularly branched (*i.e.* dendritic) side groups. By increasing the dendritic generation  $g$ , a dendronized polymer's diameter can be grown in discrete steps. With growing  $g$ , not only the thickness of the polymer chains but also the steric congestion of the dendritic side groups increases. The steric demand can additionally be controlled by the variation of peripheral substituents. The unparalleled fine control over the molecular structure possible through divergent dendronized polymer synthesis permits the systematic study of the influence of thickness on the behavior of macromolecules.

The synthesis of a fully homologous series of dendronized polymers from  $g = 1$  to  $g = 8$  required significant alterations to previous synthetic strategies. The  $g > 5$  members of this homologous series are of unprecedented structural perfection, and the improved, scalable synthetic protocols have provided useful quantities (200 mg to 20 g) of the dendronized polymers in this series.

These structurally near-perfect dendronized polymers provided a solid foundation for the investigation of the effects of thickness and dense intramolecular packing. Foremost among these is the maximum accessible dendritic generation  $g_{\max}$ . According to theoretical considerations, around  $g_{\max} \approx 6 - 7$ , steric congestion begins to dominate the behavior of the dendronized polymer. The dendronized polymers of  $g > 5$  in the series discussed in this thesis probably represent the best approximation of  $g_{\max}$  structures to date. Furthermore, the cause and mechanism of main chain scission in certain dendronized polymers is addressed.  $g$ -dependent solvent swelling as a direct consequence of intrinsic steric congestion plays a crucial role in this process. Finally, the thickness and compactness of dendronized polymers are responsible for providing sufficient contrast in cryogenic transmission electron microscopy. This has enabled the first three-dimensional imaging of individual synthetic polymer chains in their native state, permitting conformational analyses at length scales difficult to access by scattering measurements.

These phenomena represent only a glimpse at the possible consequences of endowing linear polymers with a significant diameter. The materials and methods described in this thesis are hoped to lay the groundwork for the systematic investigation of thickness as a heretofore neglected variable in polymer science.

## Kurzfassung

Die Dicke einer Kette wird bei der Untersuchung konventioneller linearer Polymere gewöhnlich nicht berücksichtigt – anderen Faktoren wie der Kettenlänge, der Polydispersität und der intrinsischen Steifigkeit der Kette wird viel grössere Wichtigkeit beigemessen. In dendronisierten Polymeren ist es möglich, die Dicke systematisch zu variieren: Ein dendronisiertes Polymer (DP) ist ein lineares Polymer, das mehrfach und regelmässig verzweigte Seitenketten (Dendronen) trägt. Der Durchmesser eines dendronisierten Polymers wächst in diskreten Schritten mit zunehmender dendritischer Generation  $g$ . Neben dem Durchmesser steigt mit der Zunahme von  $g$  auch die gegenseitige sterische Hinderung der Dendronen. Zusätzlich ist es durch Austausch der peripheren Substituenten möglich, den sterischen Anspruch der Dendronen zu steuern. Da die divergente Synthese von dendronisierten Polymeren exzellente Kontrolle über die Struktur und Dimensionen dieser Makromoleküle erlaubt wird die systematische Untersuchung von Dickeneffekten möglich

Die Synthese einer ununterbrochenen homologen Reihe von dendronisierten Polymeren mit  $g = 1$  bis  $g = 8$  war nur dank signifikanter Modifikation der bestehenden synthetischen Strategien möglich. Die optimierten, skalierbaren synthetischen Protokolle haben für  $g > 5$  dendronisierte Polymere mit zuvor unerreichter Strukturperfektion ergeben und haben die Herstellung von nützlichen Mengen (200 mg bis 20 g) dieser Polymere erlaubt.

Diese beinahe defektfreien dendronisierten Polymere bildeten die Basis für die Untersuchung der Effekte von zunehmender Dicke und immer dichterem intramolekularer Packung. Von grösster Bedeutung ist hierbei die maximal erreichbare dendritische Generation  $g_{\max}$ : Theoretische Betrachtungen lassen erwarten, dass interne sterische Hinderung ab  $g_{\max} \approx 6 - 7$  das Verhalten eines dendronisierten Polymers dominiert. Die dendronisierten Polymere der hier diskutierten homologen Reihe entsprechen für  $g > 5$  der wahrscheinlich besten Approximation des  $g_{\max}$ -Konzepts. Unter gewissen Bedingungen erleiden einige dendronisierte Polymere Hauptkettenspaltung, deren Ursache und Mechanismus in dieser Arbeit ebenfalls besprochen werden. Von grösster Bedeutung ist dabei das  $g$ -abhängige Quellungsverhalten der Dendronen, das wiederum eine direkte Folge intrinsischer sterischer Hinderung ist. Dank ihrer Dicke und Kompaktheit liefern dendronisierte Polymere genügend Kontrast für kryoelektronenmikroskopische Untersuchungen. Damit war es erstmals möglich, individuelle synthetische Polymerketten im nativen Zustand dreidimensional abzubilden. Die Kettentrajektorien ermöglichten eine Analyse der Polymerkonformation auf Längenskalen, die mit Streumessungen nur schwer zugänglich sind.

Dicke ist bisher in der Polymerforschung ein wenig berücksichtigter Parameter. Polymere mit signifikantem Durchmesser weisen sicherlich viele andere neue und interessante Eigenschaften auf, nebst den in dieser Arbeit besprochenen. Die hier vorgestellten Materialien und Methoden sollen eine Basis für die systematische Untersuchung solcher Effekte bieten.

## Acknowledgements

Few long-term projects are possible without the support of others – and the following thesis is no exception. Foremost, I was encouraged by **Prof. A. Dieter Schlüter**: He permitted and encouraged me to work on the topic which I had fallen in love with during my Master's studies. Though he provided the necessary dose of skepticism and realism, in the end he always permitted and indeed encouraged me to explore in those directions where I thought interesting phenomena might be found. The same is true for **Prof. Baozhong Zhang** (now at Lund University), who first piqued my interest in the topic of dendronized polymers, and who closely supervised me at the start of my time in the Schlüter group.

I thank my examiners – **Prof. Jan Vermant** (D-MATL, ETH Zurich) and **Prof. Christoph Weder** (Adolphe Merkle Institute, Université de Fribourg) and the head of department, **Prof. Ralph Spolenak**, for sacrificing their valuable time to read my thesis and to attend my defense.

Colleagues are the most crucial part of any work environment, and I consider myself incredibly fortunate to have encountered a group as competent and personable as has been the case at ETH Zurich. Because my general messiness and my taste in music were inflicted primarily on those who I shared lab space with, my foremost thanks and apologies go to the folk who've worked in lab H528 over the years - I feel privileged to have worked with and learned from all of them: **Prof. Baozhong Zhang, Dr. Hao Yu, Dr. Max Kory, Stan van de Poll, Dr. Tim Hungerland, Prof. Yingjie Zhao**, and naturally my most recent and long-suffering victim, **Gregor Hofer**. I also owe a great debt to those of my colleagues who worked with dendronized polymers: **Dr. Chiara Gstrein**, and **Dr. Leon Scherz** – the discussions I had with of you were ever fruitful. Colleagues working on various other projects are no less important, and I always greatly enjoyed our scientific discussions: **Dr. Ralph Lange, Dr. Wei Wang, Philipp Tanner, Dr. Vivian Müller, Dr. Wenyang Dai, Dr. Sandra Serrano-Luginbühl, Dr. Andreas Kuchler, Prof. Peter Walde, Dr. Payam Payamyar, Dr. Marco Servalli, Dr. Julia Bättig, Dr. Ikhlas Gadwal, Dr. Jingyi Rao**.

I had the fortune of being able to collaborate with a number of excellent scientists outside the Schlüter group: **Prof. Martin Kröger** (D-MATL, ETH Zurich) has long been involved in my projects, providing direly needed input from a physical/mathematical standpoint, where I as a chemist have serious blind spots, and crucially he provided all the statistical analyses presented in chapter 4. He always had an open ear for my concerns and provided rapid solutions to our mathematical problems, as well as visualizations which have greatly benefited the work presented in this thesis; **Prof. Peter Walde** (D-MATL, ETH Zurich) and his coworkers (particularly **Dr. Andreas Kuchler, Dr. Philipp Spycher, Dr. Chengmin Huo** and **Nicolas Ghéczy**) found an application and continue to use dendronized polymers in enzyme immobilization; **Surendra Anantharaman** and his colleagues at the Laboratory for Functional Polymers (EMPA Dübendorf) have found another intriguing application for the deposition of *J*-aggregates; several members of the group of Prof. Jan Vermant (**Dr. Wouter Sempels, Dr. Rao Vutukuri, Gabriele Colombo**, and **Dr. Barbara Gold**) have been involved in the investigation of fluorescently labelled dendronized polymers, along with colleagues from the group of Prof. Joan Hofkens (Molecular Imaging and Photonics, KU Leuven), particularly **Dr. Susana Rocha**. Sorry that producing adequately labelled samples took so long – I hope you'll finally be able to do your long-desired measurements now; **Dr. Reinhard Kissner** (LAC, ETH Zurich) has conducted EPR measurements of dendronized polymer scission products, enabling unprecedented mechanistic insight into the

process, and provided entertaining and valuable scientific discussions; **Prof. Carlos Alemán** and **Dr. Oscar Bertran** (Universitat Polytècnica de Catalunya, Barcelona) provided helpful insights regarding the process of main-chain scission by conducting a large MD simulation; **Priv.-Doz. Dr. Christoph Böttcher** (FZEM, Freie Universität Berlin) measured and processed cryo-TEM of dendronized polymers, an impressive experimental achievement which laid the foundation for an interesting analysis of DP chain statistics; **Prof. Kurt Binder** (Uni Mainz) contributed significantly to the analysis and contextualization of DP trajectory data; **Dr. Sebastian Tacke** (formerly ScopeM, ETH Zurich, now MPI for Molecular Physiology, Dortmund), supported by former colleagues (**Dr. Harald Nüsse** and **Dr. Ulrike Keller**; both at the Institut für Medizinische Physik und Biophysik, Universität Münster), determined dendronized polymer densities by qSTEM; **Dr. Antonio Sánchez-Ferrer** from the group of Prof. Raffaele Mezzenga (D-HEST, ETH Zurich) conducted many work- and time intensive SAXS measurements, also with the goal of measuring DP densities; **Dr. Chiara Gstrein** provided dendronized polymer samples permitting the classification of solvent quality; **Dr. Sara Mantellato** (D-BAUG, ETH Zurich) is gratefully acknowledged for ICP-OES measurements to determine residual Pd content in polymer samples; Various people outside the group have always had an open ear for scientific discussions, particularly **Dr. Mohammad Divandari** (D-MATL, ETH Zurich). To all of the above, I would like to express my sincerest gratitude: You have volunteered much of your time, on occasion to no outcome. Without your support, only very little of the work presented in this thesis would have come to fruition. Lastly, I would like to mention the late **Prof. Avraham (Avi) Halperin**. He was a long-time collaborator of our group with a keen interest in the scaling behavior of DPs, whom I was fortunate enough to meet on multiple occasions. It was in no small part his curiosity which prompted the investigations of density and shape of DPs presented in this thesis. In early 2018, he lost his battle with long illness, and I am saddened by his passing.

An important factor for successful research is good instrumentation, but truly crucial are the experts who run, maintain and provide access to such equipment. In this context, **Dr. Thomas Schweizer** has been an invaluable facilitator of my work – he’s a true wizard with all things mechanical and electronic, and likely our group would have come to a rapid standstill without his constant support: He has maintained the all-important tools for polymer characterization, especially the GPC machines (no small feat in view of much adversity from recalcitrant instruments and users), has provided first-hand knowledge in the fields of polymer characterization and processing, constructed specialized apparatus and conducted rheological studies. People outside our research group provided similarly competent and crucial services: **Dr. René Verel** from the NMR service of the LAC (D-CHAB, ETH Zurich); the staff of MoBiAs at LOC (D-CHAB, ETH Zurich), particularly **Louis Bertschi** and **Rolf Häfliger** of the MS service; **Prof. Roger Wepf**, **Dr. Stefan Handschin** and **Maja Günthert** at ScopeM (ETH Zurich) provided aid in electron microscopy; The staff at the HCI shop, who competently fulfilled all the mumbled requests of many an overworked grad student. I was also granted access to equipment by other research groups within and outside ETH. I’d particularly like to mention the groups of **Prof. Nicholas Spencer** (AFM, DLS) and of **Prof. Jan Vermant** (microscopes, processing equipment).

I had the privilege of supervising several students during my time in the Schlüter group. Your work greatly aided mine, and I hope that you learned a few things about chemistry and polymer science during your time with me – even though I might not always have been the ideal supervisor. **Jens Sesseg**, **Nadia Zuurbier**, **Valentina Gasser**, **Raphael Gmünder**, **Ralph Werner** – I wish all of you the best in your future endeavors, and I hope you remember your time under my tutelage with some fondness.

For providing some refuge away from work, I would like to thank my family – my mother **Käthi**, my father **Robert**, my brother **Lukas** and all members of my extended family. I could always rely on you for emotional support, an excellent meal on Sundays and delicious produce from the home farm. I'd like to thank my closest friends – **Michi, Francesco, Nicole, and Marcella** – for keeping me company away from work, and my roommates over the years for making our flat a place to call home. I am sorry for not being the best family member/friend/roommate at all times – particularly during the writing of this thesis, which has absorbed me thoroughly for too long a time. I'd also like to express my gratitude to those who most regularly partook of some hot beverage, the occasional sugary treat and – most importantly – a good old break during the traditional 3 o'clock tea time: **Gregor, Ralph, Vivian, Stan, Bernd, and Chiara**.

Perhaps unwisely, I started a new hobby during my PhD, and Dungeons & Dragons has grown truly close to my heart in the past couple of years; I thank **Michi, Francesco, Nicole, Marcella, Natascha, Alvaro, Sandy, Chiara, Stan, Vivian, Jay, Gregor, Richard, and Moh** for witnessing my first, often stumbling attempts at DMing, and I thank **Sacha, Beni, Mathias, Christoph** and particularly **Bea** for allowing me to join them as a player. I greatly enjoyed the stories we've told together so far, and I hope you did, too – I seem to have infected at least a few of y'all with the D&D bug. I hope there is much more great collaborative storytelling to come in the future – once all this science stuff is done, let's get together again and slay some monsters :D . I'd also like to thank the authors who gave me some respite when research got a little too real. I'd have been lost in this world if it weren't for yours: Stephen Erikson, the late and great Sir Terry Pratchett, Susanna Clarke, N. K. Jemisin, Kameron Hurley, J. R. R. Tolkien, Neal Stephenson, Jeremy Crawford/Mike Mearls/Chris Perkins & Co.

Lastly, I would like to give a special thank you to those who read and corrected parts of my thesis: **Francesco, Ralph, Leon, Gregor, Philipp, Moh** – you have greatly contributed to the quality of this document, noticing all the errors big and small which I was simply not capable of perceiving, anymore.





## Contents

Abstract.....	iii
Kurzfassung.....	iv
Acknowledgements.....	v
1. Introduction .....	6
1.1. A brief history of polymers: From obscurity to commodity .....	6
1.2. Polymers – terminology & structure.....	9
1.3. Macromolecular structures .....	11
1.3.1. Linear polymers.....	11
1.3.2. Complex polymer topologies .....	13
1.4. Dendronized polymers.....	19
1.4.1. General features .....	19
1.4.2. Synthesis of DPs .....	21
1.4.3. Applications of DPs .....	25
1.5. $g_{\max}$ of dendritic molecules .....	26
1.5.1. Definitions and implications .....	26
1.5.2. $g_{\max}$ of some dendritic structures .....	29
1.6. The $\text{PG}g_n^{\text{NHBoc}}$ DP series .....	34
1.6.1. Structure, synthesis & nomenclature .....	34
1.6.2. Synthesis of $g > 5$ DPs .....	38
1.6.3. Properties of $\text{PG}g_n^{\text{NHBoc}}$ .....	40
1.6.4. Prior investigations and modifications .....	44
1.7. Scope and Objectives .....	46
2. Overcoming Main-Chain Scission.....	47
2.1. Motivation/goals.....	47
2.2. Protecting group strategies.....	49
2.3. Failed attempts .....	51
2.3.1. Boc.....	51
2.3.2. Fmoc* .....	52
2.3.3. Cbz.....	54
2.4. Implementation of an NHAloc-based strategy for route <b>C</b> .....	55
2.4.1. Rationale & selection of conditions .....	55
2.4.2. Syntheses of $\text{DG1}^{\text{NHAloc}}$ and $\text{PG5}_{500}^{\text{NHAloc}}$ .....	57

2.4.3.	Model reactions .....	58
2.4.4.	Optimization of the “ $g + 1$ ” synthesis of $\text{PG6}_{500}^{\text{NHBoc}}$ from $\text{PG5}_{500}^{\text{NHAlloc}}$ .....	60
2.4.5.	Particularities of $\text{C-PG6}_{500}^{\text{NHBoc}}$ analytics .....	63
2.5.	Syntheses of $\text{C-PG7}_{500}^{\text{NHBoc}}$ and $\text{C-PG8}_{500}^{\text{NHBoc}}$ .....	65
2.6.	Comparison of polymers of $g = 5 - 8$ .....	67
2.6.1.	Gel permeation chromatography .....	67
2.6.2.	Atomic force microscopy .....	69
2.6.3.	Sanger labelling .....	74
2.7.	Discussion of $g_{\text{max}}$ and structural perfection: $\alpha$ and a pragmatic view of “dense” packing ..	77
2.8.	Summary and conclusions .....	82
3.	Investigations Concerning DP Main-Chain Scission .....	84
3.1.	Introduction .....	84
3.2.	General remarks on polymer chain degradation .....	85
3.3.	Prior evidence for charge-induced main-chain scission .....	87
3.3.1.	Summary of previous findings .....	87
3.3.2.	The hypothesis of charge-induced main-chain scission.....	90
3.4.	Additional investigations concerning main-chain scission in charged DPs.....	92
3.4.1.	Deprotection of $\text{PG5}_{500}^{\text{NHAlloc}}$ in absence of base .....	92
3.4.2.	Treatment of $\text{PG5}_{500}^{\text{NH}_2}$ with acid .....	93
3.4.3.	Deprotection of mixed-substitution $g = 5$ DPs in absence of base .....	95
3.4.4.	Scission in a polyanionic DP of $g = 5$ .....	99
3.4.5.	Scission in $g > 5$ DPs .....	102
3.4.6.	Summary .....	103
3.5.	Main-chain scission in solutions of uncharged DPs .....	104
3.5.1.	Initial observations.....	104
3.5.2.	Influence of solvent.....	106
3.5.3.	Influence of temperature.....	108
3.5.4.	Influence of shear .....	111
3.5.5.	Influence of dendritic generation $g$ .....	112
3.5.6.	Influence of structural perfection .....	115
3.5.7.	Influence of peripheral substitution .....	116
3.5.8.	Characterization of low molecular mass scission products .....	120
3.5.9.	Mechanistic insights from EPR spectroscopy.....	124
3.5.10.	Insights from MD simulations .....	128

3.5.11	Summary of findings .....	133
3.6	Unified hypothesis: swelling-induced main-chain scission.....	135
3.7	Conclusions & outlook .....	138
4.	Cryo-TEM of DPs and analysis of native chain conformations .....	140
4.1.	Motivation/Goals .....	140
4.2.	Previous Investigations of polymers by cryo-TEM.....	142
4.2.1.	Cryo-TEM essentials.....	142
4.2.2.	3D structures of biological filaments .....	143
4.2.3.	Cryo-EM of synthetic polymers.....	144
4.3.	Cryo-TEM of Dendronized polymers.....	145
4.3.1.	Cryo-TEM Stereography of <b>B-PG</b> <sub>500</sub> <sup>NHBoc</sup> .....	145
4.3.2.	Cryo-TEM Tomography of <b>C-PG</b> <sub>500</sub> <sup>NHBoc</sup> .....	147
4.3.3.	Overview of trajectory data.....	148
4.4.	Analysis of DP Trajectories.....	150
4.4.1.	Scattering vs. trajectory analysis.....	150
4.4.2.	Analysis of DP chain trajectories.....	151
4.5.	Summary & Conclusions .....	154
5.	Density of $PG_n^{NHBoc}$ .....	156
5.1.	Motivation/goals.....	156
5.2.	Bulk density from hydrostatic methods.....	157
5.3.	Quantitative scanning transmission electron microscopy.....	159
5.4.	Scanning and transmission electron microscopy.....	163
5.5.	Small-angle X-ray scattering .....	166
5.6.	Discussion.....	169
6.	Fluorescent Labelling of $PG_n^{NHBoc}$ for Rheological Studies .....	172
6.1.	Motivation/goals.....	172
6.2.	Selection of polymer, labelling strategy and fluorophore .....	174
6.3.	Fluorescent labelling of DPs.....	177
6.3.1.	Alexa Fluor 488 .....	177
6.3.2.	TAMRA & carboxyrhodamine B .....	178
6.3.3.	Sulforhodamine B.....	179
6.3.4.	Rhodamine B isothiocyanate .....	180

6.4.	Fluorescence microscopy.....	182
6.5.	Towards better control over labelling density.....	184
6.6.	Summary & outlook.....	186
7.	Conclusions & Outlook.....	187
8.	Experimental.....	190
8.1.	General materials & methods.....	190
8.1.1.	Syntheses.....	190
8.1.2.	Analytics.....	191
8.2.	Experimental details for chapter 2: Overcoming main-chain scission.....	193
8.2.1.	Syntheses.....	193
8.2.2.	Other experiments.....	207
8.3.	Experimental details for chapter 3: Investigations concerning DP main-chain scission.....	221
8.3.1.	Syntheses.....	221
8.3.2.	Other experiments.....	229
8.4.	Experimental details for chapter 4: Cryo-TEM of DPs and analysis of native chain conformations.....	238
8.4.1.	Cryo-TEM & image processing.....	238
8.4.2.	Supplementary information on trajectory analysis.....	244
8.5.	Experimental details for chapter 5: Density of $PG_n^{\text{NHBoc}}$ .....	245
8.5.1.	Determination of bulk density by classical methods.....	245
8.5.2.	Determination of density by qSTEM.....	249
8.5.3.	Determination of single-molecule density by SEM/TEM.....	252
8.5.4.	Determination of density by SAXS of bulk samples.....	253
8.6.	Experimental details for chapter 6: Fluorescent labelling of DPs for rheological studies..	259
8.6.1.	Syntheses.....	259
8.6.2.	Other experiments.....	264
A.	Appendix.....	265
A.1.	Example of a $g_{\text{max}}$ calculation.....	265
A.2.	How “soft” a parameter is $g_{\text{max}}$ ?.....	268
A.3.	Supplementary GPC curves.....	271
A.4.	Representations of DP trajectories from cryo-TEM.....	274

A.5. MALDI-TOF mass spectra of DP scission products.....	280
A.6. NMR spectra .....	289
Abbreviations.....	323
Curriculum Vitae .....	327
Bibliography .....	329

# 1. Introduction

## 1.1. A brief history of polymers: From obscurity to commodity

Polymers are ubiquitous in nature. To name just a few examples (Figure 1-1): Genetic information is stored in DNA and transmitted by RNA, the polymers of nucleotides. Diverse functions (enzymatic, signaling, structural *etc.*) are fulfilled by polypeptides, the polymers of amino acids. Carbohydrate polymers are used in structure formation and energy storage, tasks fulfilled *e.g.* by cellulose and starch, respectively. The latter two are both polymers of the same monomer (glucose) linked together in different fashions. Polymers which are inherently hydrophobic (*e.g.* natural rubber) or heavily cross-linked (cured plant resins) serve as barriers and for wound closure in the originating plants. Humans have utilized such naturally occurring polymers for centuries untold: Cellulosic materials and their composites alone have found applications ranging from construction materials (wood), clothing and other textiles (cotton, linen, hemp *etc.*) to substrates for writing (papyrus, paper). However, the chemical manipulation and the preparation of entirely synthetic polymers are much more recent.

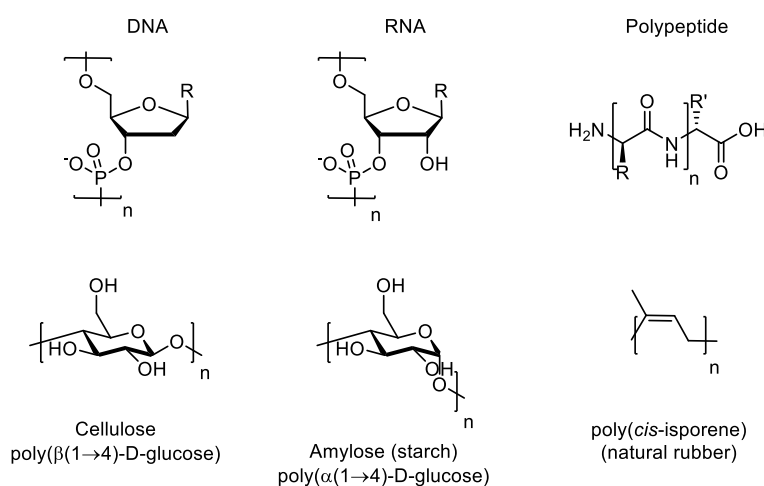


Figure 1-1: Chemical structures of some biopolymers.

The first steps toward polymer science were mid-19<sup>th</sup> century attempts to generate soluble and processable forms of cellulose (see Figure 1-2). A first step in this direction was nitrocellulose, the product of the nitration of cellulose, producing a first (semisynthetic) polymer soluble in organic solvents.<sup>2</sup> Nitrocellulose found use as an explosive in mining, as a propellant in military applications, and as a film base for photography and – eventually – cinematography. Nitrocellulose has been largely superseded as an explosive and also as a plastic (*e.g.* by cellulose acetate<sup>3,4</sup> a far less flammable film base), but still finds application in coatings, *e.g.* as nail polish. Simultaneous with the rise of semisynthetic polymers which provided entirely new properties – particularly thermoplasticity and the possibility of solution processing – the use of naturally derived polymers expanded. Natural rubber was of particular importance, especially after the development of the vulcanization process which cross-links the polyisoprene chains, thereby turning the initial soft, sticky thermoplast into a thermoset polymer with adjustable physical properties.

The age of fully synthetic polymers began before the chain-like structure of this class of materials was understood: In 1907, the thermoset Bakelite (a heavily cross-linked phenol-formaldehyde resin) was first prepared in a controlled manner by Baekeland.<sup>5</sup> Bakelite found applications in electrical insulation, as well as for the manufacture of household goods and of decorative items.

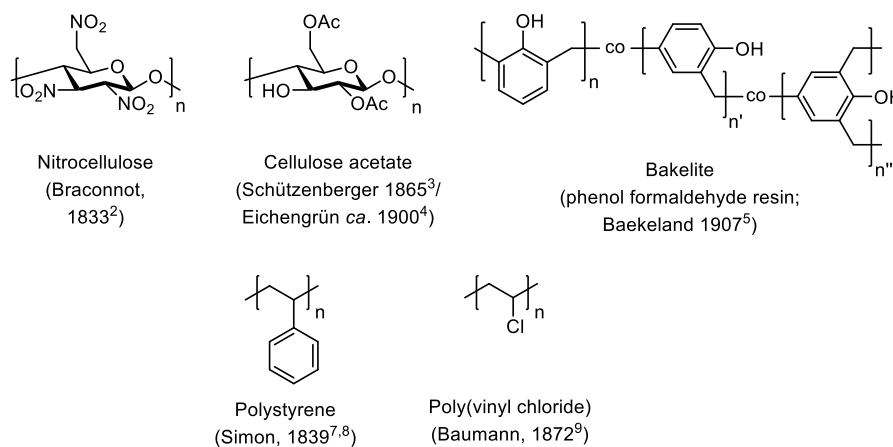


Figure 1-2: Chemical structures of some early (semi)synthetic polymers.

In spite of the increasing industrial use of thermoset resins and the continued development of celluloid materials such as cellophane (regenerated cellulose),<sup>6</sup> the macromolecular nature of such compounds was only poorly understood. To at least some degree this appears to have prevented the use of synthetic polymeric materials: Polystyrene by way of example was likely prepared accidentally as early as 1839 (“metastyrene”<sup>7,8</sup>), and likewise poly(vinyl chloride) was first prepared during the 19<sup>th</sup> century,<sup>9</sup> but the polymeric nature of these substances was realized only in the early 20<sup>th</sup> century realized, and nigh a hundred years would pass before *e.g.* the commercial-scale synthesis of polystyrene began in 1931.<sup>10</sup>

The realization that polymeric materials do indeed consist of chain-like molecules which can have very high molar masses is in large parts owed to Hermann Staudinger,<sup>11,12</sup> who was honored with the Nobel Prize in Chemistry for his work on macromolecular chemistry in 1953.<sup>13</sup> Staudinger’s ideas that polymers comprise a very large number of covalently connected, similar or identical subunits was initially met with skepticism in the chemical and crystallographic communities: Hypotheses of “partial valences” of olefinic monomers were somewhat entrenched,<sup>14</sup> and there was doubt whether molecular species exceeding molar masses of a few kDa could exist at all.<sup>15</sup> Staudinger’s endeavors in polymer modification<sup>16</sup> provided first pieces of evidence for the true macromolecular nature of such substances. These investigations were substantiated by the use of novel, continuously improving techniques such as viscosimetry, membrane osmometry and light scattering, as well as by Staudinger’s work on polymer synthesis.

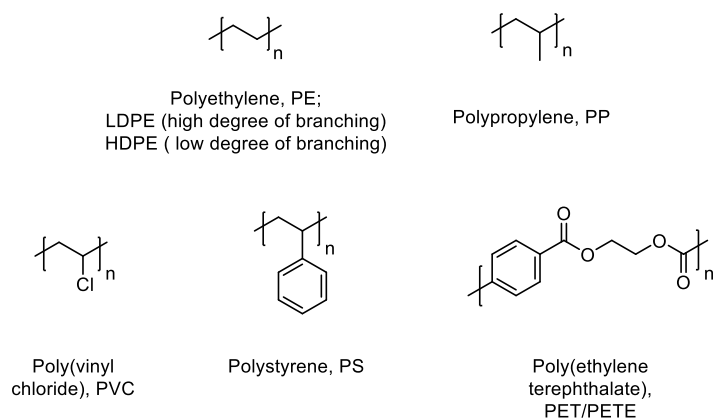


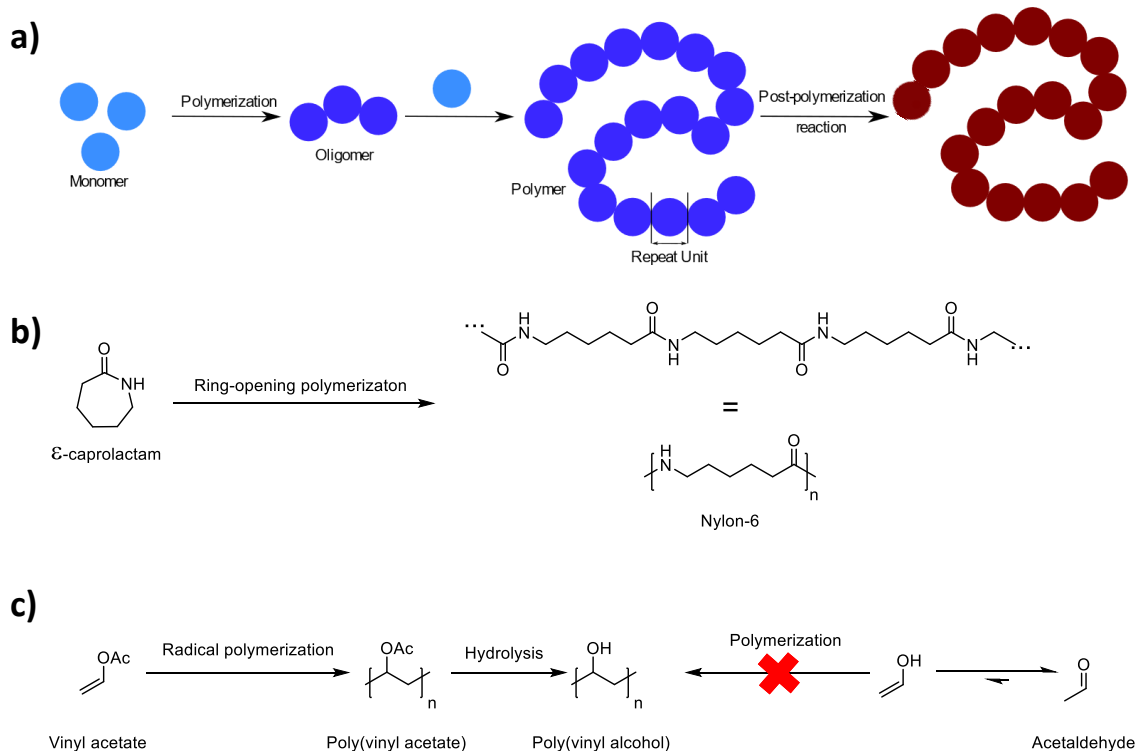
Figure 1-3: Chemical structures of the “Big Six” plastics.

The understanding of the structure and chemistry of polymers, a growing demand for novel, light-weight materials, and the increasing supply of petrochemical precursors paved the way for the industrial-scale synthesis of polymers. Today, the polymer market ( $> 300 \text{ Mt a}^{-1}$ ) is dominated in volume by the “Big Six” plastics (LDPE, HDPE, PP, PVC, PS, PET; see Figure 1-3), each of which is synthesized in quantities  $> 20 \text{ Mt a}^{-1}$ .<sup>17</sup> While simple free-radical polymerization is still frequently used, *e.g.* in the synthesis of polystyrene, other polymerization techniques have been developed and have gained importance. Particularly, condensation polymerization and coordination polymerization are of great commercial utility, and further developments in the field of “precision” polymerization reactions continue to provide access to ever more elaborate polymers, tailored to smaller-scale, but higher-value applications.



## 1.2. Polymers – terminology & structure

The word “*polymer*” was coined by Jöns Jacob Berzelius, from the ancient Greek “πολύ” (*polý*, “many”) and “μέρος” (*méros*, “parts”).<sup>18</sup> Differing significantly from Berzelius’ original usage in 1833, the term modernly refers to a substance composed of “[...] molecule[s] of high relative molecular mass, the structure of which essentially comprises the multiple repetition of units derived, actually or conceptually, from molecules of low relative molecular mass.”<sup>19</sup> The molecules of low relative molecular mass serving as actual or conceptual precursors are accordingly called *monomers*. As such, monomers are chemically different from the corresponding elements in the polymer. These elements within the polymer structure are called *constitutional repeating units*,<sup>19</sup> more commonly referred to as *repeat(ing) units* (RUs).



*Scheme 1-1: a) Schematic representation of a polymerization reaction and the species involved; b) concrete example of the polymerization of  $\epsilon$ -caprolactam to polycaprolactam (Nylon-6). Note that a polymer structure is often represented simply by its RU, particularly when end groups are of little relevance. The subscript  $n$  near the square brackets conventionally corresponds to  $P_n$  (Eq. 1-1). c) Example of a post-polymerization modification reaction, the synthesis of poly(vinyl alcohol) (PVA) from poly(vinyl acetate). PVA cannot be obtained directly from vinyl alcohol, which is tautomericly instable with respect to acetaldehyde.*

Typically, a polymer takes the shape of a long linear chain of RUs. In most economically and scientifically relevant cases, the polymer can be assembled from its monomers in a *polymerization* reaction (Scheme 1-1a). For linear chains, monomers are typically bifunctional molecules, *i.e.* they contain two functional groups or functional groups which offer two reactive centers. The latter is *e.g.* the case in olefins, but also in cyclic monomers which are polymerized by ring-opening polymerization, as is the case with the polyamide shown in Scheme 1-1b. In cases where a polymerization reaction cannot produce the desired polymer, for instance because the monomer directly corresponding to the desired RU is not stable, one may instead have to rely on *post-polymerization modification* (historically

called “polymer analogous reactions”). This involves the chemical transformation of a suitable polymeric precursor to the desired polymer. A prominent example for this is the preparation of poly(vinyl alcohol) from poly(vinyl acetate) (Scheme 1-1c).

A polymer is distinguished from an *oligomer* (from ancient Greek ὀλίγοι, oligoi, “a few”) by its “high relative molecular mass” such that the addition or removal of a single RU does not significantly alter the properties of the macromolecule.<sup>a</sup> The number of RUs in a polymer or oligomer is the *degree of polymerization*, usually given as the number-average degree of polymerization  $P_n$ , which is defined by (Eq. 1-1), where the number-average molar mass  $\overline{M}_n$  is given by Eq. 1-2 and  $M_{RU}$  is the molar mass of a repeating unit.

$$P_n = \frac{\overline{M}_n}{M_{RU}}$$

Eq. 1-1

$$\overline{M}_n = \frac{\sum_i M_i N_i}{\sum_i N_i}$$

Eq. 1-2

$$\overline{M}_w = \frac{\sum_i M_i N_i^2}{\sum_i M_i N_i}$$

Eq. 1-3

It is a characteristic of most polymers, with a few prominent exceptions such as RNA, DNA or polypeptides, that molar masses are not exact but statistically distributed: Typically, polymeric samples contain polymers of varying chain length and therefore varying molar mass.  $\overline{M}_n$  (Eq. 1-2) is the first moment of this distribution, containing  $N_i$  particles of molar mass  $M_i$ . A measure for the breadth of this distribution is the *dispersity*  $\mathfrak{D}$  (Eq. 1-4), defined as the ratio between  $\overline{M}_n$  and the weight-average molar mass  $\overline{M}_w$  (Eq. 1-3, the second moment of the molar mass distribution). For an ideally monodisperse sample with  $\overline{M}_n = \overline{M}_w$ ,  $\mathfrak{D} = 1$ .

$$\mathfrak{D} = \frac{\overline{M}_w}{\overline{M}_n}$$

Eq. 1-4

---

<sup>a</sup> The above statement is largely true for synthetic polymers, with the significant exception of end groups, where alterations may significantly impact the utility of the polymer. The removal of single repeat units in information-carrying biopolymers such as RNA or polypeptides however can have deleterious effects on their function, although bulk physical and chemical properties are largely unaffected.

### 1.3. Macromolecular structures

This section will provide a selection of the wide diversity of polymer structures – both linear and more complex. Particularly methods of controlled and living polymerization such as living anionic polymerization,<sup>20,21</sup> ring-opening metathesis polymerization (ROMP),<sup>22,23</sup> atom transfer radical polymerization (ATRP)<sup>24,25</sup> or radical addition/fragmentation transfer (RAFT) polymerization<sup>26</sup> have allowed polymer chemists to become truly creative: The design of intricate structures and the tailoring of polymer properties to very specific applications have become possible.

#### 1.3.1. Linear polymers

Even the structures of at first glance simple homopolymers can be quite diverse, impacting macroscopic properties. A prominent example of this is polypropylene (PP) – a commodity thermoplastic the properties of which depend significantly on the stereoregularity (more commonly: *tacticity*), of the repeat units (see Figure 1-4). Atactic PP does not solidify at room temperature and is comparatively well soluble, whereas highly isotactic PP is microcrystalline, with a melting point of 165 °C. The case of PP simultaneously provides the prime example of fine control over tacticity, as demonstrated prominently and impressively by the Brintzinger-type (ansa)metallocene catalysts.<sup>27</sup> These catalysts permit the controlled synthesis of different PP tacticities, including syndiotactic PP.

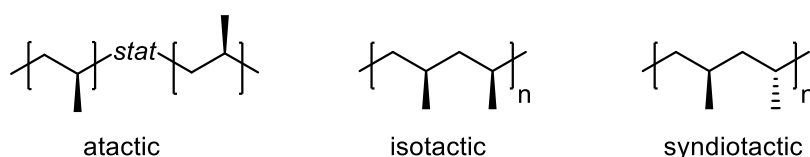


Figure 1-4: Structures of atactic, isotactic and syndiotactic PP.

A great variability of structures and properties in linear polymers can be achieved by using more than just one monomer: Using only two monomers, a significant diversity of structures is imaginable, as illustrated in Figure 1-5, which shows only the most basic variations.

Simple free-radical polymerization (FRP; to this day the most commonly employed polymerization method) only permits limited sequence control, depending on the reactivity ratios of monomers. Monomers of strongly differing reactivities tend to form mixtures of homopolymers rather than copolymers in FRP, but in the case of similar reactivities the synthesis of copolymers is possible. This usually affords random copolymers. Controlled and living polymerization reactions open up a greater diversity of linear polymer structures. For instance, the complete and rapid initiation in controlled polymerization processes permits the synthesis of gradient copolymers,<sup>28</sup> consuming first the more activated monomer before gradually adding the less activated one – similar reactions are difficult to achieve *e.g.* with FRP, as initiation usually occurs throughout the course of polymerization. Living polymerization techniques offer further possibilities, namely the synthesis of well-defined block copolymers using living anionic polymerization.<sup>29</sup> The same is true for controlled, living radical polymerization techniques (*e.g.* ATRP and RAFT) or ROMP. Block copolymers offer interesting properties: As many polymers are immiscible, phase segregation occurs on a nanoscopic scale for block copolymers. Very regular structures are accessible in this manner, the precise geometry being

determined by interfacial parameters and the relative chain lengths of the blocks.<sup>30,31</sup> Block copolymers can also self-assemble in solution, impressively demonstrated by Manners' block copolymers of ferrocenyldimethylsilane, in which the formation of a large diversity of micellar assemblies is driven by the crystallization of one block.<sup>32-34</sup>

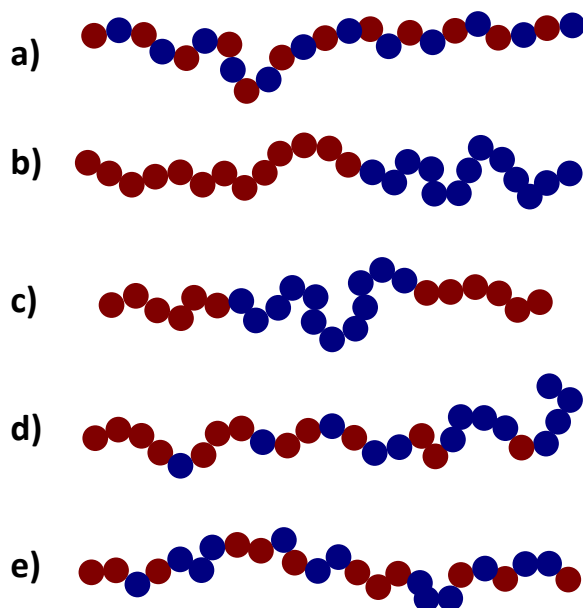


Figure 1-5: Schematic representations of 1:1 copolymers of two different monomers A and B, represented by red and blue circles. a) Alternating copolymer; b) A-B diblock copolymer; c) A-B-A triblock-copolymer; d) gradient copolymer; e) random copolymer.

The copolymerization of more than two monomers further increases the space of possible sequences, allowing in particular the synthesis of tri- and multiblock copolymers. A logical continuation of this is the synthesis of sequence-controlled polymers, *i.e.* absolute synthetic control over monomer sequence, similar to what is achieved by ribosomal peptide synthesis. Quite naturally, this is hoped to provide tight control over the properties of synthetic polymers. While this lofty goal is certainly being pursued,<sup>35</sup> most approaches thus far employ either sequential chemistry, *e.g.* by generation of many short blocks by ATRP,<sup>36</sup> or they employ pre-encoded sequences which then repeat in the resulting polymers, *e.g.* by ring-opening polymerization of macrocyclic monomers.<sup>37,38</sup>

### 1.3.2. Complex polymer topologies

A factor of great influence on polymer properties is topology: The possibility of branching further expands the playing field of the synthetic polymer chemist (Figure 1-6). The following represents only a selection of some of the most commonly investigated topologies, but naturally it is possible to extend this range significantly *e.g.* by substituting homopolymers for copolymers in Figure 1-6. In the following, the most salient features of the structure types depicted in Figure 1-6a-g will be discussed briefly. Dendronized polymers (Figure 1-6h) will be treated separately and in more detail in section 1.4.

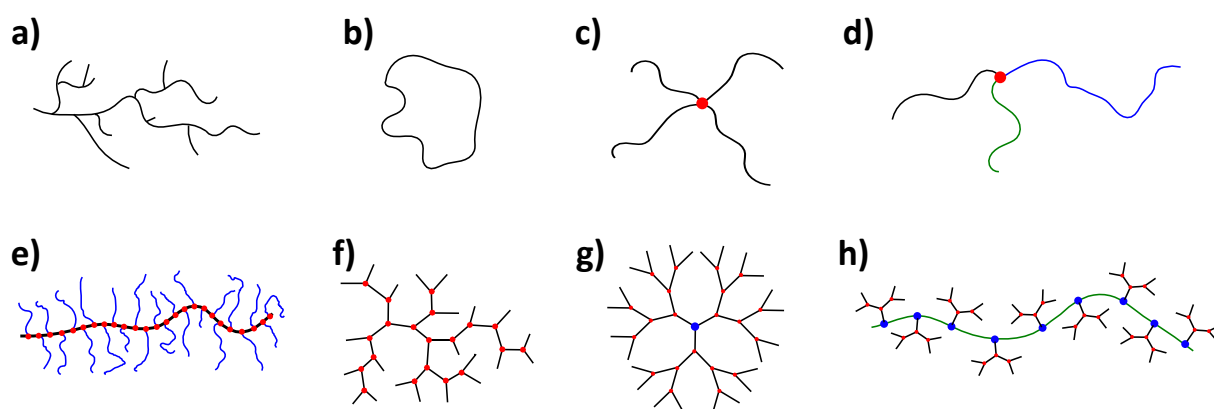


Figure 1-6: Schematic representations of some polymer topologies: a) Irregularly branched polymer; b) cyclic polymer; c) star polymer; d) miktoarm star (co)polymer; e) bottle-brush copolymer; f) hyperbranched polymer; g) dendrimer; h) dendronized polymer (see section 1.4). Dots mark well-defined branching or connection points, different colors indicate possibly, but not necessarily distinct chemical structures.

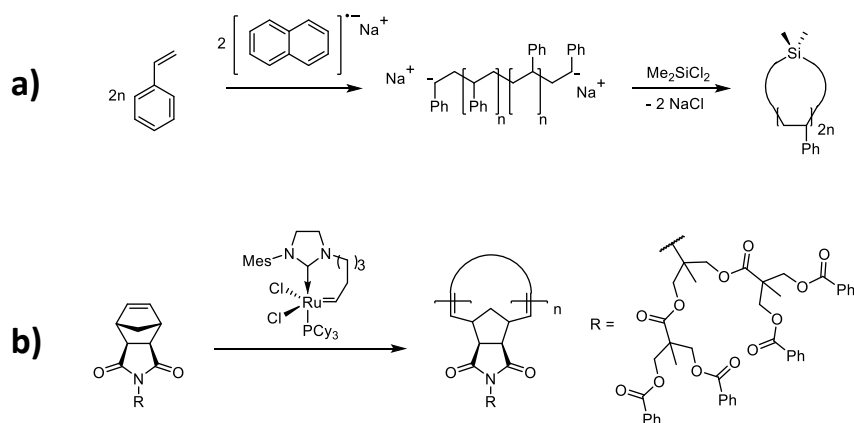
#### Irregularly Branched Polymers

Branching can greatly influence the properties of polymers. Polyethylene is certainly the prime example of this: The degree of branching affects polymer properties to such an extent that the polyethylene market is commonly coarsely subdivided into usually highly branched low-density polyethylene (LDPE) and largely branch-free high-density polyethylene (HDPE).<sup>17</sup> The former is prepared by high-pressure FRP, whereas the latter is synthesized by coordination polymerization, using Ziegler-Natta catalysts<sup>39-41</sup> or the homogenous, single-site Kaminsky<sup>42</sup>, Brintzinger<sup>27</sup> and post-metallocene catalysts.<sup>43</sup> Aside from the differing densities of these constitutionally identical polymers, properties relevant to processing and applications are markedly different: Unbranched polyethylene can form crystalline nanostructures, *e.g.* folded chain lamellae or shish-kebab structures,<sup>44</sup> and possesses high tensile strength. Branched LDPE meanwhile cannot pack into large crystalline domains and is therefore more ductile, possesses better flow properties<sup>45</sup> and is suitable *e.g.* for film applications.

#### Cyclic Polymers

Ring-shaped polymers may be synthesized either by ring closure of end-functional polymers (*e.g.* by ring-closing metathesis or using suitable reagents; see *e.g.* Scheme 1-2a for the ring-closure of a telechelic polymer),<sup>46,47</sup> or by ring-expansion polymerization (Scheme 1-2b).<sup>48-50</sup> The properties of cyclic polymers have long been expected to be distinct from those of their linear analogs – particularly

due to the absence of end groups, which affects both physical and chemical properties (*e.g.* diffusion rates, crystallization behavior *etc.*).<sup>51,52</sup> One phenomenon expected for cyclic polymers is the formation of “topological glasses” *above* the glass transition temperature of the parent linear polymer by the threading of rings throughout the melt or concentrated solution.<sup>53</sup> The precise rheological properties of ring polymers have however proven quite elusive, in large part owing to the difficulty of removing linear impurities, an obstacle which has been overcome only recently.<sup>54,55</sup>



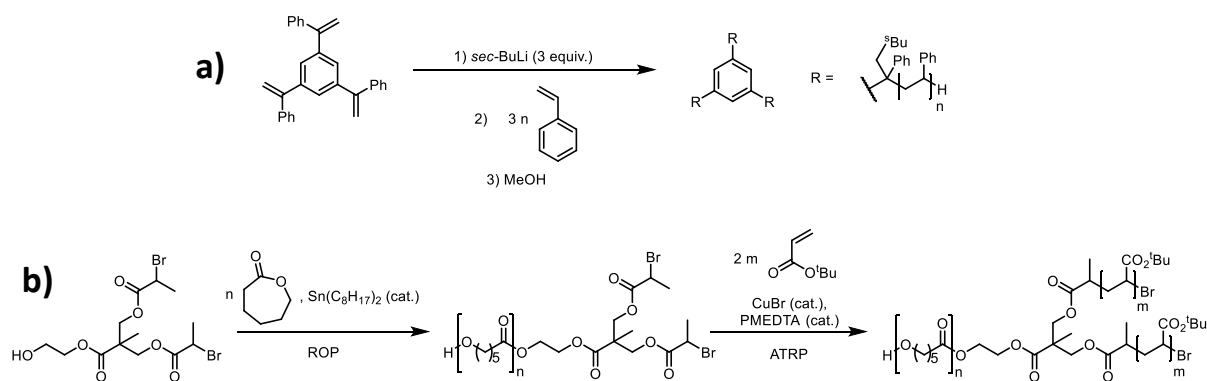
Scheme 1-2: Examples of the synthesis of cyclic polymers by a) ring closure of a telechelic polystyrene<sup>56</sup> and b) ring expansion metathesis polymerization of a dendronized norbornene derivative.<sup>49</sup>

### Star Polymers and Miktoarm Star (Co)polymers

A three-arm star polymer represents the simplest branched polymer topology. Star-shaped polymers have therefore inspired polymer chemists as early as 1948<sup>57</sup> as a means to introduce branching in a conscious and controlled manner, rather than relying on the then available, mostly poorly controlled polymerization methodologies. The syntheses of star polymers follow two principal routes: The divergent “core first” approach in which polymerization is initiated by a multifunctional core, and the convergent “arm first” approach in which end-functional polymers are attached to a multifunctional core.<sup>58</sup>

The “core first” approach demands very high initiation efficiency and few side reactions (*e.g.* radical recombination)<sup>59</sup> – anionic polymerization is particularly useful in this context<sup>29</sup> (see *e.g.* Scheme 1-3a). In the “arm first” approach, very efficient coupling chemistry is necessary, since functional end groups are present at relatively low concentrations and since partially functionalized cores may be sterically masked by the already attached chains.

A variation on the theme of star polymers are miktoarm star (co)polymers,<sup>60,61</sup> in which the arms of a star are different, varying in molar mass and/or chemical structure. In the synthesis of miktoarm structures, arm-first and core-first approaches are often mixed (see *e.g.* Scheme 1-3b), particularly when anionic polymerization and differing monomer reactivities are exploited.<sup>62</sup> Miktoarm star copolymers offer interesting opportunities for self-assembly and for functional applications.<sup>60</sup>

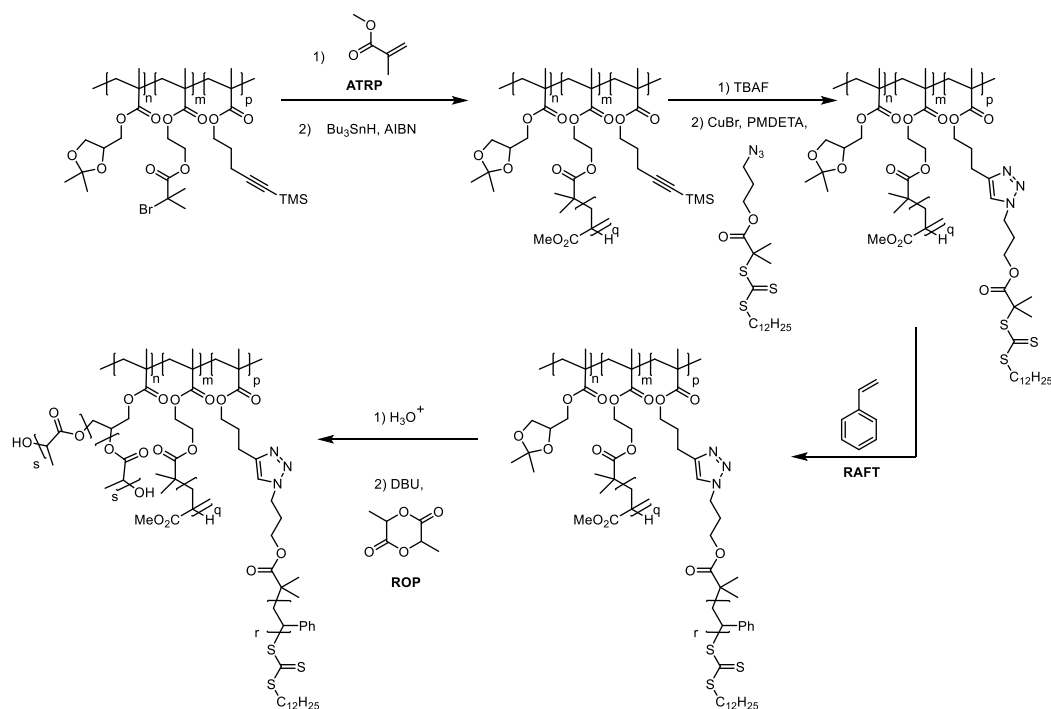


Scheme 1-3: a) Synthesis of a three-arm polystyrene star polymer by anionic polymerization;<sup>63</sup> b) synthesis of a miktoarm star copolymer by using a trifunctional initiator active in ROP of caprolactone and in ATRP of acrylates.<sup>64</sup>

### Bottlebrush Copolymers

In bottlebrush copolymers (also variously called graft copolymers or molecular brushes), a linear polymeric backbone bears linear polymeric side chains, ideally on each repeat unit. The synthesis of bottlebrushes may proceed by three principal routes:<sup>65,66</sup> i) The “grafting-through” or macromonomer approach, in which a polymer with a suitable end group undergoes polymerization; ii) the “grafting-from” approach in which a macroinitiator (a linear polymer bearing initiating side groups) is used from which side chains are grown (see *e.g.* Scheme 1-4); iii) the “grafting-to” approach, in which a side-chain functional linear polymer is coupled with end-functional polymers in order to form the brushwork (for discussions of advantages and disadvantages of the various methods, consult subsection 1.4.2 and the discussions regarding the closely related syntheses of dendronized polymers).

The first bottlebrushes were synthesized using the “grafting through” approach by radical polymerization of  $\alpha$ -olefin macromonomers.<sup>67,68</sup> More functional group tolerant polymerization methods – particularly ATRP and ROMP – have gained popularity in the synthesis of bottlebrushes in recent decades. This has been aided by the rise of click chemistry:<sup>69</sup> High grafting densities in the “grafting-to” approach can only be achieved by using very efficient chemical transformations.<sup>70</sup> When high grafting density is achieved, interesting properties arise, mainly a significant stiffening of the main chain due to the steric demand and the swelling of the polymeric side chains.<sup>71,72</sup>



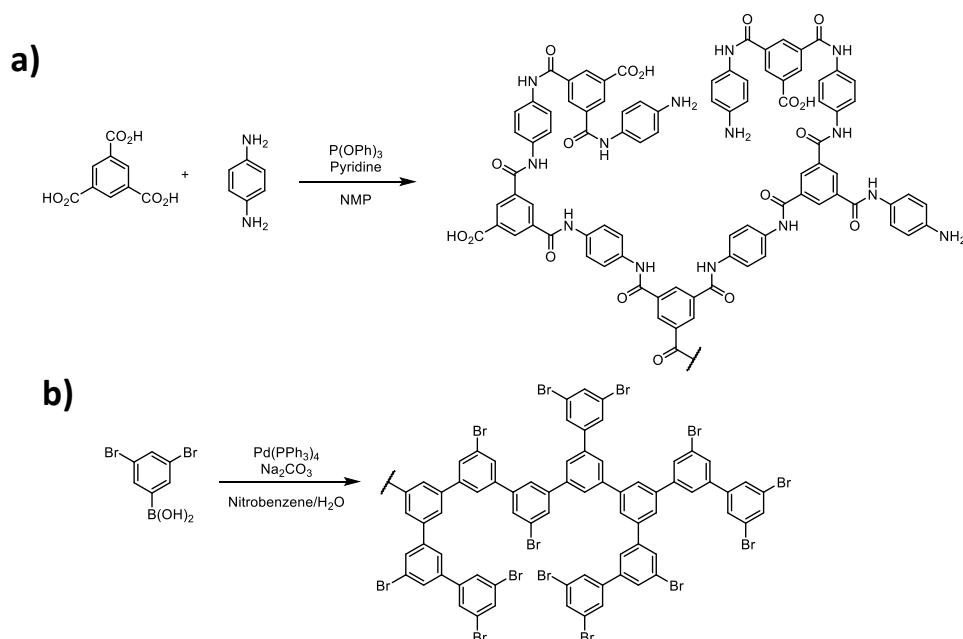
Scheme 1-4: Example of the synthesis of a triblock bottlebrush copolymer illustrating an impressive breadth of methods, employing grafting-from first by ATRP, then by RAFT polymerization after modification by CuAAC ligation, and finally by ROP. The linear precursor triblock copolymer was prepared by RAFT polymerization.<sup>73</sup>

### Hyperbranched Polymers

In hyperbranched polymers,<sup>74,75</sup> branching occurs randomly by the reaction between multifunctional monomers. The degree of branching in such systems is not controlled tightly, and therefore the repeat units within the structure may be dendritic (*i.e.* fully substituted), linear (*i.e.* incompletely substituted), or terminal. The chemistry involved in hyperbranched polymer synthesis is often quite simple. Straightforward condensation reactions are used frequently (see Scheme 1-5a for an example), but a large variety of other reaction types are used in the synthesis of hyperbranched structures. The fact that controlled branching is not required results in a large degree of freedom in the choice of chemistry. This large freedom also applies to the topologies of the monomers, and consequently a wide variety of monomer multiplicities and functionalities may be used (*e.g.* Scheme 1-5a: A<sub>2</sub>/B<sub>3</sub>; Scheme 1-5b: AB<sub>2</sub>).<sup>76,77</sup>

This large diversity provides a lot of tunability, enabling some control over the degree of branching and the density of the resulting hyperbranched polymers. Achieving the desired properties often requires careful tuning of synthetic conditions. Hyperbranched polymers are attractive for certain applications where low polydispersity is not required and where a high number of functional groups is desired. Many multifunctional monomers are available quite cheaply, and the typical polycondensation reactions involved in hyperbranched polymer synthesis are simple to implement.





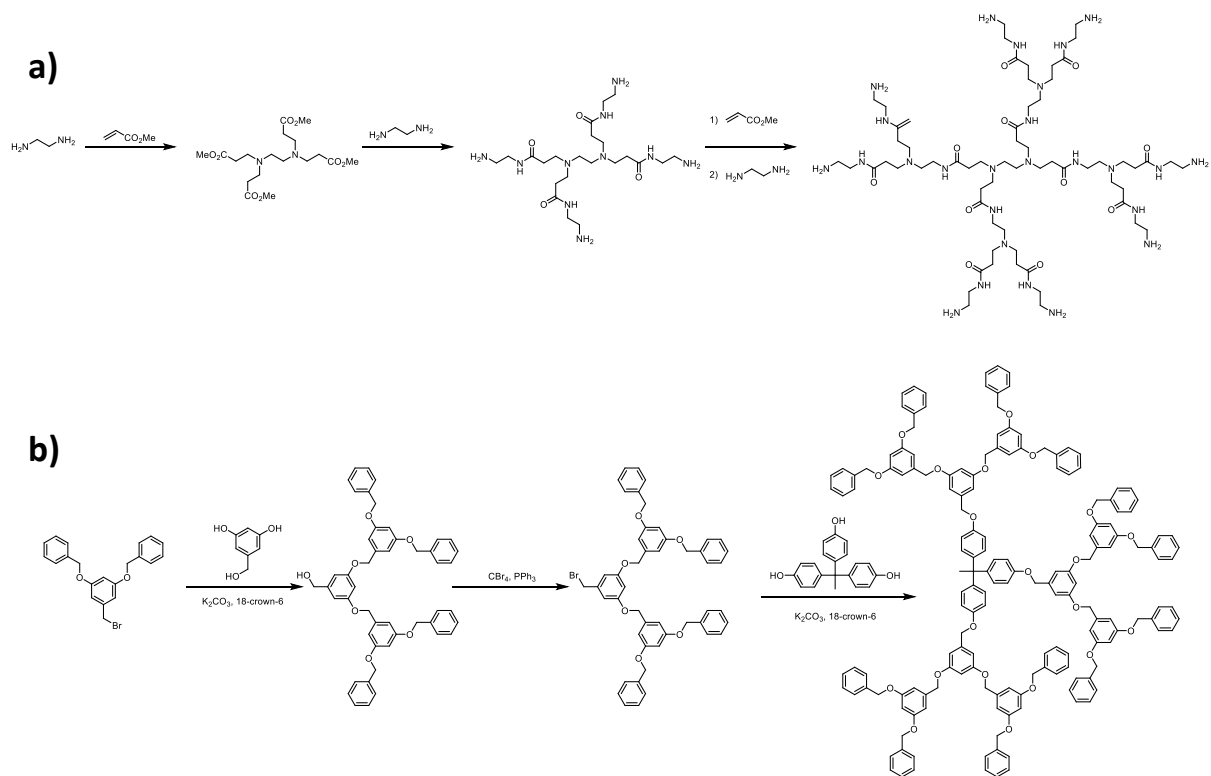
Scheme 1-5: Examples of hyperbranched polymer syntheses. a) Synthesis of a hyperbranched aromatic polyamide from an  $A_2/B_3$ -type monomer system;<sup>78</sup> b) synthesis of a hyperbranched polyphenylene from an  $AB_2$ -type monomer.<sup>79</sup>

### Dendrimers

Dendrimers are macromolecules in which multiple dendrons are attached to a common core. Dendrons are branched units containing exclusively dendritic and terminal repeat units, the latter of which are all at the same remove from the dendron's focal point. By virtue of this highly regular, repeated branching, dendrimers are more well-defined than the other classes of branched polymers presented in this section: In the ideal case – in absence of structural defects – dendrimers are monodisperse.<sup>80</sup>

Similar to star polymers, in which branches also originate from a common core, the synthesis of dendrimers usually proceeds by one of two conceptual routes: The divergent synthesis of the dendrons starting from the multifunctional core (see *e.g.* Scheme 1-6a), or the convergent attachment of complete dendrons to the core *via* their focal points (see *e.g.* Scheme 1-6b).<sup>81</sup> Dendrimers are chemically diverse and accordingly many reaction types have been employed in their syntheses. Parameters used to classify dendrimers independently of chemistry are the multiplicity of the core, the degree of branching per monomer, and the generation number  $g$ . These parameters and other aspects relevant to dendrimers will be discussed in some detail in sections 1.4 and 1.5 in the context of dendronized polymers.

The well-defined structure of dendrons and dendrimers demand good control over the reactivity of functional groups. Therefore, their syntheses rely on functional group transformations, easily removed protecting groups, or the use of multiple components with orthogonal reactivities. If such measures are not taken, hyperbranching may occur, leading to irregularities in the dendritic structure. This is usually to be avoided, as it is the defined nature of dendrimers that makes them interesting in applications *e.g.* as nanocarriers or as catalyst supports.<sup>82</sup>



Scheme 1-6: Examples of dendrimers syntheses. a) Tomalia's poly(amidoamine) (PAMAM) dendrimer ( $g = 2$ ) prepared by a divergent route using ethylenediamine as the core;<sup>83</sup> b) Convergent synthesis of a Fréchet-type polyether dendrimer using a trifunctional phenolic core.<sup>84,85</sup>

## 1.4. Dendronized polymers

### 1.4.1. General features

A dendronized polymer (DP) is a linear polymer which bears dendritic side chains (dendrons) ideally on each repeat unit. As in dendrimers, a dendron is defined as a regularly and repeatedly branched structure, *i.e.* one comprising monomers with a functionality of  $f \geq 3$  arranged such that only terminal and dendritic units are present in the branchwork, and such that all terminal units are removed from a common focal point by the same number of branching points. The number of branching points between the focal point and one peripheral group is called the dendritic generation number – often shortened to “generation” –  $g$  and is a parameter of great importance in any dendritic molecule, as discussed in more detail in section 1.5. Further parameters used to describe the dendritic structure are the functionality  $f$  of the dendritic monomer, resulting in  $(f - 1)$ -fold branching, the number of dendrons attached to the polymer RU *via* their focal points, and the number of *peripheral* groups borne by the outermost, terminal units. Figure 1-7 illustrates this terminology.

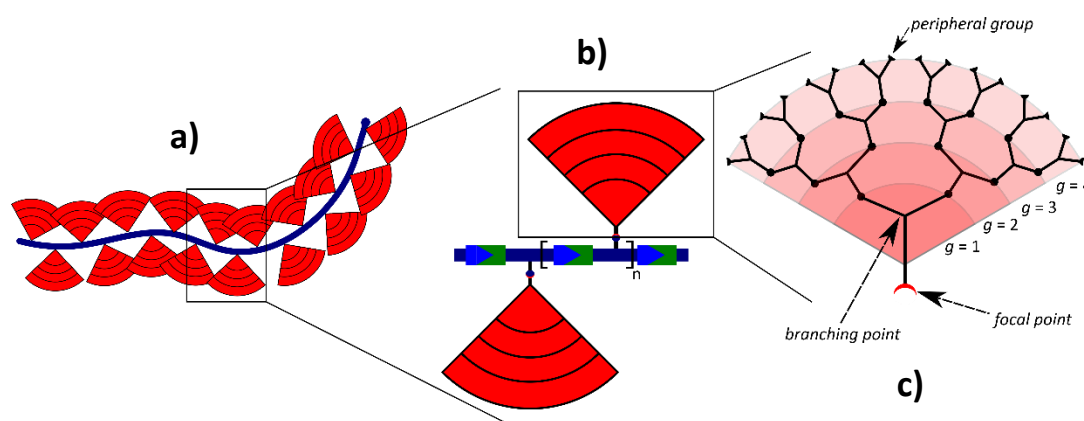


Figure 1-7: Schematic representations of a dendronized polymer at the level of a) the entire polymer, b) the repeat unit and c) the individual dendritic side chain. In this example, one dendron of  $g = 4$ , comprising trifunctional ( $f = 3$ ) dendritic repeat units, is attached to each repeat unit of the linear backbone. This results in 16 peripheral groups per RU.

DPs are a subtype of bottlebrush polymers, featuring a central linear backbone and polymeric – in this case dendritic – side chains, but they differ significantly from standard bottlebrushes with linear polymeric side chains. DPs' dendritic side chains are monodisperse and very compact, thus lending them a well-defined thickness, which can be tuned in discrete steps by varying  $g$  (see Figure 1-8b).<sup>86,87</sup> At high  $g$ , significant molar masses per repeat unit can be achieved (several dozen kDa), however unlike in regular bottlebrush copolymers the mass of the side chain is confined to a very narrow, well-defined volume. Therefore, DPs retain their by first approximation cylindrical shape even when deposited on strongly interacting surfaces, whereas bottlebrushes flatten out and spread upon adhesion (Figure 1-8a).

Additionally, due to their dendritic nature dendronized polymers may offer an unparalleled density of functional groups at high  $g$ , both in their periphery and internally within the branchwork. Due to the regular structure of the dendrons, these potentially reactive sites are very well-defined and make DPs attractive platforms for various applications (see subsection 1.4.3). The basic structural motif of the linear dendronized chain represented in Figure 1-7 can be elaborated on by combination

with other macromolecular structure elements, resulting e.g. in cyclic DPs<sup>49,88</sup> or in dendronized copolymers.<sup>89,90</sup>

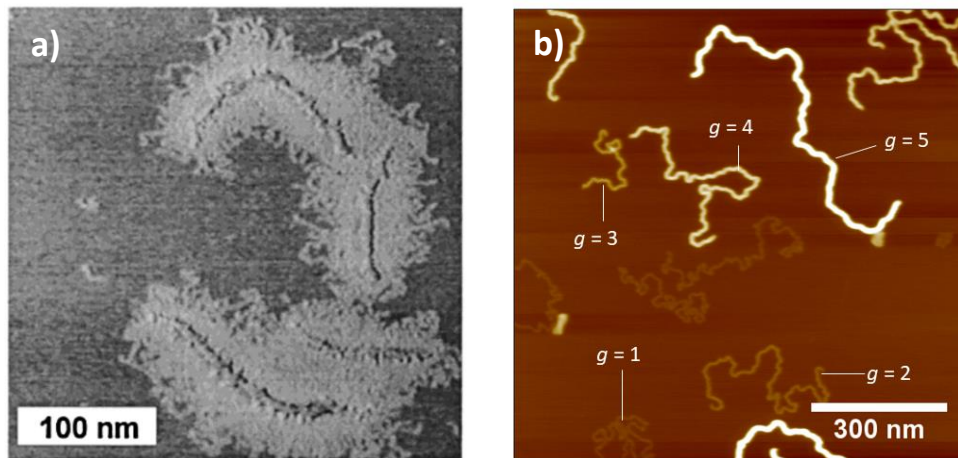


Figure 1-8: a) AFM height image of a bottlebrush copolymer (PMMA/PBA; reproduced with permission from Sheiko S. S. et al. *Macromolecules* **2001**, 34, 8354-8360, copyright 2001 American Chemical Society). b) AFM height image of DPs of  $g = 1 - 5$  (adapted with permission from Zhang, B. et al. *Angew. Chem. Int. Ed.* **2011**, 50, 737-740, copyright 2011 Wiley VCH). On strongly interacting surfaces such as mica, bottlebrushes flatten out significantly, whereas the more compact DPs retain their cylindrical shape.

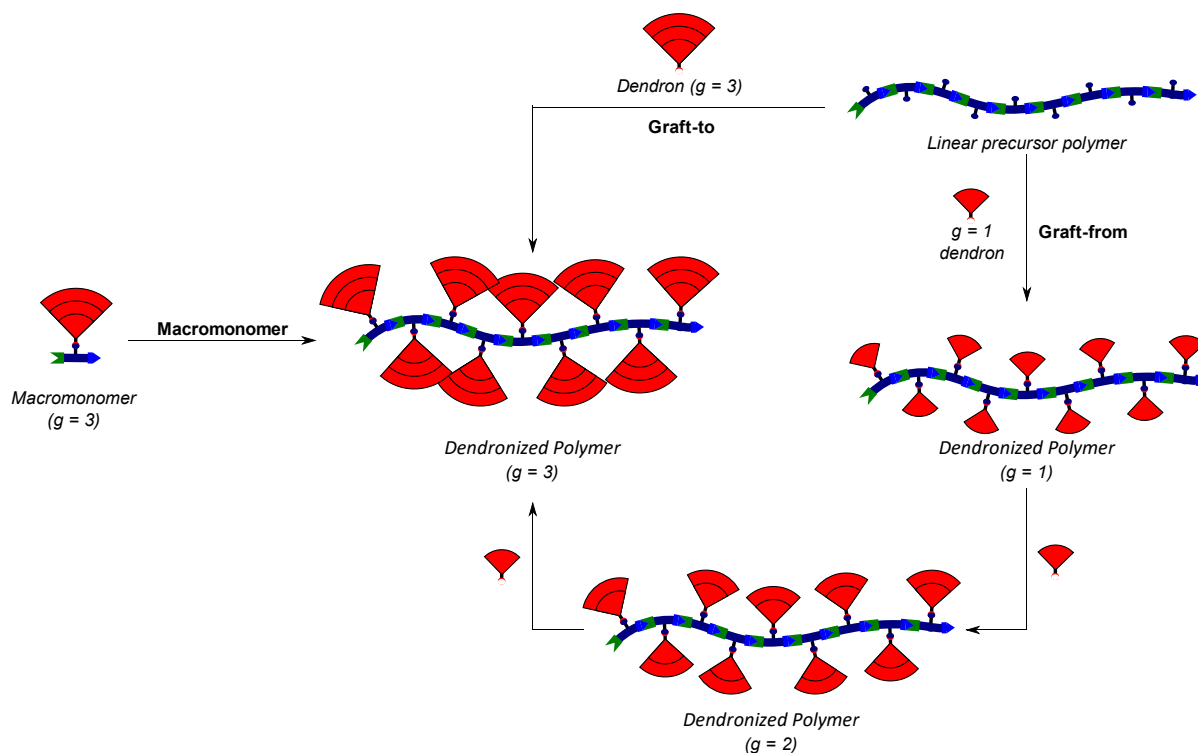
### 1.4.2. Synthesis of DPs

Similar to bottlebrushes (see subsection 1.3.2), three main routes to the synthesis of dendronized polymers exist, which are represented in Scheme 1-7 and will be discussed briefly in the following.<sup>91-93</sup> The advantages and disadvantages of each approach are outlined briefly in Table 1-1 and broadly apply to the largely analogous syntheses of bottlebrush copolymers as well.<sup>94</sup>

Other than is the case with dendrimers, which have been synthesized in some cases to very high  $g$ ,<sup>95-97</sup> syntheses of dendronized polymers are mostly limited to comparatively low generations (usually  $g \leq 4$ ). This is likely a consequence of the significant effort which high  $g$  DP synthesis requires: Convergent approaches (macromonomer polymerization & the graft-to route) require extensive, possibly  $g$ -dependent optimization, and the divergent (graft-from route) is quite time consuming. Some effects of steric congestion are already evident at fairly low  $g$ ,<sup>98,99</sup> and therefore applications-driven researchers likely see no need to proceed to higher spheres of steric congestion. There are only few exceptions to this rule, mostly relying on divergent (graft-from) syntheses: Yoshida *et al.* have prepared polyester-based DPs up to  $g = 5$ ,<sup>100</sup> and work from the Schlüter group (which forms the basis for this thesis) has progressed formally up to  $g = 8$ .<sup>101,102</sup> A notable exception is work by Mynar *et al.* which employed CuAAC “click” ligation to dendronized a dendronized polymer, bringing the resulting heterostructure to (formally)  $g = 6$ .<sup>103</sup>

Table 1-1: Main advantages and disadvantages of the synthetic approaches to DP synthesis.

Method	Advantages	Disadvantages
<b>Macromonomer</b>	<ul style="list-style-type: none"> <li>- Directly affords DP with a full complement of perfect dendrons</li> <li>- Few steps</li> </ul>	<ul style="list-style-type: none"> <li>- Suppression of polymerization at high <math>g</math> (steric demand of dendrons)</li> <li>- Macromonomer synthesis may be tedious for high <math>g</math></li> <li>- Compatibility between polymerization chemistry and dendrons necessary</li> </ul>
<b>Graft-To</b>	<ul style="list-style-type: none"> <li>- Control over DP chain length</li> <li>- Can provide DPs of high <math>P_n</math> and high <math>g</math></li> <li>- Ample combinatorial opportunity</li> </ul>	<ul style="list-style-type: none"> <li>- Requires highly efficient coupling chemistry</li> <li>- Incomplete substitution of linear precursor at high <math>g</math> due to steric demand of already attached dendrons</li> </ul>
<b>Graft-From</b>	<ul style="list-style-type: none"> <li>- Can provide DPs of high <math>P_n</math> and high <math>g</math> with full coverage</li> <li>- Comparatively simple precursors (linear polymers &amp; <math>g = 1</math> dendrons)</li> </ul>	<ul style="list-style-type: none"> <li>- Requires many post-polymerization steps (<math>g</math> by <math>g</math> dendronization)               <ul style="list-style-type: none"> <li>- Long reaction times</li> </ul> </li> <li>- Requires highly efficient chemistry for complete dendronization</li> </ul>



Scheme 1-7: Representation of the principal synthetic routes using the example of a  $g = 3$  DP.

### Macromonomer approach

In the macromonomer approach,<sup>104</sup> DPs are synthesized directly by polymerization of a suitable macromonomer (a molecule bearing a polymerizable unit and at least one dendron of the desired  $g$ ). Diverse polymerization techniques have been employed in the synthesis of DPs by the macromonomer route, including FRP (e.g. **1**),<sup>105</sup> ATRP,<sup>106</sup> RAFT polymerization,<sup>107</sup> ROMP,<sup>49,88,90</sup> Suzuki polycondensation (e.g. **3**),<sup>108,109</sup> and “click” polycycloaddition (e.g. **2**)<sup>110</sup> (Figure 1-9).

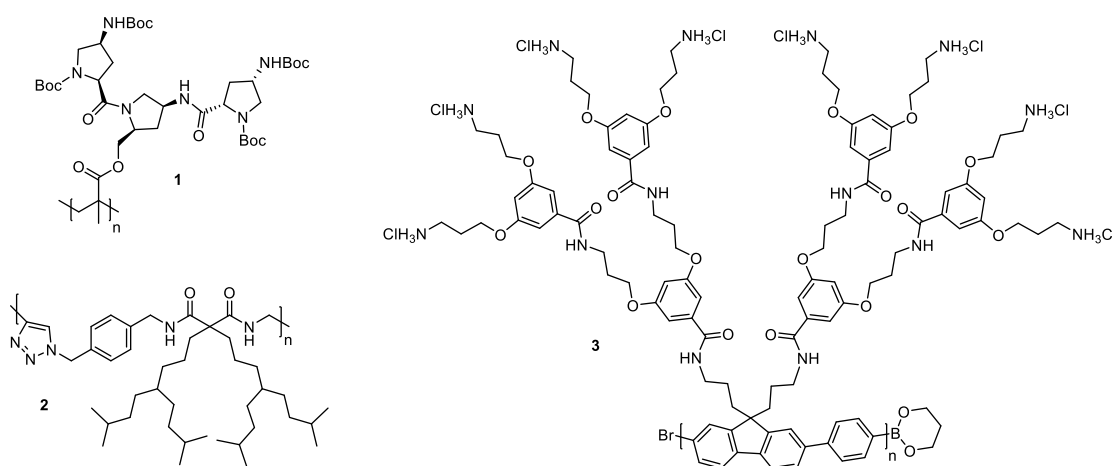


Figure 1-9: Examples of DPs prepared by the macromonomer approach:  $g = 2$  poly(methacrylate) DP bearing proline-based chiral dendrons (**1**), synthesized by FRP;<sup>111</sup>  $g = 2$  aliphatic DP (**2**) synthesized by CuAAC polycycloaddition;<sup>110</sup>  $g = 2$  water-soluble dendronized polyfluorene (**3**) synthesized by Suzuki polycondensation of AA/BB monomers.<sup>108</sup>

The greatest advantage of the macromonomer approach is that it produces polymers which are ideally dendronized: Each repeat unit in the polymer bears the intended number of perfectly formed dendrons, given pure precursor monomers (which may not be trivial to access, particularly for high  $g$  where purification tends to become difficult).

The macromonomer approach is limited particularly for high  $g$ : The dendritic side chains may inhibit polymerization both sterically – by enveloping the polymerizable functional group(s) – and chemically, by providing opportunity for side reactions. Steric inhibition can be moderated by the insertion of spacers, either in the main chain (*i.e.* by generating “long” repeat units, see **2** or **3**, Figure 1-9) or in the side chain, by inserting a tether between the polymerizable unit and the focal point of the dendron.

Studies of the polymerization behavior of different  $g$  macromonomers have indeed shown that the achievable  $P_n$  decreases with  $g$ ,<sup>112</sup> to the extent that very high  $g$  macromonomers may become incapable of polymerizing.<sup>113</sup> Due to this  $g$  dependence of polymerizability, there is a lack of control over molar mass and molar mass distribution particularly for high  $g$ , and it is nigh impossible to prepare homologous series of DPs with similar chain lengths throughout. Furthermore, the possible combinations of dendrons and linear backbones are somewhat limited due to chemical (in)compatibility of polymerization conditions with dendrons: For instance, olefinic dendrons would likely be incompatible with vinyl polymerization, and nucleophilic side chains (*e.g.* amines) would interfere with RAFT polymerization. This may, however, be circumvented by post-polymerization functionalization, installing the desired moieties after formation of a dendritic precursor polymer, or by removing suitable protecting groups.

#### Graft-to approach

In the graft-to route, dendrons of the desired  $g$ , bearing suitable functional groups in their focal points, are attached to a linear polymer bearing reactive partners on each repeat unit (see Figure 1-10).

Advantageously, this approach permits the polymerization of the linear precursor to the desired  $P_n$ , thereby giving better control over the length of the eventual DP, utilizing the toolbox of polymerization chemistry to its fullest. By attachment of suitable dendrons, high  $g$  may be achieved simultaneously. Particularly at high  $g$  however, steric hindrance causes problems: An attached dendron of high  $g$  (with a correspondingly significant steric demand) will inhibit the attachment of further dendrons to neighboring functional groups on the linear polymer.<sup>114</sup> Longer reaction times and large excesses of dendron may improve the degree of substitution, but full conversion may not be possible even under more forcing conditions.

In spite of these limitations, the graft-to route is of particular interest for the modification of biopolymers (*e.g.* **4**)<sup>115–117</sup> and it is potentially useful in the rapid synthesis of DP libraries,<sup>118</sup> as it enables the relatively straightforward combination of dendrons and polymer backbones. Diverse reactions have been employed in the attachment of dendrons to suitable backbones. Naturally, “click” reactions such as Sharpless’ CuAAC<sup>69</sup> are particularly attractive for such coupling reactions (see *e.g.* **5**).<sup>103,119</sup> Ester<sup>120</sup> and amide<sup>121</sup> bond formation reactions are likewise popular.

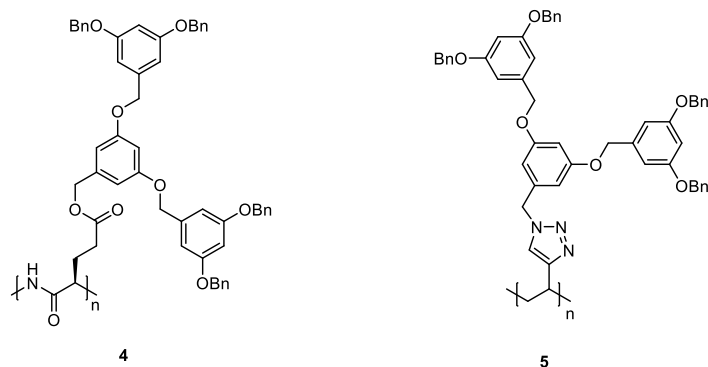


Figure 1-10: Examples of DPs prepared by the graft-to approach: A poly(glutamic acid) backbone to which  $g = 2$  Fréchet-type dendrons were grafted (**4**) by reaction of the carboxylic acid residue with a diazo-functionalized dendron;<sup>115</sup> another example of  $g = 2$  Fréchet-type dendrons, this time attached to a polyethylene-derived backbone using CuAAC, resulting in (**5**).<sup>119</sup>

### Graft-from approach

In the graft-from approach, dendrons are synthesized one  $g$  at a time, starting from a suitable linear polymeric precursor. As with the graft-to approach, this permits good control over the initial polymer chain length, and therefore DPs of both high  $g$  and high  $P_n$  may be synthesized. As the  $g = 1$  dendrons grafted to the initial linear precursor or the DP are comparatively small molecules (usually of the type  $AB'_n$ , such that protected functional groups can be liberated after dendronization), steric congestion preventing complete substitution is not as much of a problem as it is in the graft-to approach.

However, this comes at the cost of having to perform many post-polymerization reactions: Many deprotection and dendronization steps are necessary to prepare high  $g$  DPs by the graft-from route, each step usually including some form of work-up and purification. Simultaneously, the number of reactions per molecule is easily in the thousands or tens of thousands, requiring comparatively long reaction times which increase with  $g$  due to the mounting steric congestion. For even prolonged reaction times to result in complete substitution, the dendronization reaction needs to be both efficient and free from side reactions which might block terminal groups, both of which would lead to imperfect dendritic structures.

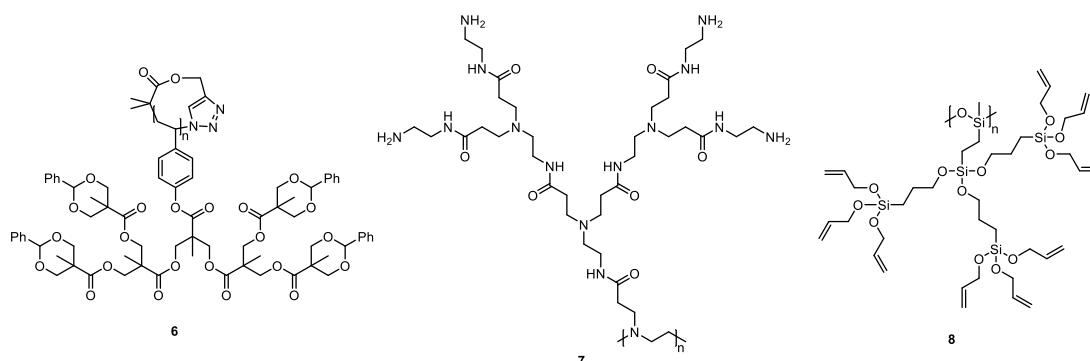


Figure 1-11: Examples of DPs synthesized by the graft-from approach: Cyclic polymer from which a  $g = 3$  polyester dendron was grown (**6**);<sup>88</sup> PAMAM-dendronized poly(ethyleneimine) of  $g = 2$  (**7**);<sup>122</sup> polysiloxane bearing a  $g = 2$  threefold-branching siloxane-based side chain (**8**).<sup>123</sup>



### 1.4.3. Applications of DPs

A key feature of dendronized polymers are their many peripheral groups, which offer a platform for the attachment of various functional molecules and which provide interesting modes of interaction with other entities. As the synthesis particularly of high  $g$  DPs is complex and time consuming (no matter which synthetic approach is used), DPs have thus far not found wide-spread use; Academic research groups have however found some promising applications for DPs.<sup>92</sup>

With their large number of peripheral, often functional groups and their well-defined structure, DPs lend themselves to functionalization *e.g.* with ligands suitable for the formation of catalytically active transition metal complexes.<sup>124,125</sup> Dendronized polymers bearing complexes active in catalytic asymmetric hydrogenation close to the backbone have likewise been used, providing good solubility of the transition metal complexes while facilitating their removal and recycling.<sup>126,127</sup> The Walde group has extensively used the class of DPs described in section 1.6 for the immobilization of enzymes, utilizing their multitude of free amines for covalent attachment of proteins as well as for the deposition of the resulting polymer-enzyme conjugates on oxide surfaces.<sup>128</sup> The dimensions of the  $g = 2$  DP used permit the immobilization of many copies of one or several enzymes on one polymer molecule,<sup>129</sup> enabling enzymatic cascade reactions with potential use in biosensing.<sup>130</sup>

The well-defined cylindrical shape of DPs and their capability of chemospecific interaction *via* peripheral or branchwork functional groups make them promising candidates for self-assembly into complex structures, such as columnar assemblies<sup>131,132</sup> and well-ordered monolayers,<sup>133,134</sup> or to act as templates *e.g.* in the synthesis of hollow nanotubes.<sup>135</sup>

## 1.5. $g_{\max}$ of dendritic molecules

### 1.5.1. Definitions and implications

The concept of the maximum dendritic generation  $g_{\max}$  is of particular importance not only to this work, but to the investigation of dendritic structure in general. Briefly after the first dendrimer syntheses by Vögtle<sup>136</sup> and Denkewalter,<sup>137</sup> de Gennes and Hervet realized that there are limitations to growth in any dendritic structure.<sup>138</sup> The scaling arguments first invoked in Ref. 138 are a seminal contribution to the science of dendritic matter, however it has since been realized that the assumed density profile is unrealistic: In de Gennes' model, peripheral groups are crowded on the outer "shell" of the dendrimer, leading to an increase in density going from the core to the periphery. This assumption disregards the possibility of backfolding, first invoked by Muthukumar.<sup>139,140</sup> Backfolding has since been confirmed experimentally,<sup>141</sup> and supported by atomistic simulations.<sup>142-144</sup> It occurs in most dendrimers to some degree, perhaps with the exception of particularly rigid systems such as Müllen's polyphenylene dendrimers.<sup>145</sup>

The choice of density profile influences the location of  $g_{\max}$ , but the essential concept of a maximum dendritic generation holds: When only one type of  $f$ -functional monomer is used in the construction of a dendron, the maximum possible extension of the dendron constructed thereof increases by first approximation linearly with  $g$  (see Eq. 1-7);<sup>146</sup> The maximum extension of the dendritic structure  $R_{\max}$  is given by the longest possible all-trans zig-zag path traced within the dendritic structure from the core to the very periphery. Meanwhile, the molar mass  $M$  of the dendron increases exponentially with  $g$ , depending on the functionality  $f$  ( $f \geq 3$ ) of the dendron:

$$M \sim (f - 1)^g$$

Eq. 1-5

As  $M$  at least doubles for each increment in  $g$ , the volume occupied by the dendron grows exponentially with  $g$  for isolated dendrons. A lower limit for the volume occupied by the dendritic molecule is given by dense packing at an average density  $\rho_{\text{packing}}$ . Depending on the geometry of the dendritic structure in question, the corresponding characteristic lengths  $R_{\text{packing}}$  scale according to:

$$R_{\text{packing}} \sim (f - 1)^{g/D}$$

Eq. 1-6

In Eq. 1-6,  $D$  is the dimensionality of the dendritic geometry:  $D = 3$  for dendrimers (Eq. 1-9),  $D = 2$  for DPs (Eq. 1-10), in both cases resulting in radii  $R_{\text{packing}}$ , and  $D = 1$  for surface-grafted dendritic brushes, where  $R_{\text{packing}}$  is a minimum value for the thickness of the grafted layer. With increasing  $g$ ,  $R_{\text{packing}}$  invariably surpasses  $R_{\max}$  (also compare section 1.5.2).<sup>146</sup> Above this crossing point, true dendrons (*i.e.* branched units comprising only terminal and dendritic units, with all the terminal units being situated

at the same  $g$ ) cannot exist without significant alterations to basic structural parameters.<sup>b</sup> It becomes necessary to include defects into the structures, thereby lowering  $M$  such that  $R_{\text{packing}} \leq R_{\text{max}}$ .

In this text,  $g_{\text{max}}$  shall be defined as the *highest value of  $g$  for which defect-free dendrons are theoretically possible*, i.e. as the value of  $g$  immediately below the crossing point of the curves describing  $R_{\text{max}}$  and  $R_{\text{packing}}$  (Figure 1-12). This concept first appeared in work by Tomalia,<sup>147</sup> but was not expounded. The Schlüter group has in recent years attempted to systematically apply the concept to the study of the class of DPs which are the topic of this thesis<sup>148–150</sup> and which are described in detail in section 1.6.

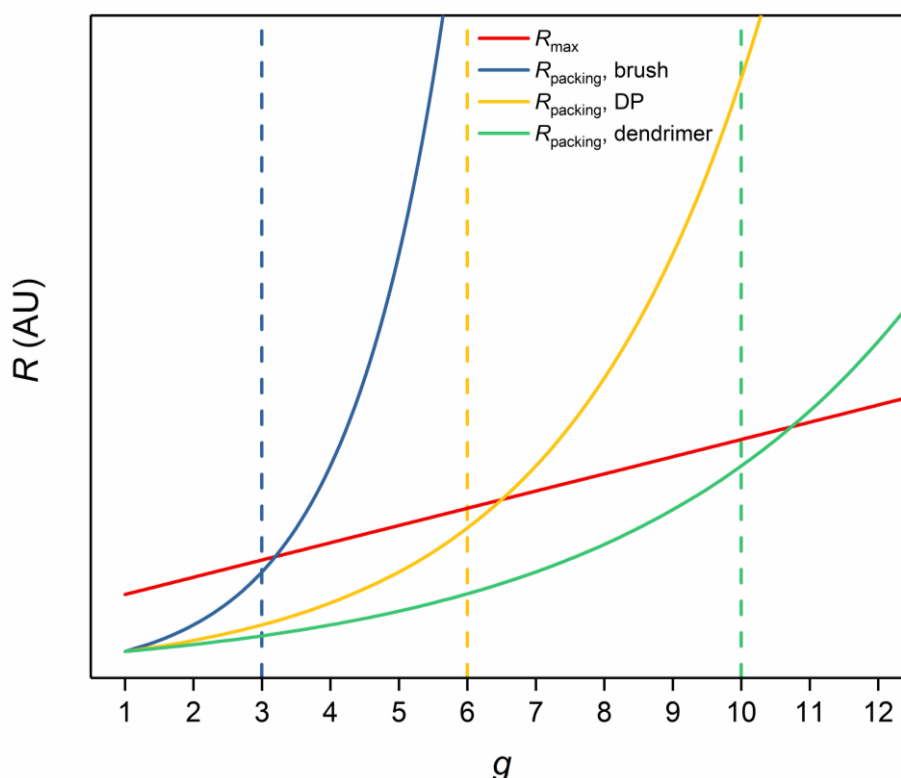


Figure 1-12: Illustration of the differences in  $g_{\text{max}}$  (marked by dashed vertical lines) resulting from geometry-dependent differences in scaling of  $R_{\text{packing}}$  ( $f = 3$ , assuming the same  $R_{\text{max}}$  for all systems; arbitrary numbers).  $R_{\text{packing}}$  scales with  $2^g$  for a surface-grafted brush,  $2^{g/2}$  for a DP and  $2^{g/3}$  for a dendrimer (Eq. 1-6).

As is evident from the scaling behavior of  $R_{\text{packing}}$  illustrated in Figure 1-12, the geometry of a dendritic structure type (*i.e.*  $D$ ) strongly influences the location of  $g_{\text{max}}$ . For comparable dendrons,  $g_{\text{max}}$  is highest for dendrimers, intermediate for DPs and lowest for surface-grafted dendritic brushes. In dendrimers, dendrons may spread over a spherical volume, whereas in DPs they are constrained by neighboring dendrons along the DP backbone, *i.e.* confined on average to a cylindrical slice of the linear DP chain. In dendritic brushes, the volume available to each dendron is a column defined by its

<sup>b</sup> For dendritic molecules to be structurally perfect beyond this limit, chemical bonds either need to be stretched considerably (shifting  $R_{\text{max}}$  to higher values), or the packing density needs to increase quite significantly (lowering  $R_{\text{packing}}$ ); see Appendix A.1. This is an approximation to some extent in that backfolding is not considered – the geometry considered for  $R_{\text{max}}$  corresponds to the density profile assumed by de Gennes,<sup>138</sup> which as previously mentioned is unrealistic.

neighboring dendrons, having the same cross-sectional area as the “footprint” of the point of connection to the surface.

The synthesis of structures around  $g_{\max}$  is most readily achieved by divergent methods: Convergent methods involving the necessary extremely bulky dendrons are likely to fail at providing complete coverage of the core, whereas the  $g = 1$  branched monomers typically involved in divergent protocols may permit for the synthesis of very high  $g$  dendritic systems starting from densely “seeded” precursors (*i.e.* dendrimer cores, linear polymeric precursors of DPs, and suitably functionalized surfaces). In terms of steps required to access structures at and beyond  $g_{\max}$ , surface-grafted brushes are ideal, due to the scaling behavior displayed in Figure 1-12. However, the analysis of such surface-bound systems is anything but trivial: The amounts of material resulting from surface-grafting are minute, rendering solution-phase measurements of properties such as *e.g.* molar masses quite challenging,<sup>151</sup> if the structures can be cleaved from the surface at all. Additionally, the synthesis of truly densely grafted, homogeneously confined brushes is hampered by a multitude of factors, including surface defects (steps and edges) and diffusion limitations near the surface.

For dendrimers, these issues are of no concern: Dendrimers are usually prepared by solution-phase synthesis – indeed branched macromolecules are often more soluble than chemically similar linear polymers<sup>152</sup> – and may be prepared in large quantities. However, the number of steps required to achieve  $g_{\max}$  is largest among the three structure types discussed here. Dendronized polymers offer the same advantages of solubility and accessible quantity, while the number of steps necessary to achieve  $g_{\max}$  in a divergent protocol is reduced. They are therefore the candidates for which, given suitably efficient dendronization chemistry, a divergent protocol is most likely to successfully afford DPs at  $g_{\max}$ .

The regime at and above  $g_{\max}$  is fascinating: Up to  $g_{\max}$ , divergent dendritic growth may proceed with perfect structures, but for  $g > g_{\max}$  the growth proceeds stochastically, though the inner, truly dendritic “core” is retained. Above  $g_{\max}$ , one would ideally expect a “dendritic”<sup>c</sup> molecule or a “dendritic” brush to resemble a densely packed object, consisting of very well-defined chemical entities which interact with the environment, *e.g.* solvent, only through the outermost periphery.

In this sense, dendritic molecules of  $g > g_{\max}$  more closely resemble densely cross-linked colloids than classical small molecules or polymers, and hence the terms “molecular colloid” and “molecular object” have been used for such structures.<sup>87</sup> Unlike for classical colloids, the dimensions of such objects are very tightly controlled in discrete steps of a few nm (correlated with  $R_{\max}$ ), a feat difficult to achieve with microfabrication techniques.<sup>153</sup> Furthermore, dendritic molecules inherently are of very low (dendritic) polydispersity and offer anisotropy in shape (*e.g.* DPs as cylindrical molecular objects) and potentially in chemistry (*e.g.* using Janus-type dendrimers).<sup>154</sup>

---

<sup>c</sup> Structures above  $g_{\max}$  are *not* strictly speaking dendritic, as they need contain linear repeat units. For simplicity, such structures will still be referred to as dendritic/DPs/dendrimers *etc.* in the following; They do contain a dendritic core inherited from the  $g \leq g_{\max}$  precursors.

### 1.5.2. $g_{\max}$ of some dendritic structures

To illustrate the points made in the preceding section,  $g_{\max}$  of some dendritic systems is estimated here, demonstrating the consequences of the scaling relations invoked previously (Eq. 1-5, Eq. 1-6). The estimation of  $g_{\max}$  follows a simple procedure, with the sole necessary inputs being the chemical structure of the dendrimer or dendronized polymer in question and an estimate of the system's packing density. The approach below has previously been applied to estimate  $g_{\max}$  of DPs (see Ref. 148) and is here extended to dendrimers for the purpose of illustration and comparison.

Stated explicitly, the scaling relations noted in subsection 1.5.1 yield Eq. 1-7 for all dendritic structures, in which  $R_0$  corresponds to radial extension of the core plus an eventual tether,  $R_1$  corresponds to the length added to the dendron by an all-trans zig-zag path within a dendritic repeat unit, and  $R_p$  corresponds to the contribution from peripheral (*e.g.* protecting) groups:

$$R_{\max}(g) = R_0 + R_p + g \cdot R_1$$

Eq. 1-7

Values of  $R_{\max}$  can be estimated *e.g.* using molecular mechanics simulations.  $R_{\text{packing}}$  can be calculated in a fairly straightforward manner from the dendritic chemical structure (see Appendix A.2 for details). The necessary inputs here are  $M(g)$ , determined by the explicit chemical structure, and a value for the packing density  $\rho_{\text{packing}}$ .  $M(g)$  is of the form:

$$M(g) = M_0 + X \left( M_1 \left[ \sum_{i=0}^{g-1} (f-1)^i \right] + M_p (f-1)^g \right)$$

Eq. 1-8

where  $X$  denotes the multiplicity of the core and  $M_0$ ,  $M_1$  and  $M_p$  denote the molar masses of core, dendritic repeat unit and peripheral group fragments within the dendron structure. The scaling relation Eq. 1-6 then explicitly translates in the case of dendrimers to the following expression, assuming the dendrimer adopts a spherical volume:

$$R_{\text{packing}} = \sqrt[3]{\frac{3}{4\pi} \frac{M(g)}{\rho_{\text{packing}}}}$$

Eq. 1-9

For dendronized polymers, the explicit expression (Eq. 1-10) further uses the length  $\delta$  of one repeat unit within the dendronized polymer, defining the height of the cylindrical slice available to one dendronized repeat unit:

$$R_{\text{packing}} = \sqrt{\frac{M(g)}{\delta \pi \rho_{\text{packing}}}}$$

Eq. 1-10

$g_{\max}$  for each system can be estimated by simply determining the point of crossover between  $R_{\max}$  and  $R_{\text{packing}}$ , as already demonstrated in Figure 1-12. Details for the calculations presented below and a rationale for  $g_{\max}$  being a fairly solid parameter are given in sections A.1 and A.2 of the Appendix.

Figure 1-14 depicts  $g_{\max}$  plots for a selection of dendrimers (Figure 1-13) from the literature. The featured dendrimers were all prepared by divergent syntheses. They include Tomalia's PAMAM dendrimers (**9**),<sup>83</sup> a class of very compact aliphatic polyamide dendrimers (**10**) recently introduced by Perez-Inestrosa *et al.*<sup>155</sup> and improved upon by Percec *et al.*,<sup>156</sup> the phosphazene-based dendrimers (**11**) investigated by Majoral *et al.*,<sup>95</sup> the compact polyester dendrimers (**12**) investigated by Hult *et al.*<sup>157,158</sup> and later Fréchet *et al.*,<sup>159</sup> Astruc's threefold-branching silane-based dendrimers (**13**),<sup>96</sup> and Müllen's polyphenylene dendrimers (**14**).<sup>145,d</sup>

These dendrimers, the  $g = 2$  representatives of which are depicted in Figure 1-13, display a fairly wide range of core multiplicities, RU structures and connecting chemistries, but nevertheless the respective  $g_{\max}$  values fall into a narrow band of  $g \approx 10 - 13$  (Figure 1-14, Table 1-2). The sole exception to this trend among the dendrimers depicted in Figure 1-13 is Astruc's silane-based, threefold-branching dendrimer, for which  $g_{\max}$  lies significantly lower than for the remaining, twofold-branching dendrimers. This suggests that the location of  $g_{\max}$  more strongly depends on scaling behavior (dominated by  $D$  and  $f$ , see Eq. 1-5 and Eq. 1-6) than it does on "compactness" or concrete chemical structures, again underlining the suitability of DPs for the investigation of the  $g_{\max}$  regime. For the class of DPs which this thesis is mainly concerned with, it has been estimated that  $g_{\max} \approx 6 - 7$  (Figure 1-20a). By virtue of the number of necessary dendronization steps being much lower than in similar dendrimers (*e.g.* PAMAM), access to  $g_{\max}$  structures should be more readily possible.

Table 1-2:  $g_{\max}$  of some dendritic structures (see Figure 1-13, Figure 1-14).

Chemistry	Core multiplicity $X$	Branching multiplicity $f$	$g_{\max}$
PAMAM ( <b>9</b> ); Tomalia <sup>83</sup>	4	2	12 - 13
"aliphatic amide" ( <b>10</b> ); Perez-Inestrosa/Percec <sup>155,156</sup>	4	2	10 - 11
Phosphazene ( <b>11</b> ); Majoral <sup>95</sup>	6	2	12 - 13
Polyester ( <b>12</b> ); Hult/Fréchet <sup>158,159</sup>	3	2	9 - 10
Allyl/silane ( <b>14</b> ); Astruc <sup>96</sup>	3	3	7 - 8
Polyphenylene ( <b>15</b> ); Müllen <sup>145</sup>	4	2	9 - 10
DP-mimetic dendrimer ( <b>38</b> ) (hypothetical, see Figure 1-20b)	6	2	11 - 12
$\text{PGg}_n^{\text{NHBOC}}$ ( <b>21 etc.</b> ); Schlüter (see Figure 1-20a) <sup>148</sup>	1	2	6 - 7

<sup>d</sup> The described treatment is not quite applicable for Müllen-type and similarly inflexible dendrimers in which backfolding is disfavoured. In such cases, the de Gennes dense packing limit<sup>138</sup> is likely a more accurate descriptor of synthetic limitations.

It must be noted that dendrimers of very high  $g$  have been synthesized. In particular this is true for PAMAM dendrimers, which are available commercially up to  $g = 10$ ,<sup>160</sup> Majoral's phosphazene-based dendrimers which have been prepared up to  $g = 12$ ,<sup>95</sup> and Astruc's silane-based dendrimers which have been synthesized up to  $g = 9$ .<sup>96</sup> While the corresponding routes are therefore capable of nominally approaching or even surpassing  $g_{\max}$ , the divergent syntheses of these dendrimers often suffer from significant deficiencies: PAMAM dendrimers are prone to backbiting side reactions, and commercially available samples of as low as  $g = 5$  have been found to bear significant numbers of defects.<sup>161,162</sup> The structural perfection of polyphosphazene dendrimers is difficult to assess, as the dendrimers fragment in mass spectrometry.<sup>163</sup> The synthesis of Astruc's silane-based dendrimers, which has proceeded nominally farthest into the territory beyond  $g_{\max}$ , suffers from side reactions, such that defective structures become dominant in the product mixtures already at  $g = 3$ .<sup>96</sup> In other cases, reactivities were found to decline drastically at  $g \ll g_{\max}$ . An extreme example is a recent report by Percec *et al.* in which aliphatic polyamide dendrimers (in the series containing **10**, see Figure 1-13) reportedly did not react at all beyond a certain  $g$ , the "limiting generation" depending on the core used for the dendrimer.<sup>156</sup> Similarly, Vögtle *et al.* in the initial poly(propyleneimine) (PPI) dendrimer synthesis had reported declining yields of the reduction of peripheral nitrile groups at comparatively low  $g$ .<sup>136</sup> However, Meijer *et al.* were subsequently able to synthesize higher  $g$  PPI dendrimers by improving the synthetic methodology.<sup>164</sup> These examples underline the previously mentioned necessity of highly effective chemical transformations, if high  $g$  dendritic molecules are to be synthesized. Accordingly, great attention has been paid to the quantification of functional group conversion values in the synthesis of DPs, as discussed in detail in subsection 1.6.1.

Defects at  $g \ll g_{\max}$  have a significant impact on the molecular structure when they are propagated to higher  $g$ , either leading to missing "arms" in the dendritic branchwork or to a sort of low-dispersity hyperbranching. Defects arise either from side reactions which terminate dendronization in that branch entirely, or from inefficient reactions, in which case further growth from low  $g$  may still be possible later on. In either case, the structures are not dendritic anymore per the strict definition. In order to reach a truly densely functionalized state and approach  $g_{\max}$  in the defined sense, such defects must be avoided. As this goal is far easier to achieve when fewer divergent growth steps are involved in the synthesis of dendritic structures, DPs provide a suitable platform for the synthesis of dendritic molecules at  $g_{\max}$ .

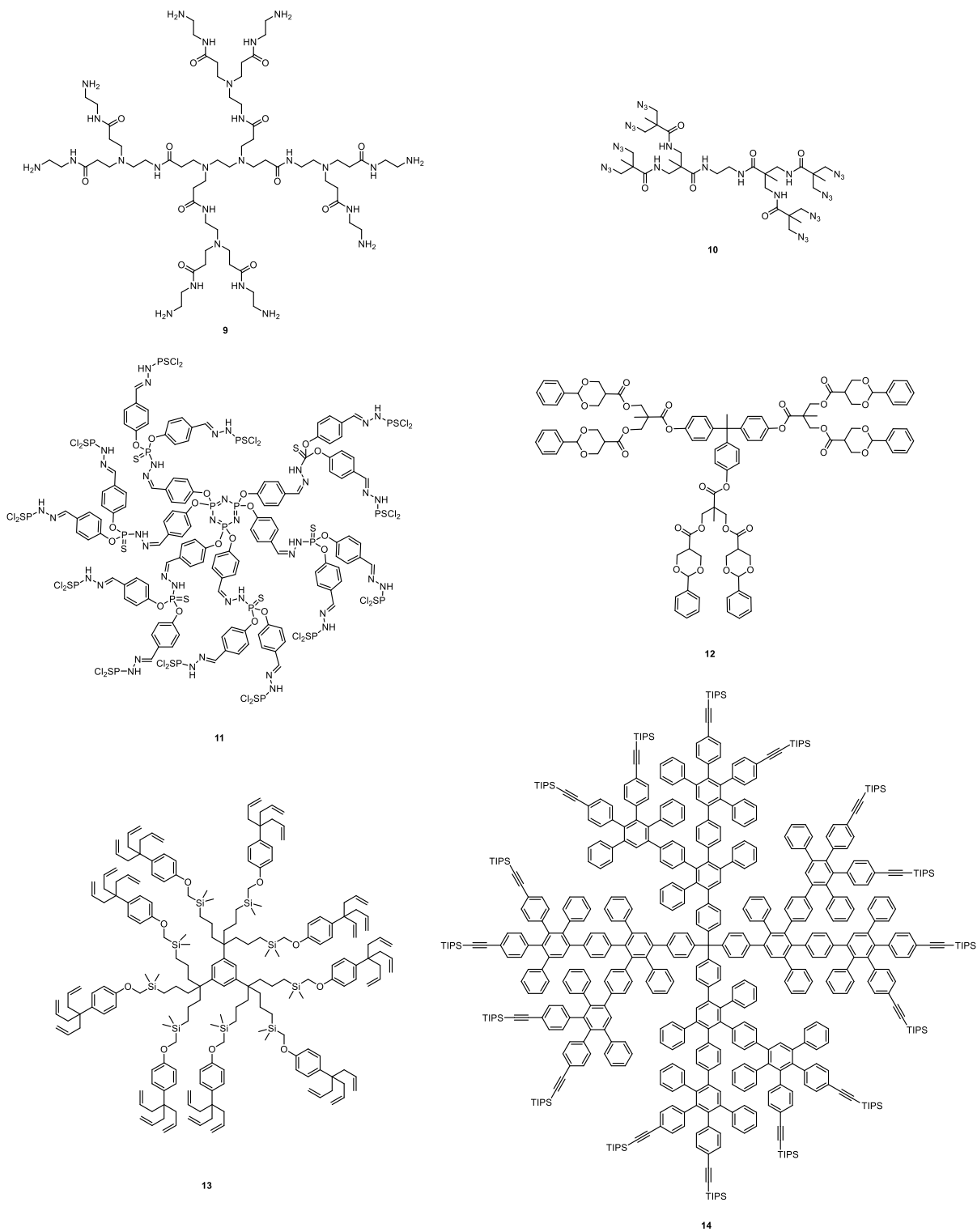


Figure 1-13: Chemical structures of dendrimers ( $g = 2$ ) for which  $g_{max}$  was calculated (see Figure 1-14). Where relevant (**10**, **12**, **14**) the form of the dendrimer bearing protecting groups was chosen.



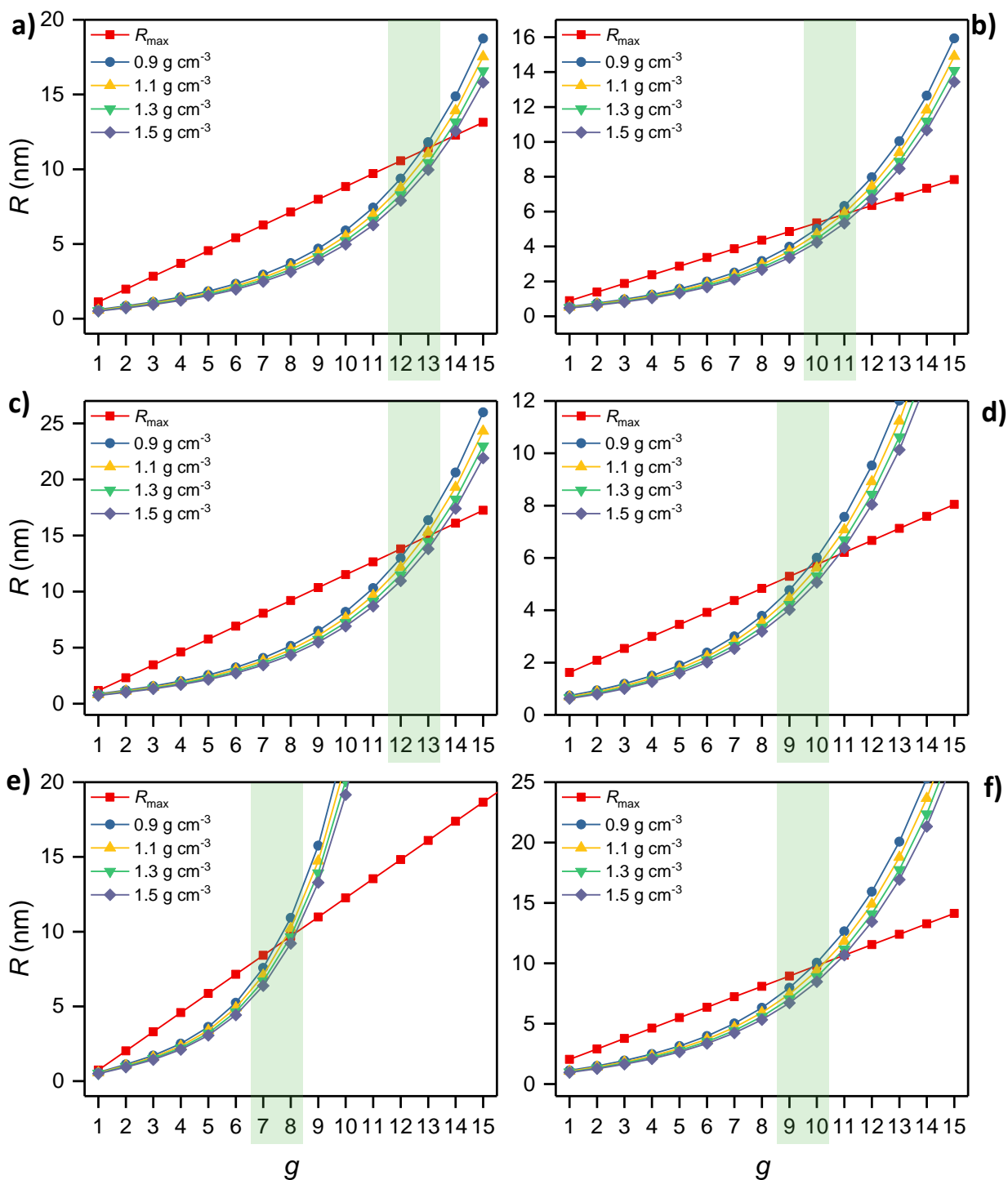


Figure 1-14:  $g_{\max}$  plots of various dendrimer series: a) PAMAM dendrimer (ethylene diamine core); b) "aliphatic polyamide" dendrimer (ethylene diamine core); c) phosphazene dendrimer (hexachlorotriphosphazene core); d) polyester dendrimer (tris-4-hydroxyphenylmethane core); e) silane-based dendrimer (mesitylene core); f) polyphenylene dendrimer (tetraphenylmethane core). The green band marks the range of  $g_{\max}$ . See Figure 1-13 for  $g = 2$  representatives of the respective DPs.

## 1.6. The $\text{PGg}_n^{\text{NHBoc}}$ DP series

### 1.6.1. Structure, synthesis & nomenclature

DPs similar or identical to those discussed in this thesis have been investigated intensely in the past two decades by the Schlüter group. The dendron is based on a 1,3,5-trisubstituted benzene ring as a branching unit (similar to Fréchet-type dendrons), with a carboxylic acid group as the “root” and tethered primary amines in the periphery. The connection between dendritic monomers is achieved by means of an amide bond. As in Denkewalter’s polylysine dendrimers,<sup>137</sup> the amine is protected during dendronization and later deprotected to permit amidation.

Multiple variations of this central theme have been implemented over the years,<sup>165–167</sup> but in recent years our group has focused on the implementation depicted in Scheme 1-8. This DP is based on a poly(methacrylate) backbone to which the dendrons are attached on each repeat unit *via* a benzyl ester moiety. This implementation is particularly suited to the study of  $g_{\text{max}}$  effects, as the spacing between the polymer backbone and the first branching point is particularly short and because the length of the repeat unit,  $\delta$ , is small.

The branching unit is derived from the readily available precursor methyl 3,5-dihydroxybenzoate (**15**) using straightforward chemical transformations (Scheme 1-8a; compounds **16** and **20** are commercially available from Synwit Technology Co. Ltd., Beijing).<sup>128</sup> A mixture of the macromonomer and graft-from approaches is used in the synthesis of these DPs: The  $g = 1$  “macro” monomer **18** at a molar mass of 523 Da is still readily polymerizable using FRP or RAFT polymerization.<sup>168,169, e</sup> After polymerization to the  $g = 1$  DP **21**, the graft-from synthesis of  $g > 1$  DPs relies on highly efficient reactions adapted from solid phase peptide synthesis which are optimized to proceed in very high functional group conversions with minimal side reactions.<sup>170</sup> In detail, the peripheral Boc groups in **21** are removed by treatment with trifluoroacetic acid (TFA), affording the *N*-deprotected, polyelectrolytic intermediate **22**. This is reacted under basic conditions with the *N*-hydroxysuccinimide ester dendronization agent **20**, resulting in the corresponding  $g = 2$  DP **23** (Scheme 1-8b).

The DPs discussed in this thesis are all derived from the above synthetic route. For ease of reference, it is convenient to introduce a nomenclature identifying the crucial components of dendronized polymer structure and synthesis. This includes three types of compounds:

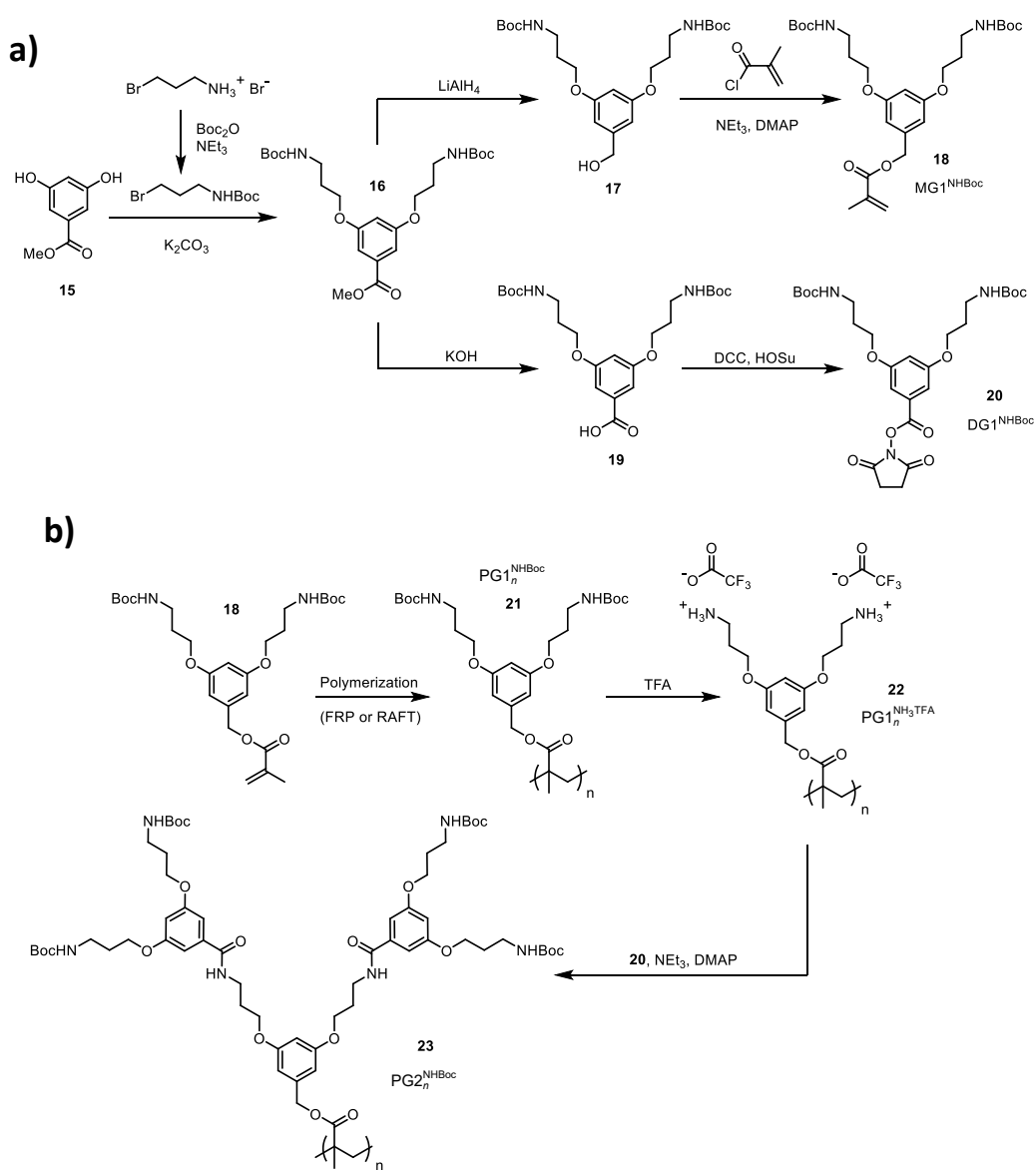
- *Monomers*, *i.e.* methacrylates such as **18** for which descriptors of the type  $\text{MGg}^{\text{X}}$  will be used.
- *Dendronization agents*, *i.e.* active esters similar to **20** for which descriptors of the type  $\text{DGg}^{\text{X}}$  will be used.
- *Dendronized polymers*, for which descriptors take the form  $\text{PGg}_n^{\text{X}}$  (Figure 1-16, Figure 1-17).

In these descriptors,  $g$  corresponds to the generation number of the dendritic molecule in question. The subscript  $n$  in the case of a DP corresponds to the average degree of polymerization  $P_n$ . The superscript X denotes the peripheral functionality, *i.e.* the functional group borne at the end of the propyl chain in each arm of the dendron. Usually, these are amines or carbamates, as is the case

---

<sup>e</sup> ATRP was used for monomers similar to **18** earlier,<sup>166</sup> however with **18**, RAFT was found to provide superior control at  $P_n > 100$ .<sup>189,395</sup>

with the compounds in Scheme 1-8, however other functional groups such as esters will be discussed in this thesis as well (see Figure 1-17). The nomenclature is illustrated in Scheme 1-8, where the relevant compounds are named accordingly:  $MG1^{NHBoc}$  (**18**),  $DG1^{NHBoc}$  (**20**),  $PG1_n^{NHBoc}$  (**21**),  $PG1_n^{NH_3TFA}$  (**22**) and  $PG2_n^{NHBoc}$  (**23**).



Scheme 1-8: a) Syntheses of the  $g = 1$  monomer **18** ( $MG1^{NHBoc}$ ) and dendronization agent **20** ( $DG1^{NHBoc}$ ) from widely available precursors; b) polymerization of **18** to the  $g = 1$  DP **21** ( $PG1_n^{NHBoc}$ ) and the two-step dendronization to **23**, its  $g = 2$  homolog ( $PG2_n^{NHBoc}$ ).<sup>128</sup>

Higher  $g$  DPs (Figure 1-16, Figure 1-17) may be accessed by simple iteration of the two-step protocol shown in Scheme 1-8b, up to and including  $PG5_n^{NHBoc}$ .<sup>101</sup> The only alteration to the procedure lies in progressively longer reaction times for dendronization. This is necessary to achieve full functional group conversion and accounts for two factors which become increasingly more prevalent with increasing  $g$ : The very large number of functional group transformations to be performed on a single molecule (easily in the thousands) and the increasing steric hindrance in the periphery of the DP.

This two-step sequence proceeds with excellent functional group conversion values  $\chi > 99.5\%$ , as determined by the labelling of unreacted amines with Sanger's reagent (2,4-dinitrofluorobenzene). The dinitroaniline resulting from the reaction between Sanger's reagent and an amine (Figure 1-15a) absorbs strongly at *ca.* 360 nm ( $\epsilon_{360} = 16'400 \text{ M}^{-1} \text{ cm}^{-1}$ ).<sup>171</sup> This UV/Vis spectroscopic quantification of defects permits a detailed analysis of this class of DPs by recursive analysis.<sup>150, f</sup> Unfortunately, attempts at characterization by MALDI-TOF-MS were not successful for this class of DPs.

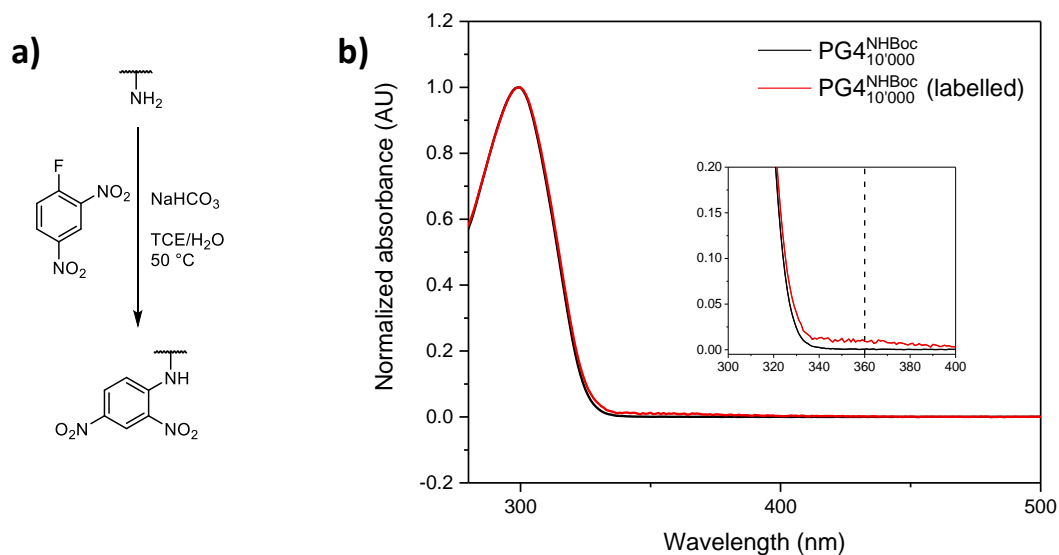


Figure 1-15: a) Conditions for the labelling of amines remaining unreacted after dendronization, schematically shown for a single amine; b) typical UV/Vis spectra of DPs in TCE before (black) and after (red) Sanger labelling.

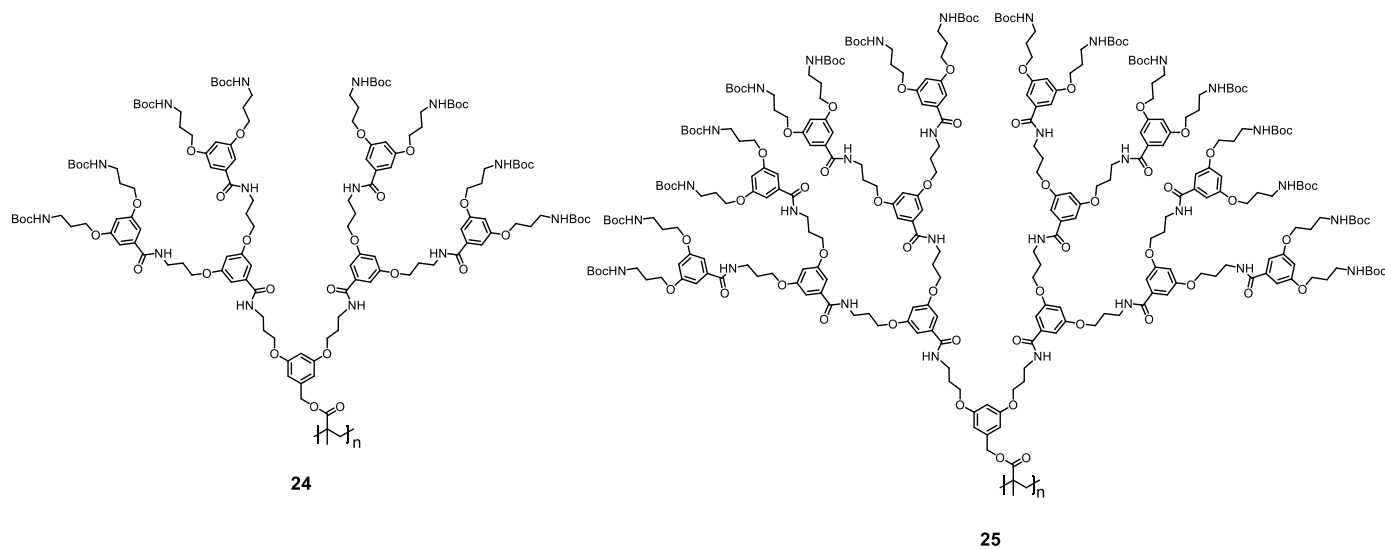


Figure 1-16: Chemical structures of  $\text{PG}_3^{\text{NHBOC}}_n$  (**24**) and  $\text{PG}_4^{\text{NHBOC}}_n$  (**25**).

<sup>f</sup> Functional group conversion values  $\chi$  given in this thesis rely on the recursive relations defined in Ref. 140; as these values assume more realistic (lower) molar masses per RU of precursor DPs, the functional group conversion values appear slightly higher than in other publications, see *e.g.* Ref. 175.

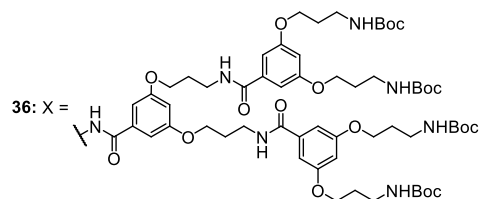
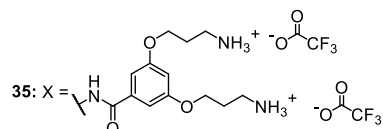
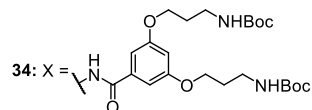
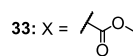
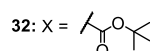
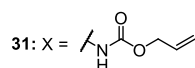
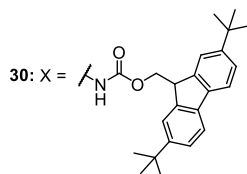
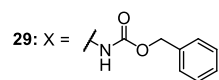
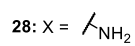
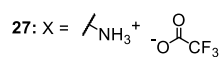
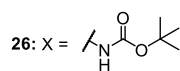
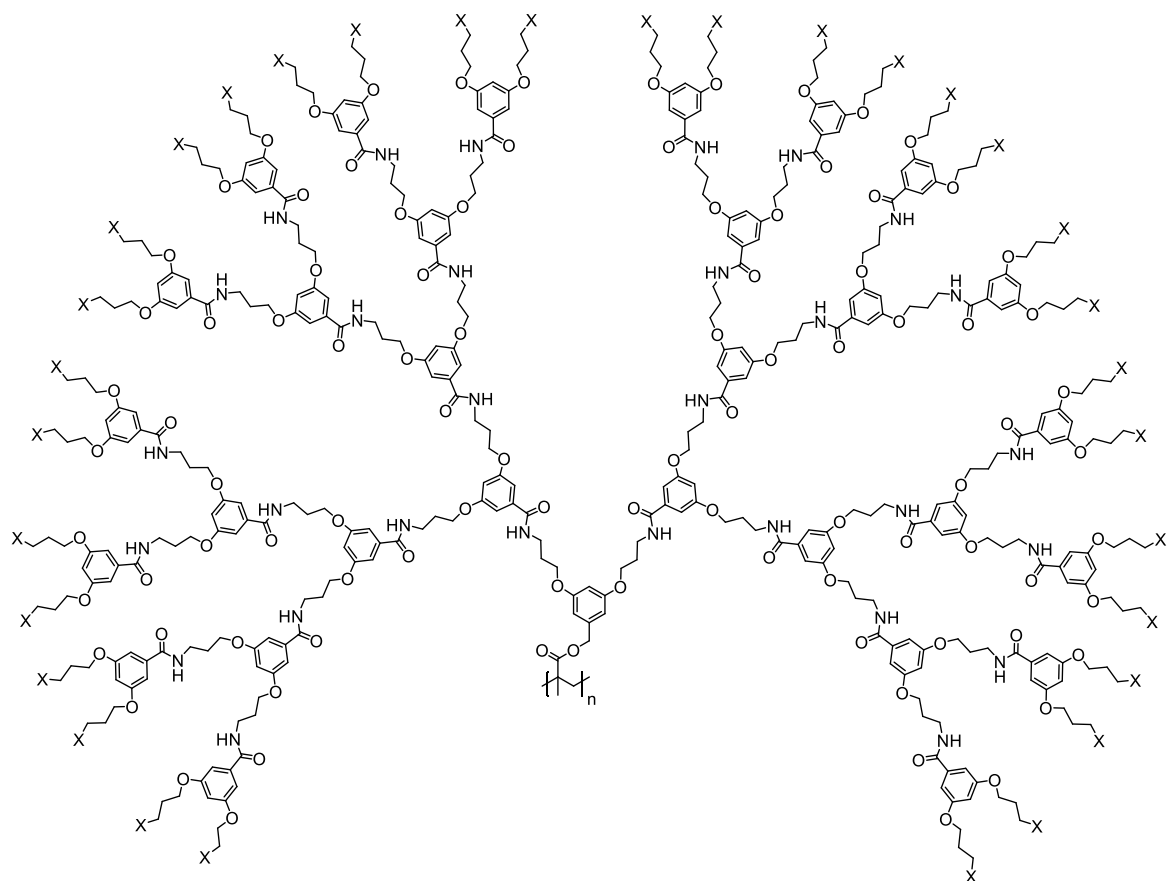


Figure 1-17: Chemical structures of some  $g \geq 5$  DPs of relevance to this thesis:  $PG5_n^{NH_{Boc}}$  (26),  $PG5_n^{NH_3TFA}$  (27),  $PG5_n^{NH_2}$  (28),  $PG5_n^{NHCbz}$  (29),  $PG5_n^{NHFmoc^*}$  (30),  $PG5_n^{NHAlloc}$  (31),  $PG5_n^{CO_2tBu}$  (32),  $PG5_n^{CO_2Me}$  (33),  $PG6_n^{NH_{Boc}}$  (34),  $PG6_n^{NH_3TFA}$  (35),  $PG7_n^{NH_{Boc}}$  (36).

### 1.6.2. Synthesis of $g > 5$ DPs

Past  $g = 5$ , the NHBoc deprotection/dendronization protocol does not proceed as desired: When  $\text{PG5}_n^{\text{NHBoc}}$  of sufficient chain length ( $n \gg 50$ , e.g.  $\text{PG5}_{500}^{\text{NHBoc}}$ , Figure 1-18a), is subjected to acid-mediated deprotection, the resulting products are not the expected polymers of the same main chain length, e.g.  $\text{PG5}_{500}^{\text{NH}_3\text{TFA}}$ , but instead much shorter oligomeric species (Figure 1-18b, also compare Figure 3-2) most closely resembling  $\text{PG5}_{50}^{\text{NH}_3\text{TFA}}$ .<sup>169,172</sup> At the time of discovery, it was reasoned that this is a result of charge-charge repulsion in the densely substituted periphery of the  $g = 5$  DPs. This hypothesis will be discussed in detail in chapter 3, which is concerned with the elucidation of main-chain scission in high  $g$  DPs.

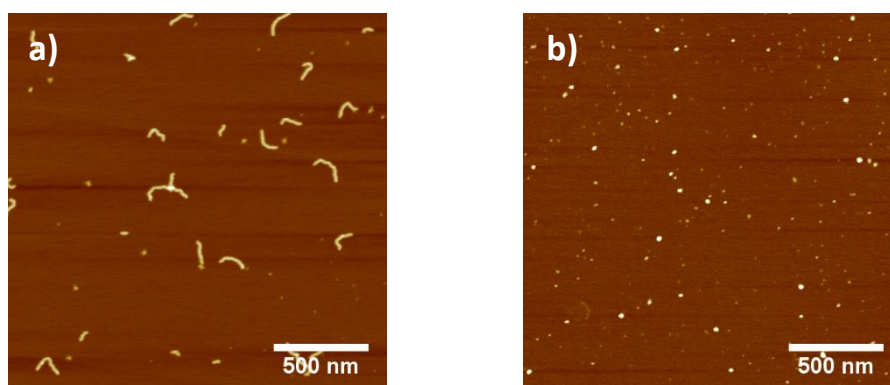


Figure 1-18: AFM height images (tapping mode, mica) of a)  $\text{PG5}_{500}^{\text{NHBoc}}$  and b) the short-chain products obtained after TFA-mediated NHBoc deprotection.

The main-chain scission at  $g = 5$  represented a significant synthetic roadblock, as it occurred in unfortunate proximity to the estimated  $g_{\text{max}} \approx 6 - 7$  (Figure 1-20). The oligomers of  $P_n \approx 40 - 50$  are unsuitable for the study of  $g_{\text{max}}$  as they are essentially ellipsoid in shape rather than wormlike. They therefore more closely resemble dendrimers, in which it is likely that  $g_{\text{max}} \geq 10$  (see Figure 1-20b), as the dendrons are not confined to cylindrical geometry anymore.

Significant effort was devoted to preventing main-chain scission. This resulted in the adaptation of a “double-exponential” graft-from procedure, employing a  $g = 2$  dendronization agent ( $\text{DG2}^{\text{NHBoc}}$ , **37**, see Figure 1-19a). Similar strategies had previously been used to reduce the number of steps required to access high  $g$  in dendrimers.<sup>173</sup> By using the stable  $\text{PG4}_{500}^{\text{NH}_3\text{TFA}}$  as a starting material, this approach was indeed successful in providing the desired DP of *nominally*  $g = 6$ . The resulting polymer proved amenable to the standard synthetic protocol laid out in Scheme 1-8b, and therefore the synthesis of polymers up to (nominally)  $g = 8$  became possible (Figure 1-19b).

However, the step from  $g = 4$  to  $g = 6$  did not proceed with the usual high values of functional group conversion: Only *ca.* 90 % conversion was achieved in this transformation. This significant number of defects means that the resulting polymers of  $g = 6$  are not strictly dendritic anymore, though for simplicity they will still be referred to as dendronized polymers ( $\text{PG6}_{500}^{\text{NHBoc}}$ ,  $\text{PG7}_{500}^{\text{NHBoc}}$ , etc.). A discussion of  $g_{\text{max}}$  is not possible on the basis of such defective structures, just as it is not for high  $g$  dendrimers bearing many defects (see subsection 1.5.2). The precise implications of this imperfect

transformation and alternative synthetic methods to prevent main-chain scission will be discussed extensively in chapter 2.

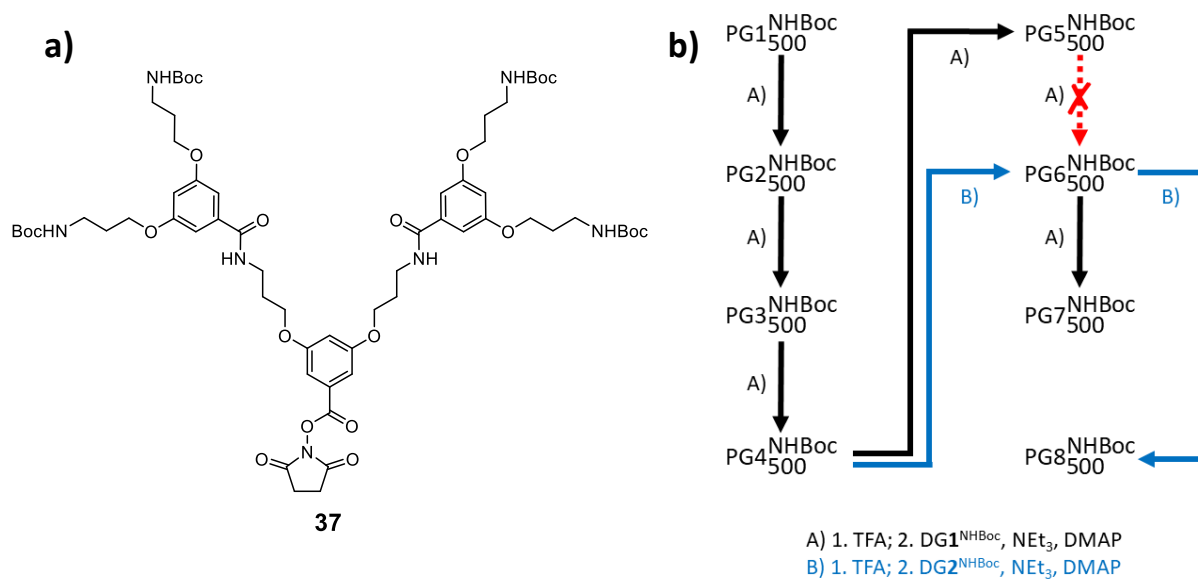


Figure 1-19: a) Chemical structure of the  $g = 2$  dendronization agent DG2<sup>NHBoc</sup>(**37**); b) schematic representation of previous DP syntheses up to  $g = 8$ .<sup>174</sup> Compare Scheme 2-1.

### 1.6.3. Properties of $PGg_n^{NHBoc}$

$g_{max}$

The maximum generation  $g_{max}$  up to which DPs of the type  $PGg_n^{NHBoc}$  are theoretically accessible without defects has been calculated to lie in the range of  $6 \leq g_{max} \leq 7$  (Figure 1-20a, compare section 1.5 and Appendix A.1).<sup>148</sup> This compares favorably to dendrimers containing different dendrons (see Figure 1-14, Table 1-2) as well as to a hypothetical dendrimer **38** which features the same dendrons as  $PGg_n^{NHBoc}$  (Figure 1-20b,c). This is true even though this example of a potential dendrimer structure is particularly crowded, being based on a hexafunctional graphitic acid core; For this structure,  $11 \leq g_{max} \leq 12$  has been estimated.

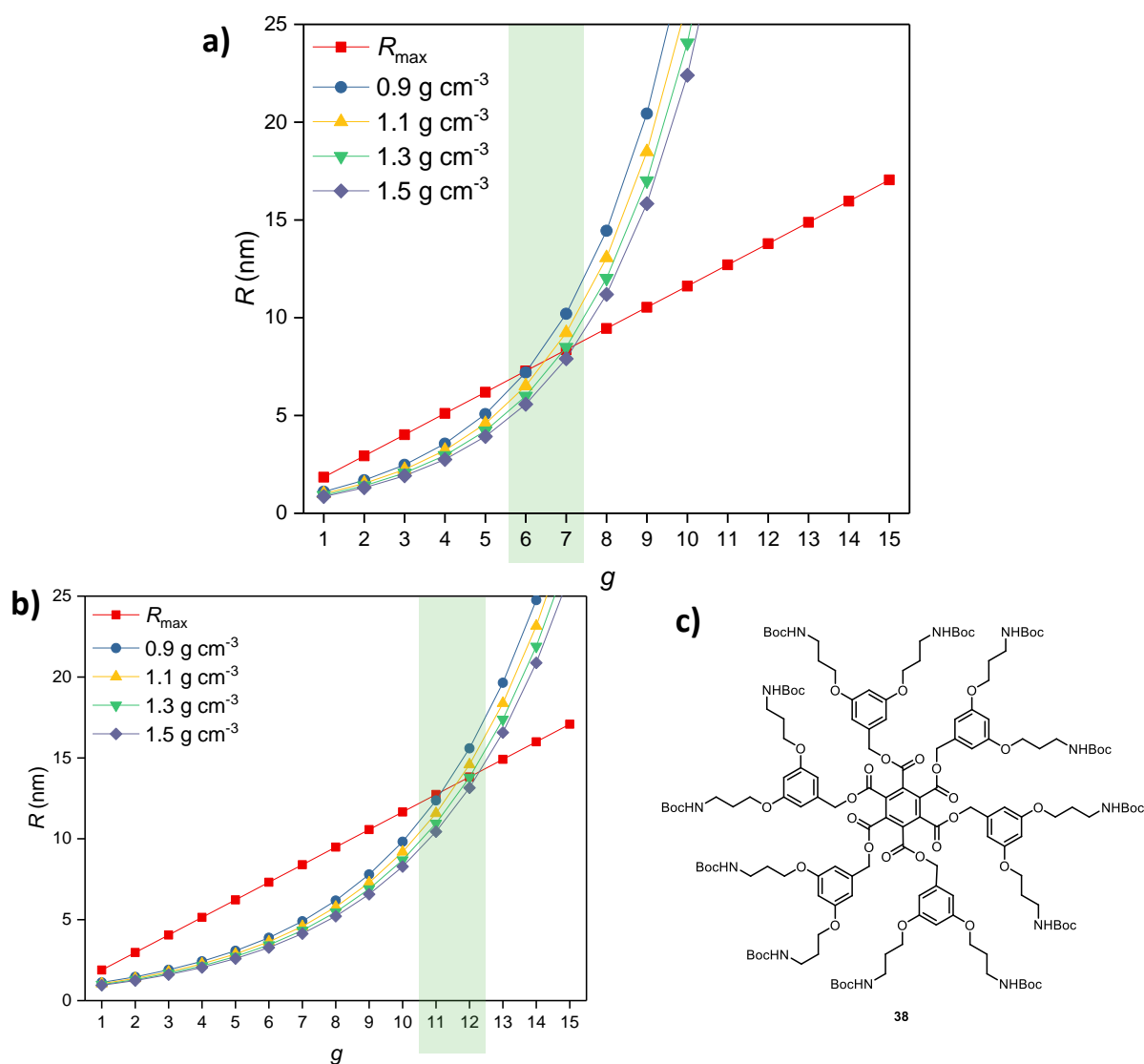


Figure 1-20:  $g_{max}$  plots for a)  $PGg_n^{NHBoc}$  ( $n > 100$ ; for  $n \approx 50$  chain end effects dominate) and b) a possible dendrimer series based on the dendritic structure found in  $PGg_n^{NHBoc}$ ; c) chemical structure of the hypothetical  $g = 1$  dendrimer, **38**.



## Solubility

The solubility of DPs in both the Boc-protected and *N*-deprotected states is of great importance to the synthesis and modification of high *g* DPs and will therefore be addressed in some detail below. These remarks are of a qualitative and observational nature – with the significant exception of the work of Gstrein *et al.*<sup>98,99</sup> – and are drawn mainly from experience in handling these substances and from communications with co-workers.

The Boc-protected DPs of the type  $\text{PG}g_n^{\text{NHBoc}}$  are soluble to at least some degree in a fairly broad range of solvents, spanning from alcohols such as MeOH to aromatics such as toluene or xylene. Polar aprotic solvents such as DMF, DMSO and DMAc are particularly good solvents for this class of DPs. DMF is the solvent of choice for synthesis and for analytical purposes, permitting the preparation of polymer solutions of at least 25 % w/w. Alcohols and other organic solvents of middling polarity, such as acetone, EtOAc, or methylene chloride are still fairly good solvents. A notable, somewhat puzzling exception sitting well within this range of solvents is acetonitrile, which is a very poor solvent for DPs of the type  $\text{PG}g_n^{\text{NHBoc}}$ . Solvents of middling quality include some chlorinated solvents such as 1,1,2,2-tetrachloroethane (TCE) and 1,4-dioxane. Aromatics such as toluene, benzene and xylenes make up the tail end of DP solubility. Notable nonsolvents for  $\text{PG}g_n^{\text{NHBoc}}$  are water, aliphatics such as hexane or pentane, and some ethers such as Et<sub>2</sub>O (although cyclic ethers such as THF and 1,4-Dioxane are moderately good solvents).

The solubility of the *N*-deprotected DPs is significantly different: The polyelectrolytes  $\text{PG}g_n^{\text{NH}_3\text{TFA},g}$  dissolve well in water, MeOH and polar-protic solvents such as DMF and DMSO. Less polar solvents, starting with fairly polar candidates such as acetone and acetonitrile, are nonsolvents and lead to the precipitation of  $\text{PG}g_n^{\text{NH}_3\text{TFA}}$  when introduced in relatively small proportions into solutions of these polymers. The solubility of  $\text{PG}g_n^{\text{NH}_2}$  is, by and large, identical to that of  $\text{PG}g_n^{\text{NH}_3\text{TFA}}$ , although quantitatively the solubility of the free base appears lower.

The free-base form  $\text{PG}g_n^{\text{NH}_2}$  – while soluble when generated *in situ* by deprotonation of  $\text{PG}g_n^{\text{NH}_3\text{TFA}}$  *e.g.* in DMF – is best not isolated as a solid: Once precipitated or isolated by evaporation of solvent, polymers of the type  $\text{PG}g_n^{\text{NH}_2}$  tend to remain insoluble for good. Likely, this is due to the formation of very strong hydrogen bonding networks among the highly branched, interdigitating polyamines: Even hot TFA is in some cases not capable of disrupting this network within a reasonable time frame (hours). The polyelectrolytes  $\text{PG}g_n^{\text{NH}_3\text{TFA}}$  by contrast can be liberated of solvent *e.g.* by freeze drying without loss of solubility.

The range of solubilities dictates the choice of solvents for the synthesis, handling and analysis of DPs: The synthesis of  $\text{PG}1_n^{\text{NHBoc}}$  and most post-polymerization reactions are performed preferentially in DMF or in similar polar-protic solvents such as DMSO, DMAc, or NMP. For these solvents, the solubilities of  $\text{PG}g_n^{\text{NHBoc}}$ ,  $\text{PG}g_n^{\text{NH}_3\text{TFA}}$ , and  $\text{PG}g_n^{\text{NH}_2}$  conveniently overlap. Furthermore, this class of solvents is capable of dissolving a very large range of organic substances, as well as some inorganic salts. Methylene chloride dissolves  $\text{PG}g_n^{\text{NHBoc}}$  well and rapidly and is easily removed by evaporation, making it the favorite choice for work-up and handling after post-polymerization functionalization. Solvents such as <sup>t</sup>BuOH and 1,4-dioxane do not dissolve DPs in high concentrations but are useful as

---

<sup>g</sup> The statements made for  $\text{PG}g_n^{\text{NH}_3\text{TFA}}$  are largely valid for other salts such as  $\text{PG}g_n^{\text{NH}_3\text{Cl}}$  as well.

solvents for lyophilization of  $PGg_n^{NHBoc}$ . Solution phase analytics of DPs are usually performed in either DMF or DMSO; Solvents which dissolve  $PGg_n^{NHBoc}$  well but are not in the class of polar-aprotics may produce erratic results, as is the case with GPC performed on  $CHCl_3$  solutions (see the comments on swelling vs. dissolution in the following paragraphs). The handling of  $PGg_n^{NH_3TFA}$  mostly occurs in aqueous or methanolic solutions, and  $PGg_n^{NH_2}$  is generated almost exclusively by deprotonation of  $PGg_n^{NH_3TFA}$  *e.g.* in DMF and then used in post-polymerization modification reactions, immediately. The particular insolubility of *N*-deprotected DPs in organic solvents such as methylene chloride – in which protected DPs and other reaction components are usually very well soluble – provides a simple qualitative tool *e.g.* to assess whether in a deprotection reaction significant transformation to  $PGg_n^{NH_3TFA}$  or  $PGg_n^{NH_2}$  has occurred.

Solubility as used above in a qualitative and somewhat colloquial sense should however not be confused with the term solvent quality as it is commonly employed in the context of linear polymers: There, depending on the binary polymer/solvent system and the exact temperature, a polymer may be in one of three states: Well-swollen in a good solvent where the interactions between solvent and RUs are fairly strong, the  $\Theta$  state where the interactions among RUs and between solvent and RU are in balance, and the collapsed state in a poor solvent, which interacts less strongly with the polymer RUs than they do among themselves.

The discussion of DP solvent quality requires more differentiated consideration, as the RUs are not compact: Chain diameters for high  $g$  can reach 10 – 20 nm, and particularly at high  $g$  there is an “interior” and “exterior” part of the structure. Work by Gstrein *et al.* has established a semiquantitative understanding of solvent quality in this context by use of a solvatochromic probe attached close to the DP backbone.<sup>98</sup> This has provided information on the degree of swelling/solvent penetration for polymers up to  $g = 4$ . In this series, the polar-aprotic solvents such as DMSO and DMF are best able to penetrate the DPs, followed by 1,4-dioxane, alcohols and less polar aprotic solvents and lastly aromatic solvents. As periphery and branchwork differ structurally, it is possible that some solvents which are capable of interacting peripherally with the DPs do not significantly penetrate the DP structure. Such a solvate more closely resembles a colloidal dispersion in which only the outermost, solvent-accessible parts of the structure determine solubility, rather than a typical polymer solution. A possible representative of this state is *e.g.* methylene chloride, high  $g$  DP “solutions” of which tend to appear slightly blueish, likely as a result of Tyndall scattering. This is not the case in the more deeply penetrating solvents such as DMF, DP solutions of which tend to appear clear at similar polymer concentrations, even though DMF ( $n_D = 1.431$ ) and methylene chloride ( $n_D = 1.424$ ) have quite similar refractive indices.<sup>175</sup>

#### Peculiarities of molar mass determination

Gel permeation chromatography (GPC) is the most frequently used technique for the determination of the molar mass and the molar mass distribution of polymeric samples. For polymers soluble in organic solvents, PS or PMMA prepared by anionic polymerization are commonly employed as calibration standards.

However, for DP samples GPC is generally unable to provide accurate molar masses: With every increment in  $g$ , the molar mass per repeat unit approximately doubles, while by virtue of the branched nature of the dendritic side chains the increased molar mass is confined to a relatively small volume. This results in an *underestimate* of molar mass for DPs, with molar masses of > 10 kDa/RU for high  $g$

when compared to conventional linear polymers with molar masses per repeat unit in the range of ca. 100 – 500 Da. Running counter to this trend, and thereby complicating matters, the increased steric demand of dendritic side chains by first approximation is expected to result in an increase of the DPs' persistence lengths with  $g$ . This factor leads to an *overestimate* of molar mass when compared to more flexible conventional polymers. While the interplay of these two factors is complex, the *underestimate* of molar mass due to increasing molar mass per unit length appears to dominate at high  $g$ . An additional factor of uncertain impact is the exclusion of solvent from the DPs' interior which becomes more prominent with  $g$ :<sup>98</sup> Not the entire volume of the DP is swollen equally well.

These peculiarities mean that commercial calibration standards are not suitable for the accurate molar mass determination of the DPs discussed here. Only the DPs themselves would be able to accurately mirror the particular  $g$  dependence of the variables discussed above. Such series of DPs can be synthesized,<sup>167,176</sup> however establishing suitable calibration curves would be connected with an amount of synthetic and analytical effort which is beyond the scope of this work. While therefore GPC is not able to provide accurate results in terms of molar mass, the very high reproducibility of the method is extremely useful in the qualitative assessment of molar mass changes, as will be demonstrated in the course of this thesis (particularly chapter 3).

Attempts at alternatively determining molar masses by light scattering were made but suffered from significant inconsistencies. Preliminary static light scattering measurements in methanolic solutions were conducted in the group of Prof. Manfred Schmidt (Uni Mainz). The issues appeared related to  $g$ -dependent solvent quality, as significant solubility issues (loss of material after filtering) were encountered for  $g > 4$  even when fairly short DPs ( $P_n \approx 50$ ) were employed (unpublished results). Results presented particularly in chapter 4 of this thesis suggest that the application of uniform model assumptions used in the analysis of scattering data may likewise be inappropriate. An accurate method of molar mass determination for thick molecules such as DPs, which approach colloidal dimensions, remains elusive.

#### 1.6.4. Prior investigations and modifications

The DPs of the type  $PGg^{NH^Y}$  have been employed for a variety of purposes over the course of investigations spanning more than a decade. A wide range of modifications has been possible in particular thanks to the peripheral amines which serve as an extremely versatile platform for the attachment of functional groups. Simultaneously, *N*-hydroxysuccinimide esters such as *e.g.*  $DG1^{NHBoc}$  (**20**) are readily available and a great variety of functional groups can be attached to the periphery of DPs in a straightforward manner. One illustration of this is the previously mentioned method used to covalently attach enzymes or other bio(macro)molecules to  $PGZ_n^{NH_3TFA}$ .<sup>128,129</sup> There, the DPs mostly serve as a glue, creating a strong contact with oxide surfaces while also covalently connecting multiple enzymes.

More extensive modifications vary from simple anion exchange, *e.g.* from trifluoroacetate to mesogenics such as lauryl, sulfate, permitting  $PG3_n^{NH_3(lauryl\ sulfate)}$  **39** to self-assemble into liquid crystalline structures,<sup>168,177</sup> over functional group modifications such as the addition of a succinimidyl ester in **40** which enables the DP to be charged negatively,<sup>178</sup> to conscious manipulation of DP rheology and assembly behavior by modification of peripheral groups, *e.g.* replacing standard NHBoc moieties with far more strongly interacting ureidopyrimidinone groups (**42**)<sup>179</sup> or with less strongly interacting oligoethylene-based dendrons (**41**).<sup>176</sup> This displays the breadth of possible peripheral modifications and forms an important precedent for the work presented in this thesis, which is mostly focused on the modification and investigation of high-generation DPs ( $g > 4$ ).

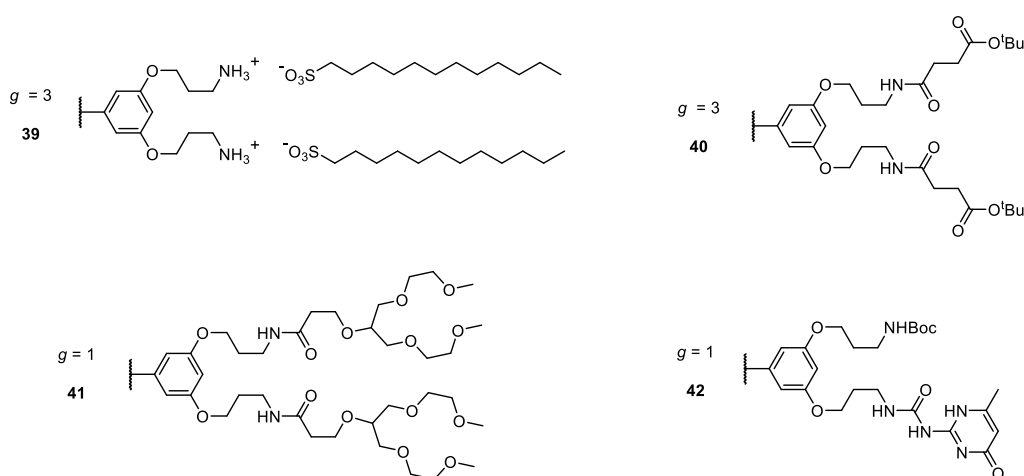


Figure 1-21: Examples of peripheral modifications to DPs of the type  $PGg^{NH^Y}$ . Only the peripheral units are shown for a polymer of the indicated  $g$ .

Other investigations performed on this class of DPs have focused more on the interior of the DPs than the very periphery. In particular, this concerns effects of steric crowding. Studies by Gstrein *et al.*<sup>98,99</sup> and Scherz *et al.*<sup>179</sup> recently demonstrated that functional groups forming specific “dead ends” installed in proximity to the DP backbone (*e.g.* **42**, Figure 1-21) are rapidly and efficiently shielded from interactions with the environment (solvents, reactants, and parts of the same or another DP molecule) with increasing  $g$  of the surrounding dendritic side chains. Agreeing with general trends

regarding the scaling behavior of dendritic structures discussed in section 1.5, such effects become apparent at far lower  $g$  for DPs than is the case for comparable dendrimers.<sup>180</sup>

The nature of DPs as molecules with a significant and variable thickness has also been the object of several studies. In particular, DPs have proven easy to manipulate by atomic force microscopy (AFM). Studies by Rabe *et al.*<sup>181,182</sup> have demonstrated that individual, suitably functionalized DPs can be manipulated and covalently connected by physically moving them with an AFM tip. Borkovec *et al.* have exploited the particular properties of DPs for the application of sophisticated nano-handling techniques.<sup>183–185</sup> In relation to DPs' thickness, a series of investigations have been concerned with the size, shape and compactness of DPs in various states. These include investigations on the adsorbed state, *e.g.* by AFM<sup>148,174</sup> or by electron microscopy,<sup>148,172</sup> as well as first attempts at solution-phase characterization by neutron scattering<sup>186</sup> or by cryo-TEM (which will be expanded in this thesis, see chapter 4). Hinderberger *et al.* have investigated the guest uptake capabilities of DPs of the type  $\text{PGg}_n^{\text{NH}_3\text{TFA}}$ , using EPR spectroscopy to probe the local environment of spin-labelled guest molecules.<sup>187,188</sup>

## 1.7. Scope and Objectives

Only very few DP syntheses have progressed much beyond  $g = 3$ . This is in curious contrast to dendrimer syntheses, which in many cases have progressed beyond  $g = 5$  (see section 1.5). This may be suggestive of the syntheses of DPs being more demanding than that of dendrimers – certainly, the preparation of structurally perfect DPs by divergent methods is time-demanding (as several ten thousand reactions may have to proceed on a single, sterically strongly congested molecule). However, the chemical transformations involved in DP synthesis are no more exotic than those employed for the preparation of dendrimers. More likely, this difference is the consequence of a lack of interest in DPs in the general research community. This is unfortunate, as DPs offer interesting opportunities which dendrimers do not. In particular, as discussed in section 1.5, DPs offer the potential to achieve structures at  $g_{\max}$  at far lower  $g$  than would be possible in similar dendrimers.

Structures at and above  $g_{\max}$  are of fundamental interest to polymer science, as they represent a transition from classical molecules to well-defined structures more closely resembling colloids. Such molecular colloids or “molecular objects” are expected to behave differently from their classical small-molecule and polymer analogues in some respects.<sup>87</sup> For instance, they are expected to interact with solvents only in their very periphery, as their interior is densely packed with dendritic matter. Unlike classical soft colloids produced *e.g.* by microfabrication techniques or by miniemulsion polymerization,<sup>153</sup> dendritic molecules above their  $g_{\max}$  are structurally very well-defined, nanometer sized objects the dimensions of which can be very tightly controlled, usually in discrete steps of a few nanometers. DPs with  $g > g_{\max}$  are of particular interest as they are worm-like or potentially rod-like soft colloids, *i.e.* anisotropic molecules within which properties may vary along multiple geometric axes.

The work presented in the following therefore had two main objectives: The first goal was to access DPs of the type  $\text{PG}g_n^{\text{NHBoc}}$  with high average chain lengths ( $P_n \gg 100$ ) at and above  $g_{\max} \approx 6 - 7$ . To that end, DP main-chain scission at  $g = 5$  needed to be prevented, *i.e.* the synthetic barriers which in the past had prevented the preparation of  $g > 5$  DPs of high structural perfection had to be overcome. In order to permit a systematic study of the effects of dense crowding near  $g_{\max}$ , the strategies to be developed not only needed to prevent main-chain scission. They also had to provide  $g > 5$  DPs with higher structural perfection than previously possible.

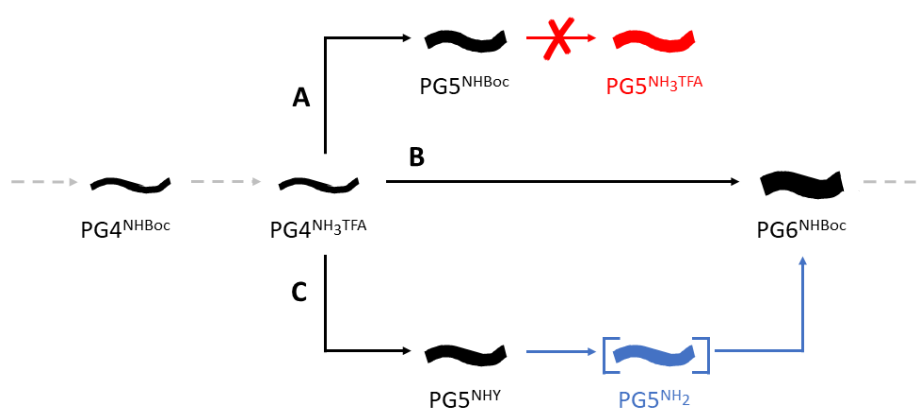
The prevention of backbone degradation in the key synthetic step from  $\text{PG}6_n^{\text{NHBoc}}$  to  $\text{PG}5_n^{\text{NHBoc}}$  was anticipated to open the path for the preparation of even higher  $g$  DPs, at least of  $g = 8$ , where the estimated value of  $g_{\max}$  would certainly be surpassed. The exploration of the properties of such very high  $g$ , structurally more perfect DPs was the second main objective of the work presented here. As systematic access to  $g > g_{\max}$  structures had not been possible prior to the solution of the problem of main-chain scission, these questions were of fundamental interest. A particular focus lay on the dependence of properties such as rheological behavior, DP conformations *etc.* on the dendritic generation  $g$ .

## 2. Overcoming Main-Chain Scission

The contents of the following chapter have in large parts been published as: Messmer, D.; Kröger, M.; Schlüter, A. D. *Macromolecules* **2018**, *51*, 5420-5429.

### 2.1. Motivation/goals

This chapter is concerned with circumventing main-chain scission; More in-depth investigations of this synthetic barrier are presented in chapter 3. The occurrence of main-chain scission at  $g = 5$  in the standard synthetic approach (route **A**, Scheme 1-8b)<sup>169</sup> represented a major roadblock on the path to DPs at and above  $g_{\max}$  (i.e. DPs of  $g \geq 6$ ). A “ $g + 2$ ” route was devised to circumvent the issue of main-chain scission, skipping  $g = 5$  entirely and instead reacting  $\text{PG4}_n^{\text{NH}_3\text{TFA}}$  with a 2<sup>nd</sup> generation dendronization agent (**37**, see Figure 1-19) to directly afford  $\text{PG6}_n^{\text{NHBoc}}$ . This synthetic approach will in the following be referred to as route **B** (Scheme 2-1).<sup>189</sup> While this strategy successfully prevented chain degradation in the synthesis of  $\text{PG6}_n^{\text{NHBoc}}$ ,<sup>174</sup> it came at a significant cost: **37** (Fig. Figure 1-19a) is fairly large in its own right, at  $M = 1266 \text{ g mol}^{-1}$  and a corresponding steric bulk. Its reaction with amines in  $\text{PG4}_n^{\text{NH}_2}$  was incomplete: The conversion of functional groups in the resulting  $\text{PG6}_{500}^{\text{NHBoc}}$  was low at  $\chi \approx 92 \%$  when compared to  $\chi \geq 99.5 \%$  achieved in the “ $g + 1$ ” steps usually employed in the standard graft-from procedure (Scheme 1-8b).<sup>174</sup> The remaining reactive amines were not accessible to **37** even after prolonged reaction times, but the  $g = 1$  dendronization agent **20** was still able to react some of the amines.<sup>172</sup>



Scheme 2-1: Visualization of the attempted routes to  $\text{PG6}_n^{\text{NHBoc}}$ . **A**: classical NHBoc-based “ $g + 1$ ” pathway (Scheme 1-8b), resulting in main-chain scission at  $g = 5$  for  $n > 50$ . **B**: NHBoc-based “ $g + 2$ ” route to (imperfect) **B**- $\text{PG6}_n^{\text{NHBoc}}$ .<sup>174</sup> **C**: Envisioned route via  $\text{PG5}_n^{\text{NHY}}$  and  $\text{PG5}_n^{\text{NH}_2}$ , affording **C**- $\text{PG6}_n^{\text{NHBoc}}$ ; Y is a protecting group suitable for N-deprotection under neutral or basic conditions. Reprinted with permission from Messmer, D.; Kröger, M.; Schlüter, A. D. *Macromolecules* **2018**, *51*, 5420-5429, copyright 2018, American Chemical Society.

While this discrepancy might seem fairly minor at first glance, it translates to significant deficiencies in molar mass. Even for relatively short 500mers, the losses are substantial when compared to ideal structures:  $\sim 1 \text{ MDa}$  of the overall theoretically achievable molar mass are lost on the path to **B**- $\text{PG6}_{500}^{\text{NHBoc}}$ .<sup>150</sup> Moreover, the defects introduced in the preparation of the  $g = 6$  DPs propagated are propagated and amplified at higher generations through continued dendritic growth.

In studies of these structurally deficient polymers by AFM and by electron microscopy, increasing corrugation of the DP chains was observed for  $g > 6$ , ascribed precisely to this propagation of defects to the higher  $g$  polymers.<sup>174</sup>

This situation is unsatisfactory particularly with regard to  $g_{\max}$ : By virtue of the very high functional group conversion values achieved, the dendritic side chains of DPs up to  $g = 5$  are essentially monodisperse and closely approach the perfect structures.<sup>150,169</sup> This does not hold true for **B**-PG6<sub>500</sub><sup>NHBoc</sup> and the higher  $g$  DPs derived therefrom. This renders  $g_{\max}$  considerations moot due to side-chain polydispersity. Further complicating matters, because of the “ $g + 2$ ” nature of steps on route **B**, the polymers synthesized in this manner do not constitute a homologous series of DPs.

Circumventing main-chain scission on the  $g = 5$  level was therefore a main motivator for the work presented in this thesis. Based on the initial hypothesis that charge-charge repulsion is the culprit responsible for main-chain scission in PG5 <sub>$n$</sub> <sup>NH<sub>3</sub>TFA</sup> ( $n > 50$ ), the direct synthesis of the corresponding free-base DPs PG5 <sub>$n$</sub> <sup>NH<sub>2</sub></sup> was attempted, in the hope that this polymer would not undergo scission. The synthetic implementations of this rudimentary strategy, relying on protecting groups or deprotection methods other than the acid-mediated cleavage of NHBoc will in the following be referred to as route **C** (Scheme 2-1).

In order to facilitate the differentiation between the synthetic families of DPs presented in this thesis, particularly DPs prepared by route **B** and **C** will in the following often be denoted with an identifying prefix where clarity is required. For example, **B**-PG6<sub>500</sub><sup>NHBoc</sup> shall refer to PG6<sub>500</sub><sup>NHBoc</sup> prepared by route **B**, *i.e.* in a “ $g + 2$ ” step from PG4<sub>500</sub><sup>NH<sub>3</sub>TFA</sup>, using the  $g = 2$  dendronization agent **37**. Similarly, **C**-PG6<sub>500</sub><sup>NHBoc</sup> will refer to PG6<sub>500</sub><sup>NHBoc</sup> prepared using an implementation of route **C**, starting from a suitable precursor polymer of  $g = 5$ . For simplicity of reference, the nomenclature for  $g > 6$  DPs will be based not on the synthetic step leading directly to the polymer in question, but on the step by which the crucial precursor at the  $g = 6$  level was derived; **C**-PG7<sub>500</sub><sup>NHY</sup>, by way of example, is derived from a precursor of the type **C**-PG6<sub>500</sub><sup>NHY</sup>.



## 2.2. Protecting group strategies

The synthesis of high  $g$  DPs requires many steps and is quite time-consuming due to extremely long reaction times. Careful consideration of suitable protecting groups and deprotection strategies is therefore necessary ahead of synthetic attempts, in order to avoid wasting time and precious material. Next to standard considerations applicable for small-molecule synthesis, such as functional group compatibility, the following requirements specific to DP synthesis should be addressed in the selection of prospective chemistries, roughly in the order presented below:

- *Acidity*: Following the initial working hypothesis for the cause of main-chain scission, (compare chapter 3) the unstable polyelectrolytic intermediates such as  $\text{PG5}_n^{\text{NH}_3\text{TFA}}$  must be avoided. To this end, removal of the protecting group must proceed under neutral or preferably basic conditions, such as to afford the free-base intermediate  $\text{PG5}_n^{\text{NH}_2}$  instead.
- *Solubility*: The intermediates of the type  $\text{PG}g_n^{\text{NH}_2}$  are problematic as they are soluble in only a limited range of solvents, largely limited to MeOH and strongly polar aprotic solvents such as DMF or DMAc. In all other solvents, DPs of the type  $\text{PG}g_n^{\text{NH}_2}$  tend to precipitate and aggregate (often irreversibly), likely due to the formation of strong hydrogen bond networks. The protected polymer and the deprotection conditions should therefore be compatible with a polar-aprotic solvent.
- *Compatibility of deprotection with dendronization*: This requirement is a direct consequence of the above criterion of solubility. The polyelectrolytes  $\text{PG}g_n^{\text{NH}_3\text{TFA}}$  are readily isolated as solids which redissolve in water, MeOH, TFA, and polar-aprotic solvents. As this is not true for the free-base analogs  $\text{PG}g_n^{\text{NH}_2}$  (see subsection 1.6.3), the isolation and purification of the target intermediate  $\text{PG5}_n^{\text{NH}_2}$  is likely not possible. Preferentially, the deprotection conditions and the products of deprotection should therefore be compatible with dendronization in a tandem or sequential reaction. This may be challenging for some conditions widely applied to small-molecule synthesis, particularly because of the very long reaction times (weeks). Steps used to quench or remove such reagents and/or products need to comply with the above conditions in order to be viable.
- *Efficiency*: In order to surpass the functional group conversion values achieved using route **B**, the deprotection reaction involved in route **C** should proceed close to quantitatively.
- *Simplicity*: While not a strict necessity, operationally demanding conditions (*e.g.* strict exclusion of moisture or oxygen) should be avoided, especially in view of the very long reaction times, which complicate the adherence to such conditions.
- *Popularity*: Myriad protecting groups exist – particularly for amines, which are highly relevant to peptide and natural product synthesis. While this is a very crude generalization, much-used protecting groups are to be preferred because their popularity is associated with a) facile access, b) chemical robustness and wide-ranging compatibility and c) the availability of varied deprotection protocols.

Using the above criteria, the expansive collections of  $N$ -protecting groups in the literature<sup>190–192</sup> were surveyed for suitable candidates. Initially, the protection of reactive amines in the form of amides (specifically: acetamides and trifluoroacetamides) appeared attractive, as amides are very easily prepared. However, preliminary experiments revealed significant problems with their removal,

which demands relatively harsh conditions. Due to concerns regarding chemoselectivity vs. amides in the interior of the dendrons, amide protecting groups were therefore not investigated in a more than cursory fashion and will not be discussed here. Fortunately, carbamate protecting groups provide more viable alternatives, offering greater reactivity and a large structural diversity with a corresponding wealth of possible deprotection mechanisms and conditions. Naturally, the following selection of protecting groups is heavily influenced by findings from SPPS and natural product synthesis, fields in which issues of N-protection have been explored thoroughly.

- *tert*-Butyloxycarbonyl (Boc): In addition to Brønsted acid-mediated deprotection using *e.g.* TFA, HCl or HF, pH-neutral deprotection conditions for the cleavage of NHBoc do exist. Specifically, these include thermolysis, Lewis acid-mediated cleavage, and attack by nucleophiles such as F<sup>-</sup>.
- 2,7-Di-*tert*-butylfluorenylmethyloxycarbonyl (Fmoc\*): The more frequently employed Fmoc protecting group cannot be applied to DP syntheses due to solubility issues; However, the more soluble Fmoc\* protecting group offers a convenient alternative. Both groups can be removed by simple treatment with a suitable organic base, although the cleavage of NHFmoc\* is slower than that of NHFmoc.<sup>190</sup> Attractively, NHFmoc\* has previously been employed to orthogonally protect DPs,<sup>193</sup> demonstrating the feasibility of quantitative deprotection in a DP.
- Benzyloxycarbonyl (Cbz): The Cbz group offers orthogonality to many other protecting group chemistries as it is fairly stable to acids and bases, but labile under reducing conditions. Specifically, hydrogenation – mediated by homogenous or heterogenous catalysts, using molecular H<sub>2</sub> or transfer hydrogenation – is a very mild method of NHCbz cleavage with a high tolerance for other functional groups.
- Allyloxycarbonyl (Alloc): Similar to NHCbz, the NHAlloc group is cleaved under conditions widely orthogonal to other groups, proceeding *via* a transition-metal catalyzed deallylation, typically using a Pd<sup>0</sup> species. The conditions for cleavage are much more involved than is the case for the above options, but Alloc is still attractive as a small, well-soluble moiety for the removal of which many different catalytic conditions have been developed.

Among these candidates, only the Alloc protecting group led to the desired success. The reasons for the failure of the other approaches are outlined briefly in section 2.3. The remainder of this chapter discusses the successful implementation of route **C** using the Alloc protecting group and the characterization of the resulting DPs.

## 2.3. Failed attempts

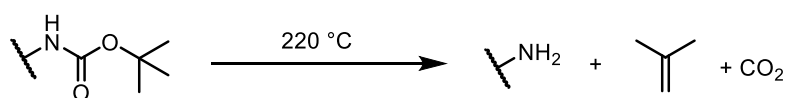
The following section briefly outlines deprotection methodologies for NHBoc protecting groups other than NHALloc which were investigated for the desired synthesis of  $PG5_n^{NH_2}$ . Details can be found in the Experimental chapter (section 8.2).

### 2.3.1. Boc

The Boc protecting group is particularly attractive since no modifications of DP structures would be necessary, if an alternative to acid-mediated NHBoc cleavage were available. Although treatment with a Brønsted acid (most commonly HCl or TFA) is by far the most popular option, the very diverse applications of the Boc protecting group in natural product synthesis have led to the development of other methods not based on protic acids.

#### Thermolysis

The chemically simplest approach to Boc removal is thermolysis: The NHBoc moiety is thermally labile and spontaneously decomposes at temperatures above 200 °C (Scheme 2-2). In DPs of the type  $PG_n^{NHBoc}$ , the thermally induced decomposition occurs at *ca.* 220 °C in N<sub>2</sub> atmosphere. Thermolysis proceeds to completion and is moderately useful for analytical purposes.<sup>174</sup>



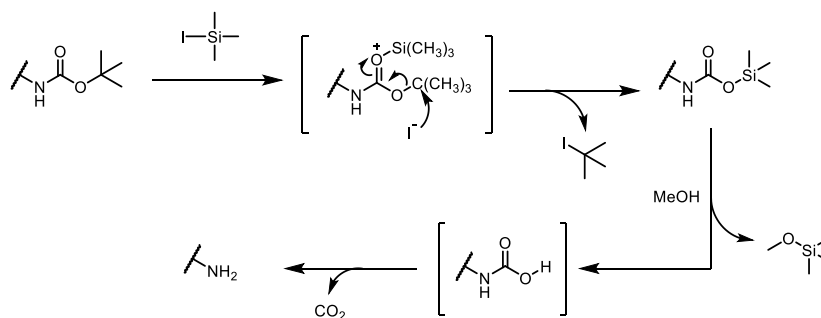
Scheme 2-2: NHBoc thermolysis; isobutylene and CO<sub>2</sub> are the most likely byproducts under thermolytic conditions.

Thermolysis by simple heating of neat polymer led to apparently complete deprotection, however the resulting polymer was entirely insoluble *e.g.* in DMF. Likely, this is the result of the formation of a strong hydrogen bond network among the polyamines resulting from deprotection, to which the tendency of the DPs to form aligned fibers certainly contributes (compare section 5.5 and Figure 3-15a).

Solvent-assisted thermolysis of Boc-protected amines is possible,<sup>194</sup> *e.g.* using hexafluoroisopropanol at reflux (58 °C).<sup>195</sup> Even after prolonged times (3 d) at reflux, precipitation testing did not indicate sufficient deprotection. When higher-boiling, good solvents for DPs (DMF, DMSO) were used, degradation of the polymers likely occurred, rather than clean deprotection.

#### Lewis acid-mediated cleavage

As is the case for Brønsted acids<sup>196</sup>, Lewis acids may coordinate to the NHBoc carbamate, thereby activating it toward nucleophilic attack. This may be achieved for example using Sn(OTf)<sub>2</sub>,<sup>197</sup> BF<sub>3</sub>·Et<sub>2</sub>O,<sup>198</sup> or Iodotrimethylsilane (TMSI).<sup>199</sup> The latter reacts with carbamates to form an intermediate trimethylsilyl carbamate, which can be treated with methanol or water to afford the desired amine under fairly mild, non-acidic conditions (Scheme 2-3).

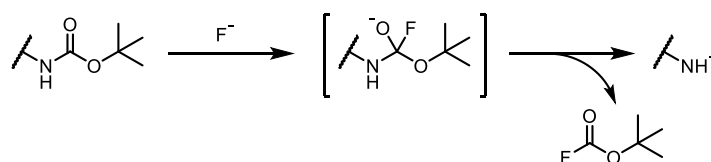


Scheme 2-3: TMSI-mediated NHBoc cleavage and successive methanolysis, following the suggested mechanism for ester scission.<sup>199</sup>

This in principle offers a convenient mode of deprotection. Attempts at removing NHBoc using a fourfold excess of TMSI indeed did result in the desired change in solubility, and <sup>1</sup>H-NMR spectra indicated significant deprotection (see Experimental, subsection 8.2.2). However, deprotection was by no means complete: Likely, more forcing conditions would be required. Furthermore, with strong Lewis acids such as TMSI, there is an inherent risk of accompanying ether cleavage within the dendritic branchwork, leading to the abandonment of this approach.

#### Nucleophile-mediated cleavage

Nucleophilic reagents are used only rarely in the removal of the Boc protecting group. The reason for this can perhaps be found in the fairly high stability of NHBoc towards commonly encountered conditions involving nucleophilic species, such as base hydrolysis or reduction by metal hydrides. However, “naked” fluoride (usually in the form of anhydrous tetrabutylammonium fluoride, TBAF) has been shown to cleave carbamates, in a reaction proposed to follow the mechanism shown in Scheme 2-4.<sup>200</sup> However, even upon prolonged exposure to TBAF, no significant change in polymer solubility was observed, indicating no or only very little deprotection.



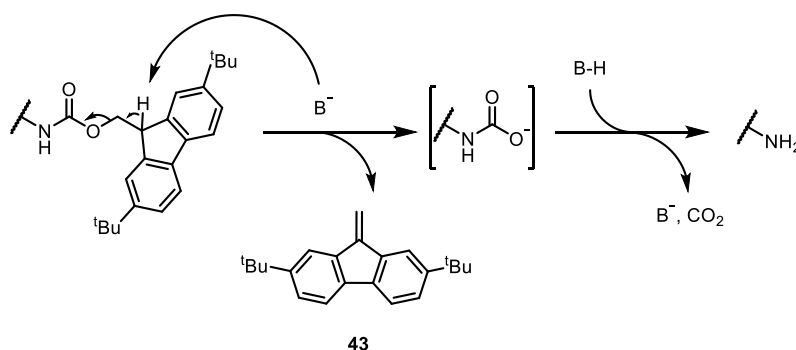
Scheme 2-4: Proposed pathway of carbamate decomposition for NHBoc.<sup>200</sup>

#### 2.3.2. Fmoc\*

The main attraction of Fmoc\* as an *N*-protecting group<sup>201</sup> for the purposes of DP synthesis are the simple deprotection conditions, which consist of the treatment of protected amines with suitable organic bases. For Fmoc, secondary amines such as piperidine or morpholine are usually employed,<sup>202</sup> simultaneously acting as scavengers for the liberated dibenzofulvene. This is desirable particularly in SPPS, where the spontaneous polymerization of dibenzofulvene to an insoluble product may present significant issues. Piperidine was successfully used in the NHFmoc\* deprotection of low *g* DPs bearing orthogonally protected peripheral amines. The polymers in that case were synthesized using the macromonomer approach.<sup>193</sup> However, in the case of DP deprotection, followed by or conducted in

tandem with dendronization, secondary amine bases would be counterproductive, as they would consume the dendronization agents (*e.g.* **20**).

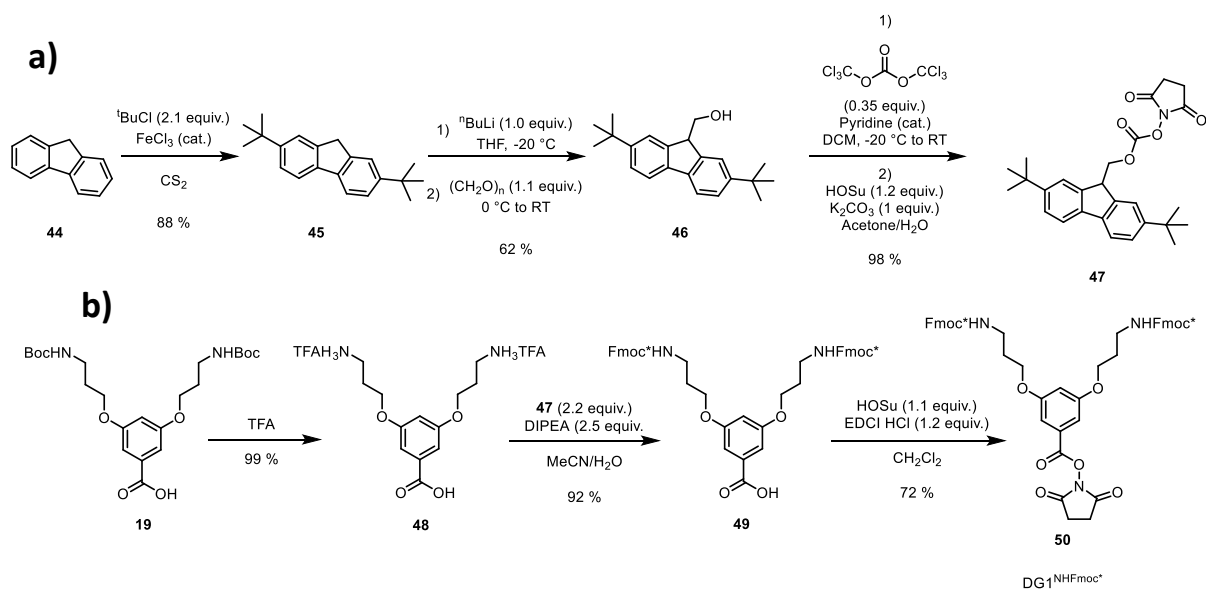
Non-nucleophilic bases such as triethylamine or Hünig's base (diisopropylethylamine, DIPEA) also promote the deprotection reaction (Scheme 2-5), however at much lower rates than the standard secondary amines.<sup>203</sup> This reactivity profile is well-established for the case of Fmoc, and likely the overall trends can be transferred to its more soluble, but slightly less reactive cousin Fmoc\*. An even more promising alternative to morpholine or piperidine is DBU,<sup>204</sup> a non-nucleophilic base often used as a catalyst, *e.g.* in amide bond formation reactions,<sup>205</sup> making it a suitable agent for promoting dendronization, as well.



Scheme 2-5: Base-mediated cleavage of NHFmoc\*.

It was therefore hoped that it would be possible to prevent main-chain scission by subjecting  $\text{PG4}_n^{\text{NH}_3\text{TFA}}$  to dendronization with a suitable, NHFmoc\*-bearing dendronization agent to afford  $\text{PG5}_n^{\text{NHFmoc}^*}$  (**30**), which would then be subjected to tandem deprotection/dendronization involving a suitable basic promoter such as DBU. This required, first, the synthesis of a suitable Fmoc\*-bearing dendron. The synthesis of multi-gram quantities of an *N*-hydroxysuccinimide-based reagent Fmoc\*OSu (**47**) was achieved starting from fluorene (**44**), mostly following literature procedures<sup>193,201</sup> (Scheme 2-6a, also see Experimental, subsection 8.2.2). Using **47**, a dendronization agent  $\text{DG1}^{\text{NHFmoc}^*}$  (**50**) was prepared in multi-gram quantities, permitting the exploration of dendronization conditions (Scheme 2-6b).

Unfortunately, a number of attempts using different approaches to the synthesis of model DPs of  $g = 2$  or  $g = 3$  led to the realization that the use of the Fmoc\* protecting group is not compatible with graft-from synthesis: Slightly basic conditions are required for complete dendronization to occur. When substoichiometric amounts of base were employed, no polymer could be isolated; when a stoichiometric amount of base or a very slight excess were used, partial deprotection was observed, as evidenced by the formation of 2,7-di-*tert*-butyldibenzofulvene **43** (Scheme 2-5) during dendronization (see Experimental, subsection 8.2.2, for details). As a large excess of the dendronization agent (5 equiv./amine) is usually employed in dendronization, simultaneous partial deprotection would lead to hyperbranching. Just as is the case with large numbers of defects, this leads to polydisperse, non-dendritic side chains and cannot be tolerated.



Scheme 2-6: Syntheses of a) **47** (Fmoc\*OSu) and b) **50** (DG1<sup>NHFmoc\*</sup>). The standard synthetic route for the synthesis of similar dendronization agents starting from a methyl ester such as **16** was deemed unfeasible in this case due to the base lability of Fmoc\*.

### 2.3.3. Cbz

The NHCbz moiety has previously been employed in the synthesis of low *g* DPs.<sup>206</sup> The Cbz group can easily be removed by catalytic hydrogenolysis in small molecules. A suitable polymer, PG5<sup>NHCbz</sup><sub>500</sub> (**29**), had been prepared previously<sup>172</sup> and its synthesis has been improved significantly for this work (see Experimental, subsection 8.2.2). Preliminary work on the deprotection of PG5<sup>NHCbz</sup><sub>500</sub> had been performed by Dr. Hao Yu,<sup>172</sup> and further attempts were made here.

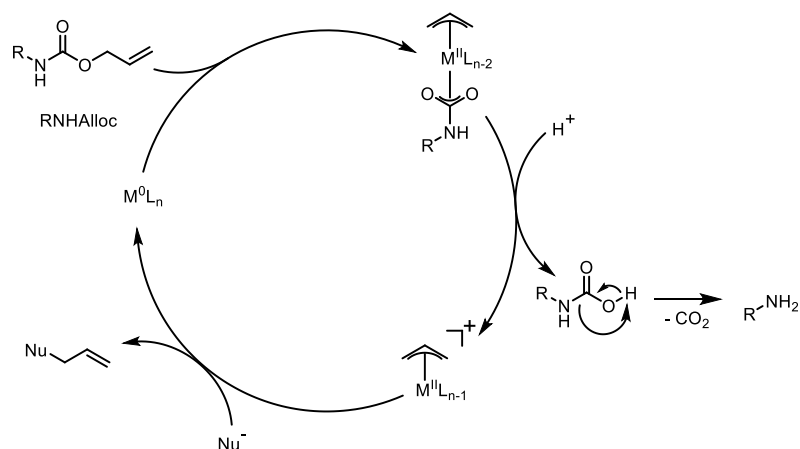
Both direct hydrogenation (using H<sub>2</sub>) and catalytic transfer hydrogenation (using ammonium formate<sup>207</sup>) were attempted. However, in all cases, no significant deprotection – as indicated by precipitation testing in DCM – was achieved. In light of the simultaneously achieved very encouraging progress in the deprotection and dendronization of Alloc-protected DPs (section 2.4), no further experiments involving the deprotection of PG5<sup>NHCbz</sup><sub>500</sub> (*e.g.* using homogenous hydrogenation catalysts) were made.

## 2.4. Implementation of an NHALloc-based strategy for route C

### 2.4.1. Rationale & selection of conditions

Boc, Fmoc and Cbz are essential protecting groups in SPPS, but Alloc is less frequently used.<sup>190</sup> While not commonly employed in terminal *N*-protection, it is often used for side-chain protection,<sup>208</sup> and therefore many conditions for the cleavage of the NHALloc moiety exist. Advantageously, Alloc-protected amines are readily accessible and well-soluble. Their deprotection, however, is less straightforward than is the case for the moieties discussed in section 2.3.

While the deprotection of NHALloc may be achieved by conditions generally applicable to carbamates – *e.g.* treatment with strong mineral acids<sup>190</sup> – the main attraction of this protecting group is the orthogonality to other commonly employed protecting groups: Alloc can be cleaved *via* deallylation promoted by transition metal catalysts (see Scheme 2-7 for a general mechanism). The resulting carbamic acid undergoes decarboxylation, liberating the desired free amine, and the catalytic cycle is closed by scavenging of the M<sup>II</sup>-allyl complex by a nucleophile.<sup>209</sup> Typically, the catalysts used are simple, commercially available Pd<sup>0</sup> species, such as Pd(PPh<sub>3</sub>)<sub>4</sub> or Pd<sub>2</sub>(dba)<sub>3</sub>.<sup>209</sup> Alternatively, Pd<sup>II</sup> precatalysts such as Pd(OAc)<sub>2</sub>,<sup>210</sup> or Ni<sup>0</sup> complexes (*e.g.* Ni(CO)<sub>4</sub>)<sup>211</sup> may be used. As judged from the literature, Pd(PPh<sub>3</sub>)<sub>4</sub> is by far the most popular catalyst for this application and was selected for attempts at DP deprotection; Pd(PPh<sub>3</sub>)<sub>4</sub> is fairly stable and readily available.



Scheme 2-7: Generalized catalytic cycle of NHALloc deprotection.<sup>209</sup>

A crucial role in the deprotection reaction is occupied by the nucleophilic scavenger employed to regenerate the catalytically active species. In the absence of an additional nucleophile, the liberated amine may act as a scavenger of the  $\pi$ -allylpalladate, leading to overall *N*-allylation rather than deprotection. To suppress this, a wide range of nucleophilic scavengers have been investigated and used.<sup>208,209,212</sup> In addition to capturing the allyl fragment, some scavengers (*e.g.* Me<sub>2</sub>NTMS) capture the carbamic acid anion, forming labile carbamates which can later be hydrolyzed. Figure 2-1 provides an overview of the fairly diverse structure types used.

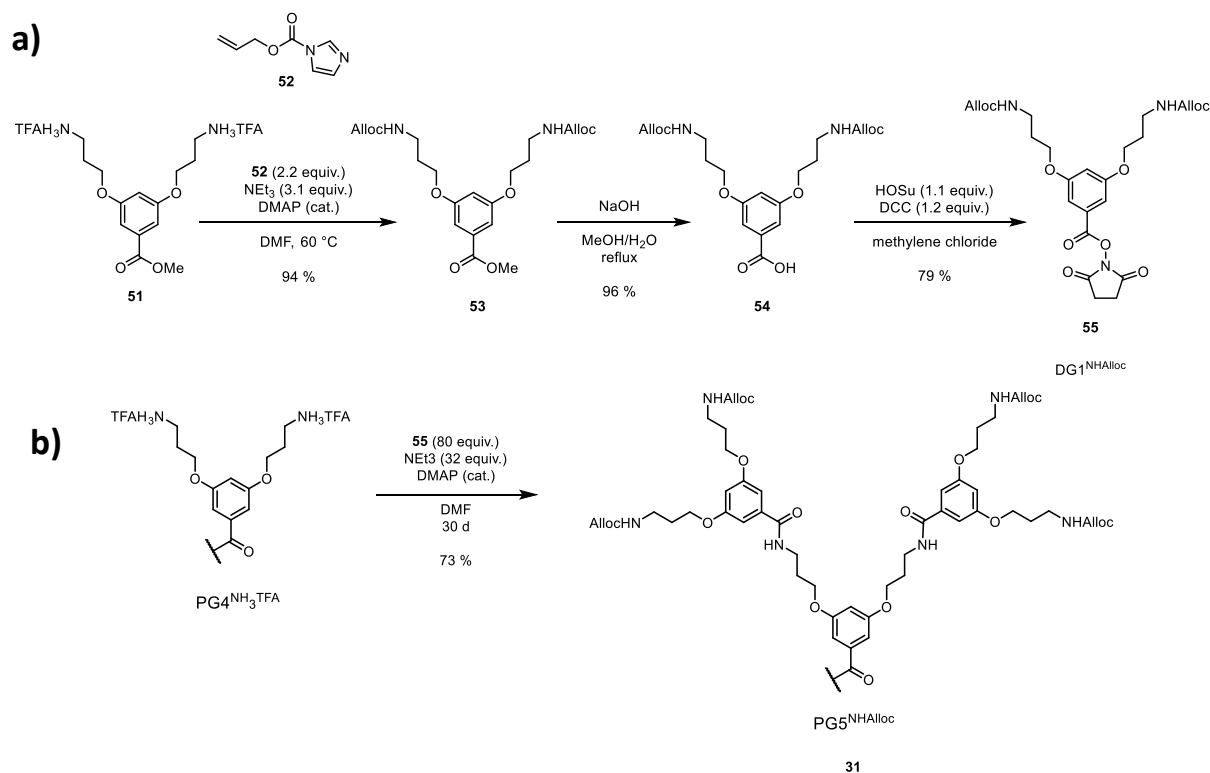




## 2.4.2. Syntheses of DG1<sup>NHAlloc</sup> and PG5<sub>500</sub><sup>NHAlloc</sup>

As was the case for the other protecting groups, the quantitative introduction of NHAlloc into a  $g = 5$  DP necessitated first the synthesis of a suitable dendron DG1<sup>NHAlloc</sup> (**55**) for use in a *graft-from* procedure. This was straightforward due to the favorable reactivity profile of NHAlloc.

Allyl chloroformate can be purchased at a reasonable price at the time of writing (Spring 2018).<sup>219</sup> This was not the case when first experiments using the Alloc protecting group were performed, and therefore initially the Alloc group was introduced using either the corresponding *N*-hydroxysuccinimide ester (synthesized from allyl alcohol, closely following the protocol for the synthesis of **47**) or allyl 1*H*-pyrrole-1-carboxylate (**52**), readily accessed from allyl alcohol and CDI.<sup>220</sup> The reaction of the *N*-deprotected dendron **51** with any of these three reagents afforded the NHAlloc-bearing methyl ester **53** in satisfactory yields. **53** was then saponified to the carboxylic acid **54**, in a direct adaptation of the synthesis of DG1<sup>NHBoc</sup> (**20**, see Scheme 1-8a). Upon esterification with HOSu, this afforded the desired active ester DG1<sup>NHAlloc</sup> (**55**) in overall good yields and 10 g quantities (Scheme 2-8a, see Experimental, subsection 8.2.1, for details).



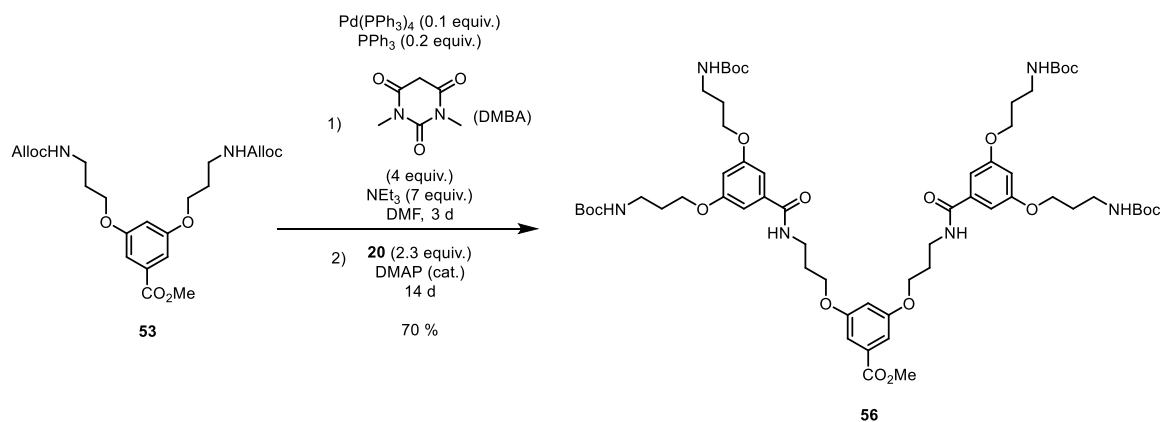
Scheme 2-8: a) Synthesis of DG1<sup>NHAlloc</sup> (**55**) using the CDI-derived **52** to introduce the protecting group. b) Synthesis of PG5<sub>500</sub><sup>NHAlloc</sup> (**31**).

Using DG1<sup>NHAlloc</sup>, the synthesis of PG5<sub>500</sub><sup>NHAlloc</sup> (**31**) was conducted using the well-established graft-from protocol, proceeding in satisfactory yields and with high functional group conversion (Scheme 2-8b). PG5<sub>*n*</sub><sup>NHAlloc</sup> was found to exhibit a solubility profile generally similar to that of PG5<sub>*n*</sub><sup>NHBoc</sup>, greatly facilitating the choice of solvents for later reactions. For testing purposes (see next section), PG2<sub>500</sub><sup>NHAlloc</sup> was prepared similarly, starting from the  $g = 1$  precursor.

### 2.4.3. Model reactions

In order to test the efficacy of the selected catalyst/nucleophile pair, Pd(PPh<sub>3</sub>)<sub>4</sub>/DMBA, two model reactions were conducted. First, a small-molecule reaction involving the deprotection of a low-*g* dendron was devised to test the compatibility with dendronization using the *N*-hydroxysuccinimide ester **20**. This was to check for acylation, a potential side reaction of concern in view of the reported reactivity of DMBA towards strongly activated carboxylic acids,<sup>217</sup> which needed to be addressed before proceeding to the actual polymer case.

To that end, the NHAlloc-bearing dendron **53** was subjected to deprotection conditions mimicking those envisioned for DP synthesis. In particular, this encompassed the use of excess base in order to ensure the full deprotonation of the liberated amines as well as the selected scavenger, DMBA (pK<sub>a</sub> ≈ 4.7). Such strongly basic conditions are slightly unorthodox for the removal of Alloc, but the only real concern in this regard is the occurrence of *N*-allylation, which is disfavored in the presence of acidic scavengers such as dimedone<sup>221</sup> or DMBA due to protonation of the liberated amines. The combination of Pd(PPh<sub>3</sub>)<sub>4</sub> and DMBA was selected specifically with this possibility in mind. A second change compared to standard small-molecule NHAlloc cleavage was the much-extended reaction time. Dendronization is controlled by the diffusion of amines to the periphery of the DP, as well as by the diffusion of fairly bulky reagents such as **20** into the periphery of DPs – which is quite densely substituted after the initial, well-accessible amines have reacted. Reaction times of several weeks must therefore be tolerated, instead of the few hours typical for such transformations in small-molecules synthesis.



Scheme 2-9: Reaction conditions for the *N*-deprotection and successive dendronization of **53**, affording the *g* = 2 dendron **56**.

The reaction proceeded as desired and provided the target dendron **56** in an isolated yield of 70 %, in range of values commonly achieved for similar small-molecule dendronization reactions using NHBoc-based chemistry. Having found that deprotection works well in the presence of a large excess of base, and that DMBA does not interfere significantly with dendronization, the deprotection/dendronization sequence was attempted using a comparatively rapidly accessible 2<sup>nd</sup> generation DP, PG2<sub>500</sub><sup>NHAlloc</sup> (see Experimental, subsection 8.2.1). The synthesis of **56** had shown that the solubility of Pd(PPh<sub>3</sub>)<sub>4</sub> in DMF is limited. Therefore, a mixture of DMSO and NMP was used, the addition of NMP being necessary as DMSO and NEt<sub>3</sub> are not freely miscible.

The reaction proceeded well, as judged by solubility tests, and the very first attempt indeed afforded the desired polymer **C-PG3**<sup>NHBoc</sup><sub>500</sub> (**24**). As judged by <sup>1</sup>H-NMR spectroscopy (Figure 2-2) the removal of Alloc proceeded to completion, and indeed the spectrum of the product of this first test reaction on a polymeric substrate was effectively superimposable with that of **A-PG3**<sup>NHBoc</sup><sub>500</sub>. Encouraged by this early success, further optimization of reaction conditions was performed directly on the target substrate, **PG5**<sup>NHAlloc</sup><sub>500</sub>.

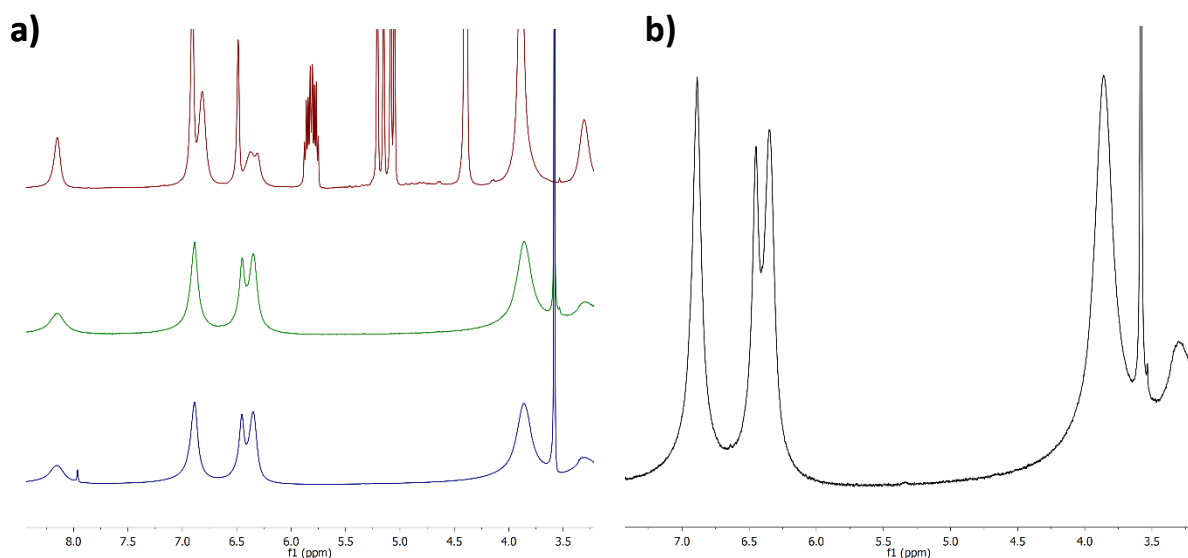


Figure 2-2: a) <sup>1</sup>H-NMR spectra of **PG2**<sup>NHAlloc</sup><sub>500</sub> (red), **A-PG3**<sup>NHBoc</sup><sub>500</sub> (green), and **C-PG3**<sup>NHBoc</sup><sub>500</sub> (blue). b) Magnification of the spectral region in which allylic signals appear for **C-PG3**<sup>NHBoc</sup><sub>500</sub>, which have disappeared completely.

#### 2.4.4. Optimization of the “g + 1” synthesis of PG6<sup>NHBoc</sup><sub>500</sub> from PG5<sup>NHAlloc</sup><sub>500</sub>

In switching to PG5<sup>NHAlloc</sup><sub>500</sub>, the need for some optimization rapidly became evident, particularly regarding the reaction solvent. The solubilities of Pd(PPh<sub>3</sub>)<sub>4</sub> and the intermediate *N*-deprotected polymer PG5<sup>NH<sub>2</sub></sup><sub>500</sub> proved problematic, which had not been the case with the small-scale, comparatively high-dilution model reaction starting from PG2<sup>NHAlloc</sup><sub>500</sub> (see subsection 2.4.3). Incomplete dissolution of reagents and, particularly, precipitation of the deprotected intermediate, should be avoided as these factors prevent reactions from proceeding to completion. To address these issues, a small screening of polar-aprotic solvents was conducted. The reasons for the failure of most solvent systems are listed in Table 2-1.

Table 2-1: Results of solvent screening for NHAlloc-based implementation of route C (Pd-catalyzed PG5<sup>NHAlloc</sup><sub>500</sub> deprotection, followed by dendronization to C-PG6<sup>NHBoc</sup><sub>500</sub>).

Solvent	Outcome of deprotection/dendronization
DMF	Only moderate solubility of Pd(PPh <sub>3</sub> ) <sub>4</sub> ; polymer precipitated briefly after addition of catalyst.
DMAc	Polymer precipitated briefly after addition of Pd(PPh <sub>3</sub> ) <sub>4</sub> .
NMP	Only limited solubility of PG6 <sup>NHBoc</sup> <sub>500</sub> at RT.
DMSO	Low solubility of Pd(PPh <sub>3</sub> ) <sub>4</sub> ; insufficiently miscible with NEt <sub>3</sub> ; polymer precipitated briefly after addition of Pd(PPh <sub>3</sub> ) <sub>4</sub> .
DMPU	Good solvent for all stages of deprotection/dendronization and all reagents; the resulting polymer appeared to have undergone a process of main-chain scission (compare chapter 3).
DMSO/NMP	Suitable solvent mixture for both deprotection and dendronization in ratios of ca. 3:2 – 2:1 (DMSO:NMP).

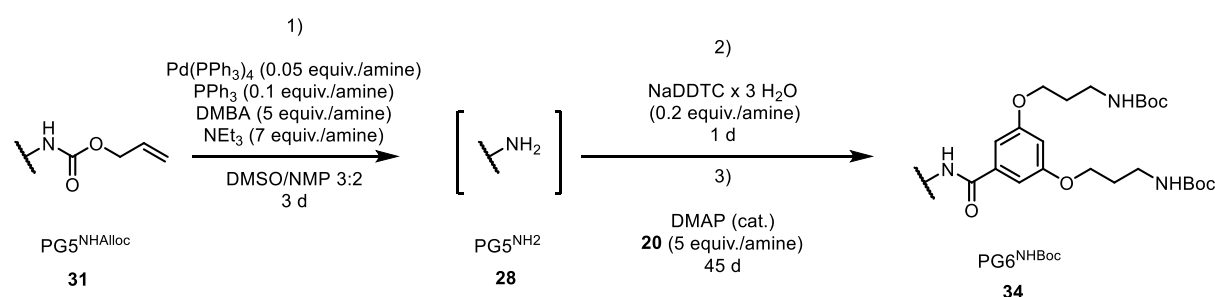
A notable case is that of DMPU (*N,N'*-dimethylpropyleneurea), which was selected as a very strong, polar-aprotic solvent, comparable to hexamethylphosphoramide but less carcinogenic.<sup>222</sup> As all components and intermediates of the deprotection/dendronization sequence are well soluble in DMPU, this solvent initially seemed to be the best solution for the aforementioned issues. However, rather discouragingly, this particular implementation of route C did not afford C-PG6<sup>NHBoc</sup><sub>500</sub>, but rather provided short, oligomeric fragments – apparently the products of main-chain scission in spite of the strongly basic conditions. This was initially very puzzling, in view of the successful implementation of route C in which only the solvent differs (see next paragraph). The finding of main-chain scission even under basic conditions will be discussed in chapter 3.

The solvent of choice for the deprotection/dendronization sequence was a mixture of DMSO and NMP, in ratios (DMSO:NMP) between 3:2 and 2:1. This combines the good solubility of NEt<sub>3</sub>, Pd(PPh<sub>3</sub>)<sub>4</sub> and PG5<sup>NH<sub>2</sub></sup><sub>500</sub> in NMP with the better solubility of the product PG6<sup>NHBoc</sup><sub>500</sub> in DMSO. Either solvent on its own was not capable of fully dissolving all components of the reaction at the desired concentrations. Depending on the exact polymer or reagent concentrations, slight adjustments to the ratio of solvents were necessary in the starting phases of deprotection and dendronization in order to avoid permanent precipitation.

Polymeric products isolated from model experiments and the solvent screening were in all cases colored, rather than colorless or slightly off-white as usually observed in routes **A** and **B**. This coloration – most commonly yellow, but occasionally brown or even purple – was ascribed to traces of Pd compounds retained by the polymers (see subsection 2.4.5). To mitigate this issue, the reaction sequence was further modified by the addition of a Pd scavenging agent, sodium *N,N*-diethyldithiocarbamate (NaDDTC), which has been shown to be effective in the removal of trace metal from products of Pd-catalyzed reactions.<sup>223,224</sup> Additionally, the strong complexation of Pd by this ligand was hoped to reduce the risks of Pd-promoted side reactions over the lengthy course of dendronization.

Further optimization mainly concerned reaction times: The initially arbitrary duration of deprotection of 3 d was found to be adequate in fully removing Alloc groups as judged by <sup>1</sup>H-NMR, and a total time for dendronization of *ca.* 45 d was deemed sufficient to permit complete reaction of all amines as judged by GPC (see Experimental, subsection 8.2.2).

The optimized conditions summarized in Scheme 2-10 were used for the implementation of route **C** based on an NHAloc-protected *g* = 5 DP, encompassing three steps: First, the deprotection of PG5<sup>NHAloc</sup> using Pd(PPh<sub>3</sub>)<sub>4</sub>/DMBA under strongly basic conditions; second, the quenching of reactive Pd species after 3 d by addition of the scavenging agent NaDDTC; third, dendronization using DG1<sup>NHBoc</sup> (**20**) for 45 d to the next-higher *g* DP, **C**-PG6<sup>NHBoc</sup>.



Scheme 2-10: Optimized conditions for the implementation of route **C** based on the NHAloc protecting group. For simplicity, transformations of only one peripheral group are shown, for complete chemical structures please refer to Figure 1-17 in the introduction.

Using these conditions, the synthesis of PG6<sup>NHBoc</sup> proceeded in isolated yields of *ca.* 60 – 70 % at scales up to 1.5 g product, comparable with the results of DP synthesis using routes **A** and **B**.<sup>101,174</sup> The polymers synthesized using the conditions shown in Scheme 2-10 appear to be **C**-PG6<sup>NHBoc</sup> by all measures, *i.e.* they have not undergone main-chain scission (also see section 2.6). This is readily evident from AFM images, in which **C**-PG6<sup>NHBoc</sup> (Figure 2-3d) presents itself as consisting of many chains, appearing very similar in length to the precursor PG5<sup>NHAloc</sup> (Figure 2-3c), rather than the small, dot-like objects observed in the case of main-chain scission such as in the failed attempts to access **A**-PG6<sup>NHBoc</sup>, which ends up being closer to **A**-PG6<sup>NHBoc</sup> (Figure 2-3b).

In combination with very high functional group conversion values of  $\chi \geq 99.3$  %, as determined by labeling with Sanger's reagent (see Experimental, subsection 8.2.1), the implementation of route **C** discussed here represents the aimed-for advance over route **B**: Main-chain scission has successfully been avoided, and structural perfection has been improved quite significantly. As discussed in section 2.5, this has also opened the path to DPs of even higher *g*. Further properties of **C**-PG6<sup>NHBoc</sup> will be

discussed in section 2.6, as they are relevant to the comparison with polymers previously synthesized using route **B** and to discussions of  $g_{\max}$ .

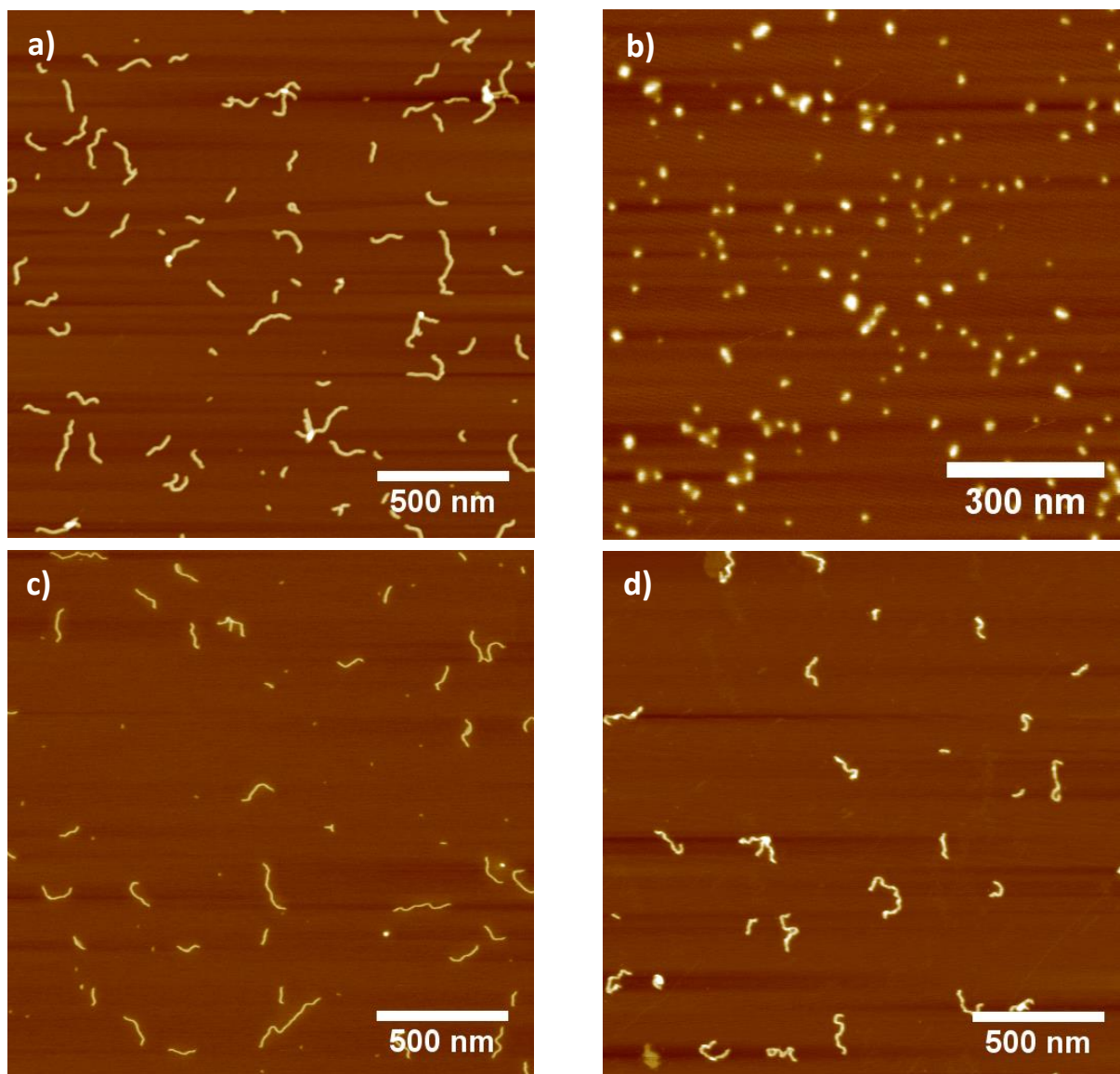


Figure 2-3: AFM height images of a)  $PG5_{500}^{NHBOC}$ , b)  $PG5_{\sim 50}^{NH_3TFA}$  obtained after NHBoc deprotection (route **A**), c)  $PG5_{500}^{NHAlloc}$ , and d)  $C-PG6_{500}^{NHBOC}$ . Adapted with permission from Messmer, D.; Kröger, M.; Schlüter, A. D. *Macromolecules* **2018**, 51, 5420-5429. Copyright 2018, American Chemical Society.

#### 2.4.5. Particularities of $\text{C-PG6}_{500}^{\text{NHoc}}$ analytics

Due to the novelty and the particular implementation of the “ $g + 1$ ” step used in the synthesis of  $\text{C-PG6}_{500}^{\text{NHoc}}$  – which involves fairly complex conditions – two remarks concerning characterization should be made.

The first concerns trace impurities: Initial trials had afforded polymers of rather erratic coloration – yellow, brown, even greyish-purple in one instance (Figure 2-4a-c). The strong and at times not persistent colorations in solution (Figure 2-4b) suggested the presence of Pd species remaining after purification of the final polymer. This led to the decision to additionally employ a Pd scavenging agent, NaDDTC,<sup>223</sup> between the deprotection and dendronization steps (see Scheme 2-10). Even with this precaution, samples of  $\text{C-PG6}_{500}^{\text{NHoc}}$  were always yellow in color (see Figure 2-4c, 2&3), raising the suspicion that trace Pd species might be retained within the DPs in spite of the use of a reportedly very effective scavenger.<sup>224</sup>

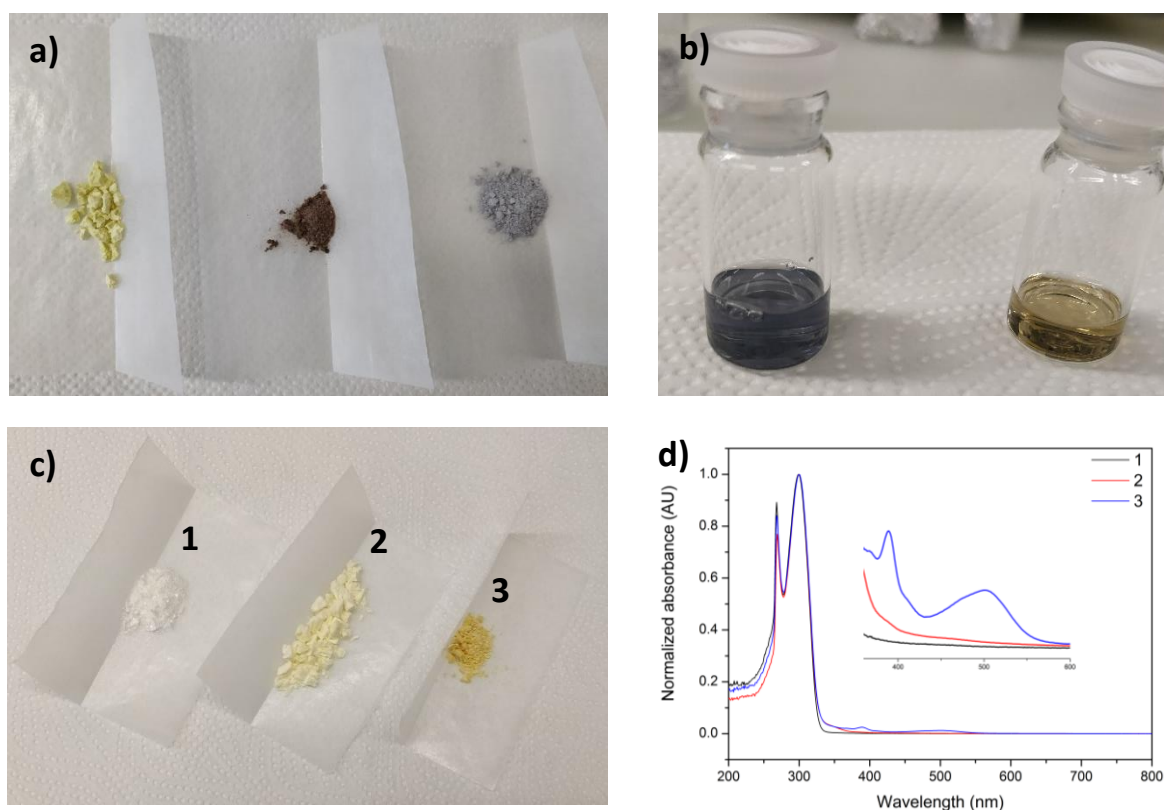


Figure 2-4: a) Photograph of different batches of  $\text{C-PG6}_{500}^{\text{NHoc}}$  from preliminary experiments (compare Figure 2-4c for samples obtained using optimized conditions). b) Solutions of the rightmost batch in Figure 2-4a in methylene chloride. left: freshly prepared, right: after standing for 3 d. The color change indicates oxidation of residual Pd species. c) Comparison of (1)  $\text{PG}_{500}^{\text{NHoc}}$  and (2, 3) two batches of  $\text{C-PG6}_{500}^{\text{NHoc}}$  prepared using optimized conditions from Scheme 2-10. d) Normalized UV/Vis spectra of the samples in Figure 2-4c in TCE, showing significant absorption at 360 nm for 2 & 3. Adapted with permission from Messmer, D.; Kröger, M.; Schlüter, A. D. *Macromolecules* **2018**, 51, 5420-5429. Copyright 2018, American Chemical Society.

The residual Pd content was first estimated using the colorimetric method of Krebs *et al.*<sup>225</sup> which relies on the formation of a strongly colored complex between an azthioformamide ligand and  $\text{Pd}^0$

(see Experimental, subsection 8.2.2). By this method, no residual Pd was detected, indicating Pd concentrations in the final polymers were below *ca.* 50 ppm. To achieve better sensitivity, polymer samples were acid digested and investigated by ICP-OES.<sup>226</sup> The detected Pd content was above the limit of detection, but below the limit of quantification, leading to an estimate of  $0.27 \text{ ppm} < [\text{Pd}] < 0.88 \text{ ppm}$  in the two polymer samples investigated thus. In view of this low value, it appears possible that not residual Pd species, but organic trace impurities are responsible for the yellow coloration observed in **C-PG6**<sub>500</sub><sup>NHBoc</sup>.

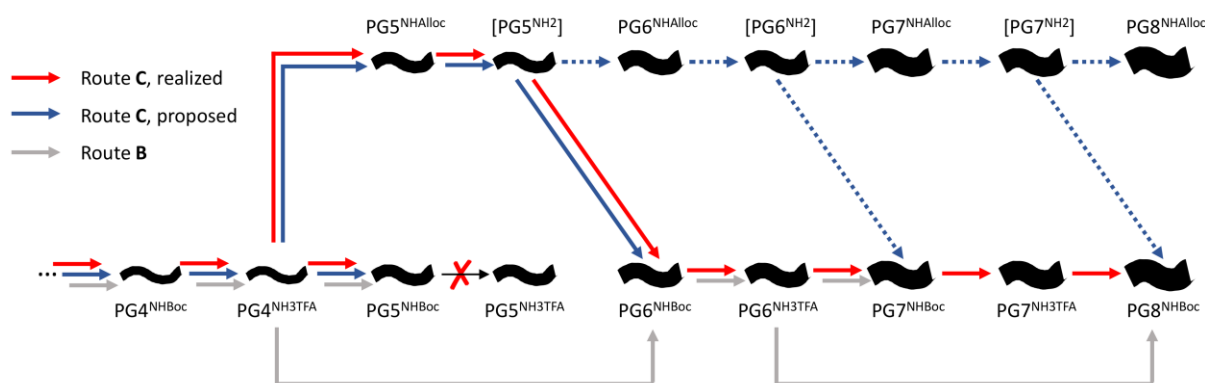
This leads into a second remark regarding Sanger labelling: The labelling results for **C-PG6**<sub>500</sub><sup>NHBoc</sup> may provide overestimates of the defect frequency, due to a residual yellow coloration of these samples even when NaDDTC was used as a scavenger (Figure 2-4d). The source of coloration remains obscure, and it is unclear whether or not the responsible impurity is removed during Sanger labelling or the subsequent workup, which involves a number of washing and precipitation steps. Because of this uncertainty, a conservative approach was taken and the absorbance at 360 nm was fully attributed to labelled amines, although there is some likelihood of colored impurities contributing to the resulting defect frequency. As the fate and identity of the colorant(s) are unclear, it cannot presently be estimated by how much the defect frequency is overestimated. In any case, the resulting uncorrected functional group conversion values of  $\chi \geq 99.3 \%$  for **C-PG6**<sub>500</sub><sup>NHBoc</sup> (possibly slight *underestimates*) are a substantial improvement when compared to those achieved using route **B** ( $\chi \leq 93 \%$ ).



## 2.5. Syntheses of $\text{C-PG7}_{500}^{\text{NHBoc}}$ and $\text{C-PG8}_{500}^{\text{NHBoc}}$

The implementation of route **C** presented in section 2.4 was based on the hypothesis that peripheral charges cause main-chain scission. That the synthesis of  $\text{C-PG6}_n^{\text{NHBoc}}$  *via* the charge-neutral intermediate  $\text{PG5}_n^{\text{NH}_2}$  proceeded without main-chain scission may be seen as a vindication of this hypothesis (compare chapter 3). Following that hypothesis, DPs of  $g = 6$  with sufficiently high structural perfection (and consequentially high density of peripheral functional groups) should also undergo main-chain scission, as they should carry higher charge densities than  $\text{PG5}_n^{\text{NH}_3\text{TFA}}$ .

Therefore, it was expected that  $g > 6$  DPs would need to be synthesized using further iterations of route **C** – *i.e.* proceeding to  $\text{C-PG7}_n^{\text{NHBoc}}$  *via*  $\text{PG6}_n^{\text{NH}_2}$  (see Scheme 2-11, blue arrows). This in turn would have necessitated the synthesis of  $\text{C-PG6}_n^{\text{NHAlloc}}$ , which might have been problematic: The presence of a Pd catalyst – necessary for NHAlloc deprotection at the  $g = 5$  level – could lead to hyperbranching growth upon addition of  $\text{DG1}^{\text{NHAlloc}}$  (**55**). As was the case in the attempted synthesis of  $\text{PG}_n^{\text{NHFmoc}^*}$  (see subsection 2.3.2), this would be detrimental. The scavenging agent NaDDTC was introduced partially with this in mind: Only the complete inactivation or removal of residual Pd species would permit the continued use of route **C** following Scheme 2-11 (blue path).



Scheme 2-11: Representation of synthetic pathways up to  $g = 8$ . Blue arrows: Proposed “all route **C**” pathway. Grey arrows: Previously realized pathway relying on route **B** (“ $g + 2$ ”).<sup>174</sup> Red arrows: Pathway discussed in this thesis, employing only one NHAlloc-based step.<sup>227</sup>

Quite surprisingly, this turned out to be unnecessary: When  $\text{C-PG6}_{500}^{\text{NHBoc}}$  was treated with TFA, the predicted main-chain scission did not occur according to AFM images (see Figure 2-5a). This finding is astounding in light of the above considerations and will be addressed in chapter 3. It was simultaneously auspicious from a synthetic point of view: The NHBoc-based protocol from route **A** is significantly easier to execute and requires less stringent conditions than route **C**. The synthesis of  $g > 6$  DPs was therefore conducted following the well-established protocol from route **A**, *i.e.* removal of Boc using TFA, followed by reaction with the active ester **20** under amide bond formation conditions, as had been the case previously up to  $\text{PG5}_{500}^{\text{NHBoc}}$ . The reaction was found to proceed without issue, affording  $\text{C-PG7}_{500}^{\text{NHBoc}}$  without the observation of main-chain scission (Figure 2-5b). The reaction proceeded with a very high calculated functional group conversion of  $\chi = 99.8\%$ .

The analogous treatment of  $\text{C-PG7}_{500}^{\text{NHBoc}}$  resulted in identical findings: No main-chain scission was found upon deprotection with TFA to  $\text{C-PG7}_{500}^{\text{NH}_3\text{TFA}}$  as judged by AFM imaging (Figure 2-5c), and the

dendronization reaction to  $\mathbf{C-PG8}_{500}^{\text{NHBoc}}$  proceeded with similar ease and a high calculated functional group conversion of  $\chi = 99.7\%$ .

The synthesis of  $\mathbf{C-PG6}_{500}^{\text{NHBoc}}$  has therefore given rise to the first fully homologous series of DPs ranging from  $g = 1$  to  $g = 8$ , with an intermittent change in tactics, but strict adherence to a “ $g + 1$ ” synthetic strategy. Together with the very high calculated functional group conversion values ( $\geq 99.3\%$  for each step),  $\mathbf{C-PG8}_{500}^{\text{NHBoc}}$  represents the first DP which should be firmly above  $g_{\text{max}}$ , a conjecture which is discussed in depth in section 2.7.

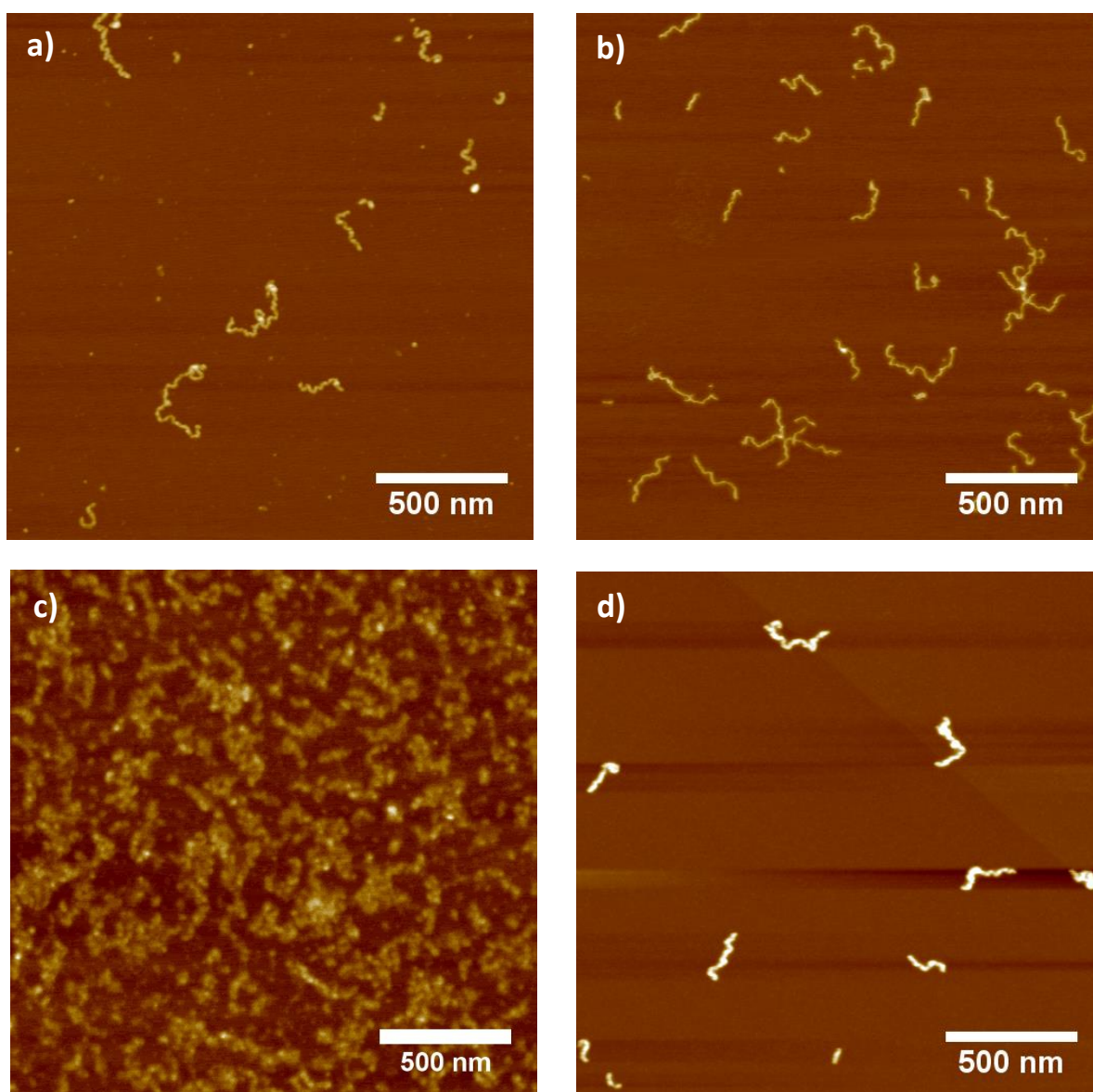


Figure 2-5: AFM height images of a)  $\mathbf{C-PG6}_{500}^{\text{NH}_3\text{TFA}}$ , b)  $\mathbf{C-PG7}_{500}^{\text{NHBoc}}$ , c)  $\mathbf{C-PG7}_{500}^{\text{NH}_3\text{TFA}}$ , and d)  $\mathbf{C-PG8}_{500}^{\text{NHBoc}}$ . Adapted with permission from Messmer, D.; Kröger, M.; Schlüter, A. D. *Macromolecules* **2018**, *51*, 5420-5429. Copyright 2018, American Chemical Society.

## 2.6. Comparison of polymers of $g = 5 - 8$

With the successful syntheses of **C-PG6**<sub>500</sub><sup>NHBoc</sup>, **C-PG7**<sub>500</sub><sup>NHBoc</sup>, and **C-PG8**<sub>500</sub><sup>NHBoc</sup> presented in the previous sections, a homologous series of DPs from  $g = 1$  to  $g = 8$  of significant main-chain length has become available. A similar, but non-homologous series of DPs had been prepared previously using route **B**<sup>h,174</sup> (see Scheme 2-11 or Figure 1-19b for synthetic pathway). For reasonable values of  $\rho \approx 1.0 - 1.4 \text{ g cm}^{-3}$  (also see section 1.6),  $g_{\text{max}}$  has been calculated to have a value of 6 or 7. **B-PG8**<sub>500</sub><sup>NHBoc</sup> bears a significant number of defects, introduced in the synthesis of its precursor **B-PG6**<sub>500</sub><sup>NHBoc</sup>. These holes in the structure do not merely push  $g_{\text{max}}$  to higher values, but the polydisperse nature of the dendrons in **B-PG6**<sub>500</sub><sup>NHBoc</sup> and DPs derived therefrom calls into question whether the concept of  $g_{\text{max}}$  is applicable to these polymers, at all. By comparing the two DP series from  $g = 5$  up to  $g = 8$ , the following section will demonstrate the synthetic improvements made thanks to route **C**, in preparation for a discussion of  $g_{\text{max}}$  in section 2.7.

### 2.6.1. Gel permeation chromatography

As discussed in subsection 1.6.3, solution-based methods for determining the size and molecular mass of polymers are not in all cases fully applicable to DPs. Suitable standards for the overall very high molar masses ( $> 10 \text{ MDa}$ ) and the particular concentration of molar mass in DPs ( $> 10 \text{ kDa}$  per RU) do not exist. While therefore commonly used GPC calibration methods *e.g.* using monodisperse PMMA are of limited utility at best, qualitative interpretation of GPC retention curves – in particular of peak retention times – is still possible and will be used in this section.

A somewhat curious observation made previously for DPs synthesized *via* route **B** was the *increased* peak RV of **B-PG6**<sub>500</sub><sup>NHBoc</sup> when compared to **PG5**<sub>500</sub><sup>NHBoc</sup> prepared from the same precursor (Figure 2-6b).<sup>174</sup> This is peculiar, seeing as peak RV *decreased* monotonically up to  $g = 5$ , in concert with the expected approximate doubling of molar mass with each dendronization step (see Experimental, subsection 8.2.1 Figure 8-1 and Figure 8-2). The synthesis of **B-PG6**<sub>500</sub><sup>NHBoc</sup> proceeded with much lower detected functional group conversion (91 – 93 %) than for conventional “ $g + 1$ ” steps in route **A**, but nevertheless the molar mass of **B-PG6**<sub>500</sub><sup>NHBoc</sup> is around 180 % that of **A-PG5**<sub>500</sub><sup>NHBoc</sup>, based on results from Sanger labelling confirmed by TGA.<sup>174</sup>

Experimental evidence supported by MD simulations<sup>98,99</sup> suggests that the periphery of DPs is only partially swelled by solvent already at  $g = 4$ , following a trend which suggests DPs at  $g = 5$  should be even less accessible. The defects arising from the “ $g + 2$ ” step to **B-PG6**<sub>500</sub><sup>NHBoc</sup> could lead to a break in this trend by providing “holes”, created by the omission of  $g = 2$  dendritic units, which are fairly large. This notion is supported by a recent EPR-based study of guest uptake.<sup>188</sup> As a result, a sizeable portion of the molecule becomes available to swelling by DMF, a very good solvent for DPs which served as the eluent in all GPC measurements discussed here. Increased swelling should by first approximation increase the apparent molar mass detected by GPC, but the concomitant increase in

<sup>h</sup> The precise polymer batches derived from route **B** discussed in this thesis were prepared according to the procedures reported in Ref. 175 and are closely comparable but not identical to those polymers. In particular, some differences in the functional group conversion values in the “ $g + 2$ ” steps to **B-PG6**<sub>500</sub><sup>NHBoc</sup> and **B-PG8**<sub>500</sub><sup>NHBoc</sup> were found, resulting in correspondingly different calculated molar masses. Other measurements delivered very similar results throughout; see Experimental, subsection 8.2.1, Table 8-2.

flexibility of the dendritic side chains – and perhaps of the overall contour of the DP – appears to tip the scales in favor of a very slight increase in peak RV, *i.e.* a decrease in apparent molar mass. Continuing in this synthetic sequence, **B-PG7**<sub>500</sub><sup>NHBoc</sup> and **B-PG8**<sub>500</sub><sup>NHBoc</sup> (the latter derived in a “*g* + 2” step from **B-PG6**<sub>500</sub><sup>NHBoc</sup>) show a similar pattern, in that they have a very similar peak RV.

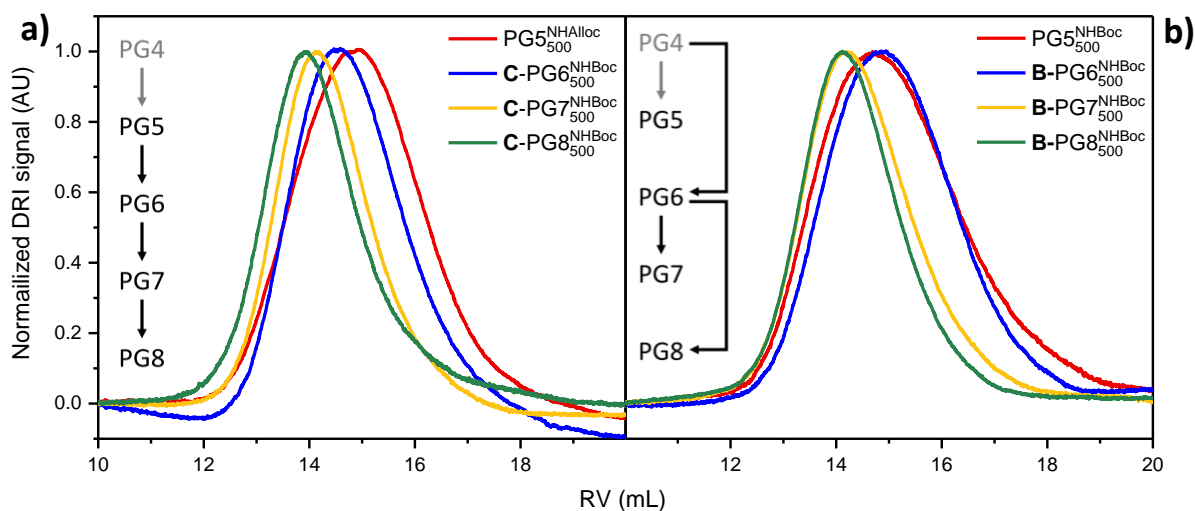


Figure 2-6: Normalized GPC traces (DRI signal) of DPs of *g* = 5 – 8, where **PG6**<sub>500</sub><sup>NHBoc</sup> was synthesized a) by route C and b) by route B. The curves in each graph were measured in a single run. Curves were shifted to account for minuscule variabilities in the retention volume of the flow marker (max. ± 0.05 mL). Reprinted with permission from Messmer, D.; Kröger, M.; Schlüter, A. D. *Macromolecules* **2018**, 51, 5420-5429. Copyright 2018, American Chemical Society.

For the homologous polymers from route C on the other hand, peak RV decreases monotonically in the series **PG5**<sub>500</sub><sup>NHAlloc</sup>, **C-PG6**<sub>500</sub><sup>NHBoc</sup>, **C-PG7**<sub>500</sub><sup>NHBoc</sup>, **C-PG8**<sub>500</sub><sup>NHBoc</sup> – just as expected for the large molar mass increases involved (Figure 2-6a). If indeed “holes” due to defects are the main cause of the surprising elution behavior of **B-PG6**<sub>500</sub><sup>NHBoc</sup> compared to **PG5**<sub>500</sub><sup>NHBoc</sup>, the absence of similar effects in the case of **C-PG6**<sub>500</sub><sup>NHBoc</sup> vs. **PG5**<sub>500</sub><sup>NHAlloc</sup> indicates that no such large, readily solvent-accessible peripheral locations are present. This is not surprising considering route C proceeds solely using “*g* + 1” steps – which result in less structurally disruptive defects, if present. The observed GPC elution behavior is in support of the improvement in functional group conversion over route B calculated from labelling data (see subsection 2.6.3).

Additionally, in both routes B and C, the absence of a decrease in apparent molar mass confirms the visual impression from AFM imaging (see Figure 2-3 and also the discussion in section 2.7) that no significant main-chain scission has occurred. In combination with the improved structural perfection as indicated by Sanger labeling, GPC results therefore demonstrate the substantial improvements over route B achieved by the present implementation of route C.

## 2.6.2. Atomic force microscopy

In looking at many AFM height images of multiple batches of **C-PG6**<sub>500</sub><sup>NHBoc</sup> (Figure 2-7d-f, also see Figure 2-3d), the impression of a strong undulation and corrugation of DP chains arose. This impression is particularly stark when compared with AFM images of PG5<sub>500</sub><sup>NHBoc</sup> or PG5<sub>500</sub><sup>NHAlloc</sup>, which appear as smooth and fairly straight objects (Figure 2-7, also see Figure 2-3a,c,d). This observation was curious and rather unexpected, particularly in view of the much-improved structural perfection discussed in the previous sections: By first approximation, one would expect a DP to approach a straight cylinder with increasing  $g$ , as the increasing steric congestion of the bulky dendritic side chains would force the backbone straighter and create a more densely packed corona of organic matter. The observation of undulation and perhaps also corrugation therefore warrants closer examination, particularly in view of the discussion of  $g_{max}$ , above which dense packing is expected.

To confirm the visual impression of significantly differing contours (also see Figure 8-13, Experimental, subsection 8.2.2) initially gained from disparate images and samples, co-preparations of PG5<sub>500</sub><sup>NHAlloc</sup> and **C-PG6**<sub>500</sub><sup>NHBoc</sup> were investigated. This was to reduce unconscious bias in the comparison of images, as well as to eliminate variations in tip geometry, differing states of drying *etc.* between samples. In such co-preparations (Figure 2-8a,b), the initial visual impression was rapidly confirmed: Two populations are readily visible, one consisting of fairly smooth worm-like objects of low local curvature (PG5<sub>500</sub><sup>NHAlloc</sup>), the other consisting of objects of greater height with stronger corrugation and apparent undulation (**C-PG6**<sub>500</sub><sup>NHBoc</sup>).

By comparison, PG5<sub>500</sub><sup>NHBoc</sup> and **B-PG6**<sub>500</sub><sup>NHBoc</sup> in AFM height images of analogous co-preparations were not as readily visually distinguishable from each other (Figure 8-14, Experimental, subsection 8.2.2). The DPs appear visually less clearly delineated in terms of height, smoothness, and local curvature. While not each individual polymer chain can be as clearly attributed to either population as is the case in Figure 2-8, still this is possible for at least some of the filaments. An attempt at a quantitative analysis of AFM height images can be found in the Experimental (subsection 8.2.2). This analysis reveals that height differences, averaged over a sizable number of individual polymer chains, are present roughly equally in co-images of PG5<sub>500</sub><sup>NHBoc</sup>/**B-PG6**<sub>500</sub><sup>NHBoc</sup> and in co-images of PG5<sub>500</sub><sup>NHAlloc</sup>/**C-PG6**<sub>500</sub><sup>NHBoc</sup>, which suggests that the visually greater distinguishability between polymer populations is the result of greater local curvature, *i.e.* corrugation and undulation.

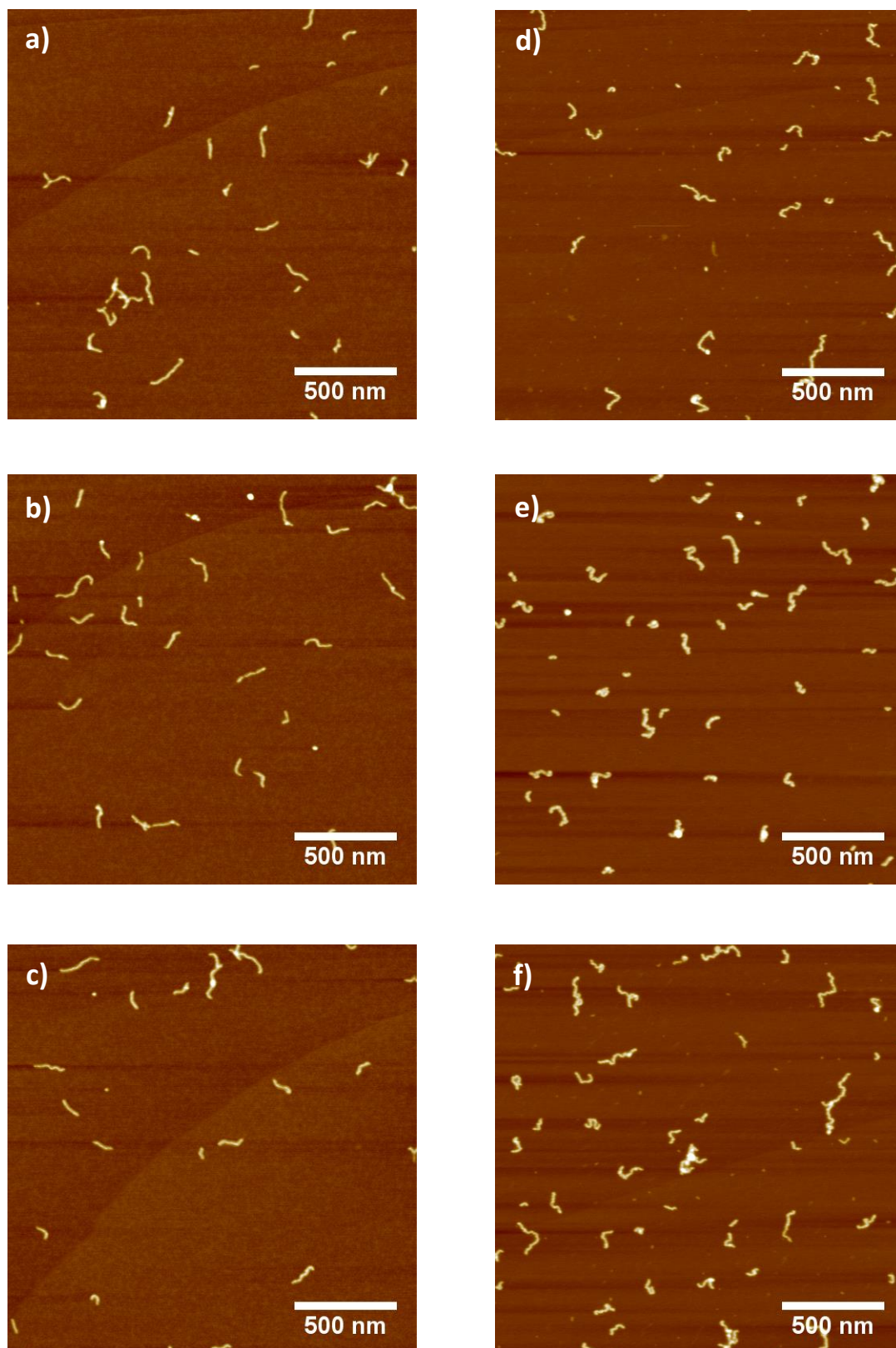


Figure 2-7: AFM height images of  $PG5_{500}^{NHAlloc}$  (a-c) and  $C-PG6_{500}^{NHBoc}$  (d-f) on mica.

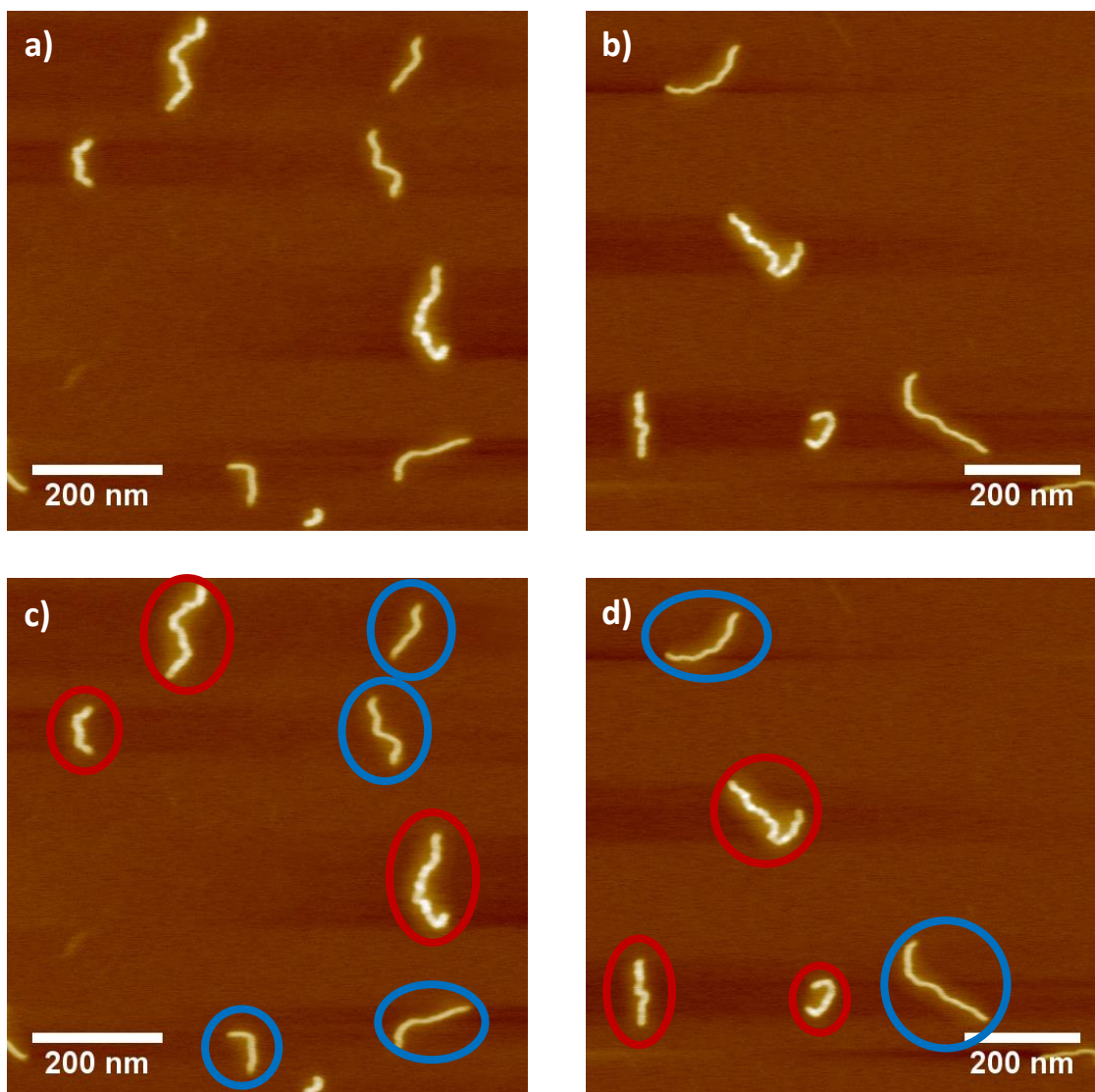


Figure 2-8: a), b): AFM height images of co-preparations of  $PG5_{500}^{NHAlloc}$  and  $C-PG6_{500}^{NHBoc}$ . c), d): The same images, with individual DPs marked as  $PG5_n^{NHAlloc}$  (blue) and  $C-PG6_n^{NHBoc}$  (red).

The finding of *increased* apparent corrugation and undulation in route **B** is puzzling: First because of the previously invoked argument that a DP should approach an ideal cylinder as it approaches  $g_{max}$ , and second because previous instances of corrugation had been ascribed to defects:  $B-PG7_{500}^{NHBoc}$  and  $B-PG8_{500}^{NHBoc}$  had previously been found to show significant corrugation. This observation was at the time ascribed to defects resulting from the “holes” left behind by low functional group conversion in the “ $g + 2$ ” steps leading to  $B-PG6_{500}^{NHBoc}$  and  $B-PG8_{500}^{NHBoc}$ .<sup>174</sup> The structural perfection of  $C-PG6_{500}^{NHBoc}$  is however significantly higher than that of  $B-PG6_{500}^{NHBoc}$ , as evidenced by GPC and Sanger labelling; The presence of undetected defects is possible, but only remotely so in view of GPC results and the fact that route **C** employs a much less sterically demanding dendronization agent (**20**). Still, it is  $C-PG6_{500}^{NHBoc}$  which appears to be the polymer of larger corrugation, suggesting that corrugation is in fact a consequence of increased structural perfection. This notion is supported by the finding that polymers of (formally)  $g = 6$  for which dendronization was stopped early appear comparatively smooth (see *e.g.* Experimental, subsection 8.2.2, Figure 8-7).

A potential explanation for this observation is depicted in Figure 2-9. The dendritic side chains might form a locally undulated (Figure 2-9b) or perhaps helical sheared cylinder around the straight backbone, rather than a cylindrical one (Figure 2-9a). Such a change in conformation is possible as long as  $R < R_{\max}$ . A sheared (helical or undulated) envelope encompasses a larger volume for the same backbone length and centerline radius  $R$  (where  $R < R_{\max}$ ). Such an interpretation is supported by results from Dr. Hao Yu (unpublished): During investigations of main-chain scission, in a serendipitous and irreproducible case, a sample of **A-PG6<sub>n</sub><sup>NHBoc</sup>** was obtained in which significant numbers of chains with fairly high  $P_n$  were apparent (Figure 2-9c). Though structural perfection in this specific case was not as high in the series leading to **C-PG6<sub>500</sub><sup>NHBoc</sup>**, at  $\chi = 96\%$  functional group conversion was much higher than in route **B**. Other than **B-PG6<sub>500</sub><sup>NHBoc</sup>** however (compare Figure 8-14) the chains appeared strongly corrugated, exhibiting a pearl-necklace like structure and strong undulation. Another result perhaps related to the present findings is that MD simulations of PG5<sub>100</sub><sup>NHBoc</sup> and PG6<sub>75</sub><sup>NHBoc</sup> in vacuum suggest that the *backbone* of the  $g = 6$  DP preferentially assumes an overall helical conformation (compare Figure 3-31a and Figure 3-34), whereas lower  $g$  DPs assume more extended conformations.<sup>144,228</sup> Additional evidence for conformations akin to Figure 2-9b will be discussed in chapter 4 based on results from cryo-TEM.

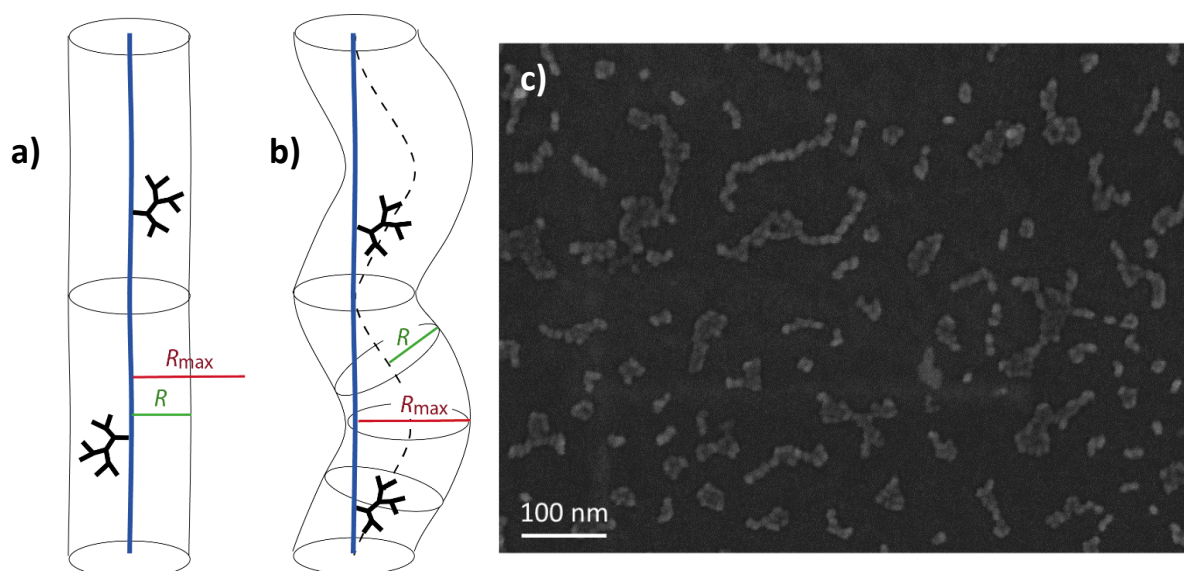


Figure 2-9: Geometric models of a) straight and b) undulated cylinders as possible conformations for high  $g$  DPs.  $V_b > V_a$  at identical backbone length; only possible for  $R < R_{\max}$ . c) SEM of serendipitously obtained **A-PG6<sub>n</sub><sup>NHBoc</sup>** ( $n > 50$ ), rotary  $W$ -shadowed, exhibiting a pearl-necklace structure (Dr. Hyo Yu, reproduced with permission).

While a conformation such as the one depicted in Figure 2-9b provides a larger volume for the same length of backbone, it also leads to an increased surface area. The transition from Figure 2-9a to Figure 2-9b for a given filament is surely subject to a complex interplay of volume and interfacial interactions, the analysis of which is beyond the scope of this thesis. However, it seems possible that the formation of an undulated or helical conformation might be driven by the increase of surface area, rather than a gain in volume, as solvent is excluded due to denser packing with increasing  $g$ . The “smoothness” of **B-PG6<sub>500</sub><sup>NHBoc</sup>** in this context is a consequence of its low structural perfection: The large defects originating from the “ $g + 2$ ” dendronization step are solvent accessible (compare subsection 2.6.1) and the overall looser peripheral substitution permits rearrangement of the dendritic matter into a fairly smooth cylinder. Meanwhile in **A-PG6<sub>n</sub><sup>NHBoc</sup>** and **C-PG6<sub>500</sub><sup>NHBoc</sup>** the much denser substitution



only permits exposure to the solvent by net rearrangement of the dendritic matter around the backbone into a sheared cylindrical conformation, providing a larger surface area for solvent interaction, while largely maintaining internal contacts. Swelling in the traditional sense is possible only to a limited degree, due to the fairly dense packing of the dendritic matter. Again, this is supported by results discussed in chapter 3, where additional evidence may be found for the above notion:  $g = 6$  DPs which are known to feature many defects (due to partial peripheral deprotection of the  $g = 5$  precursor) appear smooth in AFM images (Figure 3-8b,d,f,h).

Certainly, the balance of interactions governing the “straight-sheared” transformation suggested above must be delicate, seeing as the presumed change in this frame of reasoning is induced by comparatively minor structural changes (*ca.* 10 % of overall mass). Solvent quality – which might need to be considered separately for peripheral groups and the DP branchwork – is therefore likely to have a significant effect on the shape of DPs. Also see chapter 3 and subsection 1.6.3 for closely related discussions.

According to the above hypothesis, objects with  $R = R_{\max}$  – as needs be for  $g > g_{\max}$  – should *not* exhibit a helical or undulated shape: The rearrangement of the dendritic matter around the backbone as depicted in Figure 2-9b is only possible for  $R < R_{\max}$ . However, in AFM images both **C-PG7**<sub>500</sub><sup>NHBoc</sup> and **C-PG8**<sub>500</sub><sup>NHBoc</sup> appear strongly undulated and corrugated (see Figure 2-5b/d, respectively as well as Experimental, subsection 8.2.2, Figure 8-13). While **C-PG7**<sub>500</sub><sup>NHBoc</sup> may be at or above  $g_{\max} \approx 6$  or 7, **C-PG8**<sub>500</sub><sup>NHBoc</sup> should be firmly above  $g_{\max}$  for this class of polymers (see Figure 1-20). This observation warrants further discussion which relates closely to  $g_{\max}$ , as presented in section 2.7.

A caveat to the observations and hypotheses laid out above is the fact that they stem from observations made on *adsorbed* polymers – The shape which a polymer adsorbed on a solid substrate adopts does not necessarily represent its solution state. The direct observation of native polymer chain conformations is usually not possible, and instead the properties of large ensembles of chains are probed using scattering techniques such as static light scattering. However, for the specific case of DPs it is possible, albeit not trivial, to directly observe solution-state conformations, as will be discussed in chapter 4.

### 2.6.3. Sanger labelling

By performing an iterative analysis of results from labelling with Sanger's reagent (see Experimental, subsection 8.2.1),<sup>150,171</sup> a precise characterization of the average DP repeat unit can be performed within a series of polymers. As already mentioned, the main goals of a) avoiding main-chain scission and b) improving structural perfection have been achieved in the synthesis of **C**-PG6<sub>500</sub><sup>NHBoc</sup> when compared to **B**-PG6<sub>500</sub><sup>NHBoc</sup>. This progress is shown quantitatively in Figure 2-10, which depicts the functional group conversion values  $\chi$  for DPs of the type PG $g$ <sub>500</sub><sup>NHBoc</sup> in three different series, one employing route **C** and two employing route **B**<sup>i</sup> in the syntheses of the respective PG6<sub>500</sub><sup>NHBoc</sup>. As Figure 2-10 shows, the nominal functional group conversion values deviate from the ideal particularly in the syntheses of **B**-PG6<sub>500</sub><sup>NHBoc</sup> and **B**-PG8<sub>500</sub><sup>NHBoc</sup>, a natural consequence of the use of the bulky "g = 2" dendronization agent **37**. By comparison, for the entire DP series synthesized using route **C**, functional group conversion never dips below 99.3 %.

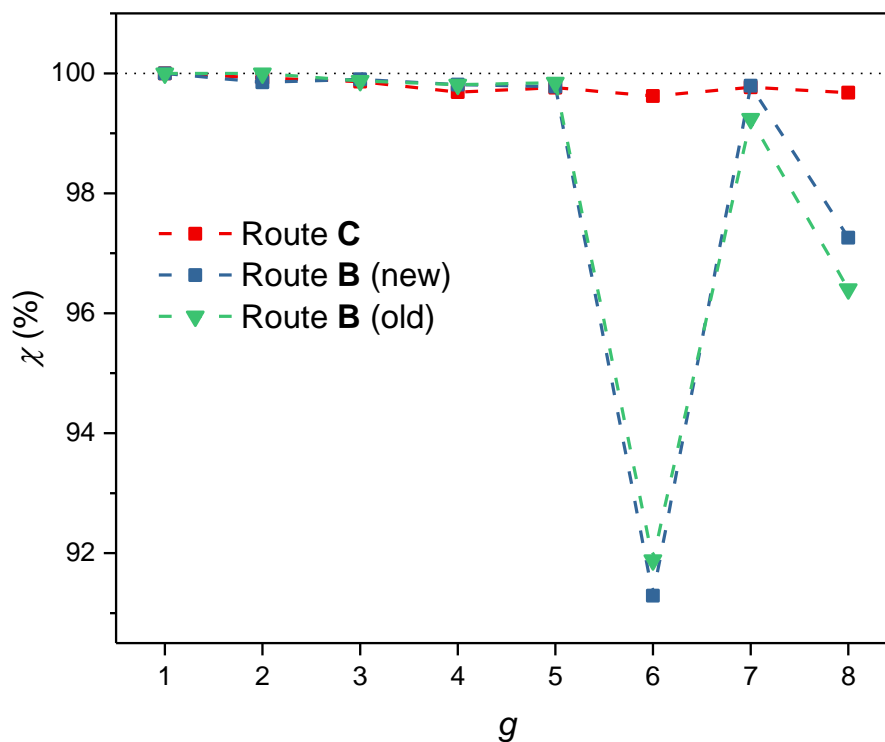


Figure 2-10: Functional group conversion values (derived from Sanger labelling data for the series of DPs synthesized using route **C** as well as two independent series of DPs involving route **B**. PG1<sub>500</sub><sup>NHBoc</sup> is assumed to be defect free in all cases.

As previously mentioned, the high defect frequencies introduced in route **B** not only lower structural perfection and effectively render the structure non-dendritic, but also result in significant losses in molar mass. They amount to *ca.* 1.1 MDa for one DP chain of **B**-PG6<sub>500</sub><sup>NHBoc</sup> when compared to the perfect structure of PG6<sub>500</sub><sup>NHBoc</sup> (a deficiency of 10 % of the theoretically achievable mass). The much-improved synthesis leading to **C**-PG6<sub>500</sub><sup>NHBoc</sup> means that this deficiency has been reduced to merely 140 kDa, or 1.3 % of the theoretically achievable molar mass.

<sup>i</sup> The two series employing route **B** correspond to a series the experimental details of which have been published previously,<sup>172,174</sup> labelled as "old" in Figure 2-10, and a re-synthesis using the same methods, labelled as "new".

However beyond  $g = 6$ , great care has to be taken when considering labelling values and molar masses; Figure 2-11a shows the average molar mass per RU calculated from Sanger labelling relative to the molar masses of theoretical, perfect RUs (blue curve), which deviates nominally by as little as 1.8 % from the ideal value ( $M_{\text{exp}} = M_{\text{RU}}$ ) for **C-PG8**<sub>500</sub><sup>NHBOC</sup>. On its face, this represents a significant improvement over route **B**: For **B-PG8**<sub>500</sub><sup>NHBOC</sup>, the deficiency in calculated molar mass corresponds to 12 % of the theoretically achievable value (Figure 2-11a, blue curve). Consider however the red curve in Figure 2-11a, which corresponds to the theoretically achievable molar mass,  $M_{\text{max}}$ : For  $g \leq g_{\text{max}}$ , *i.e.* when  $R_{\text{packing}} \leq R_{\text{max}}$ ,  $M_{\text{max}}$  is given by the molar mass of the ideal, isolated repeat unit, *i.e.*  $M_{\text{max}} = M_{\text{RU}}$  (red curve in Figure 2-11b). When  $g > g_{\text{max}}$  on the other hand,  $M_{\text{max}}$  is given by the mass that fits into the cylinder of radius  $R_{\text{max}}$  at a given density  $\rho_{\text{packing}}$  (see blue curve in Figure 2-11b; a value of  $\rho_{\text{packing}} = 1.3 \text{ g cm}^{-3}$  was assumed. Compare chapter 5).

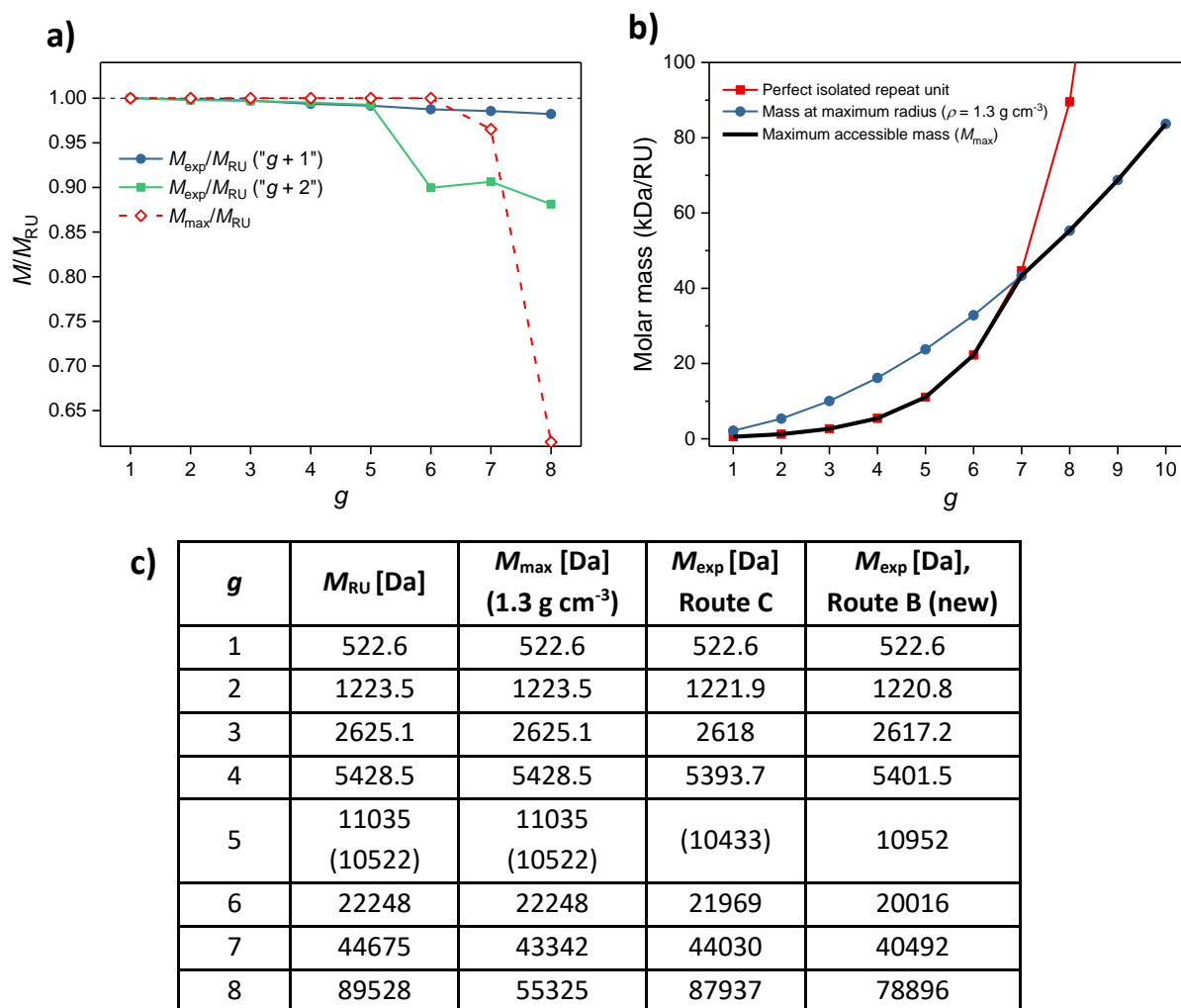


Figure 2-11: a) Average molar masses per repeat unit compared to isolated, defect free repeat units; b) " $g_{\text{max}}$  plot" expressed in terms of molar mass per repeat unit rather than radius of the DP; the black curve corresponds to  $M_{\text{max}}$ , the maximum theoretically accessible molar mass per repeat unit; c) tabulated molar masses obtained by recursive analysis of Sanger labelling as well as theoretical values; molar masses for NHAlloc-bearing DPs are in parentheses. Adapted with permission from Messmer, D.; Kröger, M.; Schlüter, A. D. *Macromolecules* **2018**, 51, 5420-5429. Copyright 2018, American Chemical Society.

As is evident from Figure 2-11a&c, there is a discrepancy between the theoretically accessible molar mass per repeat unit  $M_{\max}$  and the experimentally determined values  $M_{\text{exp}}$ : The recursive analysis of results from labelling with Sanger's reagent indicate that the average molar mass per repeat unit surpasses  $M_{\max}$ , in the series involving route **B** only for  $g = 8$  and in the series involving route **C** for both  $g = 7$  and  $g = 8$ . This conflict requires in-depth analysis and is in fact intrinsically connected to  $g_{\max}$ , as will be discussed in section 2.7.

## 2.7. Discussion of $g_{\max}$ and structural perfection: $\alpha$ and a pragmatic view of “dense” packing

For the DP series  $\text{PG}g_n^{\text{NHBoc}}$ , the maximum defect-free, dendritic generation  $g_{\max}$  has been estimated to be 6 or 7, depending on the packing density value assumed (see section 1.5). As the  $g = 6 - 8$  DPs  $\text{C-PG}6_{500}^{\text{NHBoc}}$ ,  $\text{C-PG}7_{500}^{\text{NHBoc}}$ , and  $\text{C-PG}8_{500}^{\text{NHBoc}}$  are of unprecedentedly high calculated structural perfection, the question whether any member of this series constitutes a DP above  $g_{\max}$  must be addressed. The analytical data presented in section 2.6 deliver important starting points. In particular, this concerns the average molar masses per repeat unit calculated from labelling of unreacted amines with Sanger’s reagent  $M_{\text{exp}}$ , as well as the shape of DPs as observed in AFM.

As discussed in subsection 2.6.3, the values of  $M_{\text{exp}}$  surpass the theoretically possible value  $M_{\max}$  – by a mere 1.6 % for  $\text{C-PG}7_{500}^{\text{NHBoc}}$ , but by nearly 60 % of  $M_{\max}$  for  $\text{C-PG}8_{500}^{\text{NHBoc}}$  (see Figure 2-11a,c). This is physically only possible if  $g_{\max}$  is shifted to higher  $g$ , either by significant extension of chemical bonds such that  $R_{\max}$  increases, or by significant compression of the dendritic branchwork, such that  $\rho_{\text{packing}}$  increases. Arriving at  $g_{\max} = 8$  would, for instance, require an extension of  $R_{\max}$  by nearly 20 %, or alternatively the compression to a density of  $\rho_{\text{packing}} = 2.1 \text{ g cm}^{-3}$ . These possibilities appear remote, the first because the effective force required to stretch the dendritic structure would be quite likely to result in bond rupture (compare Appendix A.2), and the second because the necessary density values are much higher than commonly encountered for organic molecules of similar composition as  $\text{PG}g_n^{\text{NHBoc}}$  (also see chapter 5).

In the more realistic case that  $g_{\max} \approx 6$ , defects should become very much apparent in DPs of  $g = 8$ ; It seems therefore more likely that the molar masses  $M_{\text{exp}}$  are an overestimate and that some defects remain undetected. In fact, for  $\text{C-PG}8_{500}^{\text{NHBoc}}$  the vast majority of defects must remain undetected to arrive at the overestimate presented in section 2.6.3. As is so often the case, reality differs from the purely theoretical ideal situation: The detection of all defects would require a perfectly quantitative labelling reaction, which appears not to be the case in this instance. At least up to  $g = 5$ , labelling does appear to be quite efficient as indicated by MALDI-TOF-MS of  $\text{MG}5^{\text{NH}_2}$  liberated during main-chain scission (see Figure 3-1a).<sup>169</sup> Above  $g = 6$ , this does not appear to be the case anymore, as already evident in route **B**:<sup>174</sup>  $\text{B-PG}6_{500}^{\text{NHBoc}}$  and  $\text{B-PG}8_{500}^{\text{NHBoc}}$  showed significant numbers of defects; the use of  $\text{DG}2^{\text{NHBoc}}$  (**37**) left large, solvent- and reagent-accessible gaps.  $\text{B-PG}7_{500}^{\text{NHBoc}}$  on the other hand – prepared from  $\text{B-PG}6_{500}^{\text{NHBoc}}$  by a “ $g + 1$ ” step – seemed to have few defects (Figure 2-10). Likely this was the result of many low  $g$  level amines still being reachable by **20** as opposed to **37**, and therefore these defects were effectively masked in  $\text{B-PG}7_{500}^{\text{NHBoc}}$ .

The question arises why, suddenly, at  $g \geq 6$  the labelling reaction becomes far from quantitative; The nucleophilic aromatic substitution in the labelling of free amines requires:

- 1) Solubilization of Sanger’s reagent and the amine nucleophile
- 2) A suitable trajectory for the formation of the intermediate Meisenheimer complex
- 3) Stabilization of the fluoride nucleofuge

While these requirements appear to be met up to  $g = 6$  for route **C**, beyond that one or several of these conditions are apparently not fulfilled. A factor influencing all these factors is steric congestion,

which is a) expected to increase strongly with  $g$  and b) negatively affects the three points listed above: In a densely crowded dendritic environment, which is only poorly solvent-swollen, the stabilization of both starting materials and products may be inadequate, and solvent shells necessary for the stabilization in particular of fluoride might not be able to form. In a similar vein, due to steric hindrance the conformational space available to the reagents is likely severely limited, thereby greatly reducing the probability of a collision trajectory leading to the intermediate Meisenheimer complex.

If the above assumptions are true for Sanger's reagent – a labelling reagent chosen for its small size, among other reasons – they would certainly also hold for the much bulkier dendronization agents such as **20**. However, the exact requirements for that reaction, a nucleophilic acyl substitution, differ from those discussed above for the  $S_NAr$  reaction of Sanger's reagent. It seems therefore all the more likely that  $M_{exp}$  is indeed an overestimate of the effectively present average molar masses per repeat unit for  $g > 6$ .

This presents a bit of a conundrum: One stated goal of the work presented here is the exploration of polymers at and above  $g_{max}$  – and labelling data, other than expected from the course of  $M_{max}$  and the concomitant expected development of defect frequencies does not provide the naively expected results: In the real dendritic system, which in this specific case employs a chemical labelling reagent for the determination of defect frequencies, reaching and indeed surpassing  $g_{max}$  (*i.e.* introducing a very large number of defects), *instead looks no different from continuing virtually defect-free synthesis!* Likewise, there is no discontinuity in GPC, as DP molar masses increase continually and as their quantification is challenging. The apparent shape transition observed in AFM images of **C-PG8**<sub>500</sub><sup>NHBoc</sup> may be seen as a transition to the  $g_{max}$  regime, as it is proposed to be the result of (pen)ultimate steric congestion.

Despite the lack of a direct discontinuity, labelling results may provide a criterion useful in determining whether a dendritic molecule has reached or surpassed  $g_{max}$ ; the ratio  $\alpha$  (Eq. 2-1) suggests itself as such a measure:

$$\alpha = \frac{M_{exp}}{M_{max}}$$

Eq. 2-1

For  $g \leq g_{max}$ , by definition  $\alpha \leq 1$ ; only for  $g > g_{max}$  is it possible for  $\alpha$  to exceed unity. The applicability of  $\alpha$  is however subject to certain requirements:  $g_{max}$  must be a fairly well-defined parameter. As shown in Appendix A.2,  $\rho_{packing}$  influences the exact value of  $g_{max}$  rather more strongly than  $R_{max}$ , therefore the density of high  $g$  dendritic molecules must be a fairly well-known in order to avoid a certain definitional circularity.<sup>j</sup> For **PGg**<sub>n</sub><sup>NHBoc</sup>, a value of  $g_{max} = 6$  or 7 still appears likely.

Values of  $\alpha$  are plotted in Figure 2-12 for two polymer series up to  $g = 8$  involving routes **B** and **C** respectively. As this demonstrates, values of  $\alpha$  in isolation are not sufficient to judge whether a dendritic molecule has surpassed  $g_{max}$ : The context of the entire "dendronization history" as reflected by the course of  $\alpha$  with  $g$  must be considered. By way of example, let us consider route **B**: For **B-PG8**<sub>500</sub><sup>NHBoc</sup>  $\alpha \approx 1.42$ . However, this polymer *cannot* be regarded as a dendritic molecule which has

<sup>j</sup> If  $\rho_{packing}$  were uncertain,  $g_{max}$  would spread over a wide range of values, and  $M_{max}$  would likewise vary strongly for  $g \gtrsim g_{max}$ , making a cogent interpretation of  $\alpha$  challenging. It should be noted that this is not *entirely* outside the realm of possibility, considering the results presented in chapter 5.

surpassed its  $g_{\max}$ , as already for  $g = 6$ ,  $\alpha$  dips significantly below the ideal value of  $\alpha = 1$ , reflecting the structural imperfections caused by the use of the  $g = 2$  dendronization agent **37**. **B-PG6<sub>500</sub><sup>NHBOC</sup>** is therefore not a dendritic molecule and the concept of  $g_{\max}$  is not applicable to this polymer or its higher  $g$  derivatives. That  $\alpha$  still eventually increases to values greater than unity is a consequence of the exponential nature of dendronization: Even defect-riddled structures can eventually be fairly densely substituted and preclude the labelling of defects, as had been suspected in previous publications already.<sup>174</sup> For route **C** on the other hand – by virtue of using exclusively  $g = 1$  dendronization steps –  $\alpha \approx 1$  for  $g \leq 6$ , and only *above* the estimated  $g_{\max} = 6$  a deviation to values  $\alpha > 1$  is observed. As structural perfection is high up to that point, a reasonable discussion of whether this means that  $g_{\max}$  has been reached is possible.

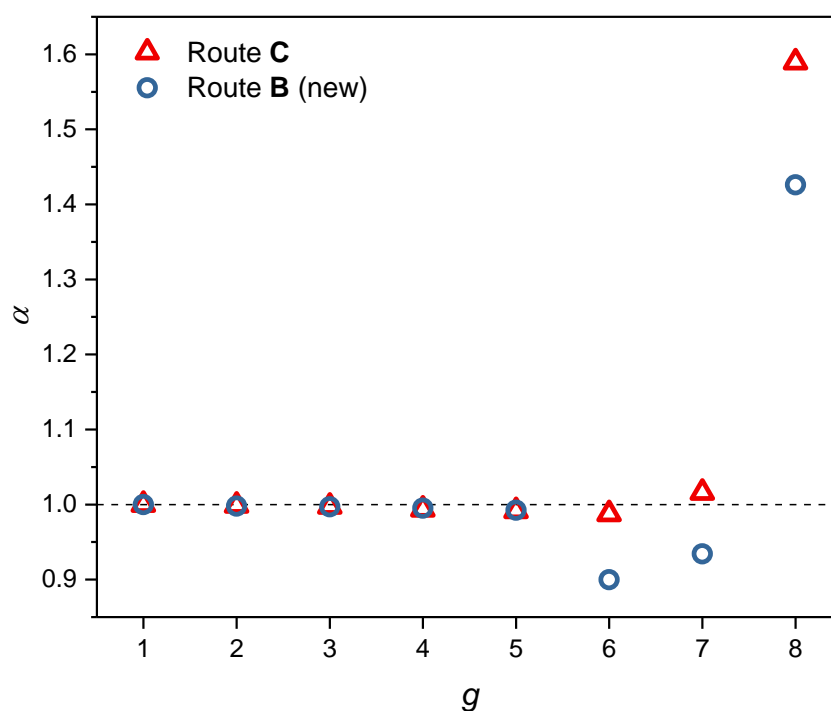


Figure 2-12: Plot of  $\alpha = M_{\text{exp}}/M_{\text{RU}}$  for two DP series, one relying on route **B** for the crucial step to  $g = 6$ , the other relying on route **C**.

For the series of DPs prepared using route **C**,  $g_{\max}$  indeed appears to have been reached, likely at  $g = 6$ .<sup>k</sup> Up to  $g_{\max}$ , very high functional group conversion values of  $\chi \geq 99.3\%$  have been achieved for every “ $g + 1$ ” step, providing nearly ideally dendritic molecules ( $\alpha \approx 1$ ). Beyond  $g_{\max}$ , a sort of controlled hyperbranching growth sets in, *i.e.* linear repeat units appear in the branchwork structure. Differing from typical hypergraft or hyperbranched polymer syntheses though, dendronization still affords densely functionalized molecules to an extent that even small labelling reagents are not capable of quantitatively reacting with all defects.

Amines at the  $g - 1$  level are apparently too crowded to quantitatively react with Sanger’s reagent above  $g_{\max}$ . The same is most likely true for the dendronization agents of the type  $\text{DG1}^{\text{NHX}}$ , *e.g.* **20**, which are bulkier, though perhaps their reactions with peripheral amines are aided by the use of

<sup>k</sup> Figure 1-20a may suggest that it is more likely that  $g_{\max} = 7$ ; however it should be noted that the estimates of  $g_{\max}$  in sections 1.5 and 1.6 rely on a maximum extension  $R_{\max}$  which is unrealistic for an entire, branched structure – this shifts the estimate to lower values of  $g_{\max}$  in the corresponding plots.

better solvents during dendronization reactions. However, as the results from AFM indicate, the periphery is not entirely densely packed: For truly dense packing, a fully cylindrical geometry would be expected, rather than the observed corrugated one. Two possibilities for the origin of corrugation present themselves: Non-equilibrium conformations could be locked in by the addition of bulky dendritic repeat units during dendronization, and the observed undulation and corrugation represent kinetically frozen states. Alternatively, the corrugated conformations of the dendritic matter around the backbone represent an energetically favorable state, possibly depending on interactions with the environment as discussed previously (subsection 2.6.2, Fig. Figure 2-9a,b).

In either case, real systems above  $g_{\max}$ , *i.e.* **C-PG8**<sup>NHBoc</sup><sub>500</sub> and perhaps **C-PG7**<sup>NHBoc</sup><sub>500</sub>, deviate slightly from the ideal picture laid out in the Introduction: They are not *completely* densely packed, and some part of the system is still available for solvent swelling or side-chain mobility – either due to “holes” created by kinetically inaccessible peripheral groups or due to the balance of bulk and solvent interactions favoring an increased surface area. This is in part a reflection of solution-phase chemistry: At some point when a regime of high steric congestion is entered, as very much appears to be the case in the DPs discussed here, reactants for labelling or dendronization cannot access peripheral reactive groups, anymore. Reactants themselves are usually much bulkier than individual solvent molecules, and sufficient solvation of reagents may be necessary in many cases for synthetically useful reaction rates.<sup>†</sup>

$g_{\max}$  can therefore also be considered in a reagent-centered view:  $g_{\max}$  is the point beyond which small reagents usually active in the modification of peripheral groups cannot react exhaustively. Above  $g_{\max}$ , further growth occurs stochastically rather than exponentially, *i.e.* in a non-dendritic fashion. The exact position of the cross-over between complete and imperfect dendronization defining  $g_{\max}$  may vary significantly depending on the “guest” species,<sup>189</sup> but for **C-PG7**<sup>NHBoc</sup><sub>500</sub> and **C-PG8**<sup>NHBoc</sup><sub>500</sub> it would appear that even very small reagents such as 2,4-dinitrofluorobenzene are precluded from reacting within the DP, as are the larger dendronization agents. This suggests that a threshold of steric congestion inherent to this type of DP has been reached. In turn, this suggests that the presented synthetic method, in route **C** relying strictly on  $g = 1$  reagents, provides the closest possible approach to a dendritic molecule at its  $g_{\max}$ .

Generalizing to any dendritic structure,  $g_{\max}$  is surpassed when  $\alpha > 1$ , but only if over the course of the entire series of dendritic molecules  $\alpha$  did not drop significantly *below* the ideal value of 1. The latter point reflects that  $g_{\max}$  is a concept applicable only to dendritic molecules. A system in which  $\alpha$  may serve as a criterion to judge whether  $g_{\max}$  has been achieved must possess functional groups which can be practically quantitatively labelled, and the detection of labels must be accurate and sensitive, as very low levels of defects are expected when highly efficient divergent chemistry is employed. Furthermore, a reasonable estimate of molecular density is required.

Spectroscopic methods alone can usually not deliver the same information as a labelling method can: A purely spectroscopic measurement of defect frequency is by first order approximation independent of steric factors. It is therefore difficult to assess by only spectroscopic methods whether dendronization defects originate in reaction inefficiencies *e.g.* due to declining solvent quality or

---

<sup>†</sup> This is a very crude generalization, as the ever widening field of synthetic mechanochemistry demonstrates. There however friction/grinding and the associate high local pressures and temperatures provide significant activation energy.



insufficient reaction times, or whether they are due to steric limitations excluding reactants at  $g > g_{\max}$ . Additionally, the fairly dense packing near and above  $g_{\max}$  may well mask defects, particularly in NMR spectroscopy. For instance, free amine defects in  $\text{PG}g_n^{\text{NHBoc}}$  are difficult to quantify by  $^1\text{H-NMR}$  spectroscopy: Amine signals are significantly broadened by H-bonding, an issue exacerbated by differences in relaxation times between the peripheral groups of the DP (which are solvent swollen and comparatively mobile) and the interior below the outermost layer(s) of dendritic repeat units, which are much more strongly entangled *and* interact with the solvent less than peripheral groups do. This results in amines not being present with a distinct peak *e.g.* in the  $^1\text{H-NMR}$  spectra of **B-PG6** $_{500}^{\text{NHBoc}}$  or **C-PG8** $_{500}^{\text{NHBoc}}$ , (Appendix A.6, Figure A-45) even though fairly large numbers of free amines are present according to Sanger labelling.

## 2.8. Summary and conclusions

After initial failures with a variety of other moieties, a successful implementation of route **C** (which aims to provide the free-base DP  $\text{PG5}_n^{\text{NH}_2}$ ) was found: It is based on the Alloc protecting group. Using a suitable catalyst/allyl scavenger pair ( $\text{Pd}(\text{PPh}_3)_4/\text{DMBA}$ ), the quantitative cleavage of  $\text{NHAlloc}$  was achieved under basic conditions. This method of amine deprotection was easy to implement on the polymer level, with only solvent composition and reaction times needing some optimization. This suggests that  $\text{NHAlloc}$ -based protecting group schemes may be of general use for post-polymerization functionalization in cases where *e.g.* acid-mediated deprotection of  $\text{NHBoc}$  cannot be tolerated, or where orthogonality to common protecting groups such as  $\text{NHBoc}$  is desired.

In line with the hypothesis that charged amines are responsible for the scission of  $\text{PG5}_n^{\text{NH}_3\text{TFA}}$ , the dendronization of  $\text{PG5}_{500}^{\text{NH}_2}$  to  $\text{C-PG6}_{500}^{\text{NHBoc}}$  was found to proceed without main-chain scission. The two-step sequence proceeded with very high functional group conversion values, providing access to the desired  $g = 6$  DP with a high degree of structural perfection for the first time. Surprisingly, it was found that  $\text{C-PG6}_{500}^{\text{NH}_3\text{TFA}}$  does not undergo main-chain scission, and as a result  $\text{C-PG7}_{500}^{\text{NHBoc}}$  was successfully synthesized using conventional  $\text{NHBoc}$ -based procedures. Similarly,  $\text{C-PG8}_{500}^{\text{NHBoc}}$  was synthesized from  $\text{C-PG7}_{500}^{\text{NH}_3\text{TFA}}$ , which was again not subject to degradation. Both of these steps proceeded with very high apparent functional group conversion, as well.

The comparison of these polymers with their analogs derived from route **B** provided insights of some consequence: GPC results agree with much improved structural perfection, in that retention volumes steadily increase with  $g$  – an assertion which cannot be made for the polymers synthesized previously *via* route **B**. This finding agreed with functional group conversion values derived from labelling with Sanger's reagent. Beyond  $g = 6$ , the molar masses calculated from Sanger labelling however are in conflict with theoretically achievable molar masses. This led to the definition of a parameter  $\alpha = M_{\text{exp}}/M_{\text{max}}$  which under certain circumstances allows one to determine whether members of divergently synthesized series of dendritic molecules have surpassed  $g_{\text{max}}$  by capturing the "excess" of experimentally determined molar mass. By this measure,  $\text{C-PG8}_{500}^{\text{NHBoc}}$  is firmly above  $g_{\text{max}}$  of the  $\text{PG}_n^{\text{NHBoc}}$  DP series.

Conflicting at first glance with approaching and surpassing  $g_{\text{max}}$  for truly dendritic molecules, the appearance of  $\text{C-PG6}_{500}^{\text{NHBoc}}$  was found to be rather irregular in AFM imaging, showing distinctly more corrugation and undulation than  $\text{B-PG6}_{500}^{\text{NHBoc}}$ . This finding may be explained as resulting from the projection of an undulated or helical state in solution, which the DP might assume in proximity to  $g_{\text{max}}$  in order to accommodate the large amount of mass, or as a consequence of kinetic trapping of certain conformations due to ultimate steric congestion having been achieved. The latter interpretation suggests itself since the irregularities observed at the  $g = 6$  level are apparently propagated to  $\text{C-PG7}_{500}^{\text{NHBoc}}$  and  $\text{C-PG8}_{500}^{\text{NHBoc}}$ .

While  $g_{\text{max}}$  has likely been surpassed for  $g = 8$ , perhaps the definition of this theoretical limitation bears rethinking. The present results (particularly AFM height imaging) indicate that at least limited solvent uptake in the extreme periphery is still possible, even above  $g_{\text{max}}$ , and so instead it may be more pragmatic to define  $g_{\text{max}}$  as lying just below the point at which proven reliable chemistry, even when utilizing fairly small reactive species and optimized reaction conditions, fails because of too-

strong steric hindrance. The impact of near-dense packing is evident in data collected in chapter 3 related to trends in solvent swelling throughout the DP series. Loading studies such as those previously conducted by Hinderberger *et al.*<sup>187,188</sup> may be able to provide more quantitative information on these points.

The present DPs of very high  $g$  represent a first push into the regime of fundamentally sterically self-obstructing growth. With the synthetic protocols at hand, single molecules with diameters in the range of 10 – 20 nm have become accessible. The tools described here – considering the synthetic relevance of results gleaned from investigations into main-chain scission (chapter 3) – should permit the synthesis of truly enormous single molecules with compact, well-defined structures and molar masses in the range of GDa.

## 3. Investigations Concerning DP Main-Chain Scission

### 3.1. Introduction

One main achievement of the work presented in this thesis is the avoidance of main-chain scission in DPs of  $g = 5$  (chapter 2). This was based on the hypothesis that Coulombic repulsion between partially unshielded ammonium cations is responsible for the scission of the DP backbone. The backbone rather than any peripheral bond was thought to be most prone to scission a) because the backbone bonds represent the point of balance of repulsive forces, assuming a symmetric distribution of the side chains around the backbone, and b) because the degree of substitution of the poly(methacrylate) is quite high, with every second carbon atom being quaternary.

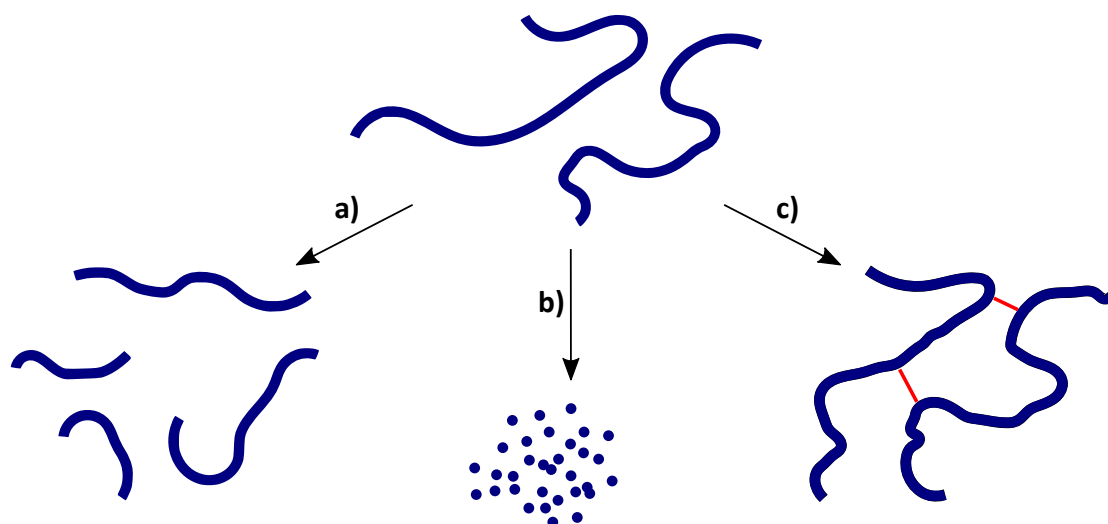
The successful implementation of an NHAloc-based protecting group strategy for the synthesis of  $\mathbf{C}$ -PG6<sub>*n*</sub><sup>NHBoc</sup> appeared to vindicate this initial hypothesis. Simultaneously however, the finding that the  $g > 5$  polyelectrolytes with improved structural perfection do not undergo main-chain scission indicated that the hypothesis of charge-induced main-chain scission needed refining, or even complete rethinking: The number of peripheral groups grows exponentially with  $g$ , whereas the maximum volume available to these charges only increases with a power of 2 – 3 (depending on how much backfolding occurs), and therefore the charge density and propensity towards scission should be increased in the polymers stemming from route **C**, rather than decreasing.

Consequently, this chapter presents a reinvestigation of main-chain scission based on two sets of data. The possibility of accessing PG5<sub>*n*</sub><sup>NH<sub>2</sub></sup> using route **C** opened intriguing possibilities. Experiments involving the protonation of DPs with acids of differing strengths and others aimed at controlling charge density in the DP periphery will be presented in this chapter. They were expected to aid in ascertaining whether a threshold of charge density exists above which the DP undergoes scission, and in situating said threshold. A second set of observations has arisen more recently: Initiated by the serendipitous discovery that PG5<sub>~5'000</sub><sup>NHBoc</sup> undergoes thermally induced degradation in solution, an entirely new set of experimental evidence pertaining to main-chain scission became available.

### 3.2. General remarks on polymer chain degradation

Polymer degradation reactions are of great significance in the application of various plastics. Molar mass, molar mass distribution,<sup>229</sup> and the degree of branching significantly influence the mechanical properties of a polymer, and changes in these parameters are usually detrimental, often leading to mechanical failure. The following brief description of different degradation phenomena will point out only those leading to topological changes, leaving aside other important types of degradation reactions not directly affecting topology, such as *e.g.* dehydrochlorination in PVC<sup>230</sup> or the hydrolysis of side chains in acrylates and methacrylates.<sup>231</sup>

Scheme 3-1 displays the major classes of topological changes involved in polymer degradation: Mechanisms involving random scission lead to a decrease in molar mass and may significantly alter the molar mass distribution, but do not lead to a significant loss in overall sample weight. Depolymerization mechanisms involve the conversion of long polymers to monomers or (more rarely) other well-defined small-molecules species, in reactions often associated with a loss of mass due to the formation of volatile or soluble products. Cross-linking leads first to increases in molar mass, and eventually to gel formation and insolubilization of soluble precursor polymers. Often, the ageing of a polymeric material is caused not by one but by a combination of multiple degradation reactions.



Scheme 3-1: Generalized modes of chain degradation. a) Random chain scission; b) depolymerization; c) cross-linking.

Random chain scission occurs *e.g.* under mechanical load: In the 1960s, it was found that the fracture of different glassy polymers produces free radicals detectable by EPR spectroscopy, and that the fracture process yields radicals only above a certain minimum chain length.<sup>232–234</sup> Mechanical scission in flow is relevant in polymer processing, particularly when extrusion is employed.<sup>235</sup> Main-chain scission may take place in sonochemical treatment of solutions of many polymers<sup>236</sup> and was also confirmed to proceed by radical mechanisms.<sup>237</sup> Sonochemical scission is likewise subject to a lower limit: The crucial parameter is a polymer's contour length rather than its molar mass, as had long been suspected but proven only very recently.<sup>238,239</sup> Random scission may also occur under conditions other than mechanical stress - the hydrolysis of polyesters and the (photo)oxidation of many olefinic polymers are examples which proceed mainly *via* random scission.<sup>240</sup> Cross-linking predominantly occurs in conjunction with random chain scission, particularly where radical

mechanisms are involved,<sup>241</sup> though the balance of the two processes is highly dependent on the polymer structures.

Depolymerization reactions occur less commonly in very high yields, although there are some prominent examples of polymers with sufficiently low ceiling temperatures ( $T_c$ ): PMMA is well known to undergo pyrolysis at high temperatures, affording methyl methacrylate in high yield.<sup>242</sup> However, depolymerization typically only occurs at temperatures ( $> 300\text{ }^\circ\text{C}$ ) significantly above  $T_c = 220\text{ }^\circ\text{C}$ ,<sup>243</sup> as some mechanism of activation is usually necessary, either at chain ends or by scission. The commercial importance of PMMA has led to attempts at stabilizing the polymer by copolymerization with *e.g.* maleic anhydride to improve heat resistance during processing.<sup>244</sup> PTFE is another commonly used polymer that undergoes significant depolymerization above *ca.*  $350\text{ }^\circ\text{C}$ .<sup>245</sup> A last prominent example is polyformaldehyde (also called poly(oxymethylene), POM): The polymer is not very chemically stable as such and needs to be end-capped after polymerization (*e.g.* by esterification) for commercial applications.<sup>246</sup> Exposure of POM to strong acids or bases may hydrolyze the terminal group and lead to catastrophic failure of the material due to the ensuing depolymerization.

Sometimes, these reactions may be desired: Particularly cross-linking is an important tool, as it renders polymers insoluble and mechanically more resistant. This fundamental shift in properties is utilized *e.g.* in photolithography,<sup>247</sup> where the irradiation of cross-linkable, photoreactive polymers (negative photoresists) renders irradiated areas insoluble, whereas unexposed areas can be washed away by a suitable solvent. Another important application for cross-linking is the vulcanization of natural rubber, which turns the natural poly(*cis*-isoprene) - a tacky, soft substance - into non-sticky rubber of adjustable hardness. Reactions leading to a reduction in molar mass can likewise be desirable, *e.g.* for applications in drug transport, where ideally a suitable stimulus-responsive polymeric nanoparticle could release its load at the target site by depolymerization or random chain scission.<sup>248</sup> Random chain scission can also be employed for photolithography, where polymers may serve as positive photoresists which reveal the underlying support after exposure and dissolution.

### 3.3. Prior evidence for charge-induced main-chain scission

#### 3.3.1. Summary of previous findings

The findings summarized below are drawn mainly from the work of Dr. Hao Yu and Prof. Dr. Baozhong Zhang and have in large parts been published<sup>169</sup> or can be found in the thesis of Dr. Hao Yu.<sup>172</sup> Where this is not the case, information is based on personal communications and other work which, in the interest of brevity, is not detailed here.

The first instance of main-chain scission was found in the course of the iteration of the “ $g + 1$ ” protocol which route **A** is based on (see Scheme 1-8b and Scheme 2-1): The deprotection of Boc-protected amines in  $\text{PG}g_n^{\text{NHBoc}}$  affords a polyelectrolyte of the type  $\text{PG}g_n^{\text{NH}_3\text{TFA}}$ ; This is followed by the dendronization of the liberated amines with the active ester  $\text{DG1}^{\text{NHBoc}}$  (**20**) under basic conditions, affording the next-higher  $g$  DP,  $\text{PG}(g+1)_n^{\text{NHBoc}}$ . This reaction sequence proceeded without issues up to  $\text{PG5}_n^{\text{NHBoc}}$ , with deprotection being effectively quantitative and dendronization very nearly so.<sup>101</sup> In the course of the next two-step sequence, *i.e.* the deprotection of  $\text{PG5}_n^{\text{NHBoc}}$  to  $\text{PG5}_{n'}^{\text{NH}_3\text{TFA}}$ , followed by dendronization to  $\text{A-PG6}_n^{\text{NHBoc}}$ , the outcome was not as desired: Instead of resulting in long chains, this sequence delivered much shorter fragments as evidenced by AFM imaging (see Figure 3-2a-c) and by GPC. AFM imaging of the intermediate polyelectrolyte  $\text{PG5}_{n'}^{\text{NH}_3\text{TFA}}$  revealed dot-like objects rather than the long chains evident in the starting material, indicating that chain degradation had taken place during the deprotection step rather than later. In-depth investigations into this process followed,<sup>169</sup> the main findings of which are:

- *The fragments observed in AFM and GPC are mostly oligomers:* From GPC of  $\text{A-PG6}_{n'}^{\text{NHBoc}}$ , it was estimated that  $n' \approx 40 - 50$ . This number was confirmed by a separate synthesis of  $\text{A-PG6}_{40}^{\text{NHBoc}}$  starting from  $\text{PG1}_{40}^{\text{NHBoc}}$ . No degradation of chain length was observed in the preparation of this series (see Figure 3-2d-f).
- *Fragment yield is high:* With isolated yields of  $\text{A-PG6}_{\sim 40}^{\text{NHBoc}} > 60\%$ , main-chain scission yielded mostly oligomeric fragments, rather than resulting in mostly macromonomer.
- *Scission occurs on the DP backbone, rather than in the periphery.* This was demonstrated by MALDI-TOF-MS of reaction products, in which the deprotected macromonomer was observed (in the form of  $\text{MG5}^{\text{NH}_2}$  **57**, see Figure 3-1), but where smaller fragments were lacking. This was corroborated by the presence of olefinic signals in  $^1\text{H-NMR}$  spectra.
- *The acid concentration does not have a significant impact.* Neat TFA is usually employed for DP deprotection. Lower concentrations (*e.g.* 20 % v/v TFA in methylene chloride) are conventionally used in SPPS, but main-chain scission also occurred at these lower acid concentrations.
- *The exact acid used for deprotection does not matter.* Scission also occurred when *e.g.* HCl was used for NHBoc deprotection instead of TFA.
- *Temperature affects main-chain scission:* When conducted at lower temperatures *and* using lower concentrations of acid, the degree of chain degradation can be moderated, but the process cannot be avoided completely.
- *Time affects scission:* In order to guarantee complete conversion of the many Boc-protected peripheral amines in a DP of the type  $\text{PG}g_n^{\text{NHBoc}}$ , reaction times of several hours are employed.

When the reaction is halted after only brief exposure to TFA (few minutes) longer chain fragments can be observed than normally. Deprotection is likely incomplete at this point, however.

- *Backbone defects do not appear responsible for scission:* In order to reduce the number of weak points in the DP backbone and to investigate the influence of end groups, the DP synthesis was modified. Head-to-head couplings are improbable because of the large substituents present in the methacrylate-based monomer **18** but may still occur rarely in the course of FRP. It was hoped that using RAFT polymerization would lead to even fewer such defects with locally extremely high steric congestion. However, if anything the propensity towards main-chain scission was found to be higher for RAFT-derived  $\text{PG5}_n^{\text{NHBoc}}$  than for FRP-derived samples.
- *Scission depends on  $g$ :* Evidently, no main-chain scission had been observed under standard synthetic conditions for  $g < 5$  DPs. However, scission was observed in the treatment of  $\text{PG4}_n^{\text{NHBoc}}$  under very harsh conditions (neat, refluxing TFA for several days). DPs of  $g < 4$  were found to be stable even in refluxing TFA. Scission was not found to occur for **B-PG6** $_{500}^{\text{NHBoc}}$ , **B-PG7** $_{500}^{\text{NHBoc}}$ , **C-PG6** $_{500}^{\text{NHBoc}}$  and **C-PG7** $_{500}^{\text{NHBoc}}$  under standard synthetic conditions, permitting for the syntheses of higher  $g$  DPs (see chapter 2).<sup>174</sup>
- *Scission appears unaffected by side-products of deprotection:* The acid-mediated deprotection of NHBoc moieties is known to generate *tert*-butyl cations.<sup>249</sup> Although the lack of chain scission at lower generations and in **A-PG5** $_{40}^{\text{NHBoc}}$  (see above) suggests that chain-end activation or indeed chemical attack is unlikely, it was nevertheless thought remotely possible that such reactive species might play a role in the main-chain scission process. Cation scavengers are frequently used in SPPS, where the presence of *tert*-butyl cations may be disruptive. Conducting the deprotection in the presence of *e.g.* triethylsilane<sup>250</sup> did however not alter the outcome, and scission was still observed.



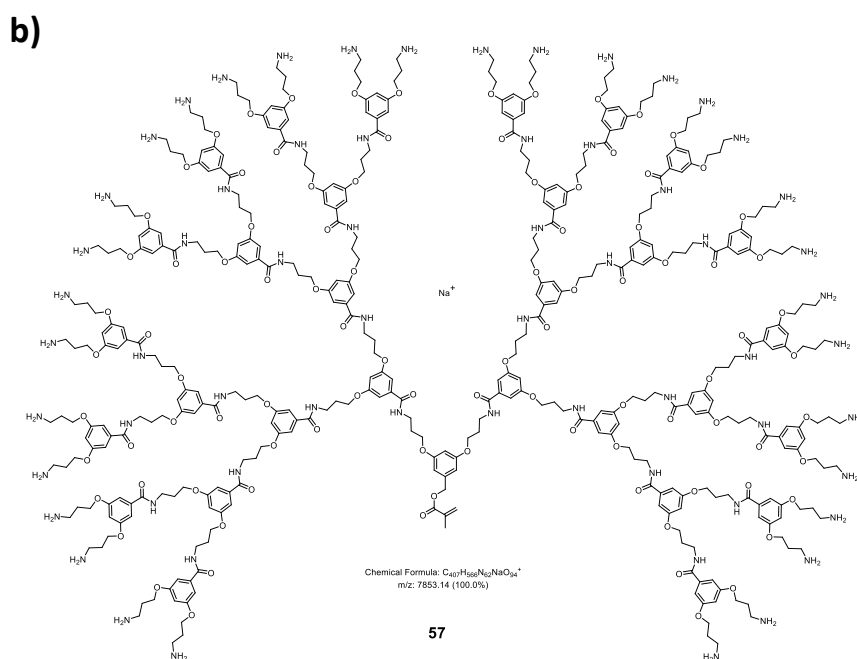
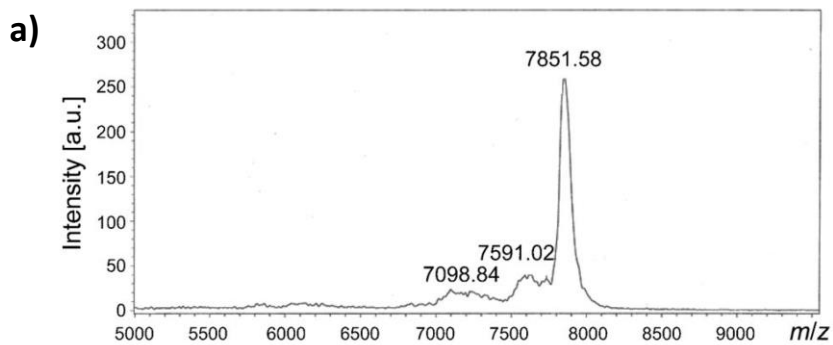


Figure 3-1: a) MALDI-TOF-MS of the product of  $PG5^{NH_{Boc}}$  deprotection using TFA,<sup>169</sup> reproduced from with permission from H. Yu et al. *Helv. Chim. Acta* **2012**, 95, 2399-2410, copyright John Wiley & Sons, 2012. b) Chemical structure of the main detected species ( $(MG5^{NH_2}+Na)^+$ , **57**; main expected mass: 7853.14 Da).

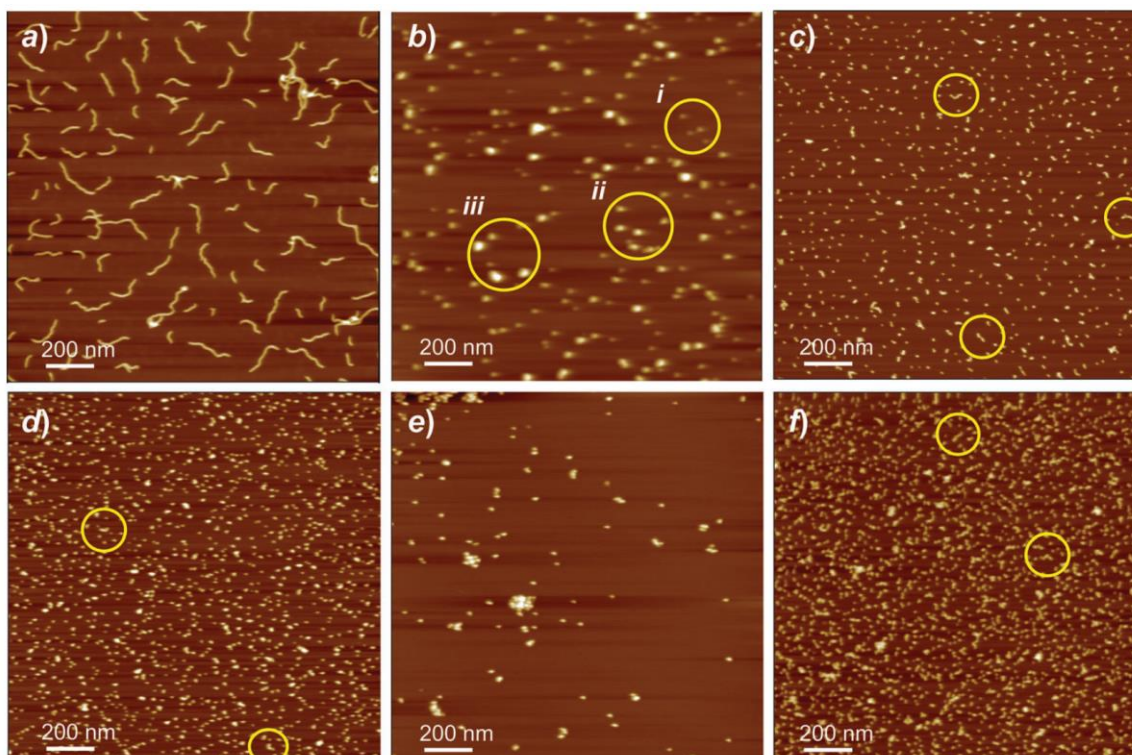


Figure 3-2: AFM height images of a)  $PG5_{500}^{NHBoc}$ , b)  $PG5_n^{NH_3TFA}$ , c)  $A-PG6_n^{NHBoc}$ , and, for comparison, the purposefully synthesized short-chain series d)  $PG5_{40}^{NHBoc}$ , e)  $PG5_{40}^{NH_3TFA}$ , f)  $A-PG6_{40}^{NHBoc}$ . Circles highlight occasionally observed chains of significant length in Figure 3-2c, d, and f, while the circles in Figure 3-2b mark feature groups with differing apparent AFM height values. Reproduced from with permission from H. Yu et al. *Helv. Chim. Acta* **2012**, 95, 2399-2410, copyright John Wiley & Sons, 2012.

### 3.3.2. The hypothesis of charge-induced main-chain scission

The observations listed in the previous section form a consistent picture: The observed decrease in molar mass during acid-mediated deprotection of  $PG5_n^{NHBoc}$  ( $n > 50$ ) is due to main-chain scission, which occurs apparently randomly along the initial DP's backbone. In this process, a small amount of macromonomer is generated, but largely and quite uniformly the products of this scission process are oligomers of  $P_n \approx 40 - 50$ , which appear as dot-like objects in AFM images (Figure 3-2).

As DPs of  $g = 5$  are already fairly close to the maximum dendritic generation  $g_{max} \approx 6 - 7$  of the class  $PGg_n^{NHBoc}$ , a ready explanation is steric congestion: The steric demand of a polyelectrolytic dendron, bearing a large number of ammonium cations, surpasses that of the Boc-protected precursor. Charges are certainly shielded partially by tightly associated counterions, but those counterions in turn contribute to the steric bulk of the dendron. Molecular dynamics simulations have supported this: The structure of a short polyelectrolyte,  $PG5_{75}^{NH_3TFA}$ , was found to appear sponge-like owing to charge-charge repulsion between dendrons in aqueous solution.<sup>228</sup> These results can unfortunately not be compared directly to parallel simulations of  $PG5_{100}^{NHBoc}$ , which were performed in the absence of solvent (however,  $PG5_n^{NHBoc}$  is insoluble in water). Other MD simulations for  $PG4_{100}^{NHBoc}$  conducted in the presence of  $CHCl_3$  (a solvent of fairly good quality) suggest that the density profile for  $PG5_{75}^{NH_3TFA}$  is markedly different from that of a dissolved DP of the type  $PGg_n^{NHBoc}$ .<sup>98</sup>

The increased repulsion between neighboring dendrons may be responsible for main-chain scission: While the individual contributions of peripheral ammonium cations are likely small, the resulting repulsive forces may be transmitted through the dendritic branchwork. Apparently, the sum of these forces is large enough for single carbon-carbon bonds to rupture at room temperature or below. That the location of bond scission is along the backbone rather than within the dendritic structure is therefore not surprising, since the backbone bonds represent the point of balance between dendrons. A related effect has previously been observed in work by Matyjaszewski *et al.*,<sup>251</sup> where the transmission of adhesion forces from the side chains led to tension and eventually backbone scission in bottlebrush copolymers.

In such a mechanically induced process, homolytic bond scission appears the most probable mechanistic course for the actual breaking of the backbone. However, a polar mechanism cannot be excluded out of hand. Whatever the initial species, it is likely that the macromonomer detected in MALDI-TOF-MS and <sup>1</sup>H-NMR is the result of partial depolymerization of an active chain end. However, depolymerization does not proceed to completion after initial random scission, suggesting either quenching of the reactive species (*e.g.* through reaction of a radical chain end with oxygen), or else the reduced degree of polymerization limiting the driving force behind initial scission and depolymerization. Likely both of these factors contribute, but the latter appears to be more relevant considering the fairly uniform, dendrimer-like appearance of the main product of scission, PG5<sup>NH<sub>3</sub>TFA</sup><sub>~40</sub>: In these ellipsoidal oligomers, chain-end effects dominate, providing sufficient space for the dendritic side chains to get out of each other's way. This may result in a lower strain on the backbone bonds and a cessation of further random scission for the short backbone segments which have remained intact.

The observed *g* dependence of this reaction partially agrees with this hypothesis: Scission does not occur in the less strongly sterically congested DPs of *g* < 4. High temperatures are necessary for PG4<sup>NH<sub>3</sub>TFA</sup><sub>*n*</sub> to undergo scission. Only then the necessary thermal energy to surmount the activation barrier is present, or intramolecular potentials due to solvent swelling, conformation, ion pairing, *etc.* are changed sufficiently to result in an increased steric demand of the dendrons. The temperature and time dependence of scission can likewise easily be explained within this scheme: At lower temperatures, scission is slower, and therefore internal rearrangement reducing the tension on the backbone may be possible before full charge-charge repulsion sets in. In the case of reduced reaction times, the less severe scission may be rationalized as originating from yet incomplete conversion of peripheral Boc groups to ammonium cations.

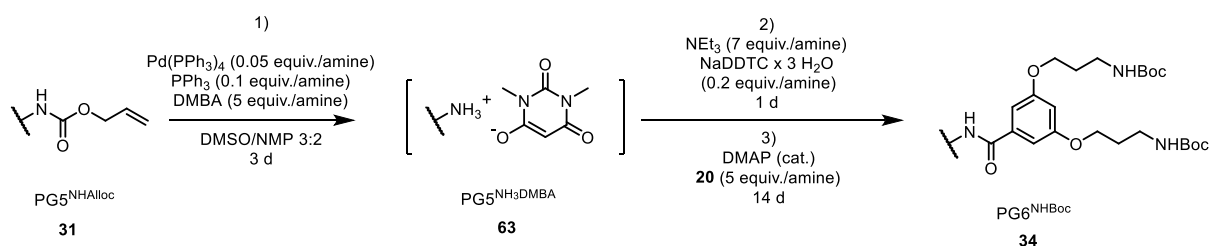
An observation which jars with the above picture is the absence of main-chain scission upon deprotection for all DPs of *g* > 5: These polymers do not undergo chain degradation under standard conditions, a fact which conveniently permitted the syntheses of **B-PG7**<sup>NHBoc</sup><sub>500</sub>, **B-PG8**<sup>NHBoc</sup><sub>500</sub>, **C-PG7**<sup>NHBoc</sup><sub>500</sub> and **C-PG8**<sup>NHBoc</sup><sub>500</sub> using standard NHBoc-based chemistry. This is puzzling in the context of the above hypothesis: For **C-PG6**<sup>NH<sub>3</sub>TFA</sup><sub>500</sub> and **C-PG7**<sup>NH<sub>3</sub>TFA</sup><sub>500</sub>, the linear density of peripheral charged amines should be higher than it is for PG5<sup>NH<sub>3</sub>TFA</sup><sub>500</sub>. The same is true for **B-PG6**<sup>NH<sub>3</sub>TFA</sup><sub>500</sub> and **B-PG7**<sup>NH<sub>3</sub>TFA</sup><sub>500</sub>, even after factoring in the large numbers of defects in these polymers. This suggests that perhaps charge-charge repulsion is not the sole or even the determining factor.

### 3.4. Additional investigations concerning main-chain scission in charged DPs

The successful deprotection of a  $g = 5$  DP under basic conditions has permitted not only the largely defect-free synthesis of  $\mathbf{C-PG6}_{500}^{\text{NHBoc}}$ , but has also provided an interesting tool with which additional insight into the main-chain scission process may be gained: It has provided direct access to  $\text{PG5}_{500}^{\text{NH}_2}$ , which may be protonated to afford the suspected instable polyelectrolytes. A point of particular interest was whether there is a charge threshold above which main-chain scission occurs, *i.e.* whether a certain proportion of peripheral amines needs to be protonated for scission to occur at all, or whether instead scission just becomes more pronounced with increasing charge density. Another question of interest was whether ammonium cations are strictly necessary for scission to occur or whether other types of charged moieties might lead to scission, *i.e.* whether the phenomenon is related to the specific structure of the type  $\text{PG}g_n^{\text{NH}_3\text{TFA}}$  or whether this could also be observed in other systems of the type  $\text{PG}g_n^{\text{X}}$ . This section describes a number of experiments aimed at addressing these and other questions related to charge-induced main-chain scission.

#### 3.4.1. Deprotection of $\text{PG5}_{500}^{\text{NHAlloc}}$ in absence of base

In the implementation of route **C** described in chapter 2 (Scheme 2-10), the addition of a large excess of base ( $\text{NEt}_3$ ) was necessary because of the acidity of the scavenger (DMBA,  $\text{pK}_a \approx 4.75^{252}$ ). Being of roughly the same strength as acetic acid, DMBA is certainly capable of fully protonating the generated amines. This is generally useful in  $\text{NHAlloc}$  deprotection, as protonation reduces amine nucleophilicity and therefore prevents *N*-allylation, but it was undesirable in the synthesis of  $\mathbf{C-PG6}_{500}^{\text{NHBoc}}$ . However, the acidity of DMBA enables a straightforward experiment to test the validity of the hypothesis of charge-induced main-chain scission: It consists of the simple omission of base during the deprotection of  $\text{PG5}_{500}^{\text{NHAlloc}}$ , followed by dendronization under basic conditions (Scheme 3-2).



Scheme 3-2: Modified reaction conditions for  $\text{NHAlloc}$  deprotection without the use of base. Compare Scheme 2-10.

The product isolated by precipitation of a sample after allowing dendronization to  $\text{PG6}_{n'}^{\text{NHBoc}}$  to progress for 14 d showed the reduction in chain length typical for main-chain scission in both AFM imaging and in GPC (Figure 3-3). This independent experiment, using different chemistry and conditions and only maintaining the protonation state of the DP, delivers evidence that indeed a polyelectrolyte of the form  $\text{PG5}_n^{\text{NH}_3\text{Y}}$  ( $\text{Y} = \text{DMBA}$ , **63** or  $\text{Y} = \text{TFA}$ , **27**) is not stable for high  $n$  and degrades to form shorter species instead. As is evident from the comparison of Figure 3-3a *e.g.* to Figure 3-2c, scission does not progress quite as far as is the case in TFA-mediated deprotection of  $\text{PG5}_n^{\text{NHBoc}}$ , leaving

behind significantly more chains of substantial length; It corresponds approximately to the result of TFA-mediated deprotection of  $PG5_n^{NHBOC}$  when halted after brief exposure to acid. The small additional peak observed in GPC at an RV of *ca.* 20.7 mL (Figure 3-3b) may correspond to macromonomer which is not separated in work-up by precipitation, hinting at a similar process in spite of the vastly different conditions applied.

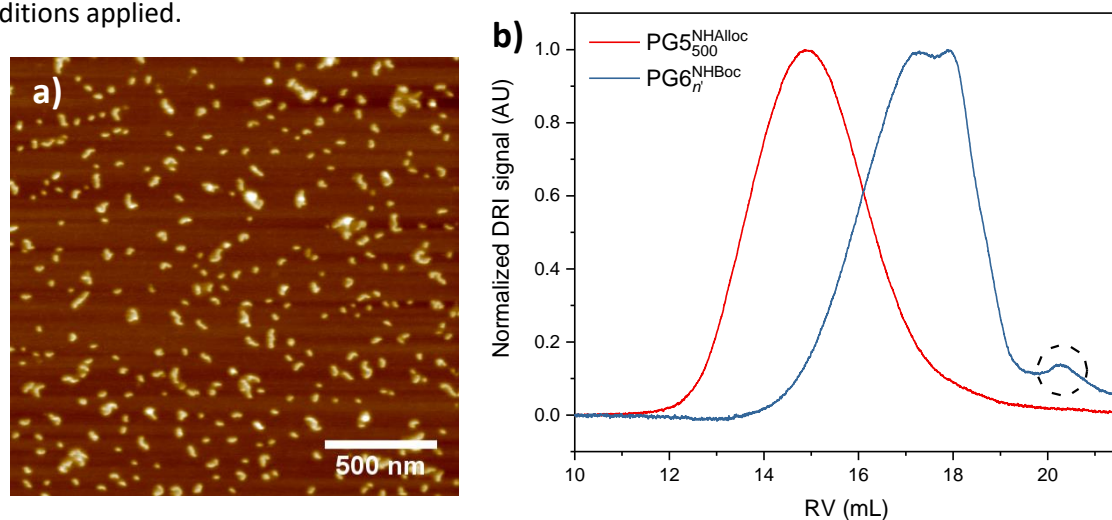


Figure 3-3: a) AFM height image of the product of base-free deprotection of  $PG5_{500}^{NHAlloc}$ , followed by dendronization to  $PG6_n^{NHBOC}$ ; b) GPC elution curves of  $PG5_{500}^{NHAlloc}$  and the product obtained after base-free  $NHAlloc$  deprotection. The dashed circle marks the peak suspected to represent macromonomer.

### 3.4.2. Treatment of $PG5_{500}^{NH_2}$ with acid

Next, an attempt was made to treat  $PG5_{500}^{NH_2}$  with defined aliquots of trifluoroacetic acid in order to determine an approximate threshold of the degree of protonation above which main-chain scission occurs, and whether perhaps the reaction time had any significant influence. To that end, deprotection was performed on a sample of  $PG5_{500}^{NHAlloc}$ , using the procedure detailed in section 2.4. Samples of the resulting solution, containing  $PG5_{500}^{NH_2}$ , were then exposed to varying amounts of excess TFA (0.8 equiv./amine, 1.2 equiv./amine, 2 equiv./amine and 4 equiv./amine). Exposure to acid was stopped in each case after 15 min, 1 h and 3 h by exposing the resulting polymer to basic dendronization conditions (see Experimental, subsection 8.3.2).

AFM imaging revealed that all samples, except for a control which had not been acidified, had undergone some scission (Figure 3-4). Accordingly, GPC retention volumes were significantly increased when compared to the control in all cases (Figure 3-5). Throughout, a progression of scission over time was observed, marked by a distinct increase in retention volume between 15 min and 1 h, followed by a far smaller increase over further 2 h of stirring under acidic conditions. This decrease over time is consistent with previous observations of main-chain scission of  $PG5_{500}^{NHBOC}$ , which can be mitigated – though never completely avoided – by employing short reaction times (minutes), however at the sacrifice of complete conversion. Under the solvent conditions of  $NHAlloc$  deprotection, it appears that charge-induced scission likewise occurs over a timescale of minutes. The present GPC data – which is admittedly too sparse to allow for the derivation of proper kinetics – suggests a “chain half-life” on the order of *ca.* 5 min. Curiously, the samples treated with the largest amount of acid

showed the least pronounced scission initially. The high-MW tail (Figure 3-5d) disappeared between 1 h and 3 h of the polymer being subjected to acidic conditions. The scission products ultimately obtained by protonation with excess TFA are by and large shorter than those obtained by protonation with DMBA (compare *e.g.* Figure 3-4c with Figure 3-3a, or Figure 3-5a with Figure 3-3b), indicating that the strength of the acid may have some influence, aside from the degree of peripheral protonation.

This last observation and the lack of distinct differences between the varied amount of acid suggested that the reaction setup did not permit for accurate control of the degree of protonation: The amounts of polymer and acid in each individual sample were quite small, making relative concentrations hard to control. Additionally and likely more importantly, deprotection required degassing to exclude oxygen, which was achieved by purging of the reaction mixture with argon prior to the addition of Pd(PPh<sub>3</sub>)<sub>4</sub>. Likely, this resulted in the loss of some NEt<sub>3</sub>, and consequently it is quite probable that a substantial excess of TFA was present in all cases. In order to gain more control over the degree of protonation, this approach was abandoned in favor of the one presented in the next subsection.

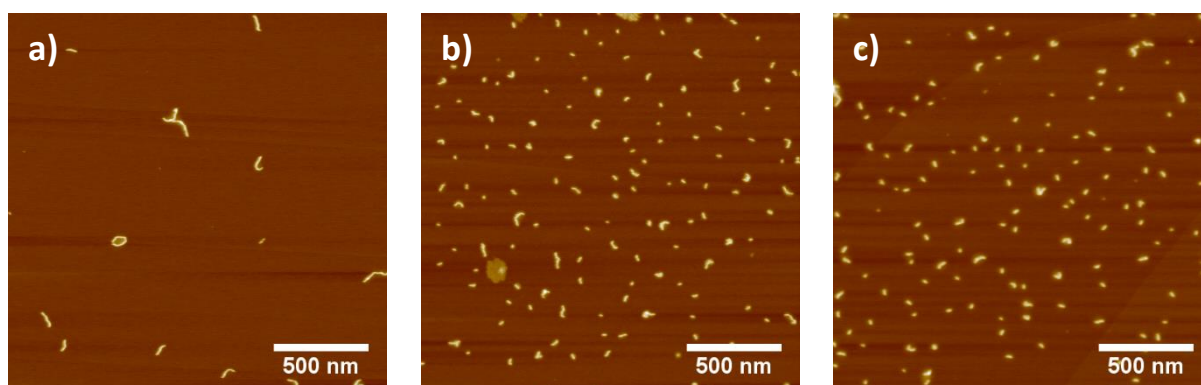


Figure 3-4: AFM height images of the products of attempted intermediate reactive titration with acid. Shown are a reaction control (a) in which no acid was added after deprotection (showing long chains) as well as the two edge cases: b) 0.8 equiv. of TFA for 15 min, c) 4 equiv. of TFA for 3 h.

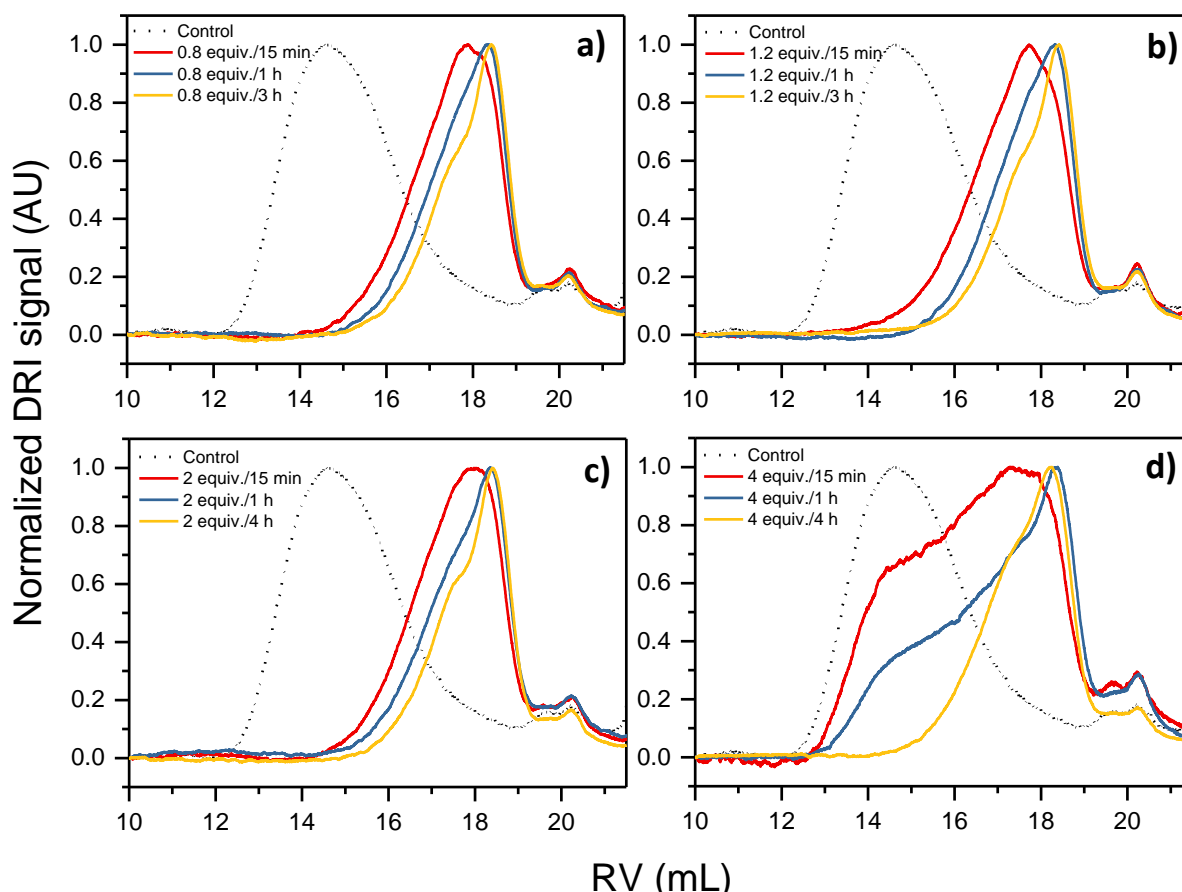


Figure 3-5: GPC retention curves of samples treated with a) 0.8 equiv., b) 1.2 equiv., c) 2 equiv. and d) 4 equiv. of excess TFA per amine, each for 15 min, 1 h, and 3 h before quenching with excess base. The dashed black curve represents the control to which no acid was added before dendronization.

### 3.4.3. Deprotection of mixed-substitution $g = 5$ DPs in absence of base

As the addition of acid directly to  $\text{PG5}_{500}^{\text{NH}_2}$  had proven difficult to control, it was anticipated that direct control of the ratio of charged and uncharged peripheral groups after *N*-deprotection could be achieved by orthogonal protection of amines. To that end, polymers with mixed peripheral substitution were synthesized. DPs with 75 %, 50 % and 25 % of peripheral Alloc-protected amines (the remainder being Boc-protected) were targeted to conduct these experiments, to cover a large range of relative protonation states. They were prepared by first reacting  $\text{PG4}_{500}^{\text{NH}_3\text{TFA}}$  with a defined amount of  $\text{DG1}^{\text{NHAlloc}}$  (**55**), followed by a large excess of  $\text{DG1}^{\text{NHBoc}}$  (**20**) in order to achieve full dendronization.

While this approach was successful in principle, the targeted ratios were not quite achieved as judged by  $^1\text{H-NMR}$  spectroscopy (Figure 3-6): Integration of NHAlloc and NHBoc signals shows that the proportion of NHAlloc is in all three cases higher than aimed for. The synthesized polymers contain 36 %, 57 % and 80 % Alloc-protected amines and accordingly will be referred to as  $\text{PG5}_{500}^{\text{Alloc36}}$ ,  $\text{PG5}_{500}^{\text{Alloc57}}$ , and  $\text{PG5}_{500}^{\text{Alloc80}}$ , respectively. Possible causes are errors in weighing and the loss of some polymer *e. g.* during workup of the deprotection reaction.

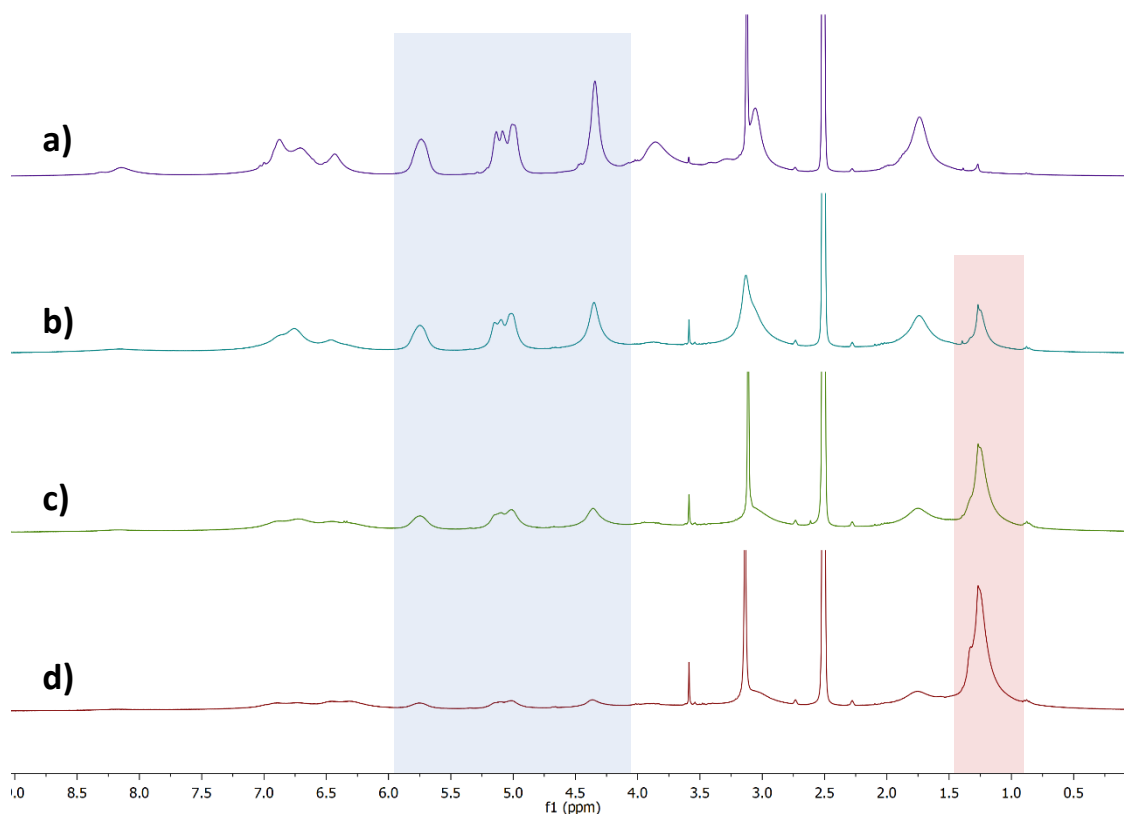


Figure 3-6:  $^1\text{H-NMR}$  spectra of  $\text{PG5}_{500}^{\text{NHAlloc}}$  (a), as well as the mixed-substitution polymers with b) 80 % ( $\text{PG5}_{500}^{\text{Alloc80}}$ ), c) 57 % ( $\text{PG5}_{500}^{\text{Alloc57}}$ ), and d) 36 % ( $\text{PG5}_{500}^{\text{Alloc36}}$ ) of  $\text{NHAlloc}$ -protected peripheral groups. Signals of Alloc and Boc protons are underlaid in blue and red, respectively.

Although the targeted substitution ratios were not quite achieved, the prepared polymers still covered a large enough range to be used in the initially planned deprotection experiments. Considering that even the weak acid DMBA is sufficient to induce scission, deprotection of these polymers was again conducted in the absence of base (see section 3.4.1).  $\text{NHBoc}$  is stable under  $\text{NHAlloc}$  deprotection conditions.<sup>253,254</sup> Using the conditions shown in Scheme 3-2, deprotection was followed by addition of excess  $\text{NEt}_3$  and dendronization with  $\text{DG1}^{\text{NHBoc}}$ . The resulting polymers were investigated by AFM imaging and by GPC.

It is evident that no main-chain scission occurred: GPC retention volumes were slightly lower than those of the respective starting materials, as opposed to showing the significant decrease observed in the base-free deprotection of  $\text{PG5}_{500}^{\text{NHAlloc}}$  (Figure 3-7). Similarly, AFM height images (Figure 3-8) showed intact chains, comparable in length to their precursors.<sup>m</sup> The observation that even  $\text{PG5}_{500}^{\text{Alloc80}}$  did not undergo main-chain scission during base-free deprotection indicates that a very high number and concomitant density of peripheral charged groups is necessary for scission to occur. With the present results, only a lower threshold of *ca.* 80 % chargeable peripheral groups can be determined, above which main-chain scission induced by charge-charge repulsion may occur, though near-complete protonation may in fact be necessary to induce backbone degradation.

<sup>m</sup> Interestingly, the chains obtained after dendronization of the liberated amines appear smoother in AFM than  $\text{C-PG6}_{500}^{\text{NHBoc}}$ , although they are of necessarily lower structural perfection. See the discussion in subsection 2.6.3.



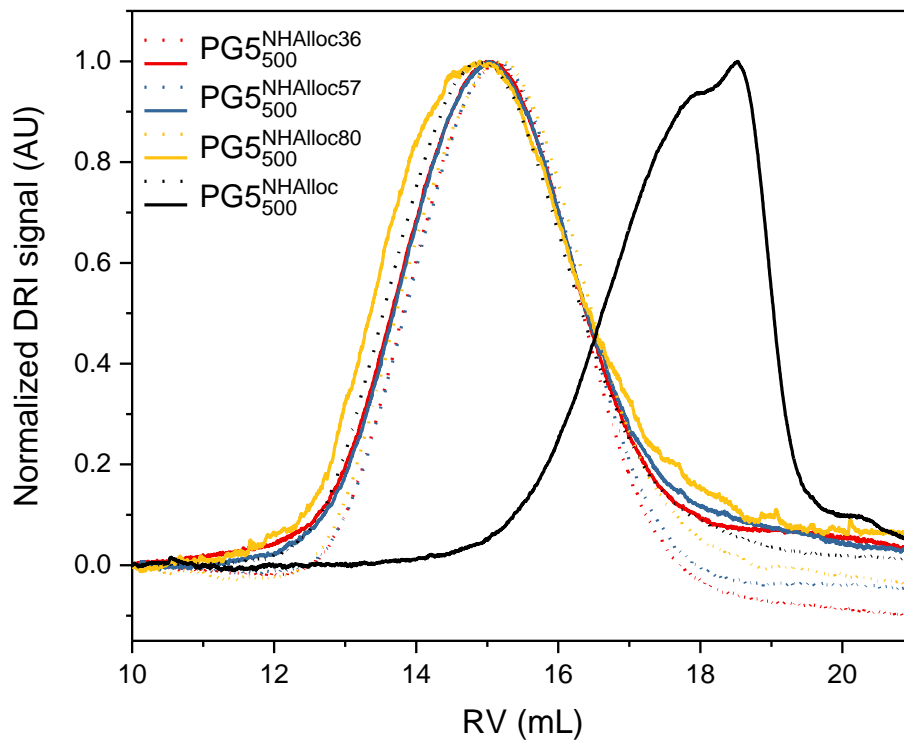


Figure 3-7: GPC of starting materials (dotted lines) and reaction products (solid lines) in the base-free deprotection of mixed protecting group DPs.

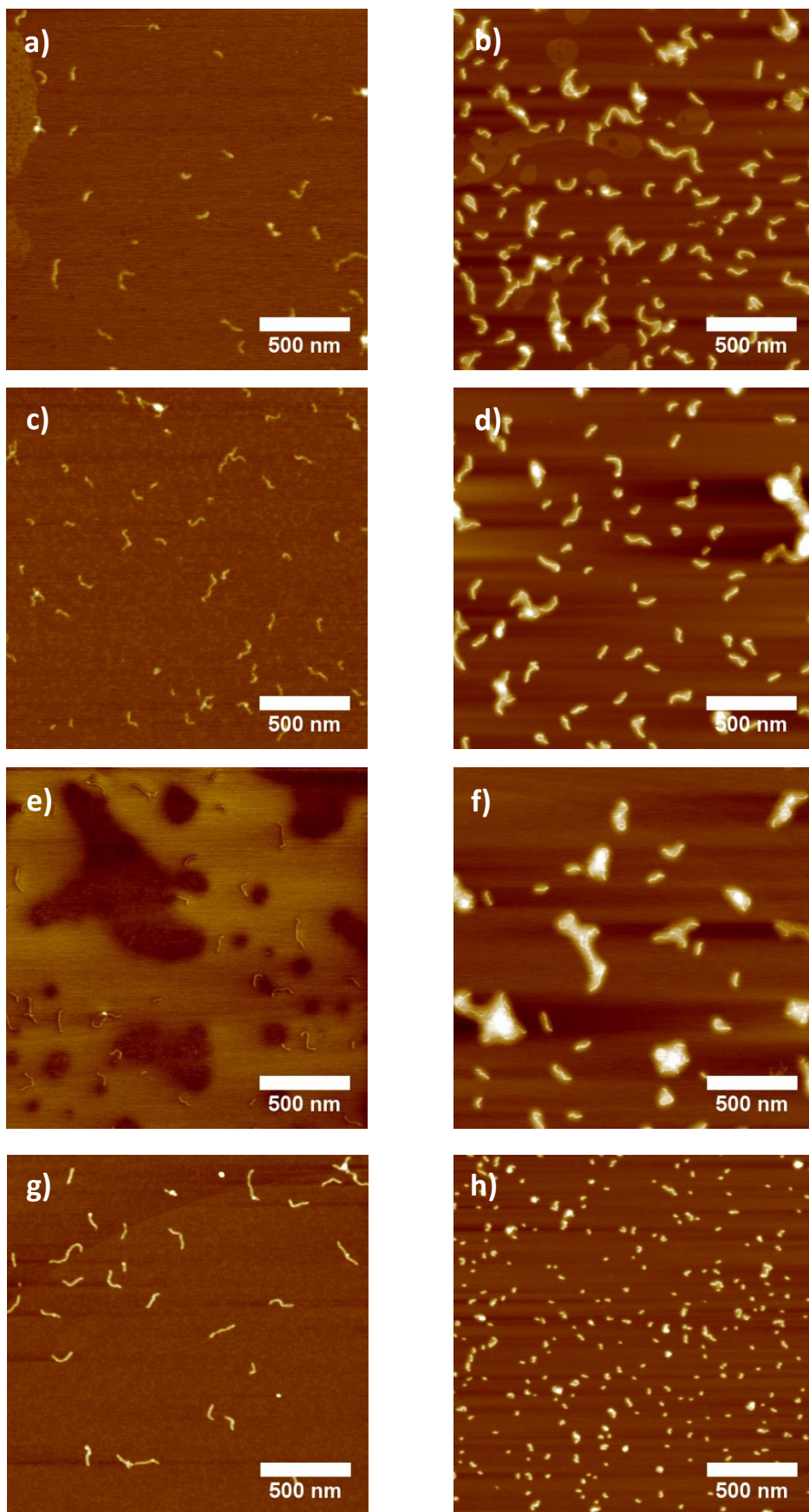


Figure 3-8: AFM height images of (left-hand column) starting polymers and (right-hand column) the products of deprotection/dendronization (Scheme 3-2): a)/b)  $PG5_{500}^{Alloc36}$ , c)/d)  $PG5_{500}^{Alloc57}$ , e)/f)  $PG5_{500}^{Alloc80}$ , g)/h)  $PG5_{500}^{NHAlloc}$ .

### 3.4.4. Scission in a polyanionic DP of $g = 5$

Though there are differences in the exact interaction parameters, depending on delocalization and the specific shielding by solvent and counterions, both cations and anions experience Coulomb repulsion when paired with like charges. Though the forces transferred to the backbone *via* the dendritic branchwork might vary, it should by first order approximation not matter whether the charges in the DP periphery are negative or positive. To test this hypothesis, a DP of  $g = 5$  bearing negatively chargeable peripheral groups was devised. Negatively chargeable DPs based on  $PGg_n^{\text{NHBoc}}$  had been prepared in previous work by reacting peripheral amines with a moiety containing a *tert*-butyl ester (Figure 3-9a; DPs up to  $g = 3$  were prepared in that case [40, Figure 1-21]).<sup>255</sup> Like NHBoc, this ester is susceptible to acid and can be removed *e.g.* by treatment with TFA.<sup>178</sup> The resulting carboxylic acid can be deprotonated, but the DPs investigated in the cited prior work are not suitable for the investigation of main-chain scission. They feature a succinimidyl spacer which results in the chargeable unit's position deviating significantly from that of the ammonium cations in  $PG5_n^{\text{NH}_3\text{TFA}}$ . To better approximate the latter's geometry, an alternative structure displayed in Figure 3-9b was devised. It also bears a *tert*-butyl ester but contains no additional spacer. A corresponding dendron suitable for the graft-from synthesis of DPs, **62**, was prepared from simple precursors as shown in Scheme 3-3a. Using **62**, the corresponding  $g = 5$  DP,  $PG5_{500}^{\text{CO}_2\text{tBu}}$ , was prepared using the standard dendronization protocol (Scheme 3-3b) modified only by the solvent composition ( $PG5_{500}^{\text{CO}_2\text{tBu}}$  is not soluble in pure DMF; see Experimental, subsection 8.3.1, for details).

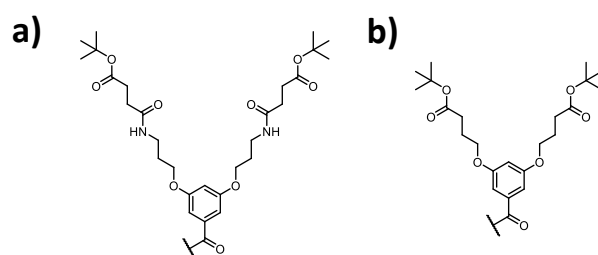
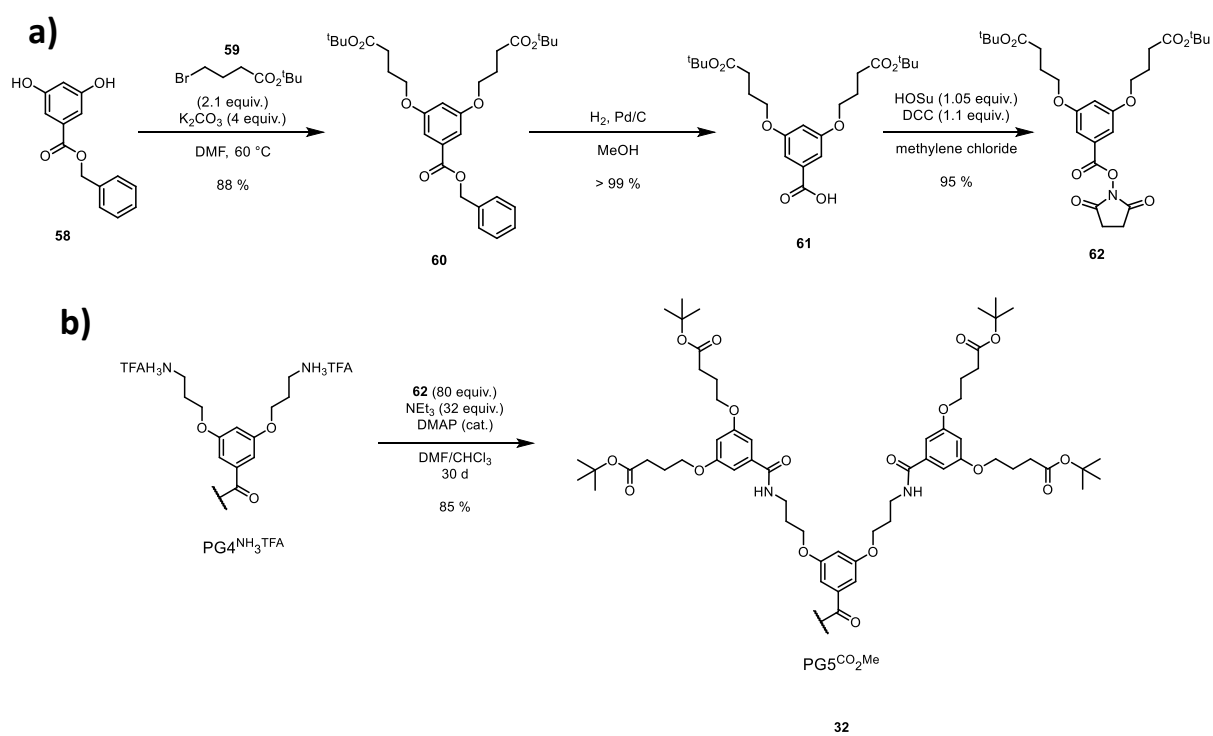


Figure 3-9: Structures of negatively chargeable dendritic units a) used in previous work<sup>255</sup> and b) in this thesis.

It was intended to first deprotect the peripheral *tert*-butyl esters with neat TFA (Figure 3-10), and then to investigate the behavior of the resulting chains when subjected to basic conditions. Surprisingly however, deprotonation was not necessary in order to provoke main-chain scission, as evidenced in DLS measurements and in AFM height images (Figure 3-10b,d).<sup>n</sup> This result contradicts previous work in which little degradation upon treatment with TFA or TFA-*d* was observed in AFM.<sup>172</sup> As distinct polymer batches were used for the two sets of experiments, reproduction of these old results was not possible. Upon deprotonation of  $PG5_n^{\text{CO}_2\text{tBu}}$  with ammonia, affording  $PG5_n^{\text{CO}_2\text{NH}_4}$ , DLS (Figure 3-10b) and AFM (Figure 3-10e) indicated no significant further scission. This finding contradicts the stated hypothesis of charge-induced main-chain scission – the weakly acidic carboxylic acid moieties of the DP should be virtually completely protonated in the presence of TFA, which is a relatively strong acid ( $\text{pK}_a \approx 0.5$ ).<sup>175</sup>

<sup>n</sup> Attempts at following this process by GPC were unsuccessful due to solubility issues.



Scheme 3-3: a) Synthesis of  $DG1^{CO_2tBu}$  **62**, d) synthesis of  $PG5_{500}^{CO_2tBu}$  (**32**), from  $PG4_{500}^{NH_3TFA}$ , showing only the transformations of the outermost functional groups.

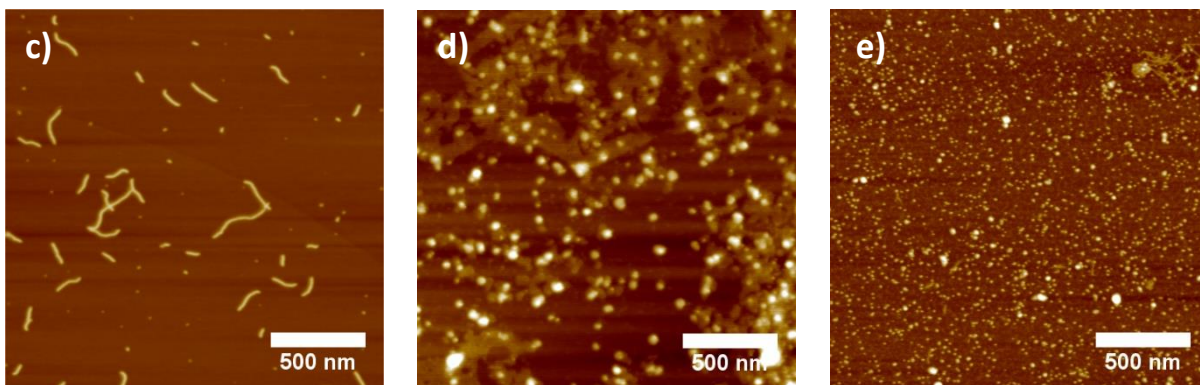
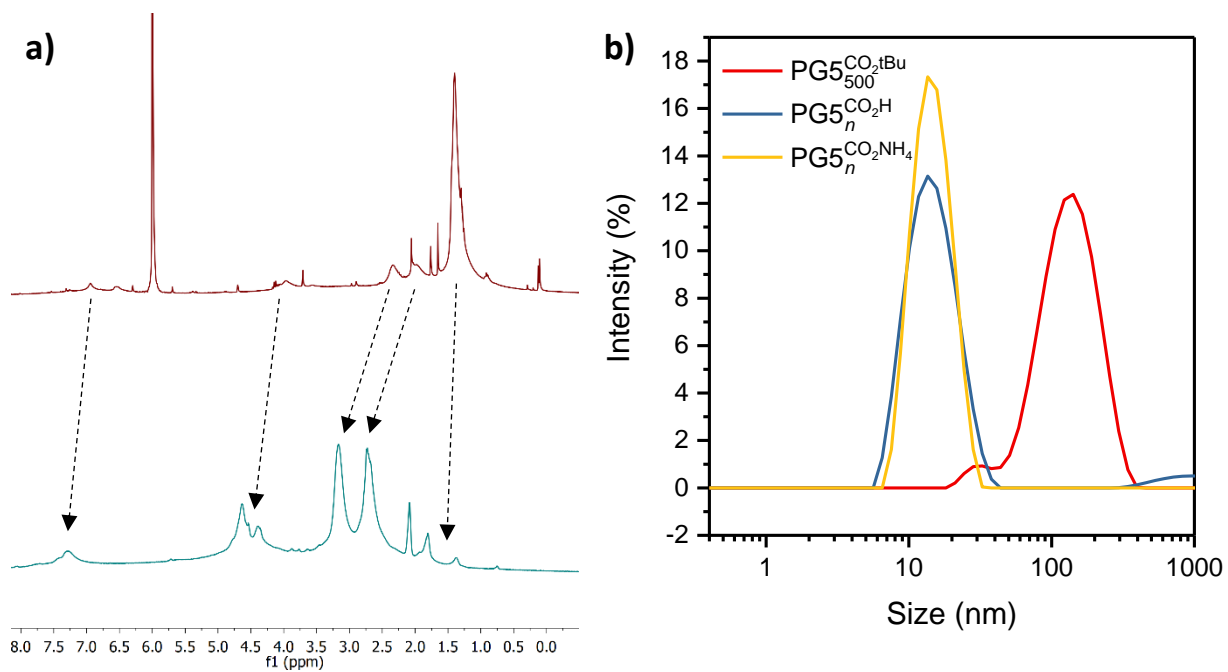


Figure 3-10: a) <sup>1</sup>H-NMR spectra of PG5<sub>500</sub><sup>CO<sub>2</sub>tBu</sup> (in TCE-d<sub>2</sub>, red) and PG5<sub>n</sub><sup>CO<sub>2</sub>H</sup> (in TFA-d, turquoise); b) DLS curves of PG5<sub>500</sub><sup>CO<sub>2</sub>tBu</sup>, PG5<sub>n</sub><sup>CO<sub>2</sub>H</sup> and PG5<sub>n</sub><sup>CO<sub>2</sub>NH<sub>4</sub></sup> (each 0.1 mg mL<sup>-1</sup> in MeOH). AFM height images of c) PG5<sub>500</sub><sup>CO<sub>2</sub>tBu</sup> on mica; d) PG5<sub>n</sub><sup>CO<sub>2</sub>H</sup> on mica; e) PG5<sub>n</sub><sup>CO<sub>2</sub>NH<sub>4</sub></sup> on PEI-1800 coated mica.

### 3.4.5. Scission in $g > 5$ DPs

As mentioned in chapter 2, the DPs  $PGg_n^{\text{NHBoc}}$  of  $g > 5$  do not undergo main-chain scission when exposed to acid. This is true for DPs synthesized both *via* route **B** (**B-PG6** $_{500}^{\text{NHBoc}}$ , **B-PG7** $_{500}^{\text{NHBoc}}$ , **B-PG8** $_{500}^{\text{NHBoc}}$ ) and *via* route **C** (**C-PG6** $_{500}^{\text{NHBoc}}$ , **C-PG7** $_{500}^{\text{NHBoc}}$ ; see Figure 2-5) over the course of the regular deployment of conditions used along route **A** (*i.e.* treatment with neat TFA at temperatures at or below RT). As Figure 3-11 shows, this stability partially extends to harsher conditions: **C-PG6** $_{500}^{\text{NHBoc}}$  does undergo main-chain scission after prolonged heating as judged by AFM height images (Figure 3-11a), however **C-PG7** $_{500}^{\text{NH}_3\text{TFA}}$  (Figure 3-11b) and **C-PG8** $_{500}^{\text{NH}_3\text{TFA}}$  (Figure 3-11c) appear to remain intact.

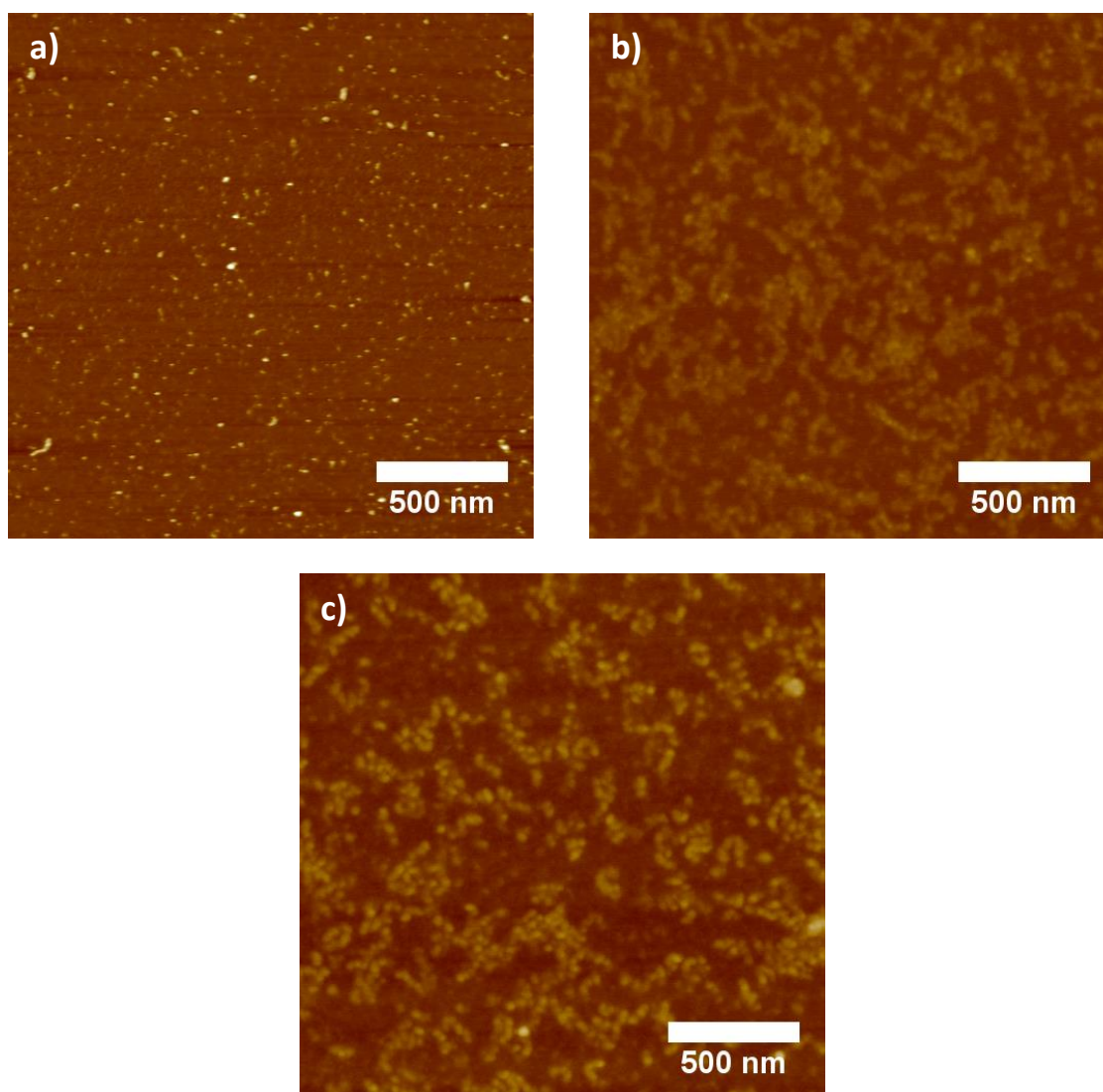


Figure 3-11: AFM height images of a) **C-PG6** $_{500}^{\text{NH}_3\text{TFA}}$ , b) **C-PG7** $_{500}^{\text{NH}_3\text{TFA}}$  and c) **C-PG8** $_{500}^{\text{NH}_3\text{TFA}}$ , prepared from the corresponding precursors (**C-PG6** $_{500}^{\text{NHBoc}}$ , **C-PG7** $_{500}^{\text{NHBoc}}$  and **C-PG8** $_{500}^{\text{NHBoc}}$ , respectively) by stirring in TFA at 80 °C for 72 h.<sup>o</sup>

<sup>o</sup> AFM imaging is more challenging for charged DPs than for their neutral counterparts. Charged DPs often appear smudged even under good imaging conditions, and additionally the tip has a high tendency to pick up debris. Additionally, it is not unlikely that the partial destruction of the DP periphery contributes to the irregular appearance of the polymers in Figure 3-11, which were subjected to very harsh conditions (boiling TFA)

### 3.4.6. Summary

Overall, the results obtained for charge-induced main-chain scission mostly match the observations previously made for the acid-mediated deprotection of  $\text{PG5}_{500}^{\text{NHBoc}}$ : Polyelectrolyte formation seems to cause main-chain scission and appears to occur on a time scale of a few minutes. This initial hypothesis has gained further support from the finding that strong acids are not necessary, and that weak acids such as DMBA are sufficient to induce main-chain scission, by virtue of being sufficiently acidic to fully protonate the peripheral primary amines.

In the solvent mixture employed for NHAloc deprotection, DPs featuring up to 80 % charged peripheral amines were still found to be stable towards main-chain scission, suggesting that a very high linear charge density is necessary for scission to occur. This is in line with the observed approximate time scale of the reaction, which is on the order of minutes for fully charged systems. This suggests that, in addition to a charged periphery, additional energy may be necessary for activation towards scission. This may be provided *e.g.* thermally, by shear from stirring (which is usually unavoidable for homogenization during DP synthesis), or by additional solvent uptake into the DP structure, *i.e.* by swelling. An observation worth mentioning is an additional small peak in GPC at *ca.* 20.7 mL for all samples which had undergone scission (Figure 3-3, Figure 3-5, Figure 3-7). As the deprotection of  $\text{PG5}_{500}^{\text{NHBoc}}$  using strong acids and scission under the much milder conditions reported above appear to proceed in a very similar fashion, it is plausible that this peak is due to macromonomer expelled from the points of scission.

While the above findings are quite consistent with the initial hypothesis of charge-induced main-chain scission, the fact that DPs of  $g > 5$  undergo scission only upon heating – if at all – requires explanation: The increase in charge density with  $g$  would lead to the opposite expectation. The observation of scission already upon deprotection of  $\text{PG5}_{500}^{\text{CO}_2\text{tBu}}$  to  $\text{PG5}_n^{\text{CO}_2\text{H}}$  under acidic conditions likewise jars with the stated hypothesis that peripheral charges are responsible for scission. It was expected that the polyacid (bearing no peripheral charges) would be stable and only undergo main-chain scission after deprotonation *e.g.* to form  $\text{PG5}_n^{\text{CO}_2\text{NH}_4}$ .

These two sets of observations cannot be explained within a hypothesis in which charge-charge repulsion among peripheral groups alone dictates the stability of the DP in question. While protonating a suitable DP does cause scission, peripheral charges are apparently neither sufficient nor necessary for scission to occur, as section 3.5 will demonstrate. This suggests that some more fundamental mechanism unrelated to, but partially influenced by charge-charge repulsion is at work. The hypothesis outlined in subsection 3.3.2 requires some rethinking at the very least, as discussed in section 3.6.

## 3.5. Main-chain scission in solutions of uncharged DPs

### 3.5.1. Initial observations

A second mode of main-chain scission, initially thought to stand apart from charge-induced main-chain scission, was discovered quite by accident: In the preparation of highly concentrated samples needed for fluorescence microscopy (see chapter 6), mixtures of  $\text{PG5}_{\sim 5'000}^{\text{NHBoc}}$  and DMF were heated to 60 °C for extended periods (> 1 h) or more briefly to 80 °C (*ca.* 15 min) to achieve complete and rapid mixing.

While complete dissolution of the polymer was achieved, the viscosity of the resulting solutions was – alarmingly – far lower than expected *e.g.* from comparison with solutions of  $\text{PG4}_{10'000}^{\text{NHBoc}}$  (Figure 3-12a).<sup>p</sup> Investigation of the polymer precipitated from the obtained solution by GPC (Figure 3-12b) and AFM (Figure 3-12c,d) revealed that significant chain degradation had taken place during the brief period of heating  $\text{PG5}_{\sim 5'000}^{\text{NHBoc}}$  in DMF, without the addition of any reagents. After similar treatment,  $\text{PG4}_{10'000}^{\text{NHBoc}}$  did not show signs of significant chain degradation (Figure 3-12a,f,g). The change in the GPC elution behavior of  $\text{PG4}_{10'000}^{\text{NHBoc}}$  (significant decrease of peak RV; Figure 3-12e) is likely a consequence of heating to 80 °C, a procedure which may favor interdigitation for very long chains as that temperature is above the glass transition temperature of the DP. AFM imaging (Figure 3-12f,g) did not indicate significant changes in average contour length.

The observation of main-chain scission by pure thermal induction is unprecedented. It might seem puzzling that this phenomenon had never been observed during the preceding decade of research using  $\text{PG}g_n^{\text{NHBoc}}$ . It should be pointed out however that in the normal course of handling, these polymers are never heated above 40 – 45 °C. Certainly, this finding warranted further investigation, especially in light of the previously discussed mode of charge-induced main-chain scission of  $\text{PG5}_{500}^{\text{NHBoc}}$ . To this end, a variety of experiments was conducted, which in the following are organized by the parameter investigated.

---

<sup>p</sup>  $\text{PG4}_{10'000}^{\text{NHBoc}}$  was the precursor polymer to  $\text{PG5}_{\sim 5'000}^{\text{NHBoc}}$ . Main-chain scission is not commonly observed in the synthesis of  $\text{PG5}_n^{\text{NHBoc}}$  by route **A**, though in this case partial degradation appears to have occurred. Judging by the results presented in this section, a likely cause is inadvertent heating to higher-than-usual temperatures at some point during workup; see Experimental, subsection 8.3.1.



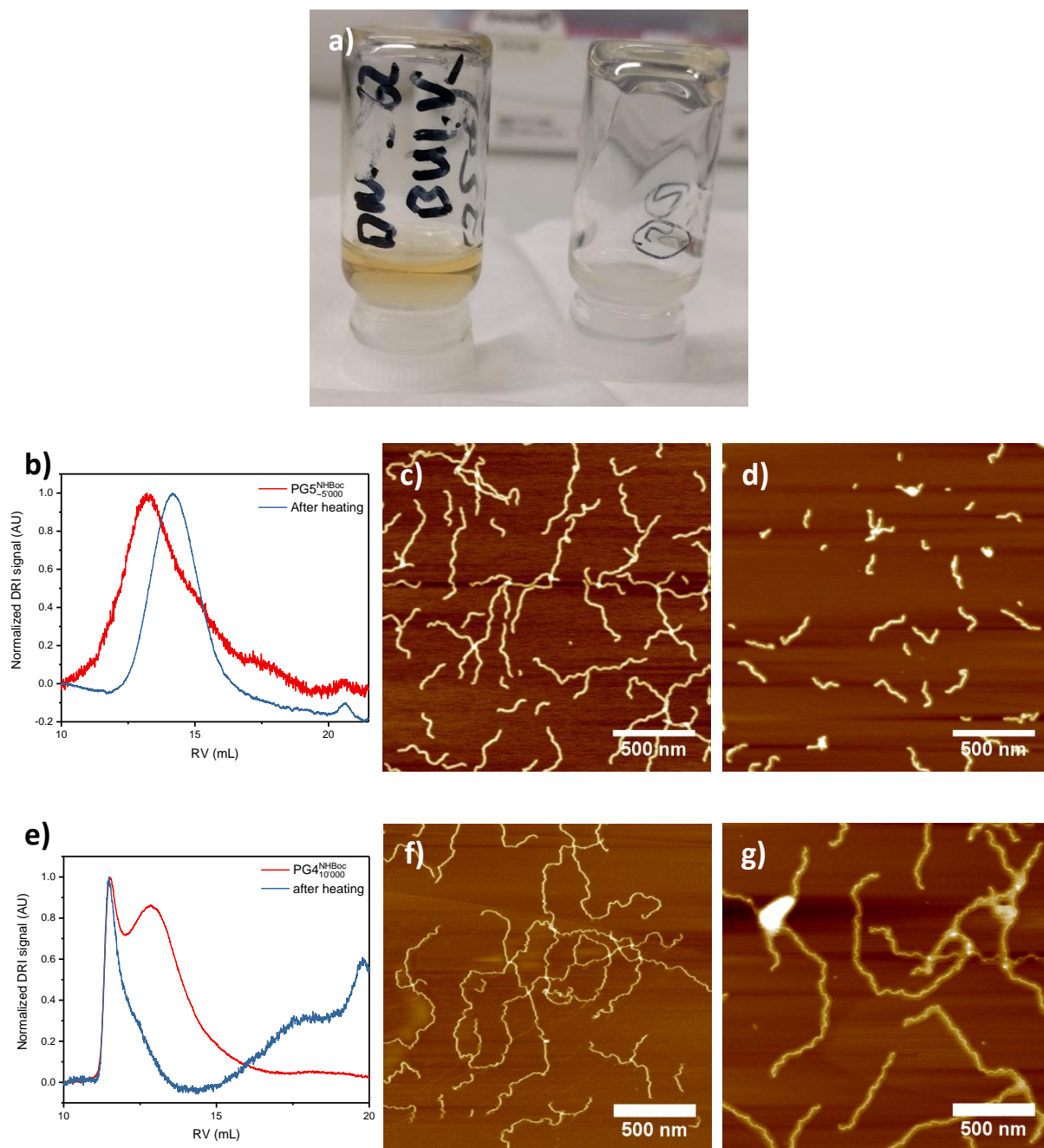


Figure 3-12: a) Photograph of solutions (ca. 10 % w/w in DMF, both after heating to 80 °C for 1 h) of PG5<sup>NHBoc</sup><sub>~5'000</sub> (left) and PG4<sup>NHBoc</sup><sub>~10'000</sub> (right), immediately after overturning of the vial. This illustrates the initially observed decrease in viscosity, which led to the findings presented in the following. b) GPC retention curves of PG5<sup>NHBoc</sup><sub>~5'000</sub> and the polymer resulting after brief heating in DMF. AFM height images of c) PG5<sup>NHBoc</sup><sub>~5'000</sub> and d) the polymer resulting after 15 min at 80 °C in DMF. e) GPC retention curves of PG4<sup>NHBoc</sup><sub>~10'000</sub> and the polymer resulting after brief heating in DMF. AFM height images of f) PG5<sup>NHBoc</sup><sub>~10'000</sub> and g) the polymer after 1 h at 80 °C in DMF.

### 3.5.2. Influence of solvent

After the initial finding that  $\text{PG5}_{500}^{\text{NHBoc}}$  degrades in DMF, a variety of other solvents was tested. To that end, a number of solvents spanning a wide range of polarity was used in scission experiments with  $\text{PG5}_{500}^{\text{NHBoc}}$ . As is evident from Figure 3-13, chain scission only occurred for the “good” polar-aprotic solvents, namely DMF, DMPU, DMSO, NMP, and DMAc. While in all of these solvents scission does occur, there are significant differences in the extent of scission: It is comparatively low for DMF, DMAc and DMSO, but much more severe for NMP and particularly DMPU. In fact, for the latter solvent, a low molar mass peak at  $\text{RV} \approx 20.7$  mL (which is present in all samples having undergone scission) becomes quite dominant, accounting for *ca.* 30 % of the total peak area. A similar low molar mass peak had already been observed in scission experiments of charged DPs (see *e.g.* Figure 3-5) and will be commented on later (see subsection 3.5.7).

For all other solvents used in these experiments, no scission was observed as judged by GPC, *i.e.* the corresponding retention curves match that of the starting material. The solvents for which no scission was found include alcohols (EtOH,  $t$ BuOH), moderately polar aprotic solvents (MeCN, EtOAc, 1,4-dioxane), chlorinated solvents (TCE), and aromatics (chlorobenzene, *o*-dichlorobenzene, and toluene).

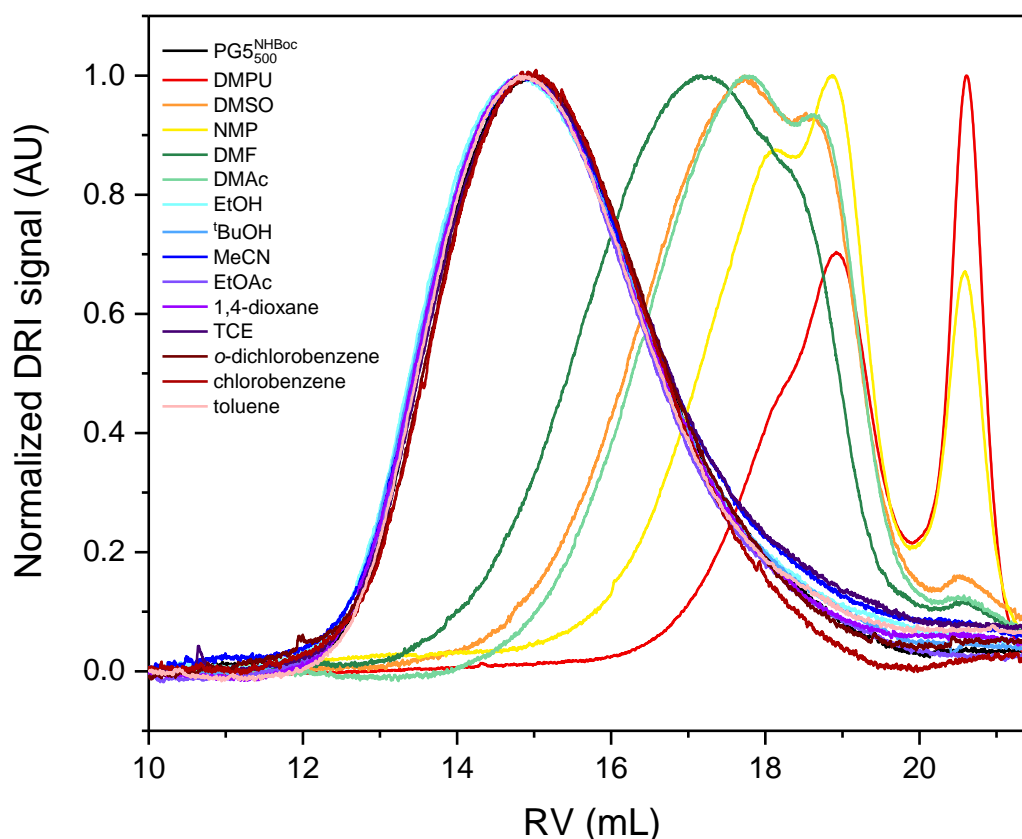


Figure 3-13: GPC elution curves of  $\text{PG5}_{500}^{\text{NHBoc}}$  (black line) and samples of the same polymer which were heated to 80 °C (or reflux, where lower) for 1 h (colored lines; color table in rough order of polarity).

Whether main-chain scission occurs upon heating to 80 °C appears to follow a rough trend of solvent polarity. An exception is MeCN: Judged by dielectric constant, MeCN is fairly polar ( $\epsilon = 36.6$ ), similar to NMP ( $\epsilon = 32.6$ ) or DMPU ( $\epsilon = 36.2$ ) – however, no scission was found. This is likely related to the curiously bad solubility of DPs of the type  $PGg_n^{\text{NH}^{\text{Boc}}}$  in MeCN. Even for toluene – which is a fairly bad solvent at RT – a clear solution was obtained at 80 °C. For MeCN, even at the low concentration of 1 % w/v, the mixture remained cloudy throughout. So, rather than in terms of solvent polarity, the observed behavior is perhaps more appropriately described in terms of solvent quality: The polar-aprotic solvents are very good swelling agents for the present class of DPs. This was demonstrated previously by using DPs functionalized with a solvatochromic probe (a 4-nitroaniline derivative).<sup>98</sup> Both DMF and DMSO were shown to be capable of swelling much of the DP branchwork. Using the same two sets of dye-labelled polymers (Figure 3-14a) of  $g = 1 - 4$  as used in the referenced work by Gstrein *et al.*, it was verified that NMP, DMAc and DMPU are likewise among the class of good swelling agents for DPs, as they show a similar behavior in terms of solvatochromic shifts (Figure 3-14b,c; solid lines). Note the previous comments regarding solvent quality in subsection 1.6.3 – solvent quality in the traditional sense and swelling capabilities might both need to be taken into account.

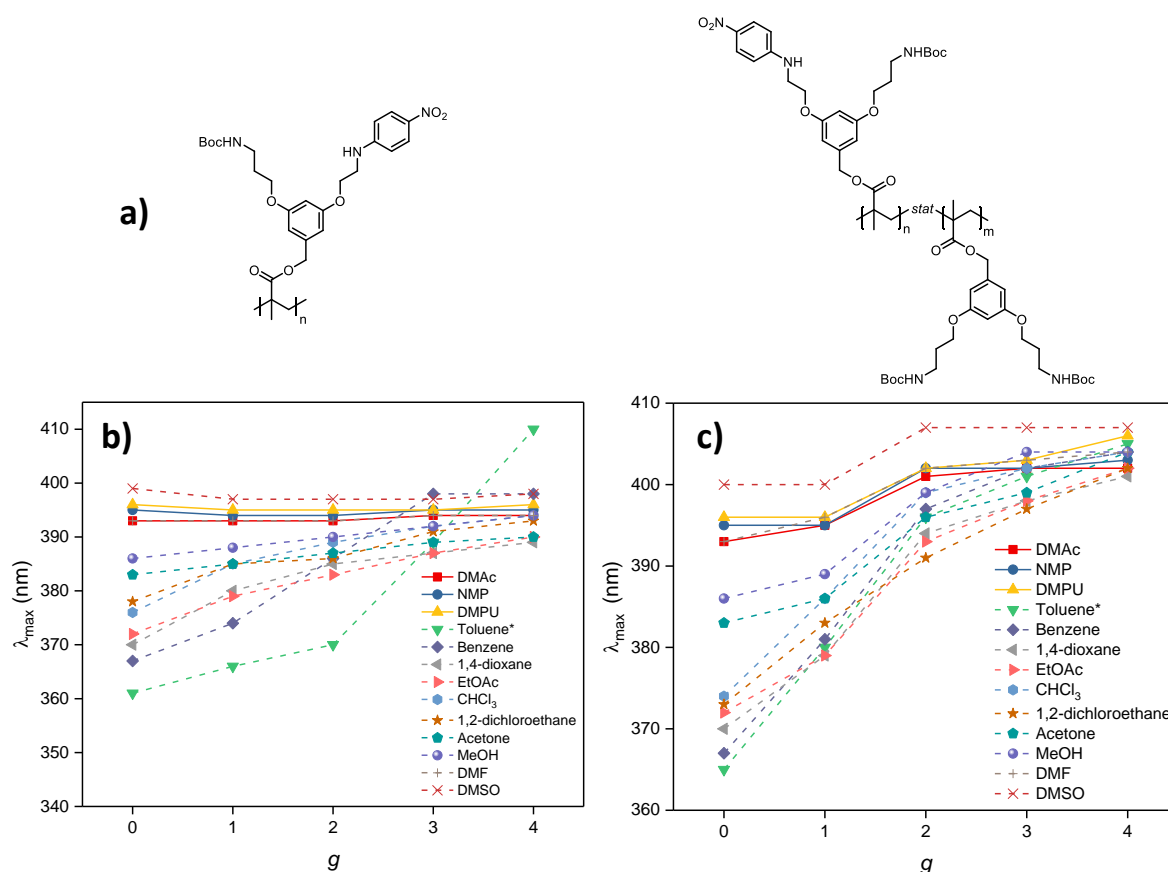


Figure 3-14: A small solvatochromic shift indicates good solvent quality: a) chemical structures of solvatochromically labelled DPs of  $g = 1$  (left: "high-substitution" homopolymer, right: "low-substitution" copolymer,  $n/m \approx 0.02$ ). The plots show  $\lambda_{\text{max}}$  of the solvatochromic probe in various solvents for a) the "high-substitution" series and b) the "low-substitution" series. Spectra were measured at  $A = 0.1 - 1$ ,  $l = 1$  cm, 25 °C (except for toluene samples, which were measured at 65 °C). Data for dashed lines was taken from Ref. 98.

By heating a sample of  $\text{PG5}_{\sim 5'000}^{\text{NH}^{\text{Boc}}}$  to 80 °C in an atmosphere of dry nitrogen, an attempt at inducing scission in the absence of any solvent was made. This produced no significant change in chain length according to AFM (Figure 3-15a), but led to an apparent *increase* in molar mass according to GPC (Figure 3-15b). Likely, this reflects the formation of fiber bundles also observed in AFM (Figure 3-15a) – probably a result of interdigitation, which in the case of the long polymers investigated here provides a sufficiently large area of interaction that not even prolonged exposure to a fairly good solvent (methylene chloride) can completely reverse the aggregation.

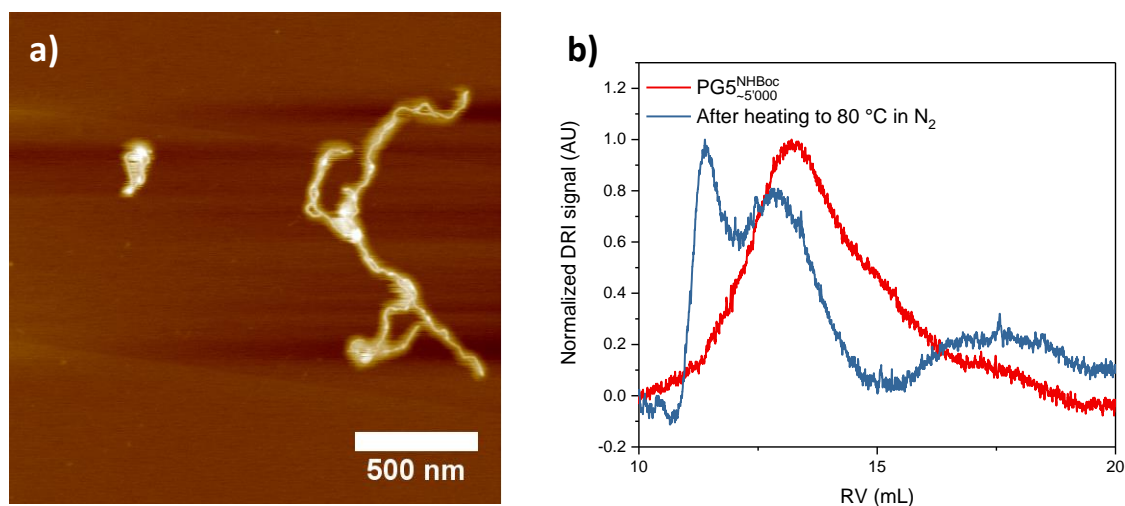


Figure 3-15: a) AFM height image of  $\text{PG5}_{\sim 5'000}^{\text{NH}^{\text{Boc}}}$  after heating to 80 °C under  $\text{N}_2$  for 1 h (compare Figure 3-12c); b) GPC traces of  $\text{PG5}_{\sim 5'000}^{\text{NH}^{\text{Boc}}}$  as synthesized and after heating in  $\text{N}_2$ .

### 3.5.3. Influence of temperature

As the extent of thermally induced scission was found to depend rather strongly on the chosen solvent, it seemed reasonable to investigate the temperature dependence of scission in different solvents. For this purpose, DMF and DMPU recommended themselves as the two extremes: In DMF, scission was found to occur, but to the lowest extent among the tested solvents, whereas for DMPU the extent of scission was largest (see Figure 3-13), suggesting differences in the reactivities of these two  $\text{PG5}_n^{\text{NH}^{\text{Boc}}}$ /solvent combinations.

Particularly the temperature onset of scission in DMF is also of significance to DP synthesis, as this solvent is the default choice for dendronization reactions. The importance of knowing this temperature threshold is illustrated by  $\text{PG5}_{\sim 5'000}^{\text{NH}^{\text{Boc}}}$  which was used in previous experiments: While still a polymer of high relatively  $P_n$ , the chains for this polymer are markedly shorter than those in the direct precursor,  $\text{PG4}_{10'000}^{\text{NH}^{\text{Boc}}}$  (see Experimental, subsection 8.3.1, Figure 8-15). Since charge-induced scission in  $\text{PG4}_n^{\text{NH}_3\text{TFA}}$  only occurs under quite forcing conditions,<sup>169</sup> it is likely that the product of dendronization was inadvertently subjected to higher-than-usual temperatures during workup. Seeing as the viscosity of concentrated DP solutions in initial experiments had decreased significantly because of main-chain scission (subsection 3.5.1), rheology was employed to determine an approximate threshold above which scission occurs in DMF (Figure 3-16).

A temperature ramp accompanied by repeated rheological testing (see Experimental, subsection 8.3.2, for details) was run in a heated rheometer. The storage and loss moduli  $G'$  and  $G''$  (Figure 3-16a) cannot be interpreted directly due to evaporation of the solvent above ca. 40 °C, which led to changes in sample concentration and geometry. The geometry-independent phase-shift angle (Figure 3-16b) shows an inflection point, indicating a thinning of the solution above ca. 65 °C which cannot be explained by evaporation. While it is difficult to disentangle this from the rather significant evaporation of the solvent, an onset of scission at about 65 °C agrees with previous results: It had been clear from the beginning that scission does not occur below 45 °C in DMF, the temperature at which GPC samples were prepared and measured. A temperature range around 65 °C also agrees quite well with the initial observation of scission in DMF, the very first instance of which was found to occur at ~60 °C.

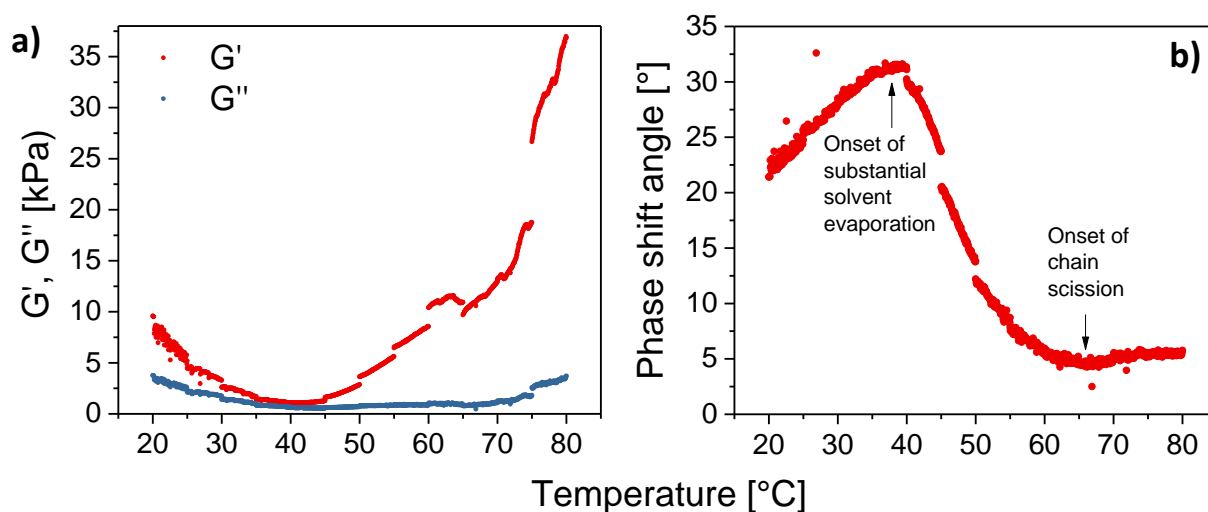


Figure 3-16: T-dependent rheological testing of a 20 % w/w solution of PG5<sup>NHBoc</sup><sub>~5000</sub> in DMF; a) dynamic moduli ( $G'$ ,  $G''$ ), b) geometry-independent phase shift angle.

As scission progresses to shorter fragments under the same heating conditions in DMPU than it does in DMF, it was expected that a similar rheological experiment would result in a lower temperature threshold for scission in DMPU. However, somewhat surprisingly, it was found that for DMPU solutions of PG5<sup>NHBoc</sup><sub>~5000</sub> and PG5<sup>NHBoc</sup><sub>500</sub> (ca. 10 % w/w), no heating whatsoever was necessary to induce main-chain scission: These mixtures were found to be of very low viscosity after shaking at room temperature already. The analysis of the scission products by AFM imaging (Figure 3-17a-c) and by GPC (Figure 3-17d) indicates that again this dramatic change in viscosity is connected to chain degradation – in fact, gentle agitation in DMPU at RT yields shorter fragments than heating of the same polymer to 80 °C in DMF (Figure 3-17d,e).

In hindsight, the finding that DMPU causes scission already at RT is not entirely new: As mentioned in subsection 2.4.4 (see Table 2-1), the use of DMPU in an attempted synthesis of PG6<sup>NHBoc</sup><sub>500</sub> yielded short fragments instead of long chains. At the time, this interesting observation had been discarded as a mere experimental fluke. As will become evident in connection with results described in subsection 3.5.6, this is likely a result of degradation of the starting material PG5<sup>NHAlloc</sup><sub>500</sub> rather than of some intermediate product.

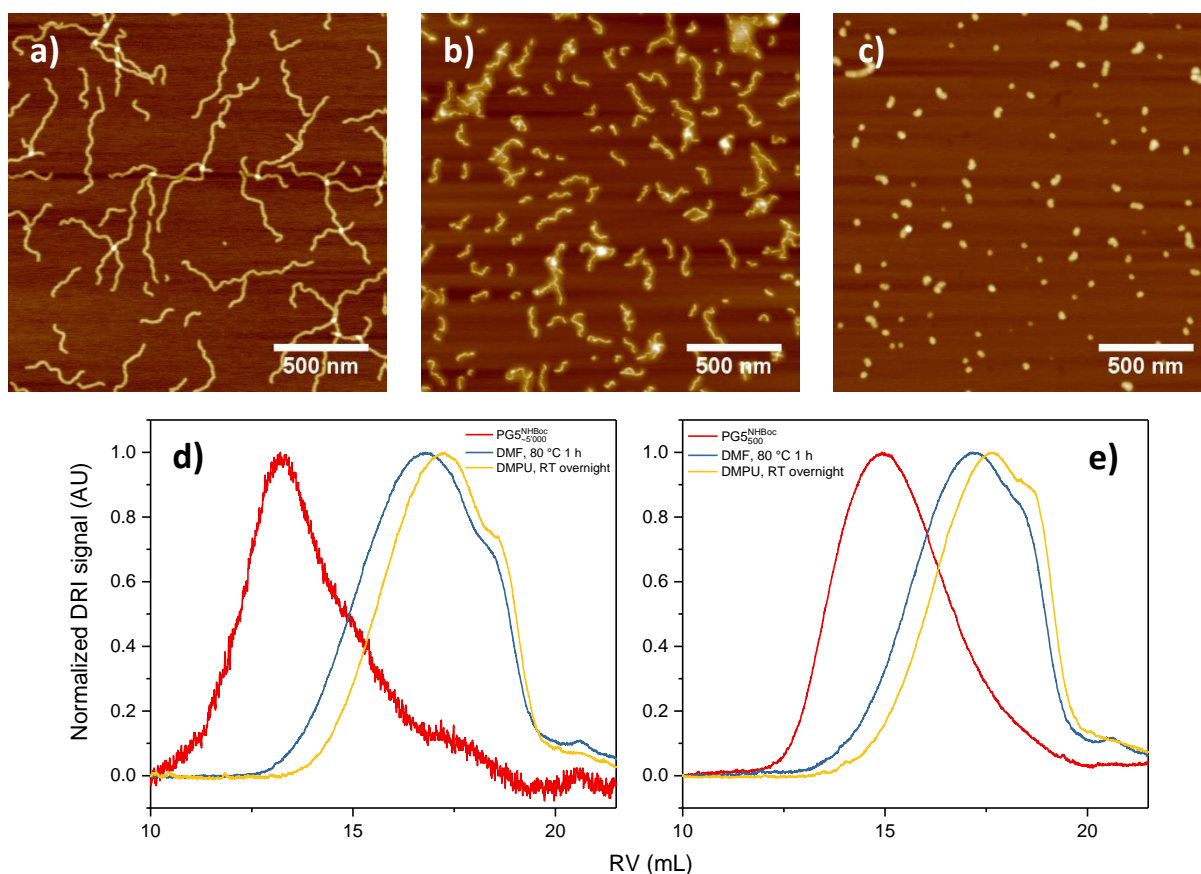


Figure 3-17: AFM height images of a)  $PG5_{5000}^{NHBoc}$  as synthesized and after b) shaking in DMF at 80 °C for 1 h or c) shaking in DMPU at RT overnight ( $\sim 10\%$  w/w for both cases); d) GPC elution curves from analogous heating experiments conducted at 1 % w/V. e) GPC elution curves for  $PG5_{500}^{NHBoc}$  treated similarly at 1 % w/V.

For all solvents in which scission upon heating (or mere exposure to solvent) was detected, a progression of scission with increased temperature was observed: Heating a solution of  $PG5_{500}^{NHBoc}$  in DMF to 120 °C for 1 h led to shorter polymeric fragments and an increase in the proportion of low molar mass fragments at  $RV \approx 20.5$  mL when compared to heating the sample to merely 80 °C for 1 h (Figure 3-18a). The same is true for DMAc, NMP, DMSO and DMPU, except that the onset of scission is shifted to much lower temperatures for the latter, occurring at RT already (Figure 3-18b).

It is difficult to ascertain from the above data whether scission merely occurs faster in DMPU than in DMF, or whether it ultimately leads to shorter products. When a solution of  $PG5_{500}^{NHBoc}$  in DMF was maintained at a set temperature for an extended period, only a minuscule shift in peak RV was observed (Figure 3-18c), suggesting that the latter is the case: The scission process appears to proceed on a time scale of minutes rather than hours at a given temperature, and shorter fragments are only produced when the temperature is increased. The end point of scission in terms of fragments size, as noted previously (see Figure 3-13), is highly dependent on the solvent at a given temperature.

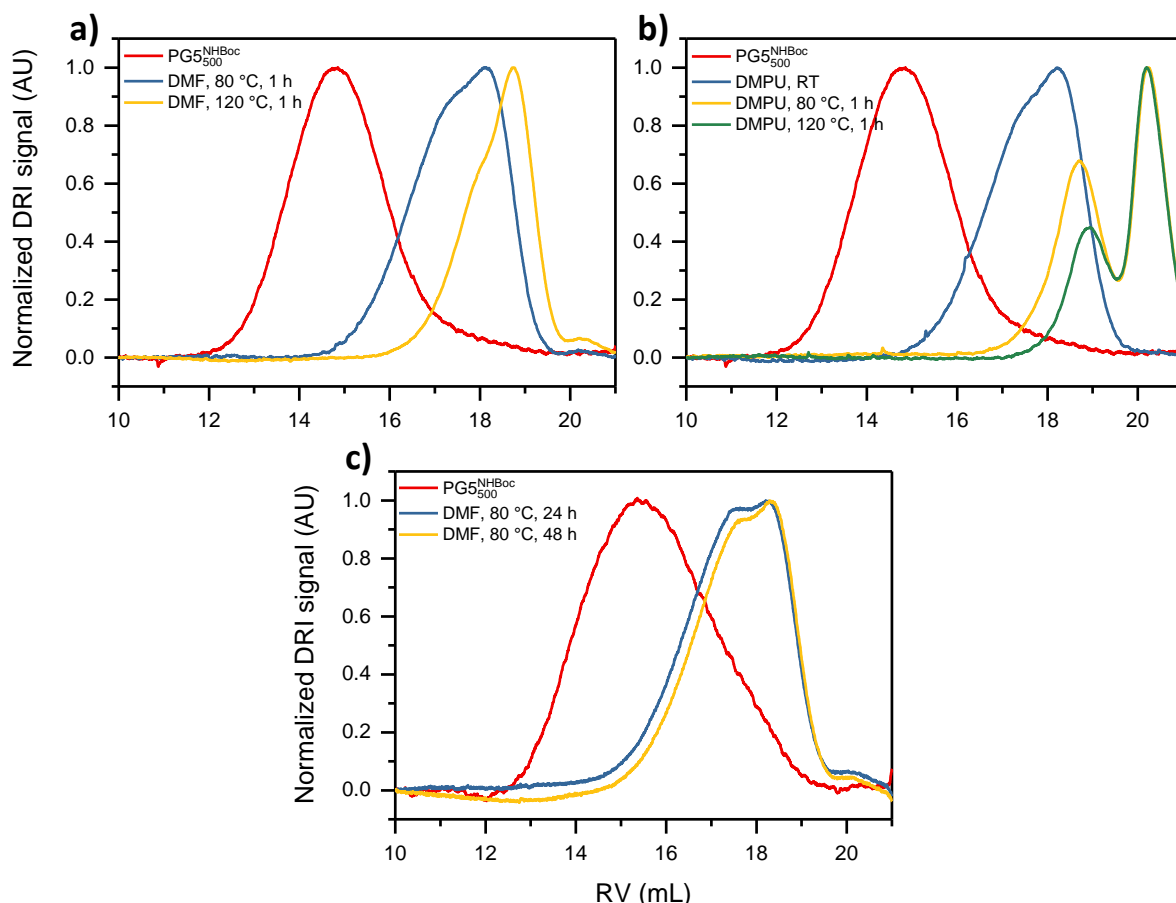


Figure 3-18: a) T-dependence of the scission process for PG5<sup>NHBoc</sup><sub>500</sub> in DMF: Scission progresses further, producing shorter fragments, upon heating to 120 °C than it does upon heating to 80 °C; b) T-dependence of scission in DMPU: Scission progresses further at 120 °C or 80 °C than it does at RT; c) Scission of PG5<sup>NHBoc</sup><sub>500</sub> in DMF after 1 d and 2 d at 80 °C, showing little progression, if any.

### 3.5.4 Influence of shear

The observation that scission in DMPU already occurs at room temperature indicates that shear stress from agitation alone (*e.g.* shaking, stirring or vortexing used initially to dissolve the DP) may be sufficient to induce scission in some cases. Seeing as the interactions between individual DP chains can be fairly strong (see Figure 3-15a), the impact of chain length and concentration as well as the applied shear rate was investigated cursorily: A high value of either parameter would be expected to promote scission, if shear was indeed an important factor.

Initial experiments regarding main-chain scission were conducted on fairly concentrated solutions of DPs (*ca.* 10 – 20 % w/w). Especially for the high- $P_n$  DPs initially investigated (PG5<sup>NHBoc</sup><sub>~5'000</sub>), such highly concentrated solutions are gel-like (see Figure 3-16a:  $G' > G''$  throughout the measurement), and consequently shear forces transmitted through entanglements and/or interdigitated chain segments might be a significant contributor to chain scission. Comparisons with experiments in more dilute solutions (1 % w/v) and with shorter polymers (PG5<sup>NHBoc</sup><sub>500</sub>) are inconclusive with respect to chain lengths: PG5<sup>NHBoc</sup><sub>~5'000</sub> affords longer fragments than PG5<sup>NHBoc</sup><sub>500</sub> during 1 h at 80 °C (Figure 3-19a). It should be noted that the respective  $g = 1$  precursors were prepared differently (FRP

for the high  $P_n$  DPs, RAFT polymerization for their shorter analogs), perhaps influencing the susceptibility to degradation. If the described intermolecular interactions were crucial to scission however, the observed result would be difficult to rationalize: Higher scission rates would be expected for the longer DPs, at least initially. Variations of concentration (Figure 3-19a) and externally applied shear (Figure 3-19b) also suggest that external mechanical force does not contribute significantly – Changes in either parameter did not lead to significant shifts in the product distributions.

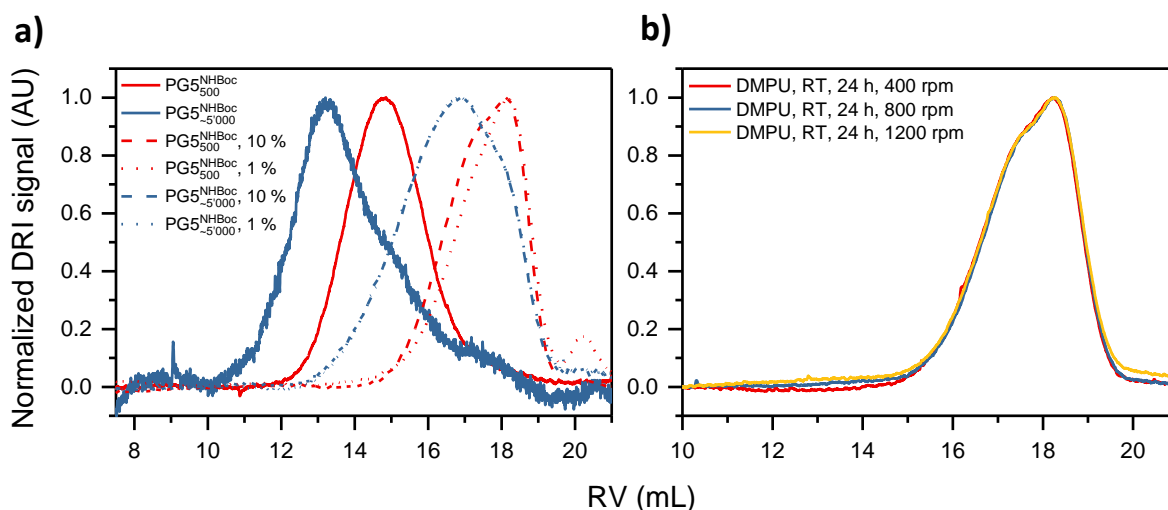


Figure 3-19: GPC elution curves of a) PG5<sub>500</sub><sup>NHBoc</sup> and PG5<sub>5000</sub><sup>NHBoc</sup>. For both polymers, solutions in DMF and DMPU (10 % and 1 % w/v) were heated to 80 °C for 1 h; b) PG5<sub>500</sub><sup>NHBoc</sup> (5 % in DMPU) subjected to different external shear rates on an orbital shaker at RT.

### 3.5.5 Influence of dendritic generation $g$

Following the initial observation of main-chain scission in samples of PG5<sub>n</sub><sup>NHBoc</sup>, an interesting question was whether in analogy to charge-induced main-chain scission a  $g$  dependence of scission could be observed. In view of the initial findings that scission in DMF at 80 °C leads to a relatively modest degree of scission and that DMPU at 80 °C provides “harsh” scission conditions, both of these conditions were applied to a wide range of DPs. Specifically, a series of high  $P_n$  ( $\approx 10'000$ ) DPs of  $g = 1 - 5$  and a range of lower  $P_n$  ( $\approx 500$ ) DPs were used. The full homologous series of DPs encompassing  $g = 1 - 8$  (derived using route **C**, *i.e.* including PG5<sub>500</sub><sup>NHAlloc</sup> [compare Figure 3-24b] **C**-PG6<sub>500</sub><sup>NHBoc</sup>, **C**-PG7<sub>500</sub><sup>NHBoc</sup>, **C**-PG8<sub>500</sub><sup>NHBoc</sup>), as well as additional polymers from route **C** ( $g = 6,7$ ). DPs derived using route **B** of  $g = 6 - 8$  (**B**-PG6<sub>500</sub><sup>NHBoc</sup>, **B**-PG7<sub>500</sub><sup>NHBoc</sup>, **B**-PG8<sub>500</sub><sup>NHBoc</sup>) were also investigated.

Samples were analyzed by GPC (see A.3 in the Appendix for a collection of all chromatograms generated in these experiments) and the peak retention volumes of the heat-treated DPs were compared to those of their starting materials to assess whether chain degradation had occurred or not (Figure 3-20b).



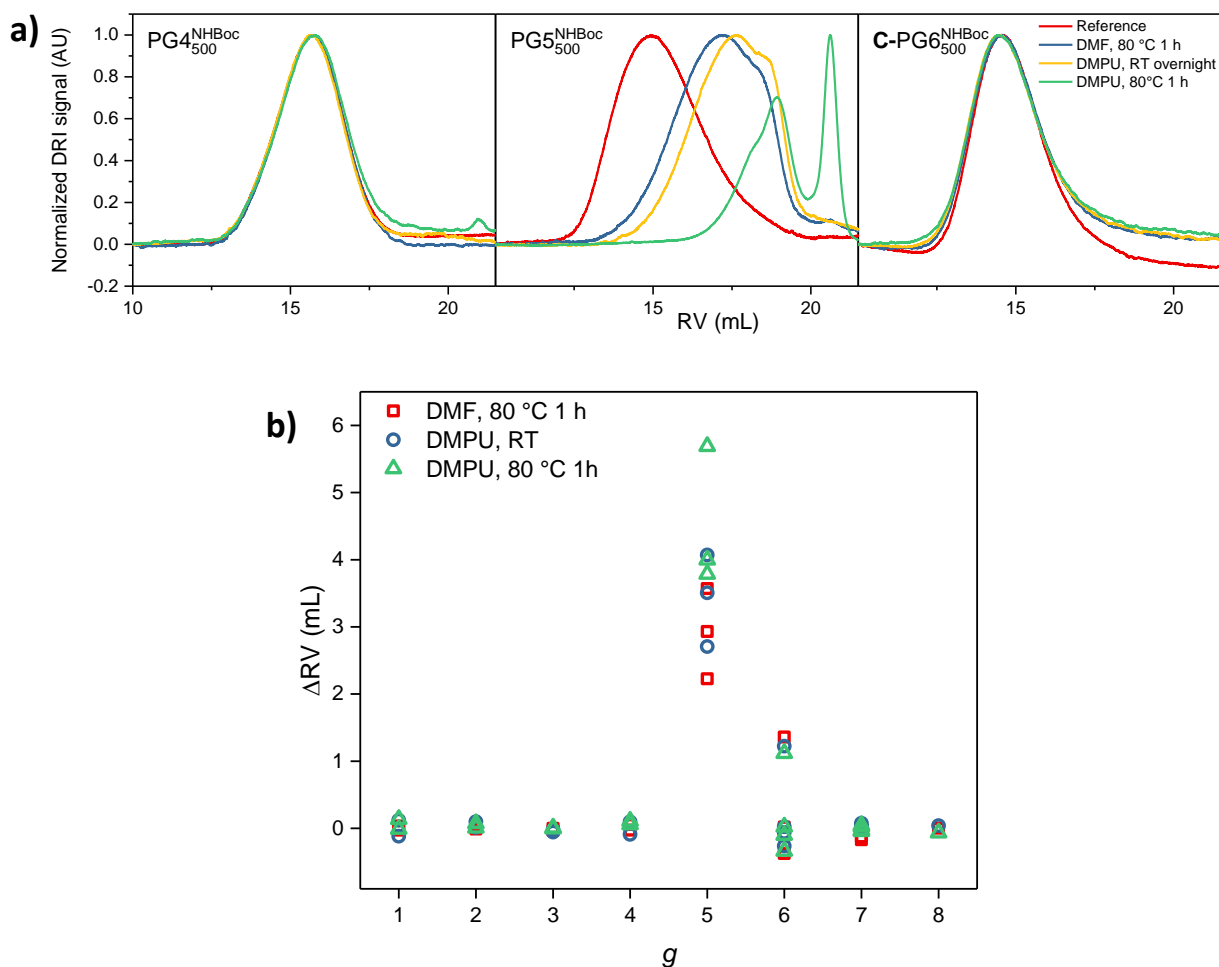


Figure 3-20: a) Representative GPC retention curves of starting DPs and the same polymers in DMPU at RT, as well as in DMF and DMPU at 80 °C; Shown are PG4<sup>NHBoc</sup><sub>500</sub>, PG5<sup>NHBoc</sup><sub>500</sub>, and C-PG6<sup>NHBoc</sup><sub>500</sub>. b) GPC peak retention volumes relative to the initial polymer after RT shaking in DMPU and “hot solvent” treatment in DMF or DMPU.

Without exception, DPs of  $g = 5$  were found to undergo significant main-chain scission ( $\Delta RV > 0$ ).<sup>9</sup> DPs other than those of  $g = 5$  experienced no significant shifts in peak retention volumes ( $\Delta RV \approx 0$ ), with the exception of one specific batch of C-PG6<sup>NHBoc</sup><sub>500</sub>. This exception (Figure 3-21) is peculiar in several ways: First, two other batches of C-PG6<sup>NHBoc</sup><sub>500</sub> – prepared using the same precursors and procedures – did not undergo main-chain scission when heated to 80 °C in DMPU (*e.g.* Figure 3-20a, right-hand pane). Second,  $\Delta RV$  remained constant no matter the applied procedure: Treatment with DMPU at RT and heating in both DMPU and DMF led to the same change in RV. Third, unlike in all other cases where a significant shift in retention volume was detected, no additional small peak at  $RV \approx 20.5$  mL was found (compare *e.g.* Figure 3-20a, center pane). No immediate explanation presents itself for this outlier.

<sup>9</sup> The shift in peak retention volume  $\Delta RV$  corresponds to the difference between peak RV of the initial polymer (heated to 45 °C in DMF during GPC sample preparation) and of the same polymer treated as indicated in Figure 3-20b.

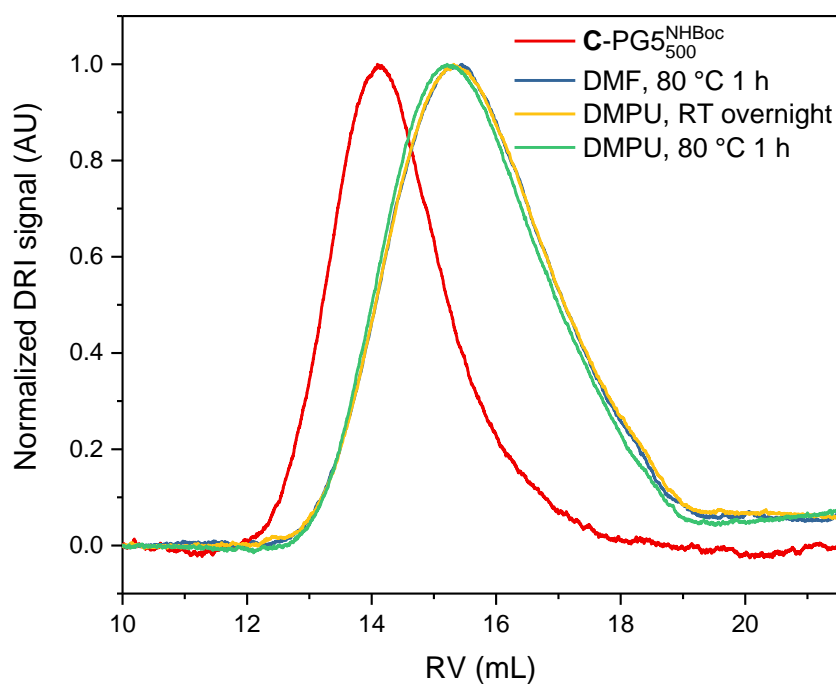


Figure 3-21: GPC retention curves for the only batch of **C-PG6**<sub>500</sub><sup>NHBoc</sup> for which a shift in retention volume was observed upon heat treatment. Compare Figure 3-20a, right-hand pane and Figure 3-23.

Aside from this exception, the values of  $\Delta RV$  suggest that *only* DPs of  $g = 5$  undergo significant degradation – as previously observed for the case of charge-induced main-chain scission. However, a closer look at the individual chromatograms reveals signs of minor degradation not captured by peak retention volumes ( $\Delta RV \approx 0$ ): Occasionally an additional small peak at  $RV > 20$  mL was observed (see e.g. Figure 3-20a, left-hand panel). In the experiments represented in Figure 3-20b, such an additional peak was only observed when heating in DMPU to 80 °C, and only for the following polymers: **PG4**<sub>500</sub><sup>NHBoc</sup> (Figure 3-22a), **B-PG6**<sub>500</sub><sup>NHBoc</sup> (Figure 3-22b) and **B-PG7**<sub>500</sub><sup>NHBoc</sup> (Figure 3-22c). No other DP samples except those of  $g = 5$  produced a clearly distinguishable second peak in these experiments (see Appendix A.3 for a collection of all chromatograms). The precise position of the second peak consistently decreased with  $g$ , the peak maxima being located at 21 mL for **PG4**<sub>500</sub><sup>NHBoc</sup>, 20.5 mL for **B-PG6**<sub>500</sub><sup>NHBoc</sup> and 20.1 mL for **B-PG7**<sub>500</sub><sup>NHBoc</sup> (Figure 3-22d), compared to *ca.* 20.6 mL for **PG5**<sub>500</sub><sup>NHBoc</sup> and **PG5**<sub>~5000</sub><sup>NHBoc</sup>.

<sup>r</sup> In **PG3**<sub>500</sub><sup>NHBoc</sup>, a similar peak might also be present ( $RV \approx 21.5$  mL, see A3, Figure A-6c), but it is far less distinct than in the cases presented here, as it is small and situated close to system signals. Compare subsection 3.5.7.

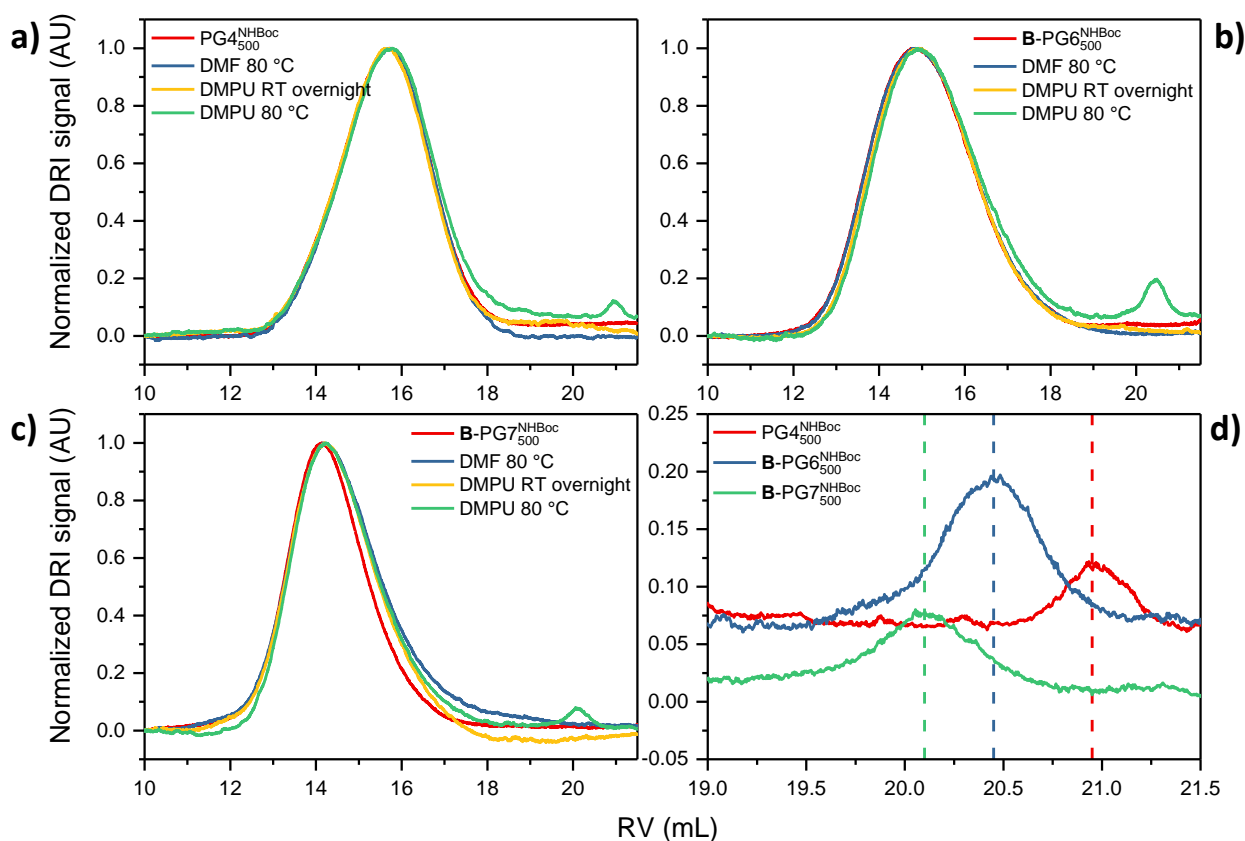


Figure 3-22: GPC elution curves for the heat treatment of samples of  $g \neq 5$  which exhibited a second peak after having been heated to 80 °C in DMPU: a)  $PG4^{NHBoc}$ , b)  $B-PG6^{NHBoc}$ , c)  $B-PG7^{NHBoc}$ . d) High-RV region of chromatograms of the same three polymers (DMPU at 80 °C), with approximate peak retention volumes indicated in dashed lines.

### 3.5.6 Influence of structural perfection

Among the previously discussed results, no scission for DPs prepared by route **C** was found up to 80 °C. Seeing as scission progresses farther at higher temperatures,  $g > 5$  samples from routes **B** and **C** were heated to 120 °C. Again with the sole exception of the aberrant batch of  $C-PG6^{NHBoc}$  (Figure 3-21), GPC showed only a negligible shift in peak RV after treatment at this much higher temperature for 1 h. Among these polymers, a distinct additional small-molecule peak was found only for  $B-PG6^{NHBoc}$  and  $B-PG7^{NHBoc}$  (Figure 3-23a,b; these are the same polymers as depicted in Figure 3-22b,c), whereas the analogous DPs from route **C** (Figure 3-23d,e) and both DPs of  $g = 8$  (Figure 3-23c,f) did not show significant peaks at high RV. It can be concluded that the DPs of higher structural perfection – those from route **C** – are far less susceptible to degradation.

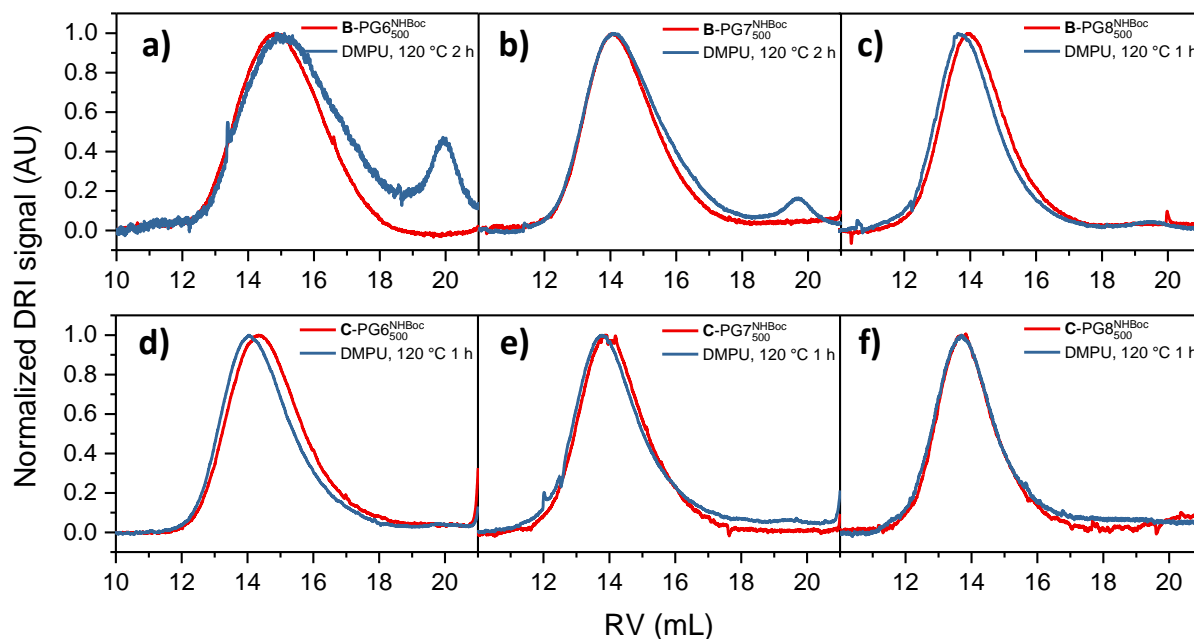


Figure 3-23: GPC retention curves of "hot solvent" treatment (1% w/V in DMPU, 120 °C for 1 – 2 h) for a) B-PG6<sup>NHBoc</sup><sub>500</sub>, b) B-PG7<sup>NHBoc</sup><sub>500</sub>, c) B-PG8<sup>NHBoc</sup><sub>500</sub>, d) C-PG6<sup>NHBoc</sup><sub>500</sub>, e) C-PG7<sup>NHBoc</sup><sub>500</sub>, and f) C-PG8<sup>NHBoc</sup><sub>500</sub>.

### 3.5.7 Influence of peripheral substitution

In addition to the standard NHBoc peripheral groups, other peripheral chemistries were available from various experiments; namely, DPs of  $g = 5$  with peripheral NHAlloc groups (PG5<sup>NHAlloc</sup><sub>10'000</sub>, PG5<sup>NHAlloc</sup><sub>500</sub>, **31**), peripheral NHCbz groups (PG5<sup>NHCbz</sup><sub>500</sub>, **29**) as well as DPs with methyl and *tert*-butyl esters instead of carbamates in their periphery (PG5<sup>CO<sub>2</sub>tBu</sup><sub>500</sub>, **32** and PG5<sup>CO<sub>2</sub>Me</sup><sub>500</sub>, **33**). In analogy to previous experiments, the polymers were heated in DMF and DMPU. As is evident from the GPC results in Figure 3-24 and the corresponding AFM images in Figure 3-25, all of these  $g = 5$  DPs – distinguished essentially only by the structure of the outermost peripheral groups – did undergo main-chain scission, though with some important nuances.

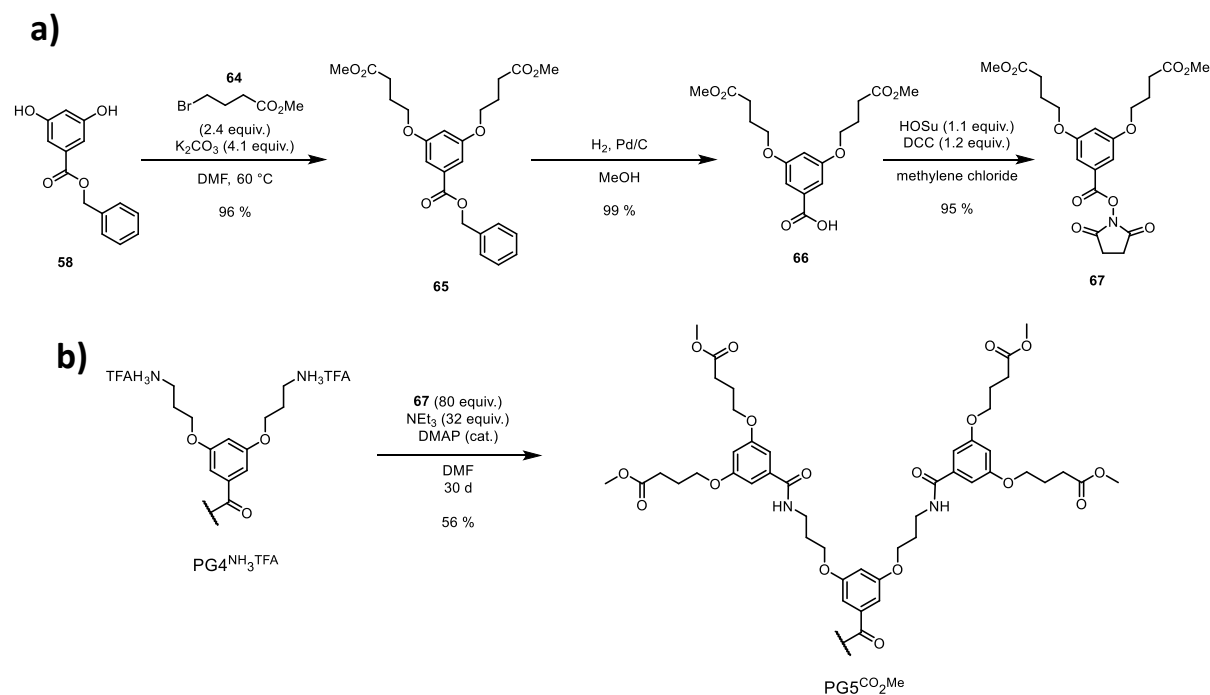
The two chain lengths of PG5<sup>NHAlloc</sup><sub>*n*</sub> behaved very similarly (Figure 3-24a,b, Figure 3-25a/b): As with their NHBoc-bearing analogs, heating of DMF solutions to 80 °C resulted in scission, as did shaking DMPU solutions at RT and at 80 °C. The severity of scission, as judged from GPC elution curves, followed the same trends as observed with NHBoc-bearing DPs, with DMPU resulting in more pronounced degradation than DMF. The overall degree of scission achieved however was significantly lower for PG5<sup>NHAlloc</sup><sub>*n*</sub> than for PG5<sup>NHBoc</sup><sub>*n*</sub>, both according to the position of the oligomeric/polymeric peak maxima and especially the relative areas of the low molar mass peaks around RV ≈ 20.5 mL. Even heating to 120 °C in DMPU for 2 h (see Figure 3-26a) did not result in a large peak corresponding to small-molecule fragments.

PG5<sup>NHCbz</sup><sub>500</sub> was likewise found to undergo main-chain scission (Figure 3-24c, Figure 3-25c/d), again following the same trends as observed for DPs of  $g = 5$  in that heating in DMF led to less scission than merely subjecting the polymer to DMPU at RT or elevated temperatures. Notably though, a significant peak corresponding to small-molecule scission products at low RV only emerged upon heating in

DMPU, although in these cases (see Figure 3-24c, purple and grey lines) the extent of scission was apparently quite significant, comparable with that occurring for  $\text{PG5}_{500}^{\text{NHBoc}}$  under the same conditions.

$\text{PG5}_{500}^{\text{CO}_2\text{Me}}$  was prepared in a synthesis very similar to that of  $\text{PG5}_{500}^{\text{CO}_2\text{tBu}}$  (Scheme 3-4, compare Scheme 3-3) and likewise underwent scission (Figure 3-24d, Figure 3-25e/f), however significant differences to the previously described cases were found: Conditions which had otherwise led to significant scission (DMF at 80 °C, DMPU at RT) did not result in degradation. Only under harsher conditions (starting with partial scission in DMPU at 80 °C) and proceeding to much shorter products on average in DMF or DMPU at 120 °C. In contrast, all these conditions did lead to main-chain scission in the case of  $\text{PG5}_{500}^{\text{CO}_2\text{tBu}}$  (Figure 3-24e, Figure 3-25g/h). Here, the familiar trends in the extent of scission are again evident *i.e.* more severe scission in DMPU than in DMF or at high temperatures than at lower temperatures.

The severity of main-chain scission for the investigated carbamate groups roughly falls in the order  $\text{NHBoc} > \text{NHCbz} > \text{NHAlloc}$ , with the bulky *tert*-butyl group producing the largest fraction of small-molecules fragments and the allyl group (which has approximately the same molar mass) producing comparatively little of the suspected macromonomer even at 120 °C in DMPU. Similarly, scission is observed under much milder conditions for  $\text{PG5}_{500}^{\text{CO}_2\text{tBu}}$  than for  $\text{PG5}_{500}^{\text{CO}_2\text{Me}}$ . This suggests an influence of steric demand not only of dendrons (all DPs mentioned in this subsection are of  $g = 5$ ; compare subsections 3.5.5 and 3.5.8), but also of the specific peripheral groups: Bulkier peripheral groups appear to lead to an increased susceptibility to degradation by main-chain scission. For the ester-substituted DPs, this stands in contrast to (qualitative) solubility, as  $\text{PG5}_{500}^{\text{CO}_2\text{tBu}}$  is only very poorly soluble in DMF unless at elevated temperatures, whereas  $\text{PG5}_{500}^{\text{CO}_2\text{Me}}$  is very well soluble.



33

Scheme 3-4: a) Synthesis of Me-ester substituted dendronization agent **67**; b) dendronization of  $\text{PG4}_{500}^{\text{NH}_3\text{TFA}}$  to  $\text{PG5}_{500}^{\text{CO}_2\text{Me}}$ , showing only the transformation of peripheral groups. See Experimental, subsection 8.3.1, for details.

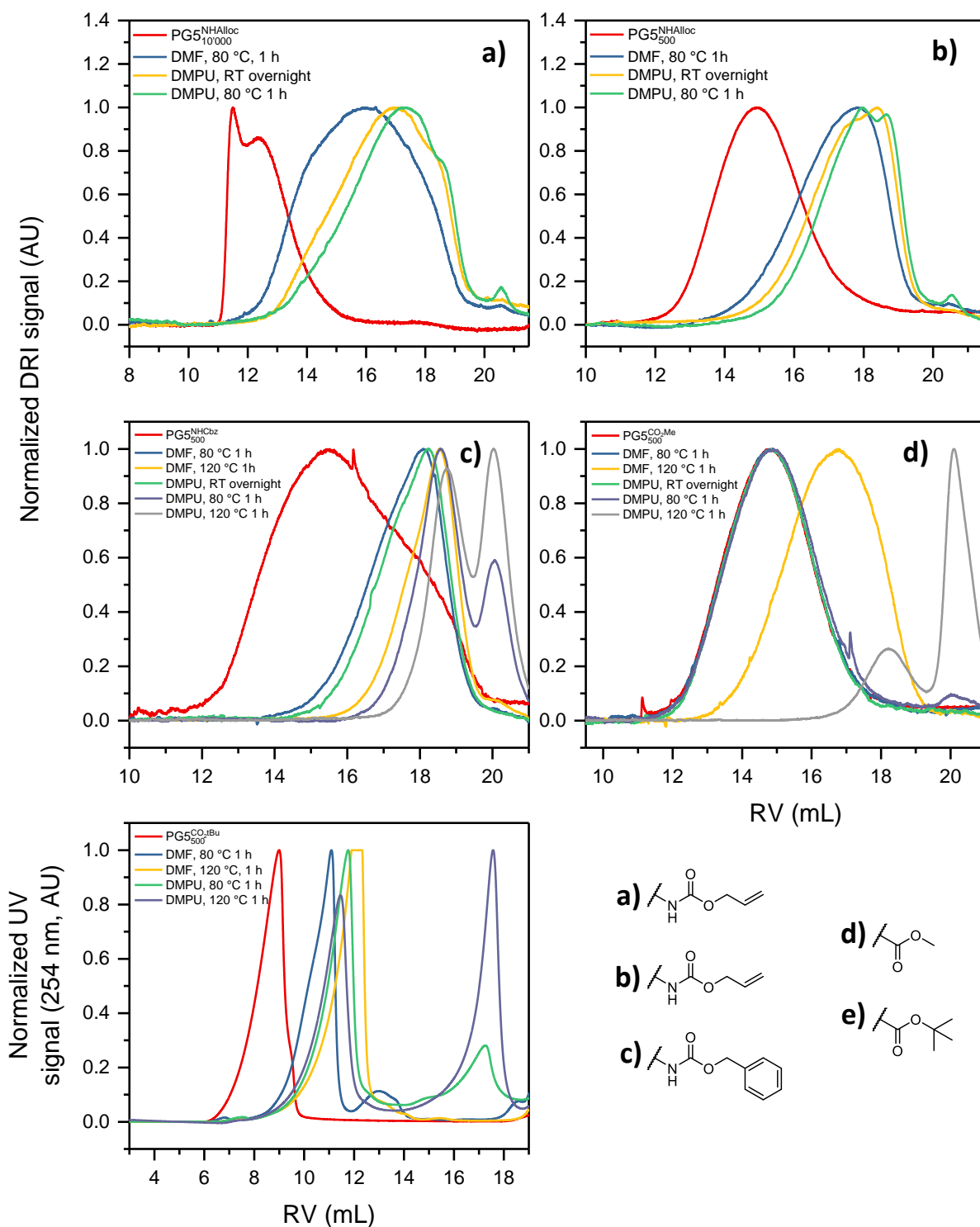


Figure 3-24: GPC elution curves representing the “hot solvent” treatment of variously substituted DPs of  $g = 5$  ( $X \neq \text{NHBoc}$ ; concentration ca. 1 % w/V for all experiments): a) PG5<sup>NHAlloc</sup><sub>10'000</sub> (31), b) PG5<sup>NHAlloc</sup><sub>500</sub> (31), c) PG5<sup>NHCbz</sup><sub>500</sub> (29), d) PG5<sup>CO<sub>2</sub>Me</sup><sub>500</sub> (33), e) PG5<sup>CO<sub>2</sub>tBu</sup><sub>500</sub> (32). The results in Fig. 3-24e for PG5<sup>CO<sub>2</sub>tBu</sup><sub>500</sub> were obtained by GPC in CHCl<sub>3</sub>; PG5<sup>CO<sub>2</sub>tBu</sup><sub>500</sub> is the only DP presented in this thesis which is not well soluble in DMF. The peripheral groups X in which these DPs differ are displayed on the bottom right (compare Figure 1-17).

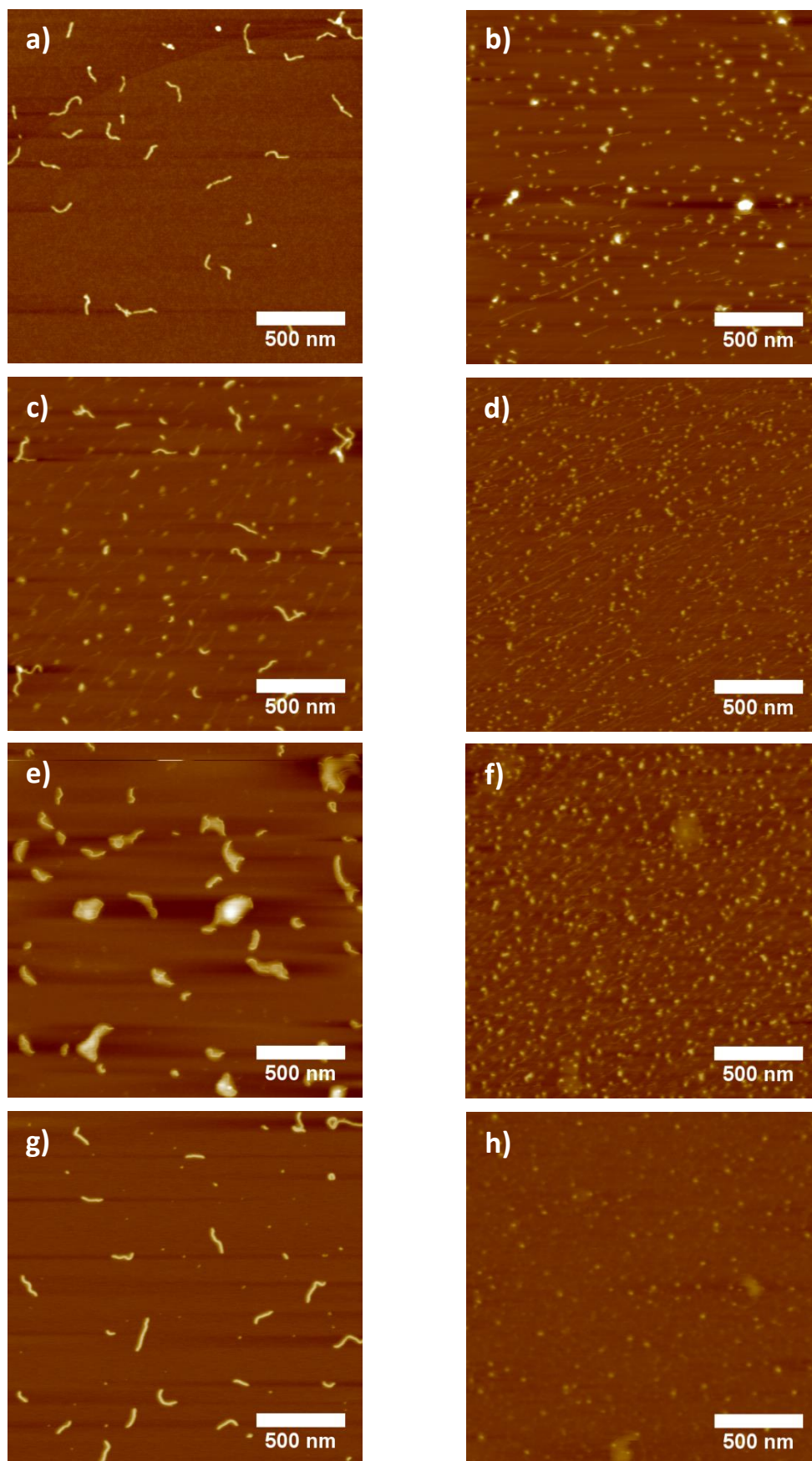


Figure 3-25: AFM height images of substituted  $g = 5$  DPs as synthesized (left-hand column) and products of "hot solvent" treatment (DMPU, 2 h at 120 °C). a), b):  $PG5_{500}^{NHAlloc}$ ; c), d):  $PG5_{500}^{NHCbz}$ ; e), f)  $PG5_{500}^{CO_2Me}$ ; g), h)  $PG5_{500}^{CO_2tBu}$ .

### 3.5.8 Characterization of low molecular mass scission products

Particularly for the degradation of  $g = 5$  DPs, low molar mass peaks detected represent a significant proportion of the products of main-chain scission as determined by GPC (Figure 3-13). As pointed out previously, peaks at similarly high RV were also detected for DPs of  $g \neq 5$  (see Figure 3-22). Under the most forcing set of conditions applied (DMPU, 120 °C for  $\geq 1$  h), indications of main-chain scission were found by GPC for the following polymers:  $\text{PG3}_{500}^{\text{NHBoc}}$ ,  $\text{PG4}_{500}^{\text{NHBoc}}$ ,  $\text{PG4}_{10'000}^{\text{NHAlloc}}$ ,  $\text{PG5}_{500}^{\text{NHBoc}}$ ,  $\text{PG5}_{\sim 5'000}^{\text{NHBoc}}$ ,  $\text{PG5}_{500}^{\text{NHAlloc}}$ ,  $\text{PG5}_{10'000}^{\text{NHAlloc}}$ ,  $\text{PG5}_{500}^{\text{NHCbz}}$ ,  $\text{PG5}_{500}^{\text{CO}_2\text{Me}}$ ,  $\text{PG5}_{500}^{\text{CO}_2\text{tBu}}$ , **B-PG6** $_{500}^{\text{NHBoc}}$ , **B-PG7** $_{500}^{\text{NHBoc}}$ . Significant peaks ( $> 10\%$  of overall GPC area) were however only detected for DPs of  $g = 5$  and for **B-PG6** $_{500}^{\text{NHBoc}}$ . All other chromatograms, small-molecule peaks were comparatively minor. A set of DPs exhibiting such peaks is found in Figure 3-26a. The peak RV of the small-molecule fraction (Figure 3-26b) decreases with increasing  $g$ , hinting at the possibility that these peaks – as for the scission observed in  $\text{PG5}_n^{\text{NH}_3\text{TFA}}$ , see Figure 3-1<sup>169</sup> – correspond to the respective macromonomers.

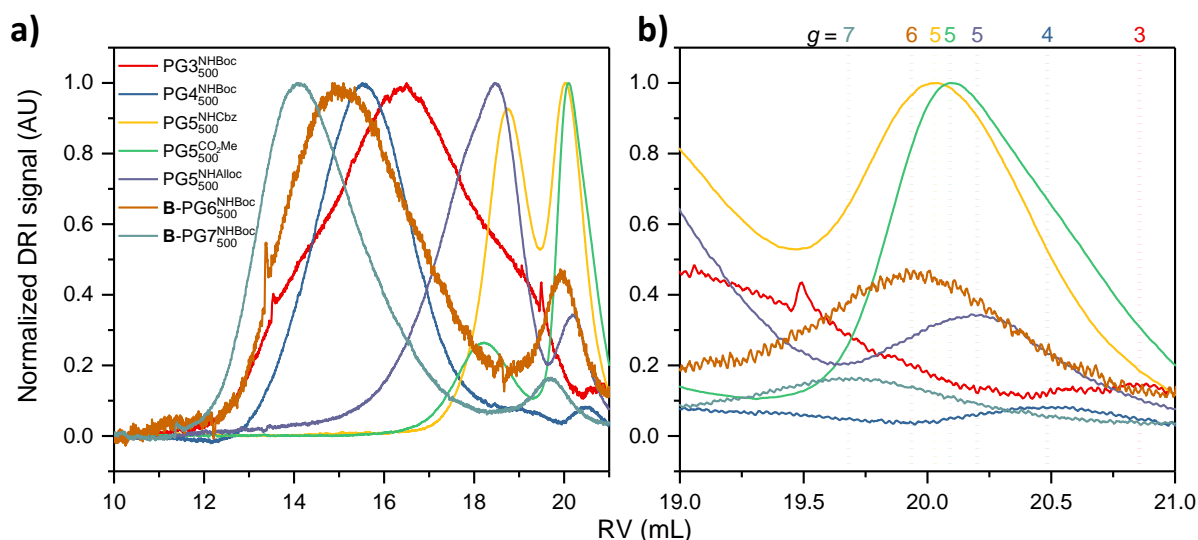


Figure 3-26: a) GPC elution curves of DPs for mass spectrometry after treatment in DMPU at 120 °C for 2h (see Appendix A.3)A.3; b) magnification of high-RV section of the chromatograms with the approximate peak retention times marked by correspondingly colored dotted lines.

For most of the above polymers, this notion is supported by MALDI-TOF-MS (Figure 3-27; full-scale mass spectra can be found in Appendix A.5): For all DPs of  $g < 6$ , peaks close to the expected  $m/z$  of the corresponding macromonomers were detected. Allocation of the main species was not possible in all cases (see Table 3-1), as the mass spectra were often insufficiently resolved. Particularly for the carbamate-bearing DPs  $\text{PG}g_{500}^{\text{NHBoc}}$ ,  $\text{PG}g_{500}^{\text{NHAlloc}}$  and  $\text{PG}g_{500}^{\text{NHCbz}}$ , it is possible that in addition to mere adduct ion formation, partial decomposition of the protecting groups accompanied by reaction with the MALDI matrix (*trans*-2-[3-(4-*tert*-butylphenyl)-2-methyl-2-propenylidene]malononitrile, DCTB) occurred.<sup>256</sup> Particularly  $\text{PG5}_{500}^{\text{NHAlloc}}$  and  $\text{PG5}_{500}^{\text{NHCbz}}$  appear to undergo significant chemical changes, in agreement with their larger potential photoreactivity. The distinct, very regular mass difference patterns observed for both of these polymers (Figure 3-27d,e) remain unexplained for now. For **B-PG6** $_{500}^{\text{NHBoc}}$  and **B-PG7** $_{500}^{\text{NHBoc}}$ , no significant peaks were detected (Figure 3-27h,i). The ionization or detection of the corresponding macromonomers may be inhibited. Limited ionizability is likely not only a result of the very high molar masses ( $m/z > 20'000$ ) but also of the high proportion of polymeric



species remaining in the samples (Figure 3-26a), with which any generated macromonomer might be tightly associated by interdigitation.

Table 3-1: Interpretation of mass spectra depicted in Figure 3-27.

Starting Polymer	Main ion found (m/z)	Macromonomer (expected m/z for M <sup>+</sup> )	Allocated species (expected m/z)
PG3 <sub>500</sub> <sup>NHBoc</sup>	2775.22	2624.40	(M+DMPU+Na) <sup>+</sup> (2774.49); also found: (M+DMPU+K) <sup>+</sup>
PG4 <sub>500</sub> <sup>NHBoc</sup>	5550.01	5426.88	(M+DMPU) <sup>+</sup> (5555.98) (also found: M <sup>+</sup> /(M+H) <sup>+</sup> )
PG5 <sub>500</sub> <sup>NHBoc</sup>	11163.27	11032.84	(M+DMPU) <sup>+</sup> (11160.93)
PG5 <sub>500</sub> <sup>NHAlloc</sup>	11008.69	10519.83	Possibly: M-DCTB reaction product, + n·DMPU (10619.94 + n·128.09)
PG5 <sub>500</sub> <sup>NHCbz</sup>	12278.66	12120.34	Possibly: (M+DMPU+Na) <sup>+</sup> (12271.42); unexplained pattern with Δm/z ≈ 420
PG5 <sub>500</sub> <sup>CO<sub>2</sub>Me</sup>	9230.90	9206.98	(M+Na) <sup>+</sup> (9229.92); also found: M <sup>+</sup> /(M+H) <sup>+</sup> , (M+K) <sup>+</sup>
PG5 <sub>500</sub> <sup>CO<sub>2</sub>tBu</sup>	10676.81	10552.49	(M+DMPU) <sup>+</sup> (10680.58)
B-PG6 <sub>500</sub> <sup>NHBoc</sup>	N/A	22245	N/A
B-PG7 <sub>500</sub> <sup>NHBoc</sup>	N/A	44670	N/A

Lastly, as noted previously for the scission products of PG5<sub>n</sub><sup>NH<sub>3</sub>TFA</sup>,<sup>169</sup> the presence of trace signals in the olefinic region in <sup>1</sup>H-NMR (4.5-5.5 ppm Figure 3-28a) of the scission products of PG5<sub>500</sub><sup>NHBoc</sup> also suggests the presence of macromonomer, as this spectral region is devoid of signals for the original DPs.<sup>5</sup> Simultaneously, much sharper dendritic signals are apparent throughout the remaining spectrum (Figure 3-28b). This observation agrees with the presence of both macromonomer and dendrimer-like oligomeric scission products as inferred from GPC measurements: For both of these product classes, the mobility of peripheral groups is expected to be far larger than in the cylindrical, highly congested parent DP.

<sup>5</sup> Oxygen was not excluded in this particular experiment, and hence some oxidation of the methacrylates *e.g.* to epoxy- or peroxy-derivatives is possible. This is potentially relevant to mass spectrometry as well, but was not considered explicitly in the evaluation in Table 3-1.

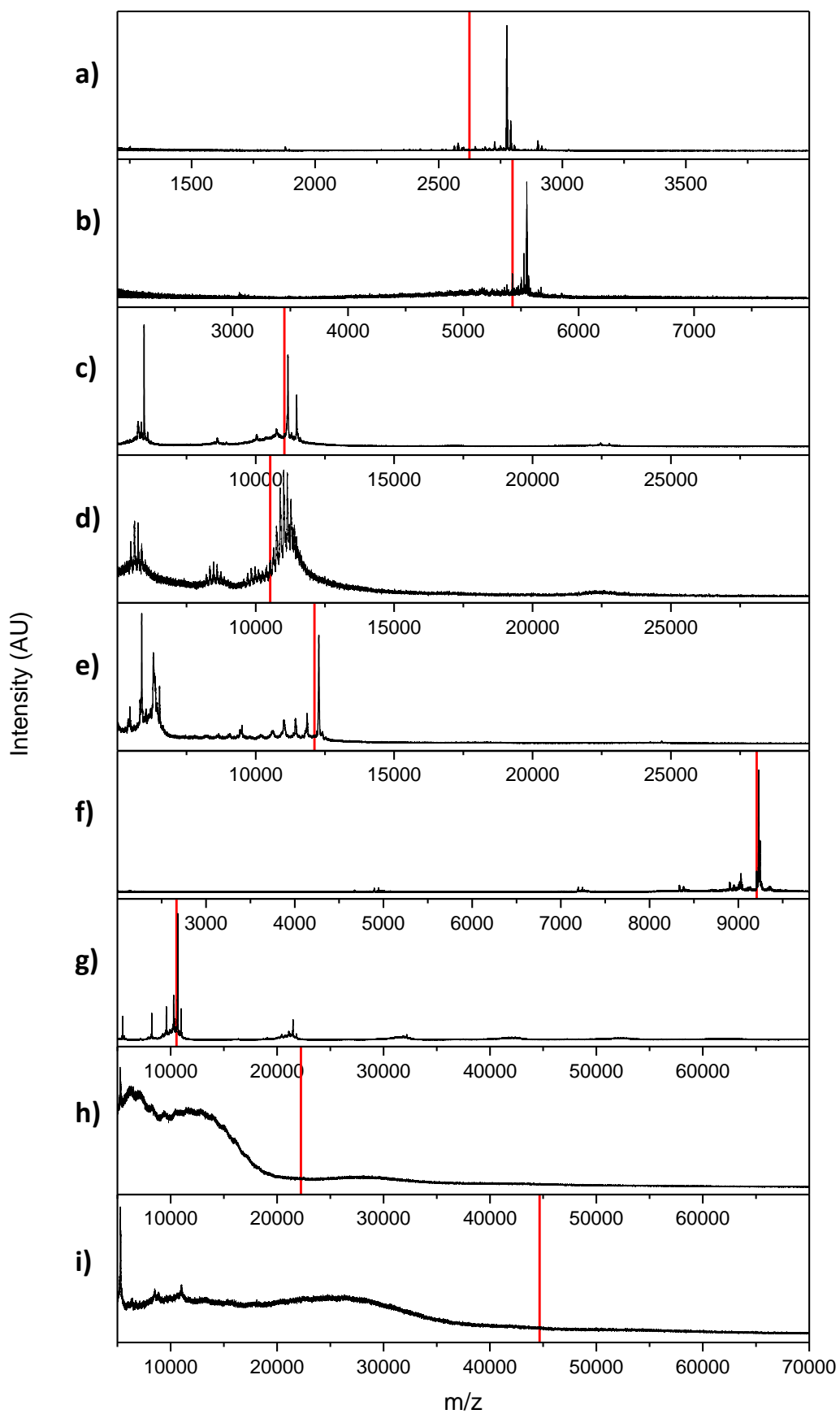


Figure 3-27: MALDI-TOF-MS of DPs after heating (DMPU, 120 °C, 2 h); red lines: expected  $m/z$  ( $M^+$ ); a)  $PG3_{500}^{NHBoc}$ , b)  $PG4_{500}^{NHBoc}$ , c)  $PG5_{500}^{NHBoc}$ , d)  $PG5_{500}^{NHAlloc}$ , e)  $PG5_{500}^{NHCbz}$ , f)  $PG5_{500}^{CO_2Me}$ , g)  $PG5_{500}^{CO_2tBu}$ , h)  $B-PG6_{500}^{NHBoc}$ , i)  $B-PG7_{500}^{NHBoc}$ .

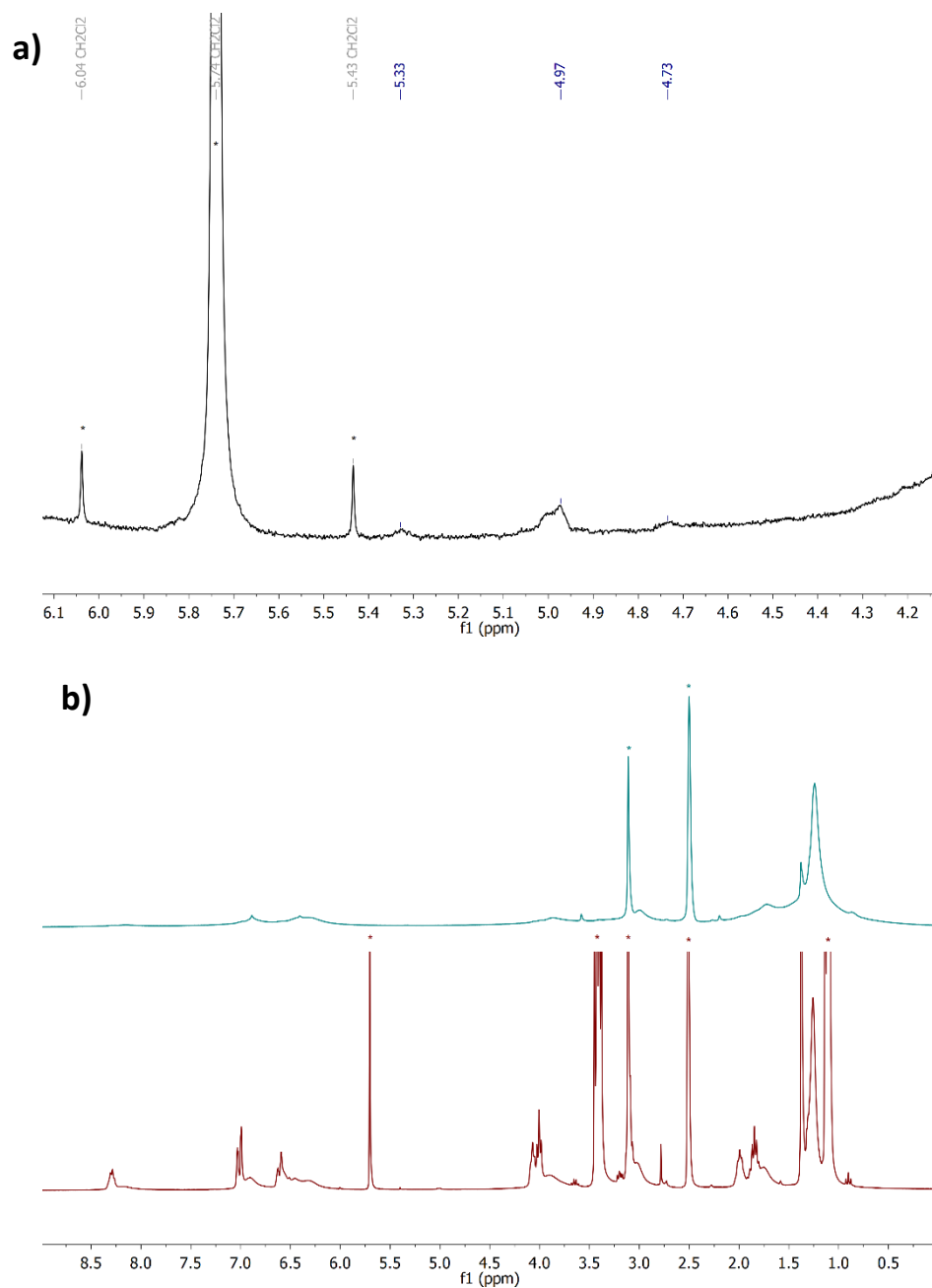


Figure 3-28: a) Olefinic region of the  $^1\text{H-NMR}$  spectrum of  $\text{PG5}_{500}^{\text{NHBOC}}$  scission products (DMPU, 80 °C, 1 h; 300 MHz, 310 K,  $\text{DMSO-d}_6$ ); b) comparison between the  $^1\text{H-NMR}$  spectra of  $\text{PG5}_{500}^{\text{NHBOC}}$  (300 MHz, 343 K,  $\text{DMSO-d}_6$ , top) and scission products (bottom); solvent peaks ( $\text{CH}_2\text{Cl}_2$ ,  $\text{Et}_2\text{O}$ ,  $\text{DMSO}$ ,  $\text{H}_2\text{O}$ ) are marked with asterisks.

### 3.5.9 Mechanistic insights from EPR spectroscopy

According to the hypothesis presented initially for acid-induced main-chain scission of  $\text{PG5}_n^{\text{NH}_3\text{TFA}}$  (subsection 3.3.2), chain degradation likely proceeds *via* homolytic scission, producing radicals at strongly congested locations along the backbone, which then undergo depolymerization to macromonomer. As the main-chain scission process discussed here appears to proceed quite similarly (see section 3.6), it seemed likely that mechanistic parallels exist. The scission process in the former case – induced by chemically aggressive strong acids and occurring even in the cold – is only poorly controllable, and therefore mechanistic insights could not be obtained previously. As the conditions are easier to control for simple “hot solvent” treatment, a more in-depth analysis of the latter process appeared much more feasible. EPR spectroscopy provides a sensitive tool for the detection of radicals and should provide some insight into the scission process, if indeed a homolytic mechanism is involved. However, as both “hot solvent” mediated and charge-induced main-chain scission proceed in highly polar media, a polar mode of scission cannot be excluded out of hand.

In an initial experiment, a mixture of  $\text{PG5}_{500}^{\text{NHBoc}}$  and DMPU was briefly brought to 80 °C, then vitrified by immersion into liquid nitrogen. In the resulting organic glass, a weak, broad EPR signal was present, centered around a Landé  $g$ -factor of  $g_{\text{I}} = 2.01 \pm 0.01$  (Figure 3-29a). The reaction was conducted under a nitrogen atmosphere, however considering the low signal-to-noise ratio it cannot be fully excluded that the detected radical is an oxygen-centered species (expectation for PMMA-derived radicals:  $g_{\text{I}} \approx 2.005$ ).<sup>257</sup> In order to provide better signal intensity and to help elucidate the character of the (likely transient) radicals produced in main-chain scission, the nitron spin trap DMPO was added in a second experiment (Figure 3-29b).  $\text{PG5}_{500}^{\text{NHBoc}}$  was heated briefly to 80 °C in the presence of DMPO/ DMPU under strict exclusion of oxygen, then vitrified (see Experimental, subsection 8.3.2, for details). EPR spectroscopy of “hot solvent” mediated main-chain scission in the presence of the radical trapping agent revealed a clear but broad, structured signal (Figure 3-29b). The influence of atmospheric oxygen was also tested for in a separate experiment (Figure 3-29d), finding that there appears to be no significant impact on the scission process.

It is evident that a radical process is involved in the main-chain scission process. As the trapped radicals proved thermally unstable upon further heating (see Experimental, subsection 8.3.2), and as spin quantification is difficult under the best of circumstances, no direct conclusions about the radical concentration and the extent of chain scission *via* a radical mechanism can be drawn. Deconvolution of the spin-trap signal (Figure 3-29c) indicates the presence of four species (see Experimental, subsection 8.3.2, Figure 8-20). The exact adducts involved can however not be identified from the present data, especially as the signals – originating from polymeric species with locally distinct chemical environments – are quite broad. Together with the thermal instability of the detected radicals (which might already be tertiary species resulting from the initial DMPO adducts), this makes the structural identification of the four apparent contributors to the signal very difficult, if not impossible from currently available data.

A potentially competing polar mechanism appeared unlikely from the start due to the higher activation barrier for heterolytic bond dissociation. GPC curves of the reaction products isolated from the EPR experiments above (Figure 3-29e) reveal that a polar pathway is indeed unlikely: Significant DP degradation has taken place in presence of the radical trapping agent, but the fragments appear

at lower RV than in the absence of DMPO. More importantly, a polar pathway would be expected to produce some macromonomer from the depropagation of the newly generated cationic or anionic chain ends. No significant peak at  $RV \approx 20.5$  mL (corresponding to macromonomer) is present in this case, however. This was corroborated by MALDI-TOF-MS, where again no macromonomer peak was found (see Experimental, subsection 8.3.2, Figure 8-19).

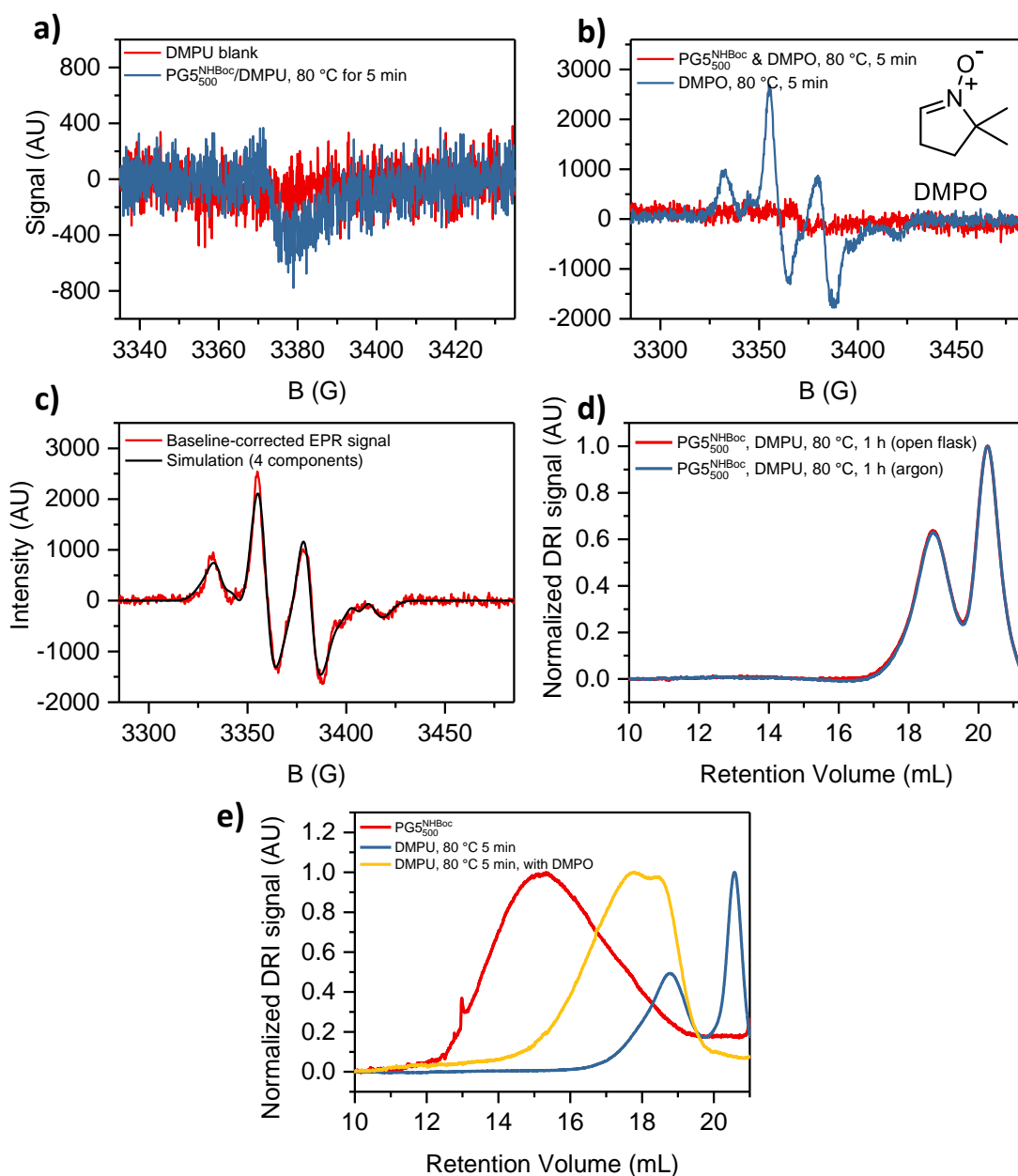
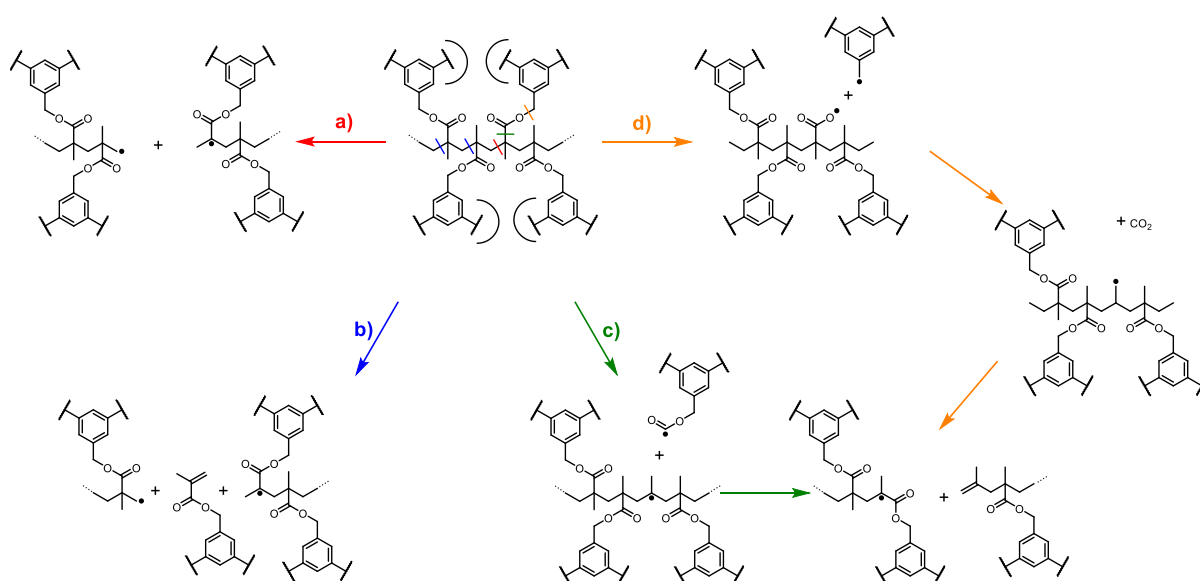


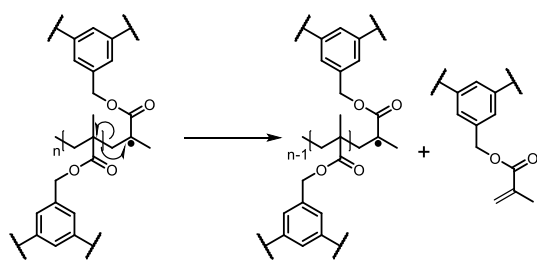
Figure 3-29: a) Line-corrected CW-EPR spectra (X-band, 200 K, 20 accumulated scans) of DMPU and a sample of  $PG5_{500}^{NHBOc}$  (ca. 2% w/w in DMPU) heated to 80 °C for 5 min. b) Uncorrected CW-EPR spectra (X-band, 200 K, 1 scan) of DMPO (ca. 1.4 M in DMPU) and of the same solution containing additional  $PG5_{500}^{NHBOc}$  (ca. 5% w/w), both after heating to 80 °C for 5 min. c) Baseline-corrected EPR spectrum and simulated spectrum consisting of 4 DMPO adduct components. d) GPC retention curves of “hot solvent” treatment (DMPU, 1% w/V) conducted in presence or absence of atmospheric oxygen. e) GPC retention curves of products of EPR experiments.

This shows that main-chain scission proceeds *via* a majority homolytic pathway. It also indicates that the DP backbone is the most likely site of cleavage (Scheme 3-5a, possibly Scheme 3-5b), rather than some adjacent bond. The cleavage *e.g.* of a C-(C=O) bond (Scheme 3-5c)<sup>258</sup> or a benzylic bond (Scheme 3-5d) in the side chains would produce small-molecule fragments which are not detected by GPC in the presence of DMPO (Figure 3-29). MALDI-TOF-MS of scission products both in presence and absence of DMPO (see subsection 3.5.8, Figure 8-19, and Appendix A.5) also did not indicate that side-chain cleavage contributes significantly to the investigated process of DP degradation, as the corresponding dendrons were not detected. It has however been suggested that side chain cleavage plays a significant role *e.g.* in the thermal degradation of PMMA.<sup>258</sup> Theoretical studies using PMMA as a model system have suggested that other backbone fragmentation patterns such as the one shown in Scheme 3-5b may be preferred,<sup>259</sup> though the absence of a low molar mass fraction in GPC and MALDI-TOF-MS suggests that instead the simpler, direct homolytic scission process (Scheme 3-5a)<sup>260,261</sup> is the preferred pathway leading to backbone scission.



Scheme 3-5: Some potential radical pathways for initial backbone scission: a) “standard” homolytic pathway;<sup>260</sup> b) alternative initiation model obtained from reactive MD simulations;<sup>259</sup> c), d) side-chain initiated scission processes.<sup>258</sup>

The macroradicals formed in the initial backbone scission (Scheme 3-5) may expel macromonomers until either the active chain-ends are quenched or depolymerization becomes unfavorable. This may be the case *e.g.* due to conformational relaxation at the new chain end, transitioning from locally cylindrical to ellipsoid geometry. Tertiary radicals produced from simple homolytic backbone scission (Scheme 3-5a) are likely to undergo a straightforward depropagation process (Scheme 3-6). The less stable primary amines may likewise depropagate similarly to Scheme 3-6, but the literature suggests that they are subject to more complex pathways prior to actual depolymerization, *e.g.* involving  $\beta$ -elimination and cleavage of side chains.<sup>261,262</sup> These pathways however involve intermolecular radical reactions, which are very unlikely to occur between the sterically strongly congested macroradical produced in DP chain scission – the fate of the primary radicals can therefore remain unclear, as an allocation of structures to the EPR signal is currently not possible.



*Scheme 3-6: Depropagation mechanism of tertiary macroradicals formed in the initial scission process.*

### 3.5.10 Insights from MD simulations

The behavior of  $\text{PG5}_{500}^{\text{NHBOC}}$  in DMPU is quite extraordinary, particularly as the DP was found to undergo main-chain scission already at room temperature in this solvent. This and the interesting rheological behavior of  $\text{PG4}_{10'000}^{\text{NHBOC}}$  dissolved in DMPU (see chapter 6) prompted an atomistic simulation of a short DP segment ( $\text{PG5}_{100}^{\text{NHBOC}}$ ,  $\sim 160'000$  atoms) in an orthorhombic box of DMPU (35319 molecules). The entire sample contained 902601 explicit atoms (see Experimental, subsection 8.3.2). Starting from a conformation obtained by simulation in vacuum,<sup>228</sup> a productive MD trajectory of 80 ns was run. The exposure to solvent led to significant shifts in the DP conformation: Snapshots at 0 ns and 80 ns (Figure 3-30a) show a significant stretching of the DP chain, particularly of the middle segments. This stretching is accompanied by penetration of DMPU into the DP structure (Figure 3-30b). That the solvent penetration is particularly strong not only in the periphery but also for the innermost part of the DP, as the density profiles in Figure 3-31 show, is likely a consequence of the initial DP conformation (left-hand side in Figure 3-30a). The pore which is present in the interior of  $\text{PG5}_{100}^{\text{NHBOC}}$  in vacuum is potentially an artefact from the simulation setup (the system is very strongly sterically congested, after all). After 80 ns of solvent exposure, the pore has become far less prominent (Figure 3-31a). Solvent therefore not only penetrated into the DP structure, but also rendered dendritic branches more mobile, such that they were able to optimize internal interactions, as indicated by an overall contraction of the branchwork (Figure 3-31a).

As shown in Figure 3-32, the changes induced by swelling are not limited to the dendritic branches, which contract by *ca.* 9 % (see Figure 8-22). The course of backbone conformations throughout the productive simulation shows accompanying changes in the overall backbone geometry: The visual impression of an overall elongation of the backbone is verified when the time evolution of the end-to-end distance is considered (Figure 3-32a). This overall extension is not merely due to a change in the backbone conformation (*e.g.* a change in helicity): Although dihedral angles do increase (Figure 3-32b), part of the elongation appears to result from significant strain being exerted on the backbone bonds. Both the backbone bond angles (Figure 3-32c) and C-C bond lengths increase substantially (Figure 3-32d). See Table 3-2 for a summary of all numerical data.



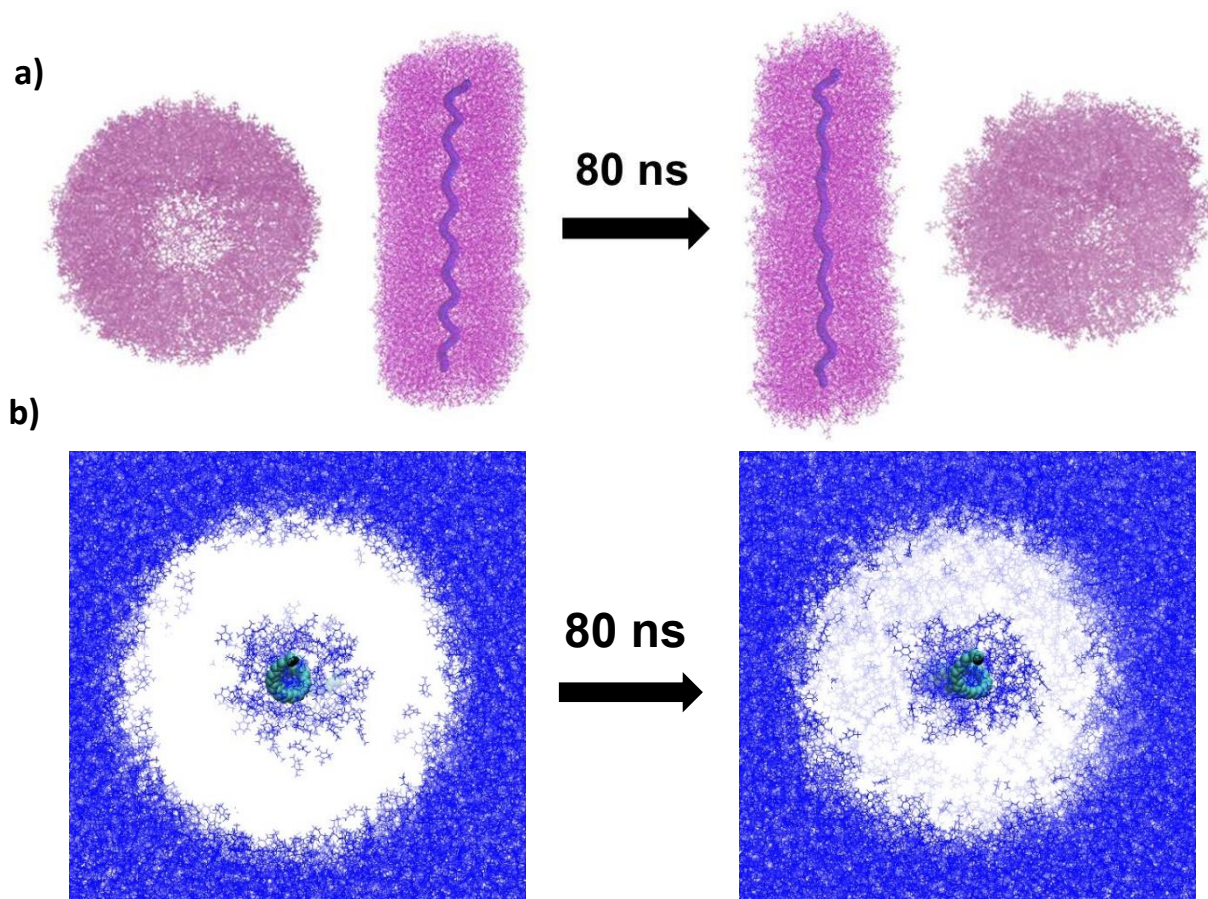


Figure 3-30 a) Axial and cross-sectional projections of  $PG5_{100}^{NHBoc}$  obtained from MD simulations in vacuum<sup>228</sup> and after 80 ns in DMPU; solvent molecules are omitted for clarity, the DP backbone is represented by the thick purple line. b) Cross-sectional profile through the DP, showing the distribution of DMPU (blue; backbone indicated in green, branchwork omitted for clarity). Images generated by Prof. Dr. Carlos Alemán (Universitat Politècnica de Catalunya), reproduced with permission.

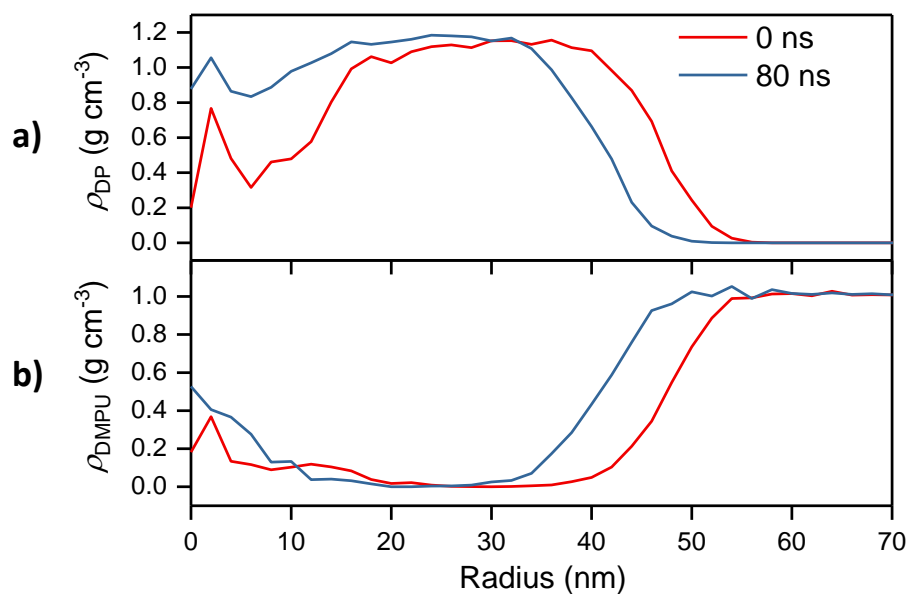


Figure 3-31: Evolution of the average radial density profiles of a)  $PG5_{100}^{NHBoc}$  and b) DMPU obtained from MD simulation (see Figure 3-30).

The average increases of bond angles by 3.1 % and of bond lengths by 1.8 % correspond to a significant gain in energy and substantial strain on the backbone, though whether this is sufficient for bond breakage at RT is difficult to tell: The harmonic potentials employed in MD simulations (AMBER force field)<sup>263,264</sup> are not designed to capture such extreme events involving significant electronic changes; The increase in strain energy is also at least partially compensated for by the formation of favourable DP-DMPU contacts. Furthermore, the data shown in Figure 3-32 are admittedly noisy. In large parts, this is due to chain-end effects, which have a large influence in the relatively short DP segment ( $P_n = 100$ ) simulated here. At the chain ends, steric congestion is lower and where there is more conformational freedom compared to the middle of the chain – where the largest changes appear to take place (Figure 3-30a).

This differential swelling effect is also shown in Figure 3-33: The middle 30 C-C bonds of the DP segment are stretched significantly – the average bond length increases by almost 7 % (Table 3-2). The bonds at the two chain ends meanwhile are relatively unaffected, with the average C-C bond length (15 bonds at either end) increasing only by 2.5 %. This strong differential swelling effect is a direct consequence of steric congestion, which is strong in the middle of the chain and relatively weak at the chain ends. In some ways, the DP-solvent interaction is therefore geometrically controlled. The swelling process also does not appear to be fully concluded at the chosen end point of the simulation. Much of the overall change appears to occur during the first 10 – 20 ns, but complete equilibrium has not been reached during the (already computationally very intensive) productive MD simulation trajectory of 80 ns shown here.

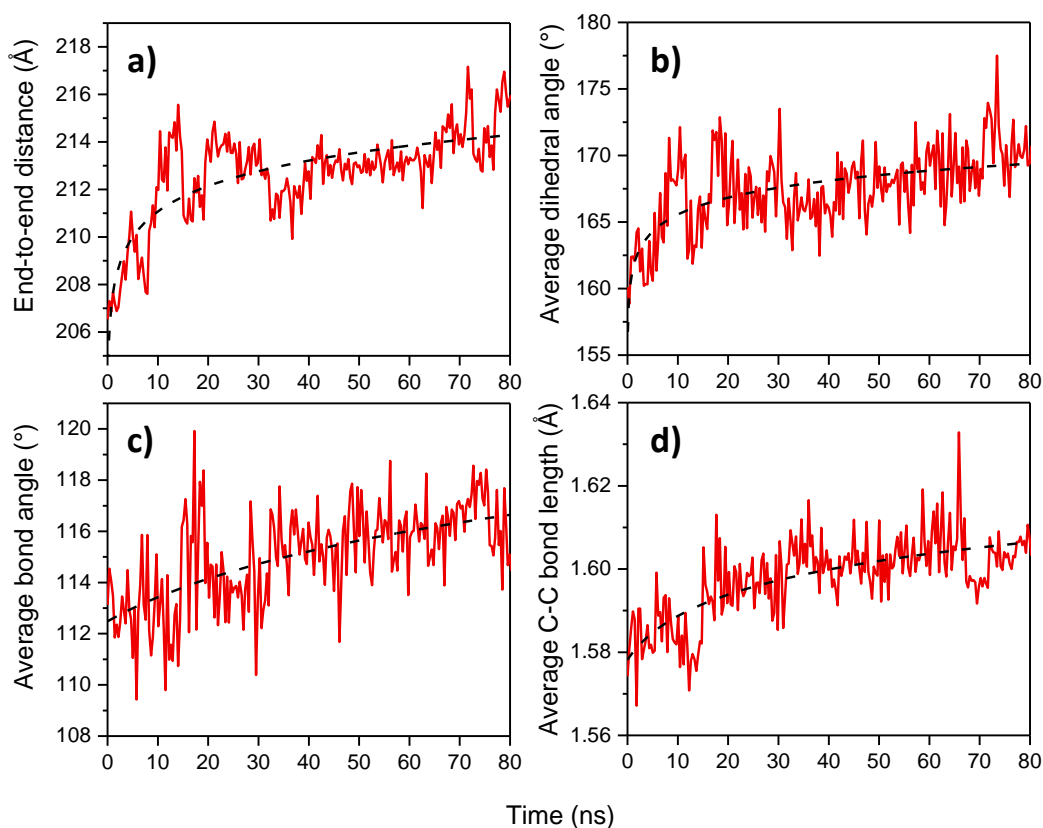


Figure 3-32: Evolution of average backbone parameters over the course of the productive MD simulation: a) end-to-end distance; b) average C-C-C-C dihedral angle; c) average C-C-C bond angle; d) average C-C bond length. The dashed lines represent logarithmic curve fits and serve only to guide the eye.

Table 3-2: Summary of changes to backbone parameters shown in Figure 3-32 and Figure 3-33; errors correspond to standard deviations where applicable. a) time-average during  $t = 0 \text{ ns} - 10 \text{ ns}$ ; b) time-average during  $t = 70 \text{ ns} - 80 \text{ ns}$ ; c) starting value at  $t = 0 \text{ ns}$ , directly after equilibration.

Parameter	Beginning of simulation	End of simulation	Change
End-to-end distance	208.9 nm <sup>a)</sup>	214.7 nm <sup>b)</sup>	+ 2.8 %
Average backbone dihedral angle (entire chain)	160 ° <sup>c)</sup>	170.8 ° <sup>b)</sup>	+ 6.8 %
Average backbone bond angle (entire chain)	113.1 ° <sup>c)</sup>	116.6 ± 1.3 ° <sup>b)</sup>	+ 1.8 %
Average backbone bond length (entire chain)	1.574 Å <sup>c)</sup>	1.603 ± 0.004 Å <sup>b)</sup>	+ 3.1 %
Average backbone bond length (30 bonds in the middle)	1.58 Å <sup>a)</sup>	1.68 ± 0.01 Å <sup>b)</sup>	+ 6.3 %
Average backbone bond length (15 + 15 bonds at chain ends)	1.57 Å <sup>a)</sup>	1.61 ± 0.01 Å <sup>b)</sup>	+ 2.5 %

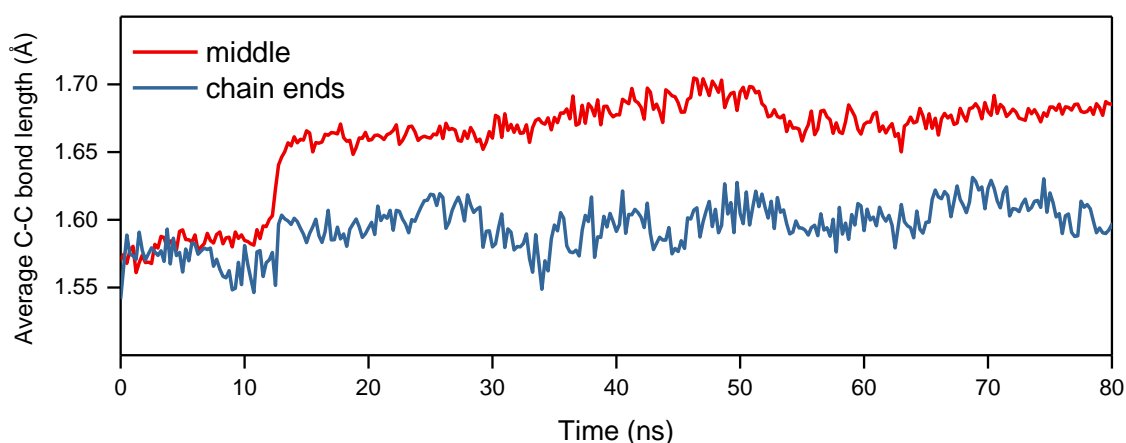


Figure 3-33: Changes in the average C-C bond length over the course of swelling for the middle of the chain (30 C-C bonds in the middle of the DP segment) and for the chain ends (15 C-C bonds at either end).

MD simulations along similar lines were previously performed for  $\text{PG5}_{75}^{\text{NH}_3\text{TFA}}$  in aqueous solution, in the context of charge-induced main-chain scission.<sup>228</sup> The results obtained there stand in intriguing contrast to those presented here: As shown in Figure 3-34, in the case of deprotection (and additional solvent exposure), a significant expansion of the dendritic corona occurred relative to  $\text{PG5}_{100}^{\text{NH}_3\text{Boc}}$  in vacuum. This was thought to be prompted by the repulsion between peripheral ammonium cations (see section 3.3) and results in a sponge-like structure which is significantly solvent-swollen. An analysis of backbone bonds similar to that shown in Figure 3-32 and Figure 3-33 was unfortunately not performed in that case, likely due to the even greater dominance of chain-end effects ( $n = 75$  instead of  $n = 100$ ). A comparative analysis of the strain exerted onto the backbone in that case might be worthwhile. That a spreading out rather than a contraction of the structure is observed in this case results in significant solvent penetration into the interior of the DP. Whether water is a solvent in which scission occurs is questionable, however: The experiments presented in section 3.4 use what are apparently good swelling agents (polar-aprotics and TFA), and the simulation run in aqueous

solution might not accurately reflect the strains exerted onto the structure during deprotection with neat (or diluted) TFA.

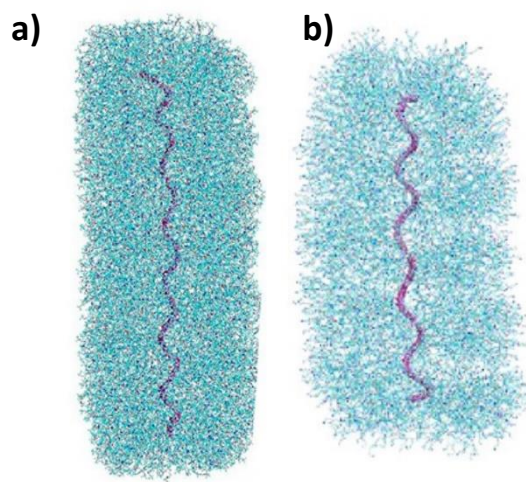


Figure 3-34: MD simulations of a)  $PG5_{100}^{NHBOc}$  in vacuum and b)  $PG5_{75}^{NH_3TFA}$  in water (chain length had been reduced for reasons of computational economy; see Ref. 229). Adapted with permission from O. Bertran et al. *J Phys. Chem. B* **2013**, 117, 6007-6017. Copyright 2013, American Chemical Society.

### 3.5.11 Summary of findings

To bring some clarity to the discussion of the novel phenomenon of main-chain scission in “hot solvents”, the most salient points to be drawn from the data presented above are summarized below:

- When dissolved in certain solvents, some DPs of the type  $PGg_n^{\text{NHBoc}}$  undergo a process of main-chain scission upon heating. This occurs without the addition of any other reagents and affords mostly short polymeric or oligomeric DP fragments.
- Scission is by far the most pronounced for  $PG5_n^{\text{NHBoc}}$ ; DPs of other  $g$  were not degraded nearly as much (Figure 3-20b), though minor fragmentation may be observed from  $g = 3$  all the way to  $g = 7$  under very harsh conditions (Figure 3-26b).
- For  $g > 6$ , DPs synthesized by route **B** are more susceptible to this mode of degradation than the corresponding, structurally more perfect DPs from route **C** (Figure 3-23).
- The scission process does not appear to depend on the concentration of the polymer solution (Figure 3-19a).
- Externally applied shear does not significantly impact the extent of scission (Figure 3-19b).
- The initial chain length (and/or mode of polymerization) appears to have some influence on the absolute extent of scission (Figure 3-19a).
- The solvents in which main-chain scission is observed are exclusively of the polar-aprotic type (DMF, DMPU, DMSO, DMAc, NMP). Other moderate to good solvents for DPs (alcohols, intermediate polarity aprotic solvents, chlorinated solvents, aromatics) do *not* cause main-chain scission (Figure 3-13).
- The degree of scission varies among the solvents for which this phenomenon was observed: In DMF, the least amount of scission is observed, while in DMPU scission produces the smallest fragments under otherwise identical conditions (Figure 3-13).
- DMPU takes a special place among the solvents for which scission does occur, as it results in main-chain scission of  $PG5_n^{\text{NHBoc}}$  even when the solution is maintained at room temperature (Figure 3-17). In contrast, a temperature threshold of *ca.* 65 °C was established for  $PG5_n^{\text{NHBoc}}$  in DMF.
- The extent of scission depends on the temperature to which the solution is heated: The higher the temperature, the shorter the scission fragments for a given solvent (Figure 3-18a,b).
- The extent of scission does not appear to depend significantly on the time of exposure to the solvent, past the initial few minutes required for full dissolution of the polymer. All data suggests that the main-chain scission process occurs on a time scale of a few minutes, reaching a temperature-dependent extent of scission which may be increased by heating to higher temperatures.
- For DPs of  $g = 5$ , main-chain scission appears to be a universal phenomenon and occurs for all tested peripheral functionalities ( $X = \text{NHBoc}, \text{NHAlloc}, \text{NHCbz}, \text{CO}_2\text{Me}, \text{CO}_2\text{tBu}$ ). The exact degree of scission varies, following a very rough trend of increased susceptibility with increasing steric demand of the peripheral group (Figure 3-24).
- “Hot solvent” mediated scission produces not only shorter polymeric or oligomeric fragments, but also a small-molecule fraction appearing at very high retention volumes in GPC; its peak RV decreases with increasing  $g$  (Figure 3-26). In most tested samples, MALDI-TOF-MS (Figure 3-27) revealed species close to the expected mass for the macromonomer of the respective

DP, and  $^1\text{H-NMR}$  of scission products of  $\text{PG}5_n^{\text{NHBoc}}$  (Figure 3-28) demonstrated that indeed some macromonomer is produced.

- EPR measurements (Figure 3-29a-c) show that the main-chain scission of  $\text{PG}5_n^{\text{NHBoc}}$  in DMPU proceeds *via* a radical mechanism. Heating in the presence of a radical trapping agent results in a reduced extent of degradation and an absence of macromonomer from the product mixture (Figure 3-29e). For this specific polymer, a possibly competing polar mechanism can be largely excluded.
- MD simulations (Figure 3-30) confirm that DMPU is an excellent swelling agent for  $\text{PG}g_n^{\text{NHBoc}}$ , and that in conjunction with already strong steric congestion in a DP can lead to significant strain on the backbone (Figure 3-32), particularly in the middle of the chain (Figure 3-33) where geometric restrictions are most pronounced.

### 3.6 Unified hypothesis: swelling-induced main-chain scission

In considering all findings presented in this chapter, close similarities between charge-induced and “hot solvent” mediated main-chain scission become apparent: Both processes appear to involve random chain scission and afford shorter polymeric or oligomeric products, in addition to a fraction of small molecules which correspond to macromonomer. Both appear to proceed *via* a radical process, a mere suspicion for charge-induced scission which was proven for “hot solvent” mediated scission. For both, there is a distinct dependence on the dendritic generation  $g$ , with only the  $g = 5$  DPs readily undergoing either mode of main-chain scission. In both cases, rather forcing conditions (*i.e.* high temperatures) are required to provoke chain degradation in DPs of  $g \neq 5$ .

These parallels strongly suggest that these are not two separate phenomena, but one and the same: Main-chain scission occurs due to a common underlying cause, although superficially two very distinct processes (a chemical reaction in the deprotection of  $\text{PG5}_n^{\text{NHBoc}}$  to  $\text{PG5}_n^{\text{NH}_3\text{TFA}}$  vs. an initially purely physical process in the simple dissolution of DPs) seem to be at play. The substantial amount of data presented above suggests an alternative hypothesis explaining both phenomena: ***Swelling of the dendritic side chains of the DPs is the cause of main-chain scission observed (mainly) in  $g = 5$  DPs.***

For “hot solvent” induced main-chain scission, the “good” solvents (more specifically: *swelling agents*) which do lead to scission penetrate the dendritic branchwork quite deeply, resulting in an increased steric demand per repeat unit and thereby exerting strain on the backbone. This notion is supported by MD simulations of  $\text{PG5}_n^{\text{NHBoc}}$  in DMPU (subsection 3.5.11). In the case of main-chain scission of charged DPs, the Coulombic repulsion between charged peripheral groups certainly contributes to the strain on the backbone, but is likely insufficient by itself: As corresponding MD simulations have shown, the charge-charge repulsion between dendrons opens up the dendritic structure to significant solvent ingress.<sup>228</sup> This particularly seems to be relevant in view of the behavior of  $\text{PG}g_n^{\text{NH}_3\text{TFA}}$  with  $g > 5$ : These polymers only undergo scission at elevated temperatures, and even then only for  $g = 6 \approx g_{\text{max}}$  (Figure 3-11). If charge-charge repulsion among peripheral groups were the sole relevant factor, these high  $g$  DPs should also undergo main-chain scission. Luckily for the synthesis of this class of DPs, this is not the case (see section 2.5),<sup>227</sup> and swelling seems to be a factor of some importance.

Two factors in particular support the above hypothesis: First, the strong solvent dependence. Only the polar aprotics DMF, DMAc, DMSO, NMP, and DMPU – which appear to be strong swelling agents rather than interacting only peripherally – cause main-chain scission. Solvents of moderate or worse swelling quality do not result in main-chain scission (Figure 3-13). TFA is an interesting addendum to the previous list of polar aprotic solvents: The results in subsection 3.4.4 – chain rupture in a DP with neutral peripheral groups – suggest that TFA may also be counted among the class of good swelling agents. This is further supported by the observation that TFA leads to more severe scission than DMBA (see subsections 3.4.1 and 3.4.2). This (and consequentially, the swelling capability of TFA) may be connected to acidity: At  $\text{pK}_a \approx 0.5$ ,<sup>175</sup> TFA may well be capable of partially protonating amides within the DP structure (generally,  $\text{pK}_a$  values of protonated amides are on the order of  $-1$ ).<sup>265</sup> As mentioned already in subsection 1.6.3, solvent quality for DPs is not necessarily as easily defined as is the case for standard linear polymers, and a delicate interplay between peripheral and branchwork interactions may be at work. The available (semi)quantitative data (see Figure 3-14 and Ref. 98) suggests that the

polar aprotic solvents are capable of swelling the DP interior better than the remaining solvent classes.<sup>†</sup>

The second key factor is the strong dependence of scission on  $g$ : DPs of  $g = 5$  are very susceptible to degradation, DPs of  $g \neq 5$  on the other hand do not undergo significant scission under standard conditions. DPs of  $g < 5$  are more easily swelled,<sup>98,99</sup> however they are also sterically far less congested, and therefore high temperatures are necessary to provoke significant chain degradation. At room temperature, their structures are capable of accommodating solvent without exerting such stresses on the backbone as would lead to rupture. The situation is different for DPs of  $g > 5$ : They are intrinsically more congested than their  $g = 5$  congeners, but it appears that this prevents solvent ingress to the degree where swelling is insufficient for main-chain scission to occur (compare the discussion of  $\alpha$  and  $g_{\max}$  in section 2.7). This behavior is expected for densely packed (*i.e.*  $g \geq g_{\max}$ ) dendritic macromolecules. In further agreement with the stated hypothesis of swelling-induced scission, the less structurally defective DPs from route **C** are more resistant to chain degradation than their counterparts from route **B** (Figure 3-23).<sup>‡</sup>

In the frame of this hypothesis of swelling-induced scission, the actual chain degradation is expected to proceed essentially in the same manner as proposed for the previously hypothesized charge-induced process: Scission occurs first along the chain, at the locations of (permanently or transiently) greatest strain, and macromonomer may be expelled from the resulting active chain ends. Localized depolymerization may progress until the active chain ends are quenched chemically or until there is no more driving force for depropagation, *e.g.* because of the steric consequences of new chain ends: At the new chain ends, the dendritic side chains have sufficient space to transition from locally cylindrical to ellipsoidal geometry, thereby lowering local steric congestion. For purely swelling-induced scission of  $\text{PG5}_{500}^{\text{NHBoc}}$ , it was shown conclusively by EPR spectroscopy that it is indeed a radical process which governs main-chain scission, and that a polar side reaction is unlikely. By trapping of the primary radicals from random chain scission, it was furthermore shown that depropagation follows the initial chain break.

The hypothesis of swelling-induced main-chain scission explains essentially all observations presented in this chapter: At increased temperatures, the extent of degradation increases, as more breaks occur per chain and/or as the relative activation barrier for depolymerization is lowered.<sup>‡</sup> As the process is caused only by the inherent steric demand of the dendritic side chains, it occurs irrespective of the exact chemical nature of the peripheral groups, as demonstrated by the “hot solvent” mediated degradation of five DPs of  $g = 5$  with different peripheral groups. Within this set, the extent of scission does however depend roughly on steric demand of the peripheral groups, with bulky *tert*-butyl groups in  $\text{PG5}_{500}^{\text{NHBoc}}$  and  $\text{PG5}_{500}^{\text{CO}_2\text{tBu}}$  being the most susceptible. Peripheral groups do

---

<sup>†</sup> The solubility of DPs of the type  $\text{PG}g_n^{\text{NH}_3\text{TFA}}$  suggests that TFA may be the interesting case of a good swelling agent – it enters the DP branchwork, as chain scission of  $\text{PG5}_n^{\text{CO}_2\text{H}}$  indicates – but a bad peripheral solvent: Upon deprotection of  $\text{PG}g_n^{\text{NHBoc}}$ , milky suspensions result which require the addition of some MeOH to afford clear solutions

<sup>‡</sup> Barring the previously discussed, single outlier of **C**- $\text{PG5}_{500}^{\text{NHBoc}}$  (Figure 3-21) which remains unexplained.

<sup>‡</sup> Particularly for experiments conducted at 120 °C with the most sterically demanding dendrons, *i.e.*  $\text{PG5}_{500}^{\text{CO}_2\text{tBu}}$  and  $\text{PG5}_{500}^{\text{NHBoc}}$ , the ceiling temperature of the polymers themselves – swelling aside – is possibly reached, and depolymerization may proceed until a radical is quenched, rather than to the point where chain-end effects dominate.



play some role in the scission process, though whether peripheral interactions with the solvent or inherent steric congestion are the relevant factors is hard to tell.

This model should allow for some predictions regarding relative susceptibilities to main-chain scission, particularly in the context of solvent quality:  $\text{PG5}_{500}^{\text{CO}_2\text{tBu}}$  and  $\text{PG5}_{500}^{\text{NHBoc}}$  show starkly different solubilities, in that the former is not soluble in DMF at room temperature (although it is at elevated temperatures; see Figure 3-24e). It is however well soluble in chlorinated solvents such as 1,2-dichlorobenzene.  $\text{PG5}_{500}^{\text{NHBoc}}$  does not undergo scission in 1,2-dichlorobenzene even at 120 °C, as it is only a moderately good solvent (Figure 3-35a). However,  $\text{PG5}_{500}^{\text{CO}_2\text{tBu}}$  (Figure 3-35b) undergoes significant degradation in the same solvent. This result is well in line with the stated hypothesis of swelling-induced scission, as dichlorobenzene is likely a better solvent for the *tert*-butyl ester peripheral groups of  $\text{PG5}_{500}^{\text{CO}_2\text{tBu}}$ . As the results obtained for charged DPs do, this indicates that good peripheral solvation may open up the DP interior for the necessary solvent swelling of the dendritic branchwork.

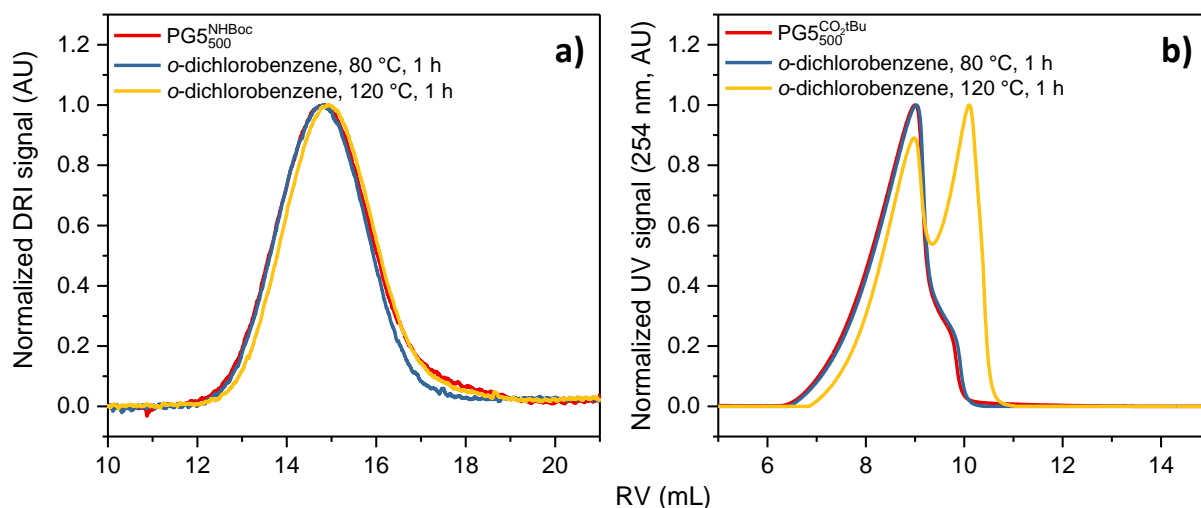


Figure 3-35: GPC traces of a)  $\text{PG5}_{500}^{\text{NHBoc}}$  (measured in DMF/0.1% LiBr) and b)  $\text{PG5}_{500}^{\text{CO}_2\text{tBu}}$  (measured in  $\text{CHCl}_3$ ) after heat treatment in *o*-dichlorobenzene.

### 3.7 Conclusions & outlook

Initial results regarding charge-induced main-chain scission seemed to largely verify the prior hypothesis of charge-induced main-chain scission, with a few notable exceptions (the resistance of  $g > 5$  DPs to charge-induced degradation and the instability of  $\text{PG5}_n^{\text{CO}_2\text{H}}$  in TFA). A large body of additional evidence from “hot solvent” mediated main-chain scission of neutral DPs has led to a more fundamental explanation which is capable of encompassing these initially perceived incongruities: Swelling of the dendritic branchwork has been established as the likely cause of main-chain scission, and random homolytic bond scission, followed by some depolymerization, has been verified as the key reaction at least for  $\text{PG5}_{500}^{\text{NHBOC}}$ .

It should be noted that this mode of chain scission is distinct from the initially noted general cases of chain degradation (Scheme 3-1): Swelling-induced main-chain scission does not involve specific reagents which attack the backbone or other parts of the DP structure. Neither is it strictly a ceiling temperature phenomenon: Unzipping depolymerization is certainly a consequence of the initial chain degradation but may be prevented entirely by trapping the initially formed radical species. Additionally, instead of going to completion above a ceiling temperature, swelling-induced main-chain scission relatively quickly (within a few minutes) reaches a temperature-dependent point of static equilibrium. Swelling-induced main-chain scission, while essentially mechanical in nature, is also not dependent on the application of external forces – the strain on the backbone appears to be of entirely internal origin. Rather, the described mode of chain degradation stands apart from these broad categories, and in solution phase such strong, swelling-induced tension appears to be a unique feature of dendronized polymers. The closest parallel to the process described here may be found in likewise strongly congested surface-grafted brushes, where sufficient grafting densities may be achieved for swelling to result in detachment of brush layers.<sup>266,267</sup> However, the observations made for DPs still remain unique in that there is no indication that *e.g.* the elongation of polymer brushes leads to a cessation of brush detachment. The instability of  $g = 5$  DPs, followed by regained stability for higher  $g$  homologs, is a singular consequence of dealing with branched, essentially densely packed organic matter, which cannot be generated easily by means other than divergent dendritic synthesis.

These results reinforce the notion that very high  $g$  DPs are “molecular objects” – single molecules of well-defined structure which in some respects resemble dense colloids. A particularly important observation in this regard is the lesser stability of DPs from route **B** when compared to their analogs from route **C**: The former are defect-riddled, and therefore partially solvent-accessible, whereas the latter are structurally more perfect and do not undergo significant scission even under forcing conditions, suggesting that little or no solvent enters their bulk – they only interact peripherally, even with very strong swelling agents such as DMPU.

A heretofore little regarded aspect of the quasi-colloidal nature of DPs has become particularly evident in the MD simulation of the DP swelling process: In an extended molecular colloid, there are substantial differences between the (nearly cylindrical) middle of the object and the chain ends (where the geometry is less restricted). Such differentiation in physical properties *e.g.* in terms swelling or backbone conformations are a feature which clearly distinguishes DPs from more standard linear polymer.

The data presented in this chapter cover a fairly large range of parameters important to “hot solvent” mediated main-chain scission of neutral DPs. However, due to the relatively recent discovery of this phenomenon, a more systematic exploration of the large parameter space (including among other factors: solvent, peripheral chemistry, temperature, reaction time, shear rates) should be conducted. Other peripheral modifications than those already investigated, *e.g.* with groups providing LCST/UCST behavior<sup>268</sup> would be of interest. The strong solvent dependence observed for DPs may pave the way for applications of swelling-induced scission. It might for instance be utilized as a tool for macromolecular engineering, opening the possibility of solvent- or pH-dependent scission *e.g.* for sensing applications or for drug release. However, considering that tedious divergent synthesis is necessary to generate the required steric congestion, such one-time “scission triggers” are likely of purely academic interest.

Potential applications aside, the knowledge of degradation tendencies is of great synthetic value in the preparation of  $g > 6$  DPs: Main-chain scission cannot be tolerated when the synthesis of GDa molar mass DPs is a goal, and careful optimization of reaction solvents is likely necessary. Scission experiments like the ones presented in this chapter (requiring as little as 5 mg of material) offer a convenient tool to avoid scission in larger-scale preparative experiments.

## 4. Cryo-TEM of DPs and analysis of native chain conformations

### 4.1. Motivation/Goals

Virus particles such as TMV,<sup>269–271</sup> protein aggregates and superstructures such as F-actin,<sup>272–274</sup> amyloid fibrils,<sup>275</sup> and dsDNA<sup>276,277</sup> are obvious and popular subjects for many microscopic techniques (AFM, TEM, STEM, optical microscopy, *etc.*), as they offer the required relatively large dimensions or provide opportunities for highly selective labelling or staining. The imaging of individual polymers is by comparison much harder: For example, the AFM imaging of ssDNA<sup>278,279</sup> or of isolated synthetic polymer chains (*e.g.* PMMA or PS) is possible,<sup>280,281</sup> but much less of a routine task. Due to lack of contrast, the imaging of such thin filaments is even more challenging with electron microscopic techniques.

In comparison to standard synthetic polymers, individual DPs are comparatively easy to image using various techniques, as illustrated in other chapters of this thesis (AFM particularly in chapters 2 & 3, TEM/SEM/STEM in chapter 5, fluorescence microscopy in chapter 6). This is owed largely to their compactness and their thickness, which for  $PGg_n^{NHBOc}$  of  $g > 5$  lies in the range of 10–20 nm (diameters in solution), approaching the dimensions of some of the aforementioned biological filaments. This is illustrated very nicely by the AFM image in Figure 4-1, which shows a chain of  $PG5_n^{NHBOc}$  alongside a TMV particle. While the AFM imaging of high  $g$  DPs is almost trivial and the TEM or SEM imaging of suitably coated specimen is fairly easy, the samples investigated in all these cases are polymers deposited onto a solid substrate (mica, HOPG *etc.*). While some inferences can be made from AFM, SEM and TEM images as to the original solution shape of such chains, they are not representative of the undisturbed native state of these molecules.

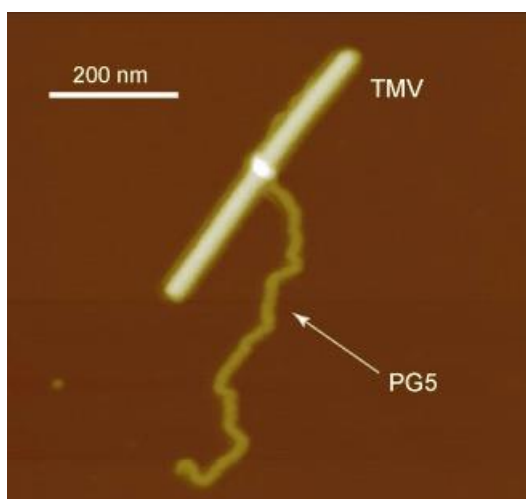


Figure 4-1: AFM height image of a single  $PG5_n^{NHBOc}$  chain and a TMV capsid, coprepared on mica. Reproduced with permission from Zhang B. et al. *Angew. Chem. Int. Ed.* **2011**, 123, 763-766, copyright 2011 Wiley VCH.

It is however the native state which is of the utmost interest: Shape, structure and structural dynamics largely determine the properties and functions of large molecules. Consequently, the (sub)molecular resolution imaging of biological specimen in their native states has taken great leaps in the past two decades or so, largely driven by the wide spread and continuing improvements in fluorescence microscopy (compare section 6.1) and in electron microscopy.<sup>282</sup> Cryogenic transmission electron microscopy (cryo-TEM) is the most important technique in this field. Sample preparation by

vitrification is central to this analytical technique, its purpose being to preserve the native structure of the specimen embedded in a glassy solvent matrix. Thereby cryo-TEM permits for the direct observation of essentially unperturbed structures. In combination with stereo-imaging or tomography, three-dimensional information on the vitrified samples can be gained.

These developments have not yet permeated the field of polymer science, although 3D shape determines the behavior of synthetic polymers much as is the case for biomacromolecules. The microscopic behavior of an individual polymer chain – the conformation it adopts in a given environment as a function of (prime among other factors) its local stiffness – forms the basis for the description of bulk specimen, *i.e.* ensembles of many chains. The models used in these descriptions vary in complexity. “Ideal” models of polymer chains (*e.g.* the freely jointed chain or the worm-like chain (WLC) model) describe 3D random walks and often provide adequate approximations. More complex models of “real” chains consider excluded volume.<sup>w</sup>

Ensemble models of polymer solutions, melts and glasses based on the models of individual chains have been very successful in describing the macroscopic behavior (*e.g.* the rheology) of bulk polymers and polymer solutions.<sup>146</sup> During the second half of the 20<sup>th</sup> century, significant effort was dedicated to the investigation of polymer microstructure, particularly using scattering techniques. These methods (SAXS, SLS, SANS, *etc.*) usually probe large ensembles of polymer chains in dilute solutions, rather than single chains. They have confirmed predictions *e.g.* from the WLC model, but a verification of such physical models based on the behavior of individual macromolecules remains difficult to this day, simply because it is not easy to probe single, individualized molecules at sufficiently high resolutions and signal intensities: Polymer chains change conformations usually on length scales of a few nm, and scattering techniques are not currently powerful enough to probe single molecules.

The following chapter details investigations of individual synthetic polymer chains based on cryo-TEM, investigating single DP molecules at nanometer resolution. Dendronized polymers are particularly suited for electron microscopy: They feature a rather densely packed corona of dendritic material, with a diameter of around 10 – 15 nm for the very highest generations. While DPs do not provide significantly more mass contrast than other polymers of similar composition<sup>x</sup> their lateral extension and compactness are expected to significantly improve detectability over standard linear polymers as the differentiation between “interior” and “exterior provides phase contrast. Their very high molar masses ( $M_L > 40 \text{ kDa nm}^{-1}$  for  $g > 4$ ) render them more radiation resistant than thinner chains, a benefit particularly for electron tomography. With these potential advantages in mind, attempts were made to resolve the three-dimensional structure of DPs in the dissolved state, in the hope that a quantitative understanding of conformations might be gained.

The following chapter is based on results by Priv.-Doz. Dr. Christoph Böttcher (CB; Forschungszentrum für Elektronenmikroskopie, Freie Universität Berlin) and Prof. Dr. Martin Kröger (MK; D-MATL, ETH Zürich), who also provided various figures (reproduced with permission). Initial samples of **B-PG6**<sub>500</sub><sup>NH<sup>Boc</sup></sup> were provided by Dr. Hao Yu (at the time D-MATL, ETH Zürich now Wuhan University, China).

---

<sup>w</sup> Excluded volume corresponds to the volume already occupied by a polymer chain, and its incorporation into polymer physical models describes the physical impossibility of self-intersection, *i.e.* of a chain crossing through the same space twice.

<sup>x</sup> Unless extraordinarily high density values are assumed; see chapter 5 for a detailed discussion of the density determination of DPs.

## 4.2. Previous Investigations of polymers by cryo-TEM

### 4.2.1. Cryo-TEM essentials

Cryo-TEM relies on the vitrification of specimen, *i.e.* the formation of a glassy state upon shock-freezing of a sample. Solvent crystallization is to be avoided for two reasons: The growth of solvent crystals may disturb the structures which are to be investigated (*e.g.* by rupturing membranes or cell organelles), and the crystalline domains introduce diffractive artefacts into the TEM image.

Figure 4-2<sup>283</sup> provides a schematic overview of a typical sample preparation work-flow for cryo-EM-based structure elucidation of a protein, which consists of conceptually simple steps: First, the deposition of the specimen solution or dispersion onto a TEM grid supporting a thin carbon film; second, the blotting-off of excess liquid; third, the vitrification of the liquid by rapid plunging into a suitable cryogen. For biological specimen dissolved in water (*e.g.* the protein shown in Figure 4-2), vitrification is achieved by plunging the sample into liquid ethane or propane.<sup>284,285</sup> For organic solvents, other cryogenic conditions may have to be applied to avoid solvent crystallization. After vitrification, the specimen is transferred into the electron microscope for imaging, all under strictly maintained cryogenic conditions. Thawing, solvent sublimation, or the formation of solvent crystals would disrupt the native structure of the sample.

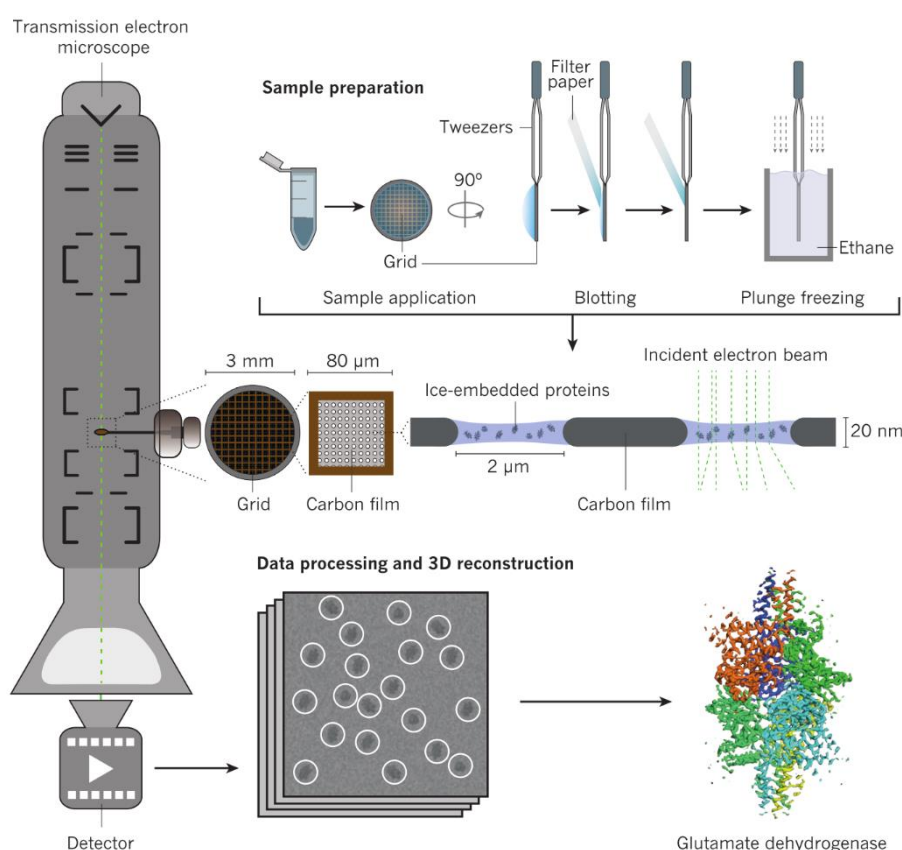


Figure 4-2: Schematic representation of cryo-TEM sample preparation and structure elucidation of a protein by the single-particle approach. Reprinted with permission from Fernandez-Leiro R., Scheres S. *Nature* **2016**, 537, 339-346, copyright Springer Nature 2016.

Cryo-TEM is still largely confined to the field of biology, where there is a high demand for the imaging of cellular structures and for the structure elucidation of proteins by electron crystallography. The latter mostly relies on the single-particle approach (see Figure 4-2).<sup>283,286</sup> Briefly, when many identical or very similar objects are present within the same image, their random orientations may be considered projections of one object, the three-dimensional structure of which may be reconstructed computationally (compare subsection 4.3.1). Cryo-TEM facilities are becoming increasingly more common, and cryo-EM may become part of the repertoire of analytical techniques routinely available to polymer scientists and chemists, much as standard TEM and SEM have.<sup>287,288</sup>

#### 4.2.2. 3D structures of biological filaments

How biological filaments behave in solution is of great significance to biological processes. Of particular interest are F-actin and dsDNA. The interest in 3D-structures of F-actin is founded in its structural function, *e.g.* as a component of the cytoskeleton (microfilaments) or as an integral part of muscle fibers. F-Actin can of course be labelled fluorescently and is large enough to be observed directly by optical microscopy,<sup>289</sup> but the filaments may also be observed by cryo-EM.<sup>290</sup> Cryo-TEM tomography (cryoET) has revealed interesting three-dimensional details of the cytoskeletal structure, *e.g.* branched and networked actin superstructures which may play roles in cellular motion<sup>274,291</sup> or in the pathogenicity of certain viruses.<sup>292</sup>

The 3D-structures of DNA are of interest as the complex systems of structural proteins, enzymes and cofactors which support DNA transcription, replication, repair *etc.* may be influenced by minor changes in the overall conformation of the polymer.<sup>293</sup> DNA is particularly suited to electron microscopic imaging as it provides fairly good mass contrast due to its phosphorous-rich backbone, its many aromatic groups, and the partial association of counterions. Dubochet *et al.* have contributed significantly to the resolution of the native conformation of dsDNA, with first examples of cryo-TEM stereography in the 1990s, in work which also produced an estimate of the persistence length of dsDNA within the WLC model.<sup>294</sup> Later work by the same group demonstrated the subtle impact of small sequence changes on the average structure of circular dsDNA, again using stereographic imaging.<sup>276</sup> Naturally, cryoET may be applied to DNA as well, as demonstrated recently in the reconstruction of *individual* DNA origami structures, showing that (with modern instrumentation) tomographic imaging may provide sufficient information to make the single-particle approach obsolete,<sup>295</sup> at least for inherently rigid and contrast-rich objects.

### 4.2.3. Cryo-EM of synthetic polymers

The three-dimensional electron microscopic imaging of synthetic polymers is less commonly attempted than that of biological specimen. Individual polymer chains (particularly polyelectrolyte bottlebrushes) have been investigated by conventional (two-dimensional) cryo-TEM. An important factor in their successful imaging were contrast-rich heavy atoms used as counterions (*e.g.* iodide as the counterion to ammonium-bearing side chains in the bottlebrush).<sup>296,297</sup> Such brushes show intriguing features (*e.g.* helical structures observed in AFM height images of deposited chains), but still “only” standard cryo-TEM imaging was performed.<sup>298</sup> No corresponding three-dimensional information is available. With the notable exception of carbon nanotubes,<sup>299</sup> no tomography or even stereography of synthetic isolated filaments appears to have been performed to date. The synthetic systems where tomography was performed are limited to superstructures, *e.g.* assemblies of DPs with cellulose nanocrystals,<sup>300</sup> filamentous assemblies of polythiophene chains,<sup>301</sup> stomatosomes assembled from amphiphilic dendrimers,<sup>302</sup> or self-assembled block-copolymer structures.<sup>303,304</sup>

In none of these cases was it possible or attempted to derive quantitative structural information on an individual polymer, the main goal usually being simply the depiction of the polymer or the aggregates in their native dissolved state. In most of the cited references, the purpose of cryo-TEM was to explain structures observed in the deposited state *e.g.* by conventional TEM or by AFM. It should also be noted that the investigated systems were usually not conventional linear polymers, with the exception of the cited case of polythiophene aggregates.<sup>301</sup> This is due to two main reasons: First, until recently cryo-EM was not capable of routinely imaging very thin filaments which provide very little mass contrast.<sup>282</sup> This situation is currently in flux: Phase plates<sup>305</sup> provide better contrast and resolution, and direct electron detectors<sup>306,307</sup> allow for lower electron doses *e.g.* in tomographic imaging. These innovations and other improvements to electron optics are becoming ever more wide spread and have led to significant improvements in cryo-TEM resolution in the past decade or so.<sup>282</sup>



### 4.3. Cryo-TEM of Dendronized polymers

In the following, two sets of experiments are described briefly. Details can be found in the Experimental chapter (subsection 8.4.1). As there was a significant pause between the two sets of experiments, different samples were used and both instrumentation and methodology were improved, although the analysis presented in section 4.4 was applied to both sets of data.

#### 4.3.1. Cryo-TEM Stereography of $\text{B-PG6}_{500}^{\text{NHoc}}$

Stereographic cryo-TEM imaging (cryo-TEM stereography) was performed on a vitrified specimen of  $\text{B-PG6}_{500}^{\text{NHoc}}$  in 1,4-dioxane, recorded at tilt angles of  $\pm 8^\circ$  (Figure 4-3a). 1,4-dioxane was selected as a thermodynamically good solvent<sup>186</sup> with a fairly low electron density (1,4-dioxane:  $0.56 \text{ mol e}^- \text{ cm}^{-3}$  at RT; water:  $0.55 \text{ mol e}^- \text{ cm}^{-3}$  at RT). At the chosen concentration (*ca.*  $0.025 \text{ mg mL}^{-1}$ ), the DPs appear as occasionally aggregated, wormlike structures and are easily distinguishable in the cryo-TEM images. From the stereographs, the trajectories of 63 individual DP chains were reconstructed (Figure 4-3b,c).

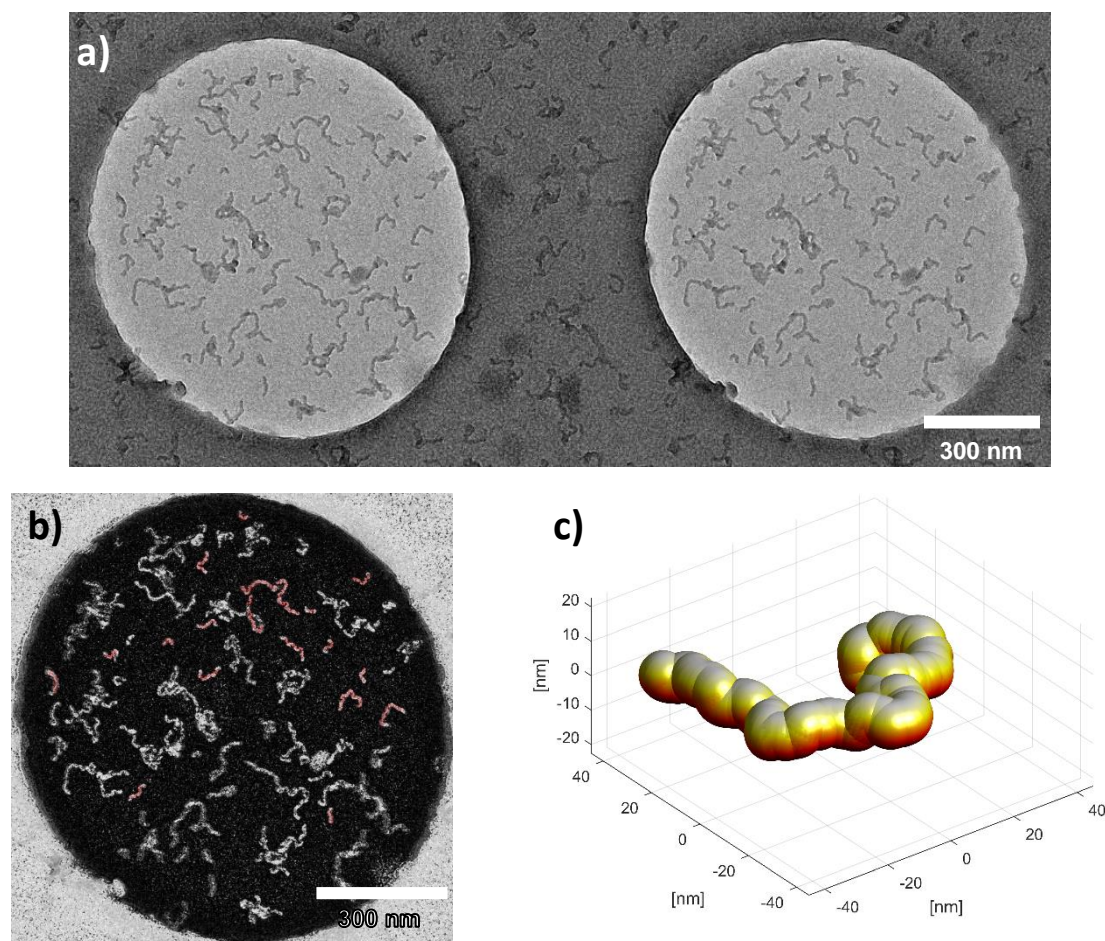


Figure 4-3: Cryo-TEM stereographic imaging of  $\text{B-PG6}_{500}^{\text{NHoc}}$  in vitrified 1,4-dioxane: a) Stereo pair of TEM images, showing one film-covered hole in the grid. The individual DPs ( $\text{B-PG6}_n^{\text{NHoc}}$ ) are visible as wormlike structures, though aggregates are frequent (CB). b) Same pore as in Figure 4-3a, but with inverted contrast and polymer trajectories marked in red (CB). c) Visualization of one filament trajectory (MK).

Stereography does not provide the same amount of three-dimensional information as full tomography: For instance, filaments which are not actually in contact may appear so in a stereo pair of images when their coordinates in the plane of the substrate overlap. Such objects had to be excluded from further analysis. However, for clearly isolated filaments, three-dimensional trajectories can be reconstructed from stereographic data. Initial analyses had indicated a fairly regular curvature, and therefore the raw cryo-TEM data was further processed by applying the single-particle approach: Locations containing clearly isolated DP segments were hand-picked for this analysis. From the resulting fairly homogenous subsets (classes) of particle projections resulting from multivariate statistical analysis,<sup>308</sup> class sum averages (Figure 4-4a) were calculated which served as the seeds for the reconstruction of a three-dimensional object.<sup>309</sup> The reconstructed object (Figure 4-4c) has a circular cross-section with a diameter of 12.5 nm (see Experimental, Figure 8-25a,b) and indicates that the selected polymer segments have a very frequently occurring curvature: A large fraction (*ca.* 60 %) of the selected DP segments can be described as projections of the object shown in Figure 4-4c, and the reprojections match the initial class sums very well (Figure 4-4b).

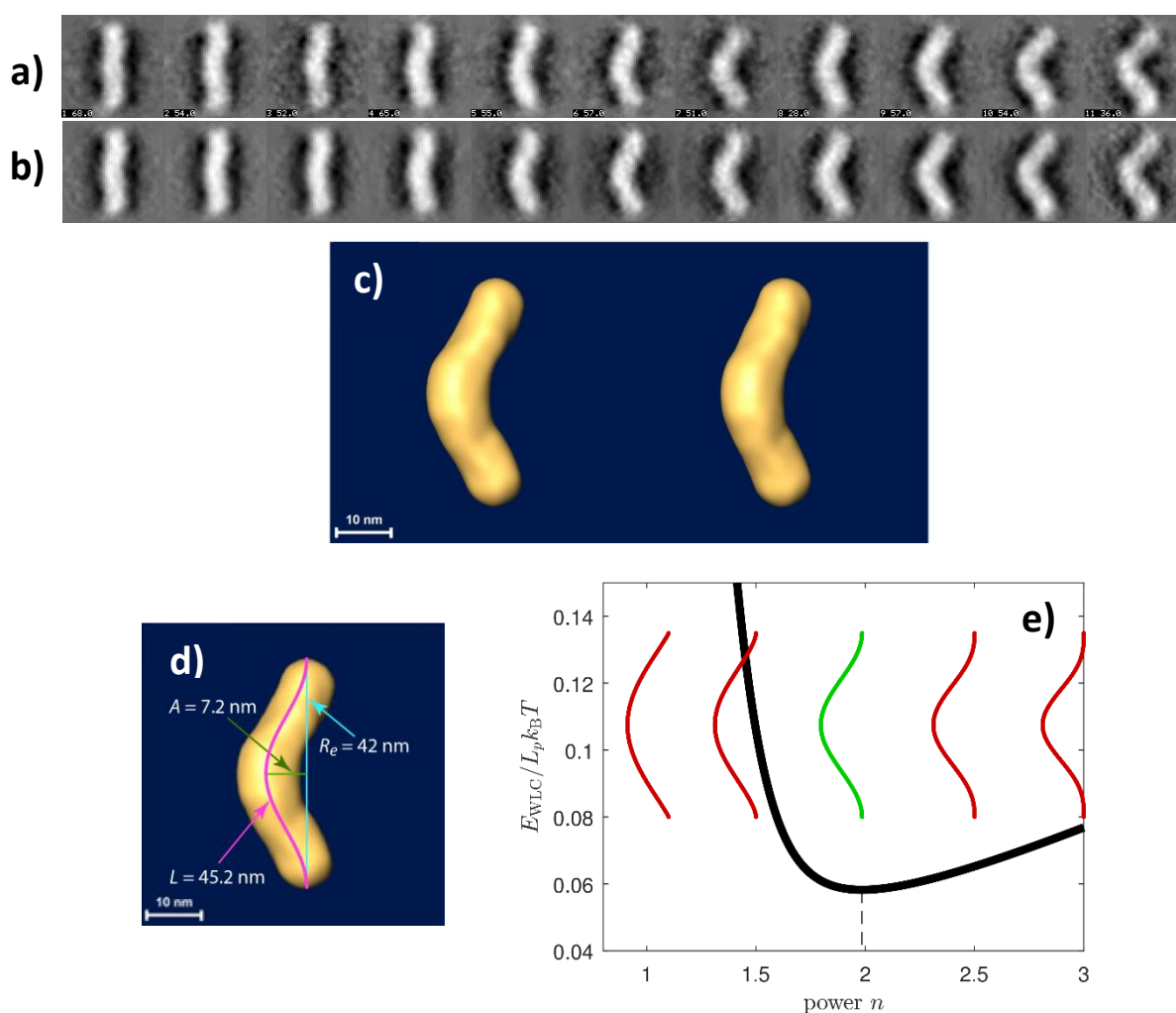


Figure 4-4: Single-particle analysis of cryo-TEM images of  $B-PG6_n^{NHBoc}$  in vitrified 1,4-dioxane: a) Selected class-sum averages extracted from the raw data (CB); b) matching reprojections of the 3D object reconstructed from 2D data (CB). c) Stereopair of the reconstructed three-dimensional object, which corresponds to a frequently-occurring, fairly uniform curvature of the selected DP segments (CB). d) Fit curve of the segment depicted in Figure 4-4c (MK); e) bending energy analysis suggests that the segment closely resembles the expected minimum-energy conformation of a worm-like chain segment (MK).

A bending energy analysis (Figure 4-4d,e) suggests that the reconstructed object approximates the minimum-energy conformation expected for a worm-like chain segment (see subsection 4.4.2). However, it is quite improbable that this specific conformation represents as large a proportion of all chain segments as the large fraction of incorporated image sections indicates. Likely, the large fraction of 60 % successfully incorporated segments is the result of bias in the manual selection of the chain segments used in this analysis.

#### 4.3.2. Cryo-TEM Tomography of C-PG7<sub>500</sub><sup>NHBoc</sup>

Tomography is capable of providing more information than stereography by sampling many more angles and typically also a far larger range of tilt angles; A typical electron tomogram covers tilt angles of  $\pm 60^\circ$  from the horizontal. Thanks to this, very precise 3D information may be gained: Even objects which overlap in the x/y-plane may be distinguished, unlike in stereography. Tomography also permits the resolution of far more complex shapes than stereography.<sup>295,310</sup> However, tomography requires the recording of many individual images: The overall electron dose is fairly high, and sensitive specimen might be damaged during a full tomographic tilt series.<sup>311</sup> High-resolution cryo-ET of soft specimen has become possible in large part thanks to improvements in detector technology: More sensitive direct electron detectors permit the application of lower electron doses for the same resolution.<sup>307</sup>

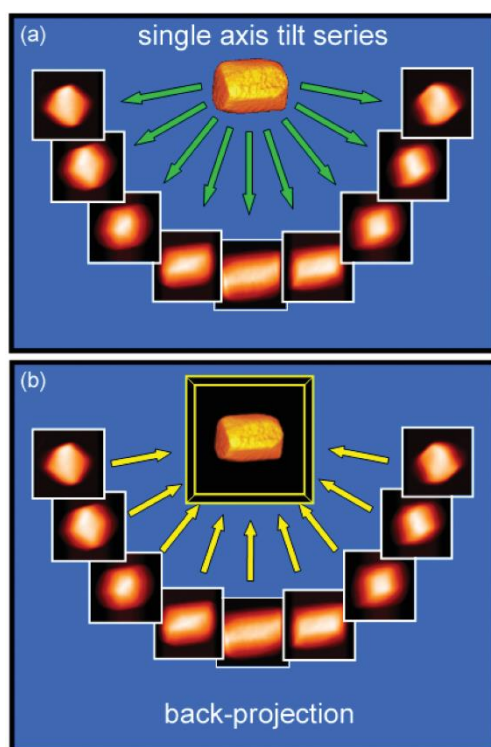


Figure 4-5: Schematic representation of the electron tomographic process. a) TEM images are recorded at various tilt angles, providing different projections of the imaged object. b) From the tilt series, the image-forming object is computationally reconstructed into three-dimensional data. Reprinted with permission from: Midgley, Paul A. et al. Chem. Soc. Rev. **2007**, 36, 1477-1494, Copyright Royal Society of Chemistry 2007.

The DP investigated by cryo-ET was **C-PG7<sub>500</sub><sup>NHBoc</sup>** prepared as described in chapter 2.<sup>227</sup> Tomographic tilt series were recorded in multiple locations of the sample, which again consisted of a vitrified solution (*ca.* 0.1 mg mL<sup>-1</sup>) of the polymer in 1,4-dioxane. In the volumes reconstructed from the tomographic tilt series of multiple locations, a total of 65 clearly isolated DP chains were then traced. The tomographic reconstructions revealed a circular cross-section with a fairly constant diameter of *ca.* 12.8 nm throughout all tomograms (see Experimental, Figure 8-25c,d).

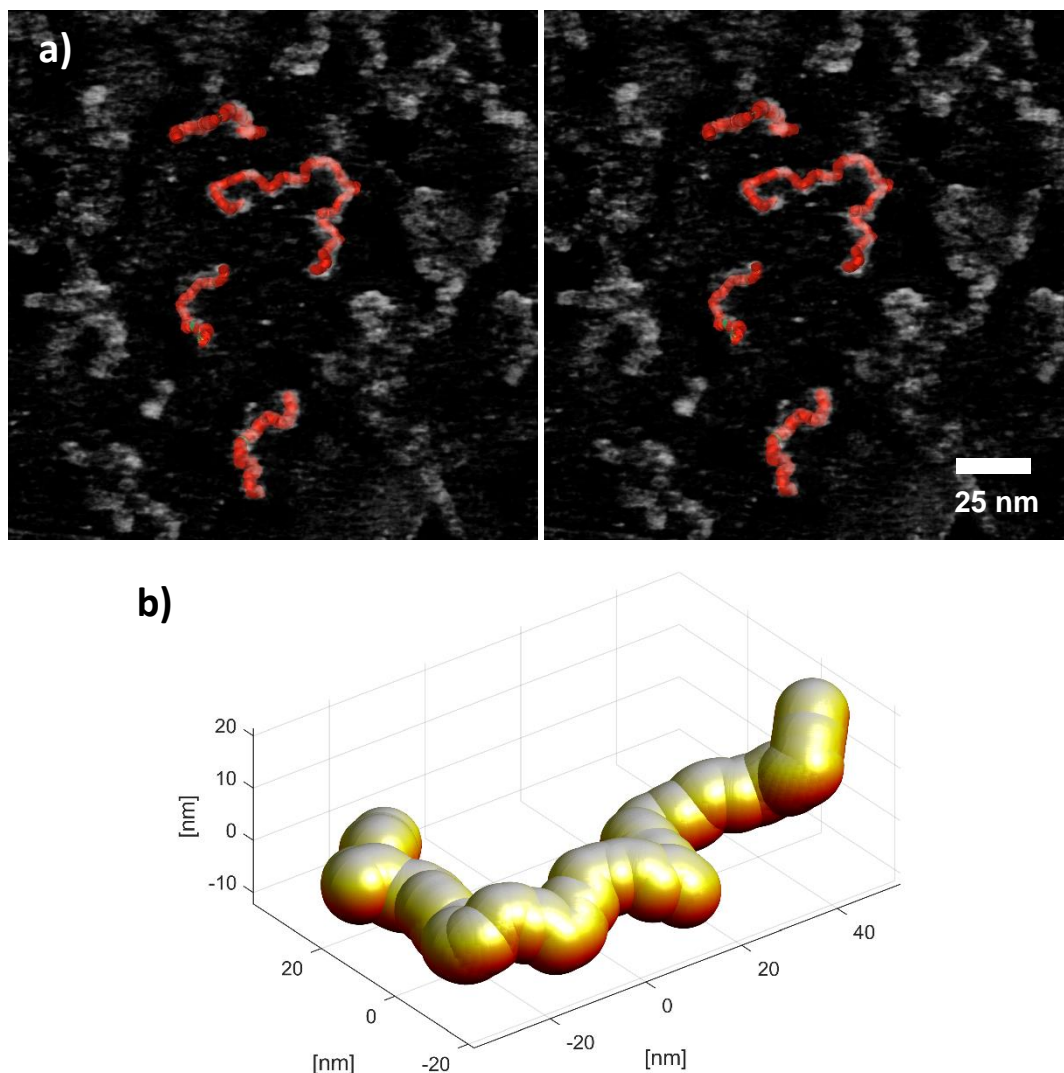


Figure 4-6: Cryo-electron tomography of **C-PG7<sub>500</sub><sup>NHBoc</sup>** in vitrified 1,4-dioxane. a) Stereo image pair (inverted contrast, tilt angle  $\pm 4^\circ$ ) reconstructed from the tomographic volume. Extracted filament trajectories shown in red. (CB) b) Visualization of one filament trajectory. (MK)

#### 4.3.3. Overview of trajectory data

Some numerical data regarding the DP trajectories is summarized in Table 4-1; Depictions of all DP trajectories can be found in Appendix A.4. The filaments of **C-PG7<sub>500</sub><sup>NHBoc</sup>** ( $\tilde{L}_c = 154$  nm) are longer on average than those of **B-PG6<sub>500</sub><sup>NHBoc</sup>** ( $\tilde{L}_c = 66$  nm). The two polymers stem from different precursors, and it is therefore difficult to assign significance to this difference. Furthermore, in stereography the selection of shorter, in-plane filaments might be favoured, and there might be differences in the aggregation behavior of the two DPs.

Table 4-1: Numerical data on trajectories from cryo-TEM stereography and from cryo-ET.

	<b>B-PG6<sub>500</sub><sup>NHBoc</sup></b>	<b>C-PG7<sub>500</sub><sup>NHBoc</sup></b>
<b>Number of filaments</b>	63	65
$L_{c,min}$	10 nm	50 nm
$L_{c,max}$	271 nm	766 nm
<b>Average contour length (<math>\bar{L}_c</math>)</b>	76 nm	184 nm
<b>Median contour length (<math>\tilde{L}_c</math>)</b>	66 nm	154 nm
<b>DP chain diameter</b>	12.5 nm	12.8 nm

Another observation worthy of comment are the diameters of the filaments: The chains of **B-PG6<sub>n</sub><sup>NHBoc</sup>** and **C-PG7<sub>n</sub><sup>NHBoc</sup>** appear fairly homogenous and exhibit circular cross-sections with diameters of 12.5 nm and 12.8 nm, respectively. Slightly different methods were applied to derive these values (see Experimental, subsection 8.4.1, Figure 8-25), but this still represents an unexpectedly small change in diameter. An increase on the order of 1 – 2 nm would have been expected; indeed in AFM height images (Figure 4-7), the two DPs are rather clearly differentiated ( $h_{AFM,PG6} = 5.5 \pm 0.5$  nm;  $h_{AFM,PG7} = 6.7 \pm 0.8$  nm).

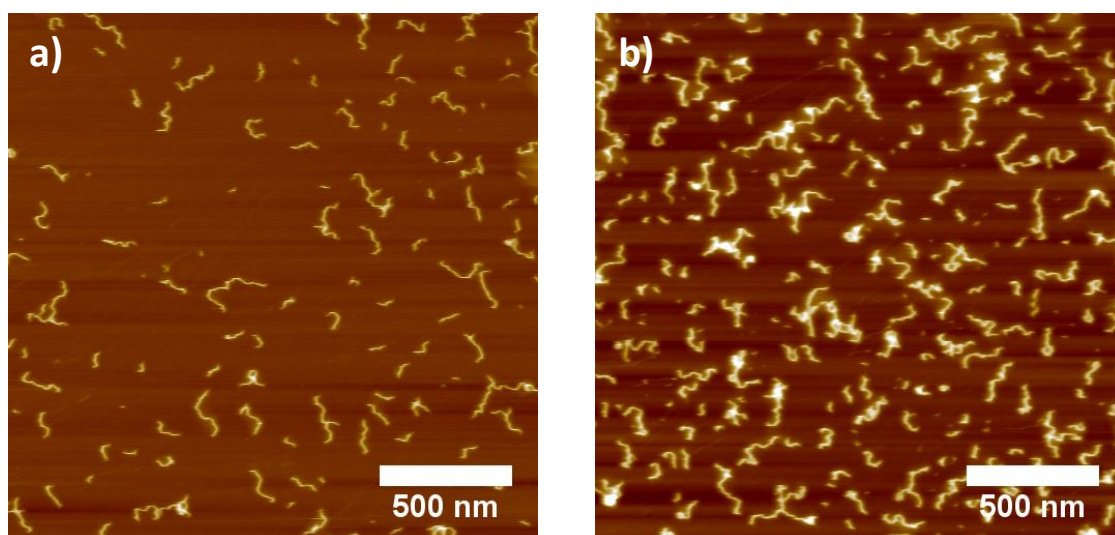


Figure 4-7: AFM height images (tapping mode) of a) **B-PG6<sub>500</sub><sup>NHBoc</sup>** and b) **C-PG7<sub>500</sub><sup>NHBoc</sup>**. Color contrast scales are identical, and the images were recorded using the same tip and imaging conditions.

A possible explanation for this is proximity to  $g_{max}$ . For a DP near or above  $g_{max}$  such as **C-PG7<sub>500</sub><sup>NHBoc</sup>**, it is expected that relatively little solvent penetrates the dendritic periphery, whereas the structurally deficient **B-PG6<sub>500</sub><sup>NHBoc</sup>** is expected to be subject to much stronger swelling. This notion is supported by results presented in chapter 3 (see subsection 3.5.6, Figure 3-23): The larger diameter of **B-PG6<sub>n</sub><sup>NHBoc</sup>** chains may result from strong swelling, whereas the dendritic branchwork of **C-PG7<sub>n</sub><sup>NHBoc</sup>** chains is essentially collapsed (because intrinsically densely packed) and only interacts with solvent in the outermost periphery.

## 4.4. Analysis of DP Trajectories

### 4.4.1. Scattering vs. trajectory analysis

As indicated in section 4.1, the analysis of DP trajectories presented in the following stands in some competition to scattering measurements, which are well-established. Before discussing concrete results, the main differences between the two methods should be pointed out: Scattering methods are – at the current level of technology – ensemble methods, and therefore all values generated are population- and time-averaged. The data extracted from cryo-TEM stereography and cryo-ET on the other hand represent instantaneous conformations of individual chains.

Scattering experiments usually cover a limited range of correlation distances in the so-called Guinier regime (where the scattering wave number  $Q \ll 1/R_g$ ). The investigation of disparate length scales may require multiple experiments (*e.g.* SAXS and  $\mu$ SAXS to cover a real-space range of *ca.* 1 nm – 100 nm), and the resulting, disparate pieces of data may be difficult to correlate. This is not the case in cryo-TEM, where objects from the resolution limit (*ca.* 1 nm in the present data) all the way to several  $\mu$ m in size may be investigated in principle.

Particularly the interpretation of scattering from filaments with significant diameters (DPs, but also more frequently encountered sample such as bottlebrush copolymers, dsDNA or actin filaments) is non-trivial. A direct analysis is often not possible, and many model parameters covering different length scales are required, including  $R_g$ , the diameter and length of the effective cylindrical tube into which the polymer conformation can be inscribed,  $L_p$ , cross-sectional density profiles, *etc.* This is particularly due to issues of interference: At length scales close to the diameter of the filament, correlations *across* the chain become increasingly relevant. Cross-section models are required to make any sense of scattering results in this regime, and the models may not in all cases be easily verifiable. The analysis of explicit trajectories from cryo-TEM does not require any such assumption, and indeed the (circular) cross-section can be obtained from the reconstruction of microscopic data. Moreover, no ensemble averaging is involved in the analysis of explicit three-dimensional trajectories, and even very polydisperse samples can easily be investigated. As will be shown in section 4.4.2, trajectory analysis also permits access to quantities and statistical analysis not attainable from scattering data.

#### 4.4.2. Analysis of DP chain trajectories

The explicit, individual trajectories of DP filaments open up interesting options for statistical analysis: The radius of gyration  $\langle R_g^2 \rangle$  is the most commonly accessed experimental quantity in scattering analysis, and it is used to determine *e.g.* persistence lengths  $L_p$ . From scattering,  $\langle R_g^2 \rangle$  is obtained as an aggregate value from the entire sampled volume, and probing the scaling of  $\langle R_g^2 \rangle$  with molar mass typically involves the preparation of polymer samples of different chain lengths. This would be a daunting task particularly for DPs, the synthesis of which is not trivial. Fortunately, the discrete trajectory data inherently contains chains of varying  $L_c$  and therefore  $M$ . Moreover, each chain trajectory can be cut into pieces of arbitrary length  $s$  along the chain contour. This provides substantial statistical power even from the relatively small sampling of chains considered here ( $\sim 60$  for both DPs).

For both **B-PG6**<sup>NHBoc</sup> and **C-PG7**<sup>NHBoc</sup>, the analysis of  $\langle R_g^2 \rangle$  (Figure 4-8) suggests that the DP chains exhibit WLC scaling (turquoise curves in Figure 4-8). The apparent persistence lengths are very similar for both polymers, with  $\mathcal{L}_{p,PG6} \approx \mathcal{L}_{p,PG7} \approx 15$  nm.

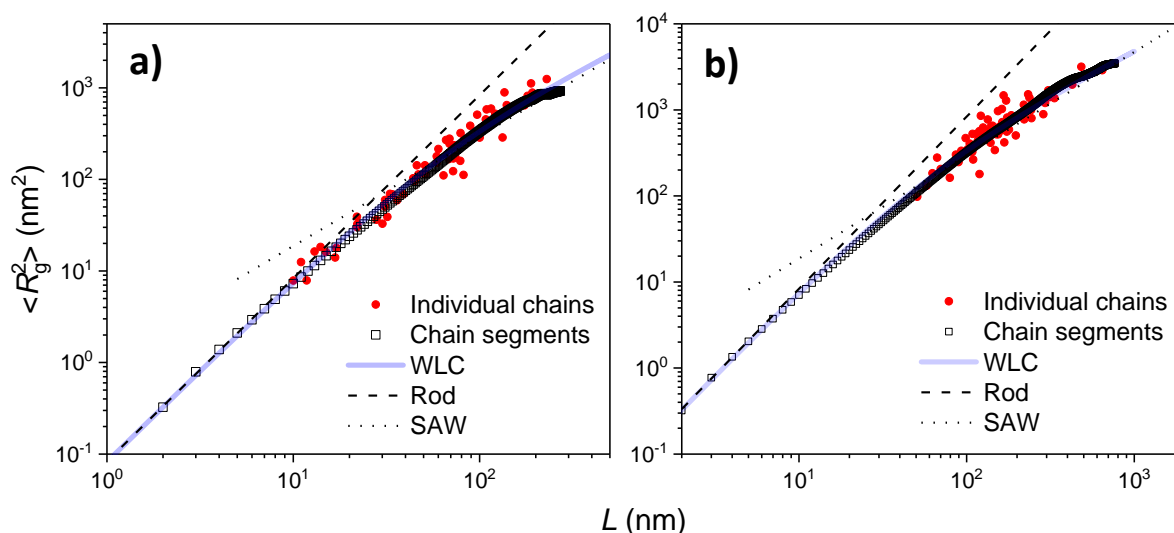


Figure 4-8:  $\langle R_g^2 \rangle$  as a function of DP segment length  $s$  (red dots: data for individual chains) for a) **B-PG6**<sup>NHBoc</sup> and b) **C-PG7**<sup>NHBoc</sup>. The indrawn lines show the scaling for rigid rods (dashed), self-avoiding walks (dotted) and worm-like chains of  $L_p = 15$  nm (transparent blue).

The explicit trajectories permit further analyses beyond the scope of scattering analysis: The structure factor  $I(q)$  in scattering measurements is the superposition of all  $n$ -point tangent correlation functions, and given experimental uncertainties and noise, it can be difficult to discern scaling differences in the analysis of  $I(q)$ . From explicit trajectories however, it is comparatively easy to calculate the two-point tangent correlation  $C(s)$  (Figure 4-9) in which scaling relations are more readily evident. Figure 4-9a,b shows the tangent-tangent correlation functions of the two trajectory datasets for low  $s$ . In the WLC model,  $C(s)$  is expected to decay exponentially (Eq. 4-1). However for the DPs, this appears to be the case only at very short length scales of *ca.* 10-20 nm, and the actual persistence lengths  $L_p$  (being measures of the truly local stiffness of the overall DP chain) are much lower than the apparent persistence lengths  $\mathcal{L}_p$  derived from the WLC fits shown in Figure 4-9 ( $L_{p,PG6} \approx L_{p,PG7} \approx 7$  nm).<sup>y</sup>

<sup>y</sup> A linear combination of two exponential functions corresponding to two different length scales of preferred curvature describes the behavior of  $C(s)$  in a much larger range (see Experimental, subsection 8.4.2, Figure 8-27). A similar interpretation had previously been used to rationalize the behavior of polyelectrolytes in Monte Carlo

The data is not very granular at such short length scales (voxel resolution  $\sim 1$  nm for both stereography and tomography), but this suggests that the chains of **C-PG7<sub>n</sub><sup>NHBoc</sup>** and **B-PG6<sub>n</sub><sup>NHBoc</sup>** are of similar flexibility, not just radius. This may be an artefact stemming from the relatively small sample size available for “short” chains of **C-PG7<sub>n</sub><sup>NHBoc</sup>**, however as previously suggested by AFM measurements, significant corrugation may in fact be a consequence of fairly high structural perfection (see Figure 2-9a/b).<sup>2</sup> The significantly lower  $L_p$  obtained from trajectory analysis also readily matches the visual impression gained e.g. from Figure 4-3c or Figure 4-6b (see Appendix A.4 for all trajectories) that the DP chains exhibit curvature on a much smaller length scale than  $L_p \approx 15$  nm would suggest. It must also be noted that such short-range scaling in scattering would be difficult to observe in scattering analysis, particularly as  $L_p$  is – surprisingly – shorter than the diameter of the DP chains ( $\sim 12.5$  nm).

The WLC model is generally thought appropriate for the description of semiflexible polymers such as DNA<sup>294</sup> or indeed DPs.<sup>186</sup> The data shown in Figure 4-9 indicate that the naïve derivation of  $L_p$  from scattering data (in analogy to the analysis in Figure 4-8) may be dangerous, at least for systems with large excluded volume effects<sup>312</sup>. This was recently pointed out by Hsu *et al.*, who re-analyzed scattering data for bottlebrush copolymers<sup>313</sup> with the help of lattice Monte Carlo simulations.<sup>314</sup> These results likewise revealed that the true, locally defined persistence length was significantly smaller than that obtained from scattering analysis. Particularly the assumption of a Gaussian cross-sectional density profile for the bottlebrush copolymers was shown to be inappropriate. In yet more extensive simulations, it was demonstrated that a transition away from WLC behavior at short length scales exists, and that the scaling of the thick bottlebrushes is dominated by excluded volume at long length scales.<sup>315,316</sup>

When excluded volume effects are taken into account,  $C(s)$  is expected to show power-law decay scaling (Eq. 4-2) with the Flory exponent  $\nu \approx 3/5$ ,<sup>317</sup> rather than the exponential decay for a worm-like chain (Eq. 4-1).

$$C(s) = e^{-\frac{s}{L_p}}$$

Eq. 4-1

$$C(s) \sim s^{-2(1-\nu)}$$

Eq. 4-2

Such a transition is indeed observed in the individual chain data for both **B-PG6<sub>n</sub><sup>NHBoc</sup>** and **C-PG7<sub>n</sub><sup>NHBoc</sup>** at length scales on the order of  $s \geq 20 - 30$  nm, as shown in Figure 4-9c,d. It should be noted that the nature of the transitional regime is somewhat ill-defined<sup>315,316</sup> and that due to increasing noise (chain-end effects, fewer chain segments of the given  $s$ ),  $C(s)$  may appear to start deviating from SAW scaling in the high  $s$  regime (Figure 4-9c,d; observe growing the error bars).

---

simulations by Kremer *et al.*<sup>386,387</sup> The simultaneous existence of two “persistence lengths” for a homogeneous polymer is however incompatible with flexibility as a local quantity.

<sup>2</sup> In considering this, it is important to note that the trajectories represent the centerline of the DP chains rather than actual backbone conformations. There is no differential contrast within the fairly densely packed DP cross-section which would allow one to distinguish between backbone and dendritic side chains.



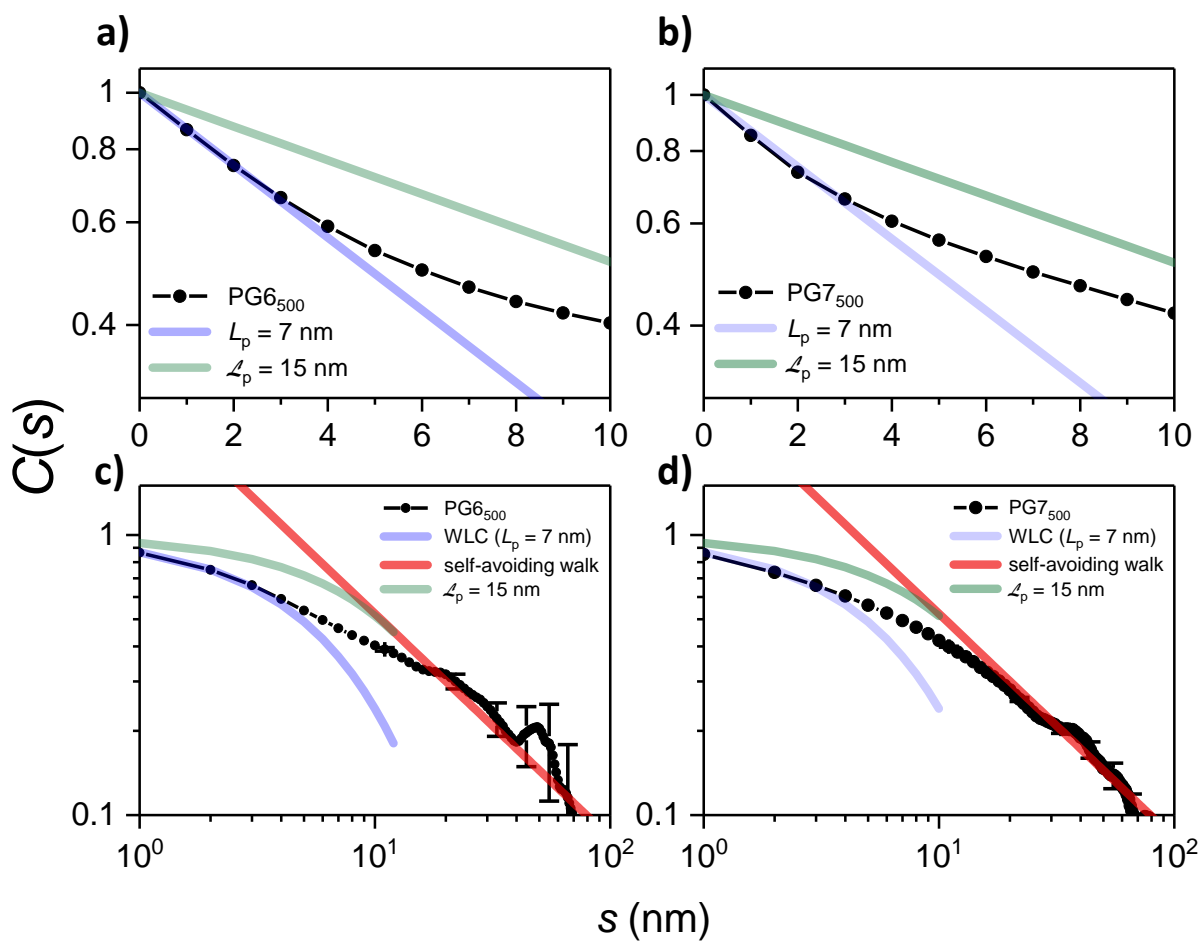


Figure 4-9:  $C(s)$  derived from DP trajectories obtained from cryo-TEM of DPs in 1,4-dioxane. Semilogarithmic plots of the tangent-tangent correlation functions  $C(s)$  with exponential (WLC) fit curves, showing an early deviation from WLC behaviour as fitted to  $C(s)$  (blue curves), and particularly as fitted to  $R_g$  (green curves); a) B-PG<sub>6500</sub><sup>NHBoc</sup>, b) C-PG<sub>7500</sub><sup>NHBoc</sup>. Logarithmic plots of  $C(s)$ , with the red line indicating SAW (power-law) scaling; c) B-PG<sub>6500</sub><sup>NHBoc</sup>, d) C-PG<sub>7500</sub><sup>NHBoc</sup>.

## 4.5. Summary & Conclusions

From the present stereographic and tomographic data, it was possible to extract 3D trajectories for individual chains of **B-PG6**<sub>n</sub><sup>NHBoc</sup> and **C-PG7**<sub>n</sub><sup>NHBoc</sup>. In the initial analysis of these trajectories, apparent persistence lengths  $\mathcal{L}_{p,PG6} \approx \mathcal{L}_{p,PG7} \approx 15$  nm were derived from the analysis of the radii of gyration  $\langle R_g^2 \rangle$ . The tangent-tangent correlation functions  $C(s)$  however show a deviation from WLC scaling for  $s \geq 20 - 30$  nm, and much shorter true persistence lengths (*i.e.* measures of local chain curvature, as defined in the WLC model) of merely  $L_{p,PG6} \approx L_{p,PG7} \approx 7$  nm. For large  $s$ ,  $C(s)$  is better approximated by power-law scaling, as expected for structures such as DPs, which feature significant excluded volume and therefore are better described by a self-avoiding walk.<sup>315,316</sup> By these measures, the two DPs behave astonishingly similar. In part, this may be the result of a relatively small sample size of only a few dozen chains each and a microscopic resolution which still leaves room for improvement. However, the previously discussed shape differences between DPs from route **B** and those from route **C** (see section 2.6) may also partially explain these observations. In this context, it would be particularly interesting to compare **C-PG7**<sub>n</sub><sup>NHBoc</sup> with its precursor polymers, **C-PG6**<sub>n</sub><sup>NHBoc</sup> and **A-PG5**<sub>n</sub><sup>NHBoc</sup>.

Classical scattering techniques do not provide access to explicit polymer trajectories of individual filaments as used in the analyses summarized above. They rely instead on statistical information from many molecules, probing *e.g.* quantities related to the hydrodynamic radius  $\langle R_g^2 \rangle$ . From such ensemble measurements, it can be difficult to differentiate between WLC and SAW scaling, demonstrating the potential power of an electron microscopic approach in the analysis of polymer behavior. Additionally, the analysis of centerline trajectories does not suffer from interferences between longitudinal and transversal correlations, which show up in scattering data on length scales close to the filament diameter. This sort of interference makes it necessary to rely on cross-section models in scattering analysis, which are not necessary in the analysis of trajectory data. Even more worryingly, it has been shown that some of these common model assumptions may result in faulty descriptions of polymer chain statistics.<sup>314</sup>

The presented results for two different DPs have demonstrated that it is in principle possible to trace individual synthetic polymers in three dimensions. This appears to be the first instance in which this has been achieved. The intrinsic properties of DPs of very high  $g$  facilitate this by providing sufficient phase contrast due to a clear separation between “interior” and “exterior”. Another crucial factor enabling this feat are recent instrumental advances: A mere decade ago, tomography as presented in subsection 4.3.2 would have been extremely difficult if not impossible for unstained, individual synthetic molecules. The continuing development and commercial implementation of innovations such as phase plates, direct electron detectors and aberration correction may at some point permit the direct observation of more standard linear polymers with smaller cross-sections. Further improvements in resolution (for the present analysis of DPs: *ca.* 1 nm) may also allow for the conformational analysis of single bonds at some point in the far future. Other than for biologically relevant, relatively large-scale features, where overarching structure is often the aim, staining is inadvisable when individual polymer conformations are targeted. Any modification is likely to significantly alter the properties of the polymer. However, intrinsically contrast-rich polymers, *e.g.* polysiloxanes, poly(ferrocenyl silanes), transition metal coordination polymers or derivatives of conventional polymers bearing contrast-rich side chains (*e.g.* poly(ferrocenylmethyl methacrylate), PFMA) might be suitable targets for this kind of investigation. First attempts in this direction were

made in the course of the work presented above (using PFMMA), which showed promise in terms of contrast (see Experimental, subsection 8.4.1, Figure 8-26).

## 5. Density of $\text{PG}g_n^{\text{NHBoc}}$

### 5.1. Motivation/goals

Determining the density  $\rho$  of DPs is of significance to the results presented in chapter 2, as it influences the precise value of  $g_{\text{max}}$ .<sup>148</sup> A range of densities typical for the composition of the class of DPs presented here ( $\rho = 0.9 - 1.5 \text{ g cm}^{-3}$ ) was typically assumed, resulting in  $g_{\text{max}} = 6 - 7$ . The transition to  $g_{\text{max}} = 7$  occurs only at fairly high density values of  $\rho > 1.35 \text{ g cm}^{-3}$  (see Figure 1-20a). The density of **16** has been determined previously ( $\rho \approx 1.1 \text{ g cm}^{-3}$ ) by extrapolating from the variation of concentration in solutions of **16**.<sup>148</sup> This simple reference compound can however not be used to infer information about the DPs, which are of slightly different structure and composition (affecting, among other things, hydrogen bonding) and in which packing and confinement effects may play a significant role. The solution-based method used for **16** cannot be employed for the density determination of DPs, as it requires comparatively large amounts of sample (*ca.* 1 g) and as  $g$ -dependent swelling of the DP periphery would significantly affect the results (see chapter 3). It should be pointed out, however, that the obtained value does agree quite well with density estimates from MD simulation of  $\text{PG}g_n^{\text{NHBoc}}$  ( $g = 1 - 6$ ) which suggests values of  $\rho \approx 0.9 - 1.1 \text{ g cm}^{-3}$ .<sup>144,228</sup>

Initial attempts at determining the density of DPs using SEM and TEM measurements predate this thesis and will be revisited in section 5.4. Extremely high density values ( $\rho > 2.0 \text{ g cm}^{-3}$ ) were obtained for the highest  $g$  DPs investigated, whereas the values for lower  $g$  DPs moved within the aforementioned reasonable-seeming range of  $\rho \leq 1.5 \text{ g cm}^{-3}$ . Such extraordinary values are not usually obtained for organic structures, with the exception of heavily halogenated substances, and clearly warrant further investigation. Moreover, such an extreme  $g$  dependence of density would have significant implications on the location of  $g_{\text{max}}$ . These observations prevented the previous publication of density values obtained from SEM/TEM measurements. Significant effort was invested into determining the density of DPs using other measurements in the bulk (hydrostatic weighing, density gradient column and SAXS) and using another microscopic method (qSTEM). In the following, the various methods will be presented, along with the obtained density values. An in-depth discussion and comparison of these values follows at the end of the chapter in section 5.6.

The investigations presented in the following were largely performed on polymers in a series prepared by Dr. Hao Yu using route **B** ( $\text{PG}1_{500}^{\text{NHBoc}}$  -  $\text{B-PG}8_{500}^{\text{NHBoc}}$ , see Figure 1-19b).<sup>174</sup>

## 5.2. Bulk density from hydrostatic methods

Although envelope density measurements may be affected *e.g.* by packing efficiency or pores within the material, they nevertheless are valuable in that they provide a baseline, minimum density value useful in assessing other methods. In order to measure the bulk density of DPs, solid, fused samples needed to be prepared first. This was achieved by vacuum hot-pressing of the freeze-dried powders obtained from DP synthesis (see Figure 2-4c), resulting in small cylindrical pills ( $\varnothing$  4 mm, thickness 1 – 3 mm, *ca.* 5 – 30 mg polymer; see Figure 5-1 and Experimental, subsection 8.5.1). The resulting pills, when fully transparent, showed no significant gas inclusions in optical microscopy. As the DPs are very brittle below  $T_g$ , samples were frequently chipped or broke apart entirely, making even a rough estimate of density from the measurement of pill dimensions impractical due to the often irregular shapes.

Initially, density was measured by hydrostatic weighing, *i.e.* the measurement of the weight of the liquid displaced by a submerged DP pill. Hexane was used as the working fluid, as it is a nonsolvent for  $\text{PG}_n^{\text{NHBoc}}$  and has a low surface tension. Water, another nonsolvent of higher density, proved impractical for the small sample size used. This approach is quite labor and time intensive, and the accuracy of hydrostatic weighing in this case was low due to the small sample size, as well as due to the low density and high volatility of hexane. The density values were in the range of 1.1 – 1.3 g cm<sup>-3</sup>, but rather uncertain (see Experimental, subsection 8.5.1, Figure 8-29b).



Figure 5-1: photographs of typical DP pills after vacuum annealing; the bulk DP samples tend to have a darker color with increasing *g*.

To achieve better accuracy, the bulk density of DP samples was determined using a density gradient column (Figure 5-2a). The density gradient was established using aqueous NaBr solutions, providing a working range of  $\rho \approx 1.0 - 1.5$  g cm<sup>-3</sup> (Figure 5-2b). Given well-calibrated standards, this method provides very accurate density values. This also requires far less manipulation of the precious and very brittle DP samples than hydrostatic weighing does. With a density gradient column, sample size and surface tension of the working fluid are also not as problematic as they are in hydrostatic weighing. The only requirement is that the sample can be submerged at the top of the column.

The spread of density values within each generation obtained by this method (Figure 5-2c) is generally lower than was the case with hydrostatic weighing, with the exception of outliers at  $g = 4$  and  $g = 6$ . The dashed trend line in Figure 5-2c shows a slight increase in from  $\rho_{\text{bulk}} \approx 1.15$  g cm<sup>-3</sup> for  $\text{PG1}_{500}^{\text{NHBoc}}$  to  $\rho_{\text{bulk}} \approx 1.21$  g cm<sup>-3</sup> for  $\text{B-PG8}_{500}^{\text{NHBoc}}$ . While this increase is significant, it is nowhere near as dramatic as that obtained previously from the analysis of SEM and TEM images (see Table 5-1). Macroscopic, accessible pores are likely not present,<sup>aa</sup> but the microstructure of these bulk samples

<sup>aa</sup> The samples are mostly transparent (although strongly colored in some cases; see *e.g.* Figure 5-1. Exploratory nitrogen adsorption isotherm measurements revealed no significant accessible pore volume.

is unknown: Packing defects necessarily decrease the bulk density compared to that of single molecular objects. Taking into account that the actual chain density must be slightly higher than the bulk value given imperfect packing density (see section 5.5), an isolated chain density value of *ca.*  $1.3 \text{ g cm}^{-3}$  appears reasonable, judging from these bulk density measurements.

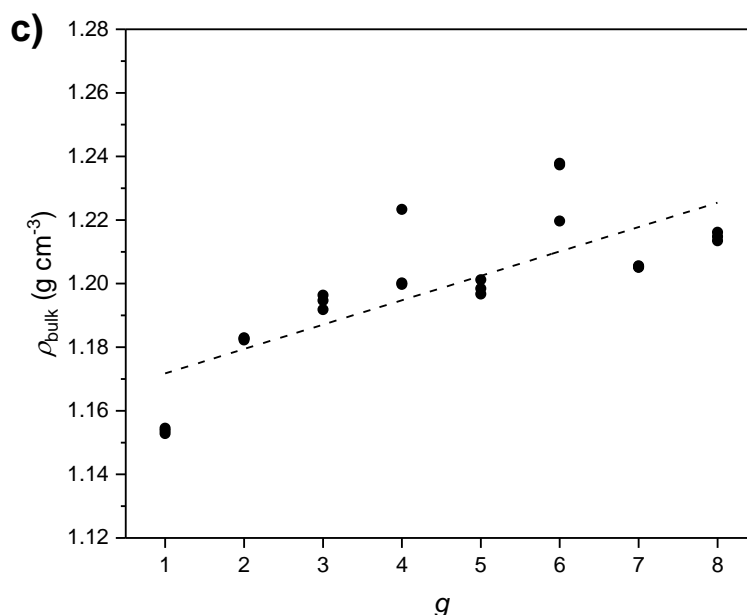
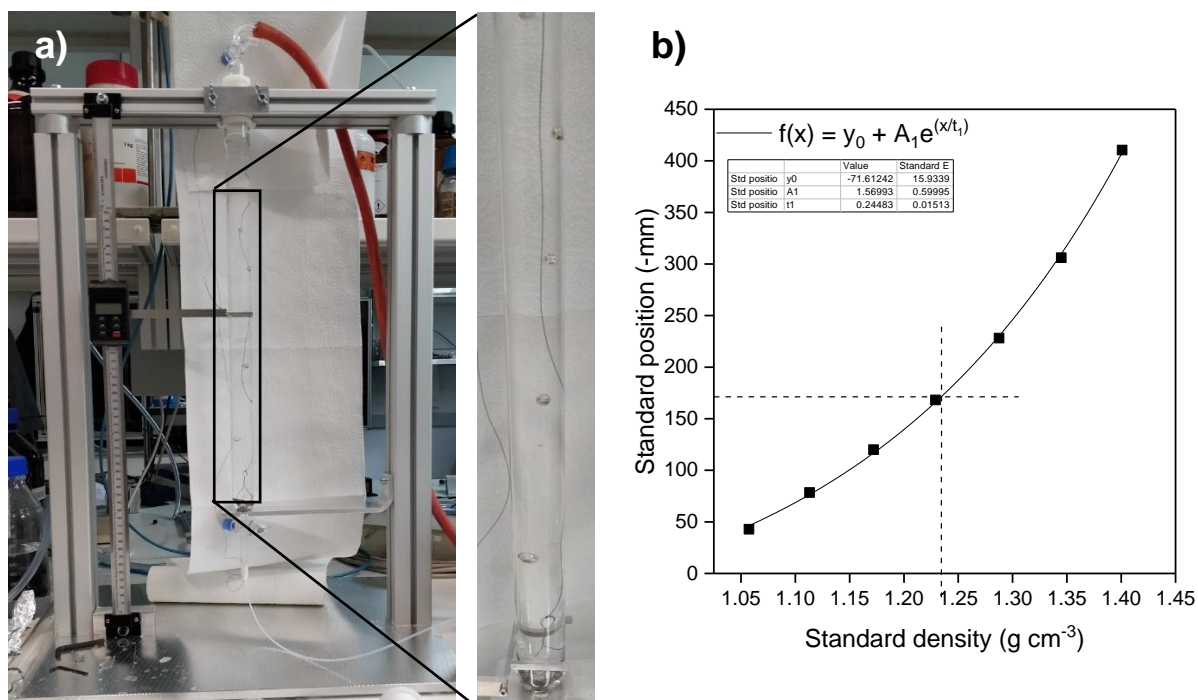


Figure 5-2: a) Density gradient column setup, the detail shot showing calibration standards within the aqueous NaBr density gradient; b) typical calibration curve of the nonlinear density gradient, the dashed lines corresponding to the position of a DP sample; c) density of hot-pressed pills of  $\text{PG}_{\text{B}_n}^{\text{NHBOC}}$  after annealing (see Experimental, subsection 8.5.1) as a function of  $g$ , determined by density gradient column. Each data point represents an individual pressed DP pill, with three pills measured per polymer sample. The errors for individual samples are negligible. The dashed trend line represents a linear fit ( $R^2 = 0.62$ ) and serves only to guide the eye.

### 5.3. Quantitative scanning transmission electron microscopy

Electron microscopy has historically been used widely for the characterization of (stained) biological specimen and of inorganic materials, but recent technological improvements also make it suitable for the analysis of soft matter, as demonstrated in chapter 4 with the example of cryo-TEM of high  $g$  DPs. Already in the 1960s – long before the advent of cryo-TEM – it was proposed that soft nanoparticles (specifically proteins) could be characterized using quantitative scanning transmission electron microscopy (qSTEM).<sup>318</sup> This method (Figure 5-3a), which has been somewhat forgotten since the advent of MALDI-TOF-MS, will be described briefly below.<sup>319</sup>

In sufficiently thin specimen, where multiple scattering events occur with negligible frequency, the (elastically) scattered intensity in the annular dark field of an STEM by first approximation depends only on the scattering mass in the incident beam path:

$$I_{\text{sca}} = I_0 t \frac{n_t}{V_{\text{voxel}}} \sigma$$

Eq. 5-1

$I_0$  is the incident electron beam intensity,  $t$  is the thickness of the sample,<sup>bb</sup>  $V_{\text{voxel}}$  is the volume of scanned by the beam, and  $n_t$  is the number of scattering atoms in the voxel (with scattering cross-section  $\sigma$ ). The scattering mass is  $M_{\text{voxel}} = n_t \cdot m_a$ , where  $m_a$  is the atomic mass; using  $V_{\text{voxel}}/t = A_{\text{pixel}}$  and replacing the atomistic constants  $m_a$  and  $\sigma$  by the respective composition weighted values  $\langle m \rangle$  and  $\langle \sigma \rangle$ , one obtains:

$$M_{\text{voxel}} = A_{\text{pixel}} \frac{\langle m \rangle I_{\text{sca}}}{\langle \sigma \rangle I_0}$$

Eq. 5-2

While the above relationship is valid in practice, adjustments to the measured electron current values  $I_0$  and  $I_{\text{sca}}$  need to be made to account for experimental reality: The incident electron current can fluctuate (which can be corrected for by using the objective aperture current as a reference), and not all scattered electrons might be detected in the annular dark field (requiring corrections for the active area and efficiency of the detector). Practically, these corrections require detailed knowledge of the operational parameters of the electron microscope, as well as extensive, up-to date calibration. To reduce the scattering background, the substrates supporting the particles of interest should be as thin as possible; Thin amorphous carbon or graphene films are predestined for this application. For soft matter specimen, it is necessary to measure at fairly low electron doses to prevent significant mass loss due to radiation damage.

For globular proteins, mass determination using Eq. 5-2 is fairly straightforward, given sufficiently isolated objects on the specimen surface. Filamentous objects (TMV particles, actin filaments, or indeed polymer chains) are rarely of uniform length and mass. It is convenient to determine the mass per unit length  $M_L$  instead; Taking the average mass-per-length value from many undisturbed, isolated

---

<sup>bb</sup> For the single-scattering approximation to hold,  $t$  must be smaller than the mean free electron path length in a material at the given acceleration voltage (30 kV). For DPs, the mean free path is approximately 30 – 35 nm.

filament segments, the density of the filament in question can then be calculated using the cross-section area  $A_{CS}$ :

$$\rho_{qSTEM} = \frac{M_L}{A_{CS}}$$

Eq. 5-3

The cross-section of the filament is not directly accessible from (q)STEM, however reasonable assumptions of the profile can be made (Figure 5-3c). On a relatively weakly interacting surface such as the amorphous carbon film used for preparation of STEM samples, ellipsoidal or circular segment cross-sections appear reasonable for a fairly compact object. While a width value of the object is available from qSTEM directly, the method does not provide direct information regarding heights. The values  $h_{TEM}$  presented in section 6.4 were used (Table 5-1).

The density of DPs was determined by qSTEM only for DPs of  $g > 4$  (PG5<sup>NHBoc</sup><sub>500</sub>, **B**-PG6<sup>NHBoc</sup><sub>500</sub>, **B**-PG7<sup>NHBoc</sup><sub>500</sub> and **B**-PG8<sup>NHBoc</sup><sub>500</sub>). For the DPs of lower  $g$ , sufficient contrast for accurate measurements of  $M_L$  would likely not have been possible with the equipment available at the time. The density values obtained for different cross-sectional models are shown in Figure 5-3c, along with  $M_L$  determined from > 1000 regions of interest for each sample (see Experimental, subsection 8.5.2, Table 8-6 and Table 8-7 for details; Figure 5-3b shows a sample image used for mass determination).

The measured values of  $M_L$  (Figure 5-3c,d) deviate quite strongly from both the absolute values and the trends observed in prior experiments (Figure 5-3d). The difference is significant already for PG5<sup>NHBoc</sup><sub>500</sub> (-13 %) and only increases for higher  $g$ . Particularly astonishing is the observation of **B**-PG6<sup>NHBoc</sup><sub>500</sub> and **B**-PG7<sup>NHBoc</sup><sub>500</sub> having the same  $M_L$  within the margin of error; Simultaneously the detected diameters of the DP filaments increase continuously with  $g$  (see Experimental, subsection 8.5.2), resulting in a local decrease in the density  $\rho_{qSTEM}$  for **B**-PG7<sup>NHBoc</sup><sub>500</sub>. Such a low or even non-existent mass increase in the “ $g + 1$ ” dendronization step leading to **B**-PG7<sup>NHBoc</sup><sub>500</sub> contradicts all other analytical data: GPC indicates a significant increase in molar mass (see Figure 2-6b), an increase in both height and width of the DP chains was observed in AFM imaging, and data from Sanger labelling and TGA are consistent with fairly high functional group conversion.<sup>174</sup> Lastly, a polymer having undergone as little conversion of amines as indicated by the  $M_L$  values shown in Figure 5-3d could likely not be isolated in the standard workup procedure: It would be only poorly soluble in methylene chloride and would be lost during normal phase flash chromatography.<sup>cc</sup>

It is possible that the  $M_L$  values suffer from a systematic deficiency resulting from the flattening of DPs: Along route **B**, the DPs have been observed to show both increasing corrugation<sup>174</sup> and flattening above  $g > 5$  (see section 5.4, Table 5-1). These observations can be ascribed to the significant defects resulting from “ $g + 2$ ” dendronization, which leave large open holes permitting for the rearrangement of dendritic matter. This might result in a significant change in the cross-section profile of the sample (e.g. transitioning from a circular segment or ellipse to a more approximately semi-circular or broad, sloped shape). This would result in fringes which contain significant mass but are

<sup>cc</sup> The reaction yield for the specific batch of **B**-PG7<sup>NHBoc</sup><sub>500</sub> used in these experiments (45 % on 150 mg scale, assuming perfect structures) does not directly contradict the low mass increase in  $M_L$ . However: 1. Workup usually involves losses due to adsorption on the column material during purification, particularly at such small scale; 2. Much higher isolated yield (64 %, assuming perfect structures) was achieved in a repetition of the same synthesis on larger scale (2 g).



not detected by the thresholding algorithm employed in qSTEM analysis. This kind of contrast issue could be alleviated in principle by increasing the overall electron dose – however, this would complicate the analysis further due to the accompanying mass loss from radiation damage. Flattening increases above  $g > 5$  (see Table 5-1), therefore it would be reasonable to expect increasing deviations due to undetected mass. This might explain the large discrepancies to other methods of mass determination: That some systematic factor is at play is also supported by the already large mass deficiency for  $\text{PG5}_{500}^{\text{NHBoc}}$ , for which far fewer defects had been found by MALDI-TOF-MS of scission fragments previously (Figure 3-1a)<sup>169</sup> as well as in this work (see Appendix A.5, Figure A-17).

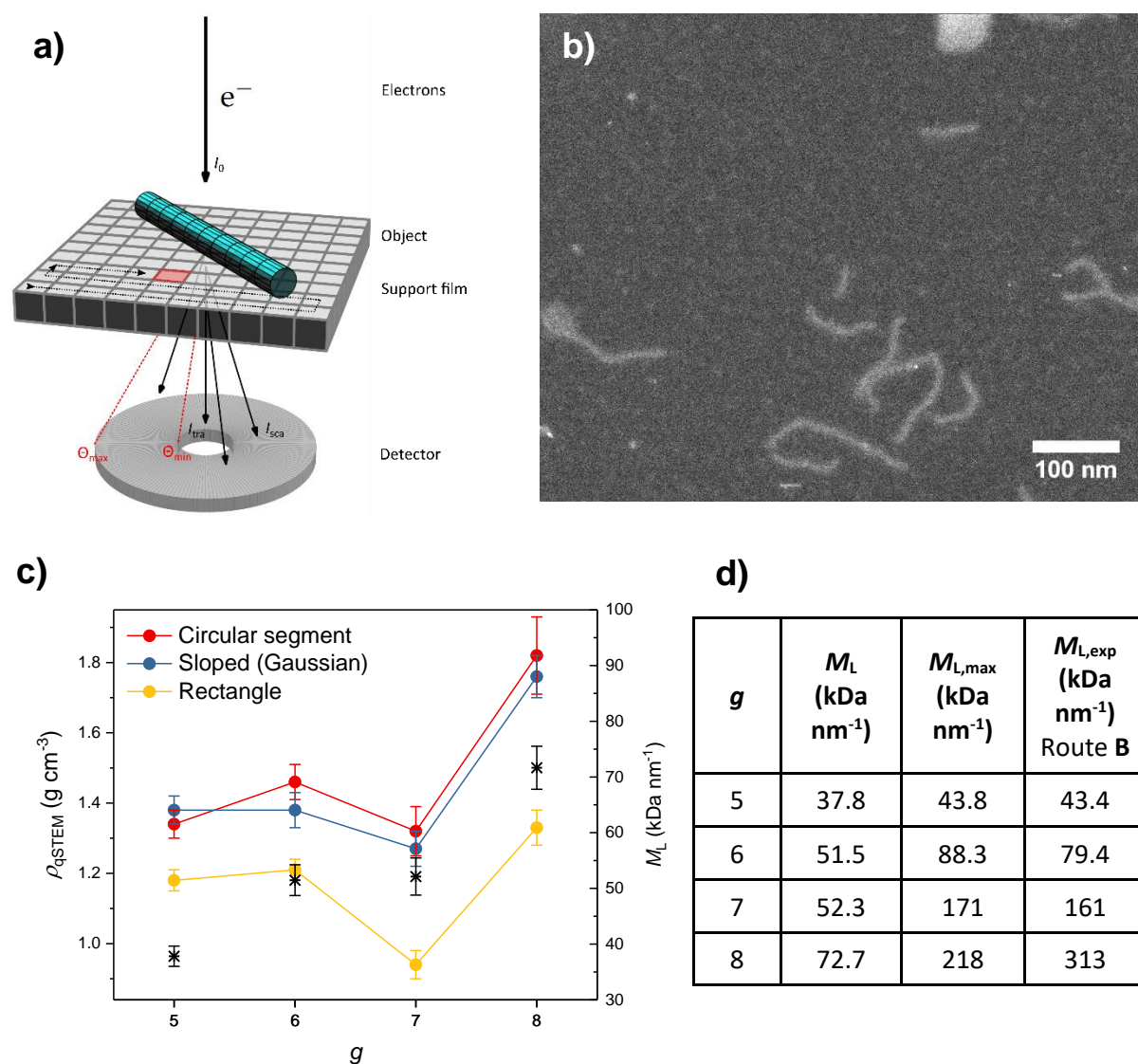


Figure 5-3: a) Schematic representation of the measurement of scattered intensity from a filament deposited on a thin substrate; Image generated by Dr. Sebastian Tacke (MPI of Molecular Physiology, Dortmund), reproduced with permission. b) Example of an STEM image of  $\text{PG5}_{500}^{\text{NHBoc}}$  used for mass analysis (Sebastian Tacke, adapted with permission). c) Density and  $M_L$  values (right-hand scale, marked by asterisks) obtained from qSTEM of  $\text{PG5}_{500}^{\text{NHBoc}}$ ,  $\text{B-PG6}_{500}^{\text{NHBoc}}$ ,  $\text{B-PG7}_{500}^{\text{NHBoc}}$  and  $\text{B-PG8}_{500}^{\text{NHBoc}}$  deposited on amorphous carbon. d) Comparison of the measured  $M_L$  with mass-per-length values derived from  $M_{\text{max}}$  and  $M_{\text{exp}}$  (see subsection 2.6.3, Figure 2-11c; calculated assuming  $\delta = 2.52 \text{ \AA}$ ).

While the values of  $M_L$  should therefore be considered with some skepticism, the density values obtained from qSTEM are likely more reliable: Some mass may not be detected in the fringes of the DP chains (particularly for  $g = 7, 8$ ), but these regions are also not considered in the evaluation of the

width of the DP, as one thresholding algorithm determines the intensity cut-off for mass and width determination. However, it is not clear in how far such a “core density” for the central portions of the DP is representative, particularly when considering the uncertainties associated with  $M_L$ . A factor of potential uncertainty here is the height value  $h_{TEM}$  employed for the calculation of  $A_{cs}$ , which has been determined by a different method for samples deposited on a different substrate type (mica; see section 5.4). The present values (Figure 5-3c) show an overall increase in density, reaching a comparatively high value of  $\rho_{qSTEM} = 1.8 \text{ g cm}^{-3}$  for **B-PG8**<sup>NHBoc</sup><sub>500</sub> (circular segment cross-section). A density value of this magnitude would indicate significant voids or packing defects in bulk samples of **B-PG8**<sup>NHBoc</sup><sub>500</sub> (compare section 5.5). The values for the lower  $g$  DPs (**B-PG5**<sup>NHBoc</sup><sub>500</sub>, **B-PG6**<sup>NHBoc</sup><sub>500</sub>, **B-PG7**<sup>NHBoc</sup><sub>500</sub>) are in a more expected range of  $\rho_{qSTEM} \leq 1.4 \text{ g cm}^{-3}$ .

## 5.4. Scanning and transmission electron microscopy

The results in this section mostly stem from work by Prof. Baozhong Zhang, Dr. Hao Yu and Prof. Roger Wepf. Density values for  $g = 1 - 5$  are derived from previously published height and width analyses,<sup>148</sup> and the remainder may be found in the doctoral thesis of Dr. Hao Yu.<sup>172</sup>

For qSTEM, no molar mass input is required, however the object size is somewhat uncertain (section 5.3). This is in part due to the limited permissible electron dose above which the soft specimen suffer radiation damage. By metal coating of deposited DPs, their heights and widths can be measured more accurately, providing an estimate of the volume of the deposited chains. The height  $h_{\text{TEM}}$  was obtained from TEM imaging of carbon replicas of unidirectionally W-shadowed DPs deposited on mica (Figure 5-4a). The length of the uncoated “shadow” is proportional to the height of the filament. The width  $w_{\text{SEM}}$  was obtained from the analysis of SEM images of rotary W-shadowed DPs deposited on mica (Figure 5-4b), taking into account an additional  $\sim 1$  nm in thickness due to the metal film.

For  $g \leq 5$ , the uncertainties in height and width values (Table 5-1) decreased with  $g$  as expected for smooth cylinders of increasing thickness and steric congestion. For  $g > 5$ , the uncertainty increased again, due to previously observed mounting corrugation, which is readily apparent in SEM (Figure 5-4b). Previously also observed by AFM, these fluctuations were ascribed to “holes” generated in the “ $g + 2$ ” steps along route **B**.<sup>174</sup> From the TEM and SEM measurements alone, it is not possible to derive an accurate cross-section geometry. As was the case for qSTEM, geometric assumptions have to be made; Figure 5-4d shows the densities obtained for two such models (rectangular and circular segment cross-sections, Figure 5-4c).

As shown in Figure 5-4d, densities increase dramatically above  $g = 5$ , in part to values of  $\rho_{\text{SEM/TEM}} > 2 \text{ g cm}^{-3}$ . Such high densities are uncommon for organic compounds, being reserved to highly halogenated compounds (*e.g.* hexachlorobenzene,  $\rho = 2.04 \text{ g cm}^{-3}$ ,<sup>320</sup> or PTFE,  $\rho = 2.16 \text{ g cm}^{-3}$ <sup>321</sup>), and are certainly extraordinary for DPs, which have the approximate composition  $\text{C}_{18}\text{H}_{26}\text{N}_2\text{O}_5$ . The significant and sudden increase in density alone requires some explanation: In the dried, deposited state, all DPs should be densely packed, only interacting with the substrate and air. An approximately constant density would be expected over the entire range of  $g$  values – as is the case for all DPs up to  $g = 5$ , with  $\rho_{\text{SEM/TEM}} \approx 1.3 \text{ g cm}^{-3}$ .<sup>148</sup> There are uncertainties associated with the applied method: Both height and width show a growing spread for  $g > 5$ , and the impact of metal coating (particularly the layer thickness for SEM) is somewhat uncertain.

Another uncertainty is the fact that the two height and width datasets ( $g = 1 - 5$  vs.  $g = 6 - 8$ ) were produced *ca.* 2 – 3 years apart. Artefacts from applying slightly different sample preparation procedures, using different materials, instruments or instrument settings can unfortunately not be excluded entirely.

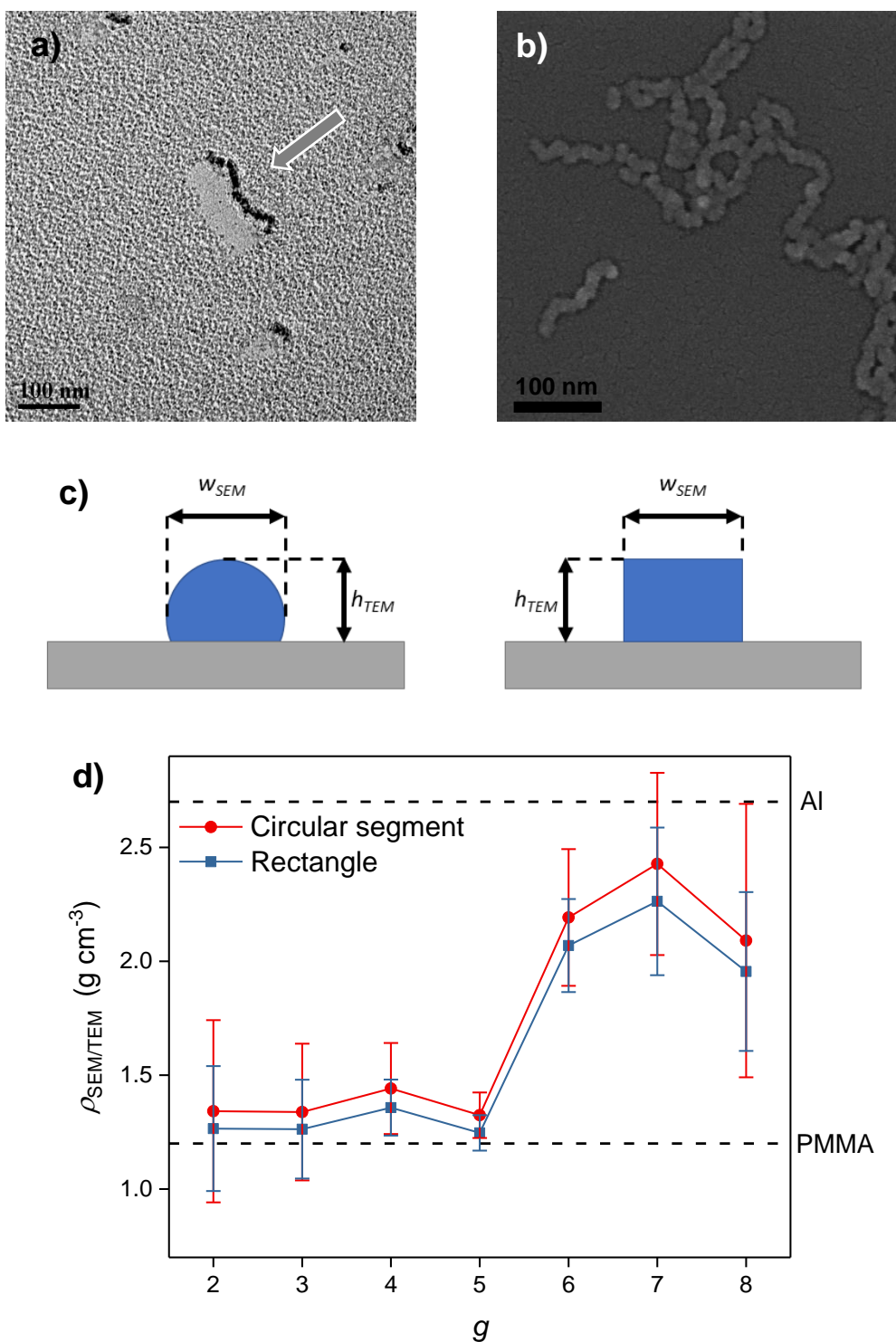


Figure 5-4: Representative electron micrographs of W-shadowed preparations used for height and width determination: a) TEM of  $B-PG7_{500}^{NHBoc}$  (carbon replica, prepared from DPs drop-cast onto mica, then unidirectionally shadowed at an angle of  $7^\circ$  from the direction indicated by the arrow; image by Dr. Hao Yu, reproduced with permission); b) SEM image of  $B-PG7_{500}^{NHBoc}$  on mica (rotary shadowed,  $45^\circ$ ; image by Dr. Hao Yu, adapted with permission). c) Circular segment (left) and rectangular (right) models for deposited DPs. d) Densities of DPs of  $g = 2 - 8$  obtained from TEM and SEM (Figure 5-4a,b, Table 5-1); the horizontal lines mark the density of a typical polymer (PMMA,  $\rho \approx 1.2\ g\ cm^{-3}$ ) and that of aluminium ( $\rho = 2.7\ g\ cm^{-3}$ ) for reference.<sup>175</sup>

Table 5-1: Data pertaining to the density calculations from SEM and TEM images shown in Figure 5-4a,b. <sup>a)</sup> values reported elsewhere.<sup>148,172</sup> <sup>b)</sup>  $M = M_{exp}$ .<sup>150</sup> <sup>c)</sup>  $M = M_{max}$  (see subsection 2.6.3). Density values were calculated assuming a cut-circular cross-section Figure 5-4c; see Experimental, subsection 8.5.3, Eq. 8-8.

<b><i>g</i></b>	<b><i>h</i><sub>TEM</sub> (nm)</b>	<b><i>w</i><sub>SEM</sub> (nm)</b>	<b>Aspect ratio</b>	<b><i>M</i> (kDa)</b>	<b><math>\rho_{SEM/TEM}</math> (g cm<sup>-3</sup>) (circular segment)</b>
<b>2</b>	2.3 ± 0.4 <sup>a)</sup>	3.1 ± 0.4 <sup>a)</sup>	0.74 ± 0.22 <sup>a)</sup>	1.2 <sup>b)</sup>	1.3 ± 0.4
<b>3</b>	3.4 ± 0.5 <sup>a)</sup>	4.5 ± 0.4 <sup>a)</sup>	0.76 ± 0.18 <sup>a)</sup>	2.6 <sup>b)</sup>	1.3 ± 0.3
<b>4</b>	4.9 ± 0.3 <sup>a)</sup>	6.0 ± 0.4 <sup>a)</sup>	0.82 ± 0.10 <sup>a)</sup>	5.4 <sup>b)</sup>	1.4 ± 0.2
<b>5</b>	7.3 ± 0.2 <sup>a)</sup>	8.9 ± 0.5 <sup>a)</sup>	0.82 ± 0.07 <sup>a)</sup>	10.9 <sup>b)</sup>	1.3 ± 0.1
<b>6</b>	7.5 ± 0.5 <sup>a)</sup>	9.6 ± 0.7 <sup>a)</sup>	0.78 ± 0.11 <sup>a)</sup>	20.1 <sup>b)</sup>	2.2 ± 0.3
<b>7</b>	9.3 ± 0.9 <sup>a)</sup>	14.2 ± 1.5 <sup>a)</sup>	0.65 ± 0.13 <sup>a)</sup>	40.2 <sup>b)</sup>	2.4 ± 0.4
<b>8</b>	11.8 ± 1.5 <sup>a)</sup>	17.6 ± 2.2 <sup>a)</sup>	0.67 ± 0.17 <sup>a)</sup>	55 <sup>c)</sup>	2.1 ± 0.6

## 5.5. Small-angle X-ray scattering

Some DPs (see Table 5-2) showed birefringence in cross-polarized optical microscopy (Figure 5-5a,b). While true birefringence was limited to small zones and most areas merely diffused light, this indicated at least some molecular order. Significant birefringence was only observed for DPs of  $g = 3 - 6$ ; Outside of this, light was not reliably transmitted in cross-polarized microscopy by either thin films or bulk samples.<sup>dd</sup> The bulk pill samples previously employed for density determination using hydrostatic methods (section 5.2) were investigated by small-angle X-ray scattering (SAXS)

SAXS is based on the elastic scattering of X-rays with the electrons in a sample (Thomson scattering); Contrast arises from density fluctuations within the sample. In SAXS, measured at around  $1-10^\circ$  relative to the axis of the incident beam, length scales of typically 1-100 nm are probed, *i.e.* the distances which are observed are usually inter- rather than intramolecular, corresponding *e.g.* to the packing of particles. This has been used previously *e.g.* to reveal the packing of liquid crystalline assemblies based on low- $g$  DPs and mesogenic additives.<sup>132,322</sup> Shorter length scales, *i.e.* intramolecular correlations at distances below a few nm, may be probed using wide-angle X-ray scattering (WAXS) or X-ray crystallography.<sup>ee</sup> Polymeric samples are often dominated by polydispersity: Even when macromolecules do align or pack in some geometry, broad scattering rather than sharp diffraction is the rule.

Matching with the observation of partial birefringence in the bulk samples, the DPs of  $g = 3 - 8$  were found to exhibit quite well-defined packing ( $\geq 3$  distinct peaks). In part, this had been the case already for freeze-dried DP powders (see Experimental, subsection 8.5.4, Figure 8-33), but the packing was significantly improved upon hot-pressing and annealing of the polymers. The  $q$  value of the first scattering peak, related to the inverse interchain distance, decreases with  $g$  throughout the DP series as expected (Figure 5-5c). Figure 5-6b shows the corresponding density values, calculated from data fits assuming columnar rhombohedral geometry (see Experimental, subsection 8.5.4).

The values of  $\rho_{\text{SAXS}}$  vary even more strongly than those obtained by other methods presented in the previous sections, ranging from  $\rho_{\text{SAXS}} \ll 1 \text{ g cm}^{-3}$  for PG1<sub>500</sub><sup>NHBoc</sup> to  $\rho_{\text{SAXS}} \approx 4 \text{ g cm}^{-3}$  for B-PG8<sub>500</sub><sup>NHBoc</sup> – the latter value is larger than the density of diamond ( $3.5 \text{ g cm}^{-3}$ ).<sup>175</sup> It should be noted that the density from SAXS is not strictly representative of the bulk, as scattering arises only from the crystalline portion of the sample. The proportions of crystalline domains likely vary by sample, and attempts to estimate the crystallinity were unsuccessful: The glass transitions especially for high  $g$  DPs are shallow and broad in DSC,<sup>323</sup> and attempts to elucidate crystallinity and real-space packing geometry by TEM were not met with success.<sup>ff</sup> At least for the high  $g$  DPs with extraordinarily high  $\rho_{\text{SAXS}}$ , amorphous domains of (much) lower density provide a possible explanation for the disparity between  $\rho_{\text{SAXS}}$  and

---

<sup>dd</sup> Only some samples (pills) of B-PG7<sub>500</sub><sup>NHBoc</sup> and B-PG8<sub>500</sub><sup>NHBoc</sup> showed significant birefringence, which was in part difficult to discern due to the relatively strong coloration of these samples (compare Figure 5-1).

<sup>ee</sup> WAXS measurements of DPs were performed in tandem with SAXS in some cases (see Experimental, subsection 8.5.4, Figure 8-34). The results indicate that the dendritic matter is essentially amorphous, as expected *e.g.* from computer simulations which show radially quite homogenous packing around the DP backbone.<sup>144</sup>

<sup>ff</sup> Thin sections of the DPs were readily prepared, however staining either with aqueous OsO<sub>4</sub> or with OsO<sub>4</sub> vapor did not reveal any structures. The staining was weak and undifferentiated, even though for these exploratory experiments PG5<sub>500</sub><sup>NHAlloc</sup> was selected as a polymer with unsaturated side groups thought particularly suited for oxidative staining.

$\rho_{\text{bulk}}$  of the corresponding samples: Amorphous domains do not produce Bragg peaks and only contribute to the background which is subtracted in the fitting procedure. Still, the obtained values require explanation in terms of effective mass per unit length – the local density of the isolated DP should not be as high as values  $\rho_{\text{SAXS}}$  for  $g > 6$ . Conversely, the densities for the DPs of  $g = 1 - 3$  are significantly lower than the corresponding values of  $\rho_{\text{bulk}}$ . These observations will be discussed in some depth in section 5.6.

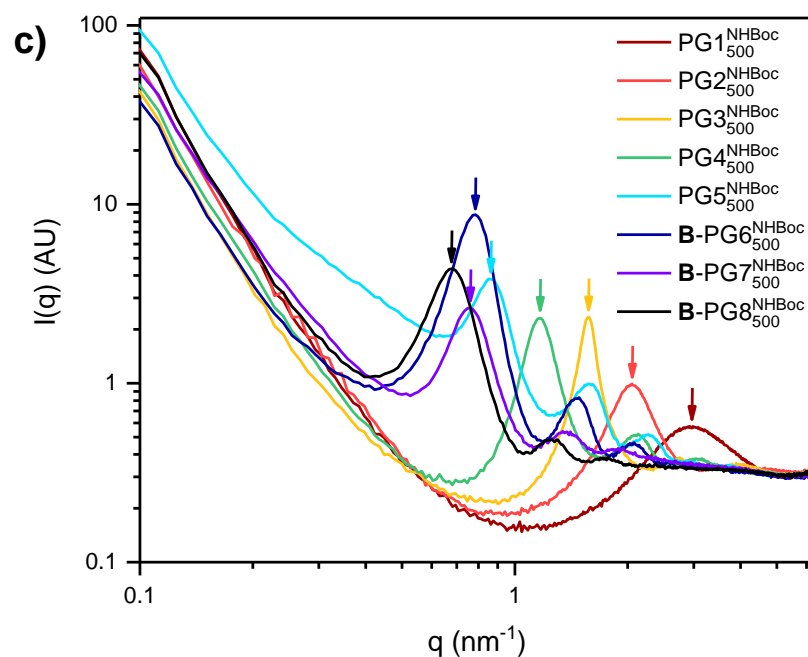
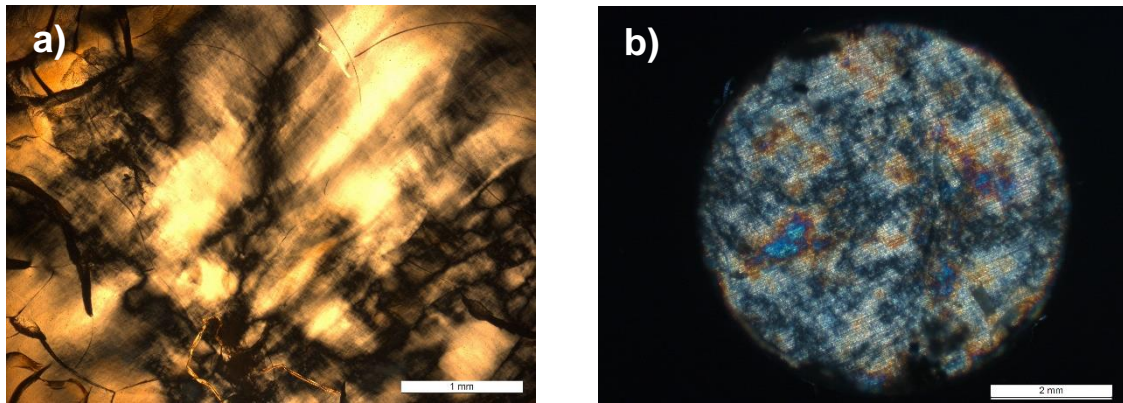


Figure 5-5: Cross-polarized optical micrographs of a) a thin film of  $\text{PG5}_{500}^{\text{NHBoc}}$  pressed at ca. 100 °C between glass slides and b) a hot-pressed pill of  $\text{PG5}_{500}^{\text{NHBoc}}$ , both displaying localized, usually diffuse birefringence. c) SAXS curves of all DP samples after annealing. The correspondingly colored arrows mark the approximate position of the first scattering peak. See Figure 8-35 for individual curves

Table 5-2: Cell & scattering parameters obtained from columnar rhombohedral fit of SAXS data.

$g$	$a$ (nm)	$\gamma$ ( $^\circ$ )	$\xi$ (nm)	$n$ (rods)	Birefringence	$\rho_{\text{SAXS, chain}}$ ( $\text{g cm}^{-3}$ )	$\rho_{\text{SAXS, unit cell}}$ ( $\text{g cm}^{-3}$ )
1	2.46	60	4	2	no	0.75	0.66
2	3.53	60	12	3	no	0.88	0.74
3	4.78	57	39	8	yes	1.08	0.90
4	6.81	52	33	5	yes	1.18	0.97
5	9.89	47	44	4	yes	1.23	1.00
6	12.63	40	54	4	yes	1.59	1.29
7	10.85	50	41	4	(yes)	3.67	2.97
8	13.67	43	48	3	(yes)	3.55	2.86

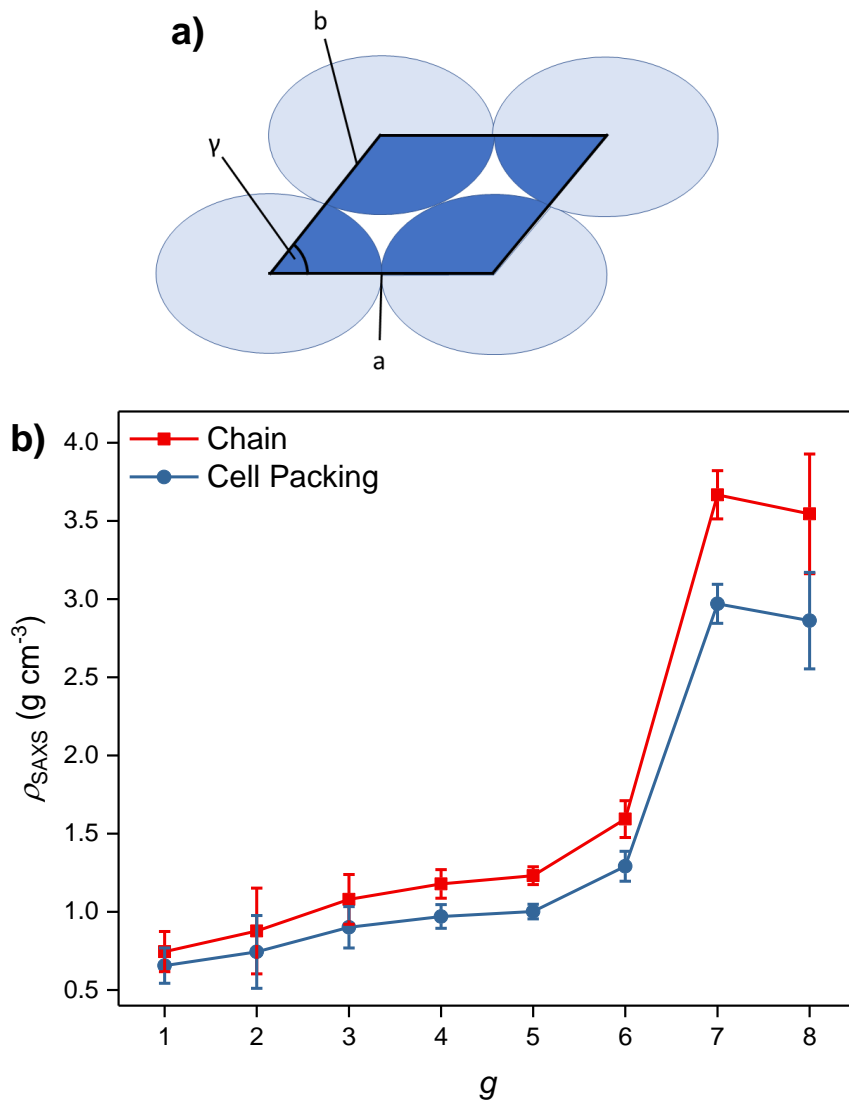


Figure 5-6: a) Cross-section through the unit cell of a columnar array; for columnar rhombohedral packing,  $a = b$ . b)  $\rho_{\text{SAXS}}$  for DPs of  $g = 1 - 8$ , calculated for the columnar rhombohedral phase.



## 5.6. Discussion

As shown in Figure 5-7, the different methods discussed in sections 5.2 – 5.5 have yielded a very wide range of density values, particularly for high  $g$ : Bulk and qSTEM measurements deliver fairly constant density values in a “reasonable” range of  $1.0 \text{ g cm}^{-3} < \rho < 1.5 \text{ g cm}^{-3}$  (excepting  $\rho_{\text{qSTEM}} = 1.8 \text{ g cm}^{-3}$  for **B-PG8**<sub>500</sub><sup>NHBoC</sup>). Conversely, the two estimates relying purely on geometric parameters – obtained either in the deposited state from combined SEM/TEM measurements or from SAXS measurements of bulk DPs – suggest a strong increase in density, to values which are frankly unphysical: Densities above  $2.0 \text{ g cm}^{-3}$  are unrealistic for matter of a composition similar to DPs, which is essentially that of a greasy peptide.

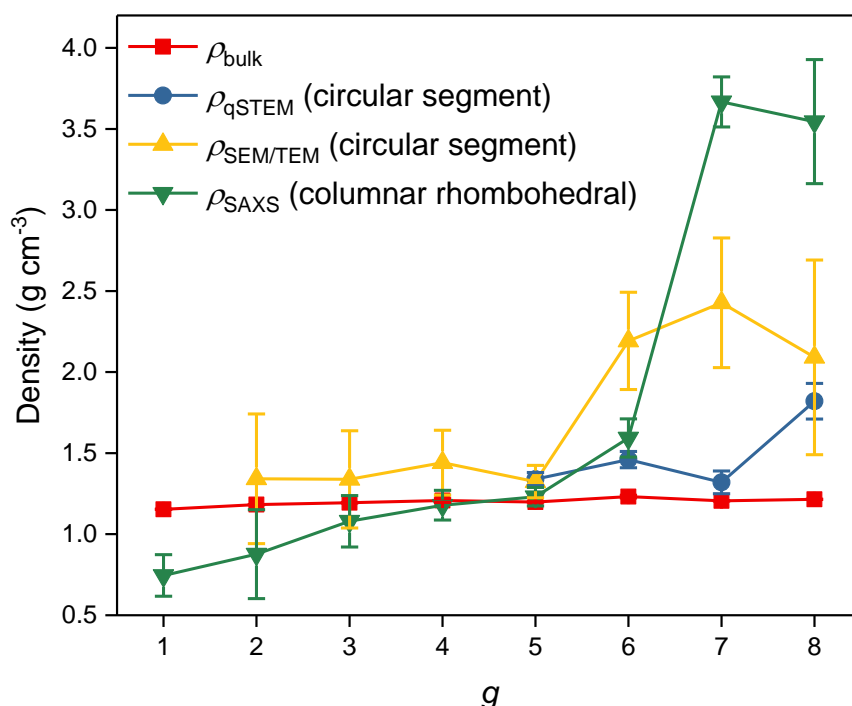


Figure 5-7: Comparison of density values obtained by the different methods.

All the methods discussed have their strengths and weaknesses, and a diversity of assumptions and approximations enters into the at times complex derivation of density values. For instance, the question of packing efficiency is significant to the density of individual DP chains. It impacts density estimates derived from envelope density values  $\rho_{\text{bulk}}$  and is also important in the discussion of  $\rho_{\text{SAXS}}$ : It is evident *e.g.* from SEM/TEM measurements presented in section 5.4 that the structurally defective DPs investigated in this chapter can be deformed significantly (Table 5-1).  $\rho_{\text{qSTEM}}$  requires the assumption of some cross-sectional geometry, the height value of which is  $h_{\text{TEM}}$  as obtained in section 5.4. A potential danger here is that TEM replicas stem from DPs deposited on mica, rather than the amorphous carbon used for qSTEM. For  $g < 5$  DPs, previous measurements had shown some differences between substrates,<sup>148</sup> a factor which is presently unaccounted for, as are the likely different detection cutoffs between the two methods.

One last assumption is of especial note: Both for SEM/TEM and SAXS, the molar mass per repeat unit is a necessary input.<sup>88</sup> As discussed in section 1.6.3, the determination of molar mass per repeat unit is far from simple for DPs, and indeed even Sanger labelling fails when steric congestion is high (see section 2.7), *i.e.* at  $g \geq 6$  where  $\rho_{\text{SAXS}}$  and  $\rho_{\text{SEM/TEM}}$  reach extraordinary values. This suggests that the values of molar mass per repeat unit determined for the  $g > 5$  DPs from route **B** investigated here are overestimates. Figure 5-8 shows the very low values of  $\alpha$  (see section 2.7) necessary to reduce DP density from SEM/TEM and SAXS measurements to “reasonable” values of  $\rho = 1.5 \text{ g cm}^{-3}$ . In light of results from GPC, AFM and Sanger labelling, molar mass values per repeat unit as calculated for SAXS are unrealistically low however – particularly the synthesis of **B-PG7**<sub>500</sub><sup>NHBOC</sup> is very unlikely to have proceeded with as low an efficiency as the data presented in Figure 5-8 suggests: such low conversion values would certainly be evident in the labelling of defects. This suggests that systematic errors leading to an underestimate of the dimensions of the DPs contribute to the present high density estimates for  $g > 5$ , though the origin of these errors is as of yet unknown.

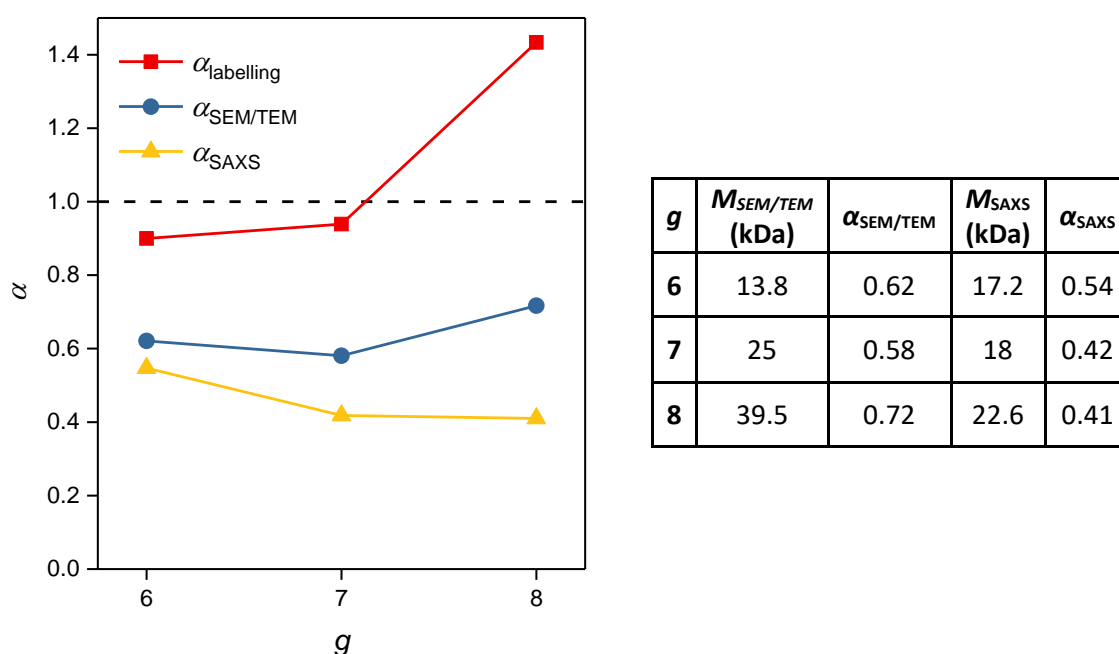


Figure 5-8: Values of  $\alpha = M_{\text{exp}}/M_{\text{max}}$  necessary to achieve  $\rho = 1.5 \text{ g cm}^{-3}$ . Values from Figure 5-3d/Figure 2-11d added for comparison.

While there are uncertainties associated with both SEM/TEM measurements (*e.g.* the hard-to-quantify influence of W-coating in SEM or the strong influence of fit geometry in SAXS), overestimates of  $M_{\text{exp}}$  may likewise contribute to such extraordinary density values. Some circularity cannot be avoided in this: The input values of  $M_{\text{max}}$  depend on the location of  $g_{\text{max}}$ , and thereby they depend on the density of the DPs. As discussed previously (section 2.7), the values  $M_{\text{exp}}$  obtained from Sanger labelling are not entirely reliable at high  $g$ . This is particularly true for the series of DPs investigated here, which was prepared using route **B** – a factor which leads to further uncertainties. Unfortunately, there was insufficient time to generate similar data for DPs prepared by route **C**. The comparison with

<sup>88</sup> As is the length per repeat unit, which is assumed to be  $\delta = 2.52 \text{ \AA}$  throughout this thesis. This is an approximation, as that value corresponds to an all-trans zig-zag conformation of the DP backbone, which may locally be bent. However, the possible range of values is much more limited than the potential error arising from overestimation of molar masses.

density values for those polymers, which by all available indicators are of higher structure perfection, would have aided in the evaluation of the present data and the localization of systematic errors of the various methods. Equally unfortunately, the MALDI-TOF analysis of oligomeric fragments obtained from the “hot solvent” induced main-chain scission of **B-PG6**<sub>500</sub><sup>NHBoc</sup> and **B-PG7**<sub>500</sub><sup>NHBoc</sup> was unsuccessful (see subsection 3.5.7). This would have provided a better than currently possible estimate of molar mass per RU.

More than anything, the results presented in this chapter unfortunately show that for polydisperse molecular objects such as DPs, density determination is far from trivial, and that it is dangerous to rely on a single type of measurement – particularly in view of the large disparities especially at high  $g$ . The “ideal” method of density determination would simultaneously provide information on the molar mass, shape and size of individual DPs. A combination of electron microscopic methods (*e.g.* qSTEM and electron tomography on one sample of deposited DPs) would likely be best suited to this purpose. Whether such an endeavor is feasible for soft specimen such as DPs is questionable however, as electron dose is a severely limiting factor.

For the work in this thesis which is concerned with  $g_{\max}$ , a density value had to be assumed. The upper limit of bulk densities  $\rho \approx 1.3 \text{ g cm}^{-3}$  was chosen for this purpose, as there are no assumptions regarding  $M_L$  or DP geometry which impact their measurement – all other methods are significantly influenced by such factors, which are currently still laden with significant uncertainty.

## 6. Fluorescent Labelling of $\text{PGg}_n^{\text{NHoc}}$ for Rheological Studies

### 6.1. Motivation/goals

The theory of polymer reptation established by Edwards,<sup>324</sup> Doi<sup>325</sup> and de Gennes<sup>326</sup> has been very successful in describing bulk properties of polymer melts and concentrated polymer solutions. Essentially, the motion of an individual polymer can be described as being restricted to a tube defined by the surrounding, entangled chains. Rather than diffusing freely as in dilute solutions where Brownian motion dominates, on short to medium time scales the polymer can only move back and forth along the long axis of the tube in a snake-like motion – hence the term reptation.

Biopolymers such as DNA or filamentous, non-covalent structures such as F-actin can achieve lengths of many  $\mu\text{m}$  and are easily labelled with fluorescent tags. Using these substrates, wide field fluorescence microscopy experiments<sup>272,327</sup> have been able to confirm the base assumptions of reptation theory on a molecular level. Due to their very specific structures, these biological systems are of limited variability and are not necessarily representative of synthetic polymers. Only recently, a first example of a fully synthetic system – a polyisocyanopeptide which forms a hydrogen bond-stabilized intramolecular helix<sup>328</sup> – was shown to allow similar microscopic investigations.<sup>329</sup> These investigations resulted in unprecedented quantitative insights into the dynamics of the reptation process. While this represented a first microscopic observation of the dynamics of synthetic polymers in their natural state, the polyisocyanopeptide system was somewhat limited in scope: Pendent groups can be altered quite readily, but the stiffness and thickness of these polymers rely on the helix-forming intramolecular hydrogen bonding network. As is the case with DNA and F-actin, this highly specific mode of intramolecular self-assembly cannot be easily altered *e.g.* to change the stiffness of the polymer, and it is sensitive to environmental conditions (*e.g.* pH).<sup>330</sup>

Not only the steady state of concentrated polymer solutions is of interest, but also their dynamic behavior under shear, *i.e.* their rheology.<sup>331</sup> Again, microscopic investigations of single molecules are limited largely to biopolymers, specifically DNA, which has been studied *e.g.* in extensional flow.<sup>332</sup> This work was recently expanded by Schroeder *et al.* to encompass greater topological diversity by investigating DNA-based comb polymers<sup>333</sup> and circular DNA.<sup>334</sup>

Recent developments in microscopy may enable the study of more classical synthetic polymer structures, and therefore the exploration of a more diverse chemical space. This has been made possible by the advent of far field optical super-resolution techniques.<sup>335</sup> One major class of such techniques relies on the manipulation of ensemble excitation states for the targeted generation of “dark” photophysical states after diffraction-limited excitation. Implementations of this general principle include ground-state depletion (GDS)<sup>336</sup> and stimulated emission depletion (STED)<sup>337</sup> microscopy. Another set of techniques, predominantly the two closely related methods of photo-activated localization microscopy (PALM)<sup>273</sup> and stochastic optical reconstruction microscopy (STORM)<sup>338</sup>, rely on the stochastic excitation and depletion or bleaching of single fluorophores, reconstructing complete images from multiple “diluted” excitation events in which the point spread functions of individual fluorophores do not overlap, thereby permitting precise localization.

While all these techniques do allow for very high spatial resolutions, the scanning rate is often limited. Structured illumination microscopy (SIM) offers the potential for imaging at higher speeds, although achievable resolution improvements (factor 2) are less impressive than *e.g.* for STED. In SIM, sub-diffraction spatial information is reconstructed computationally from Moiré patterns generated by the overlay of diffraction-limited illumination patterns with the actual image.<sup>339</sup> A similar approach, termed “instant” SIM (iSIM) can be implemented on the hardware side. While resolution improvements in iSIM are also limited to a factor of 2, this vastly improves the possible image acquisition rate compared to other super-resolution techniques; Frame rates up to 1 kHz are possible.<sup>340</sup>

Dendronized polymers are interesting subjects for dynamic studies using these microscopic techniques: They offer the rather unique possibility of controlling the intrinsic stiffness of a polymer by varying  $g$  within a homologous series. Moreover, as demonstrated previously by others<sup>179,341,342</sup> and as utilized in this thesis (see chapters 2 & 3), amide bond formation post-polymerization is a versatile tool for installing varied functional groups or solubilizing substituents in the periphery of DPs. It should be possible to leverage similar chemistry for the installation of fluorophores in the DP periphery. Lastly but importantly, DPs of this class can be synthesized with very high  $P_n$  ( $\approx 10'000 - 20'000$ ) by free-radical polymerization. The primary goal from the side of polymer synthesis, as discussed in this chapter, was therefore the preparation of DPs of high  $P_n$  and varying  $g$ , bearing peripheral fluorescent labels of sufficient density and photostability to allow for single-molecule imaging.

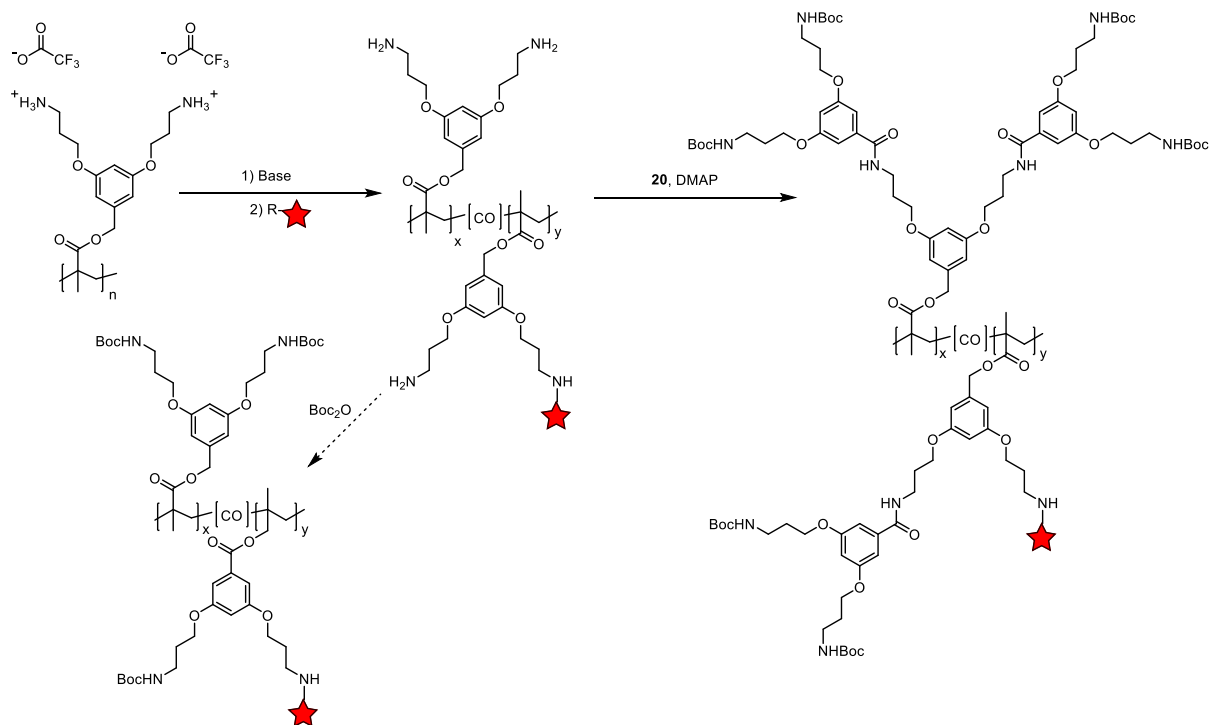
## 6.2. Selection of polymer, labelling strategy and fluorophore

For experiments in the steady state as well as for studies under shear or flow, the entangled state of DPs is of interest. In contrast to the studies discussed in previous chapters, where DPs of  $P_n \approx 500$  were used, much longer chains ( $P_n \gg 1'000$ ) are necessary to that end. Their synthesis is readily accomplished by FRP, followed by dendronization according to Scheme 1-8b, as described in subsection 8.3.1.

The fluorescent labelling of a dendronized polymer of the class discussed in this thesis had been achieved previously by Grotzky *et al.*<sup>343</sup> for the purpose of visualizing the deposition of DP-enzyme conjugates. In that work, a fluorescein tag and multiple copies each of two different enzymes were attached to  $PG1_{2000}^{NH_3TFA}$ , permitting very facile localization of the DPs once deposited on oxide surfaces. Linking was achieved by means of a UV-Vis quantifiable bis-aryl hydrazone unit.<sup>344,345</sup> While DPs containing free amines or ammonium cations are well suited for immobilization by non-covalent, but strong attachment to oxide surfaces, their limited solubility and the resulting difficulties in the purification of significant polymer quantities render DPs of the type  $PGg_n^{NH_3TFA}$  or  $PGg_n^{NH_2}$  unsuitable for the imagined purpose of dynamic imaging in concentrated (organic) solutions. The labeled polymers should therefore preferentially be of the type  $PGg_n^{NHBoc}$ . Fluorescein as a dye is likewise unsuited for the purpose of single-molecule studies: It is less photostable than other commonly used fluorescent probes,<sup>346</sup> and progressive bleaching at high laser intensities would make it difficult to follow single-chain dynamics.

The fluorescent labelling of  $PGg_n^{NHBoc}$  is not directly feasible, however amine-reactive species commonly employed in peptide chemistry (active esters, acid chlorides, acid anhydrides, chloroformates, isocyanates, isothiocyanates, *etc.*) should be readily compatible with the conditions used for dendronization. For minimum disruption of the overall DP structure, it was thought advantageous to incorporate this into a regular dendronization procedure by first partially reacting amines in  $PGg_n^{NH_2}$  with a suitable reactive dye, then completing dendronization by application of the conditions regularly applied in route **A** (see Scheme 1-8b, Scheme 2-1, and Scheme 6-1). In this manner, the impact of labelling on the solubility of DPs should be minimized, however only DPs of  $g > 1$  are accessible in this manner. The direct re-protection of amines, *e.g.* by addition of  $Boc_2O$  after labelling with a suitable dye (see Scheme 6-1), was attempted initially but then not pursued since severe solubility issues arose.

High labeling densities are desirable particularly for high frame rate imaging. However too many fluorescent labels in the DP periphery may negatively affect the solubility of the labelled polymers. Self-quenching of fluorophores in close proximity to each other is another potential issue which might put an upper limit to the aimed-for labelling density. These limitations are likely subject to variation with  $g$  and must be explored experimentally.



Scheme 6-1: Proposed labelling of DPs of  $PG1_n^{NH_3TFA}$  at a low labelling density, such that repeat units are only singly labelled. The fluorophore is represented by a red star.

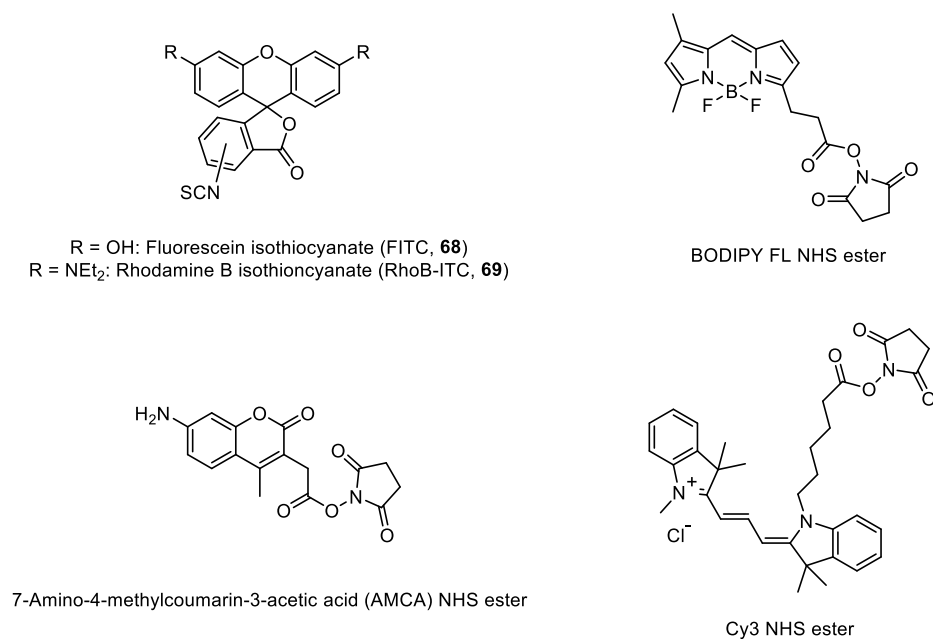


Figure 6-1: Representatives of amine-reactive fluorophores of diverse structural classes.

Various, structurally diverse classes of chromophores have been used to label reactive amines,<sup>347</sup> including xanthene,<sup>348,349</sup> cyanine,<sup>350</sup> coumarin<sup>351</sup>, rylene<sup>352</sup> and BODIPY<sup>353</sup> derivatives (see Figure 6-1). Among these, xanthenes and in particular rhodamines appear to be the most versatile, as they possess favorable photophysical properties (resistance to photobleaching, large Stokes shifts) as well as chemical properties (better stability than *e.g.* BODIPY-based dyes or cyanines). Furthermore, rhodamines are easily prepared by Friedel-Crafts type reactions involving fairly simple precursors.

The last point is of some importance as amine-reactive fluorescent probes are frequently quite expensive (> \$100/mg). This cost is not excessive for the purpose of labelling  $\mu\text{g}$  quantities of proteins and other biomolecules, often sufficing for analytical purposes. The purification of DPs however requires flash column chromatography after dendronization and imposes a lower limit of *ca.* 50 mg of material due to adsorption on the column. Smaller amounts can be isolated by precipitation; However, this would likely lead to contamination with free dye. Synthetic or commercial access to the required quantities (several dozen mg) of the labelling agents was therefore a criterion of significant importance in the selection of fluorophores.

Accordingly, dyes were selected which are either readily prepared from commercial precursors or else commercially available, either in an amine-reactive form or one which can readily be converted. The fluorophore candidates which were examined for the labelling of DPs are depicted in Figure 6-2.

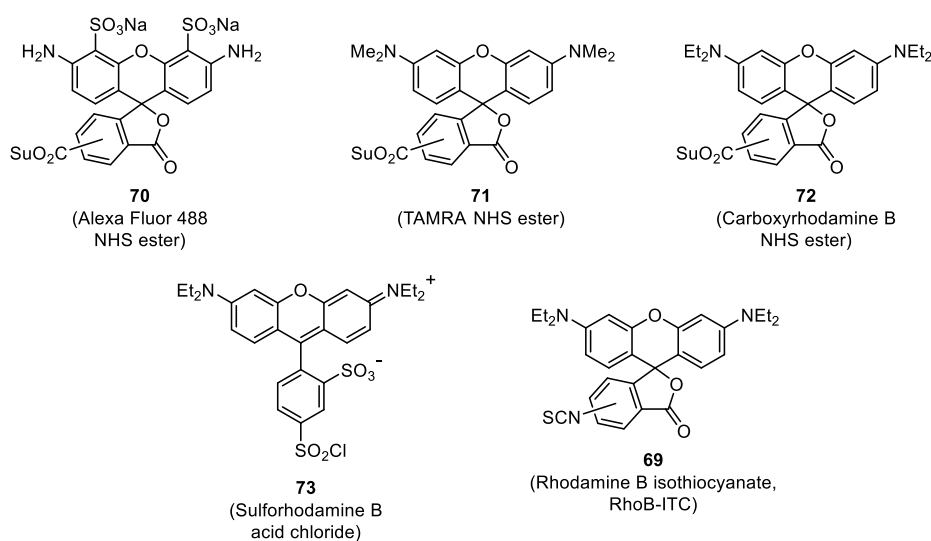


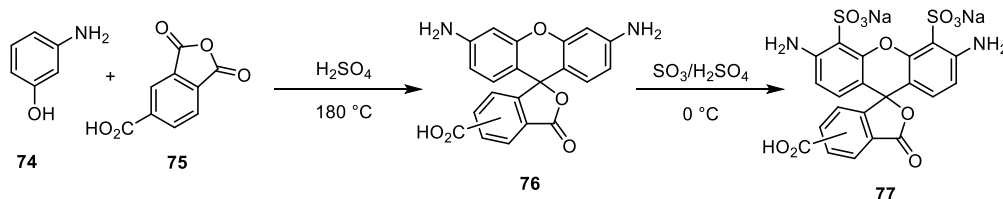
Figure 6-2: Candidate dyes for the labelling of DPs.



## 6.3. Fluorescent labelling of DPs

### 6.3.1. Alexa Fluor 488

Alexa Fluor 488 (AF488, **77**) is a sulfonated carboxyrhodamine. It is commercially available in the form of the corresponding *N*-hydroxysuccinimide ester **70**, however at > \$500/mg it is prohibitively expensive for the purpose of DP labelling. The dye can in principle be synthesized from readily available, cheap precursors as depicted in Scheme 6-2.<sup>354</sup>

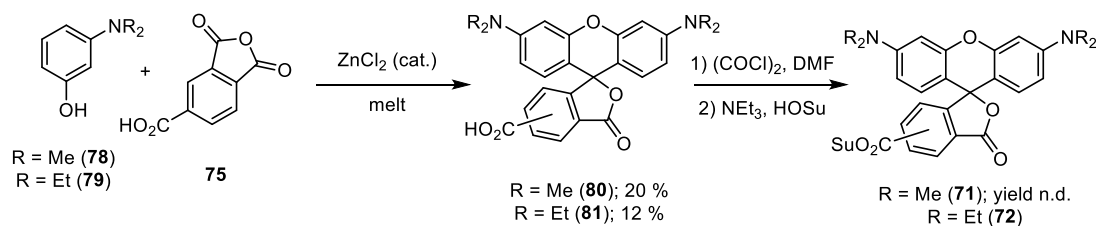


Scheme 6-2: Proposed synthesis of Alexa Fluor 488 **78**.

Starting from 3-aminophenol **74** and trimellitic anhydride **75**, the rhodamine precursor **76** (5(6)-carboxyrhodamine 110) is accessed by a Friedel-Crafts type reaction sequence catalyzed by strong acids. Subsequent sulfonation with oleum to Alexa Fluor 488 **77** would then be followed by the synthesis of the corresponding active ester **70**. The success with which this reaction sequence was executed in the course of this work is questionable: While spectroscopic characteristics (emission and absorption maxima) matched those reported in the literature,<sup>346</sup> yields were low and purification by flash chromatography proved difficult; The products obtained were mainly used as crudes. Attempts at labelling of  $\text{PG1}_n^{\text{NH}_3\text{TFA}}$  with **77** were initially encouraging (see Experimental, subsection 8.6.1), resulting in a soluble polymer with *ca.* 3 % of repeat units labelled as judged by UV/Vis spectroscopy. However, in preliminary wide-field and STED microscopy experiments of deposited AF-488-labelled  $\text{PG2}_n^{\text{NHBOC}}$ , a significant fluorescent background was detected, even after ultrafiltration of the labelled polymers. In all likelihood, the anionic nature of the sulfonated dye **77** resulted not exclusively in covalent labelling, but also in non-covalent inclusion of unreacted dye which survived chromatographic workup. Related to this, the “labelling density” as determined by UV/Vis spectroscopy did not correlate with the amount of **77** added to the reaction mixture initially. Neutral rhodamine-type dyes were employed in further attempts.

### 6.3.2. TAMRA & carboxyrhodamine B

5(6)-Carboxytetramethylrhodamine (TAMRA, **80**) and 5(6)-carboxytetraethylrhodamine (carboxyrhodamine B, **81**) may be obtained by simple condensation of trimellitic anhydride **75** and the suitable *N*-dialkylated 3-aminophenols **78** and **79**. These reactions proceeded in low yields (Scheme 6-3), but nevertheless provided synthetically useful quantities of both dyes.<sup>355</sup> The carboxyrhodamines were then either converted into the corresponding active esters **71** and **72** or used for labelling directly, employing activating agents such as TBTU (see Experimental, subsection 8.6.1, for details).



Scheme 6-3: Synthesis of carboxyrhodamines and their active esters

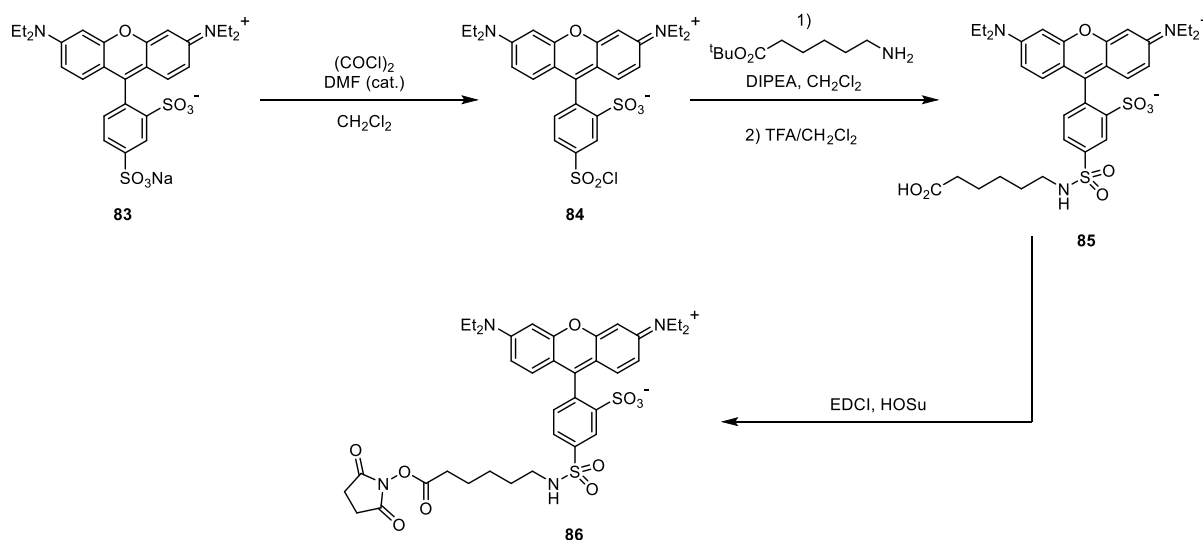
Both approaches were attempted for TAMRA in model reactions with  $\text{PG1}_{500}^{\text{NH}_3\text{TFA}}$ , followed by dendronization of the remaining amines and correspondingly affording labelled,  $g = 2$  DPs (TAMRA-PG2 $_{500}^{\text{NH}^{\text{Boc}}}$ ). When **71** was used, up to 30 % of RUs were successfully dye-labelled according to UV/Vis spectroscopy (the proportion was lower for *in situ* activation of **80** with TBTU), and the polymers remained well soluble after purification. However, labelling yields<sup>hh</sup> were low at < 20 % and somewhat inconsistent, permitting only limited control over the degree of labelling. In iSIM, the labelled DPs were found to aggregate quite significantly, with only occasional objects corresponding to the dimensions of single (short) polymer chains being in evidence. In combination with the low isolated yields of labelled DP, this suggests that some cross-linking may have taken place, possibly as a result of difunctionalization of the carboxylic acid moieties in the open form of TAMRA.

The labelling of DPs with carboxyrhodamines **80** or **81** directly or as their active esters **71** and **72** was abandoned due to greater success using rhodamine B isothiocyanate (see subsection 6.3.4), however the access to significant quantities of these dyes from simple precursors permitted their use in an exploratory study aimed at providing improved control over the degree of labelling, as presented in section 6.5.

<sup>hh</sup> The labelling yield is number of labelled amines relative to the amount of labelling agent employed. This value is independent from the isolated polymer yield.

### 6.3.3. Sulforhodamine B

Sulforhodamine B (**83**, also known as Acid Red 52 or Food Red 106) is readily available and comparatively cheap (~ 3 CHF/g). It can easily be converted into the corresponding sulfonyl chloride **84** by treatment with oxalyl chloride<sup>356</sup> (Scheme 6-4), however the direct labelling of *e.g.* PG1<sub>500</sub><sup>NH<sub>3</sub>TFA</sup> with **84** under basic conditions caused significant solubility issues: The polymer either precipitated directly from the reaction mixture, particularly for high *g*, or turned insoluble once solvent was removed after column chromatography.



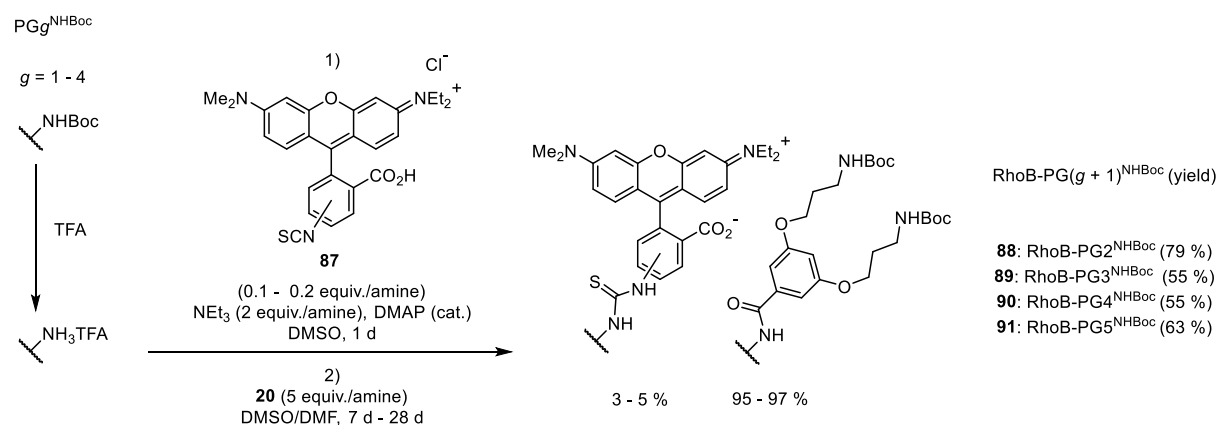
Scheme 6-4: Activation of Sulforhodamine B **83** to the sulfonyl chloride **84** and proposed subsequent synthesis of a tethered active ester **86**. The synthesis of **85** is described in the literature.<sup>356</sup>

The attachment of a solubilizing alkyl chain to the dye is straightforward,<sup>356</sup> granting access to active esters such as **86**. Due to the concurrent success of labelling with Rhodamine B isothiocyanate (6.3.4), labelling with Sulforhodamine B was not pursued further. It was not clear whether this approach – though permitting the variation of tethers – would ultimately be successful in improving the solubility of the polymer-dye conjugate. It appears likely that the poor solubility of the DP-dye conjugates is at least partially caused by the inherent zwitterionic nature of sulforhodamine B derivatives.

### 6.3.4. Rhodamine B isothiocyanate

Rhodamine B isothiocyanate (RhoB-ITC) can be obtained as the hydrochloride salt (**87**) from commercial suppliers at a cost of *ca.* 500-1000 CHF/g, which is cheap compared to other commercially available fluorescent labels. Amides are more hydrolytically stable than thioureas, particularly at high pH, resulting perhaps in somewhat reduced stability of the resulting conjugates. However, isothiocyanates compare favorably to active esters in terms of hydrolytic stability,<sup>357</sup> providing hope that labelling yields might be increased.

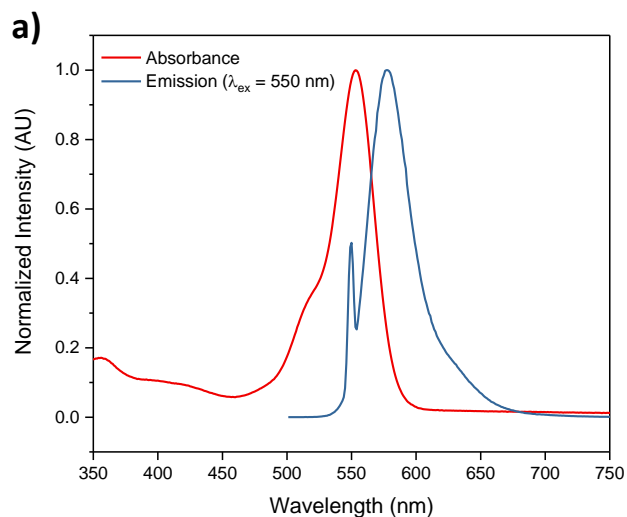
The treatment of  $PG1_{500}^{NH_3TFA}$  with **87** under basic conditions, followed by dendronization of the remaining amines with **20** afforded the desired labelled  $g = 2$  DP RhoB-PG2 $_{500}^{NHBoc}$ . The polymer was a well-soluble solid, obtained in better DP yield than was the case in previous labelling attempts. Encouragingly, the labelling yield obtained was higher than with other reagents and fairly consistent (~30 % relative to **87**). After some optimization, the reaction conditions shown in Scheme 6-5 were successfully used in the fluorescent labelling of DPs of  $g = 1 - 4$ .



Scheme 6-5: Labelling and subsequent dendronization of high- $P_n$  ( $\approx 10'000$ ) DPs of  $g = 1 - 4$ , affording the corresponding labelled DPs of  $g = 2 - 5$  with the indicated degrees of labelling.

The synthesis of RhoB-PG $g_{10'000}^{NHBoc}$  ( $g = 2 - 5$ ) proceeded with acceptable isolated DP yields (55 - 80 %) and labelling yields of approx. 20 - 30 %. While still fairly low, the labelling yields for all preliminary experiments with lower  $P_n$  DPs and those described in Scheme 6-5 were at least consistent, providing some control over the degree of labelling. The addition of significantly more than 0.2 equiv. of **87** per amine in tests using  $PG4_{500}^{NH_3TFA}$  resulted in solubility issues either during labelling and dendronization or after purification of the labelled polymers.

The polymers obtained by addition of 0.1 - 0.2 equiv. of **87** per amine (Scheme 6-5) however were well soluble and showed the desired bright fluorescence ( $\lambda_{max} = 553$  nm,  $\lambda_{em} = 578$  nm, Figure 6-3a). The achieved degree of labelling per unit mass was fairly constant over the explored range of  $g$ , corresponding to *ca.* 3 - 5 % of initially available amines (Figure 6-3b), which translates to an increasing linear labelling density due to the exponentially increasing number of amines (Figure 6-3b). Along with the expected increased stiffness of the DP chains up to  $g = 5$ , the highest  $g$  DPs therefore suggested themselves as targets for preliminary investigations by fluorescence microscopy.



**b)**

Sample	Labels/amine (%)	Labels/RU
RhoB-PG2 <sup>NHBoc</sup> <sub>10'000</sub> ( <b>89</b> )	3.3	0.07
RhoB-PG3 <sup>NHBoc</sup> <sub>10'000</sub> ( <b>90</b> )	4.5	0.18
RhoB-PG4 <sup>NHBoc</sup> <sub>10'000</sub> ( <b>91</b> )	4.6	0.37
RhoB-PG5 <sup>NHBoc</sup> <sub>10'000</sub> ( <b>92</b> )	3.1	0.5

Figure 6-3: a) Typical absorption ( $\lambda_{max} = 553$  nm) and emission spectra ( $\lambda_{ex} = 550$  nm,  $\lambda_{em} = 578$  nm) of a DP labelled with RhoB-ITC (RhoB-PG5<sup>NHBoc</sup><sub>10'000</sub>, 3.1 % of amines labelled). b) Labelling densities of the series of long-chain DP.

## 6.4. Fluorescence microscopy

Samples for fluorescence microscopy were usually prepared from a matrix containing *ca.* 10–20 % w/w of unlabeled  $\text{PG}g^{\text{NHBoc}}$  ( $g = 2 - 4$ :  $n \approx 10'000$ ;  $g = 5$ :  $n \approx 5'000$ , see Experimental, subsection 8.3.1, for their synthesis) in DMF or DMPU. The matrix polymers were prepared from the long-chain precursors also used in the synthesis of the labelled DPs **89** – **92** described in the previous section. The preparation of a matrix solution of  $\text{PG}5_{\sim 5'000}^{\text{NHBoc}}$ , in an attempt to accelerate dissolution by heating was the inciting incident for the investigation of “hot solvent” mediated scission (see subsection 3.5.1). Solutions of  $\text{PG}5_{\sim 5'000}^{\text{NHBoc}}$  in DMF were thereafter prepared at lower concentrations (< 12 % w/w in DMF) at room temperature, however lower  $g$  DPs were still heated in order to ensure homogeneity in the preparation of more concentrated and more viscous solutions. Labelled DPs were added to the matrix solutions of the same  $g$  such that a final ratio of labelled to unlabeled DPs of *ca.*  $1:10^5 - 1:10^6$  was obtained.<sup>329</sup>

Initial explorative fluorescence microscopy (iSIM) focused on RhoB- $\text{PG}5_{10'000}^{\text{NHBoc}}$  in  $\text{PG}5_{\sim 5'000}^{\text{NHBoc}}$ , but the labelled DPs were found to be fairly dim and concerns arose due to the discovery of swelling-induced main-chain scission of  $\text{PG}5_n^{\text{NHBoc}}$ , which may occur locally due to laser heating in prolonged exposures. Therefore, RhoB- $\text{PG}4_{10'000}^{\text{NHBoc}}$  in  $\text{PG}4_{10'000}^{\text{NHBoc}}$  was investigated more intensely afterwards, and gratifyingly the individual objects were found to be significantly brighter than was the case for RhoB- $\text{PG}5_{10'000}^{\text{NHBoc}}$ . Why exactly this should be the case can only be speculated on, in view of the lower average labelling density per RU for the  $g = 4$  DP: Taking the linear labelling densities listed in Figure 6-3b and assuming the DPs of  $g = 4$  and  $g = 5$  to be fully swollen cylinders of  $R = R_{\text{max}}$  (see subsection 1.6.3), average dye concentrations of  $1.8 \cdot 10^{-2} \text{ nm}^{-3}$  and  $1.6 \cdot 10^{-2} \text{ nm}^{-3}$  respectively are found.<sup>ii</sup> The effective label density per unit volume is therefore only slightly larger for RhoB- $\text{PG}4_{10'000}^{\text{NHBoc}}$ , suggesting the possibility of some fluorophore degradation in the case of RhoB- $\text{PG}5_{10'000}^{\text{NHBoc}}$ , perhaps due to longer dendronization reaction times. Since this estimate of dye density suggests roughly similar distances between individual fluorophores, it is unlikely that self-quenching in rhodamine pairs<sup>358</sup> is responsible for the reduced brilliance of RhoB- $\text{PG}5_{10'000}^{\text{NHBoc}}$ .

Only preliminary results from microscopy are available to date, and no quantitative evaluation of dynamic data has taken place as of yet. However, one significant observation of particular relevance to the previous speculations regarding swelling-induced main-chain scission was made: Thanks to the significantly higher thermal stability and the higher  $P_n$  of  $\text{PG}4_{10'000}^{\text{NHBoc}}$ , more concentrated and viscous solutions could be prepared than for  $\text{PG}5_{\sim 5'000}^{\text{NHBoc}}$ . In an attempt to further increase the viscosity of the solution  $\text{PG}4_{10'000}^{\text{NHBoc}}$ , and its labelled congener RhoB- $\text{PG}4_{10'000}^{\text{NHBoc}}$  were also dissolved in DMPU, which by itself is significantly more viscous ( $2.9 \text{ mPa s}$  at  $25 \text{ }^\circ\text{C}$ )<sup>359</sup> than DMF ( $0.8 \text{ mPa s}$  at  $25 \text{ }^\circ\text{C}$ ).<sup>175</sup> Even so, the solutions at similar DP concentrations (*ca.* 20 % w/w) were of surprisingly different viscosities: Viscous flow could be observed in DMF solutions (Figure 6-4a), whereas DMPU solutions behaved essentially like cross-linked gels and did not flow noticeably under gravity (Figure 6-4b).

---

<sup>ii</sup> It is unknown whether fluorophores are exposed on the surface or significantly backfolded; the assumptions made regarding DP geometry in the estimate of volumetric dye density are certainly simplistic.

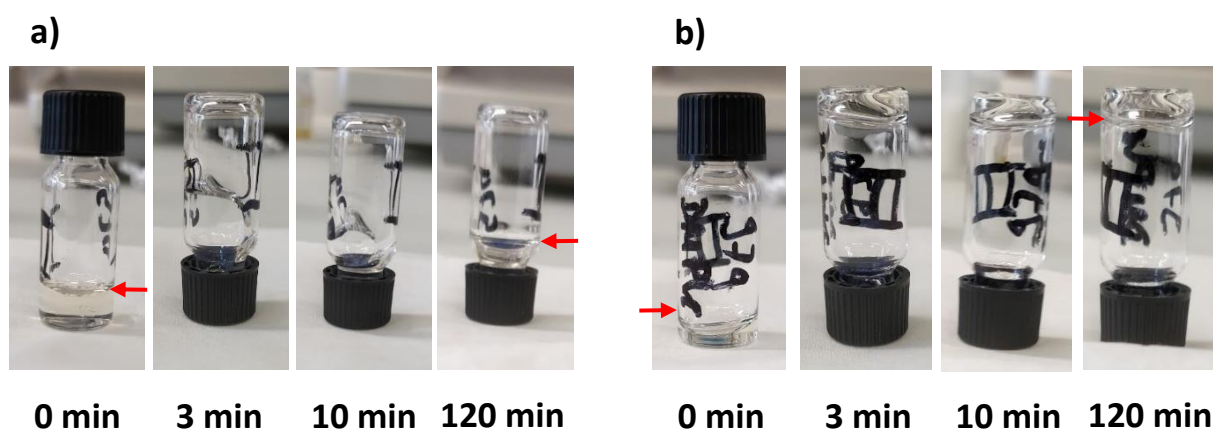


Figure 6-4: Photographs of samples of ca. 20 % w/w of  $PG4_{10'000}^{NHBoc}$  in a) DMF and b) DMPU, each showing the progressive flow or lack thereof 3 min, 10 min and 120 after overturning of the vials. The arrows indicate the liquid levels in the initial and final images.

The differences in macroscopic viscosity go along with significantly different appearances of RhoB- $PG4_{10'000}^{NHBoc}$  in iSIM: In DMF, the fluorescently labelled polymers generally appear as spherical or ellipsoidal particles (Figure 6-5a), and filamentous objects are found rarely. In the DMPU solutions of similar concentration however, labelled DPs appear as essentially straight rods (Figure 6-5b), likely representing fiber bundles of lengths up to several dozen  $\mu\text{m}$ .  $PG4_{10'000}^{NHBoc}$  in DMF – which is a fair swelling agent for this class of DPs – therefore appears to adopt coiled conformations, whereas DMPU seems to cause much stronger swelling, leading to a significant stiffening of the DP chains (compare chapter 3). As a result, in DMPU the labelled DPs take on a rod-like aspect, leading to the formation of the observed filamentous aggregates. This might also lead to gelation, as the effectively increased  $L_p$  of the DMPU-swollen rod-like  $PG4_{10'000}^{NHBoc}$  restricts the mobility within the solution and leads to a decrease in the gel point for equal chain lengths, an effect which has been observed previously with conventional polymers of differing stiffness.<sup>360</sup> This observation confirms the notion that DMPU is indeed a better swelling agent for this class of DPs than DMF.

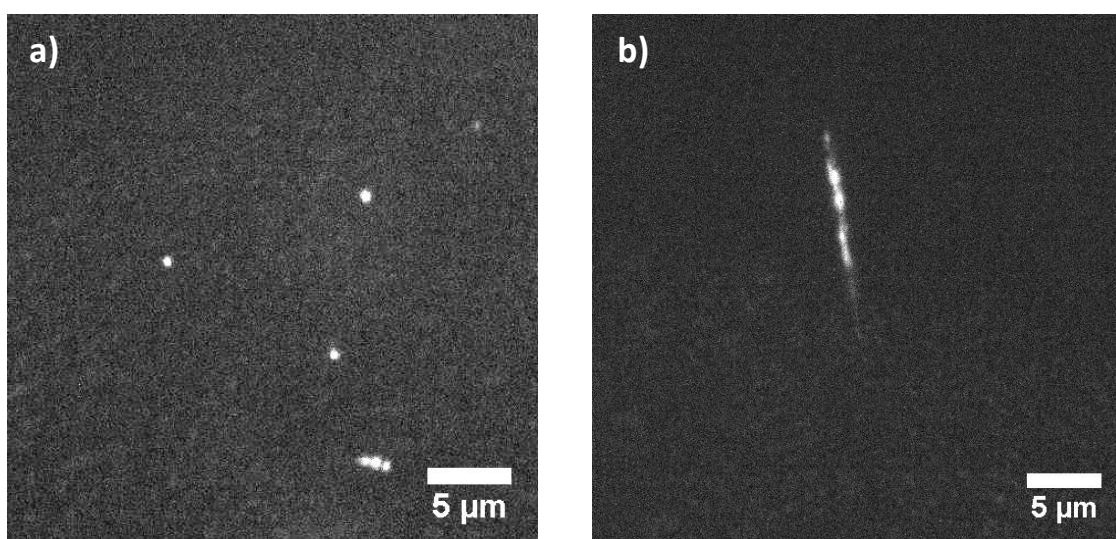


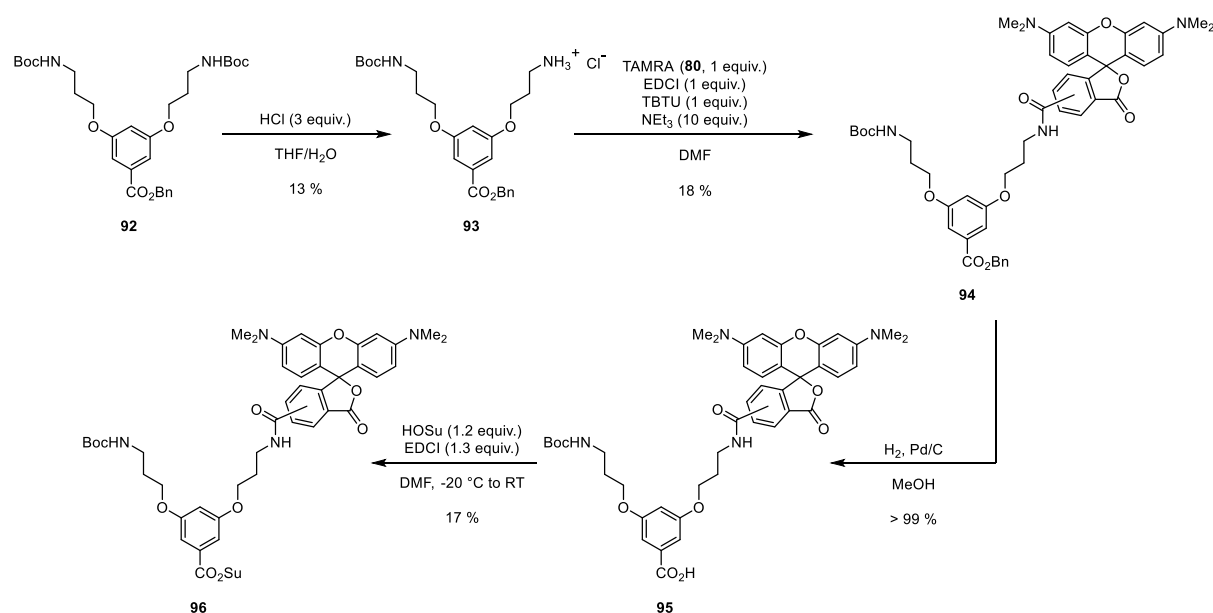
Figure 6-5: Typical fluorescence micrographs (iSIM stills, contrast enhanced in post-processing) of freshly prepared solutions of RhoB- $PG4_{10'000}^{NHBoc}/PG4_{10'000}^{NHBoc}$  of a) in DMF (measured at ca. 60 °C), showing mostly globular shapes; b) in DMPU (measured at RT) – similar rod-like aggregates were in evidence throughout the entire sample.

## 6.5. Towards better control over labelling density

The results presented in this section are the results of a semester project conducted by Ralph Werner (D-CHAB), conducted in the course of his Master's studies.

From a synthetic perspective, the lack of fine control over the degree of labelling achieved in subsection 6.3.4 is unsatisfactory. The labelling yields obtained using RhoB-ITC hydrochloride **87** were significantly higher and more consistent than those obtained *e.g.* with TAMRA-OSu **71**. Still, at *ca.* 30 % the labelling yield was low for the addition of a primary amine to an isothiocyanate, which may be expected to proceed with > 80 % yield. The cause for the inefficiency in the case of RhoB-ITC is not quite clear: It is possible that the commercial isothiocyanate had already partially degraded, although isothiocyanates are fairly hydrolytically stable in general; Two different batches of the reagent resulted in similar, fairly low labelling yields.

By attaching the rhodamine dye to a dendritic active ester similar to the dendronization agent **20**, much better labelling yields should be possible in principle, as the low-yielding conjugation step with the dye would occur not on the polymer but in a small molecule. This may also reduce the solubility issues encountered upon addition of large amounts of RhoB-ITC, which are suspected to arise from free dye. In a first step toward this goal, the synthesis of the half-labelled dendron **96** (Scheme 6-6) was undertaken. A dendron rather than some other solubilizing tether was selected in order to disturb the DP structure as little as possible, and the dendron was substituted with a fluorescent dye on only one amine group in order to avoid self-quenching in rhodamine pairs.<sup>358</sup> TAMRA **80** was used primarily in the exploration of the synthesis of a suitable dendron, as it was available in significant quantities from earlier attempts at direct labelling (see subsection 6.3.2)



Scheme 6-6: Synthesis of the TAMRA-bearing dendronization agent **96**.



Other routes to targets similar to **96** were pursued in parallel; Particularly, the use of 5(6)-carboxyrhodamine B (**81**) instead of **80** and the intermediate protection of the focal carboxylic acid group in the form of a methyl ester were attempted, but only the combination of TAMRA and intermediate protection in the form of a benzyl ester depicted in Scheme 6-6 were brought to completion.

The yields obtained were fairly low, particularly for the two ligation reactions employing EDCI: After synthetic work on this project had been concluded, it was realized that the cause for this likely lay in the use of an old batch of the coupling agent, which according to <sup>1</sup>H-NMR spectroscopy had degraded significantly. Upon optimization of conditions for the hemi-deprotection of **92**, and through the use of fresh coupling reagents, it appears likely that the overall yield of the reaction sequence in Scheme 6-6 (currently: 0.4 % over four steps) will improve significantly. The total amount of **96** prepared in this project (*ca.* 4 mg) was unfortunately not sufficient to allow for a study of DP labelling.

## 6.6. Summary & outlook

The fluorescent labelling of DPs with various rhodamine derivatives was attempted and ultimately successfully executed, using Rhodamine B isothiocyanate to covalently label  $\text{PG}g_{10'000}^{\text{NH}_3\text{TFA}}$  of  $g = 1 - 4$ . Successive dendronization with **20** afforded the desired labelled DPs  $\text{RhoB-PG}g_{10'000}^{\text{NHBoc}}$  of  $g = 2 - 5$  as well soluble, fluorescent polymers in good yields. Varying in the range of approx. 3 – 5 %, the proportion of labelled amines was fairly constant over all  $g$  values, though this translates to higher average labelling densities per unit length for the higher  $g$  DPs.

Combined with the corresponding unlabeled matrix polymers  $\text{PG}g_{10'000}^{\text{NHBoc}}$  ( $g = 2, 3, 4$ ) and  $\text{PG}5_{5'000}^{\text{NHBoc}}$ , concentrated samples (*ca.* 15 – 20 % w/w DP in DMF or DMPU) suitable for rheological investigations and for iSIM were prepared. Microscopy of the  $g = 5$  and  $g = 4$  labelled DPs in DMF showed generally well-dispersed, compact coils which tumbled in steady shear. Of the two samples,  $\text{RhoB-PG}4_{10'000}^{\text{NHBoc}}$  was found to be significantly brighter. In solutions of  $\text{RhoB-PG}4_{10'000}^{\text{NHBoc}}$  and  $\text{PG}4_{10'000}^{\text{NHBoc}}$  in DMPU, mostly large, bright filamentous aggregates were observed, and the bulk sample was gel-like rather than merely highly viscous. This suggests much stronger swelling of the DP chains in DMPU than in DMF, resulting in a coil-to-rod transformation.

With suitable samples at hand, further fluorescence microscopic and rheological studies are currently ongoing. Particularly the startup regime of mechanical deformation is of interest: Other than the tumbling observed in a steady shear field, the first moments of motion should allow for the observation of chain stretching and unfolding. The observed dependence of the overall shape of  $\text{PG}4_{10'000}^{\text{NHBoc}}$  on the swelling behavior may permit fine control over stiffness by varying solvent composition. It might be interesting to use not only good polar-aprotic swelling agents, but also more peripherally interacting solvents such as 1,2-dichlorobenzene. Additionally, the alteration of peripheral interactions may be of interest. This can be achieved *e.g.* by replacing peripheral NHBoc groups with <sup>t</sup>Bu-esters.

Yet higher labelling densities may be required for the fluorescence microscopic studies, particularly if samples prove to be of insufficient brightness to access short time scales – though higher labeling densities might be associated with increasing self-quenching of fluorophores. The synthesis of active esters such as **96** was demonstrated, though the reactions involved certainly require optimization in order to be viable for labelling. Active esters of similar structure to **96** are expected to reduce solubility issues, and to react near-quantitatively with deprotected DPs, thereby providing more accurate control over the degree of labelling. These factors are hoped to grant access to more densely labelled DPs, though due to currently insufficient quantities of **96** this has yet to be tested. All else failing, alternative dye candidates should also be considered. Particularly perylene diimide derivatives are an interesting option, as they are very photostable and can be modified in a more straightforward manner than is possible for rhodamines, permitting some adjustment of solubility.

## 7. Conclusions & Outlook

This thesis has mainly been concerned with high-generation dendronized polymers ( $g = 4 - 8$ ). Dendritic structures in general and DPs in particular are only rarely investigated up to such high values of  $g$ , as many of the desired dendritic effects (well-defined shape, large number of peripheral groups *etc.*) become relevant at lower  $g$ . The main goal of the work presented here was however not merely to push DP synthesis to ever higher generations, but to investigate the range at and above  $g_{\max}$  (for  $\text{PG}g_n^{\text{NHBoc}}$ :  $g_{\max} \approx 6 - 7$ ) and the consequences arising from increasing thickness and steric congestion.

Doing so has required significant synthetic effort: DPs of up to  $g = 9$  had been prepared prior to the work presented here, but their preparation involved synthetic steps (" $g + 2$ " dendronization reactions) which resulted in DPs of  $g > 5$  with very many defects.<sup>172,174,189</sup> It was realized later that this is far from optimal: DPs bearing so many defects are not dendritic, and the concept of  $g_{\max}$  is not applicable. Those polymers deviated increasingly more from the ideal, cylindrical shape instead of approaching it,<sup>174</sup> and instead of becoming ever more densely packed, their dendritic branchwork became more accessible with increasing  $g$ .<sup>188</sup>

One main achievement of the work presented in this thesis lies in the preparation of DPs with high structural perfection (chapter 2) by circumventing main-chain scission at  $g = 5$ . This was based on the use of protecting groups and corresponding deprotection chemistries differing from the standard route involving acid-mediated cleavage of NHBoc. The strategy behind these attempts was the synthesis of a charge-neutral intermediate  $\text{PG}5_n^{\text{NH}_2}$ , in order to avoid the suspected unstable polyelectrolyte  $\text{PG}5_n^{\text{NH}_3\text{TFA}}$ . The Alloc protecting group proved suitable for this purpose, and although the use of a Pd catalyst for deprotection complicated matters, a protocol for the generation of  $\text{PG}5_n^{\text{NH}_2}$  was developed. Successive dendronization afforded  $\text{PG}6_{500}^{\text{NHBoc}}$  without any intermediate chain degradation and with unprecedented structural perfection. From  $\text{PG}6_{500}^{\text{NHBoc}}$ , the synthesis of  $\text{PG}7_{500}^{\text{NHBoc}}$  and  $\text{PG}8_{500}^{\text{NHBoc}}$  using more conventional NHBoc-based chemistry was possible. The syntheses described here have afforded useful quantities of material ( $> 200$  mg for each generation), and all steps along this path are readily scalable.

The  $g > 5$  DPs prepared using exclusively " $g + 1$ " synthetic steps feature very few defects and likely represent the closest approximation of  $g_{\max}$  achieved in any dendritic system, considering that dendrimer syntheses usually suffer from high defect frequencies early on. This prompted an in-depth consideration of  $g_{\max}$  in the context of the applied divergent chemistry: The high structural perfection detected in defect labelling of  $g > g_{\max}$  DPs is a consequence of steric congestion, and not of the actual absence of defects. This led to a more reactant-centered view of  $g_{\max}$ : Most reactants are larger than typical solvent molecules and may need to be solvated in order for reactions to occur. The comparison of molar masses derived from defect labelling with the theoretically possible values strongly suggests that reactants are either precluded from reacting with remaining amines or even sequestered from the DP structure entirely starting at  $g_{\max} \approx 6 - 7$ . Impenetrably dense packing as proposed initially is likely unfeasible using solution-phase chemistry – more realistically, molecules above  $g_{\max}$  are *relatively* densely packed, excluding some reagents and those solvents which interact mostly peripherally, while permitting peripheral swelling with good swelling agents.

The swelling of the dendritic periphery turned out to be of paramount importance in another context: The work presented in chapter 3 has demonstrated that swelling is likely the cause of main-chain scission occurring (mostly) in DPs of  $g = 5$ . This realization arose from investigations into charge-induced main-chain scission and the newly found "hot solvent" mediated mode of DP degradation.

Swelling as a cause for main-chain scission in particular explains the strong  $g$  dependence of DP chain scission: DPs of  $g = 1 - 4$  are not sufficiently sterically congested for solvent uptake to cause much tension. The DPs of  $g = 5$  appear to feature a balance of accessibility and inherent steric congestion which causes the limited swelling to exert sufficient forces on the DP backbone for it to undergo scission. DPs of  $g > 5$  are too densely substituted for even good swelling agents to penetrate much beyond the dendritic periphery. These results also underlined the importance of structural perfection: Defect-riddled DPs from “ $g + 2$ ” routes suffered limited “hot solvent” mediated degradation, whereas the structurally more perfect DPs from the strictly “ $g + 1$ ” pathway described in chapter 2 remained intact. This is a direct consequence of very dense steric crowding, leading to the exclusion of even good swelling agents from the DP interior.

In the context of the cryo-TEM based analyses of individual DP chain conformations presented in chapter 4, swelling is a factor of interest: 1,4-dioxane is a fairly good solvent and even a moderately good swelling agent.<sup>98</sup> These novel investigations of individual, synthetic polymer chains in the native state are enabled by the particular thickness and compactness of DPs. The focus of the present results lay on exploring the possibilities arising from the availability of explicit, three-dimensional polymer conformations. This has permitted facile access to information which is quite difficult to obtain from scattering data, such as *e.g.* the behavior at length scales below the DP diameter. It would be intriguing to investigate the  $g$ - and solvent-dependent behavior of DPs in more breadth. Parameters of interest include  $g$  and structural perfection of the DPs, and particularly in light of the results presented in chapter 3 also the solvent. This work is hoped to help establish cryo-ET as a tool for the investigation of soft matter on the nanometer scale: With modern electron optics and detectors, similar investigations are in reach for more standard polymer molecules, as well.

Moreover, electron tomography might provide the solution to an unresolved issue discussed in chapter 5: The determination of the molecular density of DPs (and similar soft, polydisperse nanoparticles) is inherently difficult. None of the four methods of assessing the density of DPs (envelope density measurement, qSTEM, combined SEM/TEM measurements and SAXS) is capable of delivering molecular density without external input or strong assumptions. Specifically, no method simultaneously provides all the requisite molar mass and geometric parameters that flow into the calculation of DP density. Significant additional uncertainty arose from the use of old, structurally deficient DP samples, which may in some cases explain the extraordinarily high density values obtained. However, by using the more defect-free samples prepared in chapter 2, and by employing methods providing geometric and molar mass information from one specimen, it may be possible to unravel this puzzle in the future. A strong candidate for such a method is qSTEM, coupled with electron tomography of the same samples of deposited DPs, affording molar mass and cross-section geometry of the chains, respectively.

After these detours into analytics, chapter 6 presents a return to synthetic chemistry, namely the fluorescent labelling of high  $P_n$  DPs. The melt rheology of DPs has been explored thoroughly, at least for low  $g$  DPs.<sup>176,179,323</sup> Their solution rheology is largely uncharted territory as of yet, but intriguing dependences of their rheology on the swelling of the DP branchwork have become evident already. With suitable long-chain samples and labelled DPs at hand, these interesting phenomena are currently being explored using fluorescence microscopy and solution rheology.

A main concern of the investigations summarized above are the effects of approaching and surpassing  $g_{\max}$ . This has required a lot of synthetic effort – as is the case with the synthesis of any high  $g$  dendritic system. Likely, it is the synthesis of DPs which limits the interest they attract in the wider research community: The peptide-based chemistry involved in the synthesis of  $\text{PG}g_n^X$  is attractively

simple, highly modular and produces molecules with many functional groups and a well-defined shape, but the many synthetic steps and long reaction times are the main factors which reduce the attractiveness of high  $g$  DPs.

Considering the scaling arguments discussed in chapter 1, it might therefore be beneficial to combine the advantageous features of the divergent methodology used throughout this work with threefold branching, *e.g.* by using a branching unit based on gallic acid (**99**) instead of  $\alpha$ -resorcylic acid (**98**) as shown in Figure 7-1a. The preparation of a corresponding DP class (*e.g.* **97**) should be possible, using already established chemistry.<sup>101,361,362</sup>

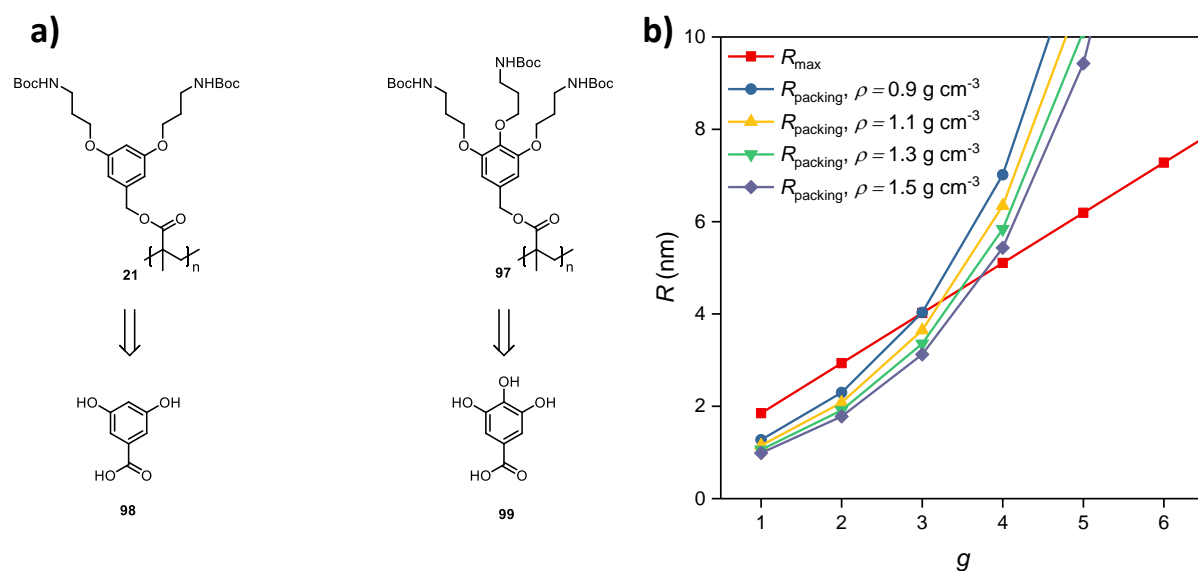


Figure 7-1: a) Comparison of  $\text{PGg}_n^{\text{NHBoc}}$  DPs and the fundamental branched precursor,  $\alpha$ -resorcylic acid **98**, with a prospective class of DPs (*e.g.* **97**) based on gallic acid **99** which might provide more rapid access to  $g_{\max}$  structures. b)  $g_{\max}$  plot for DPs in the threefold-branching series containing **97**.

For a class of DPs based on **97**,  $g_{\max} \approx 3$  (Figure 7-1b) is even lower than it is for  $\text{PGg}_n^{\text{NHBoc}}$ , requiring correspondingly fewer synthetic steps to access a molecule of ultimate steric congestion. Meanwhile, the synthetic tools developed in a large body of prior work<sup>101,193,363–365</sup> and in this thesis may be used, requiring only minimal modifications. Such a facilitated and more rapid access to dendritic molecules at and above  $g_{\max}$  may inspire yet more in-depth and systematic investigations. One main lesson gained from this work is that such further work requires particular attention to structural perfection. Substantial efforts should be made to improve the molar mass determination of DPs, *e.g.* by MALDI-TOF-MS or – if appropriate analysis can be developed to account for the particularities of dealing with thick molecules – by scattering methods. Surely, the work presented here has merely surveyed the surface of a deep pond, and there are many more intriguing consequences of increasing thickness, steric crowding and tight intramolecular packing left to uncover.

## 8. Experimental

### 8.1. General materials & methods

#### 8.1.1. Syntheses

Chemicals employed for syntheses were purchased from commercial suppliers (ABCR, Acros, Alfa Aesar, Fisher, Fluorochem, Sigma-Aldrich, TCI, Iris Biochem) and used without further purification unless specified otherwise.

**16** and **20** (DG1<sup>NHBoc</sup>) were obtained from Synwit Technology Co. Ltd. (Beijing); Pd(PPh<sub>3</sub>)<sub>4</sub> (99.9 % trace metal basis, Acros) was stored at 4 °C under N<sub>2</sub> and used only as long as the initial yellow to dark-yellow color had not significantly changed; *N,N'*-Dimethylbarbituric acid (DMBA, 99 %, < 6 % water, Alfa Aesar) was recrystallized from THF and stored in a desiccator before use; 1,4-Dioxane (analytical reagent grade, stabilized, Fisher) for use in the lyophilization of polymers was distilled by rotary evaporation prior to use; Dry solvents were either obtained from commercial sources (Acros AcroSeal bottles containing 4 Å mol sieves: DMF, DMSO, NMP, DMAc, MeCN, Toluene; Sigma Aldrich SureSeal bottles: DMPU) or prepared from HPLC grade solvents (methylene chloride and THF, Fisher) by storing over freshly activated 4 Å mol sieves for at least 24 h before use; Methacryloyl chloride (97 % stabilized, Sigma Aldrich) was vacuum distilled from hydroquinone at 10 mbar, T ≤ 40 °C and stored under N<sub>2</sub> at -20 °C before use; Solvents used for standard workup procedures (EtOAc, hexane, acetone, methylene chloride, Et<sub>2</sub>O; used for extractions, precipitations, column chromatography, and recrystallizations) were usually obtained in technical grade (Thommen Furler AG) and distilled by rotary evaporation, with the exception of Et<sub>2</sub>O which was used as received.

Where the exclusion of oxygen and/or moisture is indicated in an experimental procedure, standard Schlenk glassware and air-free handling techniques were employed unless specified otherwise, and the corresponding reactions were conducted under dry N<sub>2</sub>. Where removal of solvent is indicated, rotary evaporation at 40 – 50 °C was used unless otherwise noted. Lyophilization was conducted either using a vacuum manifold and a liquid nitrogen-cooled condenser or using a dedicated freeze dryer (Alpha 2-4 LSC, Martin Christ Gefriertrocknungsanlagen).

For purification by flash column chromatography, 230-400 mesh silica gel (SiliFlash P60, SiliCycle or high purity grade, Sigma-Aldrich) was used. For thin-layer chromatography, aluminium plates pre-coated with silica gel and a fluorescent additive (TLC Silica gel 60 F<sub>254</sub>, Merck) were used, cut into strips of ca. 6 – 7 cm in height. After development, spots were visualized with the help of a UV lamp (245 or 366 nm, CAMAG) and/or staining solutions (KMnO<sub>4</sub>, vanillin, *p*-anisaldehyde, ninhydrin).

### 8.1.2. Analytics

**NMR** spectra were measured using a 300 MHz magnet (Avance 300, Bruker) equipped with an autosampler (SampleXpress, Bruker). Deuterated solvents for  $^1\text{H}$ -NMR ( $\text{CDCl}_3$ ,  $\text{DMSO-}d_6$ ,  $\text{D}_2\text{O}$ ,  $\text{TCE-}d_2$ ,  $\text{TFA-}d_4$ ) were obtained from commercial suppliers (Cambridge Isotopes or ARMAR Chemicals). Spectra were evaluated using the MestReNova software suite (Mestrelab Research).  $^{13}\text{C}$ -NMR spectra were assigned with the help of 2D experiments (HSQC, HMBC) where necessary. Chemical shifts are given in ppm relative to tetramethylsilane and were referenced using residual solvent protons. Peak splittings are noted as follows: s = singlet, d = doublet, t = triplet, q = quadruplet, m = multiplet, b = broad. **UV/Vis spectra** were recorded on a 2-beam UV/Vis/NIR spectrophotometer (V-670, Jasco) using 2 mm or 10 mm fused quartz cuvettes (Hellma); samples were typically prepared using analytical or HPLC grade solvents. **Fluorescence spectra** were recorded at right angle on a Fluorolog 2 (SPEX) using 1 cm fused quartz fluorescence cuvettes (Hellma).

**Mass spectrometry and elemental analyses** were conducted by the Molecular and Biomolecular Analysis Service (MoBiAS) at the Laboratory of Organic Chemistry (ETH Zurich). HR-ESI-MS (maXis ESI-QTOF, Bruker Daltonics) was used for compound identification of small molecules and MALDI-TOF-MS (Ultraflex II, Bruker Daltonics) was employed for the analysis of DP chain scission products as well as for rhodamine-B labelled dendrons, using DCTB+Na as the matrix. **Melting points** were measured using a melting point determination apparatus (B-540, Büchi).

Samples for **GPC** were prepared by dissolution of the polymer in the eluent containing a small amount of toluene (*ca.* 0.1 % v/v) as a flow marker, resulting in concentrations of *ca.* 1 mg L<sup>-1</sup> of polymer. The samples were shaken at 35 °C ( $\text{CHCl}_3$ ) or 45 °C (DMF + 0.1 % LiBr) for at least 1 h on an orbital shaker (PL-SP 260, Polymer Laboratories), then filtered through 0.45  $\mu\text{m}$  pore size Teflon syringe filters into screw-cap vials. Measurements were conducted using either of two Viscotek GPCMax systems (Malvern/Viscotek) equipped with triple-detector arrays (DRI, intrinsic viscosity, right- and low-angle light scattering; Viscotek TDA, Malvern/Viscotek), both fitted with a switching valve enabling the use of two column sets. One system was operated with  $\text{CHCl}_3$  as the eluent at 35 °C and was equipped with a column set covering intermediate (2 x PLGel MIXED-B, Polymer Laboratories) and high molar masses (2 x PLGel MIXED-A, Polymer Laboratories), as well as an additional variable-wavelength UV/Vis detector (UV-Detector 2500, Viscotek). The other was operated with DMF containing 1 g L<sup>-1</sup> LiBr as the eluent and equipped with column sets covering low (1x PLGel MIXED-D, Polymer Laboratories) and high molar masses (2x D-5000, Malvern). Typically, 100  $\mu\text{L}$  of sample were injected. Where relevant, molar masses were determined from universal calibration, established using monodisperse polymer standards ( $\text{CHCl}_3$ : PS; DMF: PMMA; Polymer Laboratories). **Thermogravimetric analyses** were performed on a Q500 thermogravimetric analyzer (TA Instruments) under  $\text{N}_2$  atmosphere using a platinum pan. The base heating rate was set to 20 °C min<sup>-1</sup> unless otherwise noted. **Differential scanning calorimetry** was performed on a Q1000 differential scanning calorimeter (TA Instruments) equipped with a refrigerated cooling unit (TA Instruments) using aluminium pans, crimped tight but with a hole in the pan lid in order to accommodate gas formation. **Dynamic light scattering (DLS)** measurements were performed on a Zetasizer Nano (Malvern) using analytical grade MeOH (Fisher) and disposable polystyrene semimicro-cuvettes (VWR). A uniform refractive index of 1.51 was assumed for all polymers. DP concentrations of *ca.* 0.1 mg mL<sup>-1</sup> were used for all samples.

Samples for **atomic force microscopy** were prepared by drop-casting solutions of DPs (typically 0.5 – 20 mg L<sup>-1</sup> in methylene chloride or MeOH) onto freshly cleaved substrates (mica or HOPG, obtained from Plano GmbH) affixed to 12 mm or 20 mm diameter magnetic specimen disks (Ted Pella Inc.). Microscopy was performed either on a NanoScope Multimode IIIa (Digital Instruments) using a 10 μm x 10 μm “E” scanner (Digital Instruments) or on a Dimension Icon AFM (Bruker), in both cases using silicon cantilevers with a typical resonance frequency of 300 MHz and a typical spring constant of 26 N m<sup>-1</sup> (OMCL-160TS-R3, Olympus). Images were processed using NanoScope Analysis (Bruker), FiberApp,<sup>366</sup> and Fiji.<sup>367</sup>



## 8.2. Experimental details for chapter 2: Overcoming main-chain scission

### 8.2.1. Syntheses

The following compounds used in this subsection were prepared according to literature procedures: 3,5-bis(3-(*tert*-butyloxycarbonylamido)propyloxy)benzoyl methacrylate (**18**);<sup>168</sup> 3,5-bis(3-(*tert*-butyloxy-carbonylamido)propyloxy) benzoic acid (**19**);<sup>368</sup> 2,7-di-*tert*-butyl-9-fluorenylmethanol (**46**);<sup>201</sup> allyl 1*H*-pyrrole-1-carboxylate (**52**);<sup>220</sup> *N,N*-diethyl-(2-phenyldiazenyl)thioformamide (**101**).<sup>225</sup>

#### General Procedure A: Labelling of unreacted amines with Sanger's reagent

For the determination of functional group conversion  $\chi$  after dendronization, a modification of the previously published method<sup>364</sup> was used. A sample of the polymer (20 – 30 mg) was dissolved in TCE (2 mL). 2 mL of a solution of 2,4-dinitrofluorobenzene in TCE (25 mg mL<sup>-1</sup>) and 5 % aq. NaHCO<sub>3</sub> (4 mL) were added and the mixture was stirred vigorously at 50 °C overnight. The resulting biphasic yellow mixture was then diluted with methylene chloride (30 mL), washed with 5 % aq. NaHCO<sub>3</sub> (5 x 30 mL), then brine (30 mL), dried over Na<sub>2</sub>SO<sub>4</sub> and concentrated to a volume of ca. 1 mL. The solution was transferred to a 15 mL centrifuge tube and precipitated with Et<sub>2</sub>O (ca. 12 mL). The precipitate was sedimented by centrifugation (5 min at 4000 RPM). The polymer was precipitated twice more from little methylene chloride, then lyophilized from freshly distilled dioxane. The concentration of labelled amines was determined by measuring the absorption at 360 nm in TCE ( $\epsilon_{360} = 16400 \text{ L mol}^{-1} \text{ cm}^{-1}$ ). The functional group conversion  $\chi$  was calculated recursively according to Eq. 8-1 for routes **A** and **C** and according to Eq. 8-2 for polymers synthesized using route **B** (see chapter 3).<sup>150</sup> These relationships take the structure perfection of the precursor polymers into account.

$$\chi_{g+1}(g) = \frac{n_g + 1}{2(n_{g-1} + 1)}$$

Eq. 8-1

$$\chi_{g+2}(g) = \frac{n_g + 1}{4(n_{g-2} + 1)}$$

Eq. 8-2

#### General Procedure B: Syntheses of carboxylic acids by saponification of methyl esters

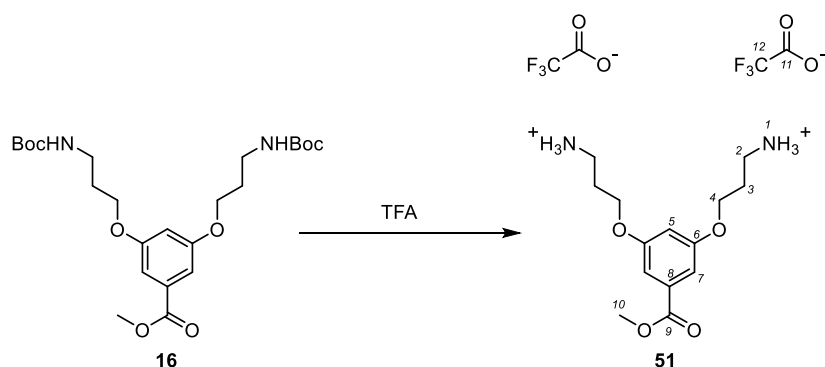
The starting methyl ester and KOH or NaOH (ca. 2 equiv.) were dissolved in MeOH/H<sub>2</sub>O 3:1 (ca. 20 mL per 1 g starting material) and refluxed for 3 h. The reaction mixture was then cooled to RT and MeOH was removed by evaporation. The resulting solution was diluted ca. 3x with water and cooled in an ice bath. Under vigorous stirring, the mixture was adjusted to pH  $\approx$  4 by slow addition of 0.5 M aq. HCl. The resulting precipitate was filtered off, washed thoroughly with water and dried in vacuum.

#### General Procedure C: Syntheses of *N*-hydroxysuccinimide esters DG1<sup>x</sup>

To a solution of the starting material and *N*-hydroxysuccinimide (1.1 equiv.) in dry methylene chloride (ca. 30 mL per 1 g starting material), DCC (1.2 equiv.) was added while stirring in an ice bath. The reaction mixture was allowed to warm to RT and stirred under N<sub>2</sub> overnight. The resulting white slurry was filtered, then concentrated in vacuum. The resulting oil or solid was dissolved in little MeCN at 40 °C, then cooled to 0 °C for at least 1 h and filtered. This procedure was repeated until no more

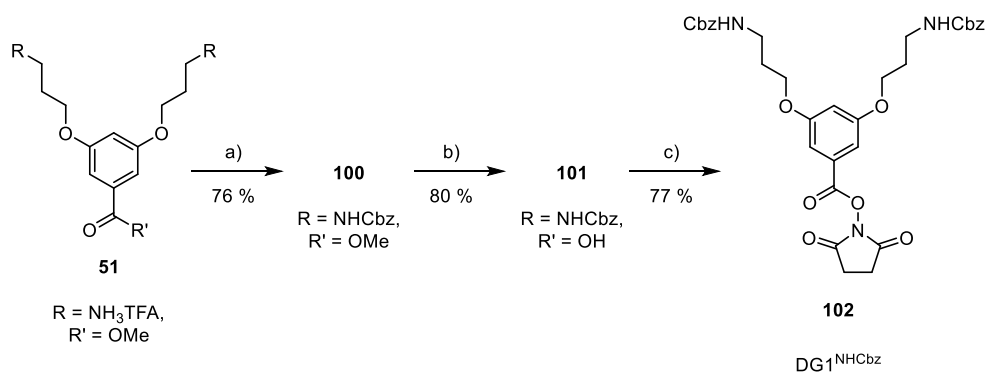
crystals of dicyclohexylurea formed after cooling, then the solution was concentrated, and the product was purified by column chromatography.

### Synthesis of methyl 3,5-bis(3-aminopropoxy)benzoate ditrifluoroacetate (**51**)



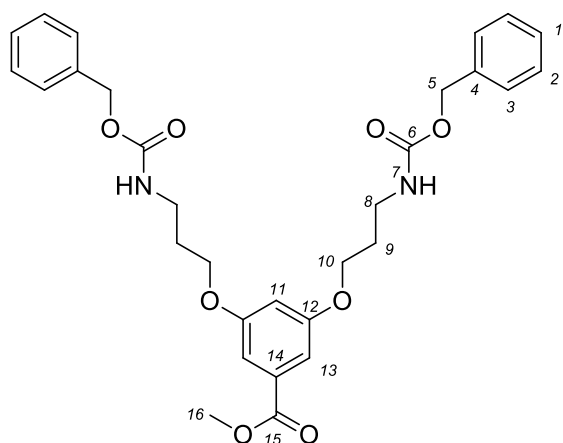
To **16** (35.06 g, 72.7 mmol) in an ice-cooled 500 mL round-bottom flask, TFA (100 g, 0.88 mol, 12 equiv.) was added slowly under vigorous stirring. After stirring at room temperature for 4 h, the flask was again cooled in an ice bath and MeOH (250 mL) was

added in portions of 50 mL. The solution was concentrated in vacuum to ca. 50 mL and more MeOH (100 mL) was added. The resulting solution was evaporated to dryness, affording the desired product as an off-white solid (**51**, 37 g, quantitative). <sup>1</sup>H-NMR (300 MHz, DMSO-d<sub>6</sub>, 298 K): 7.93 (s (b), 6H, 1), 7.10 (d, *J* = 2.2 Hz, 2H, 7), 6.80 (t, *J* = 2.3 Hz, 1H, 5), 4.10 (t, *J* = 6.1 Hz, 4H, 4), 3.84 (s, 3H, 10), 2.97 (m, 4H, 2), 2.01 (m, 4H, 3). <sup>19</sup>F-NMR (282 MHz, DMSO-d<sub>6</sub>, 298 K): -73.65 (s, 6F, 12); <sup>13</sup>C-NMR (76 MHz, DMSO-d<sub>6</sub>, 298 K): 165.89 (9), 159.25 (6), 158.62 (q, *J*<sub>C-F</sub> = 31.7 Hz, 11), 131.61 (8), 117.10 (q, *J*<sub>C-F</sub> = 298.8 Hz, 12), 107.54 (5), 106.38 (7), 65.15 (4), 52.31 (10), 36.26 (2), 26.80 (3). Melting point: 146-147 °C. HR-MS: Calc. C<sub>14</sub>H<sub>22</sub>N<sub>2</sub>NaO<sub>4</sub> (M (free base) + Na<sup>+</sup>): *m/z* = 305.1472; found: *m/z* = 305.1470. Elemental analysis: Calc. 42.36 % C, 4.74 % H, 5.4 % N; found 42.11 % C, 4.74 % H, 5.4 % N.



Scheme 8-1: Synthesis of **102** (DG1<sup>NHCbz</sup>): a) PhCH<sub>2</sub>(C=O)Cl, K<sub>2</sub>CO<sub>3</sub>, H<sub>2</sub>O/THF, 0 °C to RT; b) KOH, MeOH/H<sub>2</sub>O 3:1, reflux; c) DCC, N-hydroxysuccinimide, DCM, 0 °C to RT.

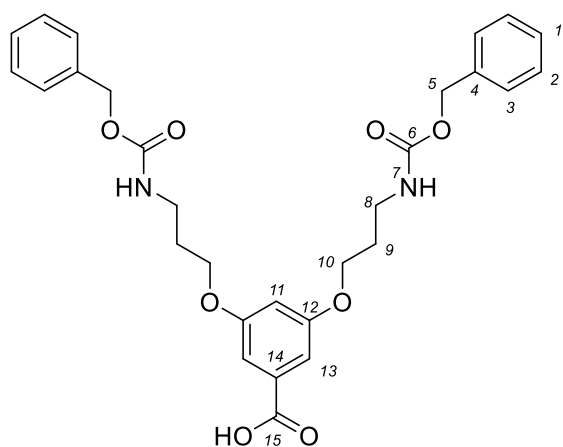
### Synthesis of methyl 3,5-bis(3-(benzyloxycarbonylamido)propyloxy)benzoate (**100**)



**51** (4.00 g, 7.8 mmol) was dissolved in water (20 mL).  $K_2CO_3$  (4.42 g, 32 mmol, 4.1 equiv.) was added, followed by THF (100 mL). The resulting solution was cooled to 0 °C in an ice bath and benzyl chloroformate (3.4 mL, 119 mmol, 3 equiv.) was added slowly. After completion of addition, the resulting solution was stirred at RT for 3 h. The solution was concentrated in vacuum, diluted with EtOAc (150 mL) and washed with water (2 x 100 mL) and brine (100 mL), then dried over  $MgSO_4$ . Purification by column chromatography

(EtOAc/hexane 3:5) afforded **100** as a colorless solid (3.27 g, 76 %).  $^1H$ -NMR (300 MHz,  $CDCl_3$ , 298 K): 7.34 (m, 10H, 1-3), 7.16 (d,  $J = 2.3$  Hz, 2H, 13), 6.61 (t,  $J = 2.3$  Hz, 1H, 11), 5.10 (s, 4H, 5), 4.98 (m (b), 2H, 7), 4.03 (t,  $J = 5.9$  Hz, 4H, 10), 3.89 (s, 3H, 16), 3.40 (m, 4H, 8), 2.00 (m, 4H, 9).  $^{13}C$ -NMR (76 MHz,  $CDCl_3$ , 298 K): 166.84 (15), 159.87 (12), 156.56 (6), 136.68 (4), 132.19 (14), 128.65 (1-3), 128.24 (1-3), 108.05 (13), 106.76 (11), 66.83 (5), 66.12 (10), 52.39 (16), 38.60 (8), 29.48 (9). Melting point: 104-105 °C. HR-MS: Calc.  $C_{30}H_{35}N_2O_8$  ( $M + H^+$ ):  $m/z = 551.2388$ ; found:  $m/z = 551.2382$ . Elemental analysis: Calc. 65.30 % C, 6.22 % H, 5.09 % N, 23.25 % O; found 65.30 % C, 6.22 % H, 4.98 % N, 23.33 % O.

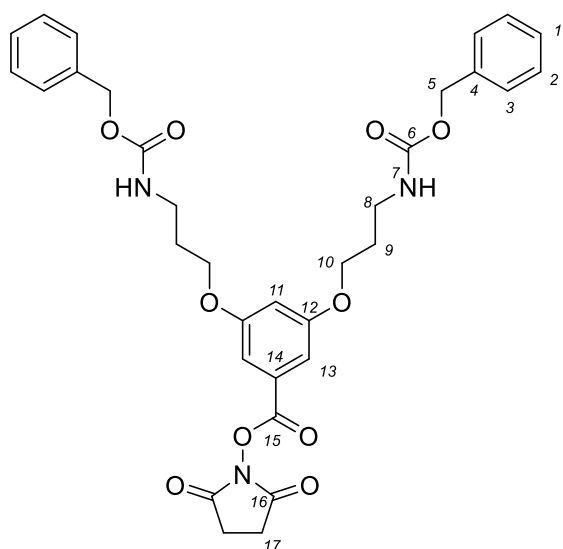
### Synthesis of 3,5-bis(3-(benzyloxycarbonylamido)propyloxy) benzoic acid (**101**)



Prepared from **100** (3.18 g, 37 mmol) according to general procedure B using KOH (0.67 g, 2 equiv.), affording **101** as a colorless solid (2.51 g, 80 %).  $^1H$ -NMR (300 MHz,  $DMSO-d_6$ , 298 K): 7.34 (m, 12H, 1-3, 7), 7.05 (d,  $J = 2.3$  Hz, 2H, 13), 6.61 (t (b),  $J = 2.7$  Hz, 1H, 11), 5.01 (s, 4H, 5), 4.98 (m (b), 2H, 7), 4.99 (t,  $J = 6.2$  Hz, 4H, 10), 3.17 (m, 4H, 8), 1.86 (m, 4H, 9).  $^{13}C$ -NMR (76 MHz,  $CDCl_3$ , 298 K):  $^{13}C$  NMR (76 MHz, DMSO)  $\delta$  167.56 (15), 159.42 (12), 156.17 (6), 137.23 (4), 135.80 (14), 128.34 (1-3), 127.73 (1-3), 107.37 (13), 104.80 (11), 65.39 (5), 65.21 (10), 37.31 (8), 29.15 (9). Melting point: 120-123 °C. HR-MS:

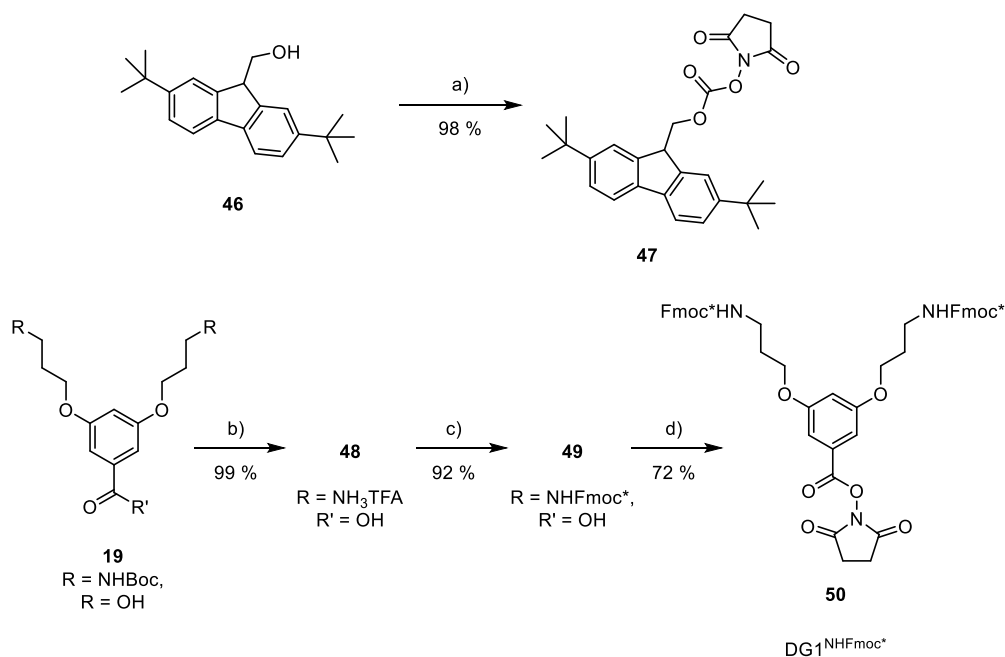
Calc.  $C_{29}H_{32}N_2NaO_8$  ( $M + Na^+$ ):  $m/z = 559.2051$ ; found:  $m/z = 559.2049$ .

Synthesis of 2,5-dioxypyrrolidin-1-yl 3,5-bis(3-(benzyloxycarbonylamido)propyloxy)benzoate (**102**)



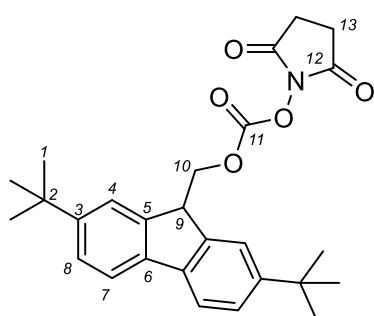
Prepared from **101** (2.33g, 4.3 mmol) following general procedure C. After purification by column chromatography (EtOAc/hexane 1:1 to 5:4), the desired product was obtained as a colorless oil of tar-like consistency (**102**, 2.07 g, 77 %). <sup>1</sup>H-NMR (300 MHz, DMSO-d<sub>6</sub>, 298 K): 7.39-7.29 (m, 10H, 1-3), 7.23 (d, *J* = 2.3 Hz, 2H, 13), 6.7 (t, *J* = 2.3 Hz, 1H, 11), 5.09 (s, 4H, 5), 5.01 (m (b), 2H, 7), 4.02 (t, *J* = 5.9 Hz, 4H, 10), 3.39 (m, 4H, 8), 2.87 (s, 4H, 17), 1.99 (m, 4H, 9). <sup>13</sup>C-NMR (76 MHz, CDCl<sub>3</sub>, 298 K): 169.28 (16), 161.74 (15), 160.09 (12), 156.56 (6), 136.67 (4), 128.62 (2/3), 128.20 (2/3), 126.80 (1), 108.83 (13), 108.67 (11), 66.78 (5), 66.14 (10), 38.37 (8), 29.41 (9), 25.77 (17). HR-MS: Calc. C<sub>33</sub>H<sub>39</sub>N<sub>4</sub>O<sub>10</sub> (M + NH<sub>4</sub><sup>+</sup>): m/z = 651.2661;

found: m/z = 651.2667.



Scheme 8-2: Synthesis of **50** (DG1<sup>NHFmoc\*</sup>): a) Triphosgene, pyridine, DCM -20 °C to RT, then N-hydroxysuccinimide, K<sub>2</sub>CO<sub>3</sub>, acetone/H<sub>2</sub>O, 0 °C to RT; b) TFA, 0 °C to RT, then MeOH; c) **47**, DIPEA, MeCN/H<sub>2</sub>O, 0 °C to RT; d) EDCI-HCl, N-hydroxysuccinimide, DCM, 0 °C to RT.

### Synthesis of 9-(2,7-di-*tert*-butylfluorenyl)methyl *N*-succinimidyl carbonate (**47**)

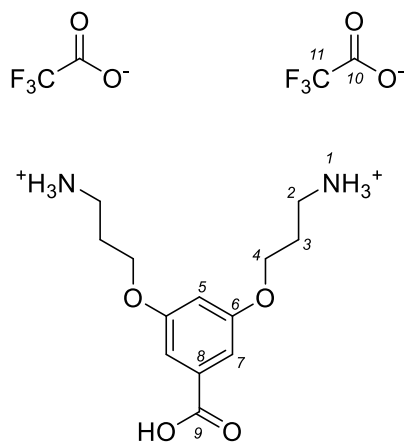


Triphosgene (3.59 g, 12.1 mmol, 0.45 equiv.) in dry methylene chloride (40 mL) was cooled to -20 °C and pyridine (0.2 mL, 2.4 mmol, 0.2 equiv.) was added. The resulting suspension was stirred at -20 °C for 40 min, at which point all solids had dissolved. **46** (8.26 g, 26.7 mmol) was added, then the cooling bath was removed and the mixture was stirred for 16 h. The resulting solution was purged with N<sub>2</sub>, the fumes being bubbled through two sequential gas wash bottles containing 2 M aq. NaOH to quench residual phosgene. The

solution was concentrated in vacuum, taken up in EtOAc (50 mL), filtered, and again concentrated to a yellow oil which was used directly.

To a solution of the obtained chloroformate in acetone (220 mL), *N*-hydroxysuccinimide (3.42 g, 29.5 mmol, 1.1 equiv.) was added, followed by a solution of K<sub>2</sub>CO<sub>3</sub> (3.62 g, 26.2 mmol, 0.98 equiv.) in water (100 mL). The resulting solution was then stirred at RT for 3 h, forming a white suspension in the process. The mixture was diluted with sat. aq. NaHCO<sub>3</sub> (250 mL) and extracted with Et<sub>2</sub>O (300 mL + 2 x 100 mL). The combined organic phases were washed with brine (200 mL), dried over MgSO<sub>4</sub> and concentrated in vacuum, affording **47** as a white, powdery solid (11.76 g, 98%). <sup>1</sup>H-NMR (300 MHz, DMSO-d<sub>6</sub>, 298 K): 7.64 (m, 4H, 7, 8), 7.44 (dd, *J* = 8.0, 1.8 Hz, 2H, 4), 4.57 (d, *J* = 7.6 Hz, 2H, 10), 4.30 (t, *J* = 7.6 Hz, 1H, 9), 2.83 (s, 4H, 13), 1.38 (s, 18H, 1). <sup>13</sup>C-NMR (76 MHz, CDCl<sub>3</sub>, 298 K): 168.60 (12), 151.74 (11), 150.43 (3), 142.67 (5), 138.82 (6), 125.39 (4), 122.20 (7), 119.51 (8), 73.45 (10), 46.44 (9), 35.06 (2), 31.69 (1), 25.60 (13). Melting point: 167-168 °C. Elemental analysis: Calc. 72.14 % C, 6.95 % H, 3.12 % N; found 73.06 % C, 7.06 % H, 2.84 % N.

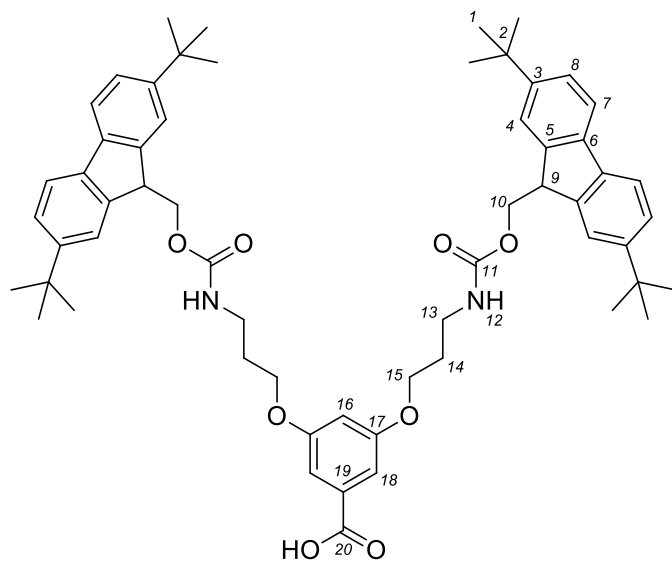
### Synthesis of 3,5-bis(3-aminopropoxy)benzoic acid ditrifluoroacetate (**48**)



Ice-cold TFA (50 mL) was added slowly to an ice-cooled 250 mL round-bottom flask containing **19** (9.89 g, 21.1 mmol). The ice bath was removed and the resulting solution was stirred at RT for 18 h. At 0 °C, MeOH (100 mL) was added slowly and the solution was concentrated in vacuum. The same procedure was repeated with further aliquots of MeOH (50 mL, each) and the solution was evaporated to afford the desired product as a yellowish, honey-like substance (**48**, quantitative) which only occasionally was found to crystallize upon prolonged standing and which was used without further purification. <sup>1</sup>H-NMR (300 MHz, DMSO-d<sub>6</sub>, 298 K): 7.95 (s (b), 6H, 1), 7.09 (d, *J* = 2.3 Hz, 2H, 7), 6.75 (t, *J* = 2.4 Hz, 1H, 5), 4.09 (t, *J* = 6.1 Hz, 4H, 4), 2.97 (m, 4H, 2), 2.01 (m, 4H, 3). <sup>19</sup>F-NMR (282 MHz, DMSO-d<sub>6</sub>, 298 K): -74.18 (s, 6F, 11); <sup>13</sup>C-NMR (76 MHz, DMSO-d<sub>6</sub>, 298 K): 166.91 (9), 159.85 (6), 158.44 (q, *J*<sub>C-F</sub> = 33.6 Hz, 10), 132.94 (8), 116.63 (q, *J*<sub>C-F</sub> = 296.1 Hz, 11), 107.64 (5), 105.99 (7), 65.04 (4), 36.29 (2), 26.80 (3). HR-

MS: Calc. C<sub>13</sub>H<sub>21</sub>N<sub>2</sub>O<sub>4</sub> (M + H<sup>+</sup>): *m/z* = 269.1496; found: *m/z* = 269.1496.

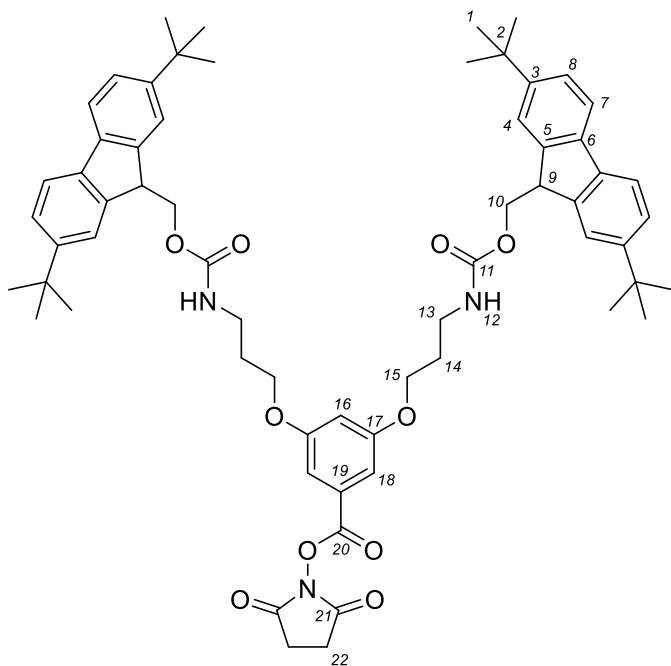
Synthesis of 3,5-bis(3-(9-(2,7-di-*tert*-butylfuorenyl)methyl)oxycarbonylamido)propyloxy)benzoic acid (49)



**48** (3.3 g, 7.1 mmol) was dissolved in water (35 mL). DIPEA (3 mL, 17.3 mmol, 2.5 equiv.) and MeCN (30 mL) were added and the resulting mixture was slowly added to an ice-cooled solution of **47** (7.03 g, 15.6 mmol, 2.2 equiv.) in MeCN (150 mL) and water (15 mL). The resulting emulsion was stirred at RT for 17 h, then taken up in Et<sub>2</sub>O (300 mL) and washed with 1 M aq. HCl (100 mL). The aqueous phase was extracted with more Et<sub>2</sub>O (2 x 50 mL) and the combined organic phases were washed with brine (100 mL), then dried over Na<sub>2</sub>SO<sub>4</sub> and concentrated in vacuum.

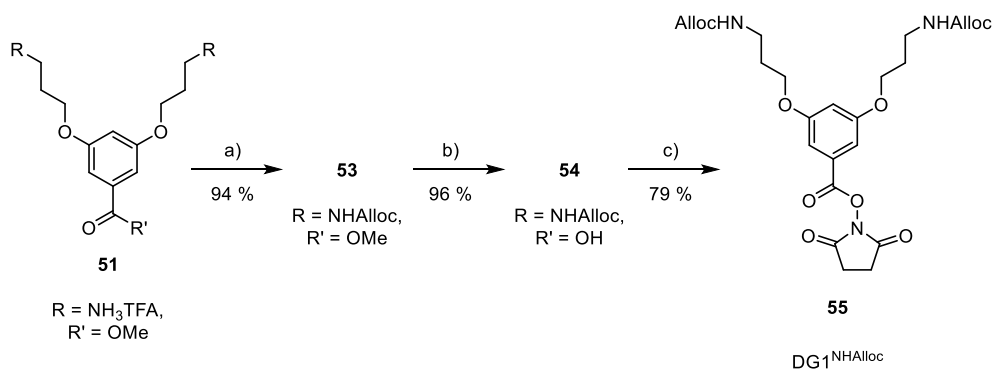
Purification by column chromatography (methylene chloride/*i*PrOH 1:0 to 95:5) afforded **49** as a white solid (6.09 g, 92 %). <sup>1</sup>H-NMR (300 MHz, DMSO-*d*<sub>6</sub>, 343 K): 12.69 (s, 1H, COOH) 7.92-7.51 (m, 8H, 7 & 8), 7.4 (d, *J* = 8.0 Hz, 4H), 7.13 (s, 2H, 12), 7.07 (d, *J* = 2.3 Hz, 2H, 18), 6.47 (t, *J* = 2.4 Hz, 1H, 16), 4.30 (d, *J* = 6.9 Hz, 4H, 10), 4.17 (t, *J* = 6.9 Hz, 2H, 9), 4.00 (t, *J* = 6.3 Hz, 4H, 15), 3.17 (m, 4H, 13), 1.87 (s, 4H, 14), 1.34 (s, 36H, 1). <sup>13</sup>C-NMR (76 MHz, DMSO-*d*<sub>6</sub>, 343 K) δ 166.59 (20), 159.39 (17), 155.77 (11), 149.13 (3), 143.71 (5), 137.79 (6), 132.76 (19), 124.01 (4), 121.37 (8), 118.81 (7), 107.46 (18), 105.76 (16), 65.45 (10), 65.31 (15), 46.71 (9), 37.14 (13), 34.21 (2), 31.03 (1), 28.88 (14). Melting point: 131-137 °C. HR-MS: Calc. C<sub>59</sub>H<sub>73</sub>N<sub>2</sub>O<sub>8</sub> (M + H<sup>+</sup>): *m/z* = 937.5361; found: *m/z* = 937.5354. Elemental analysis: Calc. 73.16 % C, 7.31 % H, 4.06 % N, 15.47 % O; found 72.97 % C, 7.22 % H, 3.97 % N, 15.56 % O.

Synthesis of 2,5-dioxopyrrolidin-1-yl 3,5-bis(3-(9-(2,7-di-*tert*-butylfuorenyl)methyl)carbonylamido)-oxypropyloxy) benzoate (**50**)



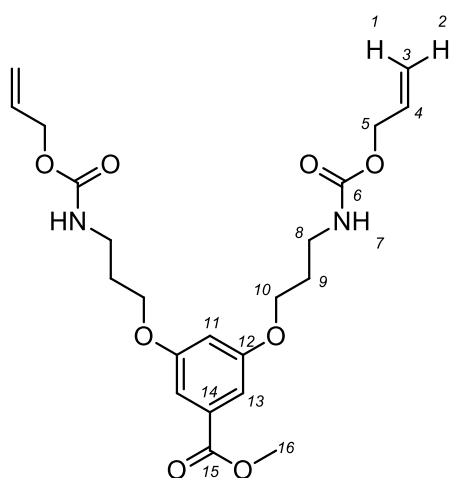
To an ice-cooled solution of **49** (12.83 g, 12.7 mmol) and *N*-hydroxysuccinimide (1.75 g, 15.2 mmol, 1.1 equiv.) in dry methylene chloride (140 mL), EDCI hydrochloride (3.05 g, 15.9 mmol, 1.2 equiv.) was added. The mixture was stirred at RT for 15 h, then washed with 1 M aq. HCl (100 mL). The aqueous phase was extracted with Et<sub>2</sub>O (2 x 200 mL) and the combined organic phases were washed successively with sat. aq. NaHCO<sub>3</sub> (200 mL) and brine (100 mL), then dried over MgSO<sub>4</sub> and concentrated in vacuum. Purification of the obtained solid by column chromatography (acetone/hexane 1:4 to 1:3) afforded **50** as a white, glassy solid (10.29 g, 72 %). <sup>1</sup>H-NMR (300

MHz, DMSO-d<sub>6</sub>, 343 K): 7.78 (m, 8H, 7, 8), 7.39 (dd, *J* = 8.0, 1.8 Hz, 4H, 4), 7.16 (d, *J* = 2.2 Hz, 2H, 18), 6.88 (t, *J* = 2.3 Hz, 1H, 16), 4.34 (d, *J* = 6.9 Hz, 4H, 10), 4.17 (t, *J* = 6.8 Hz, 2H, 9), 4.05 (t, *J* = 6.3 Hz, 4H, 15), 3.18 (m, 4H, 13), 2.9 (s, 4H, 22), 1.87 (m, 4H, 14), 1.38 (s, 36H, 1). <sup>13</sup>C-NMR (76 MHz, DMSO-d<sub>6</sub>, 343 K): 169.54 (21), 161.19 (20), 159.91 (19), 155.77 (11), 149.13 (3), 143.70 (5), 137.79 (6), 126.19 (17), 124.01 (4), 121.36 (7/8), 118.80 (7/8), 108.23 (18), 107.89 (16), 65.79 (15), 65.29 (10), 46.71 (9), 37.05 (13), 34.21 (3), 31.02 (1), 28.77 (14), 25.22 (22). Melting point: 123-131 °C. HR-MS: Calc. C<sub>63</sub>H<sub>79</sub>N<sub>4</sub>O<sub>10</sub> (M + NH<sub>4</sub><sup>+</sup>): *m/z* = 1051.5791; found: *m/z* = 1051.5791.



Scheme 8-3: Synthesis of **55** (DG<sup>1</sup>NHAlloc): a) **52**, NEt<sub>3</sub>, DMAP, DMF, 0 °C to RT; b) KOH, MeOH/H<sub>2</sub>O 3:1, reflux; c) DCC, HOSu, DCM, 0 °C to RT.

### Synthesis of methyl 3,5-bis(3-(allyloxycarbonylamido)propyloxy)benzoate (**53**)

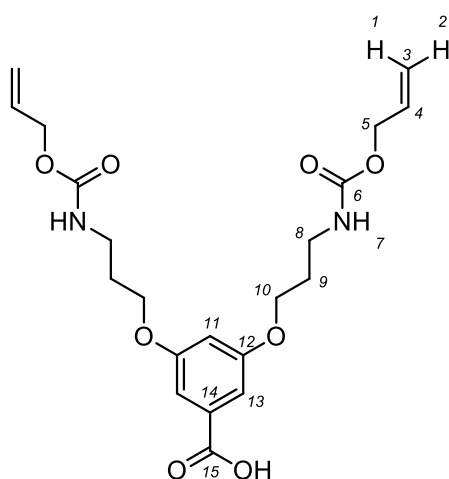


A solution of **51** (37.1 g, 72.6 mmol), allyl 1*H*-pyrrole-1-carboxylate (**52**, 24.43 g, 160.6 mmol, 2.2 equiv.), NEt<sub>3</sub> (31 mL, 223 mmol, 3.1 equiv.), and DMAP (629 mg, 0.07 equiv.) in DMF (150 mL) was stirred at 60 °C for 3 h, then concentrated in vacuum, taken up in EtOAc (400 mL) and washed successively with water (400 mL), 1 M aq. HCl (500 mL), and brine (300 mL), then dried over MgSO<sub>4</sub>. Flash chromatography (EtOAc/hexane 1:2 to 3:5) afforded **53** as a colorless solid (30.68 g, 94 %). <sup>1</sup>H-NMR (300 MHz, CDCl<sub>3</sub>, 298 K): 7.16 (d, *J* = 2.3 Hz, 2H, **13**), 6.2 (t, *J* = 2.4 Hz, 1H, **11**), 5.90 (ddt, *J* = 17.5, 10.7, 5.4 Hz, 2H, **4**), 5.29 (dd, *J* = 17.3, 1.7 Hz, 2H, **1**), 5.20 (dd, *J* = 10.4, 1.5 Hz, 2H, **2**), 4.98 (m (b), 2H, **7**), 4.56 (app. d, *J* = 5.6

Hz, 4H, **5**), 4.04 (t, *J* = 5.9 Hz, 4H, **10**), 3.89 (s, 3H, **16**), 3.39 (m, 4H, **8**), 2.00 (m, 4H, **9**). <sup>13</sup>C-NMR (76 MHz, CDCl<sub>3</sub>, 298 K): 166.84 (**15**), 159.87 (**12**), 156.43 (**6**), 133.05 (**4**), 132.19 (**14**), 117.78 (**3**), 108.04 (**13**), 106.78 (**11**), 66.15 (**10**), 65.68 (**5**), 52.39 (**16**), 38.56 (**8**), 29.48 (**9**). Melting point: 77 °C. HR-MS: Calc. C<sub>22</sub>H<sub>31</sub>N<sub>2</sub>O<sub>8</sub> (M + H<sup>+</sup>): *m/z* = 451.2075; found: *m/z* = 451.2076. Elemental analysis: Calc. 58.66 % C, 6.71 % H, 6.22 % N, 28.41 % O; found 58.56 % C, 6.68 % H, 6.21 % N, 28.50 % O.



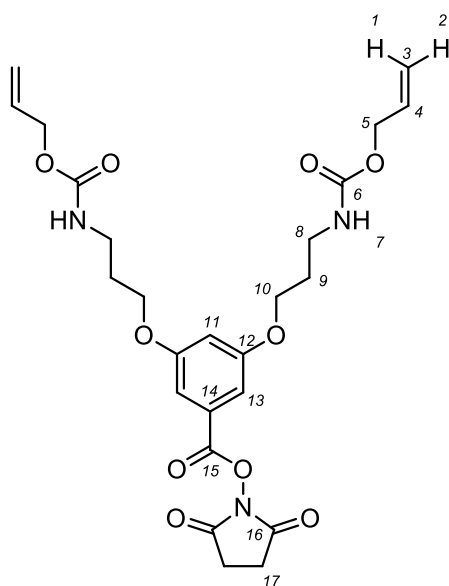
### Synthesis of 3,5-bis(3-(allyloxycarbonylamido)propyloxy)benzoic acid (**54**)



Prepared from **53** (15.14 g, 33.6 mmol) according to general procedure B using NaOH (2.07 g, 1.5 equiv.), affording **54** as a colorless solid (14.06 g, 96 %).  $^1\text{H-NMR}$  (300 MHz, DMSO- $d_6$ , 298 K): 7.29 (t,  $J = 5.7$  Hz, 2H, 7), 7.04 (d,  $J = 2.3$  Hz, 2H, 13), 6.66 (t,  $J = 2.3$  Hz, 1H, 11), 5.90 (ddt,  $J = 17.3, 10.5, 5.3$  Hz, 2H, 4), 5.26 (m, 2H, 1), 5.15 (m, 2H, 2), 4.46 (m, 4H, 5), 4.00 (t,  $J = 6.3$  Hz, 4H, 10), 3.15 (m, 4H, 8), 1.85 (m, 4H, 9).  $^{13}\text{C-NMR}$  (76 MHz, DMSO- $d_6$ , 298 K):  $^{13}\text{C-NMR}$  (76 MHz, DMSO- $d_6$ ): 167.21 (15), 159.54 (12), 155.97 (6), 134.08 (14), 133.81 (4), 116.87 (3), 107.38 (13), 105.37 (11), 65.46 (10), 64.19 (5), 37.23 (8), 29.10 (9). Melting point: 90-91 °C. HR-MS: Calc.  $\text{C}_{21}\text{H}_{29}\text{N}_2\text{O}_8$  ( $\text{M} + \text{H}^+$ ):  $m/z = 437.1918$ ; found:  $m/z = 437.1911$ .

Elemental analysis: Calc. 56.28 % C, 5.86 % H, 7.88 % N, 29.99 % O; found 56.09 % C, 5.84 % H, 8.05 % N, 30.00 % O.

### Synthesis of 2,5-dioxypyrrolidin-1-yl 3,5-bis(3-(allyloxycarbonylamido)propyloxy)benzoate (**55**)



Prepared from **54** (20.32 g, 46.5 mmol) following general procedure C. After purification by column chromatography (methylene chloride/acetone 20:1 to 9:1), **55** was obtained as a colorless solid (19.62 g, 79 %).  $^1\text{H-NMR}$  (300 MHz,  $\text{CDCl}_3$ , 298 K): 7.23 (d,  $J = 2.3$  Hz, 2H, 13), 6.72 (t,  $J = 2.3$  Hz, 1H, 11), 5.90 (ddt,  $J = 17.4, 10.8, 5.6$  Hz, 2H, 4), 5.29 (m, 2H, 1), 5.19 (m, 2H, 2), 5.00 (m (b), 2H, 7), 4.55 (app. d,  $J = 5.6$  Hz, 4H, 5), 4.04 (t,  $J = 5.9$  Hz, 4H, 10), 3.89 (s, 3H, 16), 3.38 (m, 4H, 8), 2.89 (s, 4H, 17), 2.00 (m, 4H, 9).  $^{13}\text{C-NMR}$  (76 MHz,  $\text{CDCl}_3$ , 298 K): 169.25 (16), 161.64 (15), 160.01 (12), 156.35 (6), 132.94 (4), 126.66 (14), 117.58 (3), 108.68 (13), 108.52 (11), 66.05 (10), 65.49 (5), 38.18 (8), 29.30 (9), 25.68 (17). HR-MS: Calc.  $\text{C}_{25}\text{H}_{35}\text{N}_4\text{O}_{10}$  ( $\text{M} + \text{NH}_4^+$ ):  $m/z = 551.2348$ ; found:  $m/z = 551.2349$ . Melting point: 81-83 °C. Elemental analysis: Calc. 57.79 % C, 6.47 % H, 6.47 % N; found 56.35 % C, 6.3 % H, 6.34 % N.

## Syntheses of precursor polymers

In order to provide a full homologous series of DPs, suitably large quantities (*ca.* 20 g) of  $\text{PG}g_{500}^{\text{NHBoc}}$  were prepared. Polymerization of  $\text{MG}1^{\text{NHBoc}}$  (synthesized according to literature procedures from **16**, see Scheme 1-8a)<sup>168</sup> was carried out by RAFT polymerization.<sup>189</sup> This polymer served as a starting material for the synthesis of all DPs used in route **C** (see section 2.4), using the conventional protocol denoted as route **A**, up to  $\text{PG}4_{500}^{\text{NHBoc}}$ . Thereafter, the NHAloc-based protocol central to route **C** was used to avoid main-chain scission, as indicated in chapter 2 and described in detail below; Figure 8-1 depicts GPC traces of the full homologous series of DPs (also see Figure 2-6 and the accompanying text). Table 8-1 details the results of functional group quantification by Sanger's reagent (general procedure A)<sup>150</sup> for the entire series as employed in the discussion of  $g_{\text{max}}$  in section 2.7.

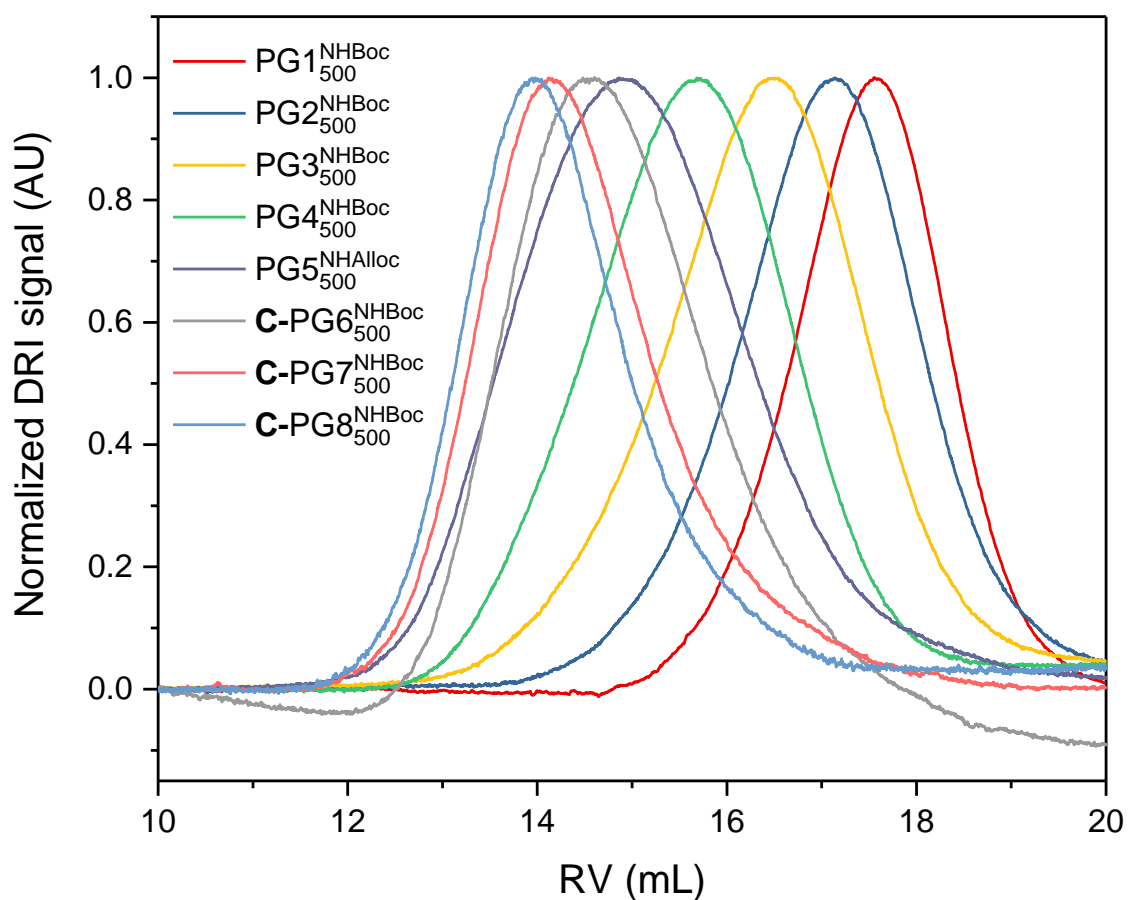


Figure 8-1: GPC traces of polymers from the homologous series of DPs from  $g = 1$  ( $\text{PG}1_{500}^{\text{NHBoc}}$ ) to  $g = 8$  ( $\text{C-PG}8_{500}^{\text{NHBoc}}$ ).

Table 8-1: Sanger labelling data and resulting functional group conversion values (recursive method) for the polymers in Figure 8-1 of  $g = 2$  to  $g = 8$ .

Polymer	Route	w [mg]	w <sub>s</sub> [g]	V [mL]	A	l [cm]	c <sub>g</sub> <sup>labels</sup> [mmol L <sup>-1</sup> ]	U <sub>g</sub>	n <sub>g</sub>	(k <sub>g</sub> <sup>blocked</sup> )	(k <sub>g</sub> <sup>labelled</sup> )	M <sub>s</sub> <sup>ideal</sup> [g mol <sup>-1</sup> ]	(M <sub>s</sub> ) [g mol <sup>-1</sup> ]	X [%]
PG2 <sup>NHBoc</sup> <sub>500</sub>	A	12.46	7.6509	4.7908	0.0231	0.2	0.0071	0.0010	2.997	3.993	0.0033	1223.5	1221.9	99.93
PG3 <sup>NHBoc</sup> <sub>500</sub>	A	10.29	7.8738	4.9304	0.0274	0.2	0.0084	0.0014	6.983	7.972	0.0105	2625.1	2618.0	99.86
PG4 <sup>NHBoc</sup> <sub>500</sub>	A	2.04	4.2350	2.6518	0.0234	0.2	0.0071	0.0032	14.916	15.866	0.0501	5428.4	5393.7	99.76
PG5 <sup>NHBoc</sup> <sub>500</sub>	A	5.66	9.1178	5.7093	0.0587	0.5	0.0072	0.0024	30.756	31.680	0.0754	10522	10433	99.69
C-PG6 <sup>NHBoc</sup> <sub>500</sub>	C	5.94	7.2185	4.5200	0.0469	0.2	0.0143	0.0038	62.272	63.033	0.2395	22248	21969	99.62
C-PG7 <sup>NHBoc</sup> <sub>500</sub>	A	3.39	5.2447	3.2841	0.0228	0.2	0.0070	0.0024	125.25	125.95	0.2968	44674	44030	99.77
C-PG8 <sup>NHBoc</sup> <sub>500</sub>	A	2.51	4.8214	3.0190	0.1242	1.0	0.0076	0.0032	250.69	250.89	0.8022	89527	87937	99.67

Due to lack of sufficient quantities of material *e.g.* for the preparation of DP pills (see section 5.2), the re-synthesis of polymers prepared by route **B** was necessary. This non-homologous series was entirely separate from the polymers prepared for the homologous series discussed above, however with a very similar chain length. The polymers were again prepared in analogy to previously published procedures,<sup>174</sup> *i.e.* using a “ $g + 2$ ” step in the syntheses of both **B-PG6**<sup>NHBoc</sup><sub>500</sub> and **B-PG8**<sup>NHBoc</sup><sub>500</sub>, with functional group conversion values very closely matching those achieved previously. As for the homologous series above, Figure 8-2 depicts GPC traces for all members of the series, and Table 8-2 details the characterization by Sanger labelling.

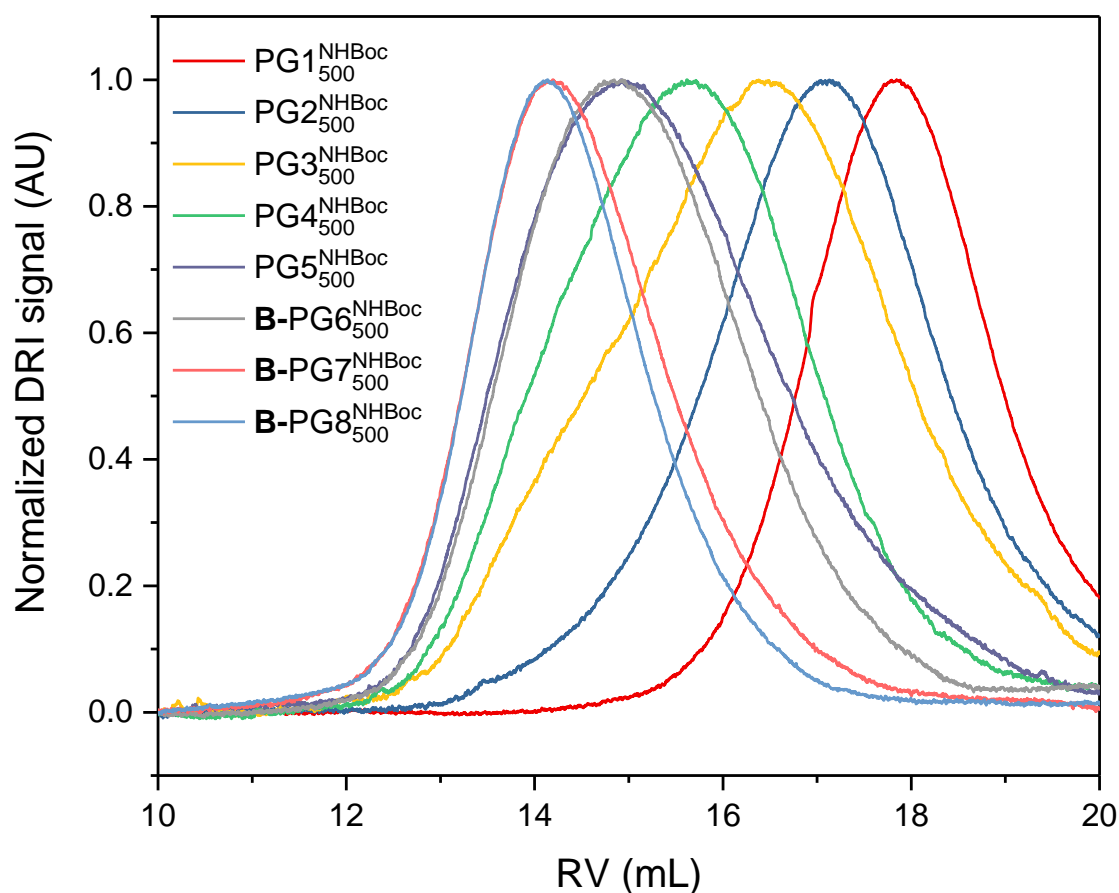
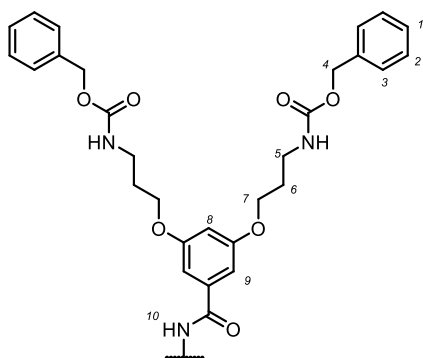


Figure 8-2: GPC traces of polymers from the homologous series of DPs from  $g = 1$  (PG1<sup>NHBoc</sup><sub>500</sub>) to  $g = 8$  (B-PG8<sup>NHBoc</sup><sub>500</sub>).

Table 8-2: Sanger labelling data and resulting functional group conversion values (recursive method) for the polymers in Figure 8-2 of  $g = 2$  to  $g = 8$ .

Polymer	Route	w [mg]	w <sub>s</sub> [g]	V [mL]	A	l [cm]	$\epsilon_{\text{labelled}}^{\text{labelled}}$ [mmol L <sup>-1</sup> ]	$U_{\text{e}}$	$n_{\text{e}}$	$\langle k_{\text{e}}^{\text{blocked}} \rangle$	$\langle k_{\text{e}}^{\text{labelled}} \rangle$	$N_{\text{e}}^{\text{ideal}}$ [g mol <sup>-1</sup> ]	$\langle M_{\text{z}} \rangle$ [g mol <sup>-1</sup> ]	$\chi$ [%]
PG2 <sup>NHBoc</sup> <sub>500</sub>	A	10.24	2.8041	1.7559	0.0946	0.2	0.0288	0.0017	2.994	3.988	0.0060	1223.5	1220.8	99.85
PG3 <sup>NHBoc</sup> <sub>500</sub>	A	12.91	7.6484	4.7892	0.0274	0.2	0.0084	0.0011	6.980	7.972	0.0081	2625.1	2617.2	99.9
PG4 <sup>NHBoc</sup> <sub>500</sub>	A	5.95	8.0218	5.023	0.0204	0.2	0.0062	0.0018	14.93	15.90	0.0283	5428.5	5401.5	99.81
PG5 <sup>NHBoc</sup> <sub>500</sub>	A	5.8	6.3433	3.972	0.0332	0.2	0.0101	0.0024	30.79	31.71	0.0760	11035	10952	99.78
B-PG6 <sup>NHBoc</sup> <sub>500</sub>	B	5.32	15.7432	9.858	0.1614	0.2	0.0492	0.0319	57.17	56.31	1.8531	22248	20016	91.29
B-PG7 <sup>NHBoc</sup> <sub>500</sub>	A	6.25	5.7884	3.6245	0.0291	0.2	0.0089	0.0018	115.1	115.9	0.2084	44675	40492	99.79
B-PG8 <sup>NHBoc</sup> <sub>500</sub>	B	5.04	9.2193	5.7729	0.077	0.2	0.0235	0.0094	225.3	224.1	2.1299	89528	78896	97.26

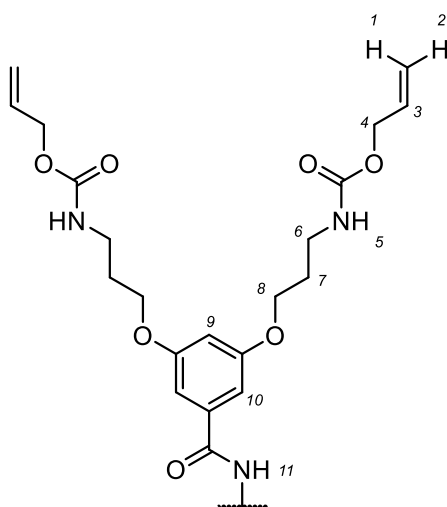
### Synthesis of PG5<sup>NHCbz</sup><sub>500</sub> (**29**)



To a solution of PG4<sup>NH<sub>3</sub>TFA</sup><sub>500</sub> (215 mg, 38  $\mu$ mol RU), NEt<sub>3</sub> (0.21 mL, 3 mmol, 40 equiv.) and DMAP (33.6 mg, 0.3 mmol, 7 equiv.) in DMF (20 mL), **102** (1.16 g, 1.8 mmol, 48 equiv.) was added at 0 °C. The reaction mixture was then stirred at RT for a total of 34 d, interrupted by addition of further aliquots of **102** after 10 d (393.6 mg, 0.6 mmol, 16 equiv.) and 20 d (390.3 mg, 0.6 mmol, 16 equiv.). The solution was then concentrated in vacuum and the polymer was purified by column chromatography (methylene chloride,  $R_f \approx 1$ ), then lyophilized from freshly distilled dioxane, affording PG5<sup>NHCbz</sup><sub>500</sub> as a white foam (305 mg,

66 %). Functional group conversion (general procedure A): 99.6 %. <sup>1</sup>H-NMR (300 MHz, DMSO-d<sub>6</sub>, 343 K): 8.10 (s(b), 10), 7.10 (app. s (b), 1-3), 6.87 (app. s (b), 9), 6.38 (app. s (b), 8), 4.85 (app. s (b), 4), 3.80 (app. s (b), 7), 3.04 (app. s (b), 5), 1.70 (app. s (b), 6).

### Synthesis of PG5<sup>NHAlloc</sup><sub>500</sub> (**31**)

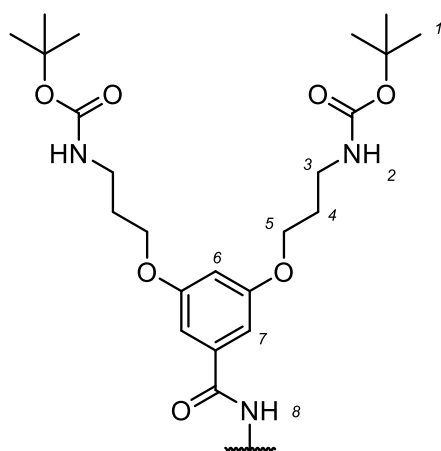


To a solution of PG4<sup>NH<sub>3</sub>TFA</sup><sub>500</sub> (3.6 g, 0.6 mmol RU), DMAP (137 mg, 1.1 mmol, 1.8 equiv.) and NEt<sub>3</sub> (2.8 mL, 20 mmol, 32 equiv.) in DMF (60 mL), **55** (16.32 g, 30.5 mmol, 48 equiv.) was added at 0 °C. The reaction mixture was then stirred at RT in the dark for a total of 35 d, interrupted by the addition of another portion of **55** (6.04 g, 11 mmol, 18 equiv.) at 0 °C after 14 d. The resulting solution was then precipitated into Et<sub>2</sub>O (ca. 3 L) and the precipitate was purified by column chromatography (methylene chloride,  $R_f \approx 1$ ). The resulting polymer was lyophilized from freshly-distilled dioxane, affording PG5<sup>NHAlloc</sup><sub>500</sub> as an off-white powder (4.92 g, 73 %).

Functional group conversion (general procedure A): 99.5 %. <sup>1</sup>H-NMR (300 MHz, DMSO-d<sub>6</sub>, 343 K): 8.11 (app. s (b), 11), 6.86 (app. s (b), 5 or 10), 6.69 (app. s (b), 5 or 10), 6.42 (app. s (b), 9), 5.71 (app. s (b), 3), 5.10 (app. d (b), J

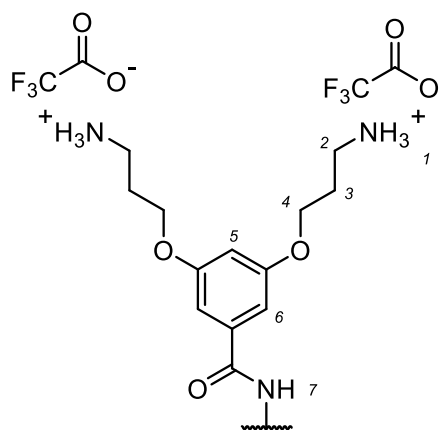
= 15.1 Hz, 2), 4.99 (app. d (b),  $J = 6.6$  Hz, 1), 4.33 (app. s (b), 4) 3.85 (app s (b), 8), 3.04 (app. s (b), 6), 1.73 (app. s (b), 7).

#### Synthesis of **C-PG6<sub>500</sub><sup>NHBoc</sup>** from **PG5<sub>500</sub><sup>NHAlloc</sup>** (route C)



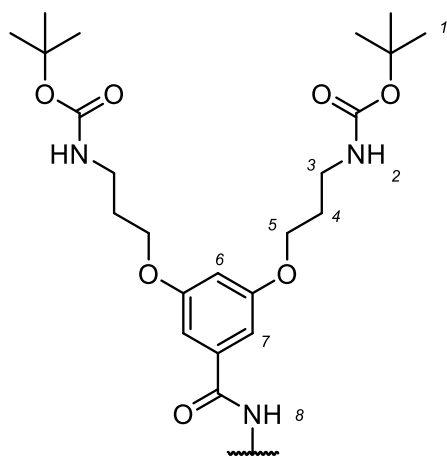
To a solution of **PG5<sub>500</sub><sup>NHAlloc</sup>** (**26** 776 mg, 73.8  $\mu\text{mol}$  RU/2.4 mmol amines),  $\text{NEt}_3$  (2.3 mL, 16.5 mmol, 7 equiv./amine), and  $\text{PPh}_3$  (63 mg, 0.24 mmol, 0.1 equiv./amine) in a mixture of dry DMSO (10 mL) and dry NMP (5 mL) at 0 °C, DMBA (1.848 g, 11.8 mmol, 5 equiv./amine) dissolved in dry DMSO (5 mL) was added slowly. The resulting solution was then warmed to RT and degassed by purging with argon supplied from a balloon. To this was added an argon-purged solution of  $\text{Pd}(\text{PPh}_3)_4$  (29.2 mg  $\text{mL}^{-1}$  in NMP; 4.7 mL, 0.16 mmol, 0.05 equiv./amine). The resulting mixture was purged with argon, then the reaction was stirred in the dark for 3 d. To the resulting clear, orange solution, sodium *N,N*-diethyldithiocarbamate trihydrate (100 mg, 0.44 mmol, 0.18 equiv./amine, dissolved in 1 mL DMSO). After purging with argon, the reaction was stirred in the dark overnight, whereupon DMAP (33 mg, 0.2 mmol, 0.11 equiv./amine) and a solution of **20** in dry DMSO (414 mg  $\text{mL}^{-1}$ ; 8 mL, 5.9 mmol, 2.5 equiv./amine) were added. Further portions of the same solution of **20** were added after 10 d (4 mL, 2.9 mmol, 1.24 equiv./amine) and 25 d (4 mL, 2.9 mmol, 1.24 equiv./amine) followed each time by purging with argon. The reaction mixture was stirred in the dark for further 20 d and then precipitated into  $\text{Et}_2\text{O}$  (1 L). The supernatant was decanted, and the residue was purified by column chromatography (methylene chloride,  $R_f \approx 1$ ). The resulting polymer was lyophilized from freshly distilled dioxane, affording **C-PG6<sub>500</sub><sup>NHBoc</sup>** (**7**) as a yellow-tinged, fluffy powder (941.1 mg, 57 %). Conversion of functional groups (general procedure A): 99.3 %.  $^1\text{H-NMR}$  (300 MHz,  $\text{DMSO-d}_6$ , 343 K): 8.19 (app. s (b), 2/8), 6.91 (app. s (b), 6/7), 6.46-6.37 (app. m (b), 6/7), 3.92 (app. s (b), 5), 3.02 (app. s (b), 3), 1.75 (app. s (b), 4), 1.26 (app. s (b), 1).

#### Synthesis of **C-PG6<sub>500</sub><sup>NH<sub>3</sub>TFA</sup>** <sup>101</sup>



While cooling in an ice bath, TFA (25 g) was added slowly to **C-PG6<sub>500</sub><sup>NHBoc</sup>** (473.7 mg). To the resulting orange-tinged slurry, MeOH (1 mL) was added, affording a clear solution which was stirred at RT overnight, then cooled to 0 °C in an ice bath. Ice cold MeOH (30 mL) was added slowly and solvents were removed from the resulting mixture by rotary evaporation at 30 °C. Addition of MeOH and solvent removal were repeated twice, then the solution was evaporated to dryness and lyophilized from deionized water, affording **C-PG6<sub>500</sub><sup>NH<sub>3</sub>TFA</sup>** as an off-white foam (quantitative).  $^1\text{H-NMR}$  (300 MHz,  $\text{DMSO-d}_6$ , 343 K): 8.39 (app. s (b), 7), 8.03 (s (b), 1), 6.98 (app. m (b), 5/6), 6.59 (app. m (b), 5/6), 4.09 (app. s (b), 4), 2.95 (app. s (b), 2), 1.99 (app. s (b), 2).

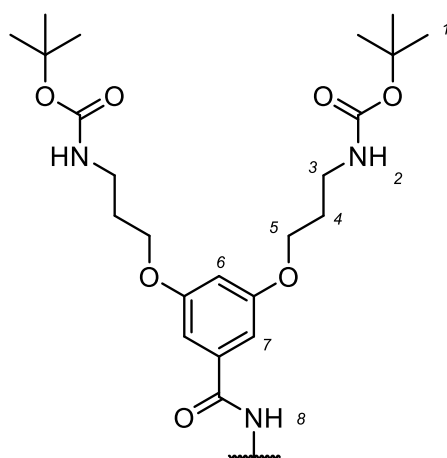
### Synthesis of **C-PG7**<sup>NHBoc</sup><sub>500</sub> 101



To a solution of **C-PG6**<sup>NH<sub>3</sub>TFA</sup><sub>500</sub> (480 mg, 21  $\mu$ mol RU) in DMF (15 mL), NEt<sub>3</sub> (0.38 mL, 2.7 mmol, 132 equiv.), DMAP (49 mg, 0.4 mmol, 19 equiv.), and **20** (2.35 g, 4.1 mmol, 198 equiv.) were added successively while cooling in an ice bath. Further portions of **20** were added at 0 °C after 10 d (776 mg, 1.4 mmol, 66 equiv.) and 25 d (783 mg, 1.4 mmol, 67 equiv.), stirring at RT in between and cooling to 0 °C for the addition of **20**. After a total of 45 d of stirring, the solution was precipitated into Et<sub>2</sub>O (500 mL). The sol was decanted, and the resulting polymer was purified by column chromatography (methylene chloride,  $R_f \approx 1$ ), then lyophilized from freshly distilled dioxane, affording **C-PG7**<sup>NHBoc</sup><sub>500</sub> as an off-white, fluffy

powder (541 mg, 55 %). <sup>1</sup>H-NMR (300 MHz, DMSO-d<sub>6</sub>, 343 K): 8.20 (app. s (b), 2/8), 6.93 (app. s (b), 6/7), 6.47-6.37 (app. m (b), 6/7), 3.95 (app. s (b), 5), 3.39 (app. s (b)), 3.02 (app. s (b), 3), 1.76 (app. s (b), 4), 1.27 (s (b), 1).

### Synthesis of **C-PG8**<sup>NHBoc</sup><sub>500</sub> 101



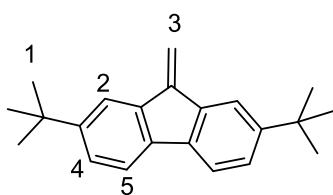
In an ice-cooled round-bottom flask, ice-cold TFA (5 mL) was added slowly to **C-PG7**<sup>NHBoc</sup><sub>500</sub> (153.1 mg,  $\mu$ mol RU). The cloudy mixture was warmed to RT and MeOH was added dropwise until the solution turned clear. After stirring overnight, the solution was cooled to 0 °C and treated with MeOH (20 mL). Solvents were evaporated and the polymer was lyophilized from deionized water. The resulting off-white powder foam was dissolved in DMF (8 mL). NEt<sub>3</sub> (0.15 mL, 1.1 mmol, 315 equiv.), DMAP (17.3 mg, 0.4 mmol, 19 equiv.) and **20** (832.5 mg, 4.1 mmol, 198 equiv.) were added successively. After 20 d and 40 d of stirring in the dark at RT, further portions of **20** (283.9 mg, 1.4 mmol, 66 equiv. and 278.8 mg, 1.4 mmol, 67

equiv., respectively) were added at 0 °C. After a total of 63 d of stirring, the solution was precipitated into Et<sub>2</sub>O (300 mL). The sol was isolated by centrifugation and purified by column chromatography (methylene chloride,  $R_f \approx 1$ ), then lyophilized from freshly distilled dioxane, affording **C-PG8**<sup>NHBoc</sup><sub>500</sub> as a dirty-white powder (205 mg, 67 %). <sup>1</sup>H-NMR (300 MHz, DMSO-d<sub>6</sub>, 343 K): 8.24 (app. s (b), 2/8), 6.96 (app. s (b), 6/7), 6.48-6.35 (app. m (b), 6/7), 3.95 (app. s (b), 5), 3.38 (app. s (b)), 3.03 (app. s (b), 3), 1.77 (app. s (b), 4), 1.26 (s (b), 1).

### Attempted synthesis of PG2<sub>500</sub><sup>NHFmoc\*</sup>

PG1<sub>500</sub><sup>NH<sub>3</sub>TFA</sup> (76.1 mg, 130 μmol RU) in DMSO (1 mL), **50** (1.408 g, 1.4 mmol, 10.5 equiv.) in DMSO (2 mL) was added. Then, a 0.188 M solution of DIPEA in MeCN (1.473 mL, 276 μmol, 2.12 equiv.) was added slowly using a syringe pump. The reaction was monitored for cloudiness and methylene chloride was added as necessary to maintain solubility (total 3 mL). After stirring in the dark for 9 d, the reaction mixture was diluted with methylene chloride (50 mL), washed with water (30 mL), then concentrated in vacuum and purified by column chromatography (methylene chloride, R<sub>f</sub> ≈ 1) to afford a colorless foam (40.3 mg, 14 %).

### Synthesis of 2,7-di-*tert*-butyl-9-methylenefluorene (**43**)



To a solution of **49** (297.4 mg, 0.7 mmol) in acetone (10 mL), NEt<sub>3</sub> (0.3 mL, 2.1 mmol, 3 equiv.) was added. After stirring for 3 h, the resulting solution was diluted with Et<sub>2</sub>O, washed with 1 M aq. HCl (40 mL), dried over MgSO<sub>4</sub> and concentrated in vacuum. The solid residue was recrystallized from hexane, affording a small amount of a colorless solid (**43**, 15 mg, 7 %). <sup>1</sup>H-NMR (300 MHz, CDCl<sub>3</sub>, 298 K): 7.74 (d, *J* = 1.8 Hz, 2H, 2), 7.56 (d, *J* = 8 Hz, 2H, 5), 7.39 (dd, *J* = 1.8 Hz, 8 Hz, 2H, 4), 6.06 (s, 2H, 3), 1.39 (s, 18H, 1). UV/Vis (THF): λ<sub>max</sub> = 262 nm; λ<sub>em</sub> = 622 nm.

## 8.2.2. Other experiments

### Attempted Deprotection of PG5<sub>500</sub><sup>NHBoc</sup>

#### a) Neat thermolysis

To test the viability of thermolysis (Scheme 2-2) by simple heating in the solid state, a TGA-based experiment was conducted. TGA permits both excellent thermal control, the TGA balance is subject to a constant flow of nitrogen protecting the DP from oxidation, and the TGA results permit fairly accurate monitoring of the progress of thermolysis, which would be difficult in standard glassware.

While the thermolysis of PG5<sub>500</sub><sup>NHBoc</sup> does indeed proceed cleanly and is well-separated from other thermal processes taking place at higher temperatures (Figure 8-3a),<sup>174</sup> neat thermolysis did not turn out to be a viable *synthetic* option: The polymer obtained after complete NHBoc thermolysis and subsequent cooling, a brittle, glassy solid (Figure 8-3b), was not soluble and barely swelled in DMF even after several days of stirring. This indicates the formation of strong – perhaps irreversible – hydrogen bonding networks. Together with the rather poor temperature control achievable in larger-scale solid-state reactions, this led to the exploration of solvent-assisted thermolysis, instead.

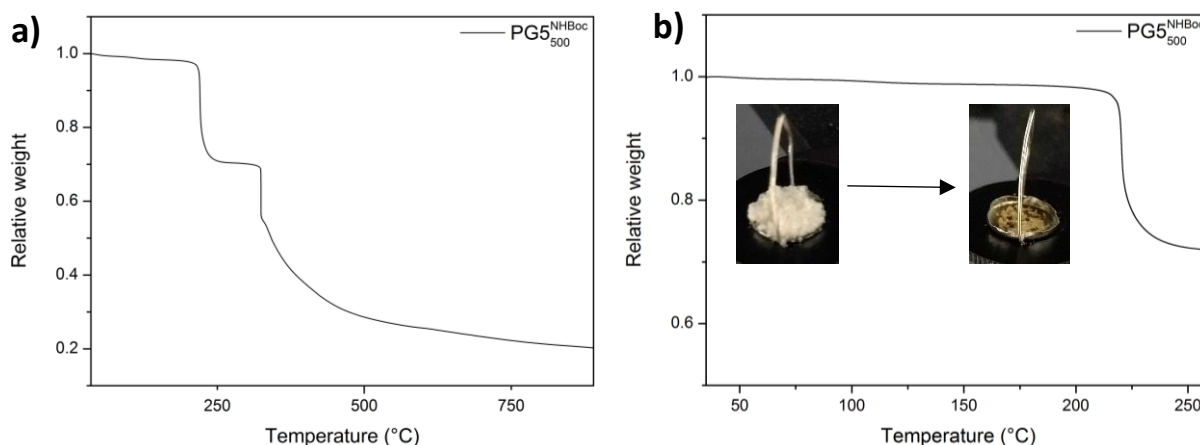


Figure 8-3: a) Complete TGA curve of PG5<sup>NHBoc</sup> (recorded in N<sub>2</sub> atmosphere). b) TGA curve of PG5<sup>NHBoc</sup> (N<sub>2</sub>) when heating was stopped at 260 °C. The insets show the polymer before and after heating. The glassy product on the right-hand side was not soluble even after prolonged exposure to DMF. Adapted with permission from Messmer, D.; Kröger, M.; Schlüter, A. D. *Macromolecules* **2018**, 51, 5420-5429. Copyright 2018, American Chemical Society.

#### b) Solvent-assisted thermolysis

For the purpose of solvent-assisted thermolysis, samples of PG5<sup>NHBoc</sup> (ca. 50 mg) were dissolved in high-purity grades of the three solvents tested (hexafluoroisopropanol, DMF, and DMSO; 5 mL each) and the solution was set to stir at the corresponding reflux temperature (58 °C for hexafluoroisopropanol, 154 °C for DMF, 189 °C for DMSO) under nitrogen for 3 d. During that time, the solutions of the DP in DMF and DMSO had turned quite brown and turbid and were therefore discarded. The HFIP solution had not changed color noticeably, and a precipitation test using methylene chloride showed no change in solubility. This indicated that only very little deprotection had occurred, if any. Microwave conditions have been demonstrated to be effective for NHBoc deprotection in fluorinated solvents,<sup>195</sup> however in view of the poor results obtained with higher boiling solvents and the apparent absence of even partial deprotection, other options of NHBoc deprotection were explored instead. In view of the results presented in chapter 3, it appears doubtful whether this approach specifically at  $g = 5$  could have led to success in avoiding scission.

#### c) Deprotection by trimethylsilyl iodide (TMSI)

Following the same mechanism as in Scheme 2-3, ester cleavage might occur during TMSI-mediated cleavage of carbamates. However since PG5<sup>NHBoc</sup> is the target of this reaction, this is a lesser concern, as previous studies with suitably modified dendrons had demonstrated that the interior of DPs is rather inaccessible to solvents<sup>98</sup> or reactive species<sup>99</sup> at  $g = 4$ , already. The benzyl ester in proximity of the backbone is therefore likely not significantly affected by TMSI-mediated reactions. A possible side reaction of larger concern is the cleavage of aryl ethers,<sup>199,369</sup> which are present in the periphery of the DPs.

To test the viability of TMSI-mediated *N*-deprotection in the DP case, PG5<sup>NHBoc</sup> in anhydrous DMF was treated with TMSI (5 equiv./amine), followed by treatment with methanol after 24 h. This resulted in the desired shift in solubility, *i.e.* the products were not fully soluble in methylene chloride. Isolation of the reaction products by precipitation into Et<sub>2</sub>O afforded a colorless solid which was soluble in DMSO-*d*<sub>6</sub>, revealing substantial deprotection as indicated by the decrease in the relative intensity of



the *tert*-butyl signal in  $^1\text{H-NMR}$  spectroscopy (Figure 8-4). However, as TMSI is also known to cleave some aryl ethers, it is not clear whether the products contain partially deprotected, intact dendrons or also partially cleaved structures. Although this result was somewhat encouraging, Lewis acid-mediated scission was not pursued further: Even with a 4-fold excess of TMSI and 3 d of reaction time, conversion was incomplete, indicating that more forceful conditions – *i.e.* the use of an even larger excess of TMSI or heating of the reaction mixture – would be necessary to push deprotection to completion. The inherently high reactivity of TMSI – the cleavage of aryl ethers, and under harsher conditions even amides appear problematic – prevented further investigations into this method of deprotection.

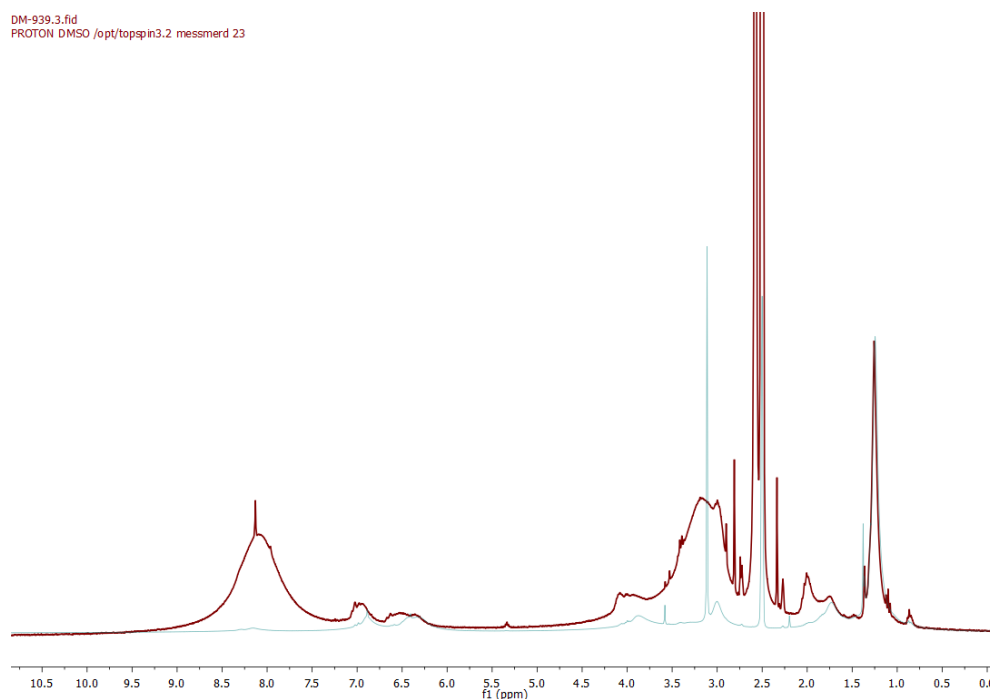


Figure 8-4:  $^1\text{H-NMR}$  spectra (300 MHz, 298 K,  $\text{DMSO-d}_6$ ) of  $\text{PG5}_{500}^{\text{NHBoc}}$  (green) and the product of treatment with TMSI followed by methanolysis (red). The signal was normalized to the *tert*-butyl signal at ca. 1.25 ppm.

#### d) Deprotection by tetrabutylammonium fluoride (TBAF)

The literature<sup>200</sup> suggests THF as a suitable solvent for the deprotection of amines using TBAF, and solutions of the reagent are commercially available in that solvent. However, THF is only a moderately good solvent for  $\text{PG}g_n^{\text{NHBoc}}$  and certainly a bad solvent for  $\text{PG}g_n^{\text{NH}_2}$ . Fortunately, TBAF is also stable in DMSO,<sup>370</sup> which dissolves the free-base DPs comparatively well.

Therefore, a solution of a small sample of  $\text{PG5}_{500}^{\text{NHBoc}}$  (ca. 50 mg) in anhydrous DMSO (5 mL) was treated with a solution of TBAF (0.8 mL, 1 M in dry THF, ca. 5 equiv./amine) and stirred at 70 °C for 24 h. A sample of the resulting clear solution was tested for precipitation with methylene chloride, but no change in solubility was found.

## Attempted Synthesis of $PGg_n^{NHFmoc^*}$

Reagents for the introduction of  $NHFmoc^*$  are commercially available, but prohibitively expensive at the required multi-gram scale and therefore were synthesized in-house (Scheme 8-2). Starting from fluorene (**44**), the solubilizing *tert*-butyl groups are readily and selectively introduced by simple Friedel-Crafts alkylation. The resulting 2,7-di-*tert*-butylfluorene (**45**) was then lithiated and reacted with paraformaldehyde to afford 2,7-di-*tert*-butylfluorenylmethanol (**46**). The corresponding chloroformate, which was prepared by reaction of **46** with *in-situ* generated phosgene, was immediately converted to the more easily storable *N*-hydroxysuccinimide ester  $Fmoc^*OSu$  **47** (Scheme 2-6a).

This reaction sequence proceeded in overall good yields (also see subsection 8.2.1) and afforded the final product in 10 g quantities. As reported in the literature,<sup>201</sup> the lithiation step in the synthesis of **46** posed some problems, necessitating titration of commercial  $nBuLi$  (1.6 M in hexanes, Sigma Aldrich) prior to use in order to ensure a precise stoichiometric match between base and **45**. The addition of even a slight excess of  $nBuLi$  resulted in drastically reduced yields or even complete failure to isolate the desired product. The use of the highly toxic gas phosgene was manageable on laboratory scales as it was generated *in situ* by pyridine-catalyzed decomposition of triphosgene, which is a weighable solid. On larger scales, this should probably be avoided by replacement with less toxic alternatives such as carbonyldiimidazole (CDI).

With sufficient quantities of  $Fmoc^*OSu$  at hand, the active ester active ester,  $DG1^{NHFmoc^*}$  (**50**), was prepared. Its synthesis from the corresponding methyl ester was not deemed feasible in this case, as  $Fmoc^*$ , unlike Boc, is not stable to base hydrolysis. Therefore, instead of the *N*-deprotected dendron **51**, the di(amino)acid **48** was used as a precursor. The synthesis of the  $NHFmoc^*$ -bearing carboxylic acid **49** was initially challenging but proceeded in good yield after some optimization of the solvent system and the base used (DIPEA proved superior to  $NEt_3$  and  $K_2CO_3$ ).

The dendronization agent **50** was then used in the synthesis of polymers of the type  $PGg_{500}^{NHFmoc^*}$ . As at least mildly basic conditions are necessary for dendronization, this step was critical due to the base-labile nature of  $NHFmoc^*$ . DIPEA was selected as the base for this process; it had proven fairly compatible with  $NHFmoc^*$  in the previous synthesis of **49**, an observation which is congruent with the fair stability of  $NHFmoc$  in the presence of DIPEA.<sup>203</sup>

However, whereas the synthesis of **49** had progressed encouragingly smoothly, no conditions suitable for dendronization of DPs with **50** were found: Initial attempts (mostly starting from  $PG1_{500}^{NH_3TFA}$ ) quickly revealed that partial deprotection of  $NHFmoc^*$  occurred under standard dendronization conditions (excess base), leading to hyperbranching. Hyperbranching, rather than the addition of a single generation in a well-defined manner, is to be strictly avoided: Excessive dendronization is just as problematic in the context of  $g_{max}$  considerations as defects are. Both lead to side-chain dispersity. Hyperbranching was evident from the appearance of a strongly fluorescent, high  $R_f$  spot in TLC of the dendronization reaction mixtures. An obvious candidate for this was the dibenzofulvene derivative **43**, which is liberated in the deprotection of  $Fmoc^*$ . The fluorescent compound was indeed successfully isolated upon treatment of **49** with excess  $NEt_3$  (see 8.2.1, Figure 8-5, Figure 8-6).

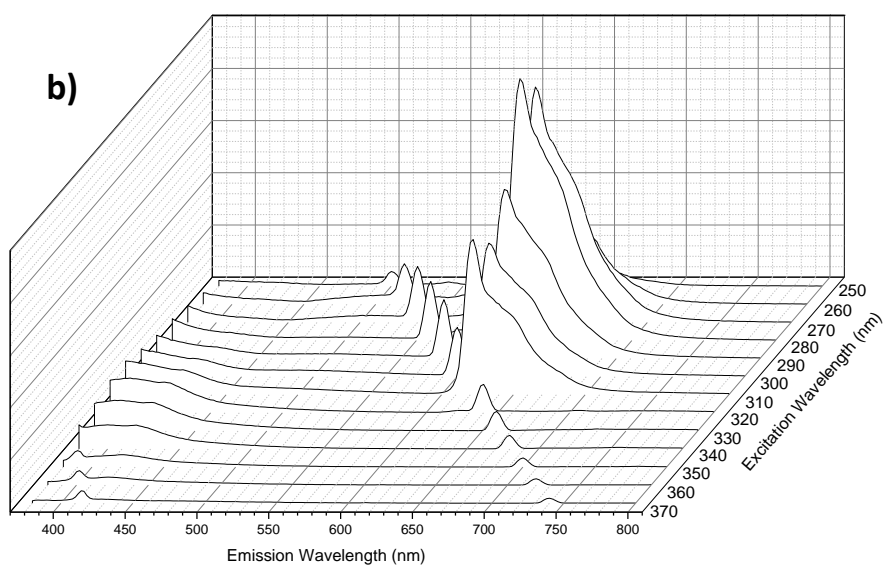
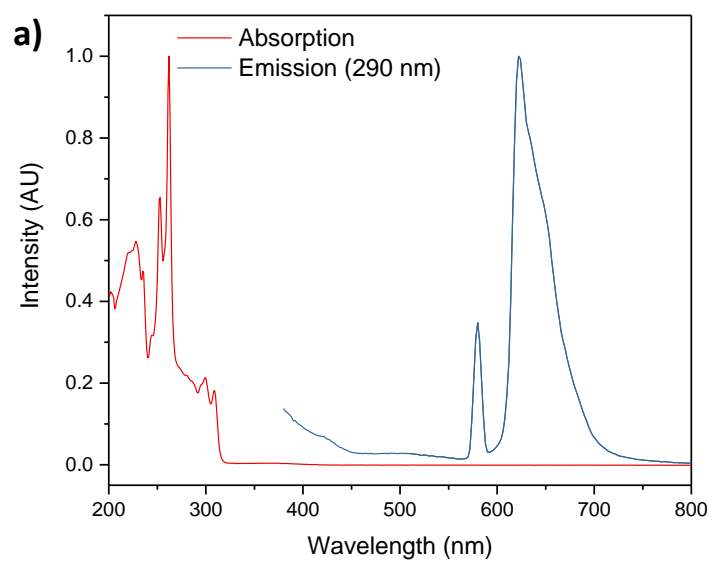


Figure 8-5: a) UV/Vis absorption and emission spectra ( $\lambda_{ex} = 290$  nm) of **43** isolated from the treatment of **49** with triethylamine. b) Excitation scan of **43** in THF, curiously showing both blue emission upon excitation at ca. 340 nm and more intense orange fluorescence upon excitation at 280 nm (both visible in Figure 8-5a).

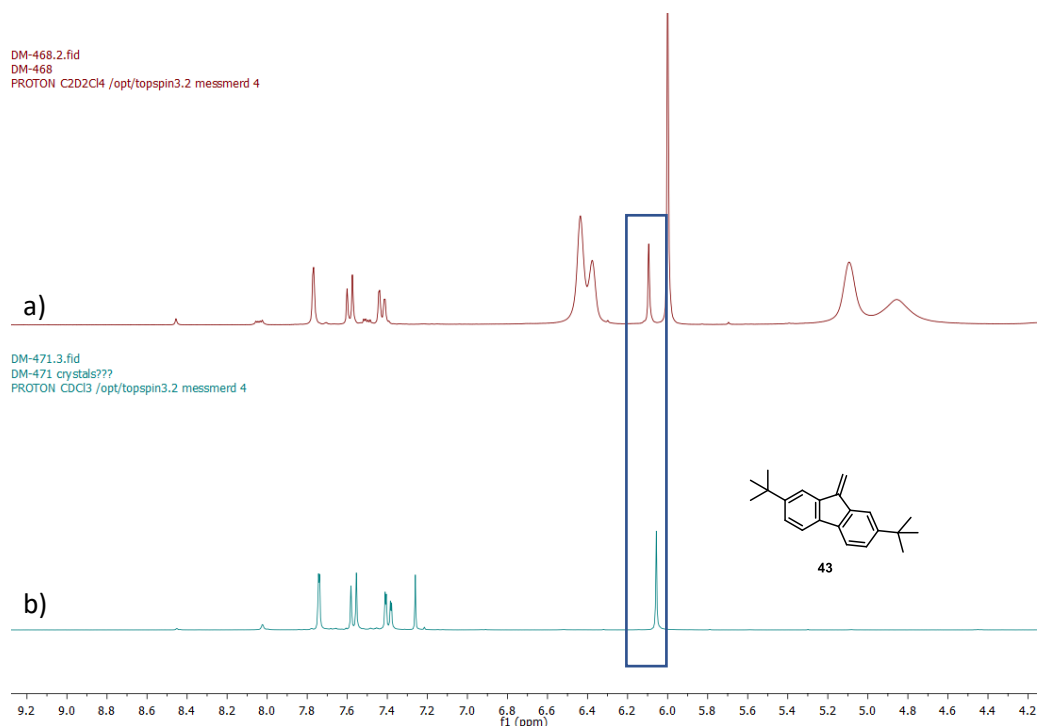


Figure 8-6: Selected regions of  $^1\text{H-NMR}$  spectra (300 MHz, 298 K) of a) the reaction product of dendronization of  $\text{PG1}_{500}^{\text{NH}_3\text{TFA}}$  with **50** ( $\text{TCE-d}_2$ ) and b) **43** ( $\text{CDCl}_3$ ) isolated from a dendronization attempt. Signals attributed to the fulvene moiety are highlighted.

Attempts to prevent this by using merely stoichiometric amounts of base, even with very slow addition of base (see subsection 8.2.1), were not able to prevent partial deprotection and the resulting hyperbranching. The addition of only substoichiometric amounts of base *was* successful in preventing partial  $\text{NHfmoc}^*$  deprotection and hyperbranching as indicated by TLC, however the resulting polymers could not be isolated successfully: Likely due to the presence of remaining free ammonium groups, their purification by flash chromatography (silica gel) afforded no or only negligible amounts of polymeric product. It had to be concluded, therefore, that the  $\text{Fmoc}^*$  protecting group is not compatible with a graft-from type synthesis aiming at the addition of precisely one dendritic generation. This is owed at least partially to the very long reaction times (weeks) necessary to achieve complete functional group conversion in the dendronization of DPs.

#### Attempted deprotection of $\text{PG5}_{500}^{\text{NHCbz}}$

Based on earlier work,<sup>172</sup> the synthesis of larger quantities of  $\text{PG5}_{500}^{\text{NHCbz}}$  was attempted. A synthesis of the necessary dendronization agent  $\text{DG1}^{\text{NHCbz}}$  (**102**) had been reported previously<sup>172</sup> but some modifications and improvements were made, providing straightforward access to **102** in multi-gram quantities (see subsection 8.2.1, Scheme 8-1). The synthesis of  $\text{PG5}_{500}^{\text{NHCbz}}$  by dendronization of  $\text{PG5}_{500}^{\text{NH}_3\text{TFA}}$  had previously only proceeded in comparatively low yield of *ca.* 40 %, which was improved here to > 65 %.

The hydrogenolytic deprotection of the resulting  $\text{PG5}_{500}^{\text{NHCbz}}$  was attempted several times, using heterogenous catalysts (Pd/C or Pd black). In a typical experiment, *ca.* 50 mg of  $\text{PG5}_{500}^{\text{NHCbz}}$  and small amount of the heterogenous catalyst in methanol or DMF were subjected to hydrogenolytic conditions (either direct hydrogenation or transfer hydrogenation, using ammonium formate as a hydrogen donor)<sup>207</sup> for several days to several weeks. Samples were taken at intervals and treated

with methylene chloride after filtration. The precipitation which would indicate *N*-deprotection was not observed in any of these attempts.

Homogenous catalysts were not used in these explorative attempts due to their higher cost and the greater difficulties connected to their removal – although they offer a greater chance of achieving complete deprotection due to the low accessibility of functional groups in DPs, and in view of the success with Pd(PPh<sub>3</sub>)<sub>4</sub>-catalyzed NHALloc deprotection, homogenous hydrogenation catalysis may be worth pursuing in the future.

#### Determination of NHALloc deprotection end point

For the determination of the amount of time necessary to achieve full deprotection, a small-scale reaction (*ca.* 200 mg PG5<sub>500</sub><sup>NHALloc</sup>) was started using the deprotection procedure for the synthesis of C-PG6<sub>500</sub><sup>NHBoc</sup> (see subsection 8.2.1). After 1 d, a third of the reaction mixture was transferred into another Schlenk tube and deprotection was terminated by first adding NaDDTC, then DG1<sup>NHBoc</sup> (5 equiv./amine). The same procedure was repeated with the remainder of the original solution after 2 d, and after 3 d the same sequence of additions was performed on the solution left in the original vessel. The three dendronization reactions were each stopped 4 d after the addition of DG1<sup>NHBoc</sup>, the polymer was isolated by precipitation into Et<sub>2</sub>O, then further purified by twice precipitating from little methylene chloride into Et<sub>2</sub>O.

<sup>1</sup>H-NMR spectra (Figure 8-8) at first glance indicated complete Alloc removal already after 1 d of deprotection. Some very small signals attributable to remaining NHALloc groups were present, but only visible in a magnified view. Even these signals disappeared completely after 2 – 3 d (Figure 8-9). The initial, purely arbitrarily selected deprotection time of 3 d was therefore also used in later experiments.

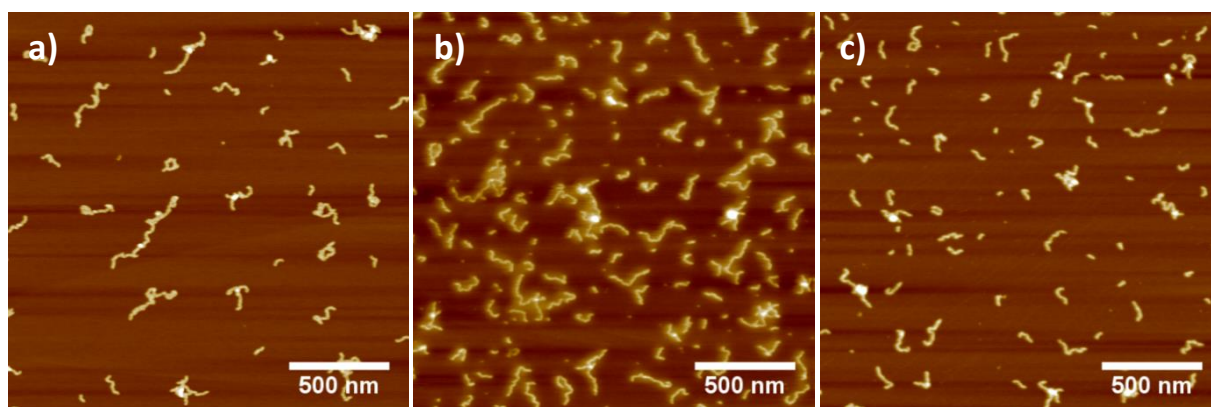


Figure 8-7: AFM height images of “PG6<sub>500</sub><sup>NHBoc</sup>” synthesized by quenching of the deprotection of PG5<sub>500</sub><sup>NHALloc</sup> with **20** after a) 1 d, b) 2 d, and c) 3 d.

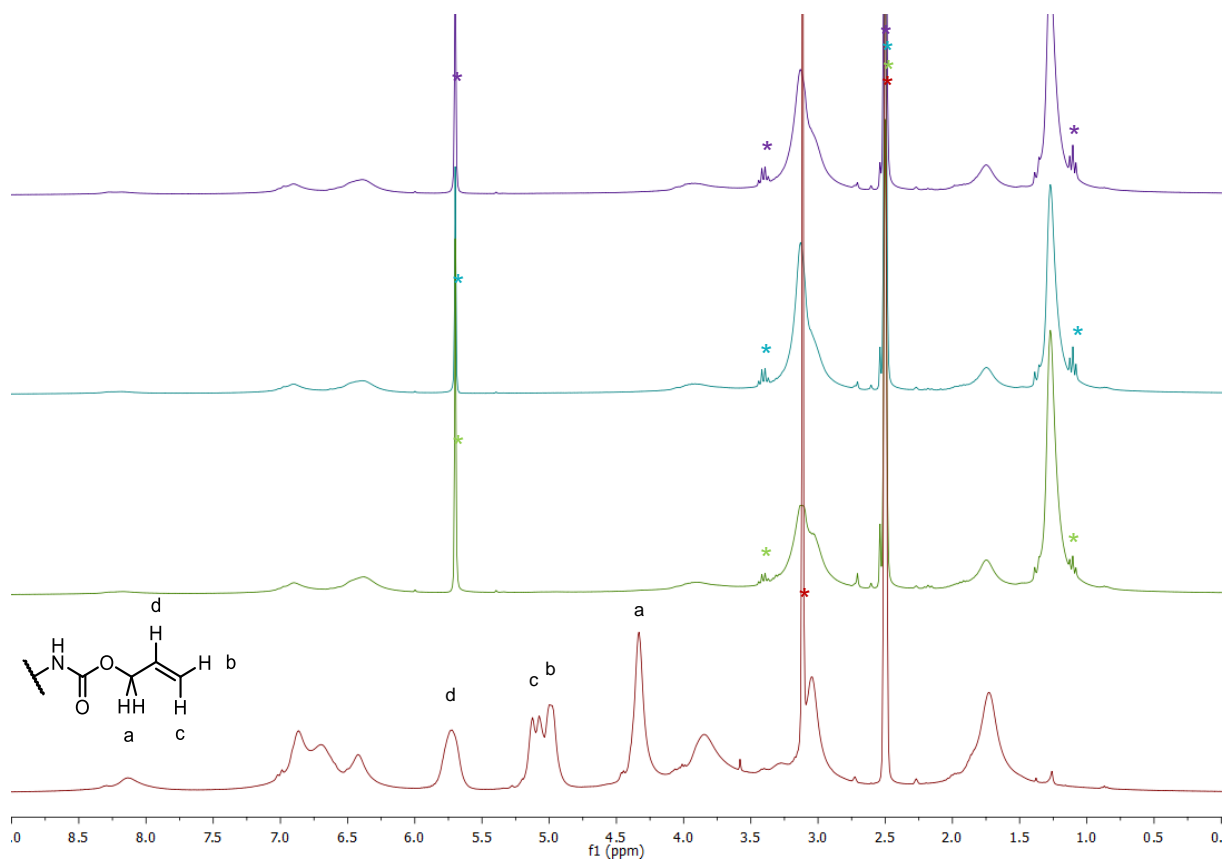


Figure 8-8:  $^1\text{H-NMR}$  spectra (300 MHz, 343 K,  $\text{DMSO-d}_6$ ) of  $\text{PG5}^{\text{NHAlloc}}$  (**31**, red, NHAlloc protons assigned) and samples quenched after 1 d (green), 2 d (turquoise), and 3 d (violet) of deprotection; the samples are nominally  $\text{PG6}^{\text{NHBOC}}$  as a result of quenching with **20**, but functional group conversion is low. Residual solvent signals (dioxane, methylene chloride, diethyl ether, DMSO) are marked with asterisks.

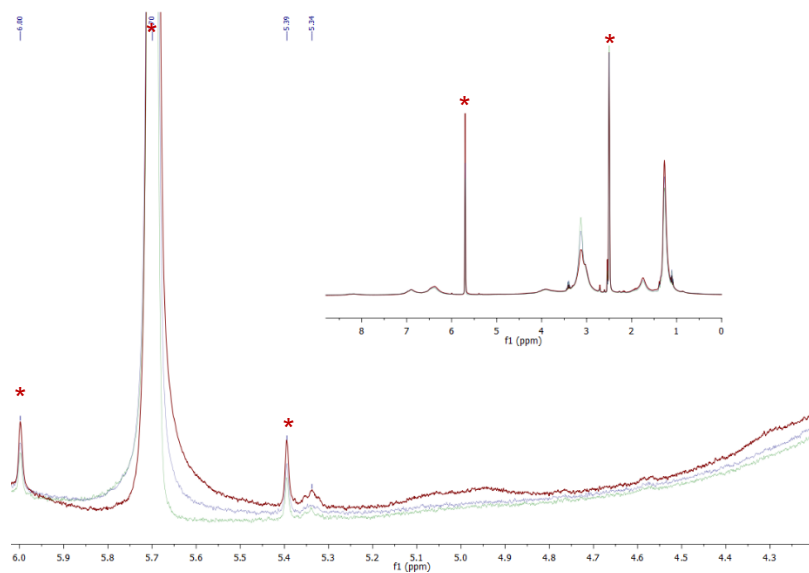


Figure 8-9: Superimposition of  $^1\text{H-NMR}$  spectra (300 MHz, 343 K,  $\text{DMSO-d}_6$ ) of samples quenched by addition of **20** after 1 d (red), 2 d (blue) and 3 d (green) under conditions of NHAlloc cleavage; also see Fig. S11. Residual solvent peaks (methylene chloride, DMSO) are marked by asterisks.

### Determination of dendronization end point

To assess when dendronization is complete, samples from an on-going dendronization reaction, performed as described for the synthesis of **C-PG**<sub>500</sub><sup>NHBoc</sup> (see subsection 8.2.1) were drawn at intervals of a few days. The samples, containing *ca.* 20 mg of polymer each, were precipitated into Et<sub>2</sub>O and the resulting products (yellow-orange, glassy solids) were analyzed by GPC (Figure 8-10a). Peak retention volumes (Figure 8-10b) ceased to change after *ca.* 35 d, continuing the previously established trend of *ca.* one additional week being required per *g* for dendronization to proceed to completion. Erring on the side of caution, 45 d was set as the duration for dendronization in experiments following this.

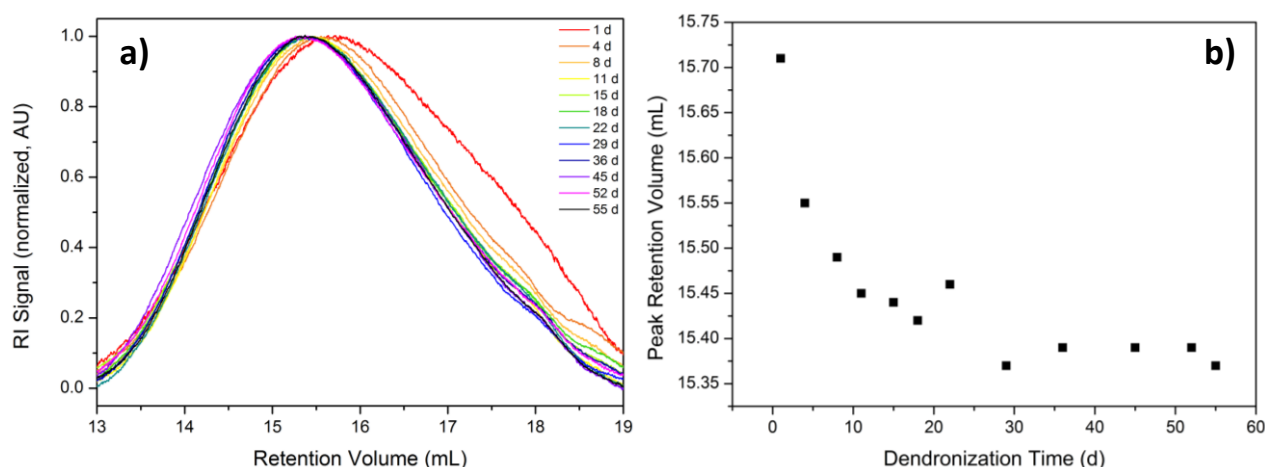


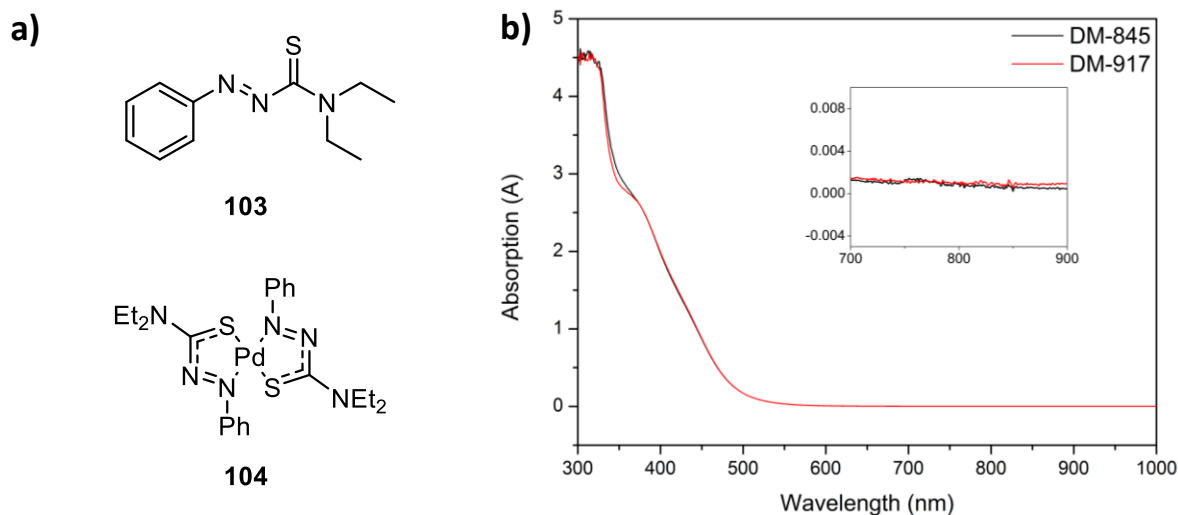
Figure 8-10: a) Normalized GPC curves (DRI signal) of samples drawn from the dendronization reaction of **PG**<sub>500</sub><sup>NH<sub>2</sub></sup>. b) Peak retention volume as a function of dendronization time. Retention volumes were adjusted to account for the small variations of the peak retention volume of the toluene flow marker ( $\pm 0.02$  mL). Reproduced with permission from Messmer, D.; Kröger, M.; Schlüter, A. D. *Macromolecules* **2018**, 51, 5420-5429. Copyright 2018, American Chemical Society.

### Quantification of residual Pd content

#### a) Colorimetric method

To provide a rough estimate of the residual amount of Pd, the colorimetric method by Krebs *et al.*<sup>225</sup> was used. This method relies on the readily synthesized azothioformamide ligand **103**, the Pd<sup>0</sup> complex of which (**104**, Figure 8-11a) absorbs strongly in the far-red end of the visible spectrum ( $\lambda_{\text{max,CHCl}_3} = 801$  nm,  $\epsilon = 10300$  M<sup>-1</sup> cm<sup>-1</sup>), appearing dark green in solution. The ligand by itself and DPs of the type **PG**<sub>*n*</sub><sup>NHBoc</sup> do not absorb in this spectral region (Figure 8-11b).

The treatment of samples of **C-PG**<sub>500</sub><sup>NHBoc</sup> with the ligand did not produce a visible green coloration, and a significant absorption peak at the expected wavelength was absent in UV/Vis spectroscopy. While this was encouraging, the detection limit of this colorimetric method is at *ca.* 40 ppm with the amount of polymer sacrificed (*ca.* 50 mg per sample). With this upper threshold, however, a determination of Pd content by ICP-OES became possible without wasting large amounts of **C-PG**<sub>500</sub><sup>NHBoc</sup> on preliminary experiments to determine the approximate calibration range.



#### b) ICP-OES

A substantial sample (ca. 3.7 g) of A-PG3<sub>500</sub><sup>NHBOC</sup> was digested in order to account for matrix effects. This provided accurate limits of detection and quantification using the Pd emission line at  $\lambda = 340.4$  nm (concentration-adjusted LOD<sub>340.4</sub> = 0.27 ppm; LOQ<sub>340.4</sub> = 0.88 ppm). Two samples of C-PG6<sub>500</sub><sup>NHBOC</sup> (200-300 mg) drawn from different synthetic batches were similarly digested for analysis.

Before digestion, all glassware employed was cleaned thoroughly by boiling 69 % aq. HNO<sub>3</sub> (ROTIPURAN Supra, Carl Roth; certified < 0.5 ppb Pd) inside the flasks and condensers, then rinsing with ultrapure water (MilliQ, > 18 M $\Omega$ ). Polymer samples were suspended in a few mL of 69 % HNO<sub>3</sub> at RT, then refluxed for 3 d. Excess HNO<sub>3</sub> was boiled off, the resulting solid was suspended in 2 % aq. HNO<sub>3</sub> by ultrasonication, then diluted to the appropriate concentration of ca. 8 mg mL<sup>-1</sup> and filtered before measurement of Pd concentration. ICP-OES followed an established procedure<sup>226</sup> and measurements were conducted by Dr. Sara Mantellato (D-BAUG, ETH Zurich) in axial view mode on an iCAP 6300 Dual-View spectrometer (Thermo Fisher) with an ASX-260 autosampler (CETAC). A Pd standard (TraceCERT 1000 mg L<sup>-1</sup> Pd in aq. HCl, Sigma Aldrich) was diluted with the matrix material derived from PG3<sub>500</sub><sup>NHBOC</sup> for calibration and determination of LOD/LOQ.

The Pd content measured by this method was above the limit of detection, but below the limit of quantification of both samples measured and is very low (Table 8-3). It is therefore conceivable that the residual yellow coloration does not stem from Pd species, but instead from organic impurities which are not completely removed during workup but present at sufficiently low concentrations so as to not appear in <sup>1</sup>H-NMR spectra or GPC retention curves.



Table 8-3: Results of Pd determination by ICP-OES. Two different batches of C-PG6<sup>NHBoc</sup><sub>500</sub> were employed (compare Figure 2-4c).

Sample	Before digestion [g]	Final sample weight [g]	Dilution factor	Measured Pd concentration (324.2 nm) [ppb]	Measured Pd concentration (340.4 nm) [ppb]
Matrix (PG3 <sup>NHBoc</sup> <sub>500</sub> )	3.73	557.82	149.5	N/A	N/A
C-PG6 <sup>NHBoc</sup> <sub>500</sub>	0.2394	31.204	130.3	3.00	3.08
C-PG6 <sup>NHBoc</sup> <sub>500</sub>	0.293	34.423	117.5	1.92	0.72

#### Analysis of AFM co-images

Samples containing approximately equimolar amounts of PG5<sup>NHAlloc</sup><sub>500</sub> and C-PG6<sup>NHBoc</sup><sub>500</sub> (Figure 8-13) or PG5<sup>NHBoc</sup><sub>500</sub> and B-PG6<sup>NHBoc</sup><sub>500</sub> (Figure 8-14) in DCM were prepared and drop-cast as described in subsection 8.2.1. Only one AFM tip each was used in the imaging of the resulting two samples, and the image series was terminated as soon as significant changes in tip geometry became evident.

The images were analyzed using FiberApp (see Figure 8-12a), a software suite permitting the automated tracking of filamentous objects in greyscale images. For both samples, greyscale values along the backbones of > 100 polymer chains or chain segments were extracted and analyzed. Histograms (Figure 8-12b,c) in both cases reveal two peaks, indicating two overlapping populations of height values. This suggests that rather than average height values, the visual distinguishability of PG5<sup>NHAlloc</sup><sub>500</sub> and C-PG6<sup>NHBoc</sup><sub>500</sub> stems from more pronounced undulation and perhaps corrugation than is the case for PG5<sup>NHBoc</sup><sub>500</sub> and B-PG6<sup>NHBoc</sup><sub>500</sub>, which appear approximately equally smooth (Figure 8-14).

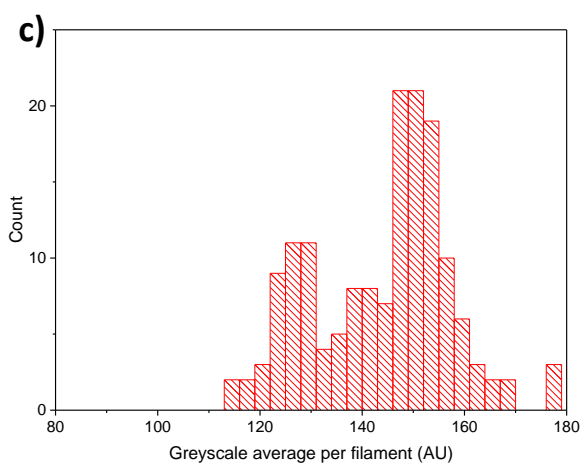
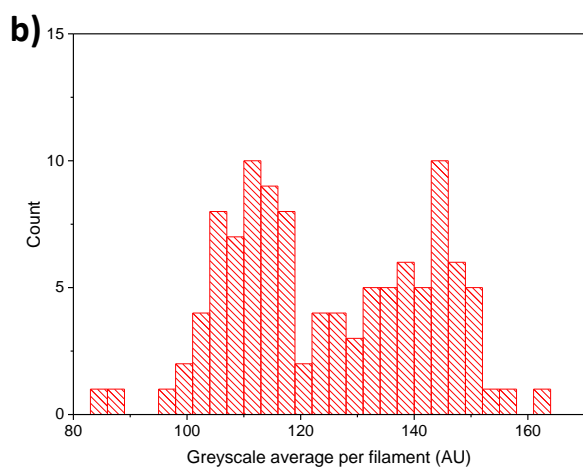
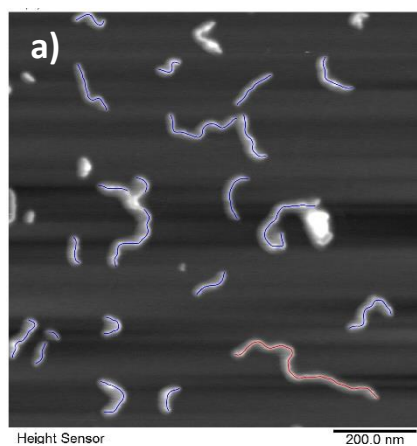


Figure 8-12: a) Example of polymer centerline tracing in FiberApp (compare Figure 2-8). Histograms of average greyscale values per polymer segment, extracted from b) 109 segments of  $PG5_{500}^{NHAlloc}/CPG6_{500}^{NHBoc}$  and c) 171 segments of  $PG5_{500}^{NHBoc}/BPG6_{500}^{NHBoc}$  using FiberApp.

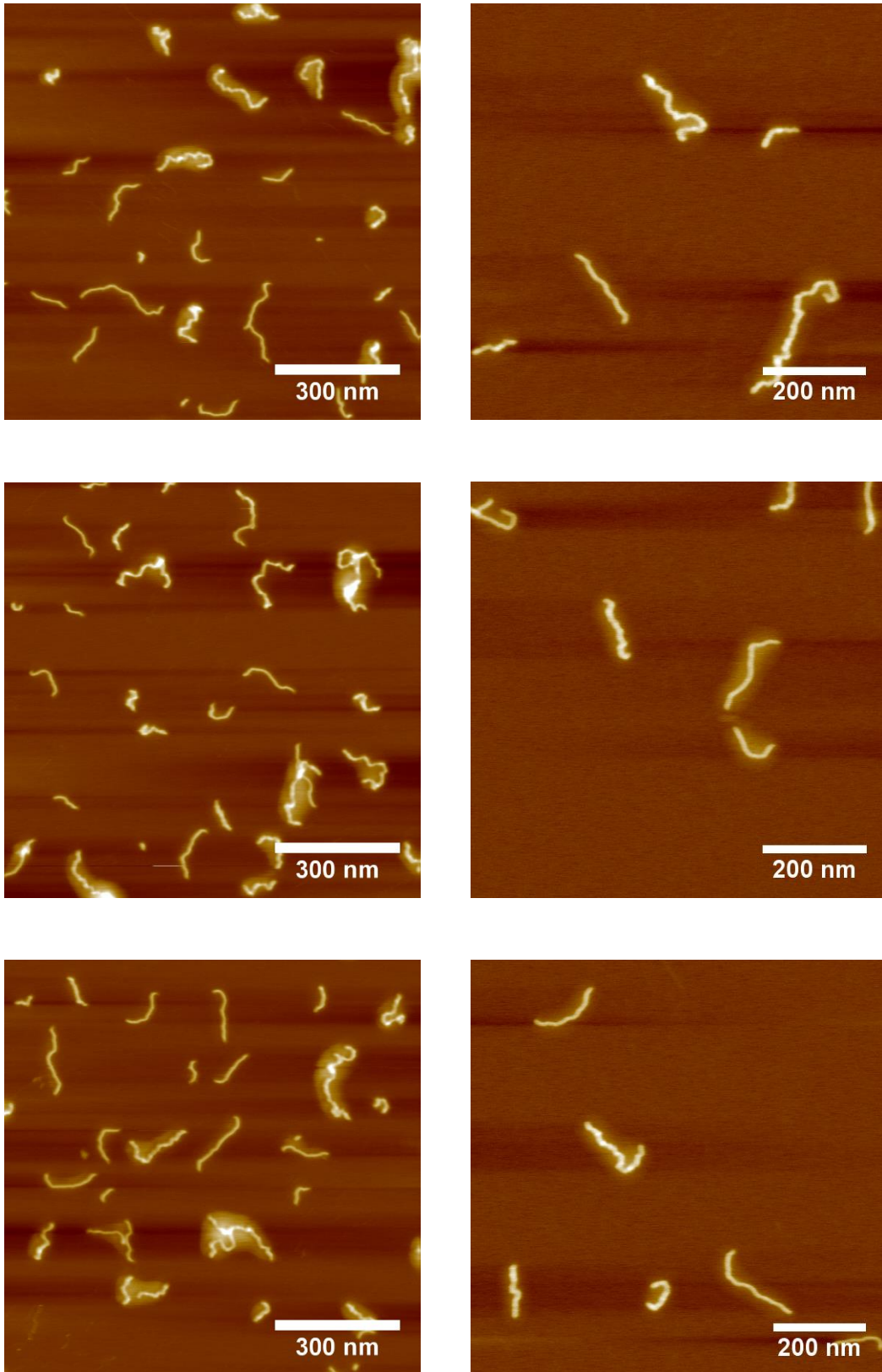


Figure 8-13: AFM height images of a copreparation of  $PG_{500}^{NHAlloc}$  and  $C-PG_{500}^{NHBoc}$  on mica.

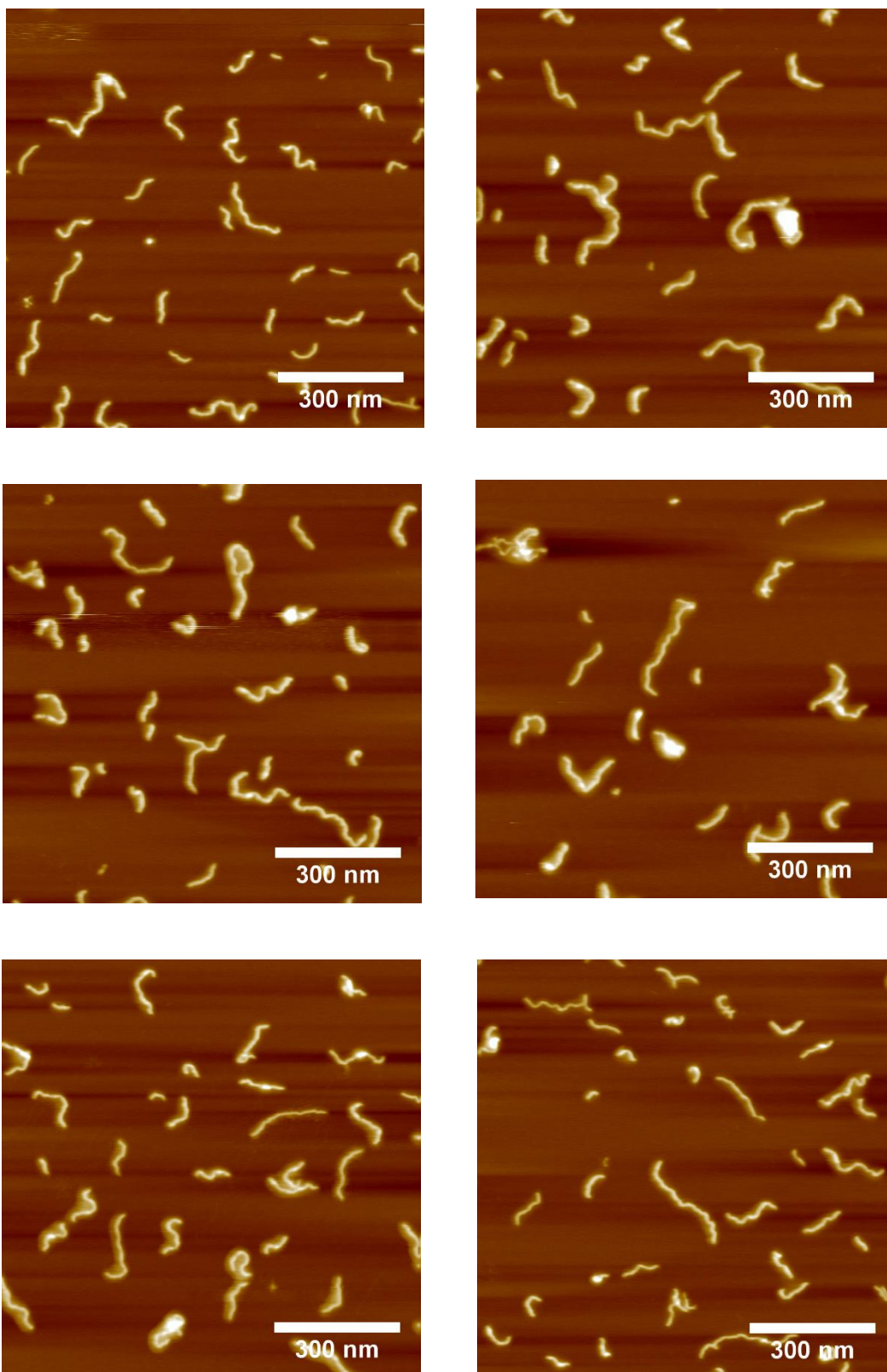


Figure 8-14: AFM height images of a copreparation of  $PG5_{500}^{NHBoc}$  and  $B-PG6_{500}^{NHBoc}$  on mica.

### 8.3. Experimental details for chapter 3: Investigations concerning DP main-chain scission

The MD simulation study presented in subsections 3.5.10 and 8.3.2 was conducted by Dr. Oscar Bertran and Pro. Dr. Carlos Alemán (both Universitat Politècnica de Catalunya); all EPR measurements and the evaluation of the preliminary EPR study in absence of radical scavenger were conducted by Dr. Reinhard Kissner (D-CHAB, ETH Zurich).

#### 8.3.1. Syntheses

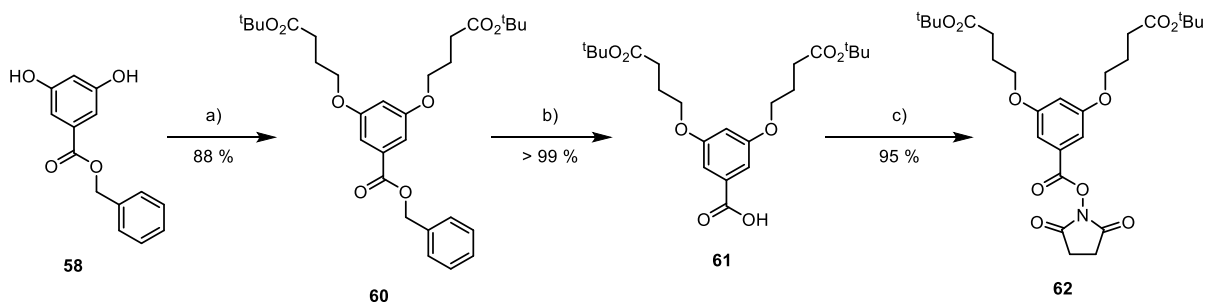
The following compounds were prepared according to literature procedures: benzyl 3,5-dihydroxybenzoate (**58**),<sup>371</sup> *tert*-butyl 4-bromobutyrate (**59**);<sup>372</sup> methyl 4-bromobutyrate (**64**).<sup>373</sup>

#### General procedure D: Deprotection of DPs of the type $PGg_n^{NHBoc}$

For NHBoc-deprotection, the polymer in question ( $PGg_n^{NHBoc}$ ) was cooled to 0 °C in a suitably sized vial or round-bottom flask. While stirring, cold, neat TFA (*ca.* 2 mL per 100 mg DP, approx. 50 equiv. TFA per amine) was added slowly. In this process, care was taken that all polymer adhering to the glass walls was flushed down. The resulting mixture (frequently a white suspension) was then warmed to RT and MeOH was added dropwise until the mixture was permanently clear (usually ~50 – 100  $\mu$ L per 100 mg DP). The polymer was stirred at RT overnight, then cooled to 0 °C in an ice bath and treated with MeOH (*ca.* 5 mL per 100 mg DP). The mixture was stirred at RT for 5 min, then solvents were removed by rotary evaporation at  $\leq$  35 °C. The addition of MeOH and removal of solvents was repeated twice, then the resulting glassy polymer,  $PGg_n^{NH_3TFA}$ , was lyophilized from deionized water.

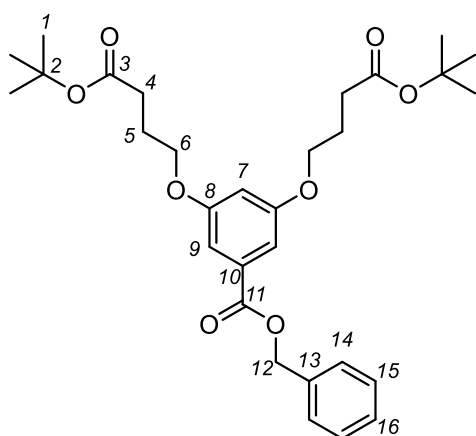
#### General procedure E: Dendronization of DPs of the type $PGg_n^{NH_3TFA}$

The lyophilizate of  $PGg_n^{NH_3TFA}$  (typically a colorless or off-white foam) was dissolved in DMF (*ca.* 1.5 mL per 100 mg DP) and the solution was cooled to 0 °C in an ice bath.  $NEt_3$  (2 equiv./amine) and DMAP (catalytic amount, *ca.* 0.05 – 0.1 equiv./amine) were added, followed by  $DG1^{NHBoc}$  (**20**, 3 equiv./amine). The reaction mixture was then warmed to RT and stirred for a total of *g* weeks (*e.g.* 3 weeks for  $PG3_n^{NHBoc}$  as the starting material). During this time, after *ca.* one third and two thirds of the total reaction time had elapsed, the reaction mixture was cooled back to 0 °C and further portions of  $DG1^{NHBoc}$  were added (1 equiv./amine on both occasions). After the indicated amount of stirring time, the reaction mixture was either concentrated in vacuum or precipitated into  $Et_2O$  (*ca.* 200 mL per 100 mg initial DP). The polymer ( $PG(g+1)_n^{NHBoc}$ ) was then purified by column chromatography (methylene chloride,  $R_f \approx 1.0$ ) and lyophilized from freshly distilled 1,4-dioxane.



Scheme 8-4: Synthesis of **62** (DG1<sup>CO2Me</sup>) Conditions: a) **59**,  $K_2CO_3$ , DMF, 60 °C; b)  $H_2$ , Pd/C, MeOH; c) HOSu, DCC, methylene chloride, 0 °C to RT.

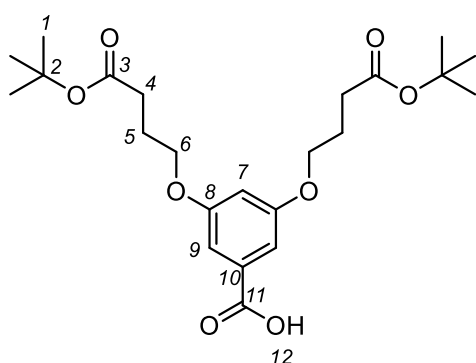
### Synthesis of benzyl 3,5-bis(3-(*tert*-butyloxycarbonyl)propyloxy)benzoate (**60**)



To a solution of **58** (21.87 g, 87 mmol) in DMF (180 mL),  $K_2CO_3$  (49.78 g, 360 mmol, 4 equiv.) was added and the mixture was stirred at RT for 30 min. Then, **59** (41.69 g, 188 mmol, 2.1 equiv.) was added as a solution in DMF (70 mL) and the mixture was stirred at 60 °C for 18 h. The resulting suspension was diluted with EtOAc (500 mL) and washed with water (2 x 800 mL) and brine (800 mL), then dried over  $MgSO_4$  and concentrated in vacuum. Column chromatography (EA/Hex 10:1) afforded **60** as a slightly yellow-tinged oil (41.5 g, 88 %).  $^1H$ -NMR (300 MHz,  $CDCl_3$ , 298 K): 7.42 – 7.21 (m, 5H, 14 – 16), 7.11 (d,  $J = 2.3$  Hz, 2H, 9), 6.56 (t,  $J = 2.4$  Hz, 1H, 7), 5.27 (s, 2H, 12), 3.92 (t,  $J = 6.1$  Hz, 4H, 6), 2.34 (t,  $J = 7.3$  Hz, 4H, 4), 1.98 (m, 4H, 5), 1.37 (s, 18H, 1).  $^{13}C$ -NMR (76 MHz,  $CDCl_3$ , 298 K): 172.56 (3), 166.33 (11), 160.06 (8), 136.13 (13), 132.07 (10), 128.73 (15), 128.37 (16), 128.34 (14), 108.17 (9), 106.58 (7), 80.55 (2), 67.37 (6), 66.97 (12), 32.12 (4), 28.27 (1), 24.82 (5). HR-MS: Calc. For  $C_{30}H_{44}NO_8$  ( $M+NH_4^+$ ):  $m/z = 546.3061$ ; found:  $m/z = 546.3064$ . Elemental analysis; Calc. 68.16 % C, 7.63 % H; found 68.19 % C, 7.7 % H.

9), 6.56 (t,  $J = 2.4$  Hz, 1H, 7), 5.27 (s, 2H, 12), 3.92 (t,  $J = 6.1$  Hz, 4H, 6), 2.34 (t,  $J = 7.3$  Hz, 4H, 4), 1.98 (m, 4H, 5), 1.37 (s, 18H, 1).  $^{13}C$ -NMR (76 MHz,  $CDCl_3$ , 298 K): 172.56 (3), 166.33 (11), 160.06 (8), 136.13 (13), 132.07 (10), 128.73 (15), 128.37 (16), 128.34 (14), 108.17 (9), 106.58 (7), 80.55 (2), 67.37 (6), 66.97 (12), 32.12 (4), 28.27 (1), 24.82 (5). HR-MS: Calc. For  $C_{30}H_{44}NO_8$  ( $M+NH_4^+$ ):  $m/z = 546.3061$ ; found:  $m/z = 546.3064$ . Elemental analysis; Calc. 68.16 % C, 7.63 % H; found 68.19 % C, 7.7 % H.

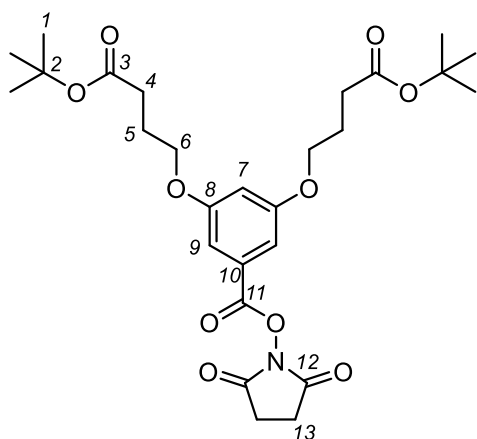
### Synthesis of 3,5-bis(3-(*tert*-butyloxycarbonyl)propyloxy)benzoic acid (**61**)



**60** (41.26 g, 52 mmol) was dissolved in MeOH (250 mL) and Pd/C (500 mg, 10 % Pd) was added. The mixture was stirred vigorously under 1 atm  $H_2$  supplied from a balloon for 15 h. The solution was then filtered through celite and concentrated in vacuum, affording **61** (34.07 g, 99.5 %) as a colorless solid.  $^1H$ -NMR (300 MHz,  $CDCl_3$ , 298 K): 7.22 (d,  $J = 2.3$  Hz, 2H, 9), 6.68 (t,  $J = 2.3$  Hz, 1H, 7), 4.02 (t,  $J = 6.1$  Hz, 4H, 6), 2.43 (t,  $J = 7.3$  Hz, 4H, 4), 2.07 (m, 4H, 5), 1.45 (s, 18H, 1).  $^{13}C$ -NMR (76 MHz,  $CDCl_3$ , 298 K): 172.63 (3), 171.46 (11), 160.12 (8), 131.17 (10), 108.50 (9), 107.56 (7), 80.63 (2),

67.41 (6), 32.13 (4), 28.28 (1), 24.83 (5). Melting point: 98-99 °C. HR-MS: Calc. for  $C_{23}H_{34}NaO_8$  ( $M+Na^+$ )  $m/z = 461.2146$ , found  $m/z = 461.2154$ . Elemental analysis: Calc. 63 % C, 7.81 % H, found 62.72 % C, 7.72 % H.

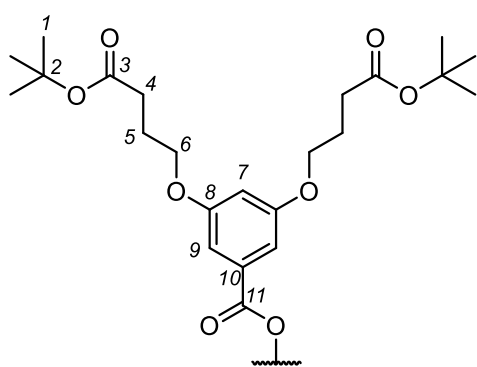
### Synthesis of 2,5-dioxopyrrolidin-1-yl 3,5-bis(3-(*tert*-butyloxycarbonyl)propyloxy)benzoate (**62**)



Prepared from **61** (15.09 g, 34 mmol) according to general procedure C (see subsection 8.2.1). After purification by column chromatography (EtOAc/Hex 1:1), **62** (22.22 g, 95 %) was obtained as a colorless solid. <sup>1</sup>H-NMR (300 MHz, CDCl<sub>3</sub>, 298 K): 7.22 (d, *J* = 2.3 Hz, 2H, 9), 6.72 (t, *J* = 2.4 Hz, 1H, 7), 4.01 (t, *J* = 6.1 Hz, 4H, 6), 2.9 (s, 4H, 12), 2.41 (t, *J* = 7.3 Hz, 4H, 4), 2.06 (m, 4H, 5), 1.45 (s, 18H, 1). <sup>13</sup>C-NMR (76 MHz, CDCl<sub>3</sub>, 298 K): 172.49 (3), 169.25 (12), 161.85 (11), 160.28 (8), 126.75 (10), 108.87 (7), 108.60 (9), 80.62 (2), 67.52 (6), 32.02 (4), 28.27 (1), 25.82 (13), 24.74 (5). Melting point: 78–79 °C. HR-MS: Calc. for C<sub>27</sub>H<sub>37</sub>NNaO<sub>10</sub> (M+Na<sup>+</sup>): *m/z* = 558.231; found: *m/z* = 558.2309. Elemental analysis: Calc.

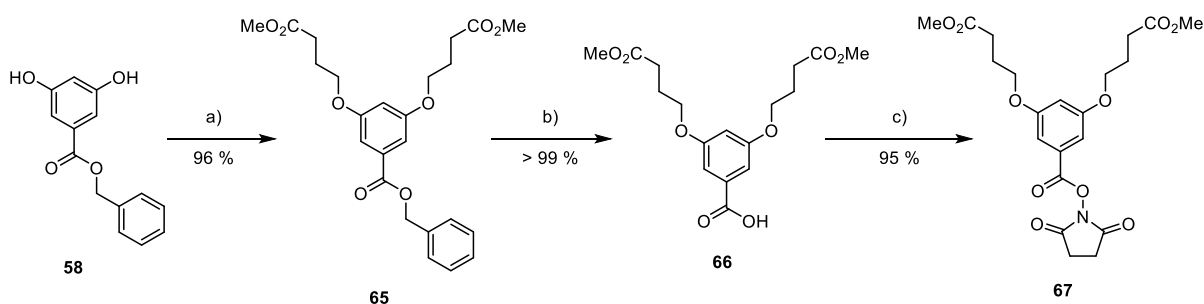
60.55 % C, 6.96 % H, 2.62 % N; found 60.38 % C, 6.97 % H, 2.67% N.

### Synthesis of PG5<sub>500</sub><sup>CO<sub>2</sub>tBu</sup> (**32**)



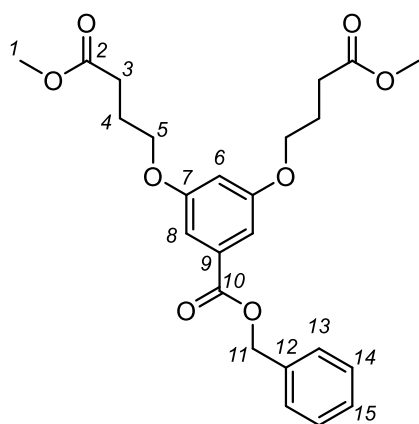
To a solution of PG4<sub>500</sub><sup>NH<sub>3</sub>TFA</sup> (513.2 mg, 91 μmol, 1.45 mmol amines), DMAP (30.1 mg, 0.2 mmol, 0.17 equiv./amine) and NEt<sub>3</sub> (0.45 mL, 3.2 mmol, 2.2 equiv./amine) in DMF (5 mL), **62** was added (2.3 g, 4.3 mmol, 3 equiv./amine) as a solution in DMF (*ca.* 5 mL) at 0 °C. The mixture was warmed to RT and monitored visually. CHCl<sub>3</sub> was added to the mixture as necessary in order to maintain a clear solution at first (*ca.* 10 mL in portions of 1 – 2 mL, added over the course of 7 d), after which no turbidity arose, anymore. The solution was stirred for an additional 2 weeks, then

precipitated into hexane. The resulting polymer was isolated by column chromatography (methylene chloride, *R<sub>f</sub>* ≈ 1) and lyophilized from freshly distilled dioxane, affording PG5<sub>500</sub><sup>CO<sub>2</sub>tBu</sup> (**32**) as a colorless powder (816 mg, 85 %). <sup>1</sup>H-NMR (300 MHz, TCE-d<sub>2</sub>, 343 K): 6.94 (app. s(b), 9), 6.47 (app. s(b), 7), 3.88 (app. s(b), 6), 2.29 (s(b), 4), 1.81 (app. s(b), 5), 1.36 (s, 1).



Scheme 8-5: Synthesis of **67** (DG1<sup>CO<sub>2</sub>Me</sup>) Conditions: a) **64**, K<sub>2</sub>CO<sub>3</sub>, DMF, 60 °C; b) H<sub>2</sub>, Pd/C, MeOH; c) HOSu, DCC, methylene chloride, 0 °C to RT.

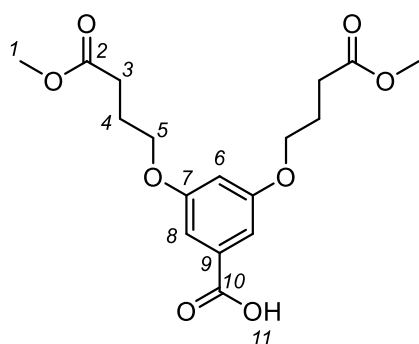
### Synthesis of benzyl 3,5-bis(3-(methyloxycarbonyl)propyloxy)benzoate (**65**)



To a solution of **58** (13.441 g, 55 mmol) in DMF (230 mL),  $K_2CO_3$  (30.87 g, 223 mmol, 4.1 equiv.) was added and the mixture was stirred at RT for 20 min. Then, **64** (24.16 g, 133 mmol, 2.4 equiv.) was added as a solution in DMF (70 mL) and the mixture was stirred at 60 °C for 16 h. The resulting suspension was diluted with EtOAc (500 mL), washed with water (2x 1 L) and brine (800 mL), then dried over  $MgSO_4$  and concentrated in vacuum. Column chromatography (EA/Hex 1:1) afforded **65** as a colorless oil (23.5 g, 96 %).  $^1H$ -NMR (300 MHz,  $CDCl_3$ , 298 K): 7.45 – 7.23 (m, 5H, 13 – 14), 7.18 (d,  $J = 2.3$  Hz, 2H, 8), 6.61 (t,  $J = 2.4$  Hz, 1H, 6), 5.34 (s, 2H, 11), 4.10 (t,  $J = 6.1$  Hz, 4H, 5), 3.68 (s, 6H, 1),

2.52 (t,  $J = 7.3$  Hz, 4H, 3), 2.1 (m, 4H, 4).  $^{13}C$ -NMR (76 MHz,  $CDCl_3$ , 298 K): 173.68 (2), 166.30 (10), 159.98 (7), 136.12 (12), 132.12 (9), 128.74 (13 or 14), 128.40 (15), 128.36 (13 or 14), 108.17 (7), 106.62 (7), 67.18 (5), 67.01 (11), 51.81 (1), 30.63 (3), 24.68 (4). HR-MS: Calc. for  $C_{24}H_{28}NaO_8$  ( $M+Na^+$ ):  $m/z = 467.1676$ , found:  $m/z = 467.1682$ . Elemental analysis: Calc. 64.85 % C, 6.35 % H, 28.8% O, found 64.79 % C, 6.35 % H, 28.97 % O.

### Synthesis of 3,5-bis(3-(methyloxycarbonyl)propyloxy)benzoic acid (**66**)

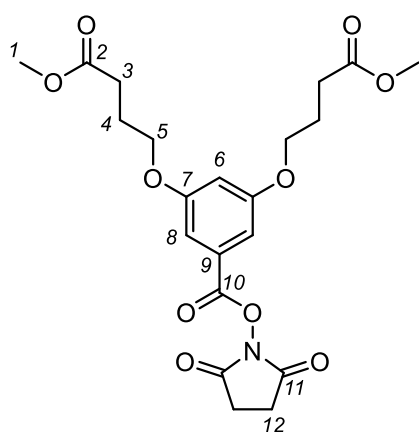


**65** (23.2 g, 52 mmol) was dissolved in MeOH (250 mL) and Pd/C (500 mg, 10 % Pd) was added. The mixture was stirred vigorously under 1 atm  $H_2$  supplied from a balloon for 15 h. The solution was then filtered through celite and concentrated in vacuum, affording **66** (19 g, > 99 %) as a colorless solid.  $^1H$ -NMR (300 MHz,  $CDCl_3$ , 298 K): 7.22 (d,  $J = 2.3$  Hz, 2H, 8), 6.66 (t,  $J = 2.3$  Hz, 1H, 6), 4.04 (t,  $J = 6.1$  Hz, 4H, 5), 3.70 (s, 6H, 1), 2.53 (t,  $J = 7.3$  Hz, 4H, 3), 2.12 (m, 4H, 4).  $^{13}C$ -NMR (76 MHz,  $CDCl_3$ , 298 K): 173.72 (2), 171.35 (10), 160.03 (7), 131.19 (9), 108.49 (8), 107.56 (6), 67.22

(5), 51.84 (1), 30.64 (3), 24.67 (4). Melting point: 89 °C. HR-MS: calc. for  $C_{17}H_{23}O_8$  ( $M+H^+$ ):  $m/z = 355.1387$ ; found:  $m/z = 355.1389$ . Elemental analysis: Calc. 57.62 % C, 6.26 % H, 36.12 % O; found 57.68 % C, 6.26 % H, 36.24 % O.



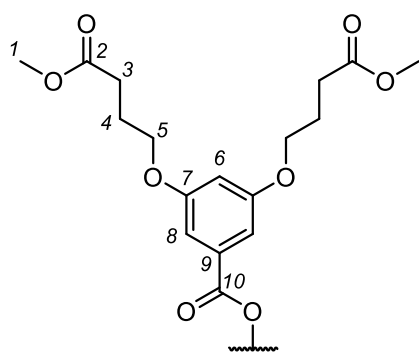
### Synthesis of 2,5-dioxopyrrolidin-1-yl 3,5-bis(3-(methoxycarbonyl)propoxy)benzoate (**67**)



Prepared from **66** (18.14 g, 51 mmol) according to general procedure C (see subsection 8.2.1). After purification by column chromatography (EtOAc/Hex 1:1), **67** (22.22 g, 95 %) was obtained as a colorless oil. <sup>1</sup>H-NMR (300 MHz, CDCl<sub>3</sub>, 298 K): 7.21 (d, *J* = 2.3 Hz, 2H, 8), 6.7 (t, *J* = 2.3 Hz, 1H, 6), 4.01 (t, *J* = 6.1 Hz, 4H, 5), 3.68 (s, 6H, 1), 2.89 (s, 4H, 12), 2.51 (t, *J* = 7.2 Hz, 4H, 3), 2.1 (m, 4H, 4). <sup>13</sup>C-NMR (76 MHz, CDCl<sub>3</sub>, 298 K): 173.58 (2), 169.27 (11), 161.79 (10), 160.17 (7), 126.7 (9), 108.81 (8), 108.61 (6), 67.31 (5), 51.81 (1), 30.52 (3), 25.80 (12), 24.57 (4). HR-MS: calc. for C<sub>21</sub>H<sub>29</sub>N<sub>2</sub>O<sub>10</sub> (M+NH<sub>4</sub><sup>+</sup>): *m/z* = 469.1817; found: *m/z* = 469.1815. Elemental analysis: Calc. 55.87 % C, 5.58 % H, 3.1 % N;

found 55.61 % C, 5.8 % H, 3.28 % N.

### Synthesis of PG5<sub>500</sub><sup>CO<sub>2</sub>Me</sup> (**33**)



To a solution of PG4<sub>500</sub><sup>NH<sub>3</sub>TFA</sup> (prepared by general procedure D, 115 mg, 20 μmol, 0.32 mmol amines), DMAP (19.3 mg, 0.16 mmol, 0.5 equiv./amine) and NEt<sub>3</sub> (0.1 mL, 0.72 mmol, 2.2 equiv./amine) in DMF (5 mL), **67** was added (440.5 mg, 0.98 mmol, 3 equiv./amine) as a solution in DMF (*ca.* 1.5 mL) at 0 °C. Further portions of **67** were added at 0 °C after 10 d (146.8 mg, 0.33 mmol, 1 equiv./amine) and 20 d (158 mg, 0.35 mmol, 1.1 equiv./amine). After a total of 30 d of stirring, the resulting solution was concentrated in vacuum and purified by column

chromatography (methylene chloride, *R<sub>f</sub>* ≈ 1). The resulting polymer was lyophilized from freshly distilled dioxane, affording PG5<sub>500</sub><sup>CO<sub>2</sub>Me</sup> (**33**) as a colorless powder (104 mg, 56 %). <sup>1</sup>H-NMR (300 MHz, DMSO-*d*<sub>6</sub>, 343 K): 8.14 (app. s(b), amide H of underlying structure), 6.85 (app. s(b), 8), 6.39 (app. s(b), 6), 3.82 (app. s(b), 5), 3.41 (s(b), 1), 2.23 (app. s(b), 3), 1.76 (app. s(b), 4).

### Synthesis of PG5<sub>500</sub><sup>NHAlloc36</sup>

PG4<sub>500</sub><sup>NH<sub>3</sub>TFA</sup> (prepared according to General Procedure D, 100.5 mg, 19 μmol RUs) was dissolved in DMF (3 mL); at 0 °C, DMAP (9.3 mg, 80 μmol, 0.25 equiv./amine) and NEt<sub>3</sub> (0.1 mL, 0.7 mmol, 2.3 equiv./amine) were added, followed by a 54.5 mg mL<sup>-1</sup> solution of DG1<sup>NHAlloc</sup> (**55**, 0.73 mL, 75 μmol 0.25 equiv./amine) in DMF. The resulting solution was stirred at RT for 5 d, then DG1<sup>NHBoc</sup> (**20**, 400 mg, 0.7 mmol, 2.3 equiv./amine) was added. After 10 more days of stirring, another portion of DG1<sup>NHBoc</sup> (**20**, 417 mg, 0.7 mmol, 2.3 equiv./amine) was added. After a total of 35 d of stirring, the reaction mixture was concentrated in vacuum and precipitated into Et<sub>2</sub>O (80 mL). Purification of the polymer by column chromatography (methylene chloride, *R<sub>f</sub>* ≈ 1), followed by lyophilization from freshly distilled 1,4-dioxane afforded a white powder (78 mg, 39 %). <sup>1</sup>H-NMR (300 MHz, DMSO-*d*<sub>6</sub>, 343 K): 8.21 (s (b)), 6.89-6.73 (m (b)), 6.45-6.3 (m (b)), 5.75 (app. s (b)), 5.1-5.01 (m (b)), 4.36 (app. s (b)), 3.02 (app. s(b)), 1.75 (app. s (b)), 1.25 (s (b)). Integration of NMR signals indicates *ca.* 36 % NHAlloc.

### Synthesis of PG5<sup>NHAlloc57</sup>

PG4<sup>NH<sub>3</sub>TFA</sup><sub>500</sub> (prepared according to General Procedure D, 108.1 mg, 20 μmol RUs) was dissolved in DMF (3 mL); at 0 °C, DMAP (6.5 mg, 53 μmol, 0.16 equiv./amine) and NEt<sub>3</sub> (0.1 mL, 0.7 mmol, 2.2 equiv./amine) were added, followed by a 54.5 mg mL<sup>-1</sup> solution of DG1<sup>NHAlloc</sup> (**55**, 2.45 mL, 0.25 mmol, 0.75 equiv./amine). The resulting solution was stirred at RT for 5 d, then DG1<sup>NHBoc</sup> (**20**, 404.9 mg, 0.7 mmol, 2.1 equiv./amine) was added. After 10 more days of stirring, another portion of DG1<sup>NHBoc</sup> (**20**, 404.5 mg, 0.7 mmol, 2.1 equiv./amine) was added. After a total of 35 d of stirring, the reaction mixture was concentrated in vacuum and precipitated into Et<sub>2</sub>O (80 mL). Purification of the polymer by column chromatography (methylene chloride, *R<sub>f</sub>* ≈ 1), followed by lyophilization from freshly distilled 1,4-dioxane afforded a white powder (91 mg, 43 %). <sup>1</sup>H-NMR (300 MHz, DMSO-*d*<sub>6</sub>, 343 K): 8.15 (s (b)), 6.88-6.73 (m (b)), 6.45-6.3 (m (b)), 5.75 (app. s (b)), 5.1-5.01 (m (b)), 4.36 (app. s (b)), 3.06 (app. s(b)), 1.75 (app. s (b)), 1.24 (s (b)). Integration of NMR signals indicates *ca.* 57 % NHAlloc.

### Synthesis of PG5<sup>NHAlloc80</sup>

PG4<sup>NH<sub>3</sub>TFA</sup><sub>500</sub> (prepared according to General Procedure D, 113.3 mg, 21 μmol RUs) was dissolved in DMF (3 mL); at 0 °C, DMAP (9.3 mg, 0.25 equiv./amine) and NEt<sub>3</sub> (0.1 mL, 0.7 mmol, 2.4 equiv./amine) were added, followed by a 54.5 mg mL<sup>-1</sup> solution of DG1<sup>NHAlloc</sup> (**55**, 0.73 mL, 0.25 equiv./amine). The resulting solution was stirred at RT for 5 d, then DG1<sup>NHBoc</sup> (**20**, 400 mg, 0.7 mmol, 2.4 equiv./amine) was added. After 10 more days of stirring, another portion of DG1<sup>NHBoc</sup> (**20**, 417 mg, 0.7 mmol, 2.4 equiv./amine) was added. After a total of 35 d of stirring, the reaction mixture was concentrated in vacuum and precipitated into Et<sub>2</sub>O (80 mL). Purification of the polymer by column chromatography (methylene chloride, *R<sub>f</sub>* ≈ 1), followed by lyophilization from freshly distilled 1,4-dioxane afforded a white powder (97 mg, 44 %). <sup>1</sup>H-NMR (300 MHz, DMSO-*d*<sub>6</sub>, 343 K): 8.15 (s (b)), 6.76 (m (b)), 6.44 (app. s (b)), 5.74 (app. s (b)), 5.14-5.0 (m (b)), 4.34 (app. s (b)), 3.12 (app. s(b)), 1.73 (app. s (b)), 1.25 (s (b)). Integration of NMR signals indicates *ca.* 80 % NHAlloc.

### Synthesis of PG1<sup>NHBoc</sup><sub>10'000</sub> (**21**)

A solution of MG1<sup>NHBoc</sup> (**18**, 15.24 g, 29.1 mmol) and AIBN (41 mg, 25 μmol, 0.8 mol%) in dry DMF (15 mL) was degassed by freeze-pump-thaw and then stirred under N<sub>2</sub> at 65 °C overnight. The resulting highly viscous solution was dissolved in methylene chloride and purified by column chromatography (methylene chloride, *R<sub>f</sub>* ≈ 1.0). The product was lyophilized from freshly distilled 1,4-dioxane, affording PG1<sup>NHBoc</sup><sub>10'000</sub> (**21**) as a glassy, colorless solid (14.5 g, 95 %). GPC (DMF, 0.1 % LiBr): *M<sub>n</sub>* > 3 MDa (partially in column cutoff; peak almost entirely out of calibration range), *Đ* ≈ 1.5. <sup>1</sup>H-NMR (300 MHz, DMSO-*d*<sub>6</sub>, 343 K): 8.15 (s (b)), 6.9 (app. s (b)), 6.48 (s), 6.39 (app. s(b)), 3.87 (app. s(b)), 3.31 (app. s(b)), 3.02 (m (b)), 1.75 (m (b)), 1.3 (s).

### Synthesis of PG2<sup>NHBoc</sup><sub>10'000</sub> (**23**)

Prepared according to General Procedures D, then E, starting from PG1<sup>NHBoc</sup><sub>10'000</sub> (3.987 g, 7.6 mmol RUs), resulting in a colorless foam (PG2<sup>NHBoc</sup><sub>10'000</sub>, 7.75 g, 83 %). Functional group conversion (General Procedure A): 99.9 %. <sup>1</sup>H-NMR (300 MHz, DMSO-*d*<sub>6</sub>, 343 K): 6.39-6.35 (m (b)), 4.78 (app. s(b)), 3.87 (app. s(b)), 3.06 (m (b)), 1.79 (m (b)), 1.34 (s), 0.93 (s (b)), 0.72 (s (b)).

#### Synthesis of PG3<sup>NHBoc</sup><sub>10'000</sub> (24)

Prepared according to General Procedures D, then E, starting from PG2<sup>NHBoc</sup><sub>10'000</sub> (4.6 g, 3.7 mmol RUs), resulting in a colorless foam (PG3<sup>NHBoc</sup><sub>10'000</sub>, 7.31 g, 74 %). Functional group conversion (General Procedure A): 99.9 %. <sup>1</sup>H-NMR (300 MHz, DMSO-*d*<sub>6</sub>, 343 K): 8.13 (s (b)), 6.88 (app. s (b)), 6.45 (s), 6.33 (app. s(b)), 3.85 (app. s(b)), 3.28 (app. s(b)), 3.0 (m (b)), 1.73 (m (b)), 1.27 (s).

#### Synthesis of PG4<sup>NHBoc</sup><sub>10'000</sub> (25)

Prepared according to General Procedures D, then E, starting from PG3<sup>NHBoc</sup><sub>10'000</sub> (3.6 g, 1.4 mmol RUs), resulting in a colorless foam (PG4<sup>NHBoc</sup><sub>10'000</sub>, 7.31 g, 76 %). Functional group conversion (General Procedure A): 99.9 %. <sup>1</sup>H-NMR (300 MHz, DMSO-*d*<sub>6</sub>, 343 K): 8.16 (s (b)), 6.87 (app. s (b)), 6.3 (app. s(b)), 3.0 (m (b)), 1.7 (app. s (b)), 1.24 (s).

#### Synthesis of PG5<sup>NHBoc</sup><sub>5'000</sub> (26)

Prepared according to General Procedures D, then E, starting from PG2<sup>NHBoc</sup><sub>10'000</sub> (1.75 g, 0.3 mmol RUs), resulting in a colorless foam (PG5<sup>NHBoc</sup><sub>5'000</sub>, 2.15 g, 60 %). Functional group conversion (General Procedure A): 99.6 %. <sup>1</sup>H-NMR (300 MHz, DMSO-*d*<sub>6</sub>, 343 K): 8.21 (s (b)), 6.89 (app. s (b)), 6.43 (app. s (b)), 3.87 (app. s(b)), 3.0 (app. s (b)), 1.72 (app. s (b)), 1.24 (s).

#### Synthesis of PG5<sup>NHAlloc</sup><sub>10'000</sub> (31)

Prepared according to General Procedures D, then E (with the sole modification that DG1<sup>NHAlloc</sup> (55) was used instead of DG1<sup>NHBoc</sup> (20), starting from PG4<sup>NHBoc</sup><sub>10'000</sub> (1.71 g, 0.3 mmol RUs), resulting in a colorless foam (PG5<sup>NHAlloc</sup><sub>10'000</sub>, 1.71 g, 52 %). Functional group conversion (General Procedure A): 99.3 %. <sup>1</sup>H-NMR (300 MHz, DMSO-*d*<sub>6</sub>, 343 K): 8.2 (s (b)), 6.82 (app. s (b)), 6.43 (app. s(b)), 4.95 – 5.1 (m (b)), 4.33 (s (b)), 3.87 (app. s(b)), 3.05 (app. s (b)), 1.73 (app. s (b)).

As noted in the main text, the DP of *g* = 5 in this series of long-chain polymers was of notably shorter length than the previous members of the series; this is evident in AFM (see *e.g.* chapter 3: Figure 3-12c vs. Figure 3-12e,f) and in GPC (Figure 8-15). Likely, this is a consequence of swelling-induced main-chain scission as discussed extensively in chapter 3: It is possible that the DMF reaction mixture resulting from dendronization was briefly heated to > 60 °C accidentally, *e.g.* during the removal of excess solvent before precipitation and purification of the polymer. Scission does not occur in the deprotection of PG4<sup>NHBoc</sup><sub>10'000</sub>, as evidenced by the maintained chain length of PG5<sup>NHAlloc</sup><sub>10'000</sub> (Figure 8-16).

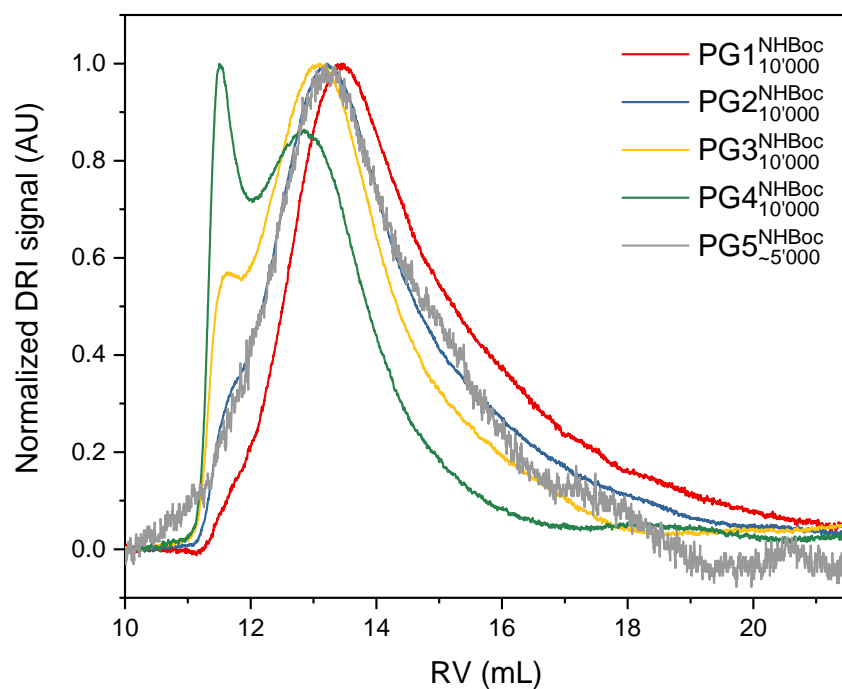


Figure 8-15: GPC retention curves of the series of long-chain DPs. Note that the peak RV increases up to  $g = 4$ , but then drops significantly for  $g = 5$ . For all DPs, the high molar mass lead of the peak is in the exclusion volume of the column set of  $RV \approx 11.2$  mL.

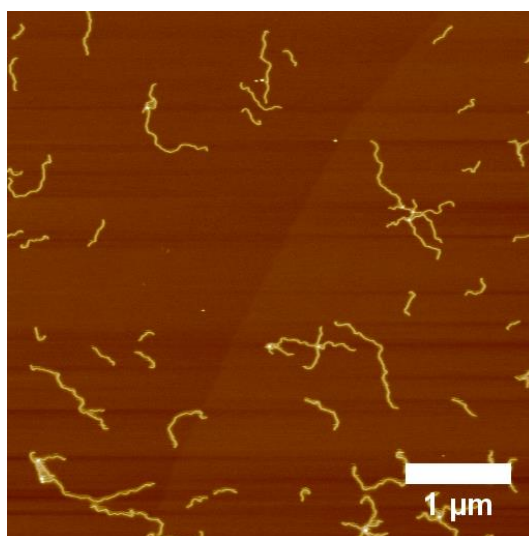


Figure 8-16: AFM height image of  $PG5^{NHAlloc}_{10^000}$ .

Table 8-4: Sanger labelling data and resulting functional group conversion values (recursive method) for the polymers in Figure 8-15 of  $g = 2$  to  $g = 5$ .

Polymer	w [mg]	w <sub>s</sub> [g]	V [mL]	A	l [cm]	c <sub>labels</sub> [mmol L <sup>-1</sup> ]	U <sub>s</sub>	n <sub>s</sub>	(k <sub>s</sub> <sup>blocked</sup> )	(k <sub>s</sub> <sup>labelled</sup> )	M <sub>s</sub> <sup>ideal</sup> [g mol <sup>-1</sup> ]	(M <sub>s</sub> ) [g mol <sup>-1</sup> ]	X [%]
PG2 <sup>NHBoc</sup> <sub>10<sup>0</sup>00</sub>	4.44	9.80737	6.141121	0.006487	0.2	0.002	0.001	2.997	3.993	0.0033	1223.45	1221.952	99.9
PG3 <sup>NHBoc</sup> <sub>10<sup>0</sup>00</sub>	3.25	9.58336	6.000852	0.004176	0.2	0.0013	0.0008	6.987	7.981	0.0062	2625.09	2619.97	99.9
PG4 <sup>NHBoc</sup> <sub>10<sup>0</sup>00</sub>	3.92	8.91712	5.583669	0.007149	0.2	0.0022	0.0011	14.957	15.941	0.0168	5428.37	5411.81	99.8
PG5 <sup>NHBoc</sup> <sub>~5<sup>0</sup>00</sub>	6.17	10.1625	6.363494	0.1661	1	0.0101	0.0037	30.8	31.686	0.1146	11034.9	10953.46	99.6
PG5 <sup>NHAlloc</sup> <sub>10<sup>0</sup>00</sub>	3.4	7.2447	4.536443	0.241217	1	0.0147	0.0069	30.7	31.485	0.2148	10521.55	10399.22	99.3

### 8.3.2. Other experiments<sup>ij</sup>

#### Deprotection of PG5<sub>500</sub><sup>NHAlloc</sup> in absence of base

The experiment very closely followed the procedure for the synthesis of C-PG6<sub>500</sub><sup>NHBoc</sup>, outlined in subsection 2.4.4, detailed in subsection 8.2.1, with the exception of the time of the addition of base and the workup procedure, which owing to the small scale of the experiment consisted only of repeated precipitation. Samples for AFM and GPC were prepared as described in subsection 8.1.2.

To a solution of PG5<sub>500</sub><sup>NHAlloc</sup> (50.5 mg, 4.8 μmol RU / 0.15 mmol amines) and PPh<sub>3</sub> (4 mg, 15 μmol, 0.1 equiv./amine) in a mixture of dry DMSO (1 mL) and dry NMP (1 mL), DMBA (119 mg, 0.8 mmol, 5 equiv./amine) was added. The resulting solution was degassed by purging with argon supplied from a balloon. Then an argon-purged solution of Pd(PPh<sub>3</sub>)<sub>4</sub> (18.9 mg ml<sup>-1</sup> in NMP; 0.46 mL, 7.5 μmol, 0.05 equiv./amine) was added. The resulting solution was purged with argon, then the reaction was stirred in the dark for 3 d. To the resulting clear, orange solution, sodium *N,N*-diethyldithiocarbamate trihydrate (9.3 mg, 41 μmol, 0.27 equiv./amine) was added. After purging with argon, the reaction was stirred in the dark overnight, whereupon NEt<sub>3</sub> (0.5 mL, 3.6 mmol, 24 equiv./amine), DMAP (5 mg, 41 μmol, 0.27 equiv./amine) and **20** (260.5 mg, 0.5 mmol, 3.3 equiv./amine) were added, followed by purging with argon. After 16 d of stirring in the dark, the resulting solution was precipitated into Et<sub>2</sub>O, further purified by twofold reprecipitation from little methylene chloride, then redissolved in little methylene chloride which was removed in vacuum to afford a glassy, yellow-orange solid.

#### Treatment of PG5<sub>500</sub><sup>NH<sub>2</sub></sup> with acid

This experiment was also set up in close resemblance to the synthesis of C-PG6<sub>500</sub><sup>NHBoc</sup>:

To a solution of PG5<sub>500</sub><sup>NHAlloc</sup> (218.7 mg, 20.8 μmol RU / 0.67 mmol amines), NEt<sub>3</sub> (0.74 mL, 5.3 mmol, 8 equiv./amine), and PPh<sub>3</sub> (17.8 mg, 79 μmol, 0.1 equiv./amine) in a mixture of dry DMSO (6 mL) and dry NMP (4 mL) at 0 °C, DMBA (520.7 mg, 3.4 mmol, 5 equiv./amine) was added. The resulting solution was then warmed to RT and degassed by purging with argon supplied from a balloon. To this was added an argon-purged solution of Pd(PPh<sub>3</sub>)<sub>4</sub> (18.9 mg ml<sup>-1</sup> in NMP; 2.1 mL, 35 μmol, 0.05 equiv./amine). The resulting solution was purged with argon, then the reaction was stirred in the dark for 3 d. From the resulting orange solution, 4 aliquots of 3 mL were removed, each transferred under argon into a separate argon-filled vessel. To each solution, a different amount of TFA was added (as a 195.25 mg/mL solution in dry DMSO; 0.765 mL/0.8 equiv. excess per amine; 0.805 mL/1.2 equiv. excess per amine; 0.875 mL/2 equiv. excess per amine; 1.045 mL/4 equiv. excess per amine). Each sample was then topped up with additional dry DMSO such that 1.5 mL total added volume was achieved.

From each of these solutions, aliquots of 1.5 mL were taken after 15 min, 1 h and 3 h and added to a vial containing a 0.6 mL portion of a premade solution of **20** (ca. 0.3 mmol per sample), DMAP (ca. 30 μmol per sample) and NEt<sub>3</sub> (ca. 0.5 mmol per sample) in dry NMP. The samples were stirred under argon for 3 d, then each was precipitated into Et<sub>2</sub>O, reprecipitated from little methylene chloride, then

---

<sup>ij</sup> It should be noted that the “solvent heating” experiments carried out in this section, corresponding to the data presented in section 3.5, partially overlap.

taken up in little methylene chloride and dried in vacuum, resulting in glassy solids, ranging in color from orange to brown.

#### Deprotection of mixed-substitution DPs of $g = 5$ in absence of base

The procedure described above for the base-free deprotection of  $\text{PG5}_{500}^{\text{NHAlloc}}$  was employed (see Scheme 3-2), *i.e.* the base was added only *after* deprotection had been completed, and the liberated amines were intermittently fully protonated by DMBA. This procedure was applied to  $\text{PG5}_{500}^{\text{NHAlloc36}}$ ,  $\text{PG5}_{500}^{\text{NHAlloc57}}$  and  $\text{PG5}_{500}^{\text{NHAlloc80}}$  on a small scale, and the resulting DPs of (partially)  $g = 6$  were isolated by repeated precipitation. Samples for AFM and GPC were prepared as noted in subsection 8.1.2.

#### Deprotection of $\text{PG5}_{500}^{\text{CO}_2\text{tBu}}$

The deprotection of  $\text{PG5}_{500}^{\text{CO}_2\text{tBu}}$  closely followed the procedure outlined for NHBoc-protected DPs (general procedure D, see subsection 8.3.1), *i.e.* the neat DP powder was treated directly with cold, neat TFA while cooling in an ice bath. In this case however, no turbidity was observed, the polymer simply dissolved; Hence no MeOH was added. Experiments were usually conducted on an analytical scale (10 – 20 mg of  $\text{PG5}_{500}^{\text{CO}_2\text{tBu}}$ ) and the reaction mixture was usually directly diluted with MeOH for AFM imaging and DLS.

#### Deprotonation of $\text{PG5}_n^{\text{CO}_2\text{H}}$

$\text{PG5}_n^{\text{CO}_2\text{H}}$  was prepared from  $\text{PG5}_{500}^{\text{CO}_2\text{tBu}}$  (*ca.* 10 mg) as described above. The polymer was isolated from the TFA solution by precipitation into  $\text{Et}_2\text{O}$ , and the resulting solid was washed twice with  $\text{Et}_2\text{O}$  before being dispersed in an ice-cold saturated solution of ammonia in MeOH, in which the polymer rapidly dissolved. The ammonia solution was prepared by passing a stream of ammonia (generated by the addition of NaOH pellets to an ice-cooled slurry of water and  $\text{NH}_4\text{Cl}$ ) through an ice-cooled flask containing MeOH.

The open vessel containing the  $\text{PG5}_n^{\text{CO}_2\text{NH}_4}$  solution was allowed to reach room temperature over *ca.* 2 h, then the mixture was purged with  $\text{N}_2$ .

### Testing for solvent influence on “hot solvent” mediated scission of PG5<sub>n</sub><sup>NHBoc</sup>:

Initial tests were performed using fairly high concentrations (10 – 20 % w/w) of PG5<sub>5000</sub><sup>NHBoc</sup> in polar-aprotic solvents. After it was found that scission occurs at far lower concentrations and also with shorter starting polymers, PG5<sub>500</sub><sup>NHBoc</sup> was used instead, as this polymer was available in larger quantities and easier to handle.

For scission experiments, a solution of PG5<sub>500</sub><sup>NHBoc</sup> (1% w/v, typically using *ca.* 10 mg of the polymer and 1 mL of the solvent in question) was prepared in a screw-cap vial and shaken at room temperature overnight to fully dissolve the polymer. The vial was set into a shaker (PL-SP 260, Polymer Laboratories) pre-heated to 80 °C and gently shaken at that temperature for 1 h. A sample of the resulting mixture was then taken and diluted to *ca.* 1 mg mL<sup>-1</sup> with DMF (containing 1 g L<sup>-1</sup> LiBr and 1 mL L<sup>-1</sup> toluene); from this solution, samples for GPC were prepared as described in subsection 8.1.2.

### Rheological testing for the determination of scission onset in DMF

To determine the temperature onset of scission, a highly concentrated solution (*ca.* 20 % w/w) of PG5<sub>5000</sub><sup>NHBoc</sup> in DMF was heated from 20 °C to 80 °C in steps of 5 °C while monitoring rheological properties using a cone-plate geometry (CP50-1) in a MCR502 rheometer (Figure 8-17, Aton Paar GmbH). To that end, a frequency sweep ( $\omega = 400 - 0.1 \text{ rad s}^{-1}$  at  $\gamma_0 = 0.02 \%$ ) was performed after equilibrating at every multiple of 5 °C. During heating between frequency sweeps (0.1 °C min<sup>-1</sup>), dynamic testing at  $\omega = 10 \text{ rad s}^{-1}$  and  $\gamma_0 = 0.02 \%$  was performed.

While a solvent-filled guard ring (Figure 8-17a) was used to reduce solvent evaporation in the hood oven, the apparatus could not be closed completely, and above *ca.* 40 °C the onset of evaporation was observed, indicated by a thickening of the solution after the expected initial decrease of viscosity with increasing temperature. This complicates the interpretation of the data: The absolute values of  $G'$  and  $G''$  (Figure 3-16a) cannot be interpreted directly due the changes in sample geometry caused by evaporation. However, in the geometry-independent phase-shift angle (Figure 3-16b), an inflection point is visible.

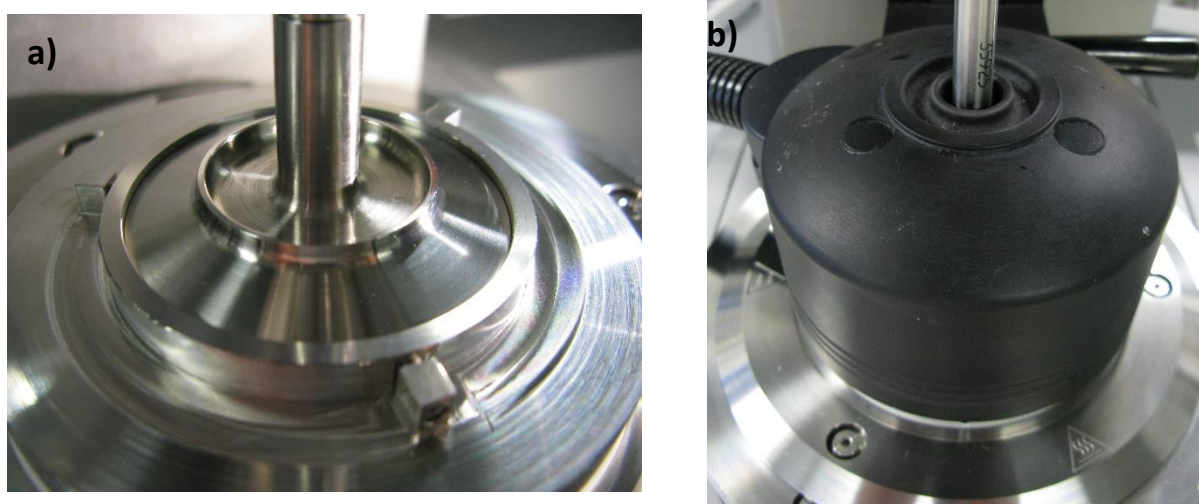


Figure 8-17: a) Cone-plate measurement geometry (CP50-1) with a guard ring (*ca.* 0.1 mm gap); during measurement, the solvent reservoir on top was filled with DMF; b) apparatus with the closed hood oven, which has no gap at the bottom.

### Testing for temperature dependence on scission of PG5<sub>n</sub><sup>NHBoc</sup>

Initial observations regarding the main-chain scission of PG5<sub>5'000</sub><sup>NHBoc</sup> at RT in DMPU were made in highly concentrated (*ca.* 10 % w/w) solutions. Later, more systematic investigations on PG5<sub>500</sub><sup>NHBoc</sup> were performed using *ca.* 1% w/V solutions in a number of solvents for which scission was found to occur (see subsection 3.5.3), and performed similar to the testing for solvent influence described above:

A solution of PG5<sub>500</sub><sup>NHBoc</sup> in the solvent in question (*ca.* 1% w/V DP) was heated to the indicated temperature for the given amount of time, using a pre-heated shaker (PL-SP 260, Polymer Laboratories). When the desired amount of time had passed, the vial was cooled to RT and a sample was diluted with DMF containing 0.1 % w/V LiBr and 0.1 % V/V toluene to a polymer concentration suitable for GPC measurement (*ca.* 1 mg mL<sup>-1</sup>), for which a sample was prepared as described in subsection 8.1.2. Samples marked as having been subjected to solvent at RT were shaken at RT overnight without any heating.

### Testing for the influence of concentration and chain length

Again, initial experiments were performed using PG5<sub>5'000</sub><sup>NHBoc</sup> and PG5<sub>500</sub><sup>NHBoc</sup> in fairly concentrated solutions (10% w/w). Later experiments were conducted at lower concentrations (1 % w/V). In either case, the samples were treated as described before, *i.e.* the solution in question was agitated using a shaker (PL-SP 260, Polymer Laboratories) pre-heated to 80 °C for 1 h, then a sample was removed, diluted to *ca.* 1 mg mL<sup>-1</sup> with DMF containing 0.1% w/V LiBr and 0.1% V/V Toluene, and then treated as described in subsection 8.1.2 to prepare a sample for GPC. Samples were first subjected to the solvent at RT overnight and *then* heated to 80 °C, a factor which is of particular importance in the investigation of DMPU.

### Testing for the influence of shear

For shear testing, samples of PG5<sub>500</sub><sup>NHBoc</sup> (5 % w/V in DMPU) were shaken at RT on an orbital shaker (IKA-VIBRAX-VXR, IKA-Werke) for 24 h at different speeds (400 rpm, 800 rpm, 1200 rpm) immediately pursuant to the addition of DMPU to the polymer. The resulting samples then diluted for GPC as described in the previous paragraph.

### Testing on the influence of *g*

To test for the influence of the dendritic generation *g*, experiments in analogy to those described in the above paragraphs were conducted: (1 % w/V) solutions of the DPs in question were shaken on a shaker (PL-SP 260, Polymer Laboratories) pre-heated to 80 °C for 1 h, then a sample was removed, diluted to *ca.* 1 mg mL<sup>-1</sup> with DMF containing 0.1% w/V LiBr and 0.1% V/V toluene, and then treated as described in subsection 8.1.2 to prepare a sample for GPC. Samples were first subjected to the solvent at RT overnight, then heated to 80 °C, and then heated further to 120 °C for 1 h after removal of another sample for GPC which was treated as usual.

### Testing for the influence of peripheral chemistry

Similar to the above cases, the DPs in question were dissolved in DMPU at *ca.* 1 % w/V and then directly put into the pre-heated shaker (PL-SP 260, Polymer Laboratories, 80 °C) for 1 h. The solutions were then cooled to RT and samples were removed and diluted to *ca.* 1 mg mL<sup>-1</sup> with DMF containing



0.1% w/V LiBr and 0.1% V/V toluene. The solutions were then subjected to further heating (1 h at 120 °C), and again samples were removed for GPC (subsection 8.1.2).

#### Sample preparation for MALDI-TOF-MS based detection of macromonomers

DPs with GPC peaks suspected to represent macromonomer or short oligomers were treated as follows: Solutions of the DPs ( $\text{PG3}_{500}^{\text{NHBoc}}$ ,  $\text{PG4}_{500}^{\text{NHBoc}}$ ,  $\text{PG5}_{500}^{\text{NHBoc}}$ ,  $\text{PG5}_{500}^{\text{NHAlloc}}$ ,  $\text{PG5}_{500}^{\text{NHCbz}}$ ,  $\text{PG5}_{500}^{\text{CO}_2\text{Me}}$ ,  $\text{PG5}_{500}^{\text{CO}_2\text{tBu}}$ , **B-PG6** $_{500}^{\text{NHBoc}}$ , **B-PG7** $_{500}^{\text{NHBoc}}$ , each *ca.* 1 % w/V in DMPU) were prepared and directly set into a pre-heated shaker (PL-SP 260, Polymer Laboratories, 120 °C) in which they were agitated gently for 2 h. The resulting solutions were then cooled to RT and precipitated (into Et<sub>2</sub>O/hexane 1:1, excepting  $\text{PG5}_{500}^{\text{CO}_2\text{tBu}}$ , for which pure hexane was employed). The resulting solids were reprecipitated from little methylene chloride, and samples for GPC (Figure 3-26) and MALDI-TOF-MS (Figure 3-27, also see Appendix A.5 for full-size individual spectra) were prepared.

#### EPR spectroscopy & associated experiments

For the initial experiment shown in Figure 3-29a,  $\text{PG5}_{500}^{\text{NHBoc}}$  (*ca.* 10 mg) was added to a quartz EPR tube which had been flushed with dry nitrogen. DMPU (0.5 mL, purged with nitrogen) was added. The contents were shaken, then inserted into an X-band EPR spectrometer (EMX, Bruker) equipped with a TM cavity and a thermostat (Eurotherm), which was pre-heated to 353 K. The sample was maintained at that temperature for 5 min, then quenched by plunging into liquid nitrogen. The thermostat was cooled to 200 K, then the sample was inserted and thermally equilibrated before measurement. Further cycles of heating/cooling were performed to discern whether radicals would accumulate, but no significant changes were found, indicating that the observed low concentration of radicals was transient. After *ca.* 20 min total at 80 °C, the sample was brought to RT and the solution was diluted to *ca.* 1 mg mL<sup>-1</sup> with DMF (containing 1 mL L<sup>-1</sup> toluene and 1 g L<sup>-1</sup> LiBr) in preparation for GPC.

For radical trapping with DMPO, the sample and all precursor solutions were prepared in a nitrogen-filled glove box (< 4 ppm O<sub>2</sub>): DMPO (352 mg; ABCR, 97 %) was dissolved in dry DMPU (*ca.* 2 mL, degassed thoroughly by cycling the glovebox antechamber). A sample of this solution was added to an EPR tube and the DMPO solution (*ca.* 1 mL) was added to  $\text{PG5}_{500}^{\text{NHBoc}}$  (*ca.* 50 mg). The resulting mixture was shaken and added to another EPR tube. The two sample tubes were tightly stoppered and wrapped in parafilm before exiting the glove box, and the samples were treated as follows without delay: The reference solution containing only DMPO was heated to 353 K for 5 min using the thermostat of the EPR spectrometer and then measured after vitrification by cooling to 200 K directly in the spectrometer. The sample solution containing  $\text{PG5}_{500}^{\text{NHBoc}}$  as well as the radical trap was treated similarly, however with two additional periods of heating to 80 °C as indicated in Figure 8-18. Rather than showing further accumulation of trapped radicals, the EPR spectra recorded after additional heating show a lower radical concentration. In agreement with other results, this indicates that main-chain scission occurs on a time scale of a few minutes, as apparently the rate of radical formation drops below that of adduct decomposition for longer heating times. A kinetic analysis of such data is however not currently possible: The thermal stability of DMPO itself is unknown, as is the stability of the radical adducts. Furthermore, the likely present multiple species are not readily identifiable, as the solid-state spectra of the polymeric or oligomeric fragments show strong line broadening. Additionally, the decrease in relative signal intensity after further heating in Figure 8-18 is not homogenous across the entire spectrum, suggesting that some of the multiple adducts present are

less stable than others. After EPR measurement, the sample was warmed to RT and precipitated into Et<sub>2</sub>O/hexane (1:1). The solid was reprecipitated from little DCM, then dried in vacuum to afford a glassy solid which was subjected to GPC (Figure 3-29e) and MALDI-TOF-MS (Figure 8-19). Neither method provided unequivocal evidence of macromonomer, further supporting the proposed homolytic scission mechanism.

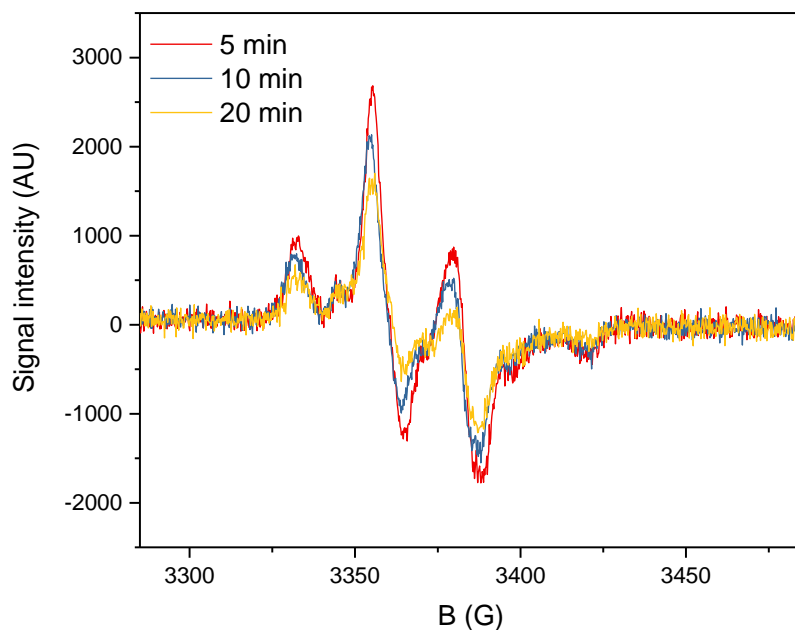


Figure 8-18: Stability of quenched radicals: PG5<sub>500</sub><sup>NH<sub>2</sub>Boc</sup> and DMPO heated in DMPU to 353 K for the indicated total time before cooling for solid-state CW-EPR measurements (X-band, 200 K, single scan).

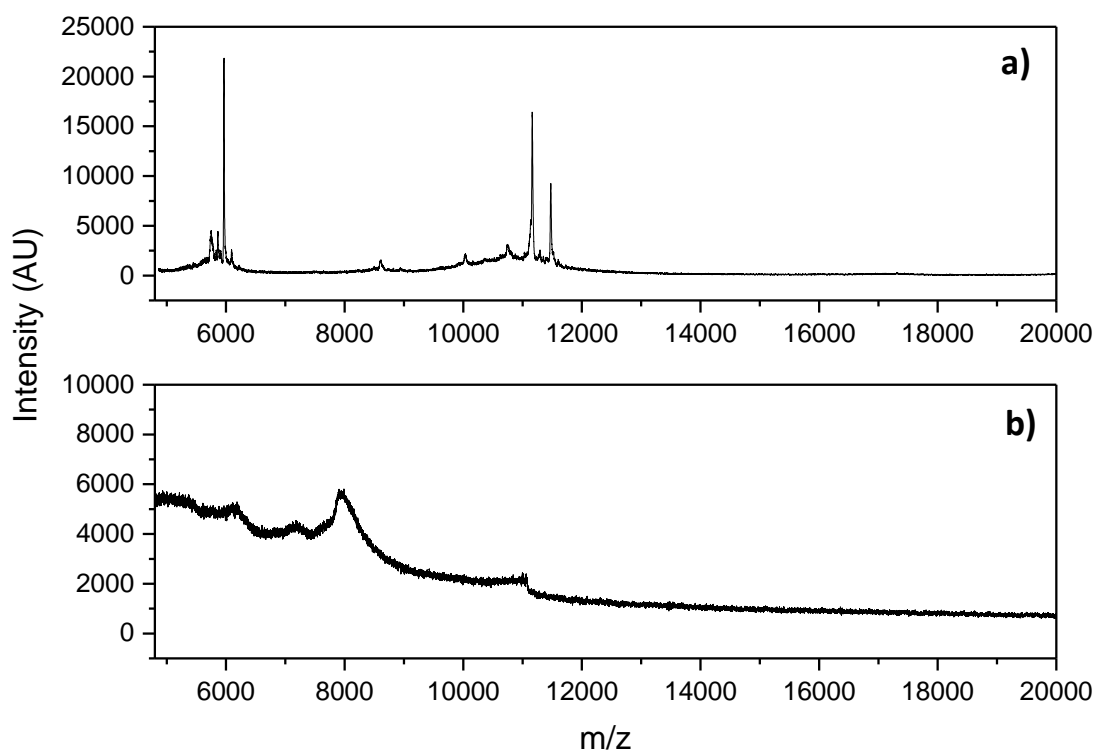


Figure 8-19: Comparison of MALDI-TOF mass spectra of PG5<sup>NH<sub>2</sub>Boc</sup> heated in DMPU a) without scavenger (see Figure A-17) and b) in presence of DMPO.

The EPR signal in Figure 3-29c (derivative form) and Figure 8-20c was fitted by a manual deconvolution approach. To that end, the signal was first integrated and baseline-corrected (Figure 8-20a). The spectrum was then simulated by Gaussian curves, assuming  $A_H \approx A_N$ , *i.e.* a simple quadruplet of peaks (Figure 8-20b, Table 8-5).

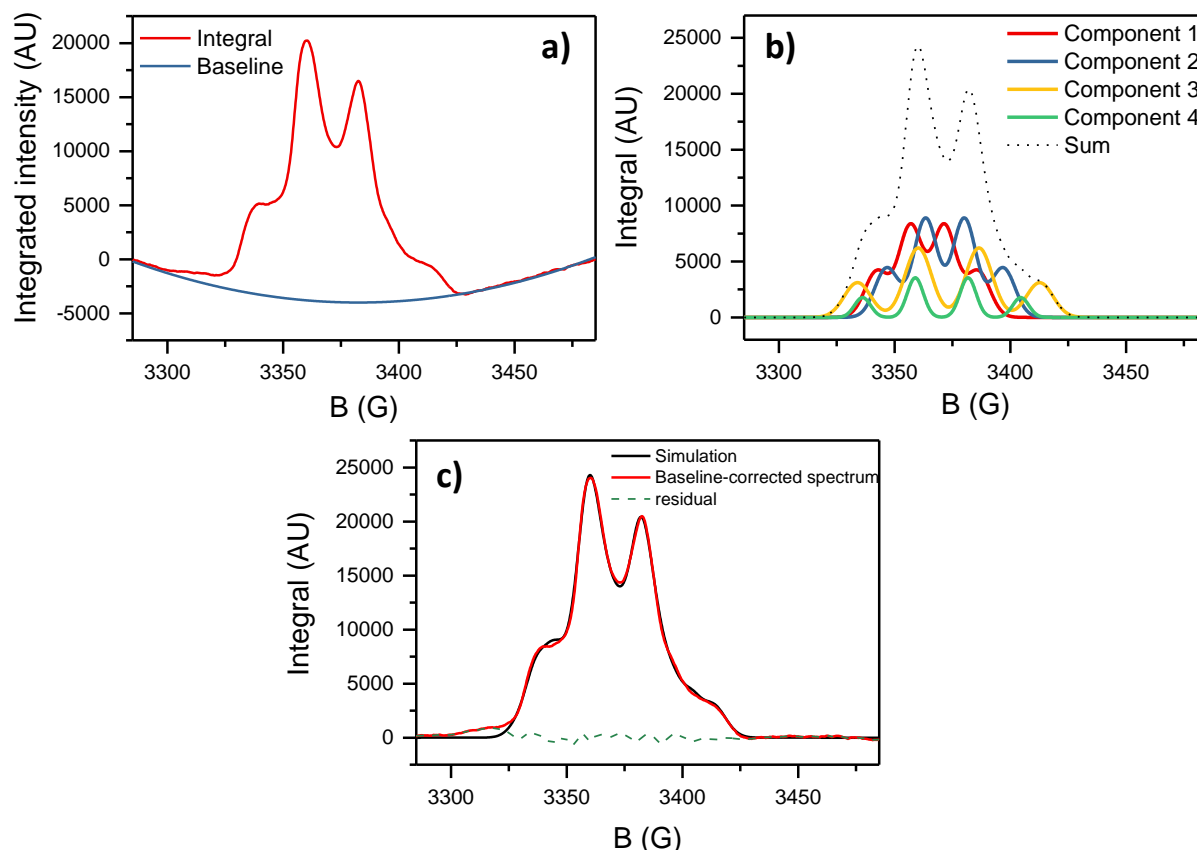


Figure 8-20: a) Baseline correction of the integrated, background-corrected EPR signal; b) deconvolution of the integral into four Gauss-broadened quadruplets (see Table 8-5); c) overlay of the corrected, integrated spectrum with the simulated spectrum. The residual is indicated by the green dashed line.

Table 8-5: Parameters for the deconvolution components shown in Figure 8-20b; <sup>a)</sup> It is assumed here that  $A_N \approx A_H = A$ , resulting in a symmetric 1:2:2:1 line split centered around  $B_{center}$ ; <sup>b)</sup>  $k$  is a dimensionless line broadening parameter for the Gaussian curve of the form  $I(B) = I_0 e^{-\frac{k}{2}(B-B_0)^2}$ .

	$B_{center}$ (G)	$A$ (G) <sup>a)</sup>	$k$ <sup>b)</sup>	Peak intensity $I_0$ (AU)
<b>Component 1</b>	3364.2	14.6	0.0191	8174.3
<b>Component 2</b>	3371.8	16.7	0.019	8839.3
<b>Component 3</b>	3373.3	26.2	0.0151	6212.5
<b>Component 4</b>	3370.3	22.8	0.0411	3540.9

### MD simulation of PG5<sub>100</sub><sup>NHBoc</sup> in DMPU

The conformation previously reported<sup>228</sup> for PG5<sub>100</sub><sup>NHBoc</sup> (160902 explicit atoms) in vacuum was the starting point for the simulation. This starting conformation requires some comment: While the simulation of PG $g$ <sub>100</sub><sup>NHBoc</sup> ( $g = 1 - 4, 6$ ) had been relatively straightforward,<sup>144</sup> the simulation of the  $g = 5$  homolog was significantly more difficult, largely due to optimization problems regarding the internal structure of the DP. Three different starting points with differing backbone helicities had been chosen for the simulation of PG5<sub>100</sub><sup>NHBoc</sup> in vacuum, and the one used as a starting point here was the energetically most favourable among these.<sup>228</sup> The “pore” in the middle of this configuration, close to the DP backbone (see Figure 3-31) may be an artefact of the initial helical setup, and may not represent real configurations, though it is also possible that the pore originates from the drive to maximize DP-DP interactions in the vacuum simulation – farther away from the backbone, there is more interaction surface available between fairly stretched out dendrons, after all. The initial pore likely significantly affects the outcome of simulation, seeing as it is initially solvent swollen due to the simulation setup as described in the following:

DMPU was represented by using an all-atom model. The energy was calculated using the AMBER force-field,<sup>263</sup> all the bonding and van der Waals parameters required for the DPs under study being taken from previous studies which had successfully modelled the structure and properties of PG1-PG6.<sup>98,144,228,374,375</sup> The bonding and van der Waals parameters required for DMPU molecules were taken from the Generalized AMBER force-field (GAFF).<sup>264</sup> Atomic charges were adjusted using the Restrained Electrostatic Potential (RESP) strategy.<sup>376</sup> The resulting electrostatic parameters are shown in Figure 8-21.

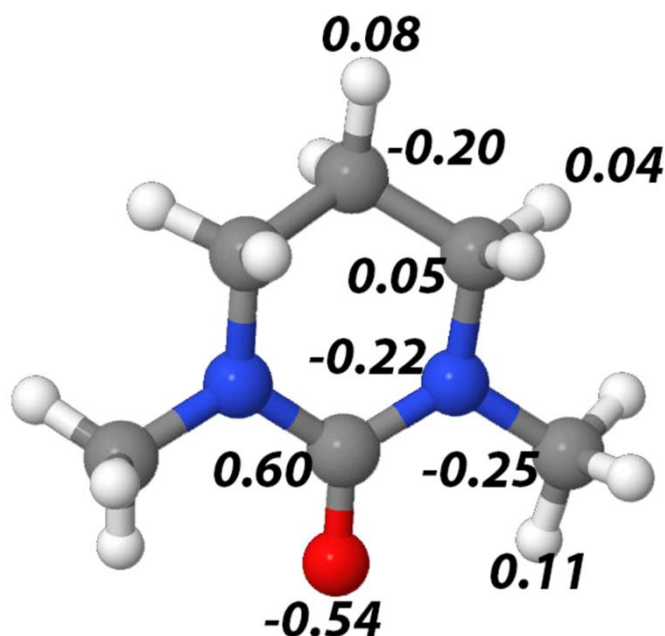


Figure 8-21: Atomic charges of DMPU. Image generated by Dr. Oscar Bertran (Universitat Politècnica de Catalunya), reproduced with permission.

For the NVT-MD simulation in DMPU solution, the DP chain was placed in the centre of an orthorhombic simulation box of  $296 \times 196 \times 153 \text{ \AA}^3$  filled with explicit solvent molecules. The simulation box was initially filled only with DMPU molecules. After 100 ns of NPT-MD at 298 K, the density had reached  $1.04 \text{ g cm}^{-3}$ , which is in excellent agreement with the experimental density ( $1.06 \text{ g cm}^{-3}$ ).<sup>377</sup>

After this, the PG5<sub>100</sub><sup>NH<sub>2</sub>Boc</sup> chain was placed in the middle of the equilibrated solvent box, eliminating those solvent molecules which exhibited overlap with the DP. A total of 35319 solvent molecules remained in the box (741699 explicit solvent atoms) and, therefore, the whole simulated system contained 902601 explicit atoms. Then, the solvent alone was thermally relaxed in three consecutive runs while the DP was kept frozen: First, 10 ns of NVT-MD at 500 K was used to re-distribute the solvent in the box. Second, 7.5 ns of isothermal relaxation at 298 K was run. Finally, the DP was set free and all atoms of the system were submitted to 25 ns of NVT-MD at 298 K (thermal equilibration). The temperature was controlled by a weak coupling method, the Berendsen thermostat<sup>378</sup> with a time constant for heat-bath coupling of 1 ps. The end of the thermal relaxation simulation was taken as the starting point of the production trajectory (80 ns) at 298 K, which was run in duplicate.

Atom-pair distance cut-offs were applied at 12 Å to compute van der Waals and electrostatic interactions. Bond lengths involving hydrogen atoms were constrained using the SHAKE algorithm with a numerical integration step of 2 fs.<sup>379</sup>

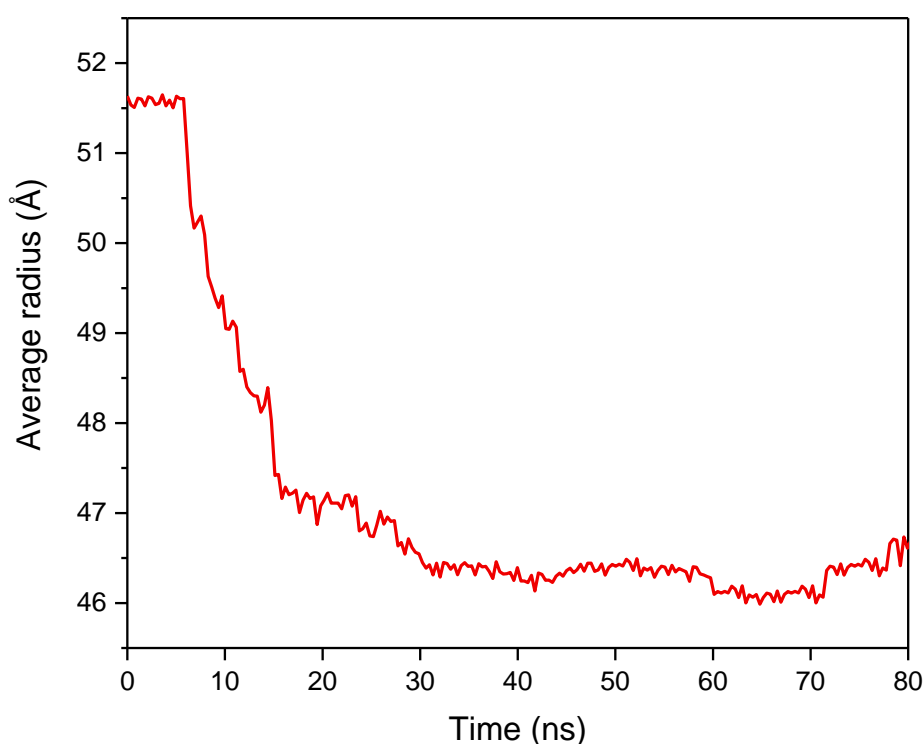


Figure 8-22: Evolution of the average diameter of the DP, showing a lateral contraction of approx. 9 %.

## 8.4. Experimental details for chapter 4: Cryo-TEM of DPs and analysis of native chain conformations

All cryo-TEM measurements & image processing were conducted by Priv.-Doz. Dr. Christoph Böttcher, and the vast majority of trajectory analyses were conducted by Prof. Dr. Martin Kröger. Images and graphs originating in their work are marked correspondingly with (CB) and (MK) respectively in the caption. Prof. Dr. Kurt Binder (Uni Mainz) aided in the interpretation and contextualization of the results as presented in chapter 4.

### 8.4.1. Cryo-TEM & image processing

#### Sample Preparation

The sample employed for cryo-TEM stereography was an old sample of **B-PG6**<sup>NHBoc</sup><sub>500</sub> provided by Dr. Hao Yu. The sample employed for cryo-ET of **C-PG7**<sup>NHBoc</sup><sub>500</sub> was prepared as described in this thesis (see Experimental, subsection 8.2.1) and Ref. 228.

A droplet (5 µL) of the sample solution (0.02 - 0.2 mg mL<sup>-1</sup> in 1,4-dioxane) was placed on a perforated carbon film grid (**B-PG6**<sup>NHBoc</sup><sub>500</sub>: R1/4, Quantifoil Micro Tools GmbH, Jena, Germany, **C-PG7**<sup>NHBoc</sup><sub>500</sub>: R1.2/1.3 on gold TEM grids, Quantifoil Micro Tools GmbH, Jena, Germany) covered with a layer of graphene (**B-PG6**<sup>NHBoc</sup><sub>500</sub>: CNM Technologies, Bielefeld, Germany. **C-PG7**<sup>NHBoc</sup><sub>500</sub>: Dr. P. Feicht, FU Berlin, Germany). The excess fluid was blotted off to create an ultra-thin layer (typical thickness of 200-300 nm) of the solution covering the graphene support film. The samples were then immediately vitrified by propelling the grids into liquid nitrogen using a standard plunging device.

#### Cryo-TEM stereography of **B-PG6**<sup>NHBoc</sup><sub>500</sub>

For PG6<sub>500</sub>, the vitrified sample grids were transferred under liquid nitrogen into a Tecnai F20 TEM (FEI company) equipped with a FEG and operated at 160 kV acceleration voltage, using a Model 626 cryo-holder (Gatan). Microscopy was carried out at -175 °C sample temperature using the microscope's low dose protocol at calibrated primary magnifications of 50k or 29k. The defocus was set to 3.98 µm or 9.81 µm, respectively. Images were recorded with a 4k-Eagle CCD camera (FEI Company) at 2k resolution (binning factor 2). Stereo-image pairs were recorded at 8°-tilt angle. See Figure 4-3a for a typical stereo image pair.

Filament tracing was performed in the context of the „Filament“ module of AMIRA 6.0 (ThermoFisher Scientific). Stereo-image pairs recorded at ± 8° tilt angles were aligned and reconstructed with Inspect 3D Version 4.1.2. (ThermoFisher Scientific). 63 individual filaments were volume-extracted in AMIRA and transferred to the Filament module. Parameters were adjusted until the complete length of individual filaments was automatically traced.

#### Single-particle reconstruction of a **B-PG6**<sup>NHBoc</sup><sub>n</sub> segment

Segments of the polymer chains were interactively extracted from micrographs as 60 px x 60 px patches (pixel resolution 0.8459 nm) using Boxer of the Eman the software package.<sup>380</sup> Care was taken

to choose only individual undisturbed polymer chains. For example, image areas where strong Fresnel fringes at the chain edges indicated an incomplete embedding in the solvent were not included in the process. The remaining processing steps were performed in IMAGIC 5 (Image Science GmbH)<sup>381</sup> Overall, 896 motifs were selected and stored in an image gallery. After band-pass-filtering to remove low- and high-frequency noise, a first centering of the motifs was performed using a featureless vertical stripe as a reference. Multivariate statistical analysis (MSA)<sup>308</sup> was applied to look for inherent structural patterns for subsequent classification procedures. 100 class sum images were allocated.

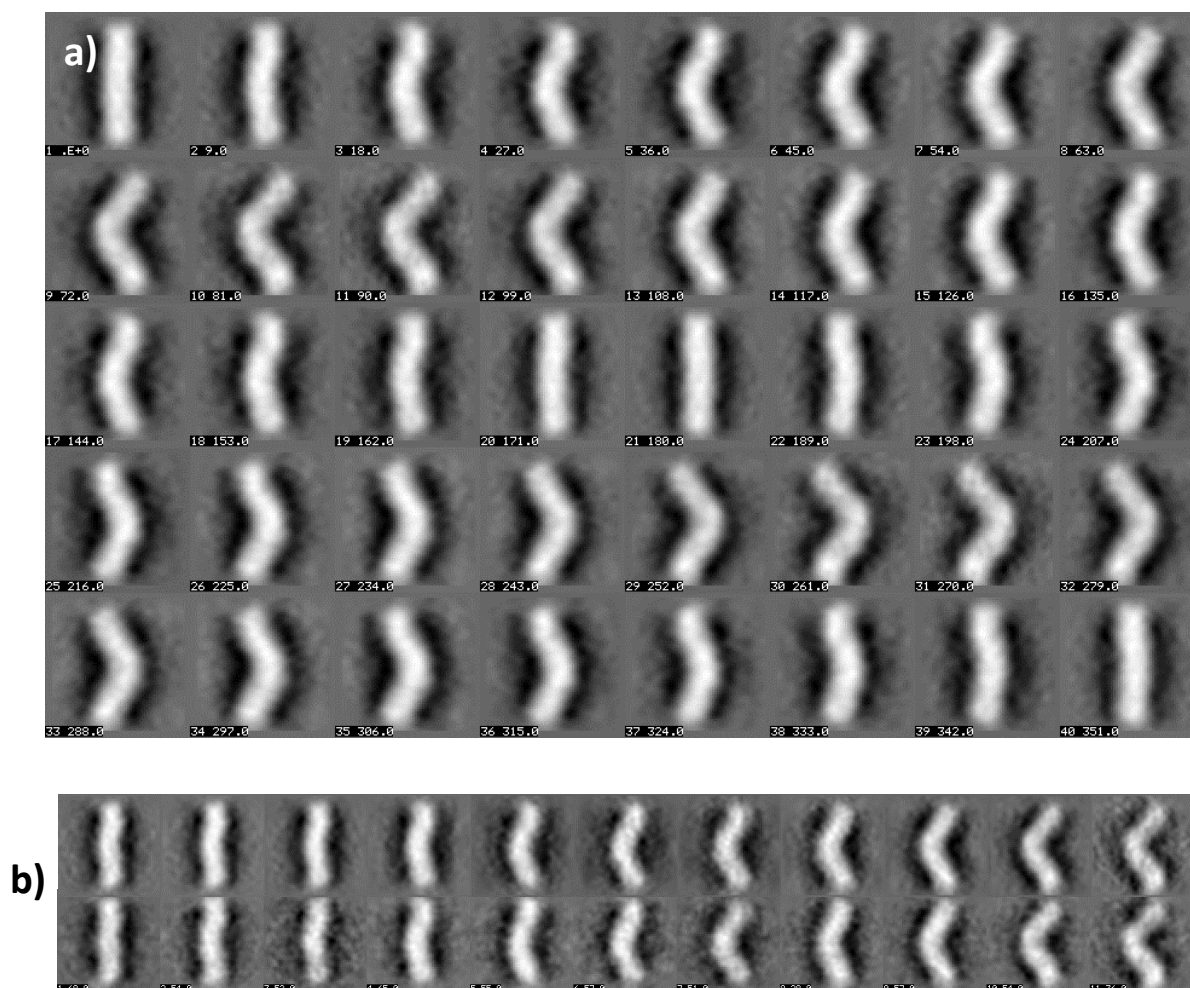


Figure 8-23: a) Projection images of the three-dimensional reconstruction of a PG6<sub>500</sub> chain segment (Fig. 2d) in a tomographic series over 360° in  $\gamma = 9^\circ$  increments ( $\gamma = 0^\circ$ ). The corresponding Euler angle  $\gamma$  is given with the second index number. b) Comparison of class sum averages of polymer sections used for 3D reconstruction (top) with the corresponding reprojections (bottom). The deviation over all Euler angles is 2.3%. (CB)

The closer inspection of these results suggested that the class sum images describe projections of a structurally very well-defined feature, the three-dimensional volume of which was reconstructed using the angular reconstitution approach implemented in IMAGIC.<sup>382</sup> The reconstruction went smoothly and a comparison of the class sum images and the corresponding reprojections from the 3D-volume (Figure 8-23a) showed high agreement (Figure 8-23b, deviation 2.32%). 566 of the total 896 images could be integrated into the 3D-volume, which confirms a high degree of consistency within the dataset. This data is however hand-picked, hence some bias is certainly inherent in the selected data (see discussion regarding Figure 4-4e).

The bending energy analysis in Figure 4-4a,b considers the two-dimensional shape curve  $\mathbf{x}(t)$  of a given segment parametrized by:

$$\mathbf{x}(t) = (-A \sin^n(\pi t), R_e t)$$

Eq. 8-3

with  $t \in [0,1]$  where  $R_e$  denotes the given end-to-end distance,  $A$  is the amplitude of the sinusoidal curve, and where the power  $n$  we obtained for given contour length  $L = \int_0^1 |\dot{\mathbf{x}}| dt$ .

The filament shape bending energy  $U$  was then calculated using:

$$U = 0.5 L_p k_B T \int_0^1 |\ddot{\mathbf{x}}|^2 / |\dot{\mathbf{x}}|^3 - (\ddot{\mathbf{x}} \cdot \dot{\mathbf{x}})^2 / |\dot{\mathbf{x}}|^5 dt$$

Eq. 8-4

### Cryo-ET of C-PG7<sub>500</sub><sup>NHBoc</sup>

For PG7<sub>500</sub>, the vitrified grids were stabilized with a copper autogrid and fixed by a spring clamp under liquid nitrogen. Autogrids were transferred under liquid nitrogen into a Talos Arctica transmission electron microscope (ThermoFisher Scientific) using the microscope's autoloader transfer routine. Tomographic tilt series were performed using the FEI Tomography software (Version 4.5.0, ThermoFisher Scientific) in the tilt range of  $-65^\circ/65^\circ$  at  $2^\circ$  increments. A total dose of  $180 \text{ e}/\text{\AA}^2$  was accumulated on the specimen at a primary magnification of 28k (Pixel size 3.733 nm). Tilt-images were recorded with the Falcon 3CE direct electron detector at full image size (4096x4096 pixel) and an exposure time of 0.28 s per image (12 frames). The defocus was set to  $4.90 \mu\text{m}$  in all cases to create sufficient phase contrast. Image stack alignment and volume reconstruction were performed in the context of the FEI Inspect 3D software (Version 4.1.2., ThermoFisher Scientific). See Figure 4-6a for a stereo image pair generated from the tomogram.

Filament tracing was performed in the context of the „Filament“ module of AMIRA 6.0 (ThermoFisher Scientific Inc., Waltham (MA), USA). Volumes from reconstructed tomographic series were loaded and subvolumes of individual filaments created and evaluated in the „Filament“ module using the manual tracing modus („trace filament“) following the central backbone of the filament in the volume. 65 filaments which were identified to be undisturbed by neighboring entities were evaluated.



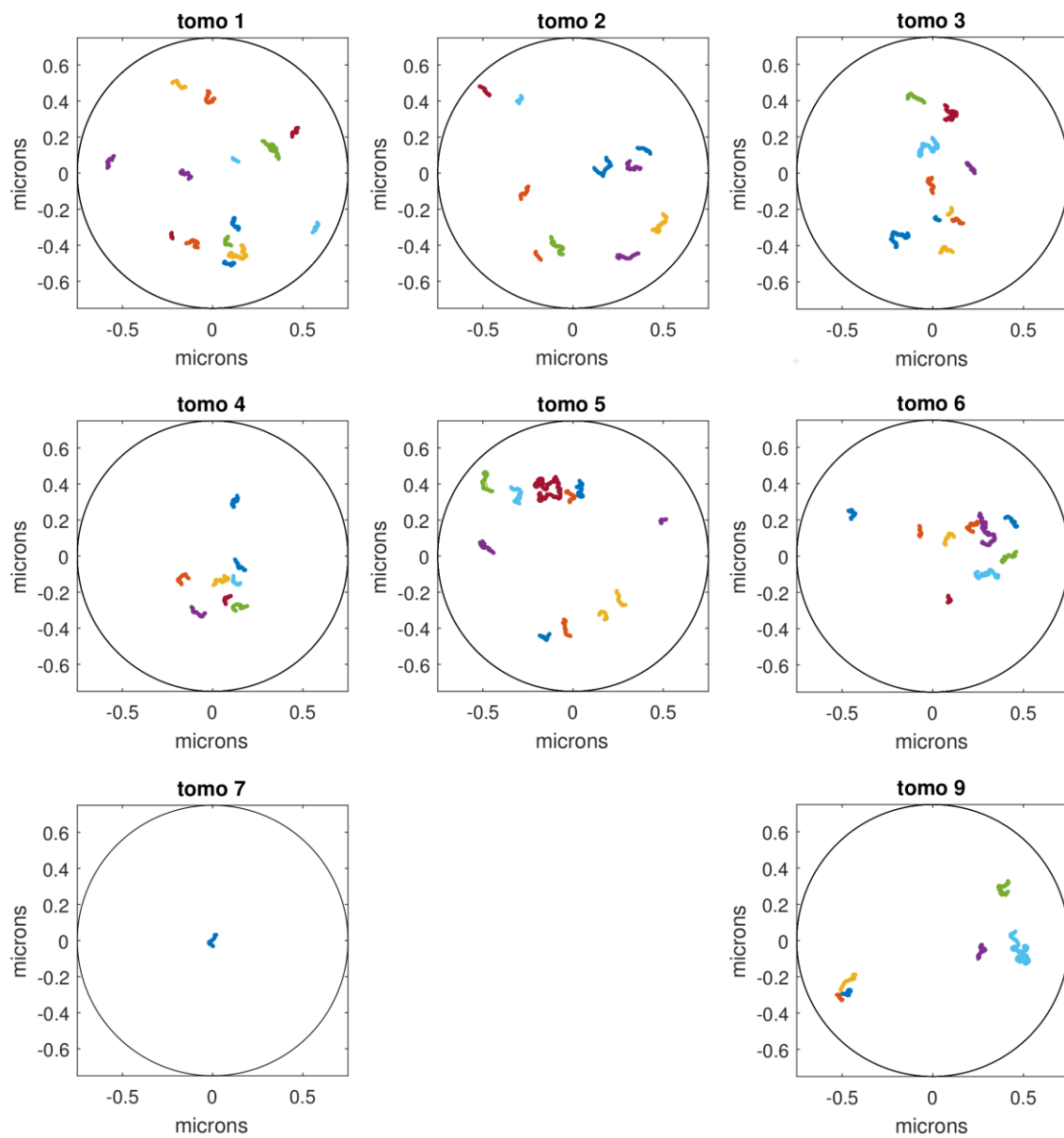


Figure 8-24: Overview of traced C-PG7<sub>n</sub><sup>NHBOc</sup> filaments throughout the 1.5 μm pores as obtained from cryo-ET.

### Derivation of DP width values

The widths of DPs were derived from sets of data with distinctly different origin: For **B-PG6**<sub>n</sub><sup>NHBoc</sup>, width values were extracted from the DP segment reconstructed using the single-particle approach (Figure 8-25a; see Figure 4-4) whereas the width of **C-PG7**<sub>n</sub><sup>NHBoc</sup> was derived from the an overlay of segments obtained topographically (Figure 8-25c). In both cases, the width was determined as the full width at half maximum of the average profile (Figure 8-25b,d).

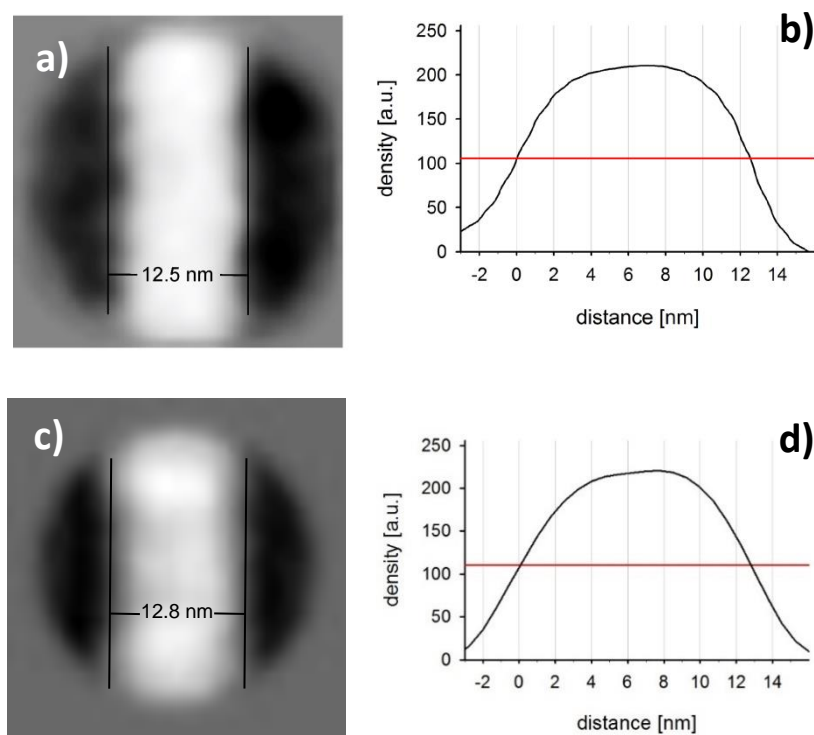


Figure 8-25: a) Class sum image of the untilted view of a **B-PG6**<sub>n</sub><sup>NHBoc</sup> segment for (Euler angle  $\vartheta = 0$  in Figure 8-23) and b) corresponding densitogram. c) Sum image of 220 aligned motifs extracted from as many different **C-PG7**<sub>n</sub><sup>NHBoc</sup> filaments of the tomography data, which allow a determination of the average filament diameter to (12.8 nm). The densitograms were generated in ImageJ using the plot profile routine along a filament length of 20 nm. (CB)

### Cryo-TEM of PFMMA

Ferrocenylmethyl methacrylate was prepared according to a literature procedure<sup>383</sup> and twice recrystallized from pentane before polymerization using a simple ATRP procedure, affording a polymer of  $P_n \approx 200$ . The polymer appears to provide sufficient mass contrast for imaging, but single-molecular resolution has not been achieved, as the polymer appears to form a networked superstructure of some kind, as shown in Figure 8-26a. Diluting the solution resulted not in the formation of individual chains which might constitute this network, but rather in stub-like filaments. The diameter of these filaments (*ca.* 2 nm) is larger than expected for an individual PFMMA chain, suggesting the formation some sort of stable complex in toluene. In view of the strong crystallization tendency of ferrocenyl-containing polymers (shown prominently in the work of Manners *et al.*),<sup>32</sup> this is not entirely surprising. Possibly, the structure formed in this case is a double-stranded helix similar to that observed in *it*-PMMA,<sup>384,385</sup> but this is mere speculation at this point. More effort needs to be invested both to find suitable sample preparation conditions for the imaging of individual, unfolded chains and to resolve the structure of the potential superstructures.

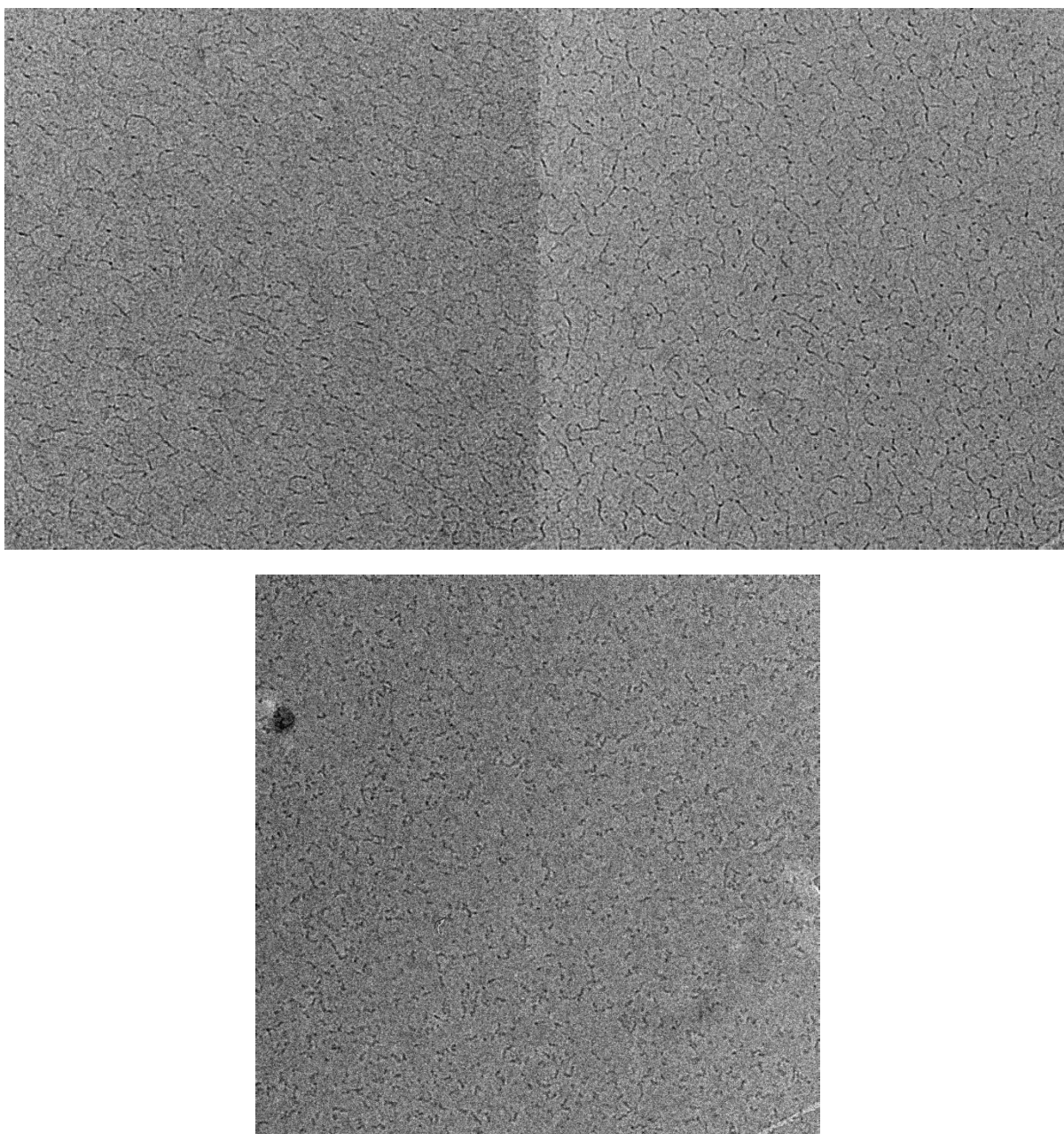


Figure 8-26: a) cryo-TEM Stereoimage pair (magnification x 50k) of a 0.1 mg mL<sup>-1</sup> solution of PFMMA in toluene, exhibiting a networked structure. c) cryo-TEM image (magnification x 62k) of a more dilute PFMMA solution in toluene. (CB)

### Analysis of DP trajectories

A tracer file available for each individual filament contains a 3D path of point locations, which were spline interpolated to allow the subsequent analysis on equidistantly spaced coordinates  $\mathbf{r}_1, \mathbf{r}_2, \dots, \mathbf{r}_N$  (resolution:  $\Delta s = 1$  nm) along the DP contour. From these coordinates were extracted: The DP end-to-end distance  $R_{ee} = |\mathbf{r}_N - \mathbf{r}_1|$ ; the total contour length  $L_c = N\Delta s$ ; the geometrical center  $\mathbf{c} = \langle \mathbf{r}_j \rangle$ ; the radius of gyration  $R_g = \langle (\mathbf{r}_j - \mathbf{c})^2 \rangle^{1/2}$ ; The tangent-tangent correlation function  $C(s) = \langle \mathbf{u}_j \cdot \mathbf{u}_{j+k} \rangle$ , where  $\mathbf{u}_j$  denotes the unit tangent vector emanating from the  $j$ th coordinate,  $\mathbf{u}_j = (\mathbf{r}_{j+1} - \mathbf{r}_j) / |\mathbf{r}_{j+1} - \mathbf{r}_j|$ . Results were found to be insensitive to the chosen interpolation scheme; All figures are based on an interpolation

with cubic splines. For the analysis of  $\langle R_g^2 \rangle$ , the following expression was employed to describe WLC scaling:

$$\langle R_g^2 \rangle = L_p \left\{ L/3 - L_p + L_p^2 \left[ L - L_p \left( 1 - \exp[-L/L_p] \right) \right] / L^2 \right\}$$

Eq. 8-5

#### 8.4.2. Supplementary information on trajectory analysis

As mentioned in the main text, the tangent-tangent correlation function  $C(s)$  can be approximated over a fairly large range of  $s$  by a linear combination of two exponential functions, as shown in Figure 8-27. This interpretation was used to rationalized simulation results in work by Kremer *et al.*,<sup>386,387</sup> however two “persistence lengths” within one system do likely not accurately reflect the behavior of the polyelectrolyte systems investigated in those simulations. It appears more likely that this is merely an expression of the strong and early deviation from WLC behavior – as is the case in the lattice Monte Carlo simulations by Binder *et al.*<sup>315,316</sup> and indeed the results presented in section 4.4.

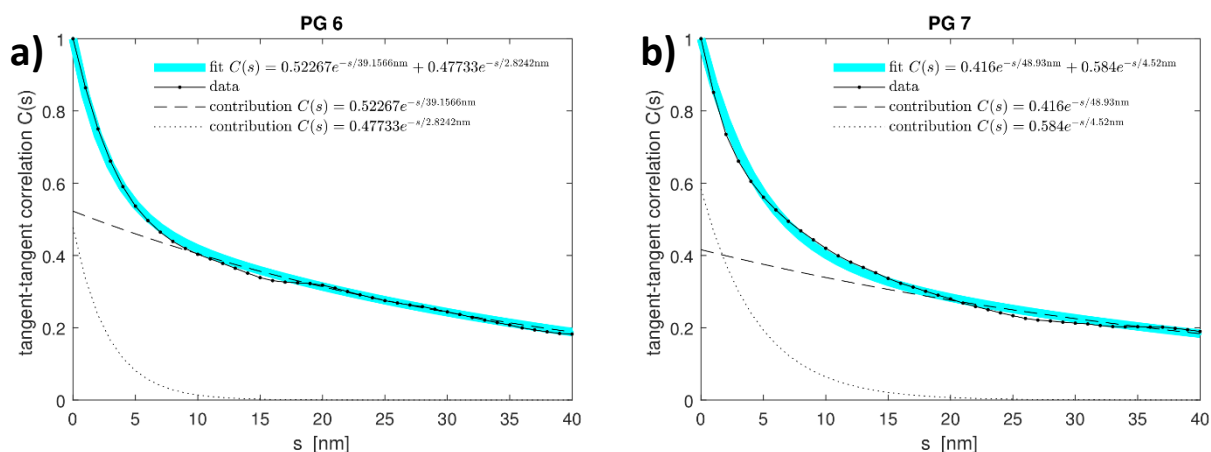


Figure 8-27: Double-exponential fits of  $C(s)$  for a)  $\mathbf{B-PG6}_n^{NHBoc}$  and b)  $\mathbf{C-PG7}_n^{NHBoc}$  apparently describing the long-range scaling of DPs rather well (MK).

## 8.5. Experimental details for chapter 5: Density of $\text{PGg}_n^{\text{NHoc}}$

SEM/TEM measurements discussed in chapter 5 were performed by Dr. Hao Yu, Prof. Dr. Baozhong Zhang and Prof. Dr. Roger Wepf (all ETH Zurich at the time) in the context of earlier work.<sup>148,172,174</sup> qSTEM measurements and corresponding data evaluation were conducted by Dr. Sebastian Tacke (MPI Dortmund), aided by Dr. Ulrike Keller and Dr. Harald Nüsse (both Uni Münster). Pills were vacuum annealed by Dr. Anontio Sánchez-Ferrer (D-HEST, ETH Zurich), who also conducted and evaluated all SAXS/WAXS measurements.

### 8.5.1. Determination of bulk density by classical methods

#### Preparation of bulk samples

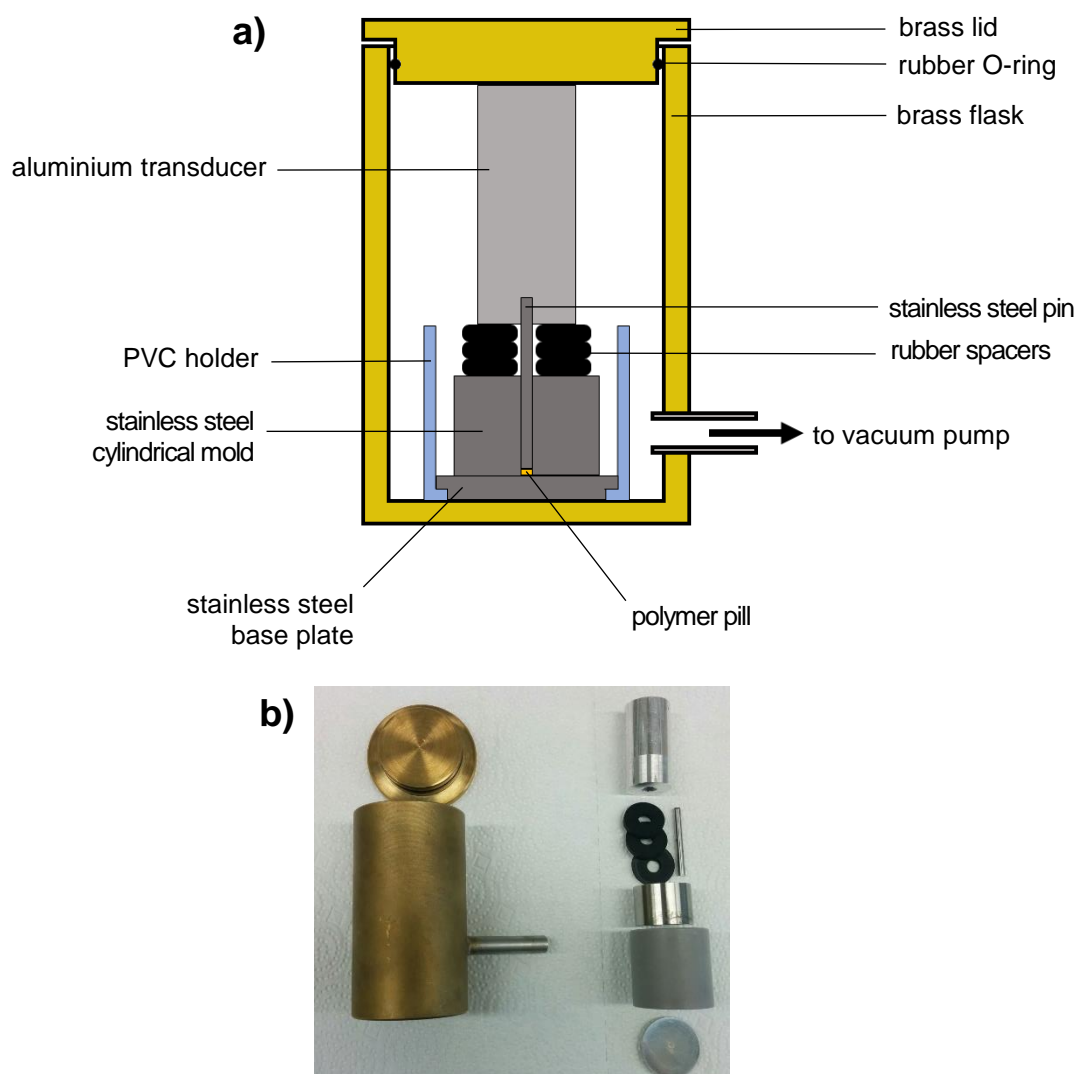


Figure 8-28: Schematic cross-section of the assembled compression molding setup used for hot-pressing of DP samples; b) photograph of the disassembled device.

In order to obtain solid bulk samples of DPs, the following method was employed, using the setup displayed in Figure 8-28, custom-built by Dr. Thomas Schweizer (D-MATL, ETH Zurich). The steel base plate and the steel mold were set into the PVC holder. The 4 mm bore of the mold was filled with the powdery DP lyophilizate, then the remainder of the interior of the setup was assembled. This was then carefully transferred into the pre-heated brass flask. The temperature chosen was slightly above  $T_g$  of the polymer in question (PG1<sub>500</sub><sup>NHBoc</sup>: 80 °C; PG2<sub>500</sub><sup>NHBoc</sup>: 90 °C; PG3<sub>500</sub><sup>NHBoc</sup> - **B**-PG8<sub>500</sub><sup>NHBoc</sup>: 100-105 °C). The entire setup was equilibrated at that temperature between the plates of the temperature-controlled, actively coolable hot press (Rondol) without applying significant pressure for 1 min, then the flask was evacuated slowly to *ca.*  $10^{-2} - 10^{-1}$  mbar. Under vacuum, a force of 0.1-0.3 kN was applied to the flask using the hot press; this was maintained for 5 min, and then clamping was released again. The press and flask were cooled to ambient temperature, then the flask was slowly filled with air, the setup was disassembled, and the pressed pill was carefully removed.

When switching DP samples, all parts in contact with polymer were carefully cleaned with methylene chloride to remove any residue. The DP pills obtained in this manner (Figure 5-1) were glassy at RT and quite brittle; edges were frequently chipped when removing the pills from the compression molding setup. Occasionally, the pills obtained were completely opaque rather than at least partially translucent. Such samples were generally discarded, although at least within the accuracy of hydrostatic weighing their density did not differ significantly from that of clear pills prepared from the same polymer. For higher *g* DPs, a progressively darker coloration of the samples after pill pressing from essentially colorless to quite yellow was observed. This deepened even further in the case of DPs derived from route **C** to dark browns, likely due to the colorants lending the initials DP samples their yellow color (see Figure 2-4).

#### Annealing of DP pills

DP samples as prepared above were found to significantly improve structurally in SAXS upon vacuum annealing. This process likely removed traces of (plasticizing) lyophilization solvent (1,4-dioxane) remaining in the samples after hot-pressing. The bulk samples investigated by SAXS and by density gradient column were therefore annealed by subjecting them to high vacuum (*ca.*  $5 \times 10^{-9}$  mbar) at 120 °C for 7 d in a special vacuum oven (Mezzenga group, D-HEST, ETH Zurich). Although annealing was conducted above  $T_g$  (60 - 80 °C) for all DPs, only PG1<sub>500</sub><sup>NHBoc</sup> was found to have softened and changed shape significantly. All other samples had remained in their original shape. This agrees with extremely long relaxation times found in rheological studies by Costanzo *et al.*<sup>323</sup> as well as unpublished findings by Dr. Thomas Schweizer, demonstrating that DPs tend to interdigitate quite strongly.

### Density determination by hydrostatic weighing

For hydrostatic weighing, a density determination kit (Mettler Toledo) suitable for a top-loading analytical balance (Mettler Toledo AE 163, Mettler Toledo) was used (Figure 8-29a). For each individual DP pill, five measurements were conducted, each consisting of weighing the sample in air ( $w_{DP}$ ), taring the balance and then submerging the sample into the working fluid, in this case *n*-hexane, giving its buoyancy ( $w_{hex}$ ). The density of hexane  $\rho_{hex}$  for each measurement day was determined separately using the calibrated sinker contained in the density determination kit in order to account for slight variations in room temperature ( $23.5 \pm 1$  °C). The density of the sample  $\rho_{DP}$  (Figure 8-29b) is then given by:

$$\rho_{DP} = -\rho_{hex} \frac{w_{DP}}{w_{hex}}$$

Eq. 8-6

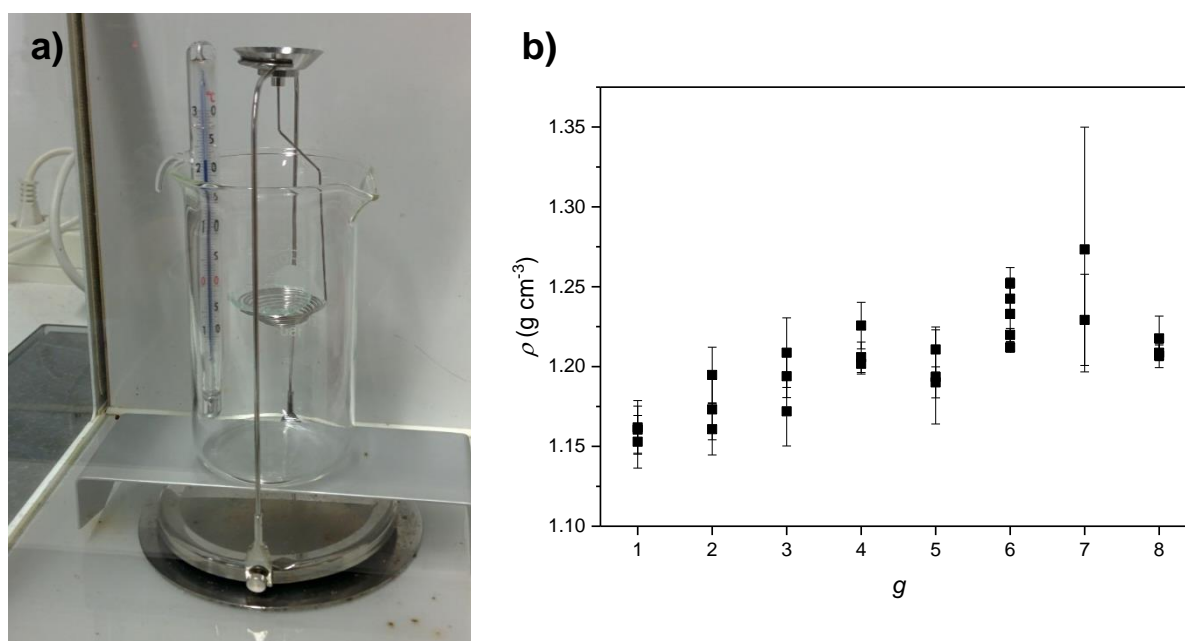


Figure 8-29: a) Photograph of the density determination kit assembled on the top-loading balance; b) densities of annealed DP samples as determined by hydrostatic weighing.

### Density determination using a density gradient column

A simple in-house built setup (Dr. Thomas Schweizer, D-MATL, ETH Zurich) was used to establish a density gradient column (Figure 8-30). It consists of a frame made from extruded aluminium profiles affixed to a heavy steel base plate. In the frame, a standard chromatography column (30 x 500 mm) was clamped rigidly. Position values were read out by means of a linear encoder bar affixed to the frame parallel to the column, to which was attached a measurement arm ending in a fork around the chromatography column to help avoid parallax errors. Samples and density standards (8 hollow glass spheres, evenly spaced between  $1.002$  g cm<sup>-3</sup> and  $1.4009$  g cm<sup>-3</sup>; H&D Fitzgerald Ltd.) were lowered into the column before establishment of the gradient by means of a titanium wire basket (weighted down with a small piece of lead), affixed to a nylon string.

Before establishment of the gradient, the two starting liquids (deionized water and sat. aq. NaBr) were degassed thoroughly to avoid bubble formation by vigorously stirring while applying vacuum (100 mbar) for at least 3 min,. The density gradient was established from the bottom by vacuum aspiration (*ca.* 800 mbar): The bottom of the column was fed from a stirred reservoir initially filled with deionized water, which was in turn connected to a reservoir of saturated aq. NaBr (Figure 8-30b). This permits the gradual mixing of the denser salt solution into the water, therefore creating a density gradient in the approximate range of  $\rho = 1.0 - 1.45 \text{ g cm}^{-3}$  in which density  $\rho$  and the distance from the top of the column  $d$  are related according to the following relation (also see Figure 5-2b for an example gradient):

$$d(\rho) = d_0 + A_1 e^{\rho/t}$$

Eq. 8-7

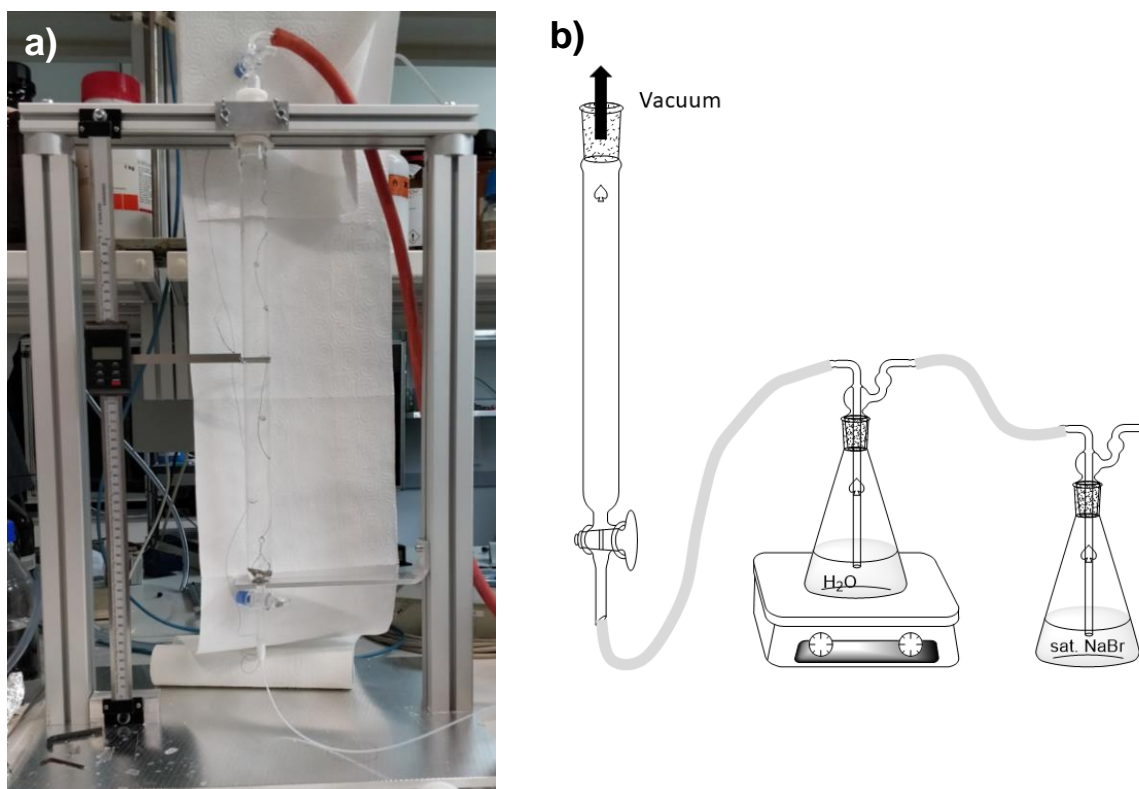


Figure 8-30: a) Photograph of the filled density gradient column setup. b) Schematic representation of the setup used for establishing the density gradient.

A new gradient was established for each set of three annealed DP pills measured per generation. Before reading out the positions of standards and samples, the column was allowed to equilibrate undisturbed for at least 16 h. Measurements were discarded when standards and/or pills were in contact with each other or when visible bubbles had formed in the column due to insufficient degassing. Room temperature was essentially constant at 23.5 °C, and temperature correction of the density standards was applied following the instructions of the manufacturer.



### 8.5.2. Determination of density by qSTEM

Samples for qSTEM were prepared by depositing a droplet of DP solutions (*ca.* 2 mg L<sup>-1</sup> in methylene chloride) onto TEM grids, carrying a lacey carbon film with a thin layer of amorphous carbon on top. The excess liquid was blotted off, the grid was propelled into liquid nitrogen, then transferred into a vacuum chamber for freeze drying. After freeze drying, all sample transfers were conducted under vacuum in a high vacuum transfer shuttle<sup>388</sup> to avoid contamination. The samples were briefly surveyed by SEM to check whether regions of suitable DP coverage were available (see Figure 8-31).

qSTEM measurements were conducted at Universität Münster by Drs. Sebastian Tacke, Harald Nüsse and Ulrike Keller, using a Hitachi STEM operating at 30 kV. The electron dose per exposure was 300 – 500 e nm<sup>-2</sup> and the pixel resolution was 0.699 nm. For data evaluation (conducted by Dr. Sebastian Tacke), a previously described approach was employed, affording mass and width values.<sup>319</sup> For cross-section models, the values  $h_{\text{TEM}}$  (section 5.4, Table 5-1) were used. Table 8-6 and Table 8-7 show the numerical results of qSTEM analyses.

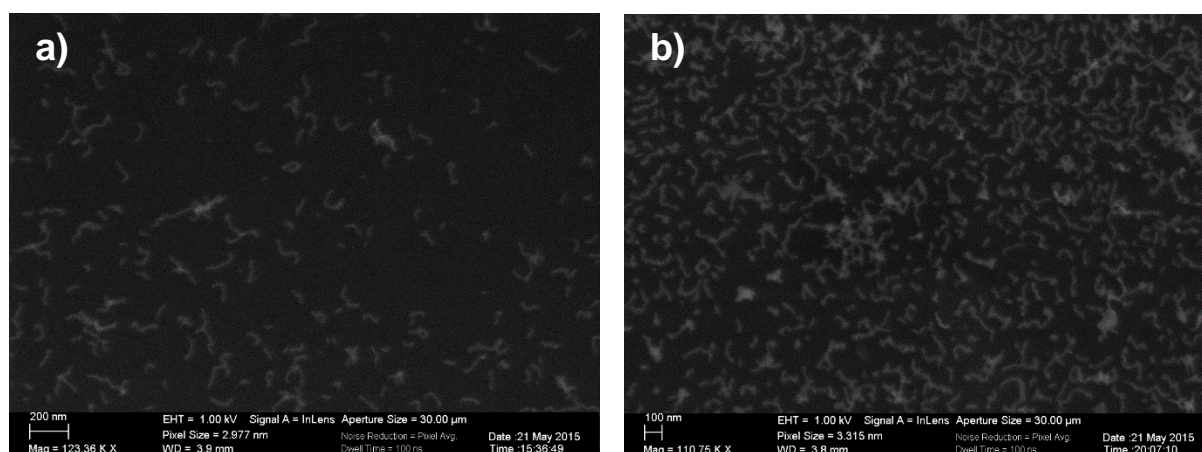


Figure 8-31: Example SEM images of samples (a) PG5<sub>500</sub><sup>NHBoc</sup>, b) B-PG6<sub>500</sub><sup>NHBoc</sup> destined for qSTEM.



Table 8-7: qSTEM evaluation for a) B-PG7<sup>NHBoc</sup><sub>500</sub> and b) B-PG6<sup>NHBoc</sup>. Sebastian Tacke, reproduced with permission.

Data		Mass		Width		Radius		Height		Square		Rectangle		Circle		Cutted Circle		Triangle		Gaussian Profile (8.2%)									
hTEM	ΔhTEM	wSEM	ΔwSEM	rFW	Δr	R(w)	ΔR	h(r)	Δh	A	ΔA	Density	Δp	A	ΔA	Density	Δp	A	ΔA	Density	Δp								
9	0.90	14.20	1.50	0.65	0.14																								
A Exp 1	34	55.04	6.75	1.16	2.75	3.18	0.48	2.60	0.48	110.46	10.09	0.83	0.05	72.34	12.74	1.26	0.14	86.71	7.92	1.05	0.07	61.84	25.69	1.48	0.37				
A Exp 3	143	51.47	9.05	0.76	2.83	1.99	0.15	2.58	0.15	99.09	2.90	0.86	0.03	64.89	10.27	1.32	0.13	77.78	2.28	1.10	0.03	55.47	8.85	1.54	0.15				
B Exp 1	159	50.34	8.55	0.68	2.61	1.77	0.23	2.59	0.23	132.87	5.22	0.63	0.02	86.89	13.90	0.96	0.09	104.15	4.10	0.80	0.03	74.27	10.59	1.13	0.10				
B Exp 2	224	52.22	10.84	0.71	2.60	1.94	0.24	2.59	0.24	125.08	5.28	0.69	0.02	81.92	13.18	1.08	0.10	88.19	4.14	0.88	0.03	40.96	6.59	2.12	0.21				
B Exp 3	119	53.30	8.91	0.82	2.63	2.14	0.26	2.61	0.26	116.59	5.61	0.76	0.03	76.36	12.43	1.16	0.12	91.52	4.41	0.97	0.04	70.02	11.66	1.24	0.13				
B Exp 4	148	46.56	12.23	1.01	2.63	2.64	0.30	2.60	0.30	116.08	6.50	0.65	0.03	76.03	12.55	1.00	0.10	91.12	5.10	0.83	0.04	65.27	13.57	1.36	0.17				
B Exp 5	253	54.28	8.46	0.53	2.60	1.38	0.21	2.60	0.21	120.15	4.52	0.75	0.02	79.69	12.98	1.15	0.11	94.32	3.55	0.96	0.03	67.26	10.51	1.34	0.13				
Average	1090	52.13	0.74	3.34						6.72	0.61	SEOM	0.94	0.04	SEOM	1.32	0.07	SEOM	0.92	0.01	SEOM	1.32	0.07	SEOM	2.20	0.08	SEOM	1.27	0.04

Data		Mass		Width		Radius		Height		Square		Rectangle		Circle		Cutted Circle		Triangle		Gaussian Profile (8.2%)									
hTEM	ΔhTEM	wSEM	ΔwSEM	rFW	Δr	R(w)	ΔR	h(r)	Δh	A	ΔA	Density	Δp	A	ΔA	Density	Δp	A	ΔA	Density	Δp								
12	1.50	17.60	2.20	0.67	0.18																								
B Exp 1	250	74.28	10.12	0.64	2.60	1.66	0.11	2.58	0.11	111.03	2.39	1.11	0.02	74.44	11.34	1.66	0.15	87.16	1.88	1.42	0.03	62.15	16.24	1.98	0.31	83.63	8.81	1.94	0.16
B Exp 2	200	71.29	10.31	0.73	2.60	1.90	0.14	2.59	0.14	116.51	2.99	1.02	0.02	78.12	11.97	1.52	0.14	91.46	2.35	1.29	0.03	65.22	17.04	1.81	0.29	66.77	10.08	1.77	0.16
A Exp 5	82	72.59	9.88	1.09	2.64	2.88	0.20	2.60	0.20	131.40	6.93	0.92	0.04	88.10	14.08	1.37	0.14	103.15	5.44	1.17	0.05	73.55	19.21	1.64	0.26	75.30	19.95	1.60	0.26
A Exp 6	140	78.89	11.03	0.93	2.63	2.45	0.21	2.60	0.21	122.10	4.57	1.07	0.03	91.86	12.79	1.60	0.15	96.85	3.59	1.37	0.04	68.35	17.85	1.92	0.30	69.97	15.80	1.87	0.25
A Exp 7	197	87.97	10.88	0.76	2.61	2.02	0.10	2.58	0.10	132.57	2.34	1.10	0.02	86.89	13.43	1.64	0.15	104.07	1.94	1.40	0.02	74.21	19.39	1.97	0.31	75.97	9.09	1.92	0.14
A Exp 8	340	61.61	8.87	0.42	2.60	1.10	0.10	2.59	0.10	112.32	2.10	0.91	0.01	75.31	11.42	1.36	0.12	88.17	1.65	1.16	0.02	62.88	16.42	1.63	0.26	64.37	6.23	1.59	0.09
A Exp 9	250	78.73	10.97	0.69	2.60	1.81	0.14	2.59	0.14	117.03	3.04	1.12	0.02	78.46	12.03	1.67	0.16	91.87	2.39	1.42	0.03	65.51	17.11	2.00	0.32	87.06	10.93	1.95	0.19
Average	1559	71.66	0.66	3.86						1.02	0.61	SEOM	1.33	0.05	SEOM	1.82	0.11	SEOM	1.30	0.01	SEOM	1.82	0.11	SEOM	3.05	0.11	SEOM	1.76	0.06

### 8.5.3. Determination of single-molecule density by SEM/TEM

#### SEM

Samples were prepared by drop-casting DP solutions (1 – 5 mg L<sup>-1</sup> in methylene chloride) onto freshly cleaved mica. The samples were air-dried and then transferred to a vacuum chamber for rotary W-shadowing (45 °). SEM images were recorded digitally on a cryo-FE-SEM (Gemini 1530, Zeiss), simultaneously in the SE and BSE modes using acceleration voltages of 2-10 kV.

#### TEM

Samples were prepared by drop-casting DP solutions (1 – 5 mg L<sup>-1</sup> in methylene chloride) onto freshly cleaved mica. The samples were air-dried and then transferred to a vacuum chamber for unidirectional W-shadowing (6 nm layer, elevation angle 7 °). The samples were then coated with an additional layer of carbon (8 nm, 90 °). The samples were removed from the chamber, the carbon replicas were floated onto ultrapure water and deposited onto copper TEM grids (400 mesh, Plano GmbH) and dried in air. TEM images were recorded using a CM12 TEM (Phillips) operated at 100 kV, equipped with a Gatan CCD camera.

#### Calculation of Density

The calculation of cross-sectional area is simple in the case of a rectangular cross-section depicted in Figure 8-32b (used mainly to arrive at slightly less outlandish density values for high  $g$ ):  $A_{\text{rectangle}} = w_{\text{SEM}} \cdot w_{\text{TEM}}$ . The calculation of cross-sectional area of a circular segment shown in Figure 8-32 is less straightforward. The total area is given by the area of a circle of radius  $\frac{1}{2}w_{\text{SEM}}$  minus the missing circular segment described by the angle  $\beta$ , *i.e.*

$$A_{\text{CS,segment}} = \frac{\pi}{4} w_{\text{SEM}}^2 - \frac{1}{8} w_{\text{SEM}}^2 (\beta - \sin\beta)$$

Eq. 8-8

Where the angle  $\beta$  of the circular segment is given by:

$$\beta = 2\cos^{-1}\left(1 - \frac{2(w_{\text{SEM}} - h_{\text{TEM}})}{w_{\text{SEM}}}\right)$$

Eq. 8-9

The volume corresponding to one DP unit can then be calculated as  $V = A\delta$ , with the length of one repeat unit within the DP chain being  $\delta = 0.252$  nm. To calculate the corresponding density values  $\rho = M/V$  (Table 5-1), the molar mass values  $M_{\text{exp}}$  noted in Table 5-1 were employed; for  $g = 1 - 7$ , they correspond to those calculated by the recursive approach based on labelling data, for  $g = 8$  they correspond to  $M_{\text{max}}$ . Some circularity in this cannot be avoided:  $M_{\text{max}}$  depends on the density  $\rho_{\text{packing}}$  (not only  $g_{\text{max}}$ ) of the DP.

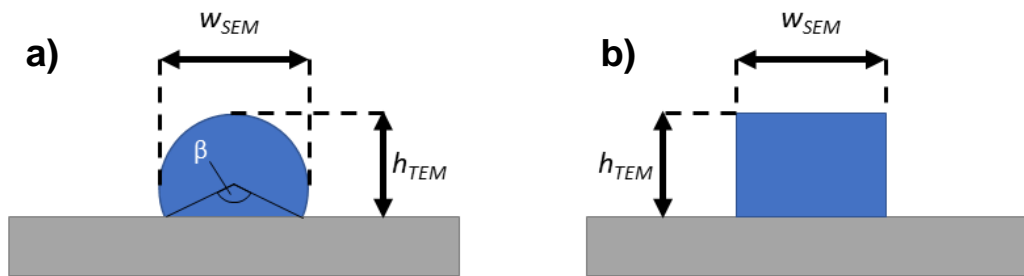


Figure 8-32: Cross-sectional models for deposited DPs: a) circular segment ( $g = 1 - 5$ ), b) rectangular ( $g = 6 - 8$ ).

#### 8.5.4. Determination of density by SAXS of bulk samples

SAXS and WAXS experiments (Dr. Antonio Sánchez-Ferrer, D-HEST, ETH Zurich) were performed using an AXS Micro (Bruker), equipped with a microfocused beam (50 W, 50 kV, 1 mA,  $\lambda_{CuK\alpha} = 0.15418$  nm) and a Dectris 2D 100K X-ray detector (Pilatus, 83.8 cm  $\times$  33.5 cm, 172  $\mu$ m resolution); An effective scattering vector range of  $0.1 \text{ nm}^{-1} < q < 25 \text{ nm}^{-1}$  was obtained). Alternatively, a MicroMax-002<sup>+</sup> (Rigaku) equipped with a microfocused beam (40 W, 45 kV, 0.88 mA,  $\lambda_{CuK\alpha} = 0.15418$  nm) collimated by three pinhole collimators (0.4 mm, 0.3 mm, and 0.8 mm), equipped with a Triton-200 gas-filled detector (20 cm diameter, 200  $\mu$ m resolution) and a two-dimensional BAS-MS 2025 imaging plate system (Fujifilm, 15.2  $\times$  15.2 cm<sup>2</sup>, 50  $\mu$ m resolution); An effective scattering vector range of  $0.05 \text{ nm}^{-1} < q < 25 \text{ nm}^{-1}$  was obtained with this instrument. Experiments were conducted at RT and the DP pills were affixed in the sample holder by a piece of adhesive tape which was measured without a sample for background subtraction.

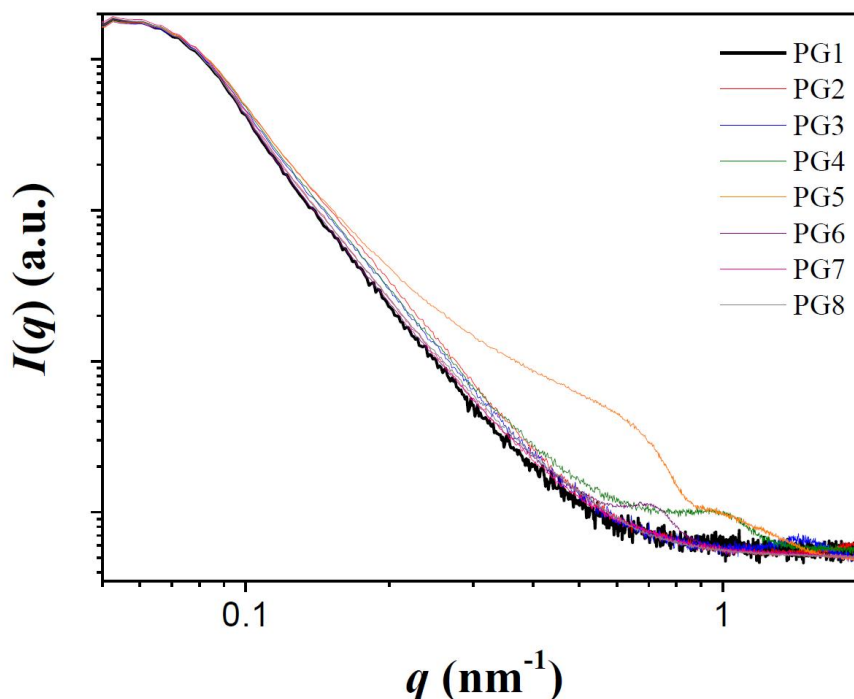


Figure 8-33: SAXS curves of freeze-dried DP powders, showing limited order for  $g = 3 - 6$ . Image generated by Dr. Antoni Sánchez-Ferrer, reproduced with permission.

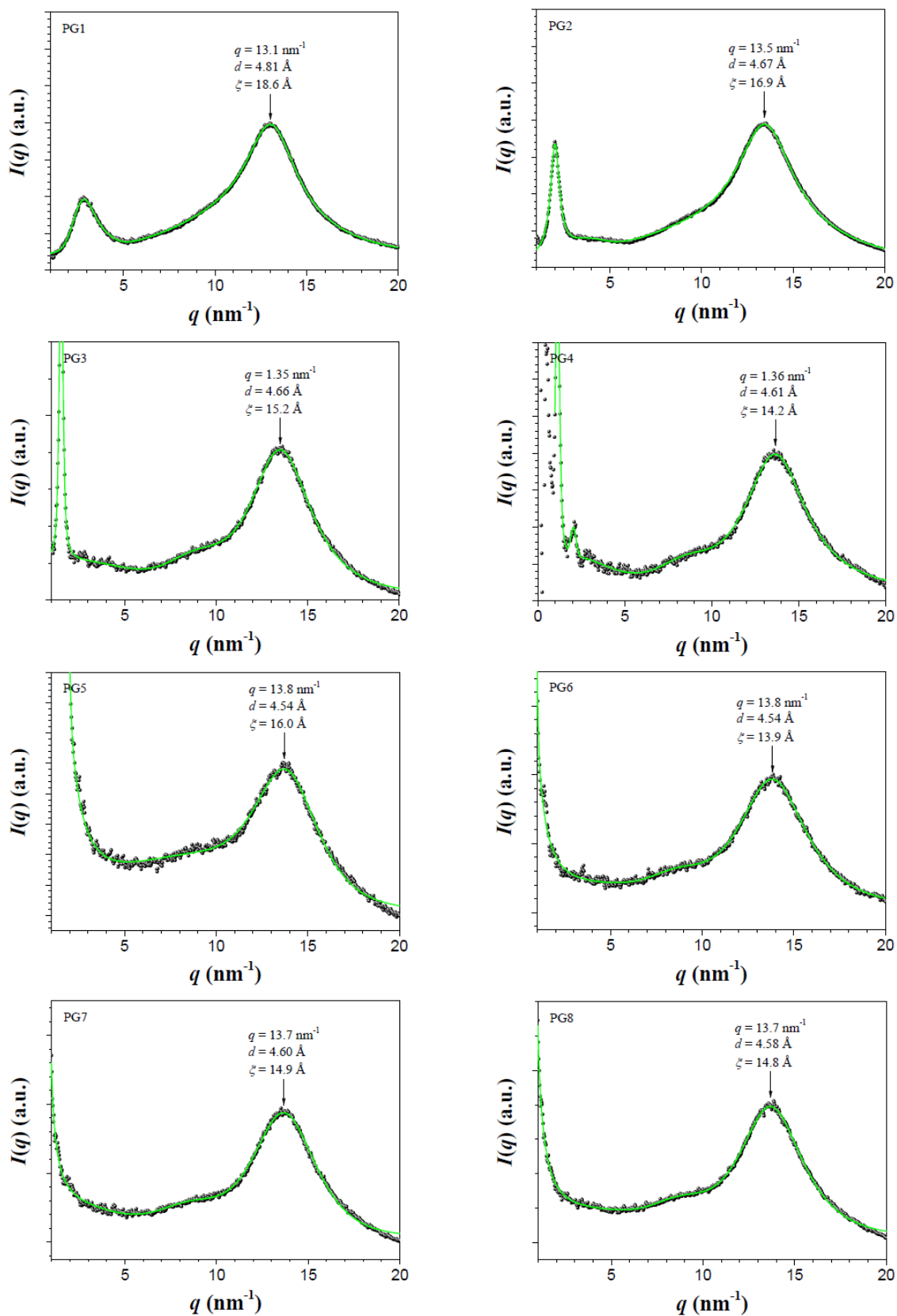


Figure 8-34: WAXS data & fits for DPs of  $g = 1 - 8$ , showing no distinct crystalline peaks. Image generated by Dr. Antoni Sánchez-Ferrer, reproduced with permission.

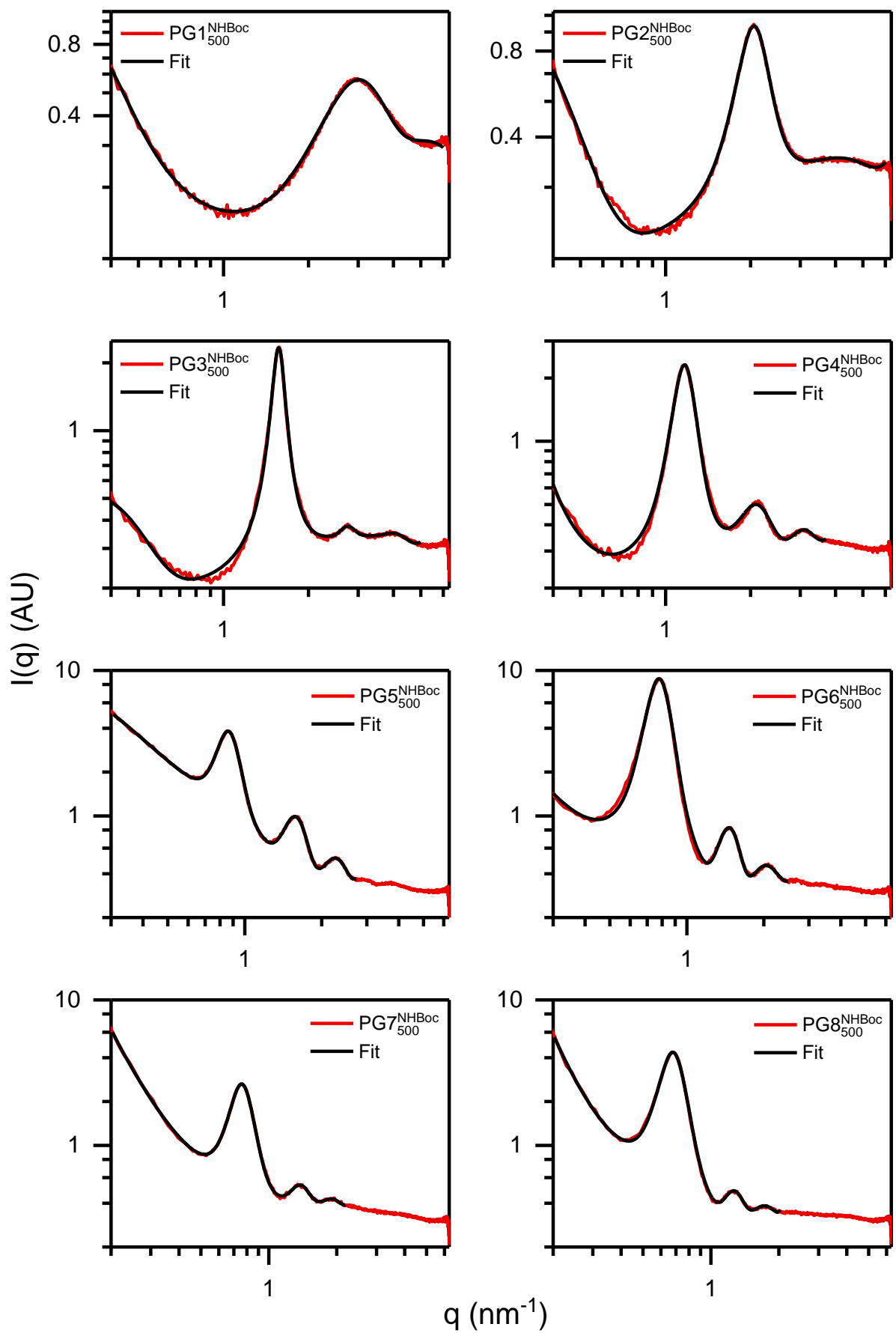


Figure 8-35: SAXS curves from Figure 5-5c including the corresponding fit curves (columnar rhombohedral packing).

Table 8-8: Cell parameters & density values obtained using other fit geometries (square, oblique, and rhombohedral packing of DP chains).

g	Col <sub>t</sub>		Col <sub>o</sub>				Col <sub>h</sub>	
	a (nm)	$\rho$ (g cm <sup>-3</sup> )	a (nm)	b (nm)	$\gamma$ (°)	$\rho$ (g cm <sup>-3</sup> )	a (nm)	$\rho$ (g cm <sup>-3</sup> )
1	2.13	0.964	2.46	2.46	60	0.746	2.46	0.72
2	3.06	1.093	3.53	3.53	60	0.878	3.53	0.82
3	4.01	1.366	6.45	3.67	38	1.439	4.63	1.02
4	5.38	1.564	8.29	4.62	40	1.777	6.21	1.17
5	7.28	1.732	10.36	5.66	45	2.186	8.41	1.30
6	8.08	2.570	10.31	5.48	52	3.730	9.33	1.93
7	8.28	4.956	9.99	5.50	56	7.337	9.56	3.72
8	9.26	5.378	10.99	5.90	57	8.338	10.70	4.03

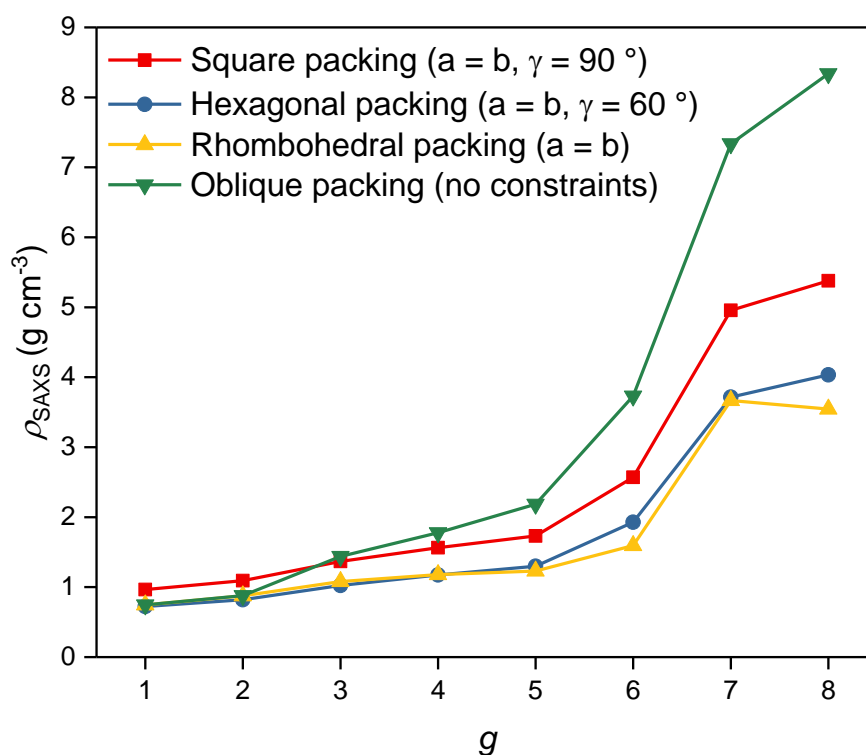


Figure 8-36: Chain densities noted in Table 5-2 and Table 8-8. Rhombohedral packing provided the best fit, however hexagonal packing fits also were fairly decent.

The density of a DP chain within the packed portions of the bulk sample as determined by SAXS can be calculated in the general (*i.e.* columnar oblique) case by assuming a dense array of ellipses (Figure 8-37a).<sup>kk</sup>

<sup>kk</sup> The array shown in Figure 8-37a assumes all ellipsoid semimajor axis are aligned with the long edge a of a parallelogram; this is not necessarily true, however a larger error is likely introduced by not considering the possibility of deformation away from an ellipsoid shape.



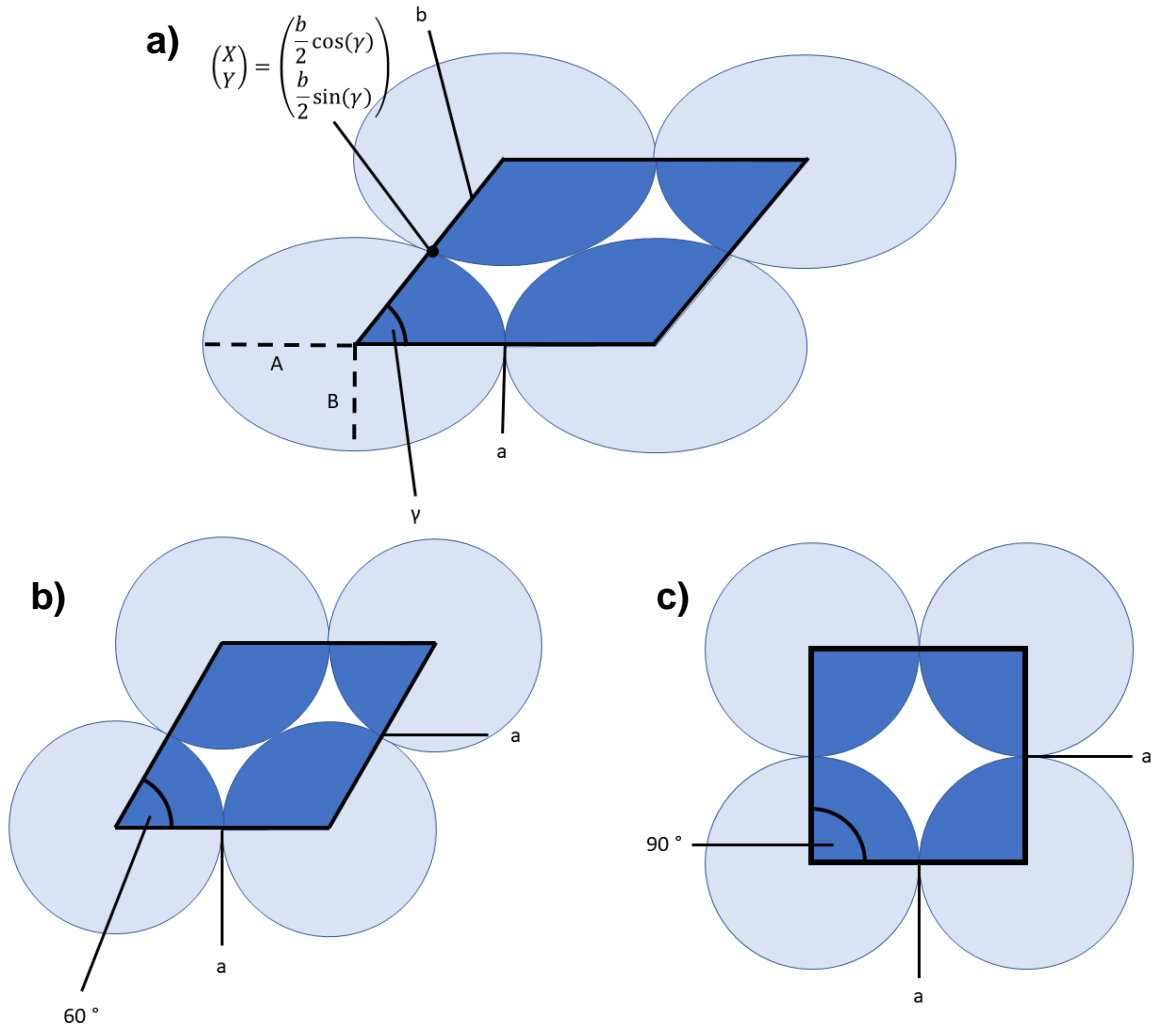


Figure 8-37: Geometric models used in the calculation of  $\rho_{\text{SAXS}}$ ; a) general, columnar oblique geometry (no geometric restrictions); b) columnar hexagonal geometry ( $a = b$ ,  $\gamma = 60^\circ$ ); c) columnar tetragonal geometry ( $a = b$ ,  $\gamma = 90^\circ$ ).

The general, columnar oblique case is parametrized by the side lengths of the parallelogram  $a$  and  $b$ , as well as by the angle  $\gamma$ . The area of the entire parallelogram is given by:

$$A_{\text{cell,obl}} = a \cdot b \cdot \sin \gamma$$

Eq. 8-10

The area of an ellipse – corresponding to the cross-section of a DP chain within this model – with the semimajor axis  $A$  and the semiminor axis  $B$  as indicated in Figure 8-37a is given by

$$A_{\text{chain,obl/rhomb}} = A \cdot B \cdot \pi$$

Eq. 8-11

The length of the semimajor axis  $A$  corresponds to  $A = 0.5a$ , and the length of the semiminor axis  $B$  can be derived from the parametrization of the ellipse, which in any configuration of  $a$ ,  $b$  and  $\gamma$  passes through two points: Taking the center of the ellipse as the origin of a cartesian coordinate system, the ellipse passes through the middle point of the base of the parallelogram ( $X = 0.5a$ ,  $Y = 0$ ), and through the middle of the upright side as indicated in Figure 8-37a. The coordinates of these two

intersection points provide the requisite information to solve the parametrization equation of an ellipse (Eq. 8-12) for the semiminor axis B.

$$\frac{x^2}{A^2} + \frac{y^2}{B^2} = 1$$

*Eq. 8-12*

These equations are valid for all fit geometries. However for the cases with fewer geometric degrees of freedom, it is convenient to use the arising simplifications. For the columnar rhombohedral case ( $a = b$ ), the area of the unit cell simplifies to Eq. 8-13, however the above derivation of the area of an ellipse must still be used. For the columnar hexagonal case (Figure 8-37b,  $a = b$ ,  $\gamma = 60^\circ$ ), the area of the individual chain is given by that of a circle of radius  $a$ . The same is true for columnar tetragonal packing (Figure 8-37c,  $a = b$ ,  $\gamma = 90^\circ$ ), where the area is of course simply that of a square of edge length  $a$ .

$$A_{\text{cell,rhomb}} = a^2 \sin \gamma$$

*Eq. 8-13*

The density of the DP chain  $\rho_{\text{SAXS}}$  is in all cases calculated using:

$$\rho_{\text{SAXS}} = \frac{M}{V} = \frac{M_{\text{exp}}}{A_{\text{chain}} \cdot \delta}$$

*Eq. 8-14*

## 8.6. Experimental details for chapter 6: Fluorescent labelling of DPs for rheological studies

Microscopy (iSIM) was conducted in collaboration with Gabriele Colombo (D-MATL, ETH Zurich); the synthetic work presented in section 6.5 was done by Ralph Werner (D-CHAB, ETH Zurich) in the course of a student research project.

### 8.6.1. Syntheses

Carboxyrhodamine 110 (**76**)<sup>389</sup> and its sulfonated derivative AF-488 (**77**) were prepared as reported elsewhere;<sup>354</sup> Purification of these two rhodamine-type dyes was only investigated cursorily, crude precipitates were used in further reactions. Food red 106 sulfonyl chloride (**84**)<sup>390</sup> was likewise prepared according to literature; TAMRA (**80**) and (5/6)-carboxyrhodamine B (**81**) were prepared following another literature procedure.<sup>355</sup> (5,6)-rhodamine B isothiocyanate hydrochloride (**69**, Bio reagent grade) was obtained from Sigma Aldrich.

#### General procedure F: Rhodamine B ITC labelling & dendronization of DPs of the type $PGg_n^{NH_3TFA}$

The lyophilizate of  $PGg_n^{NH_3TFA}$  (general procedure D) was dissolved in DMSO (*ca.* 5 mL per 100 mg initial DP) and the solution was cooled to 0 °C in an ice bath.  $NEt_3$  (4 equiv./amine) and DMAP (catalytic amount, *ca.* 0.05 – 0.1 equiv./amine) were added, followed by a solution of Rhodamine B isothiocyanate hydrochloride (**69**, 0.1 – 0.2 equiv./amine) in DMSO (*ca.* 30 mg mL<sup>-1</sup>). The mixture was stirred at RT in the dark for 2 d, and then  $DG1^{NHBoc}$  (**20**, 3 equiv./amine) and DMF (*ca.* 1 mL per 100 mg initial DP) were added at 0 °C. The reaction mixture was then warmed to RT and stirred in the dark for a total of *g* weeks (*e.g.* 3 weeks for  $PG3_n^{NHBoc}$  as the starting material). During this time, after *ca.* one third of the total reaction time had elapsed, the reaction mixture was cooled back to 0 °C and a further portion of  $DG1^{NHBoc}$  (**20**, 2 equiv./amine) was added. After the indicated amount of stirring time, the reaction mixture was precipitated into  $Et_2O$  (*ca.* 200 mL per 100 mg initial DP). The polymer was then purified by column chromatography (methylene chloride,  $R_f \approx 1.0$ ) and lyophilized from freshly distilled 1,4-dioxane.

#### Attempted labelling of $PG1_{500}^{NH_3TFA}$ with AF-488 (**77**)

A solution of  $PG1_{500}^{NH_3TFA}$  (100 mg, 0.2 mmol RU) in DMF (5 mL) was cooled in an ice bath and  $NEt_3$  (0.1 mL, 0.7 mmol, 3.7 equiv.) and DMAP (a few grains) were added. To this, a solution of **77** (crude; 25.5 mg, *ca.* 44 μmol, 0.23 equiv.), EDCI (50 mg, 0.3 mmol, 1.4 equiv.) and HOSu (25 mg, 0.2 mmol, 1.1 equiv.) in DMSO (1.5 mL) was added dropwise. The resulting mixture was stirred at RT for 3 d; an initially formed precipitate dissolved during this time. Then,  $Boc_2O$  (406.4 mg, 1.8 mmol, 9.7 equiv.) was added and the mixture was stirred at 50 °C for 10 h. The reaction mixture was concentrated in vacuum, then purified by column chromatography (methylene chloride,  $R_f \approx 1$ ). Lyophilization from <sup>t</sup>BuOH afforded a raspberry-pink solid (23.3 mg, 23 %). UV/Vis:  $\lambda_{max, MeOH} = 497$  nm; *ca.* 0.01 dyes/RU ( $\epsilon = 73'000$ ).

Attempts using this dye never progressed beyond *ca.* 1 % of RUs being labelled (as judged by UV/Vis), and in ultracentrifugation and dialysis experiments, it became evident that significant amounts of unbound dye remained after purification by column chromatography – likely bound non-covalently to the DP itself, considering the polar nature of the dye and the low polarity of the eluent (methylene chloride).

#### Labelling of PG3<sub>500</sub><sup>NH<sub>3</sub>TFA</sup> with TAMRA (**80**)

A solution of PG3<sub>500</sub><sup>NH<sub>3</sub>TFA</sup> (106.3 mg, 39  $\mu$ mol RUs) in DMF (3 mL) was cooled to 0 °C and NEt<sub>3</sub> (0.1 mL, 0.7 mmol, 18 equiv.) and a few crystals of DMAP (cat.) were added, followed by 162  $\mu$ L of a solution containing TAMRA (**80**, 71 mM; 0.3 equiv./RU) and TBTU (147 mM; 0.6 equiv./amine). The resulting dark-red solution was stirred under N<sub>2</sub> for 5 d, then DG1<sup>NHBoc</sup> (**20**, 870 mg, 40 equiv./RU) was added and the mixture was stirred in the dark for further 10 d. The resulting mixture was precipitated into Et<sub>2</sub>O (300 mL) and the polymer was purified by column chromatography (methylene chloride, R<sub>f</sub>  $\approx$  1), then lyophilized from freshly distilled 1,4-dioxane. The polymer was obtained as a deep magenta foam (130.7 mg, 62 %). UV/Vis:  $\lambda_{\text{max, MeOH}}$  = 552 nm; *ca.* 0.035 dyes/RU ( $\epsilon$  = 87'000).

#### Synthesis of RhoB-PG2<sub>10'000</sub><sup>NHBoc</sup> (**88**)

Prepared according to General Procedures D, then F, starting from PG1<sub>10'000</sub><sup>NHBoc</sup> (154.6 mg, 0.1 mmol RUs); 0.15 equiv./amine of **69** (47.6 mg, 88  $\mu$ mol) were used. RhoB-PG2<sub>10'000</sub><sup>NHBoc</sup> was isolated as a bright magenta foam after lyophilization (286 mg, 79 %). UV/Vis:  $\lambda_{\text{max, MeOH}}$  = 550 nm. Labelling density: 0.066 RU<sup>-1</sup>/0.033 per amine; labelling yield: 22 %. <sup>1</sup>H-NMR (300 MHz, DMSO-*d*<sub>6</sub>, 343 K): 8.15 (s (b)), 6.9 (app. s (b)), 6.48 (s), 6.38 (app. s(b)), 3.88 (app. s(b)), 3.3 (app. s(b)), 3.02 (m (b)), 1.75 (app. s (b)), 1.3 (s).

#### Synthesis of RhoB-PG3<sub>10'000</sub><sup>NHBoc</sup> (**89**)

Prepared according to General Procedures D, then F, starting from PG2<sub>10'000</sub><sup>NHBoc</sup> (148.7 mg, 0.3 mmol RUs); 0.16 equiv./amine of **69** (41.7 mg, 78  $\mu$ mol) were used. RhoB-PG3<sub>10'000</sub><sup>NHBoc</sup> was isolated as a bright magenta foam after lyophilization (177 mg, 55 %). UV/Vis:  $\lambda_{\text{max, MeOH}}$  = 552 nm. Labelling density: 0.181 RU<sup>-1</sup>/0.045 per amine; labelling yield: 28 %. <sup>1</sup>H-NMR (300 MHz, DMSO-*d*<sub>6</sub>, 343 K): 8.13 (s (b)), 6.88 (app. s (b)), 6.45 (s (b)), 6.34 (app. s(b)), 3.85 (app. s(b)), 3.0 (m (b)), 1.73 (app. s (b)), 1.27 (s).

#### Synthesis of RhoB-PG4<sub>10'000</sub><sup>NHBoc</sup> (**90**)

Prepared according to General Procedures D, then F, starting from PG3<sub>10'000</sub><sup>NHBoc</sup> (151.3 mg, 58  $\mu$ mol RUs); 0.13 equiv./amine of **69** (32.4 mg, 60  $\mu$ mol) were used. RhoB-PG4<sub>10'000</sub><sup>NHBoc</sup> was isolated as a bright magenta foam after lyophilization (171 mg, 55 %). UV/Vis:  $\lambda_{\text{max, MeOH}}$  = 554 nm. Labelling density: 0.372 RU<sup>-1</sup>/0.046 per amine; labelling yield: 36 %. <sup>1</sup>H-NMR (300 MHz, DMSO-*d*<sub>6</sub>, 343 K): 8.23 (s (b)), 6.91 (app. 6.35-6.45 (m (b)), 3.89 (app. s(b)), 3.01 (app. s (b)), 1.77 (app. s (b)), 1.27 (s (b)).

#### Synthesis of RhoB-PG5<sub>10'000</sub><sup>NHBoc</sup> (**91**)

Prepared according to General Procedures D, then F, starting from PG4<sub>10'000</sub><sup>NHBoc</sup> (152 mg, 28  $\mu$ mol RUs); 0.13 equiv./amine of **69** (30.5 mg, 60  $\mu$ mol) were used. The addition of further DMF was necessary after a few days of dendronization in order to redissolve precipitated polymer. RhoB-PG5<sub>10'000</sub><sup>NHBoc</sup> was isolated as a bright magenta foam after lyophilization (196 mg, 63 %). UV/Vis:  $\lambda_{\text{max, MeOH}}$  = 553 nm. Labelling density: 0.5 RU<sup>-1</sup>/0.031 per amine; labelling yield: 25 %. <sup>1</sup>H-NMR (300 MHz, DMSO-

$d_6$ , 343 K): 8.15 (s (b)), 6.89 (app. s(b)), 6.3-6.45 (m (b)), 3.88 (app. s(b)), 3.01 (app. s (b)), 1.73 (app. s (b)), 1.26 (s b)).

#### Determination of labelling density in RhoB-labelled DPs

The labelling density was estimated by UV/Vis spectroscopy: The DP was dissolved in MeOH at *ca.* 0.1-0.2 mg mL<sup>-1</sup>; UV/Vis spectra were measured in 1 cm quartz cuvettes and when necessary the solution was diluted such that  $A \leq 1.0$ . The labelling density was determined using the Lambert Beer law and the extinction coefficient of Rhodamine B ( $\epsilon = 106'000 \text{ M}^{-1}\text{cm}^{-1}$ ):

$$C_{\text{RhoB}} = \frac{A}{106'000 \text{ M}^{-1}}$$

Eq. 8-15

The labelling density per RU and amine for a DP of  $g$  were determined using:

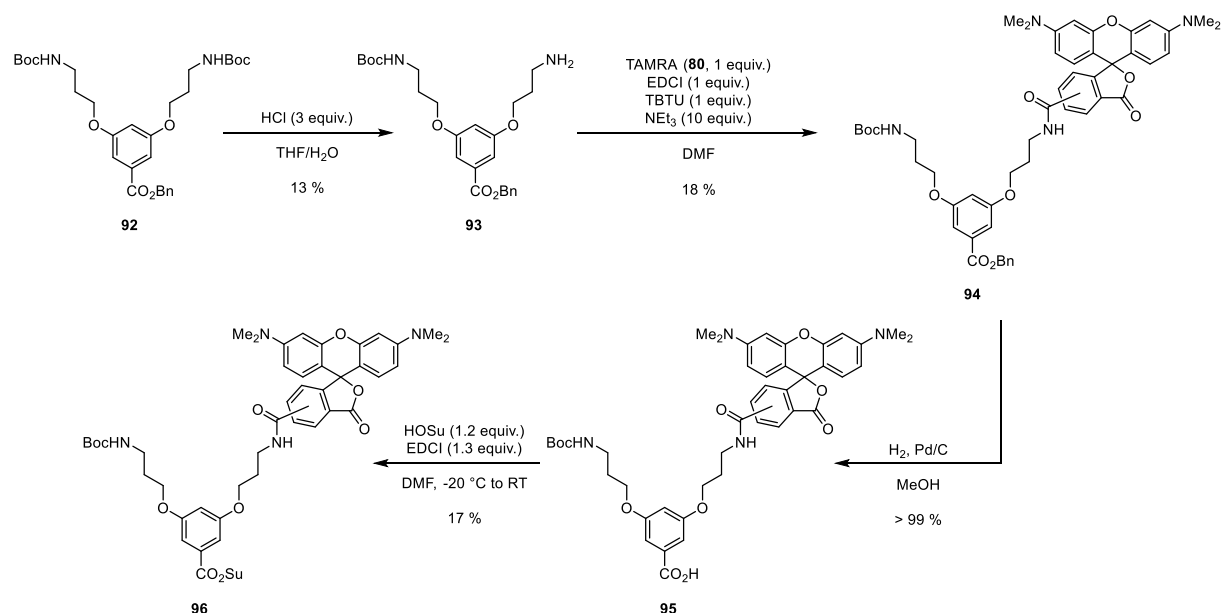
$$X_{\text{RhoB}}[\text{RU}^{-1}] = \frac{C_{\text{RhoB}}}{C_{\text{RU}}}$$

Eq. 8-16

$$X_{\text{RhoB}}[\text{amine}^{-1}] = \frac{X_{\text{RhoB}}[\text{RU}^{-1}]}{2^g}$$

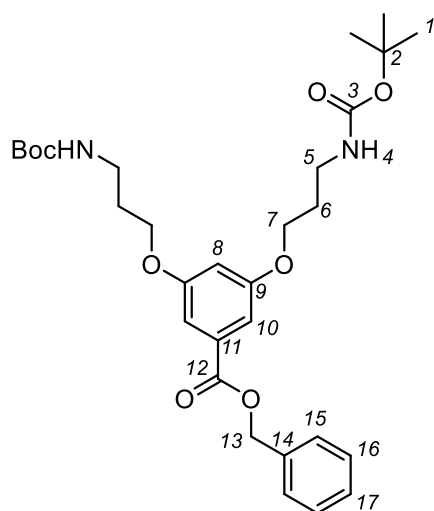
Eq. 8-17

For the calculation of the polymer RU concentration  $C_{\text{RU}}$ , the labelling density does not matter significantly, as the molar mass difference of replacing a peripheral dendritic group (derived from DG1<sup>NHBoc</sup>) with the thiourea derived from RhoB-ITC is small.



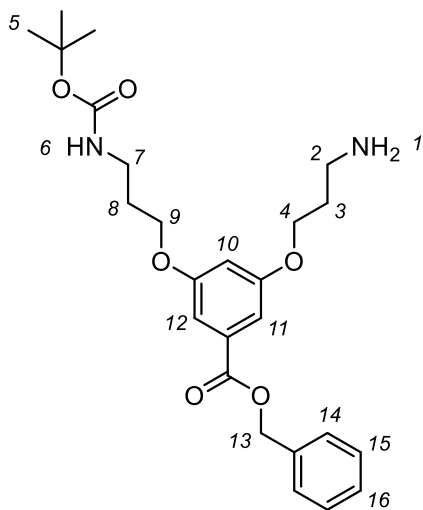
Scheme 8-6: Synthesis of TAMRA-bearing dendronization agent 69.

### Synthesis of benzyl 3,5-bis(3-(*tert*-butyloxycarbonylamido)propyloxy)benzoate (**92**)



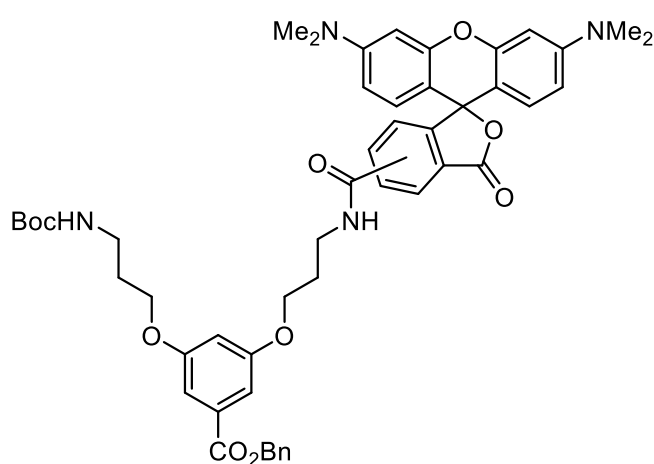
To a solution of **19** (5 g, 10.42 mmol, 1 equiv.) in DMF (50 mL),  $K_2CO_3$  (1.77 g, 12.81 mmol, 1.2 equiv.) was added and the mixture was stirred for 30 minutes at RT before benzyl bromide (2.37 g, 13.88 mmol, 1.3 equiv.) was added. The mixture was stirred at 65 °C for 16 hours, then cooled to RT and stirred for another 96 hours before the solvent was removed. The resulting white powder was dissolved in ethyl acetate and washed with 10 % aq.  $NaHCO_3$ . Flash chromatography (hexane:EtOAc 4:1) and evaporation of the solvent yielded a white solid (**92**, 5.28 g, 88.6 %).  $^1H$ -NMR (300 MHz, 298 K,  $CDCl_3$ ): 1.43 (s, 18H), 7.30-7.47 (m, 5H, 15-17), 7.19 (d,  $J = 2.4$  Hz, 2H, 10), 6.63 (t,  $J = 2.4$  Hz, 1H, 8), 5.34 (s, 2H, 13), 4.73 (br, 1H, 4(?)), 4.02 (t,  $J = 6$  Hz, 4H, 7), 3.31 (m, 4H, 5), 1.97 (m, 4H, 6), 1.43 (s, 18H, 1).  $^{13}C$ -NMR (300 MHz, 298 K,  $CDCl_3$ ): 166.26 (12), 159.96 (9), 156.11 (3), 136.09 (14), 132.15 (11), 128.74 (15), 128.41 (17), 128.37(16), 108.20 (10), 106.64 (8), 79.43 (2), 67.03 (13), 66.15 (7), 38.04 (5), 29.63 (6), 28.55 (1).

### Synthesis of benzyl 3-(3-(*tert*-butyloxycarbonylamido)propyloxy)-5-(3-amidopropoxy)benzoate (**93**)<sup>98</sup>



**92** (5.1 g, 9.13 mmol, 1 equiv.) was dissolved in THF (50 mL), cooled to 0 °C and a mixture of 37% HCl (2.26 mL, 27.4 mmol, 3 equiv.) and THF (20 mL) was added slowly. The mixture was stirred for 24 hours at room temperature and the reaction progress was monitored by TLC (EtOAc:MeOH 2:1, 1 %  $NEt_3$ ;  $R_{f,product} = 0.4$ ,  $R_{f,educt} = 0.95$ ). More 37% aq. HCl (0.37 mL, 4.57 mmol, 0.5 equiv.) in THF (13 mL) was added at 0 °C and the reaction was stirred for another 4 hours at RT. The reaction was stopped by addition of  $NEt_3$  (6.33 mL, 45.65 mmol, 5 equiv.). Flash column chromatography (EtOAc:MeOH 1:0  $\rightarrow$  2:1 + 1%  $NEt_3$ ) yielded a yellow oil (**93**, ca 0.6 g, 1.204 mmol, 13.2 %) containing some  $NEt_3$ .  $^1H$ -NMR (300 MHz, 298 K,  $CDCl_3$ ): 8.42 (s (b), 1H, ), 7.42-7.32 (m, 5H, 14-15), 7.15 (app. s (b), 2H, 11&12) 4.06 (, 6.68 (app. s (b), 1H, 10), 5.3 (s, 2H, 13), 4.82 (s (b), 1H, 6), 4.06 (m (b), 2H, 4 or 9), 3.98 (m (b), 2H, 4 or 9), 3.3-3.21 (m (b), 4H, 2&7), 2.25 (m (b), 2H, 3 or 8), 1.92 (m (b), 2H, 3 or 8), 1.41 (s, 9H, 1).  $^{13}C$ - NMR (300 MHz, 298 K,  $CDCl_3$ ): 166.20, 159.96, 159.52, 136.04, 132.02, 128.75, 128.41, 128.35, 107.81, 106.79, 79.38, 67.03 66.24, 65.69, 37.96, 29.55, 28.56, 27.27.

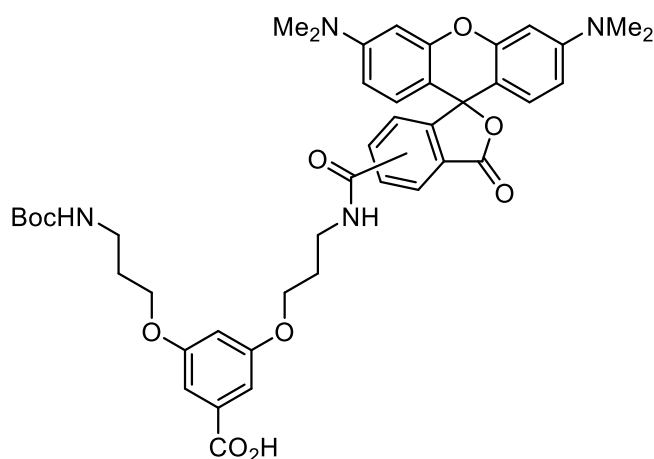
Synthesis of benzyl 3-(3-(tert-butyloxycarbonylamido)propyloxy)-5-(3-TAMRA-amidopropoxy)benzoate (**94**)



TAMRA (**80**, 100 mg, 0.231 mmol) EDCI (44.3 mg, 0.231 mmol, 1 equiv.) TBTU (74.2 mg, 0.231 mmol, 1 equiv.) and  $\text{NEt}_3$  (0.28 mL, 2.05 mmol, 10 equiv.) were dissolved in DMF (10 mL) at room temperature. After 3 hours **93** (3.81 mL of a 91 mM solution in DMF, 0.374 mmol 1.5 equiv.) was added. The reaction was stopped after 4 days, the solvent was removed in vacuo at 55 °C and flash column chromatography (DCM: MeOH, 20:1→20:2) afforded the product as a red solid (35 mg, 18 %).  $^1\text{H-NMR}$  (300 MHz, 298

K,  $\text{CDCl}_3$ ): 8.50 (s, 1H), 8.17-8.20 (m, 1H), 7.66-7.73 (m, 1H), 7.50-7.56 (m, 1H), 7.30-7.46 (m, 6H), 7.15-7.22 (m, 4H), 6.76-6.84 (m, 2H), 6.68 (s, 1H), 6.44-6.56 (m, 3H), 5.32 (s, 2H), 4.14 (m, 2H), 4.01 (t,  $J=6$  Hz, 2H), 3.73 (m, 2H), 3.27 (m, 2H), 3.08 (s, 12H), 2.18 (t,  $J=5.4$  Hz, 2H), 1.94 (m, 2H), 1.40 (s, 9H).

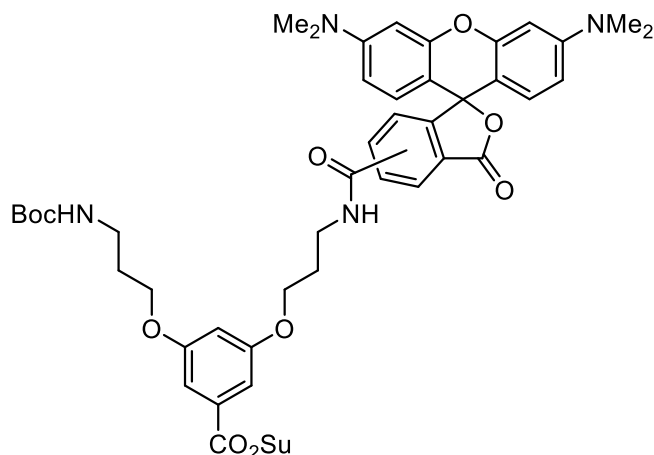
Synthesis of 3-(3-(tert-butyloxycarbonylamido)propyloxy)-5-(3-TAMRA-amidopropoxy)benzoic acid (**95**)



**94** (22.7 mg, 0.026 mmol, was dissolved in MeOH (9 mL) and 10% Pd/C (9 mg, cat.) was added. Hydrogen was bubbled through the solution for 5 minutes and the mixture was then kept under 1 atm of  $\text{H}_2$  for 4 hours. TLC (DCM:MeOH:1M:AcOH 10:4:0.5) showed complete reaction ( $R_{f,\text{educt}} = 0.95$ ,  $R_{f,\text{product}} = 0.4$ ). The mixture was filtered through a syringe filter and the solvent was evaporated. A red solid was obtained (**95**, 20.9 mg, 0.026 mmol, > 99 %).  $^1\text{H-NMR}$  (300 MHz, 298 K,  $\text{CDCl}_3$ ): 8.63 (s, 1H), 8.13 (m,

1H), 7.78 (m, 1H), 7.69 (m, 1H), 7.07-7.19 (m, 4H), 6.92-7.00 (m, 2H), 6.87 (s, 2H), 6.69 (s, 1H), 4.12 (m, 2H), 4.00 (m, 2H), 3.65 (m, 2H), 3.25 (s, 12H), 3.21 (m, 2H), 2.15 (m, 2H), 1.91 (m, 2H), 1.41 (s, 9H).

## Synthesis of 2,5-dioxopyrrolidin-1-yl 3-(3-(*tert*-butyloxycarbonylamido)propyloxy)-5-(3-TAMRA-amidopropyloxy)benzoate (**96**)



**95** (19.4 mg, 0.0247 mmol, 1 equiv.), *N*-Hydroxysuccinimide (3.42 mg, 0.0298 mmol, 1.2 equiv.) and EDCI (6.18 mg, 0.0322 mmol, 1.3 equiv.) were dissolved in DMF (10 mL) at -15 °C. The mixture was stirred for 15 hours at RT and then poured into of a mixture of Et<sub>2</sub>O and hexane (1:1, 200 mL) cooled to 0 °C. The precipitate was filtered off and dissolved in DCM. Flash column chromatography (acetone, *R<sub>f</sub>* = 0.15) afforded a red solid (**96**, 3.7 mg, 0.0042 mmol, 17 %). <sup>1</sup>H-NMR (300 MHz, 298 K,

CDCl<sub>3</sub>): 8.34 (s, 1H), 8.18 (m, 1H), 6.78 (s, 2H), 6.61 (m, 2H), 6.49 (m, 2H), 6.41 (m, 2H), 4.16 (t, *J* = 6 Hz, 2H), 4.04 (t, *J* = 6 Hz, 2H), 3.72 (m, 2H), 3.29 (m, 2H), 3.00 (s, 12H), 2.88 (s, 4H), 1.96 (m, 2H), 1.42 (s, 9H), HRMS (MALDI): calc. for [M+H]<sup>+</sup> *m/z* = C<sub>47</sub>H<sub>52</sub>N<sub>5</sub>O<sub>12</sub> 878.3612, found *m/z* = 878.3606.

### 8.6.2. Other experiments

#### Preparation of samples for rheology and iSIM

For both rheology and iSIM, samples of typically 10 – 25 % w/w DP were prepared by adding the freeze-dried DP powder to a vial, then weighing in the appropriate amount of solvent (DMF or DMPU). The vial was then stoppered and agitated overnight at room temperature on an orbital shaker (IKA-VIBRAX-VXR, IKA-Werke). If the solution proved too viscous at room temperature or if mixing was otherwise incomplete, the vial was set into an orbital shaker (PL-SP 260, Polymer Laboratories) at 60 °C or 80 °C until dissolved. This step was not performed for DP of *g* = 5 after “hot solvent” mediated main-chain scission had been discovered.

For the preparation of samples for iSIM, a diluted solution of the labelled DP of the same *g* as the above, highly concentrated DP matrix was prepared (typically 10 – 100 mg L<sup>-1</sup> in the same solvent). An appropriate amount of the solution of the labelled dye was added such that the ratio of labelled to unlabeled DPs was *ca.* 1:10<sup>6</sup> – 1:10<sup>5</sup>. The sample was then thoroughly shaken for at least 4 h at the maximum temperature previously applied under an atmosphere of argon.

#### iSIM of DP solutions

Microscopy was performed on the Rheo-iSIM setup in the group of Prof. Dr. Vermant (D-MATL, ETH Zurich), which consists of an iSIM constructed as described elsewhere,<sup>340</sup> additionally coupled to a MCR502 rheometer (Anton Paar) equipped with an additional counter-rotating motor. This permitted the observation of DP solutions not only in steady state, but also in shear.



## A. Appendix

### A.1. Example of a $g_{\max}$ calculation

Using  $\text{PG}g_n^{\text{NHBoc}}$  as an example, the process of estimating  $g_{\max}$  will be detailed in the following.

As a first step, the dendron in question was reduced to a “linear path” thought to adequately represent the dendritic structure. In the example of  $\text{PG}g_n^{\text{NHBoc}}$ , based on the corresponding macromonomer  $\text{MG}g_n^{\text{NHBoc}}$  the second substituent *meta* to the root of the dendritic repeat unit was discarded, *i.e.* only one of two branches at every branching point is contained in the linear path, as shown in Figure A-1 for  $g = 2$ .

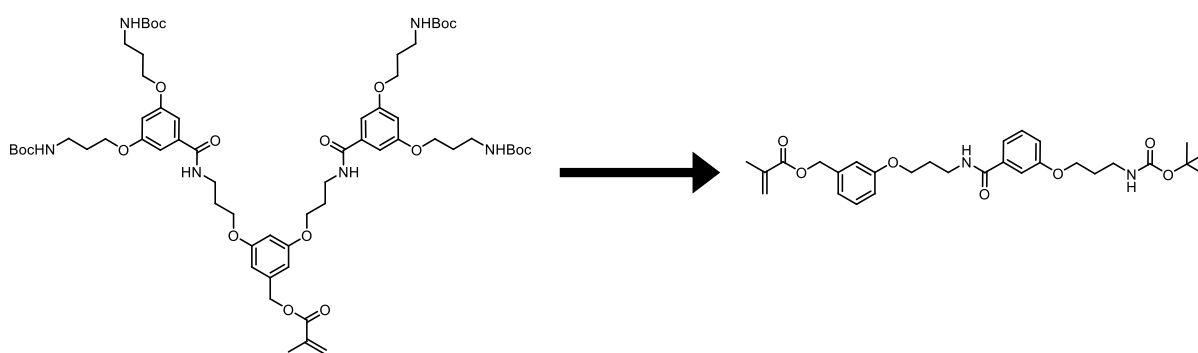


Figure A-1: Structure of  $\text{MG}_2^{\text{NHBoc}}$  and the corresponding “linear path” used for estimating  $R_{\max}$ .

The same procedure was performed for all macromonomers up to  $g = 5$  and each was pre-arranged into a suitable all-trans zig-zag conformation using Chem3D. For reasons of convenience, structure optimization was thereafter performed using Avogadro,<sup>391</sup> employing MMFF94(s) force field parameters,<sup>392</sup> under the constraint that all bonds along the backbone be in an all-trans zig-zag conformation (*i.e.*, setting linear path dihedral angles to 180 °). After energy minimization, the distance between the center point of the dendritic structure (see Figure A-2) and the outermost atom was determined. The resulting distances for  $g = 1$  to  $g = 5$  (Figure A-3a) were fitted with a linear function (Figure A-3b), such that  $R_{\max}$  can be represented by Eq. 1-7. For  $\text{PG}g_n^{\text{NHBoc}}$ :  $(R_0 + R_p) = 0.764$  nm and  $R_1 = 1.086$  nm were obtained. This fit function was used in the calculation of  $R_{\max}$  both for  $g = 1 - 5$  as well as for extrapolation to higher  $g$ .

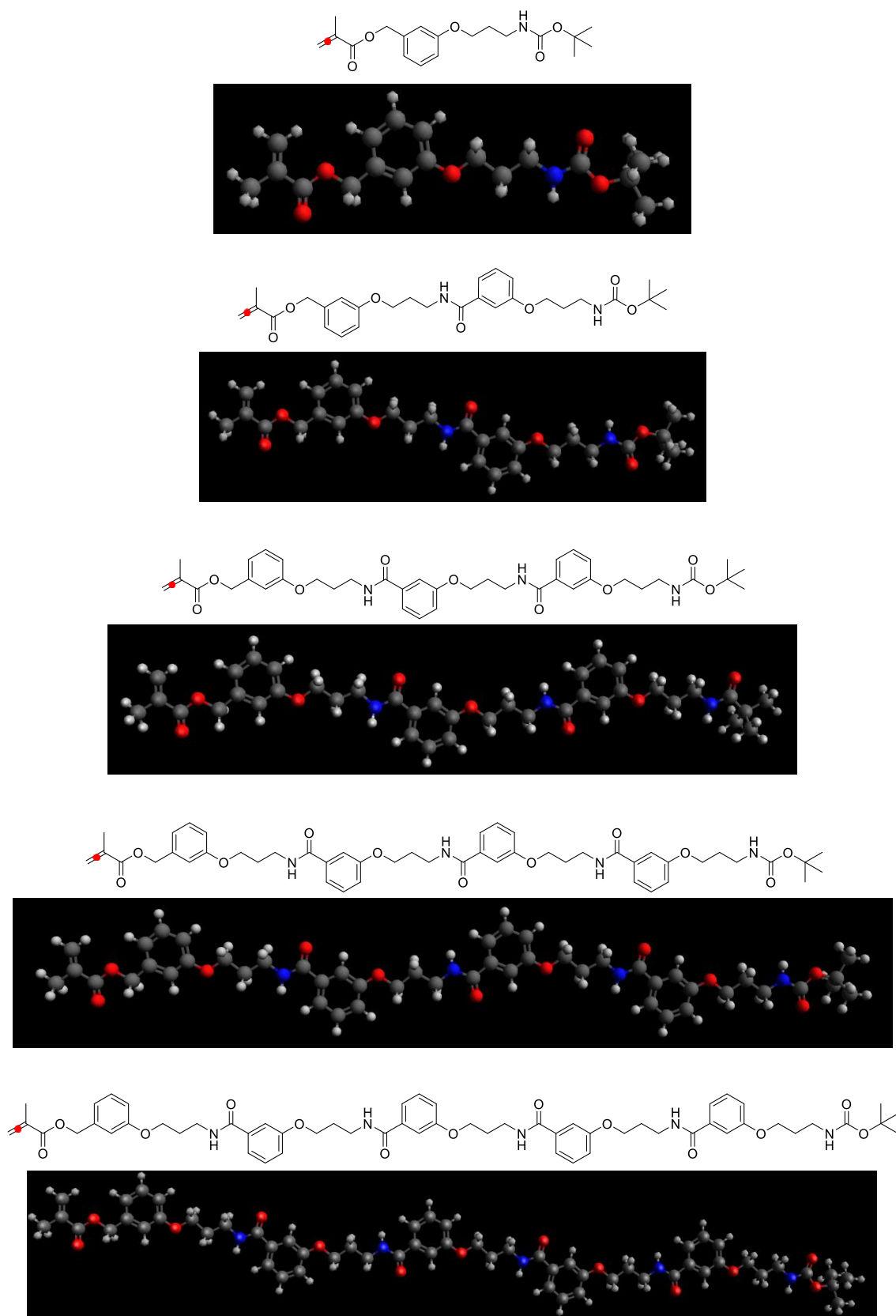


Figure A-2: "Linear paths" corresponding to macromonomers of  $g = 1 - 5$  and the corresponding optimized structures. The red dot marks the point relative to which  $R_{max}$  was measured.

a)

$g$	$R_{\max}$ (nm), structure opt.	$R_{\max}$ (nm), fit
1	1.8717	1.849
2	2.9375	2.935
3	3.963	4.02
4	5.1226	5.106
5	6.209	6.191

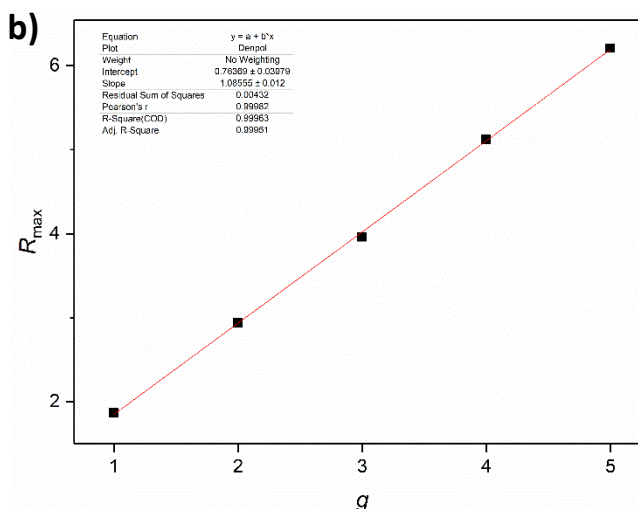


Figure A-3: a) Table listing the  $R_{\max}$  values measured from Figure A-2 and the corresponding fit values; b) plot of  $R_{\max}$  and linear interpolation (adjusted  $R^2 = 0.99951$ ).

The calculation of  $R_{\text{packing}}$  (Table A-1) follows straightforwardly from the chemical structure of the dendron, following Eq. 1-7 in the main text; rather than explicitly calculating the relevant molar masses, it is often more straightforward to determine the relevant number of atoms in a molecular fragment. Using the obtained molar masses for entire dendrimers, Eq. 1-9 is used, assuming values of  $0.9 \text{ g cm}^{-3}$ ,  $1.1 \text{ g cm}^{-3}$ ,  $1.3 \text{ g cm}^{-3}$ , and  $1.5 \text{ g cm}^{-3}$  for  $\rho_{\text{packing}}$ . The same values are used in the case of DPs, however Eq. 1-10 which is used in this instance. This furthermore requires a value for the repeat unit length, which is set to  $\delta = 0.252 \text{ nm}$ .

Table A-1: Molar mass calculations and  $R_{\text{packing}}$  for  $\text{PGg}_n^{\text{NHBoc}}$  up to  $g = 15$ .

$g$	# peripheral groups	C	H	N	O	Molar Mass $\text{g mol}^{-1}$	$R_{\text{packing}}$				
							Density ( $\text{g cm}^{-3}$ )	0.9	1.1	1.3	1.5
1	2	27	42	2	8	522.6309		1.103623	0.998264474	0.955765	0.854863
2	4	63	94	6	18	1223.45		1.688559	1.527359268	1.462335	1.307952
3	8	135	198	14	38	2625.089		2.473404	2.237278498	2.142031	1.915891
4	16	279	406	30	78	5428.365		3.556786	3.217233683	3.080267	2.755074
5	32	567	822	62	158	11034.92		5.071165	4.587041264	4.391758	3.928107
6	64	1143	1654	126	318	22248.03		7.200604	6.51319104	6.235906	5.577564
7	128	2295	3318	254	638	44674.24		10.0356	9.229467886	8.836543	7.903644
8	256	4599	6646	510	1278	89526.6		14.4444	13.06544746	12.50921	11.18858
9	512	9207	13302	1022	2558	179231.5		20.43762	18.48652474	17.6995	15.83091
10	1024	18423	26614	2046	5118	358641.2		28.91035	26.15039113	25.03709	22.39386
11	2048	36855	53238	4094	10238	717460.7		40.89048	36.98683111	35.41219	31.67363
12	4096	73719	106486	8190	20478	1435100		57.83146	52.31052584	50.08352	44.79606
13	8192	147447	212982	16382	40958	2870377		81.78858	73.98055142	70.83099	63.35316
14	16384	294903	425974	32766	81918	5740933		115.6683	104.6259229	100.1717	89.59629
15	32768	589815	851958	65534	163838	11482044		163.581	147.9645473	141.6653	126.7093
16	65536	1179639	1703926	131070	327678	22964265		231.3393	209.2542813	200.3457	179.1947

## A.2. How “soft” a parameter is $g_{\max}$ ?

The two variables entering  $g_{\max}$  calculations which are affected by some uncertainty are the density  $\rho_{\text{packing}}$  and the maximum achievable dimension of the system  $R_{\max}$ .

As the results in chapter 5 demonstrate, it is not trivial to achieve a good estimate of density for single molecules: Their packed, isolated states may be difficult to investigate and additionally there may be some variability in density dependent on  $g$ . For DPs, a density of *ca.*  $1.3 \text{ g cm}^{-3}$  appears reasonable as judged by the results obtained in chapter 5, however for other systems what constitutes a reasonable estimate is difficult to judge: For the PAMAM dendrimers – doubtless the most well investigated dendrimer system – estimates of density from MD simulations in vacuum exist for many generations, however experimental values are spread quite widely, reportedly ranging from  $0.4 \text{ g cm}^{-3}$  to  $1.23 \text{ g cm}^{-3}$ .<sup>147,162,393</sup> For other types of dendrimers, density values are difficult to obtain, relying mostly on estimates *e.g.* from simulations. Due to this comparative lack of data, a fairly wide range of densities ( $0.9 \text{ g cm}^{-3}$  to  $1.5 \text{ g cm}^{-3}$ ; compare this to the average density of proteins, which is in the much narrower range of  $1.4 \text{ g cm}^{-3}$  to  $1.55 \text{ g cm}^{-3}$ )<sup>394</sup> was chosen for the estimate of  $g_{\max}$  as presented in sections 1.6 and A.1. Generally, this results in a variation of no more than 1 integer (see Figure A-4, also compare Figure 1-14 and Figure 1-20).

$R_{\max}$  is likewise subject to some uncertainty, and in the simplistic way it is currently being determined (molecular mechanics simulation of a linear dendron fragment thought representative, see Appendix A.1) it is certainly a crude estimate. An important question, however, arises in the near-densely packed state: When dendrons are crowded, it appears possible that such a hypothetical chain could be stretched by the steric pressure exerted onto it. Certainly this scenario is not realistic for the entire dendritic structure in the case of flexible chains (it would correspond to dense packing according to de Gennes,<sup>138</sup> rather than the experimentally verified backfolding case invoked by Muthukumar<sup>139</sup>), but nevertheless the flexibility of a chain needs to be considered.

To estimate this flexibility, a very simplistic model was considered using the example of  $\text{PG}g_n^{\text{NHBoc}}$ : The linear dendritic segment (see Figure A-1) was approximated by a linear  $\text{C}_{(9g+8)}$ -chain (same number of atoms per  $g$ ) and its stiffness toward stretching was estimated using the parametrization of the MMFF94(s) force field.<sup>392</sup> Stretching of this simple C-C-C... chain can originate in the stretching of individual bonds distances  $l$  or in the opening of C-C-C angles  $\vartheta$  (Figure A-4a). It was assumed that the whole chain can only be stretched until the force exerted surpasses the typical bond dissociation energy of a C-C bond ( $84 \text{ kcal mol}^{-1}$ ), resulting in contour plots dependent on  $l$  and  $\vartheta$  such as those depicted in Figure A-4b. The “extensibility” of this model chain is then given by calculating the ratio between the equilibrium C-C “length”  $d_0$  and of the length  $d$  given by

$$d = \sqrt{l^2 \sin(\vartheta/2)^2}$$

Eq. A-1

Where  $l$  and  $\vartheta$  are solutions of  $U(\{l, \vartheta\}) = U_{\text{stretch}}(l) + U_{\text{bending}}(\vartheta) = 84 \text{ kcal mol}^{-1}$ . The solution resulting in a maximum value of  $d$  was chosen as a reference point and is reported as a percentage of the equilibrium distance  $d_0$  in Table A-2. As the amount of force required to result in breaking a single bond is distributed over an increasing number of flexible elements with increasing  $g$ , the extensibility

relative to the overall chain length naturally decreases with  $g$ , although in absolute terms it increases (Table A-2).

The calculated extensibilities for each  $g$  were applied to the prior estimates of  $g_{\max}$  in the “relaxed” state, and the resulting “stretched” values for  $R_{\max}$  were plotted in Figure A-4c along with the aforementioned range of  $\rho_{\text{packing}}$ . It is apparent that the estimated variability in  $R_{\max}$  influences the location of  $g_{\max}$  far less than that of  $\rho_{\text{packing}}$ . Even when both effects are combined, the resulting value of  $g_{\max}$  varies by no more than 1 integer. This thesis therefore unless called for only takes into account the variability in  $\rho_{\text{packing}}$ , particularly in the comparison to other dendritic systems for which densities are unknown or highly uncertain.

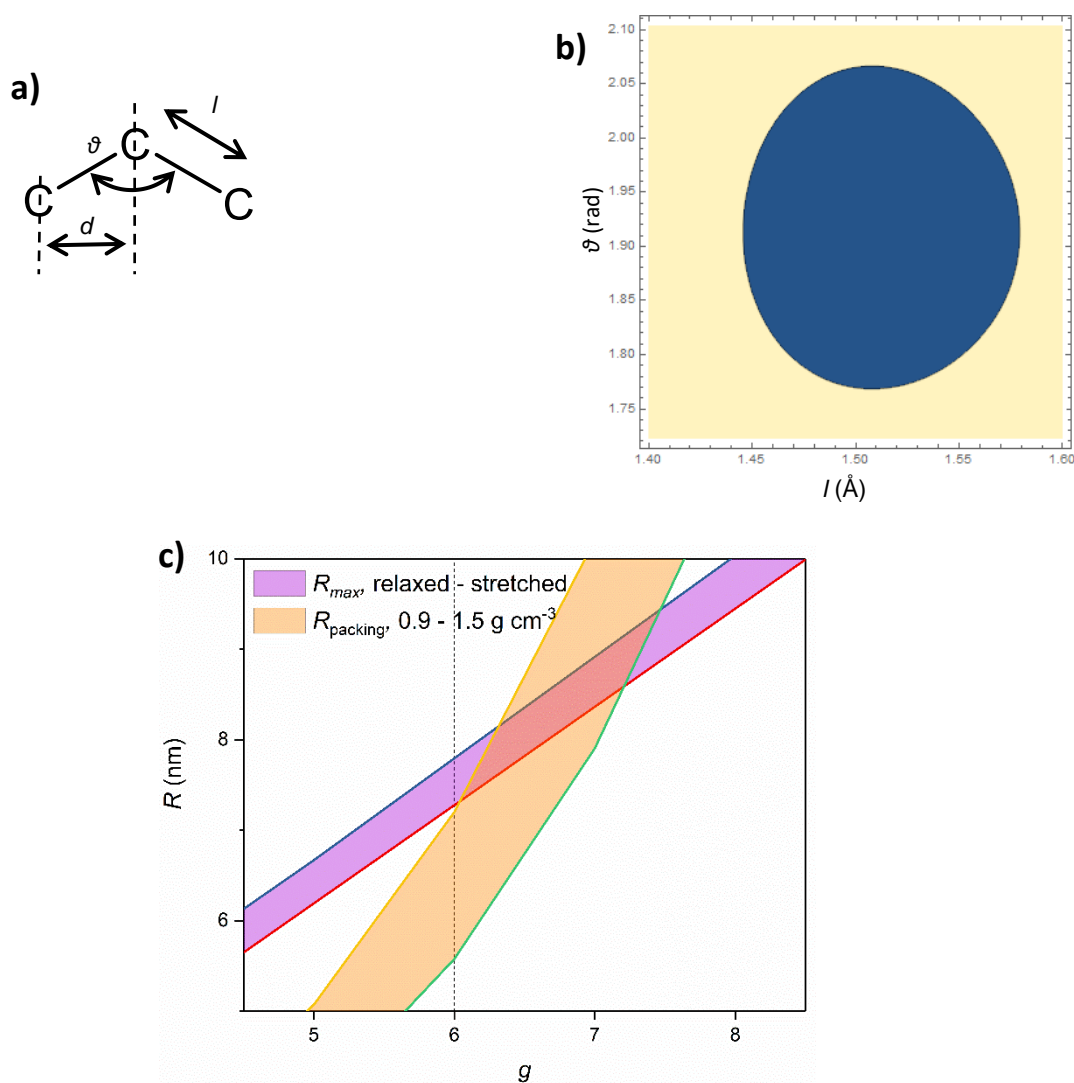


Figure A-4: a) Representation of the model for “extensibility” of a C-C-... Chain; b) Contour plot of  $U\{l, \vartheta\}$ , blue color marking  $U \leq 84$  kcal mol<sup>-1</sup>; c)  $g_{\max}$  plot for  $\text{PGg}_n^{\text{NHBOC}}$ , focusing on the crucial crossover regime and indicating the variability in  $R_{\max}$  resulting from extensibility as well as in  $R_{\text{packing}}$ , resulting from the uncertainty regarding  $\rho_{\text{packing}}$ .

Table A-2: Extensibilities of model C-C-C... chains representative of  $PGg_n^{NHBOC}$  linear segments.

<b><i>g</i></b>	<b># C atoms</b>	<b>Extensibility (%)</b>
<b>1</b>	17	13.8
<b>2</b>	26	12.5
<b>3</b>	35	11.1
<b>4</b>	44	9.5
<b>5</b>	53	7.7
<b>6</b>	62	7.1
<b>7</b>	71	6.6
<b>8</b>	80	6.2
<b>9</b>	89	5.8
<b>10</b>	98	5.5

### A.3. Supplementary GPC curves

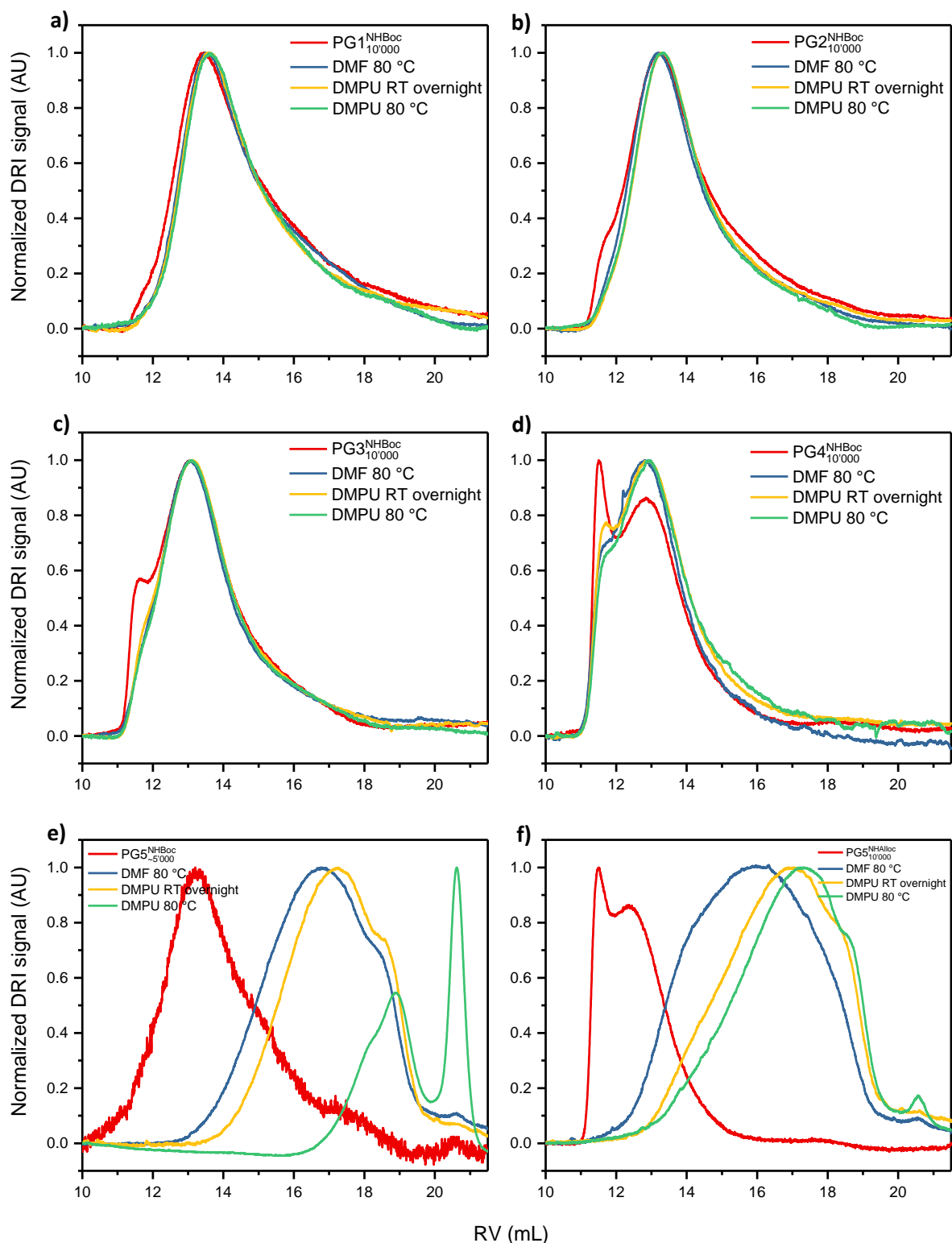


Figure A-5: GPC elution curves for solvent treatment (heating to 80 °C in DMPU & DMF, RT treatment in DMPU) of DPs with high  $P_n$ : a) PG1<sup>NHBoc</sup><sub>10'000</sub>, b) PG2<sup>NHBoc</sup><sub>10'000</sub>, c) PG3<sup>NHBoc</sup><sub>10'000</sub>, d) PG4<sup>NHBoc</sup><sub>10'000</sub>, e), PG5<sup>NHBoc</sup><sub>5'000</sub> f) PG5<sup>NHAlloc</sup><sub>10'000</sub>.

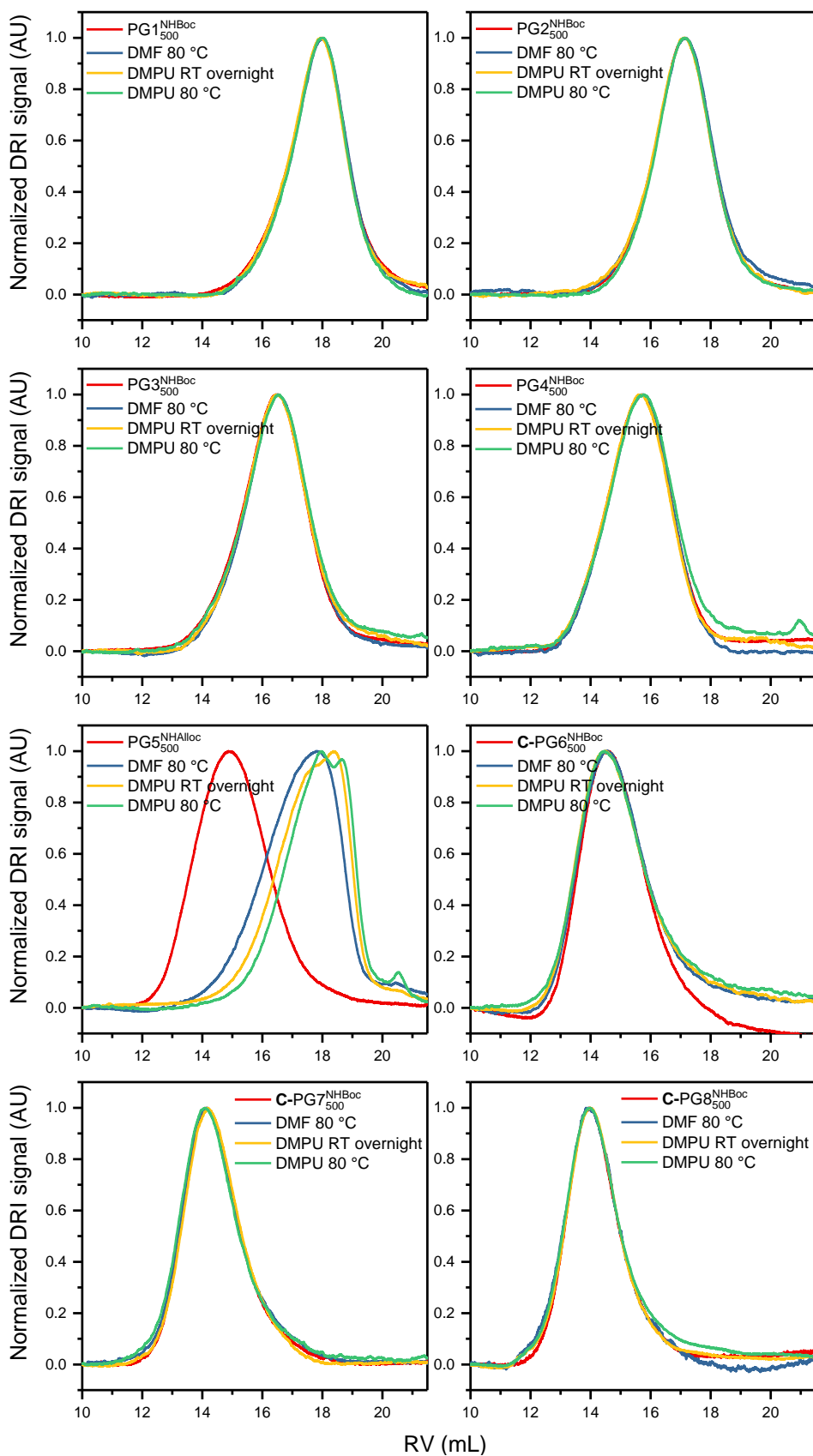


Figure A-6: GPC elution curves for solvent treatment (heating to 80 °C in DMPU & DMF, RT treatment in DMPU) of the full homologous series of DPs accessed using route C: a)  $PG1_{500}^{NHBoc}$ , b)  $PG2_{500}^{NHBoc}$ , c)  $PG3_{500}^{NHBoc}$ , d)  $PG4_{500}^{NHBoc}$ , e)  $PG5_{500}^{NHAlloc}$ , f)  $C-PG6_{500}^{NHBoc}$ , g)  $C-PG7_{500}^{NHBoc}$ , h)  $C-PG8_{500}^{NHBoc}$ .



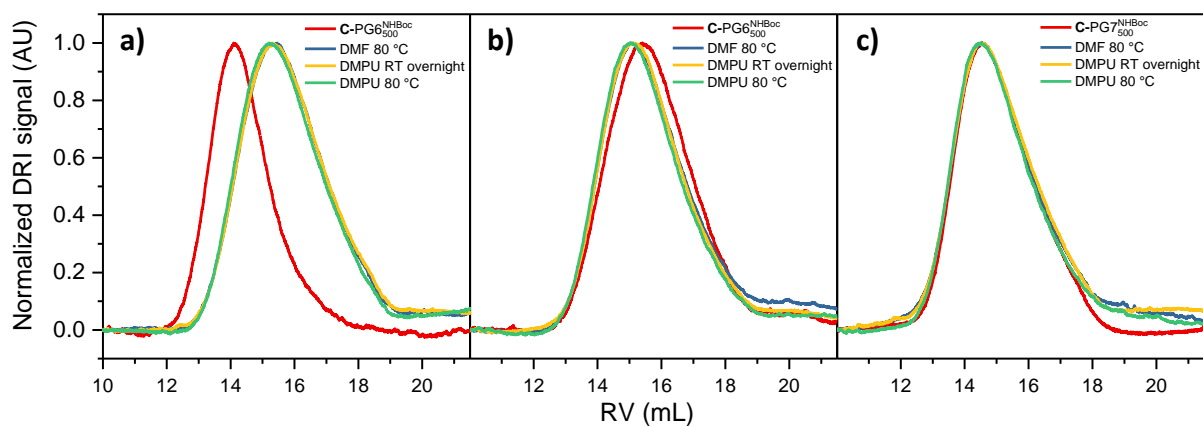


Figure A-7: GPC elution curves for solvent treatment (heating to 80 °C in DMPU & DMF, RT treatment in DMPU) of additional DPs accessed by route C; a), b):  $C\text{-PG6}^{\text{NHBoc}}$ , c)  $C\text{-PG7}^{\text{NHBoc}}$ .

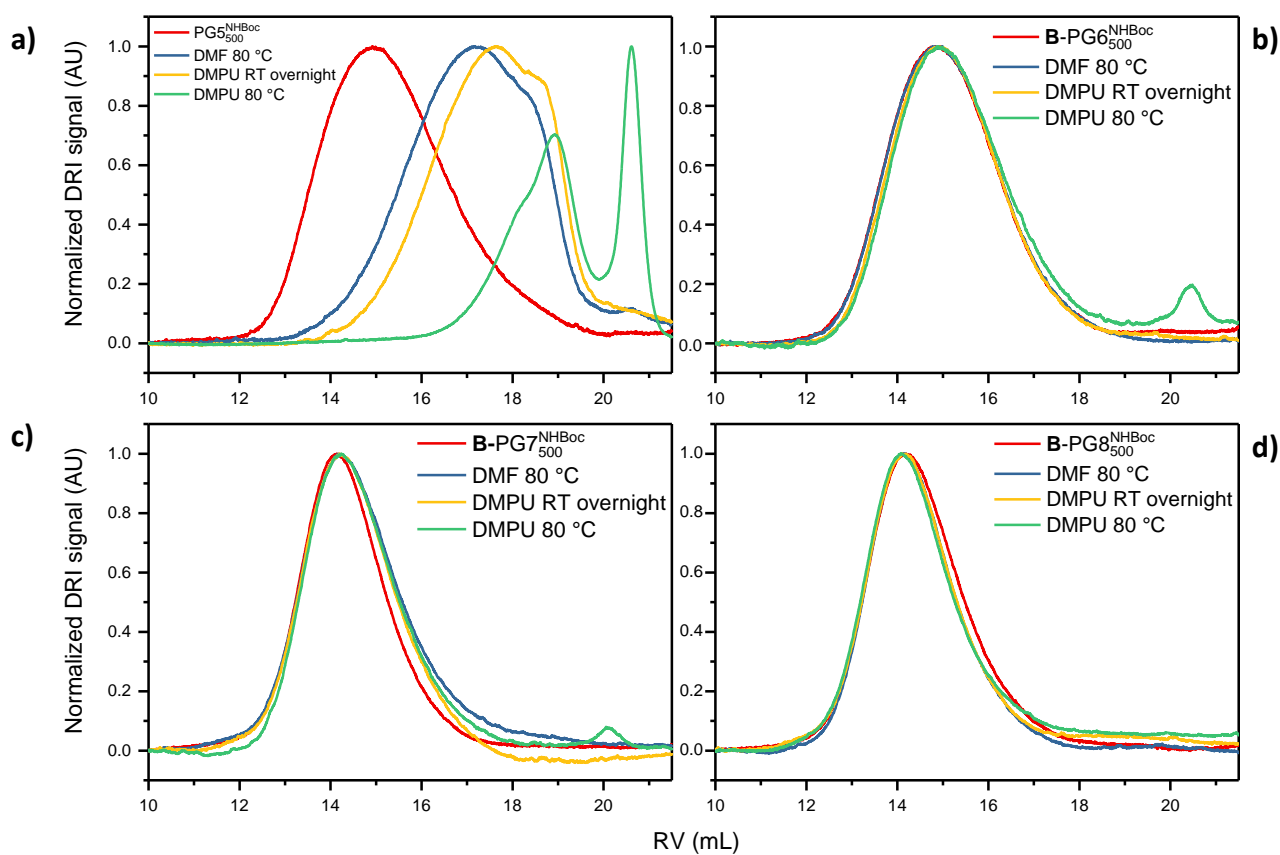


Figure A-8: GPC elution curves for solvent treatment (heating to 80 °C in DMPU & DMF, RT treatment in DMPU) of high g DPs accessed by route B: a)  $\text{PG5}^{\text{NHBoc}}$ , b)  $\text{B-PG6}^{\text{NHBoc}}$ , c)  $\text{B-PG7}^{\text{NHBoc}}$ , d)  $\text{B-PG8}^{\text{NHBoc}}$ .

#### A.4. Representations of DP trajectories from cryo-TEM

The coloration marking the extension in the 3<sup>rd</sup> dimension in the following projections is arbitrarily scaled. Scaling in the image plane has not been altered from the original trajectory data, but coordinates have been shifted so as to fit the filaments onto the grid pattern shown below. The position of one filament on the grid does not change within one set of projections. The following images (Figure A-9 – Figure A-14) only serve to provide a rough overview.

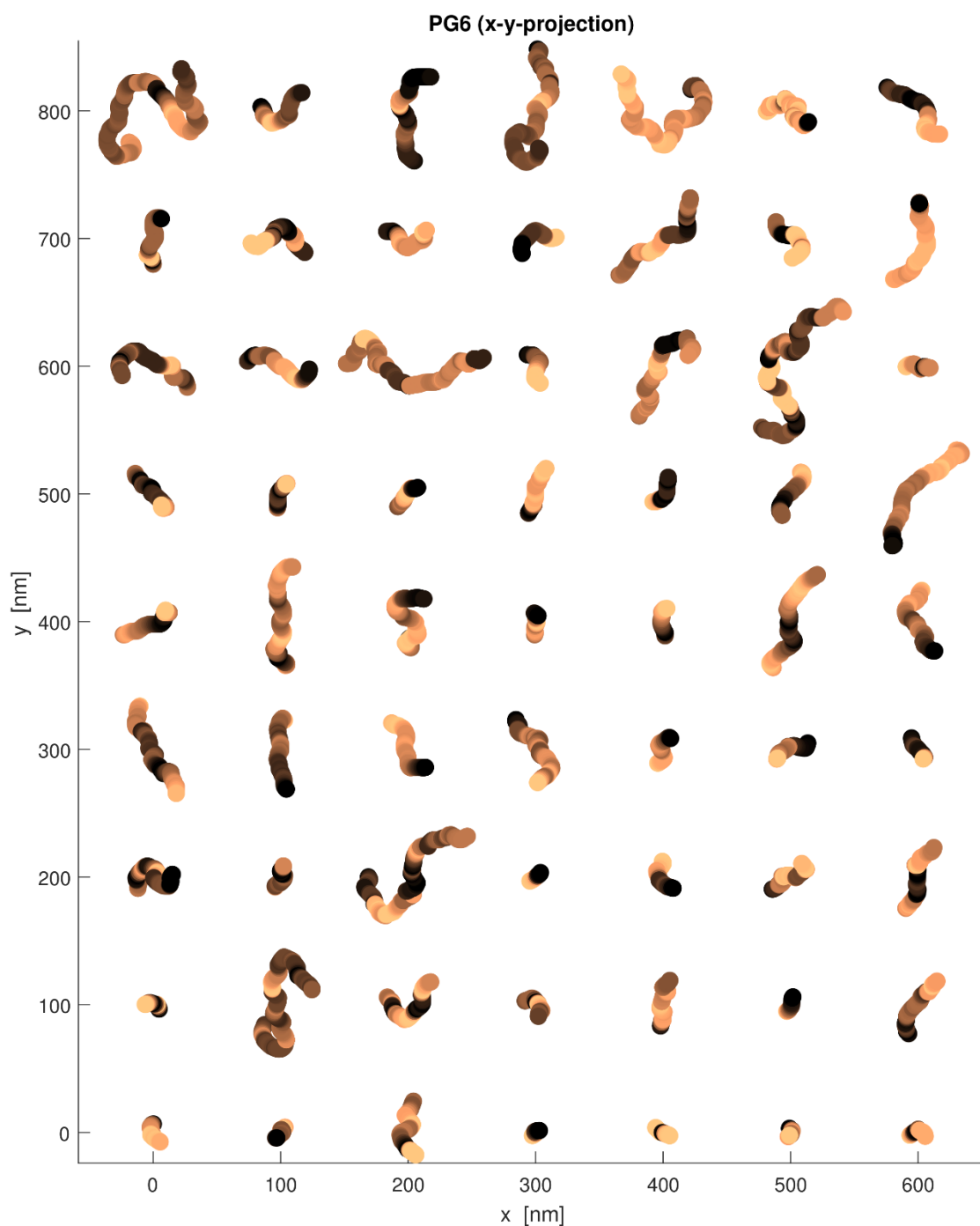


Figure A-9: XY projections of B-PG6<sub>n</sub><sup>NHBOc</sup> filaments obtained from cryo-TEM stereography.

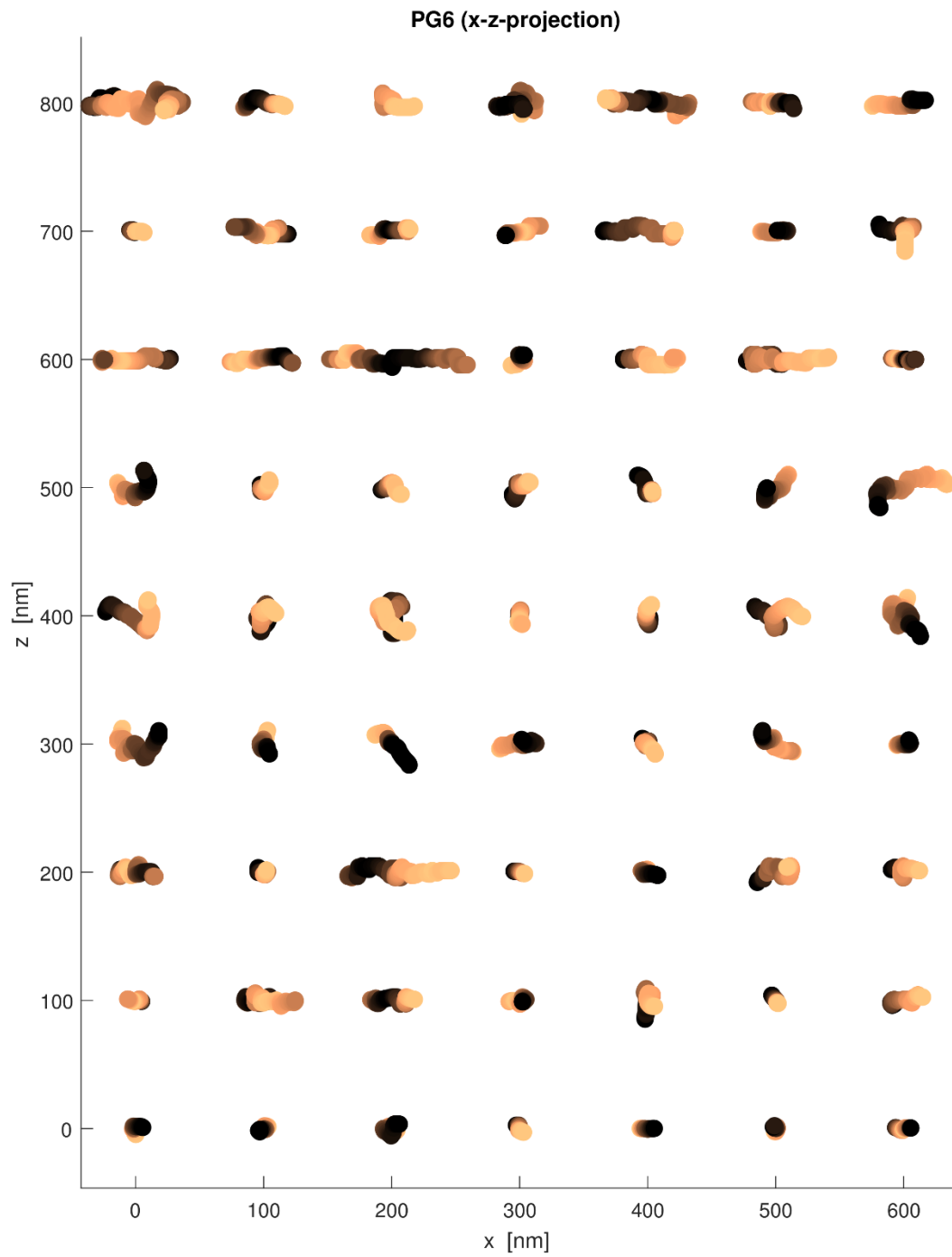


Figure A-10: XZ projections of  $B\text{-PG6}_n^{\text{NHBoc}}$  filaments obtained from cryo-TEM stereography.

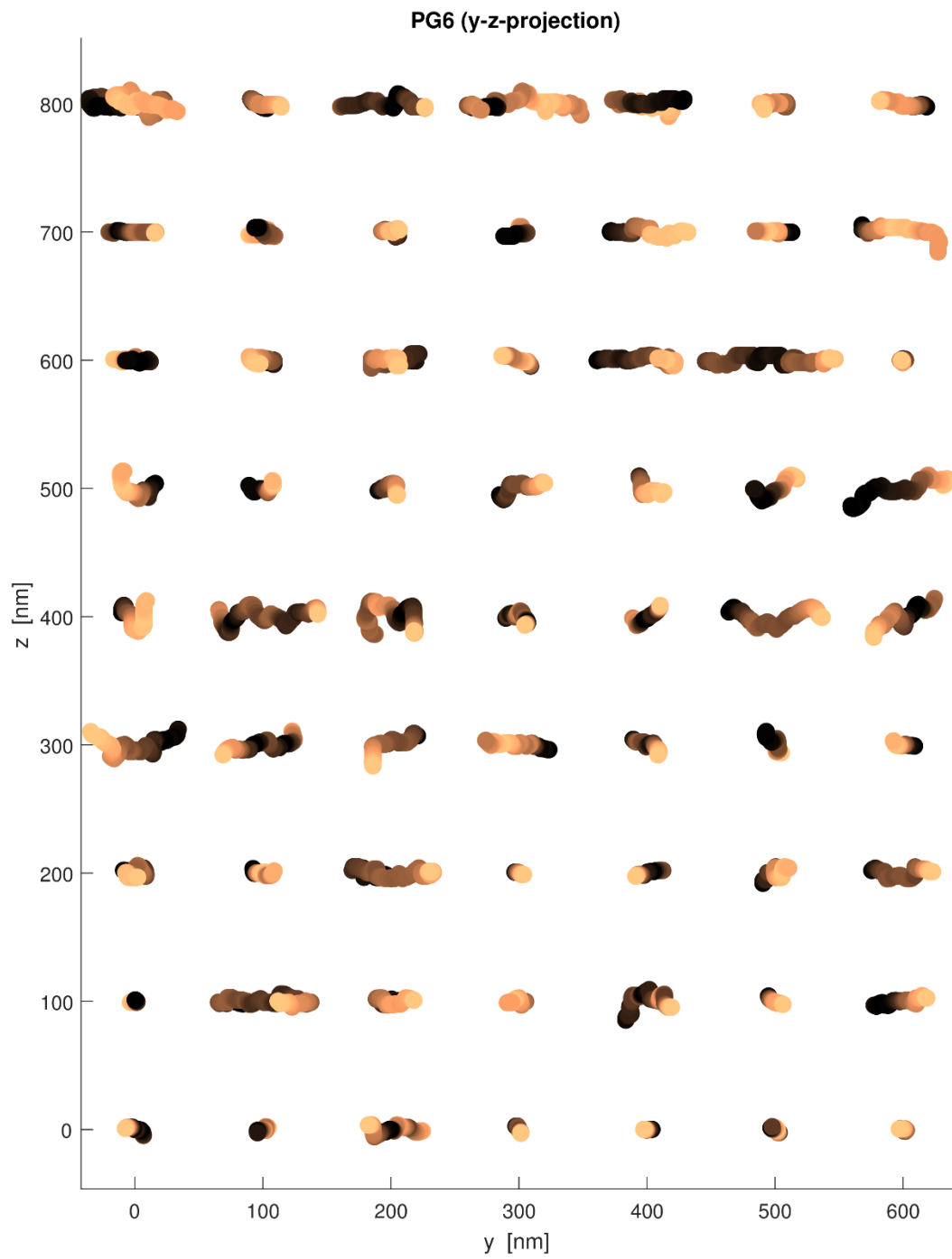


Figure A-11: YZ projections of  $B\text{-PG6}_n^{\text{NHBoc}}$  filaments obtained from cryo-TEM stereography.

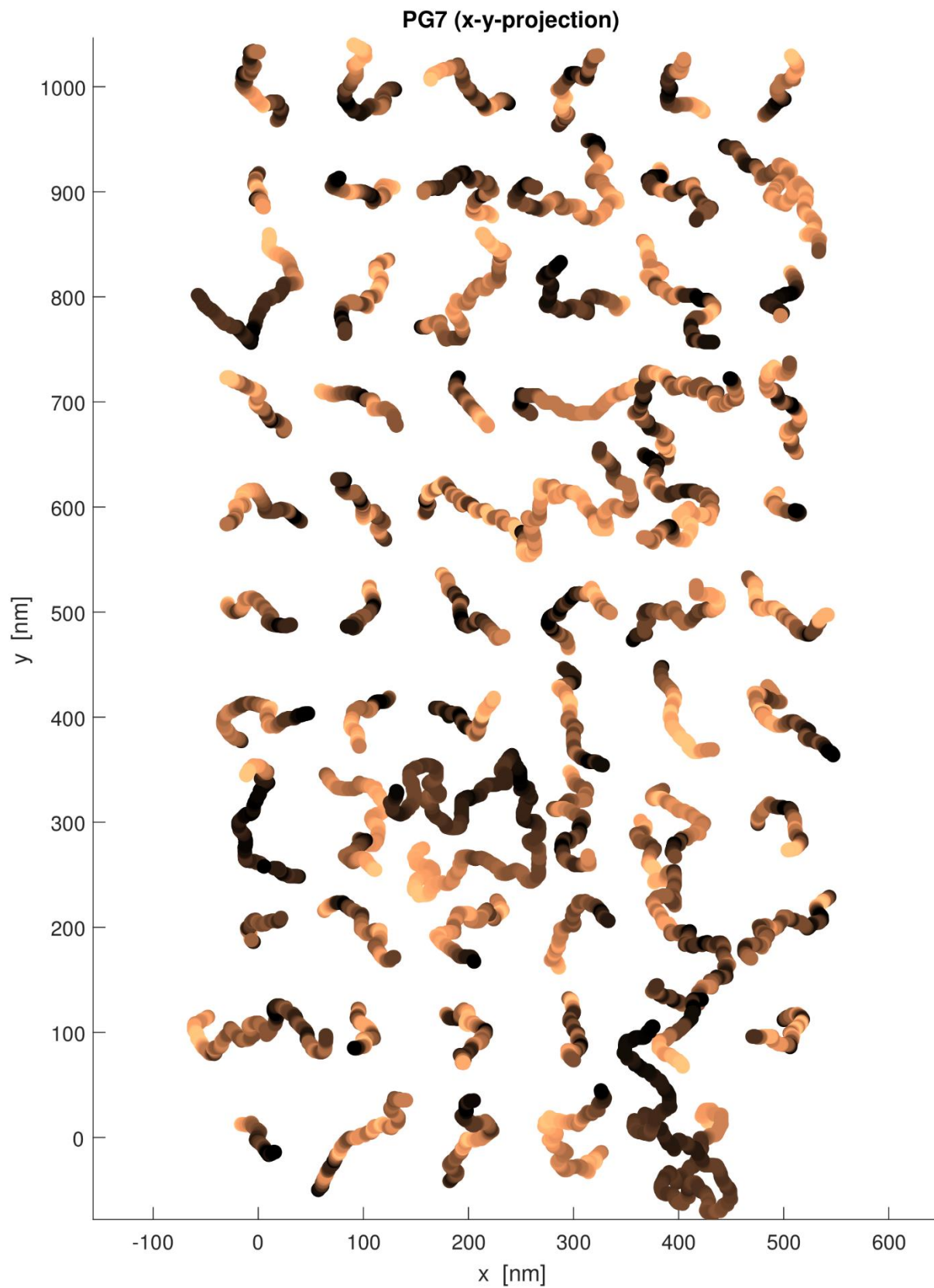


Figure A-12: XY projections of C-PG7<sub>n</sub><sup>NHBoc</sup> filaments obtained from cryo-TEM tomography.

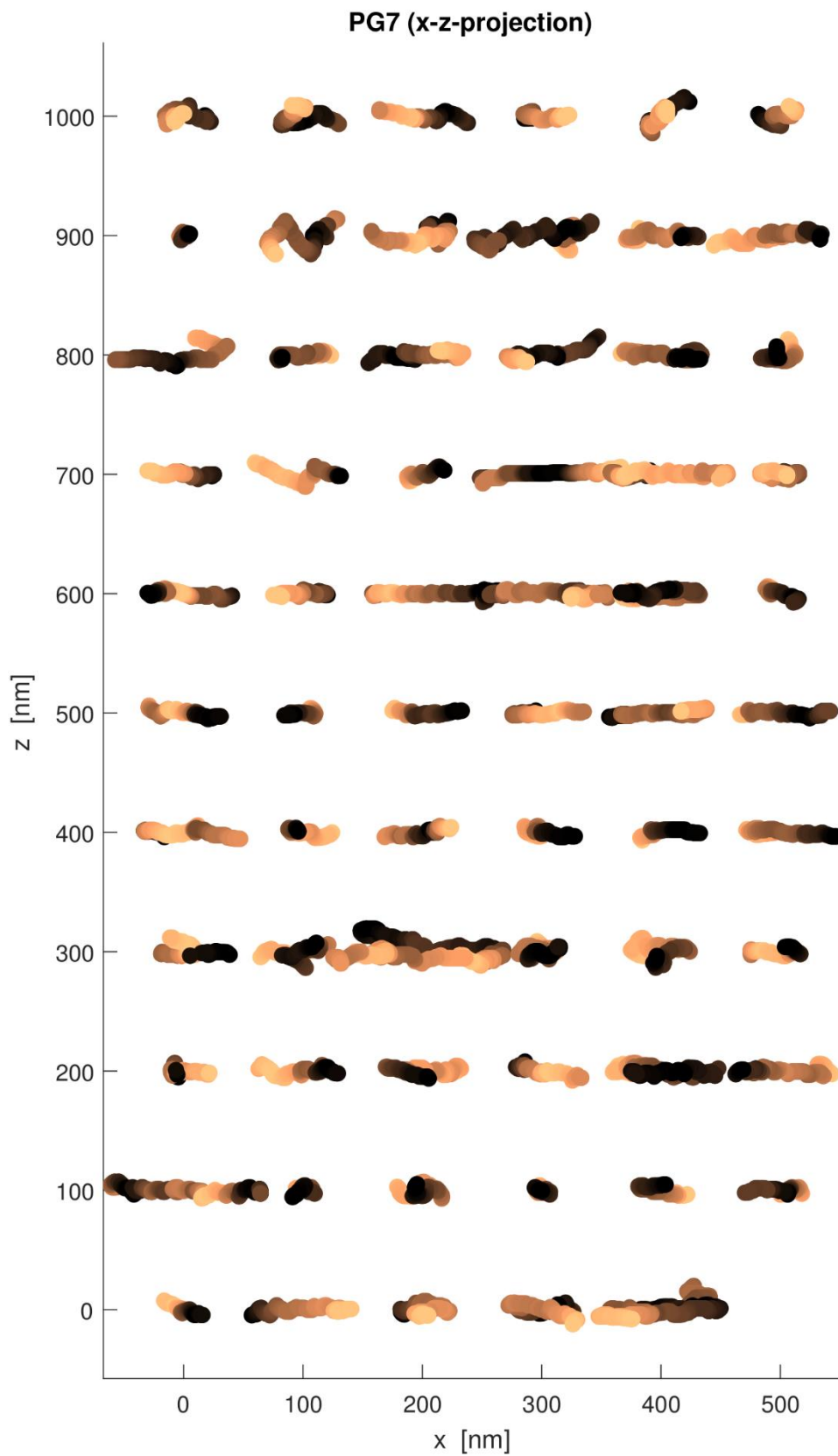


Figure A-13: XZ projections of C-PG7<sub>n</sub><sup>NHBoc</sup> filaments obtained from cryo-TEM tomography.

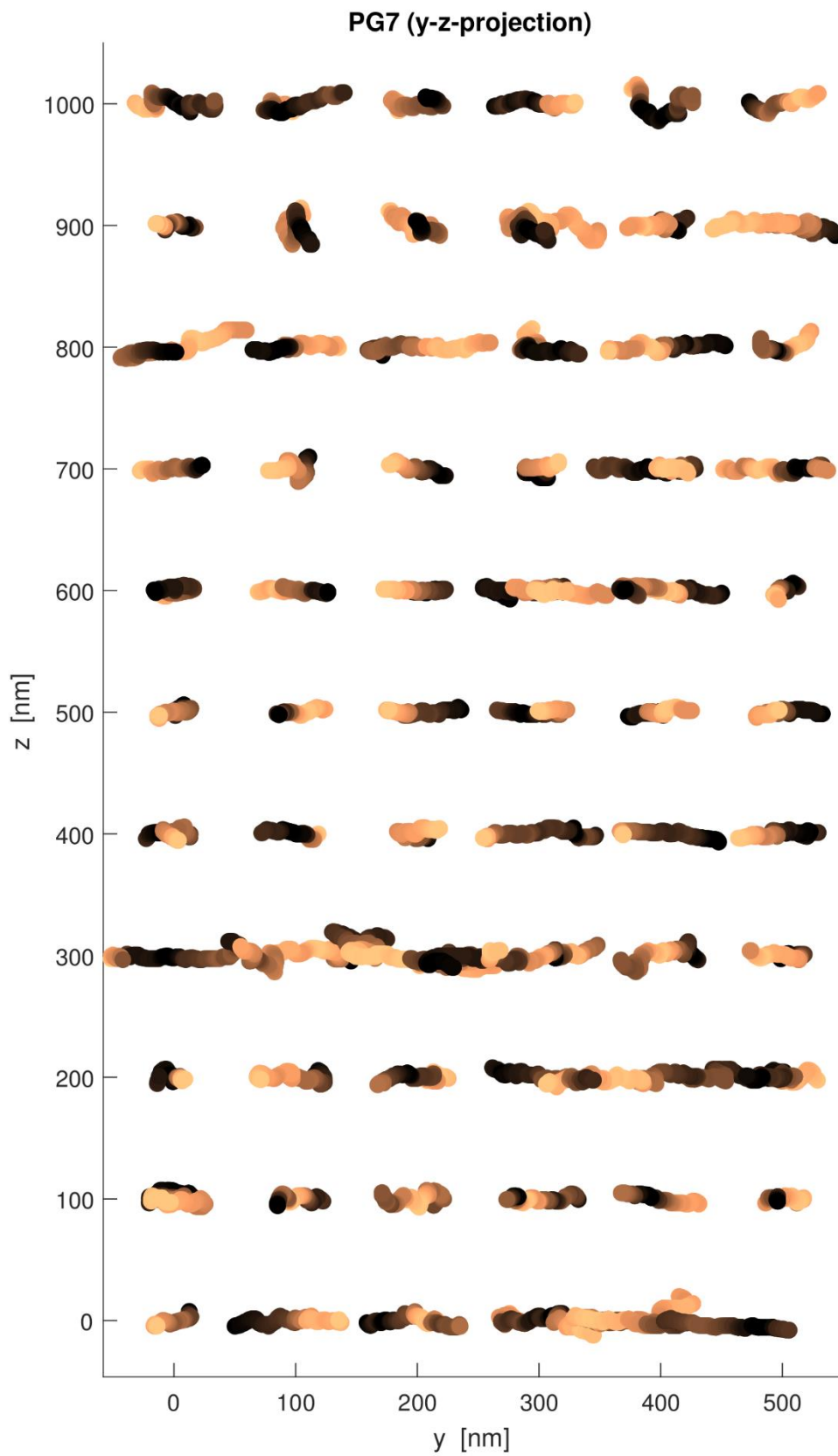


Figure A-14: YZ projections of C-PG7<sub>n</sub><sup>NH<sub>2</sub>Boc</sup> filaments obtained from cryo-TEM tomography.

## A.5. MALDI-TOF mass spectra of DP scission products

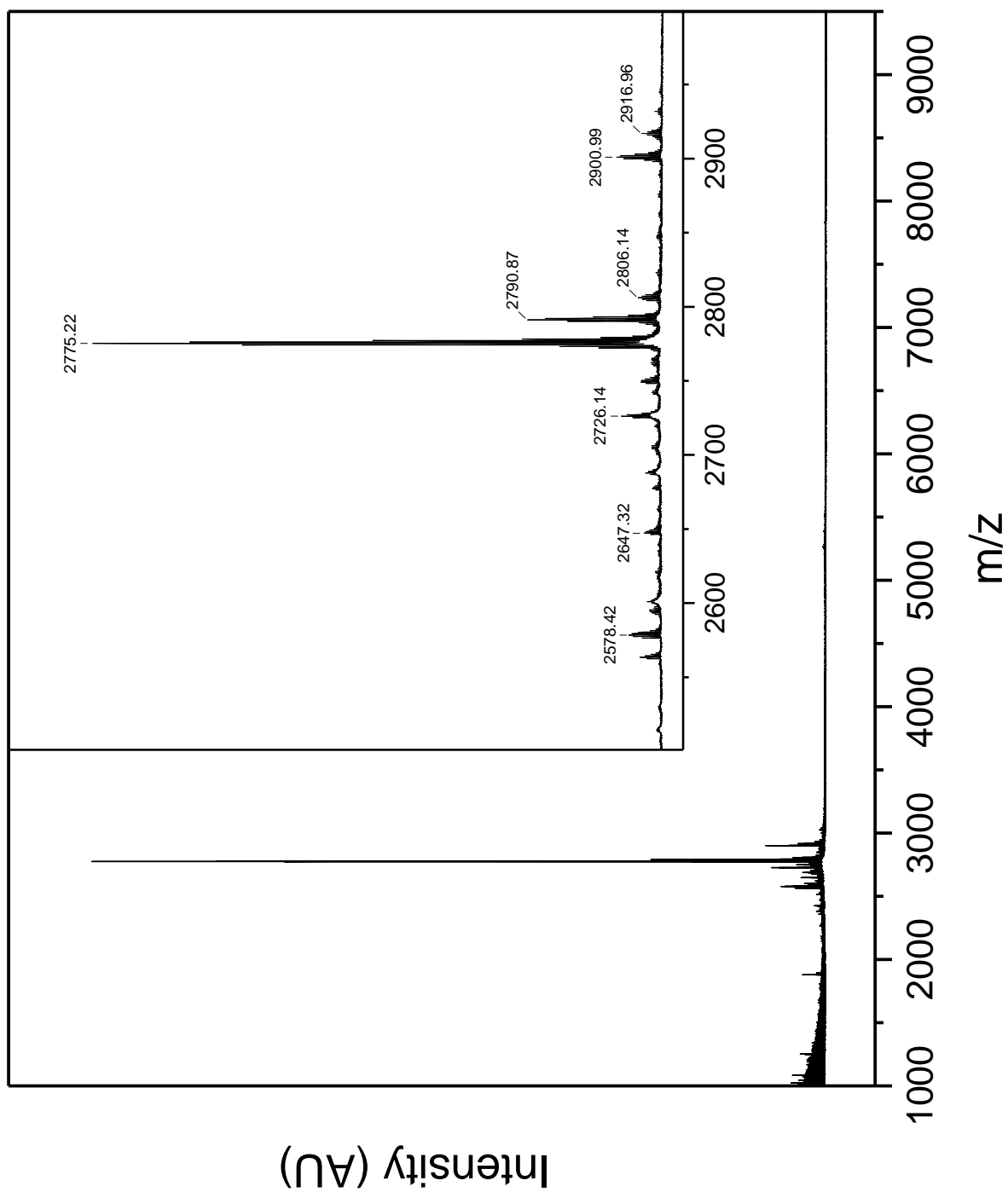


Figure A-15: MALDI-TOF mass spectrum of the products of heat treatment (DMPU, 2 h at 120 °C) of  $\text{PG3}_{500}^{\text{NH}^{\text{Boc}}}$  (**24**).



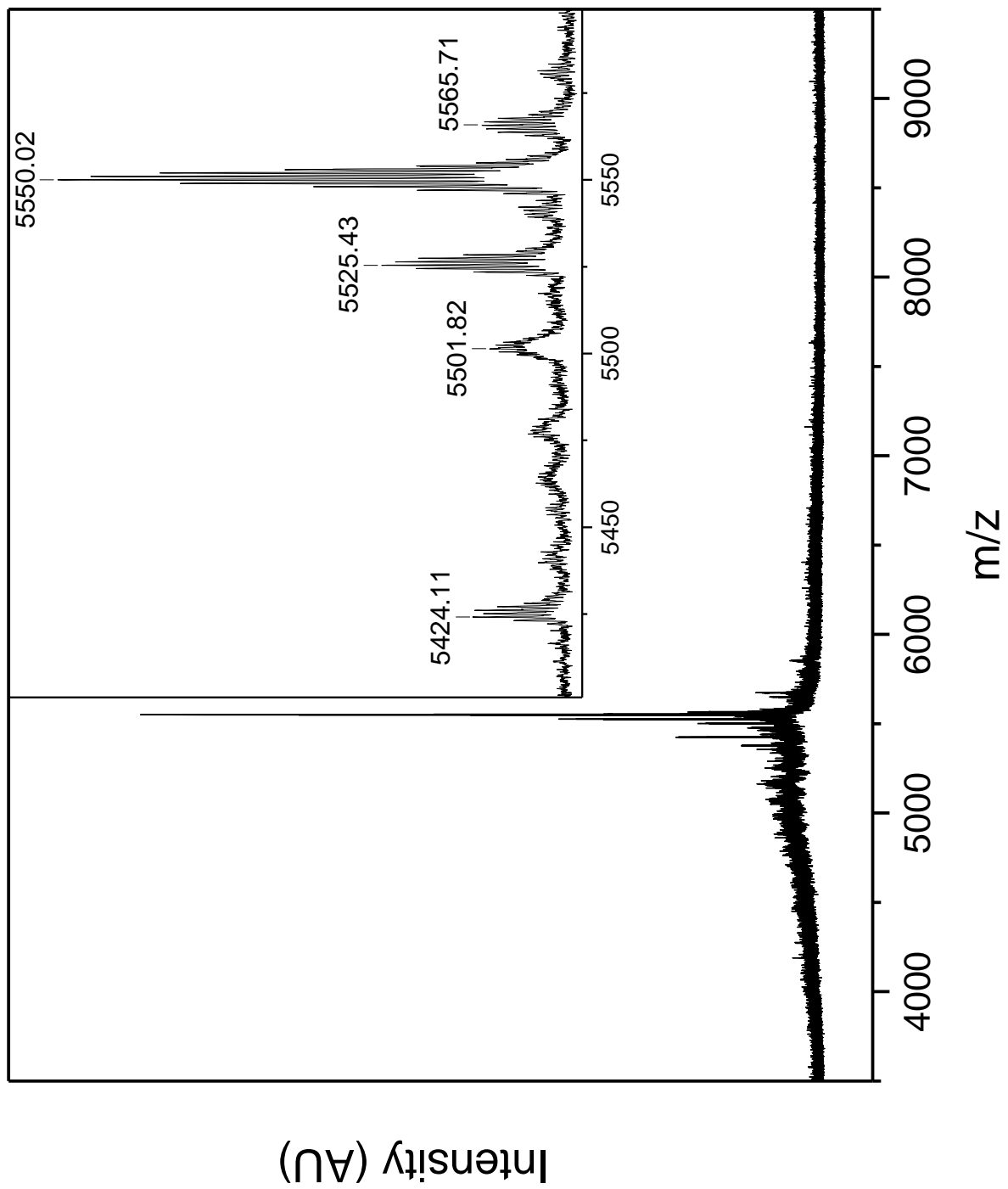


Figure A-16: MALDI-TOF mass spectrum of the products of heat treatment (DMPU, 2 h at 120 °C) of  $PG_{500}^{NHBOC}$  (**25**).

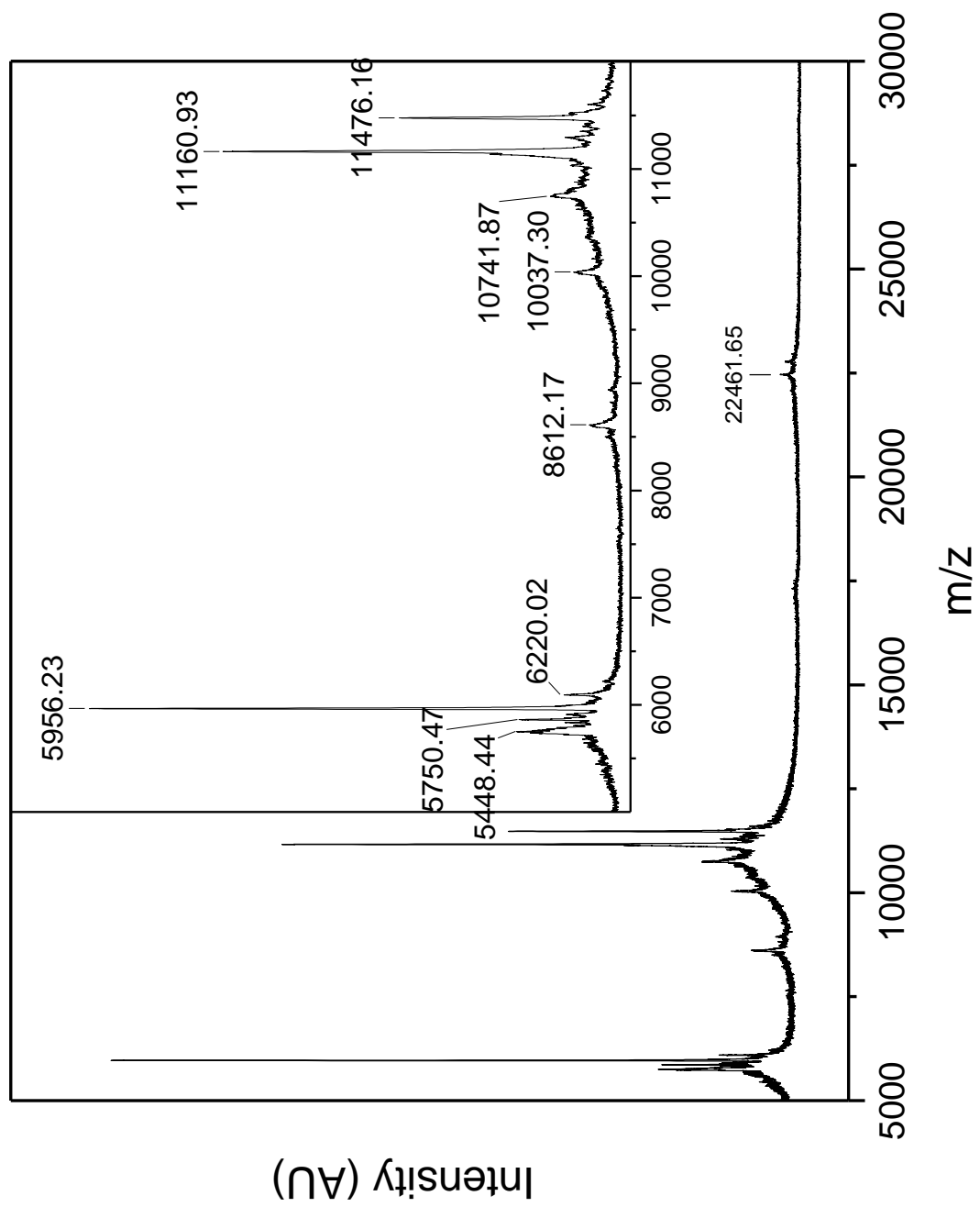


Figure A-17: MALDI-TOF mass spectrum of the products of heat treatment (DMPU, 2 h at 120 °C) of  $PG_{500}^{NHBOc}$  (**26**).

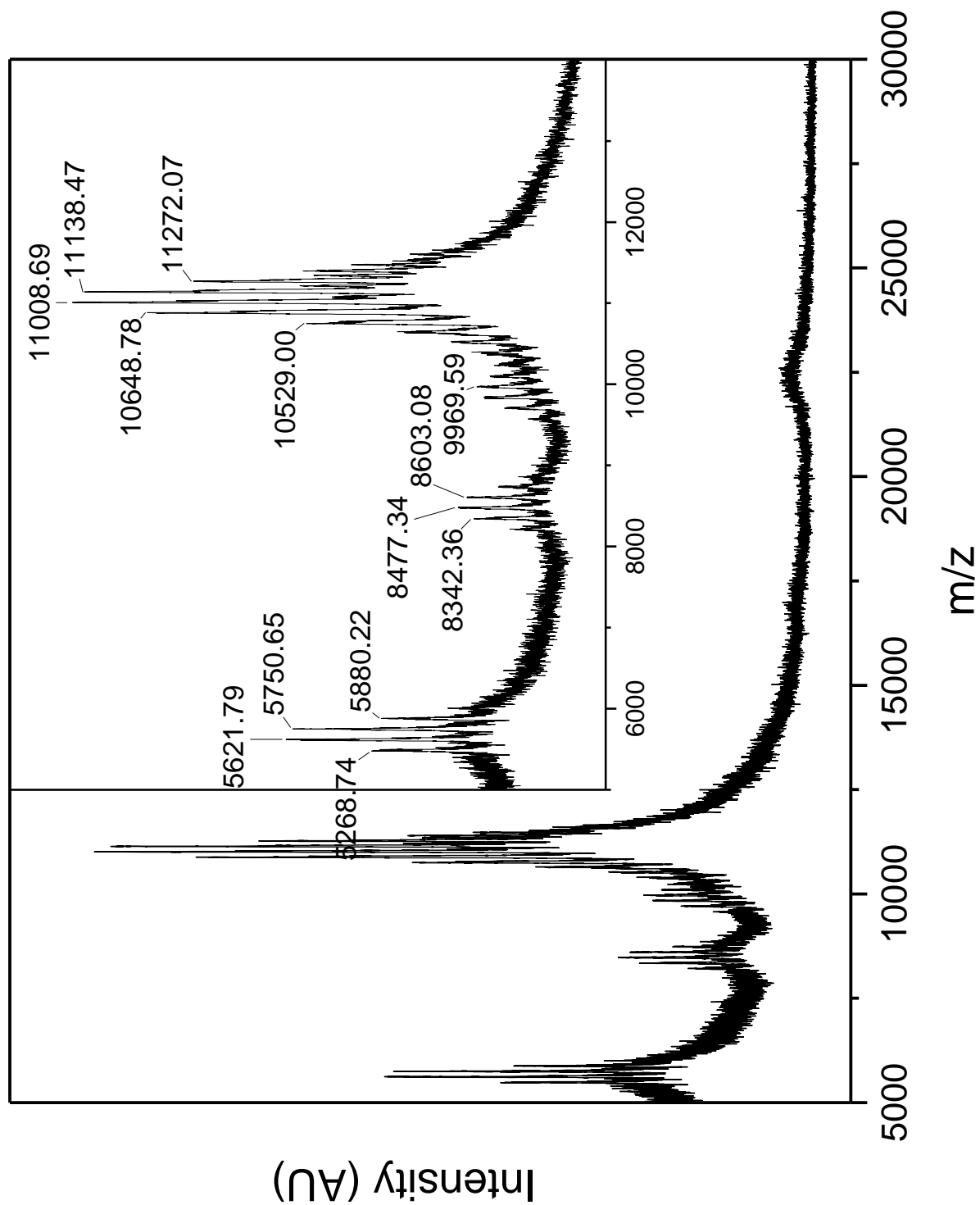


Figure A-18: MALDI-TOF mass spectrum of the products of heat treatment (DMPU, 2 h at 120 °C) of PG<sub>500</sub><sup>NHAlloc</sup> (**31**).

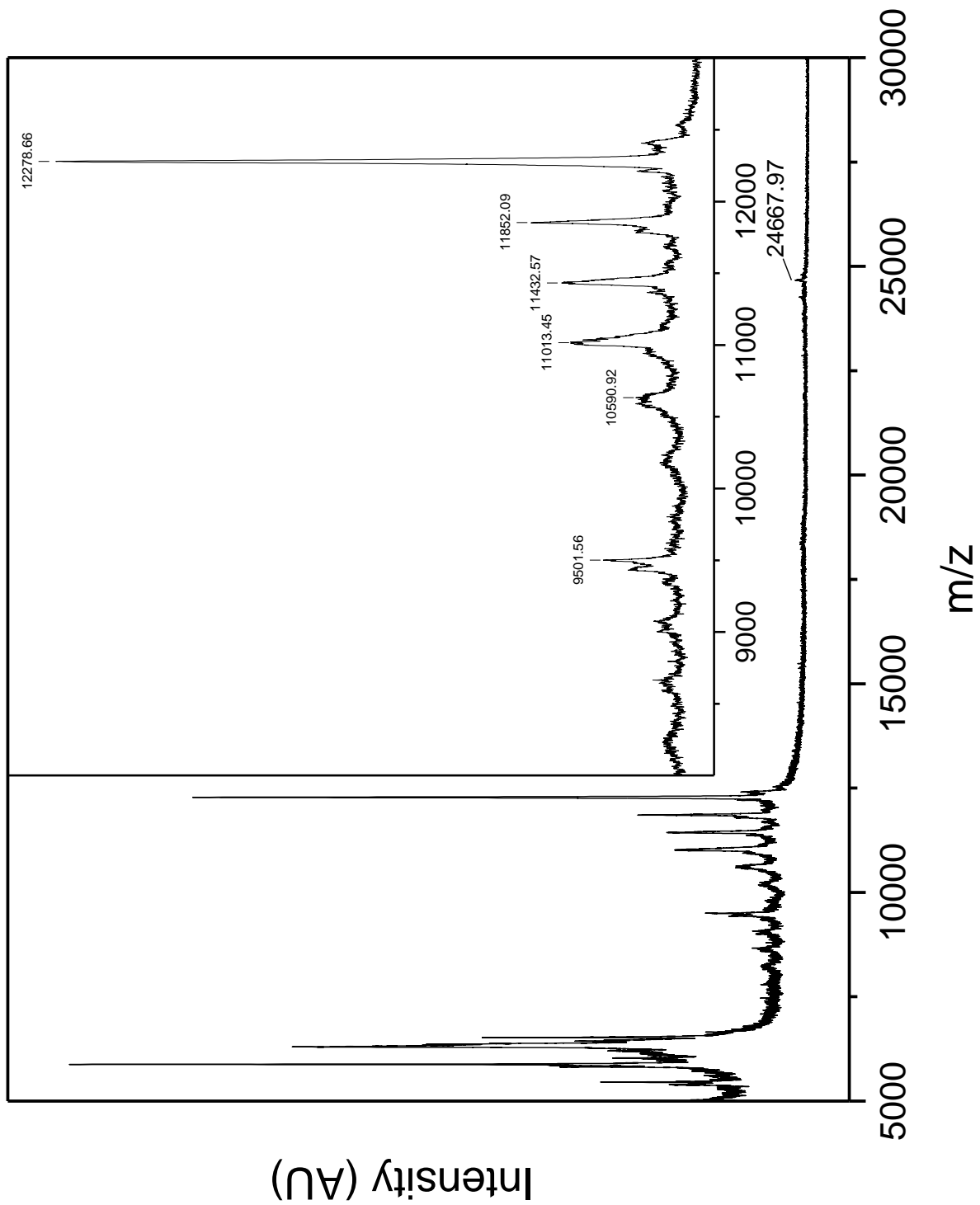


Figure A-19: MALDI-TOF mass spectrum of the products of heat treatment (DMPU, 2 h at 120 °C) of  $\text{PG}_{500}^{\text{NHCBz}}$  (29).

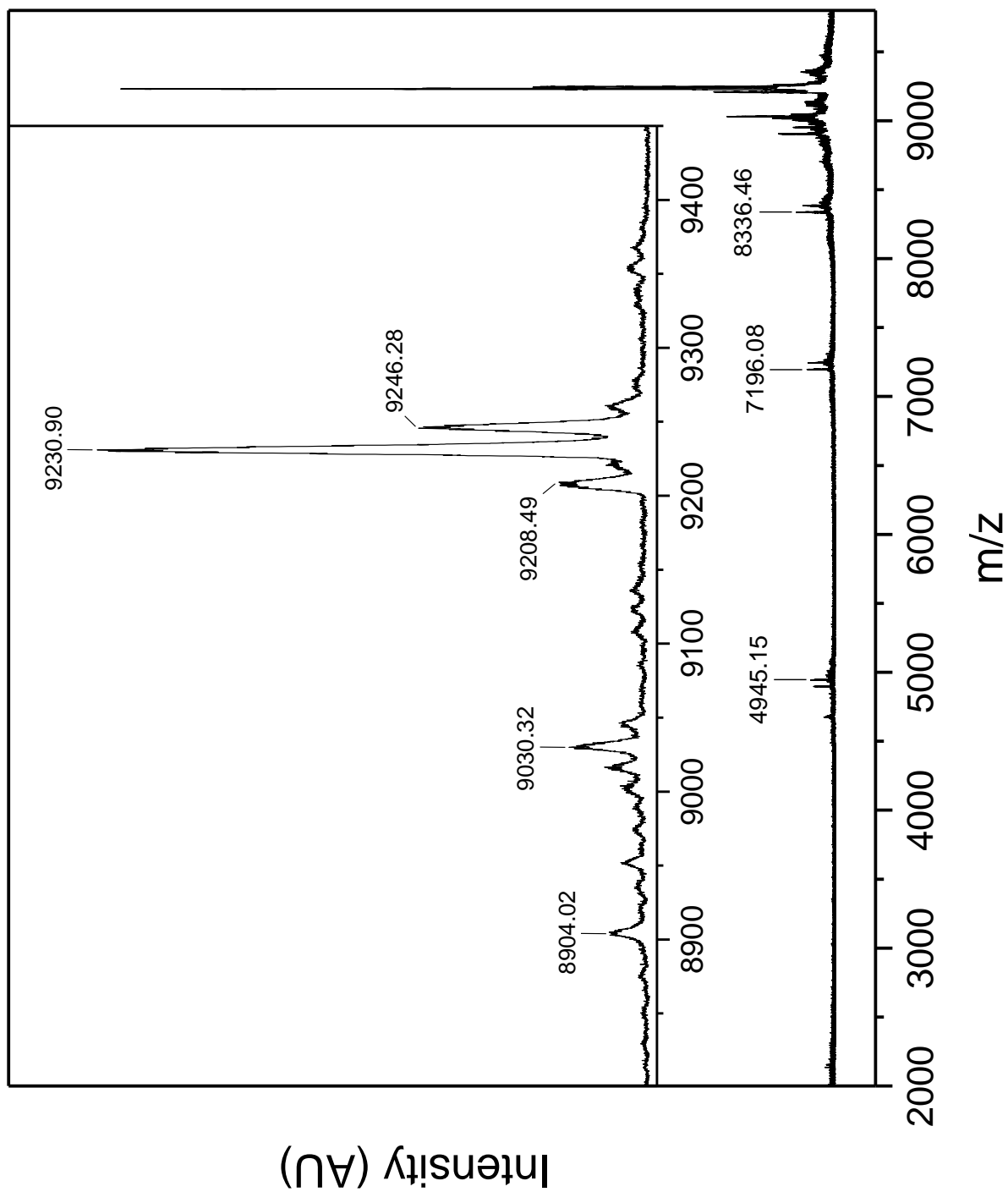


Figure A-20: MALDI-TOF mass spectrum of the products of heat treatment (DMPU, 2 h at 120 °C) of  $PG5_{500}^{CO_2Me}$  (29).

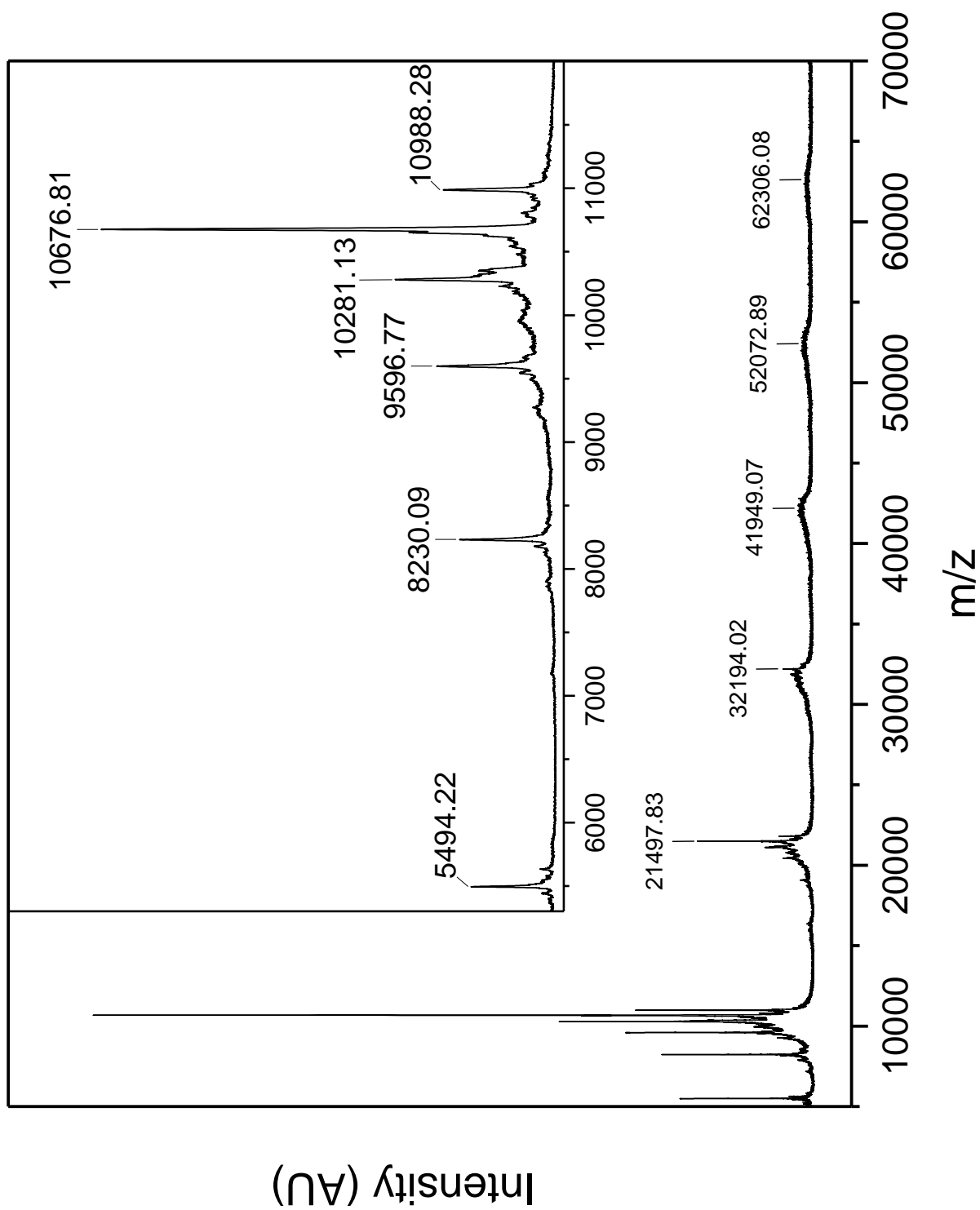


Figure A-21: MALDI-TOF mass spectrum of the products of heat treatment (DMPU, 2 h at 120 °C) of  $\text{PG}_{500}^{\text{CO}_2\text{tBu}}$  (32).

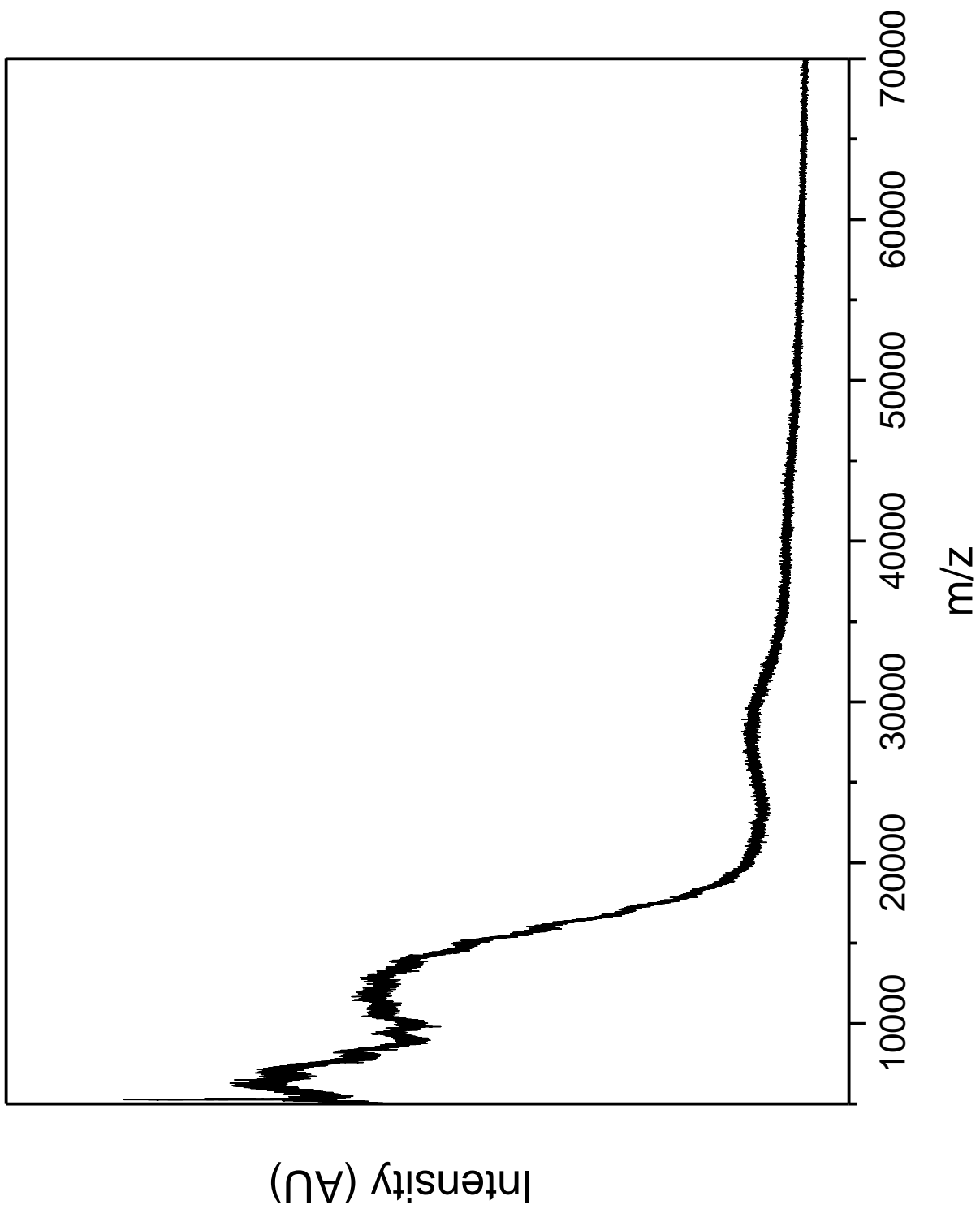


Figure A-22: MALDI-TOF mass spectrum of the products of heat treatment (DMPU, 2 h at 120 °C) of B-PG6<sub>500</sub><sup>NHBoc</sup> (**34**).

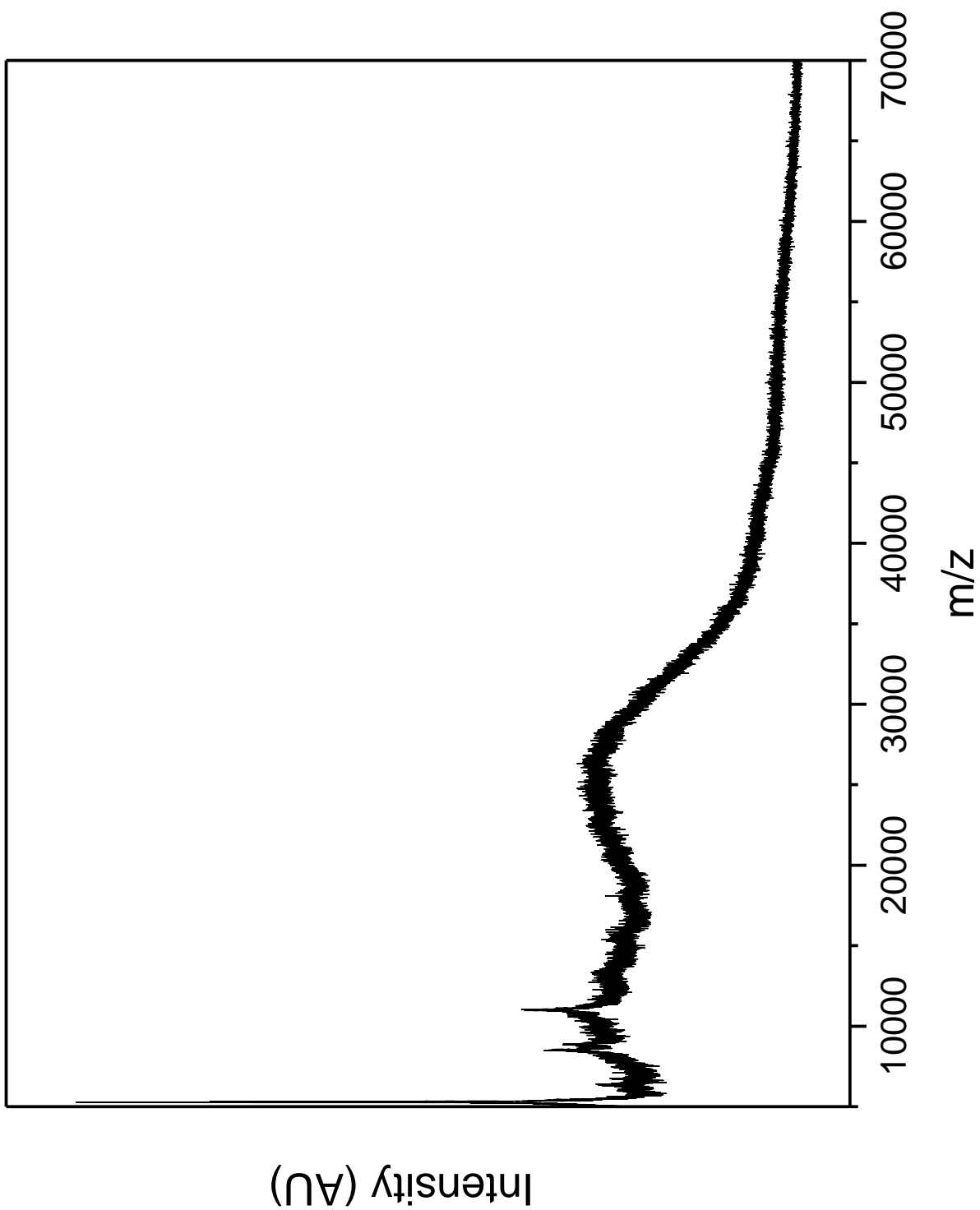
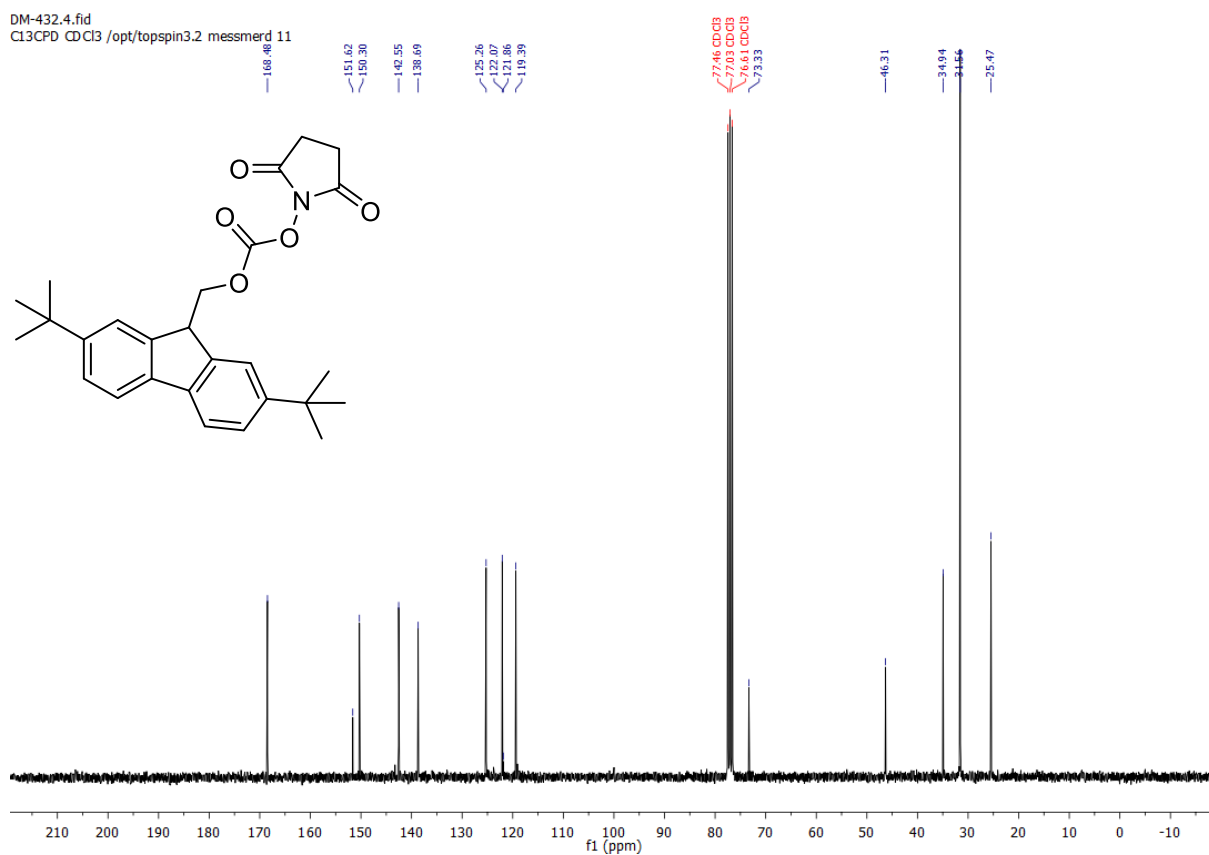
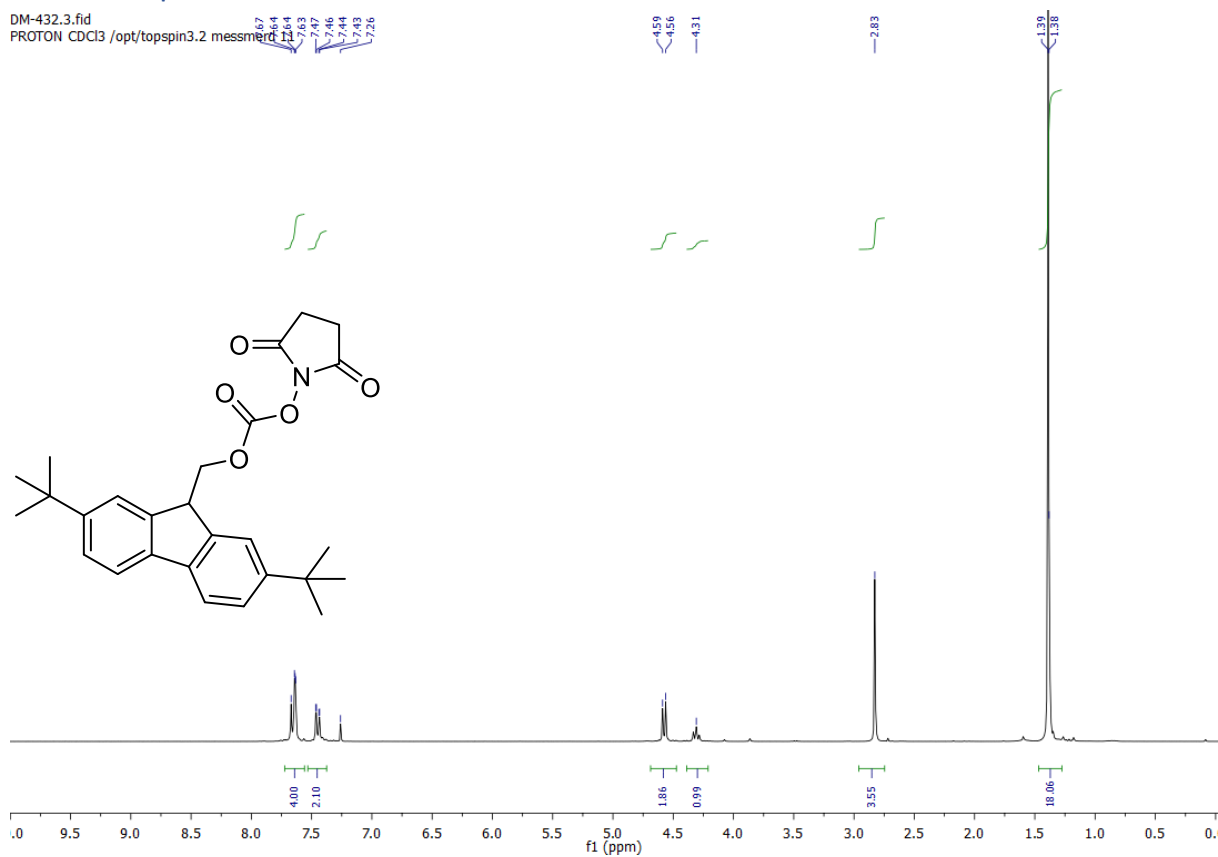


Figure A-23: MALDI-TOF mass spectrum of the products of heat treatment (DMPU, 2 h at 120 °C) of  $B-PG7_{500}^{NHBoC}$  (**36**).



## A.6. NMR spectra



DM-958.1.fid  
 DM-958 dendron all deprotected  
 PROTON DMSO /opt/topspin3.2 messmerd 49

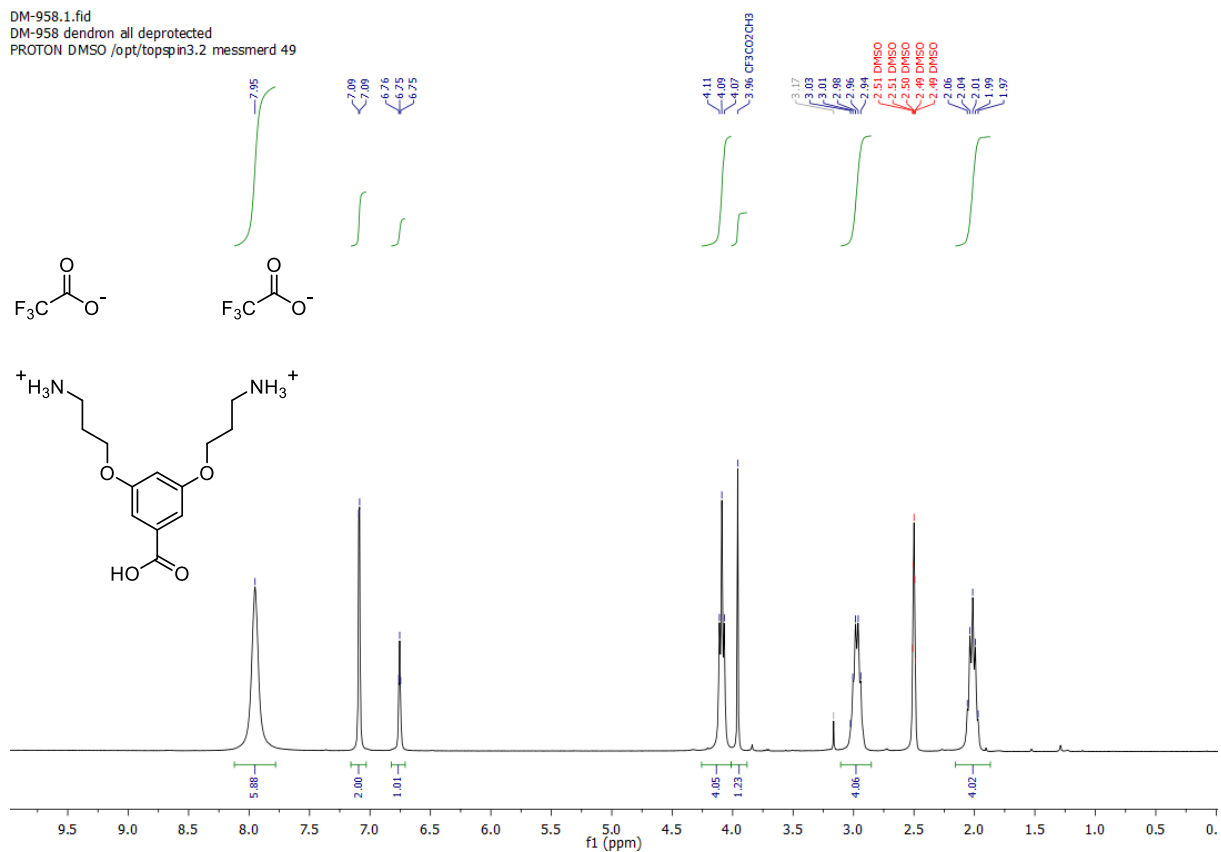


Figure A-26: <sup>1</sup>H-NMR spectrum of **48**.

DM-958.5.fid  
 DM-958 dendron all deprotected  
 F19 DMSO /opt/topspin3.2 messmerd 49

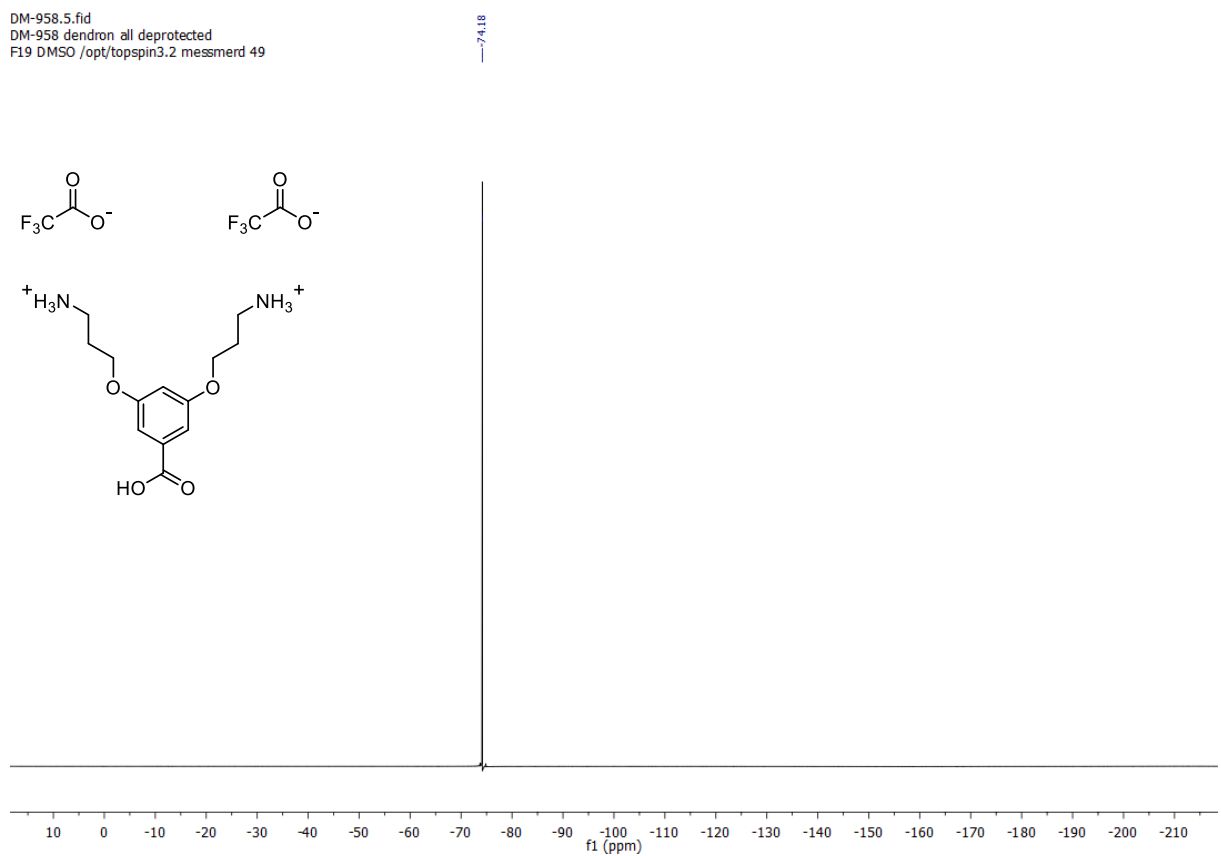


Figure A-27: <sup>19</sup>F-NMR spectrum of **48**.

DM-958.2.fid  
 DM-958 dendron all deprotected  
 C13CPD DMSO /opt/topspin3.2 messmerd 49

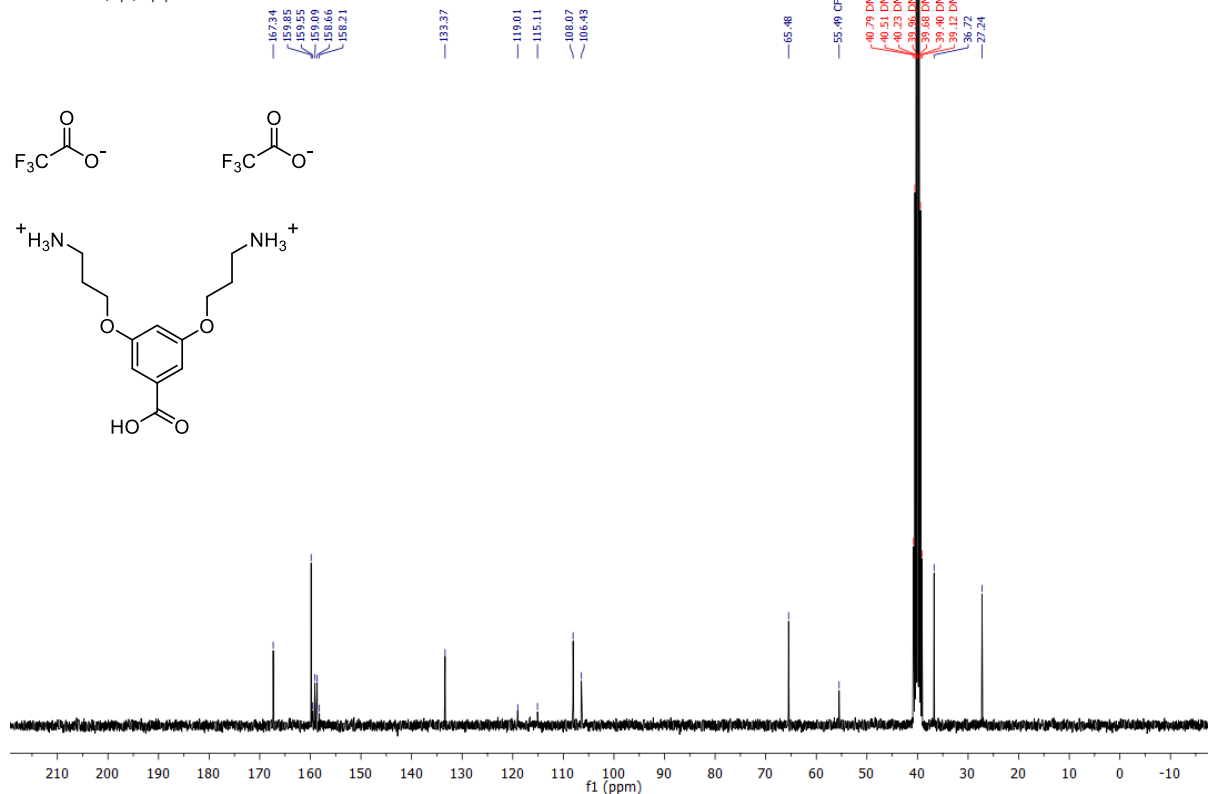


Figure A-28:  $^{13}\text{C}$ -NMR spectrum of 48.

DM-411.7.fid  
 PROTON DMSO /opt/topspin3.2 messmerd 10

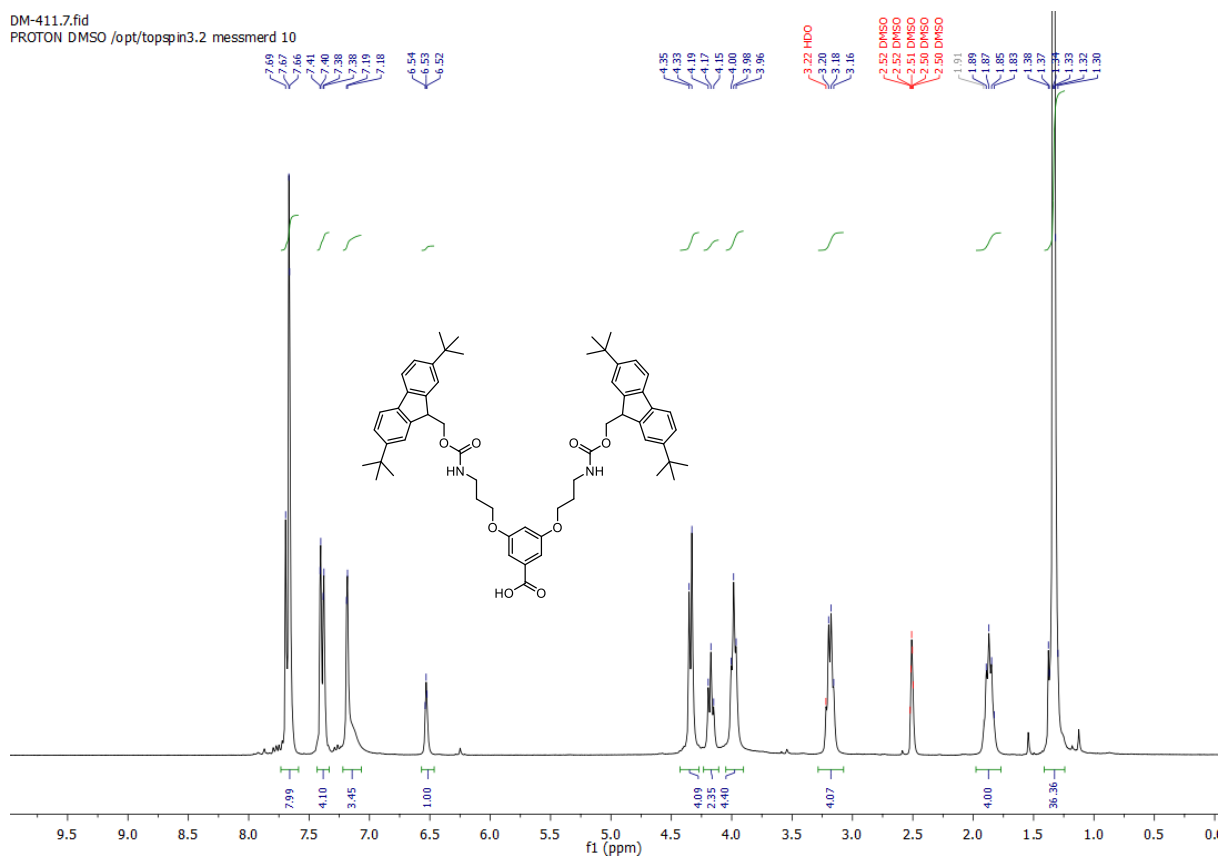


Figure A-29:  $^1\text{H}$ -NMR spectrum of 49.

DM-442.13.fid  
 C13CPD DMSO /opt/topspin3.2 messmerd 2

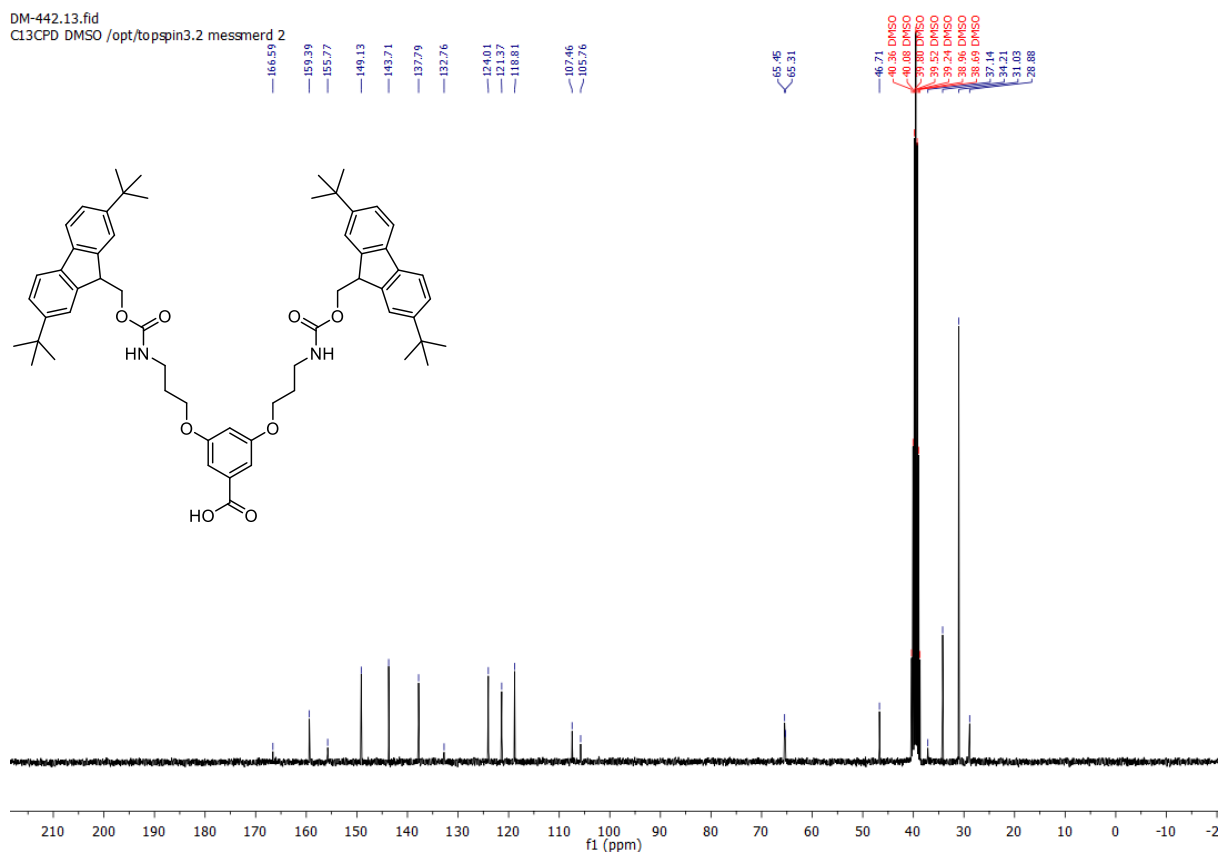


Figure A-30:  $^{13}\text{C}$ -NMR spectrum of 49.

DM-434.2.fid  
 PROTON DMSO /opt/topspin3.2 messmerd 12

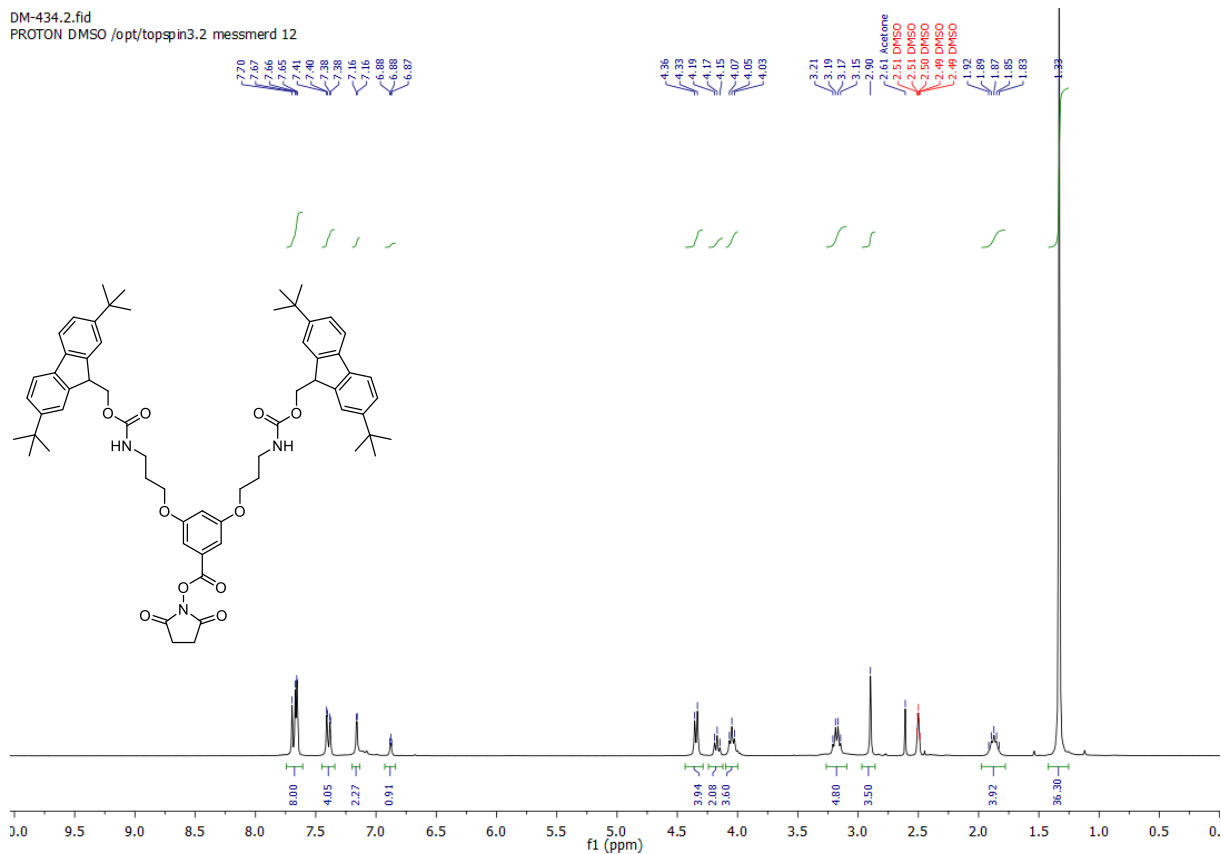
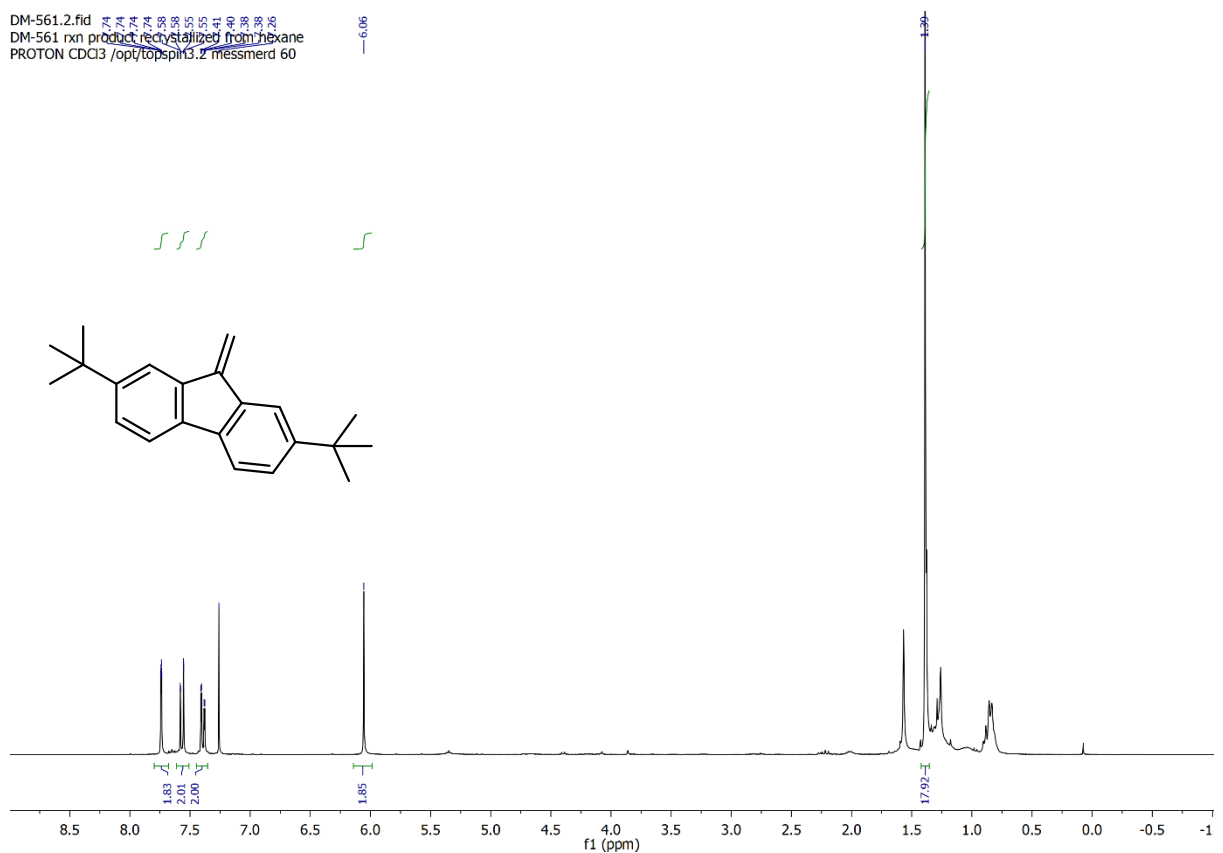
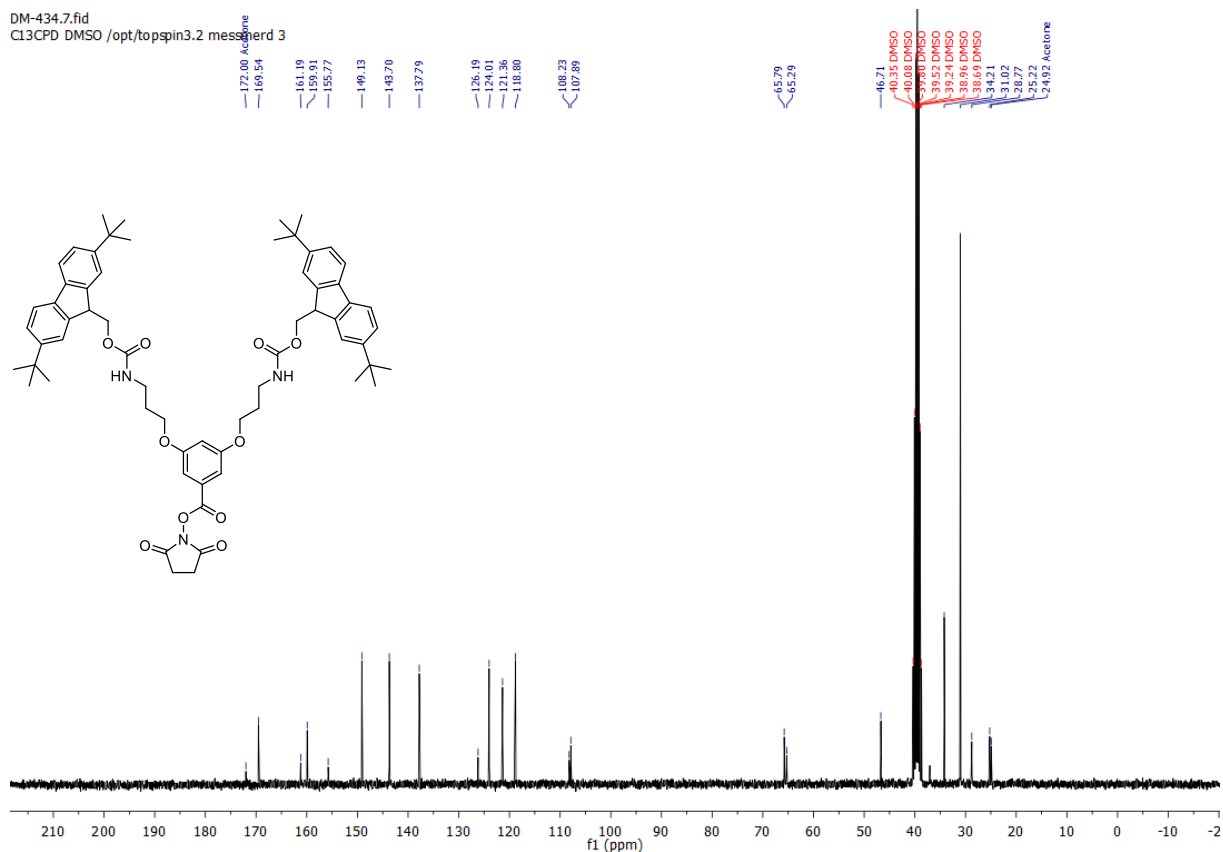
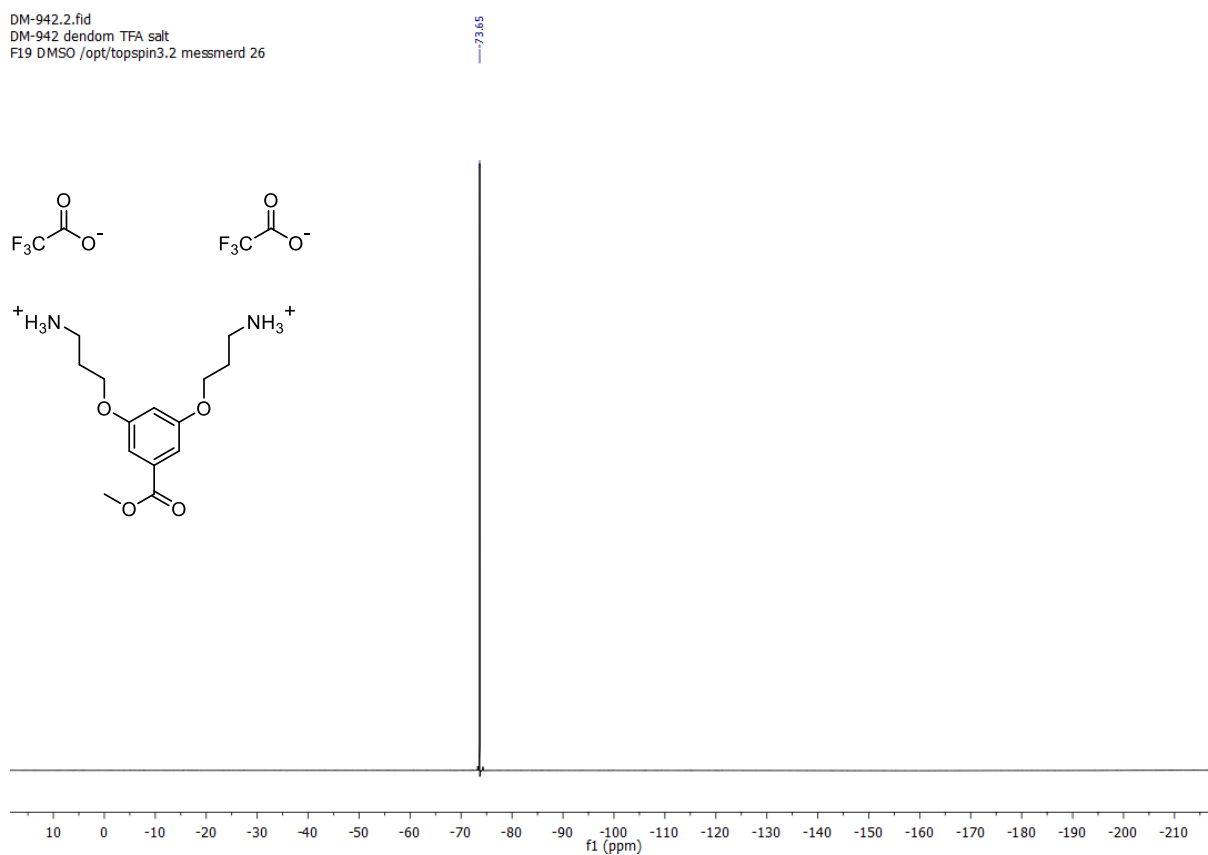
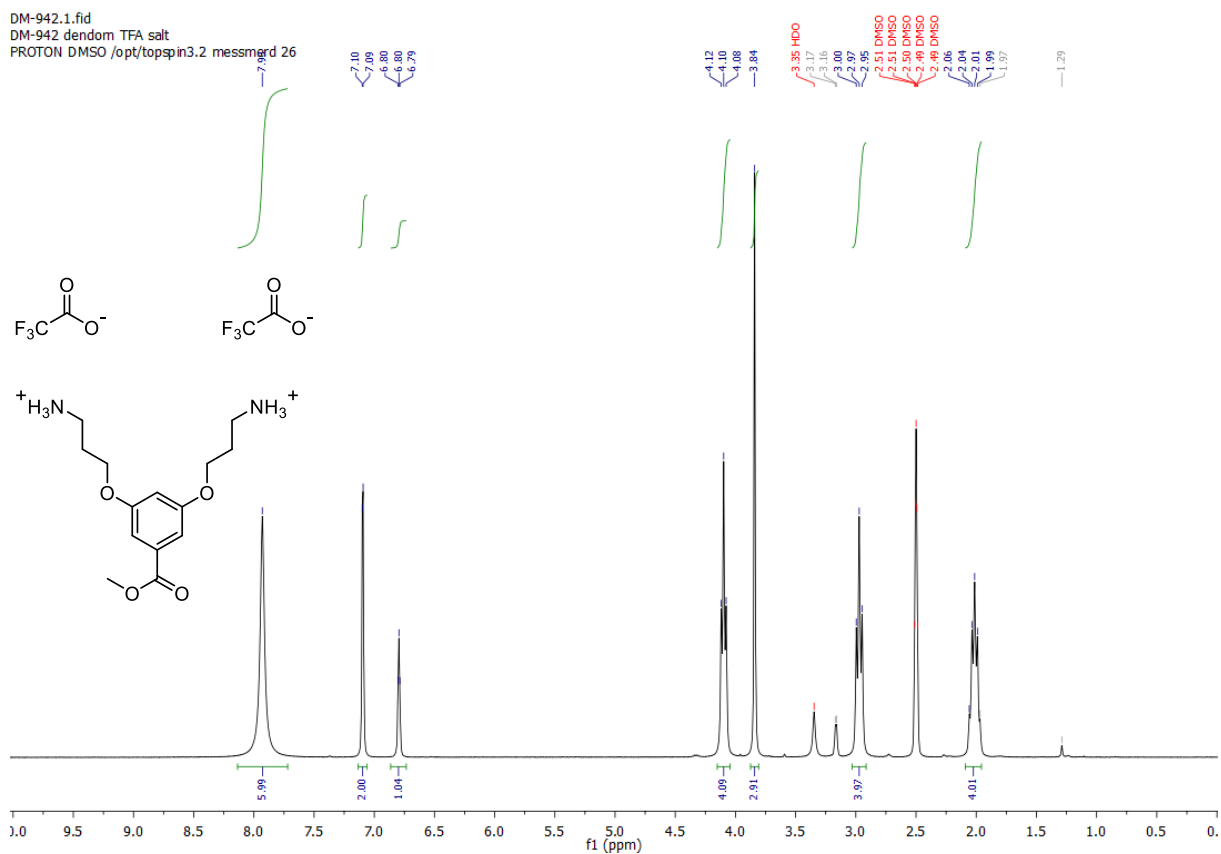


Figure A-31:  $^1\text{H}$ -NMR spectrum of 50.





DM-942.6.fid  
DM-942  
Cl3CPD CD Cl3 /opt/topspin3.2 messmerd 21

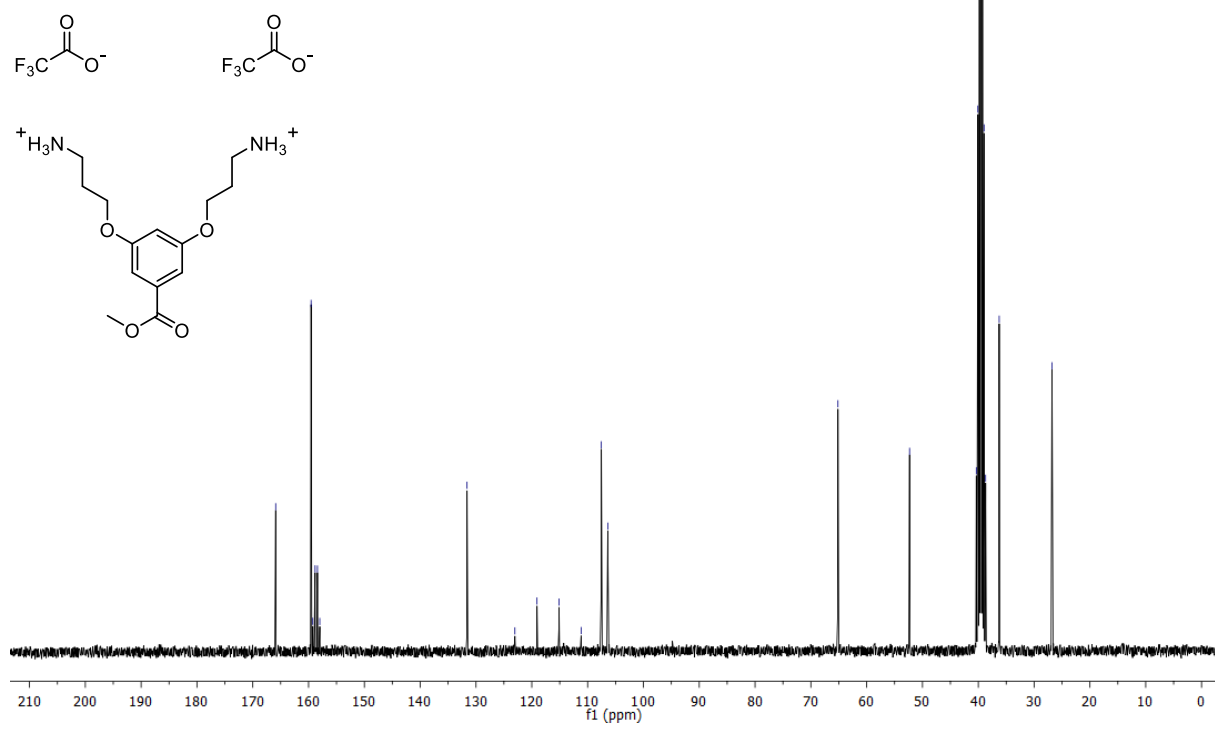


Figure A-36: <sup>13</sup>C-NMR spectrum of 51.

DM-944.1.fid  
 DM-944  
 PROTON CDCl3 /opt/topspin3.2 messmerd 7

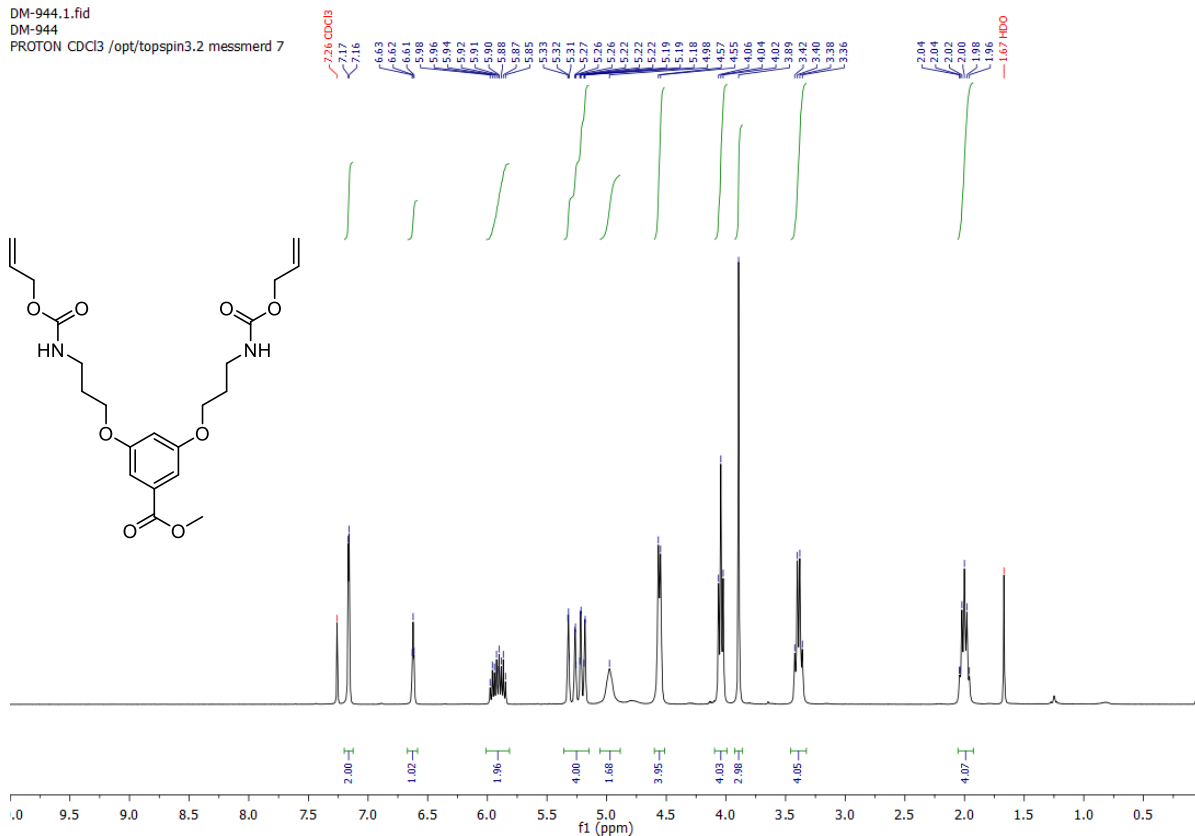


Figure A-37: <sup>1</sup>H-NMR spectrum of 53.

DM-944.2.fid  
 DM-944  
 C13CPD CDCl3 /opt/topspin3.2 messmerd 7

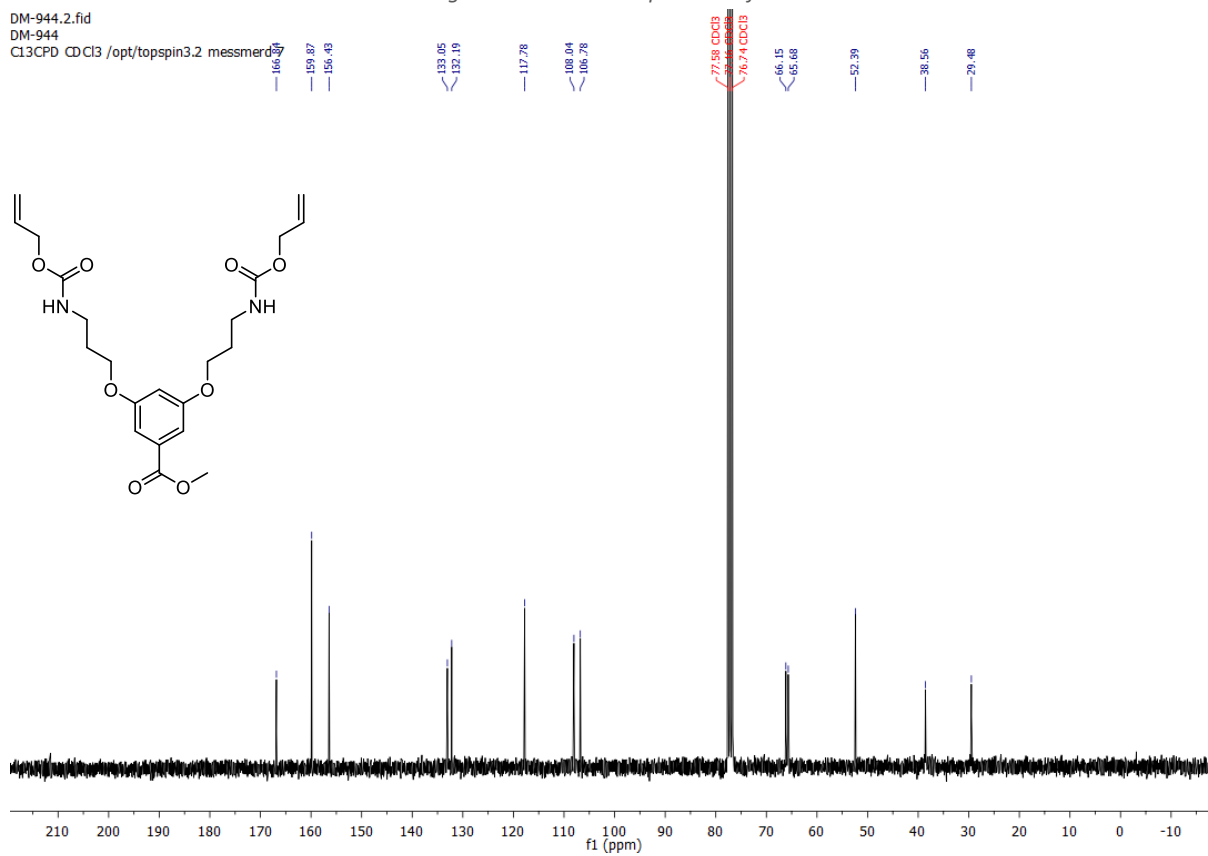


Figure A-38: <sup>13</sup>C-NMR spectrum of 53.



DM-957.1.fid  
 DM-957  
 PROTON DMSO /opt/topspin3.2 messmerd 9

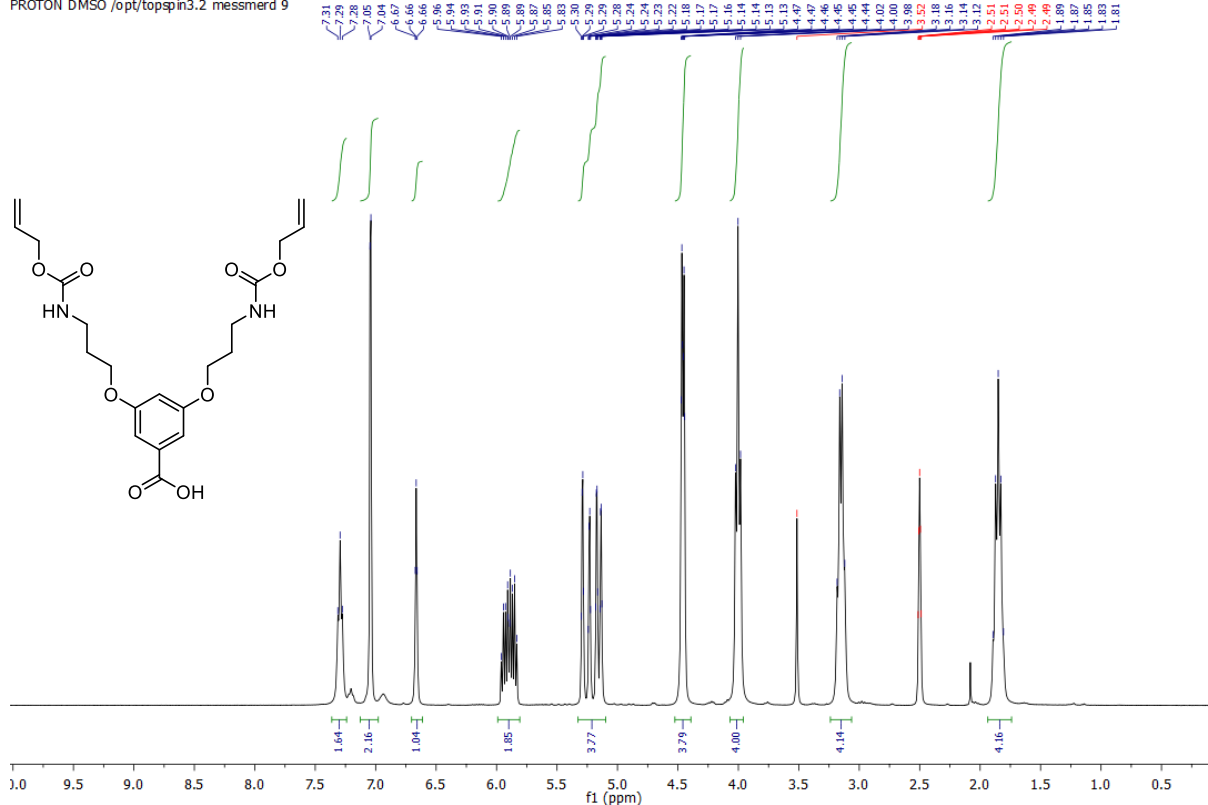


Figure A-39: <sup>1</sup>H-NMR spectrum of 54.

DM-957.4.fid  
 C13CPD DMSO /opt/topspin3.2 messmerd 15

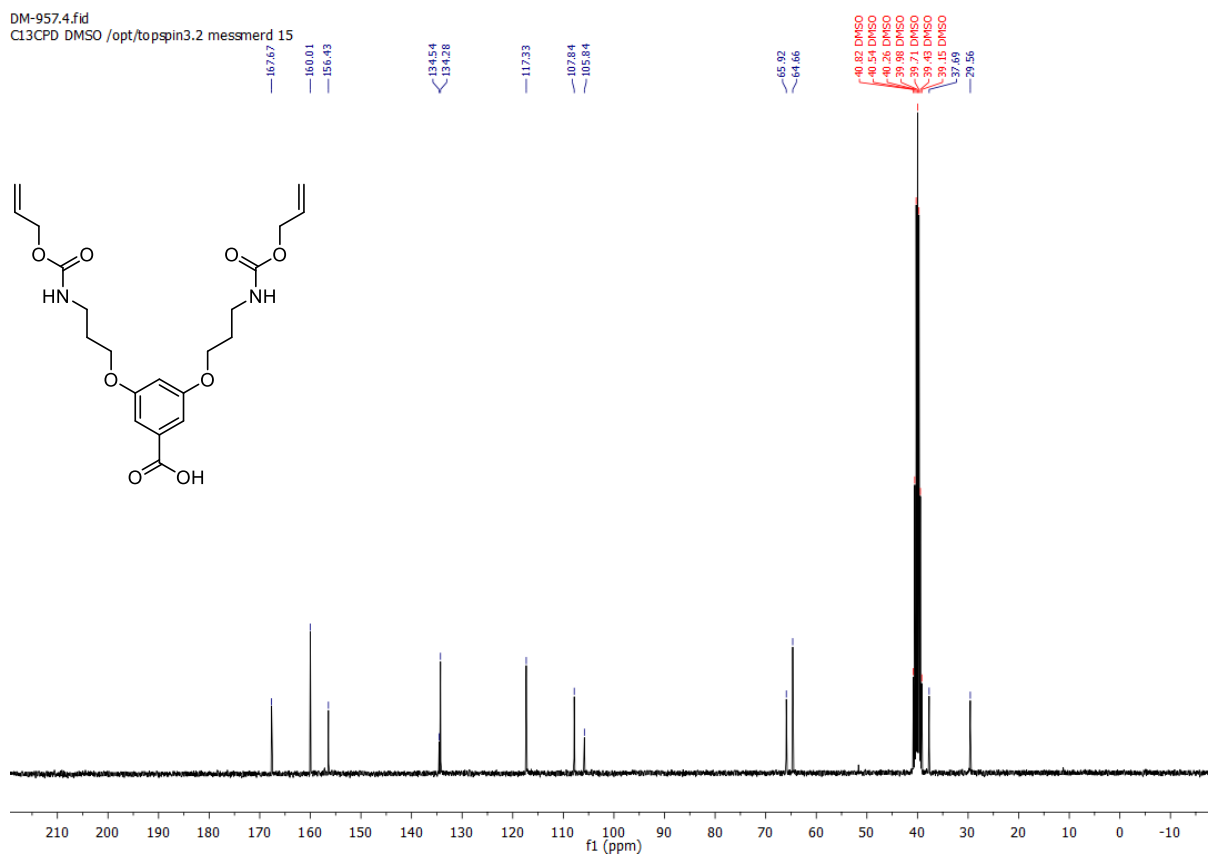


Figure A-40: <sup>13</sup>C-NMR spectrum of 54.

DM-956.3.fid  
 PROTON CDCl3 /opt/topspin3.2 messmerd 11

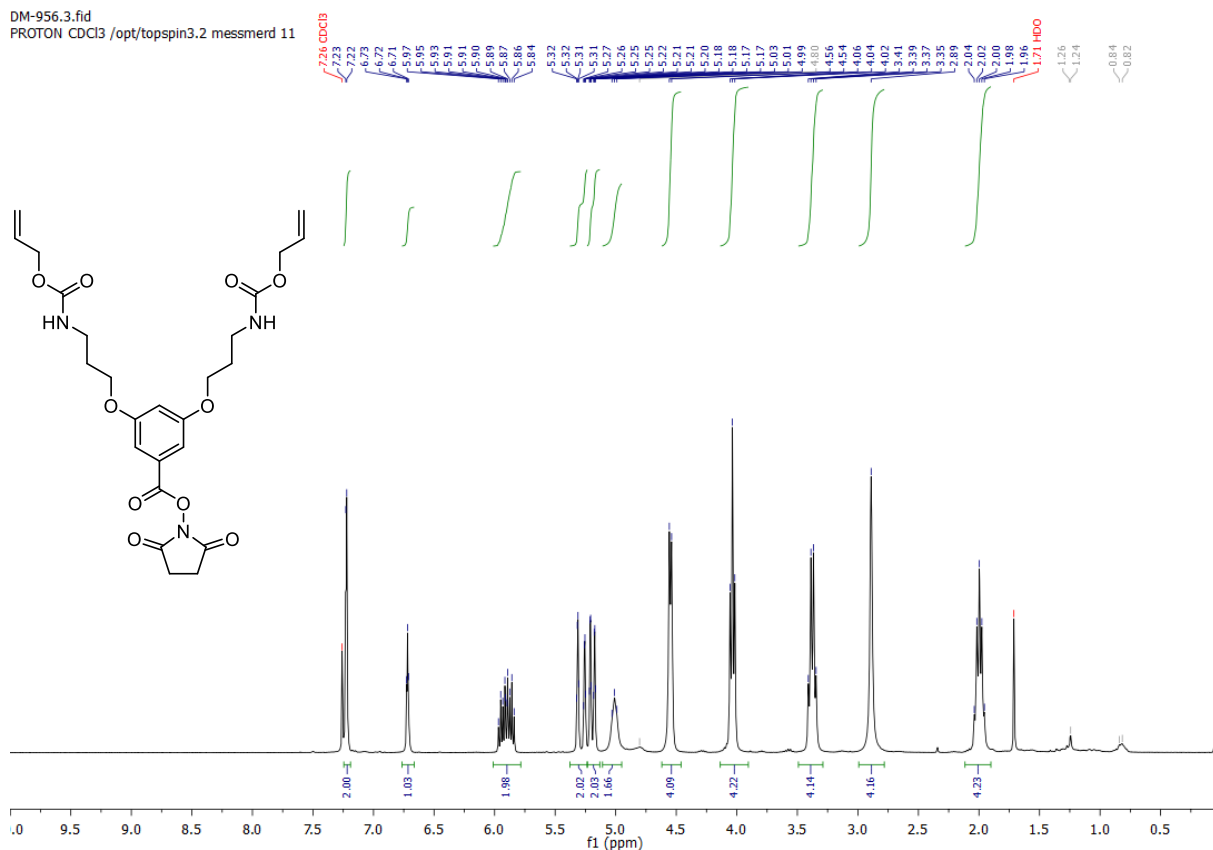


Figure A-41: <sup>1</sup>H-NMR spectrum of 55.

DM-956.8.fid  
 C13CPD CDCl3 /opt/topspin3.2 messmerd 44

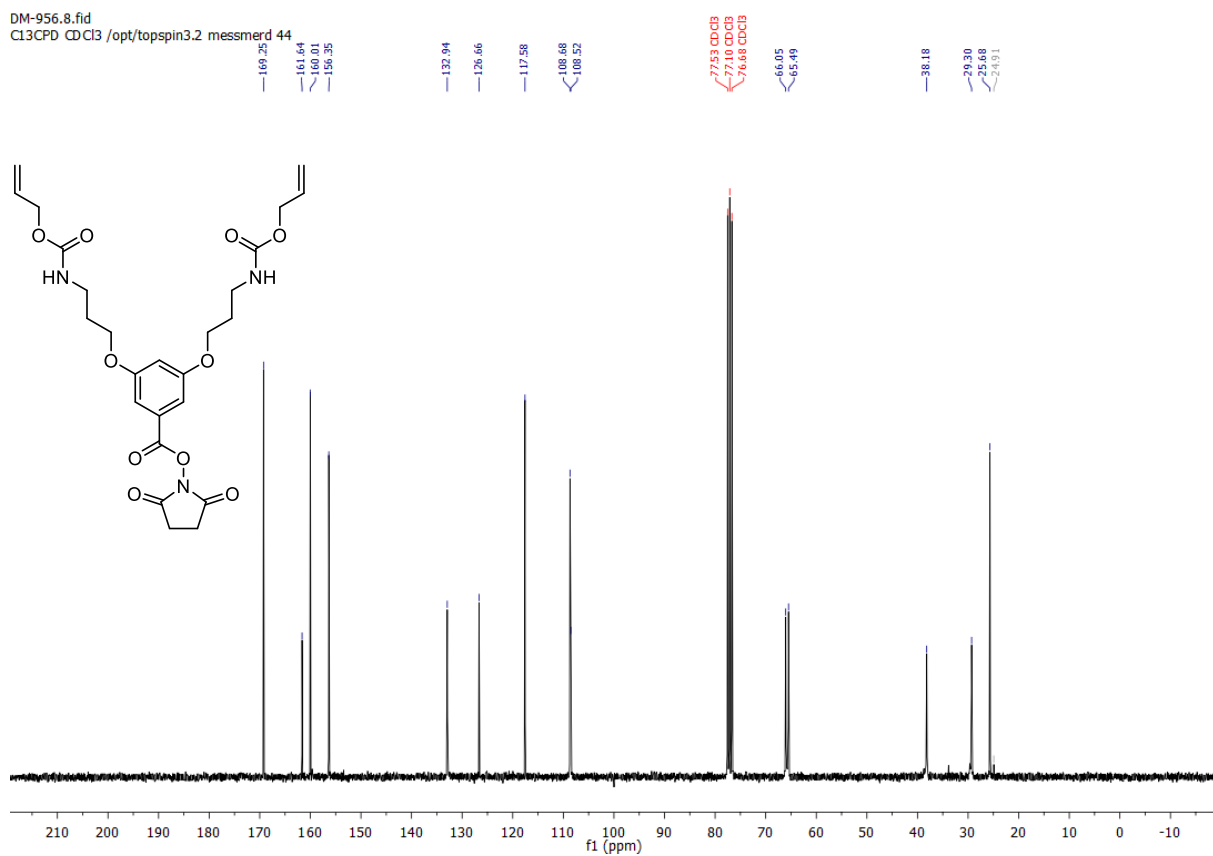


Figure A-42: <sup>13</sup>C-NMR spectrum of 55.

DM-979.3.fid  
 DM-979 purif  
 PROTON CDCl3 /opt/topspin3.2 messmerd 28

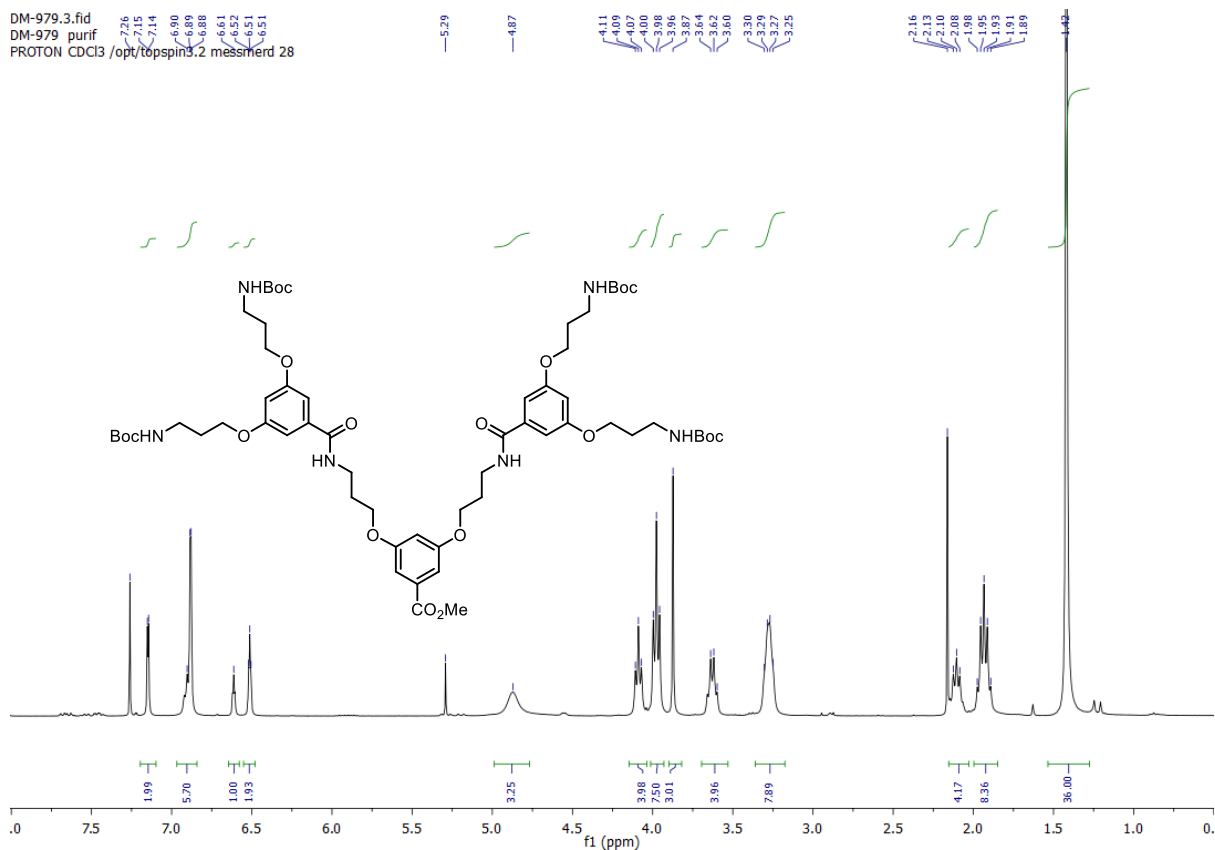


Figure A-43:  $^1\text{H-NMR}$  spectrum of **56** prepared from **53** (test reaction for  $\text{NHAlloc}$  deprotection).

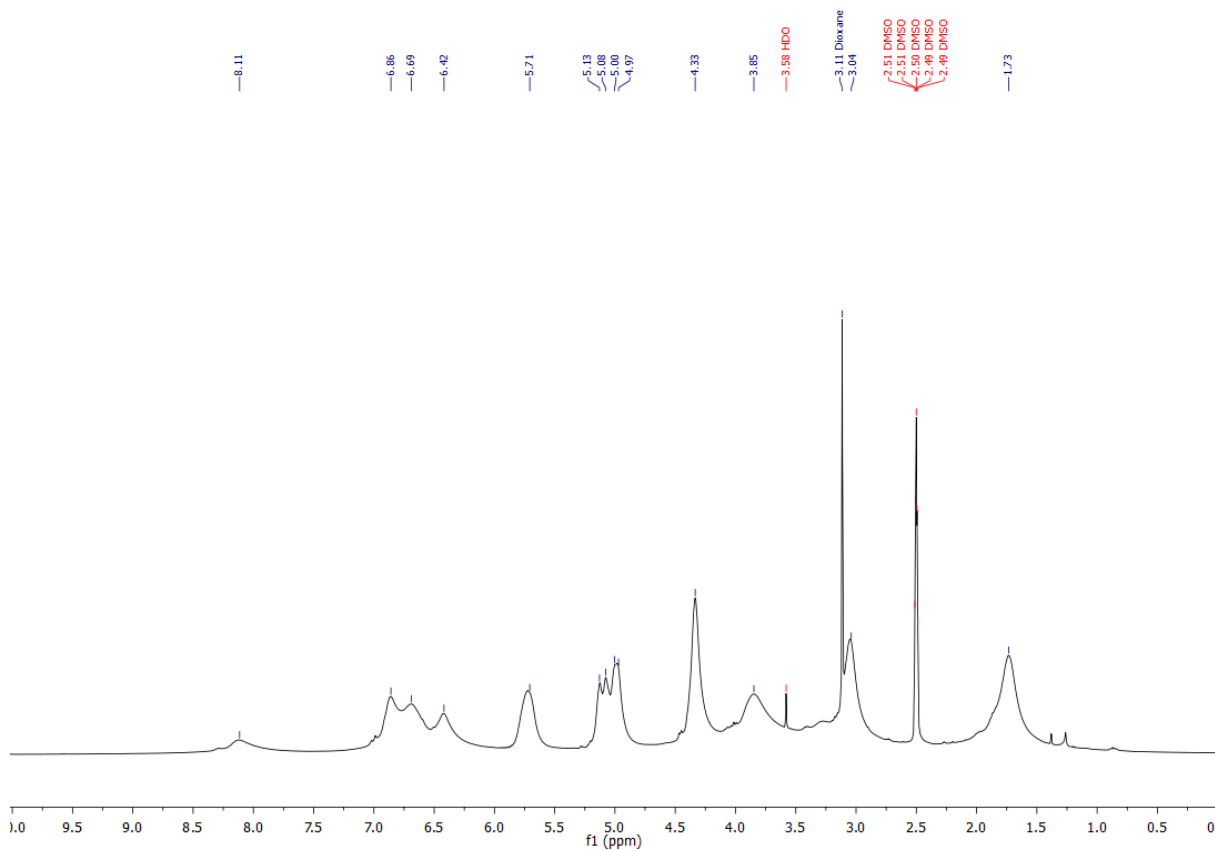


Figure A-44:  $^1\text{H-NMR}$  spectrum of  $\text{PG5}_{500}^{\text{NHAlloc}}$  (**31**).

DM-845.2.fid  
DM-845 PG6 from n+1  
PROTON DMSO /opt/topspin3.2 messmerd 42

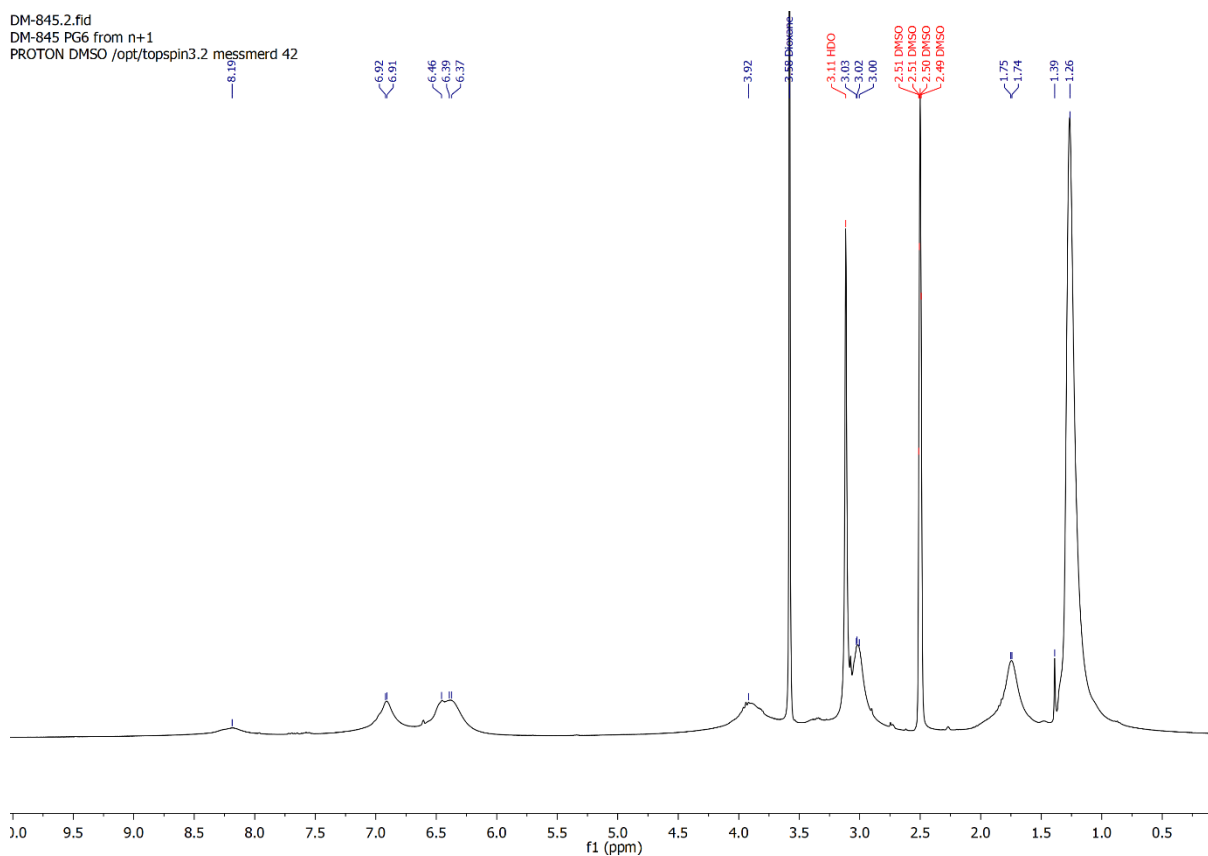


Figure A-45: <sup>1</sup>H-NMR spectrum of C-PG6<sup>NHBOC</sup><sub>500</sub> (**34**).

DM-840.1.fid  
Light brown powder, de-PG6 (500)  
PROTON DMSO /opt/topspin3.2 messmerd 26

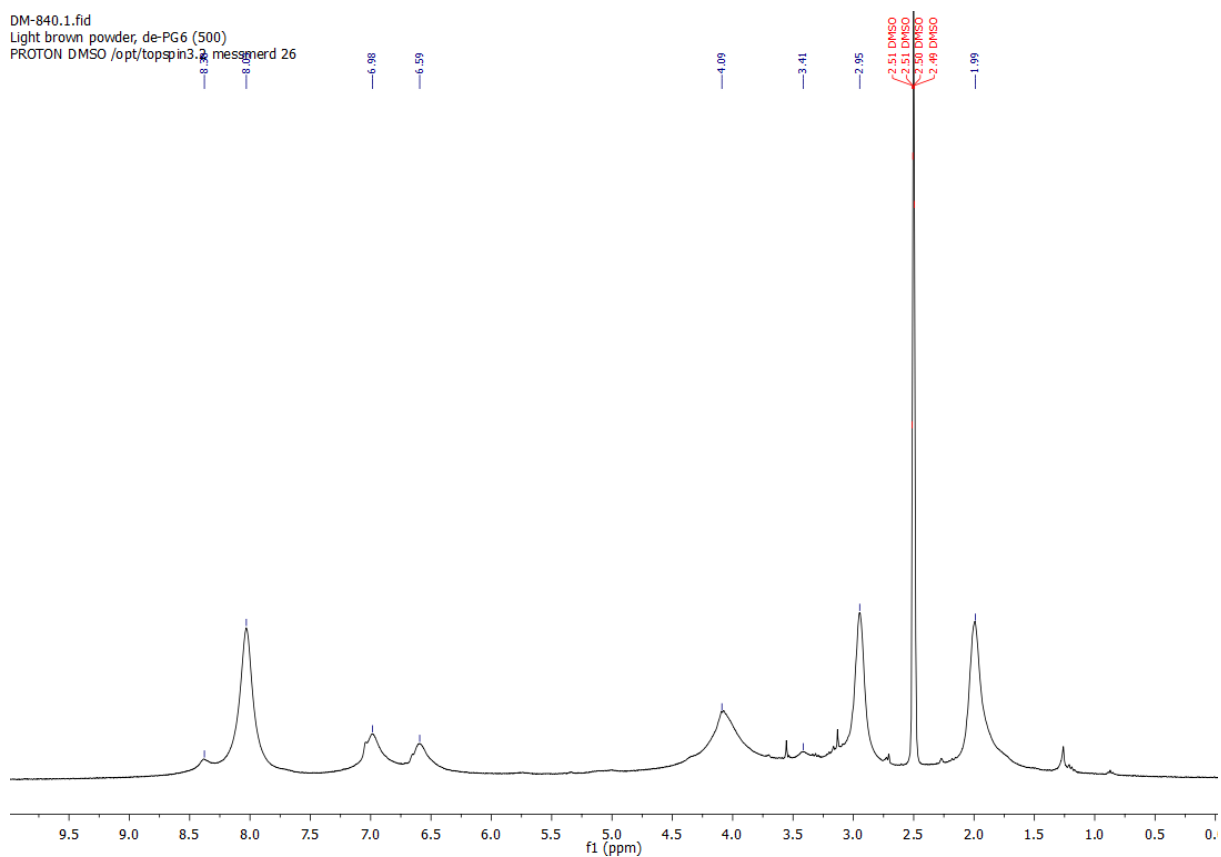


Figure A-46: <sup>1</sup>H-NMR spectrum of C-PG6<sup>NH<sub>3</sub>TFA</sup><sub>500</sub> (**35**).

DM-844.1.fid  
PROTON DMSO /opt/topspin3.2 messmerd 13

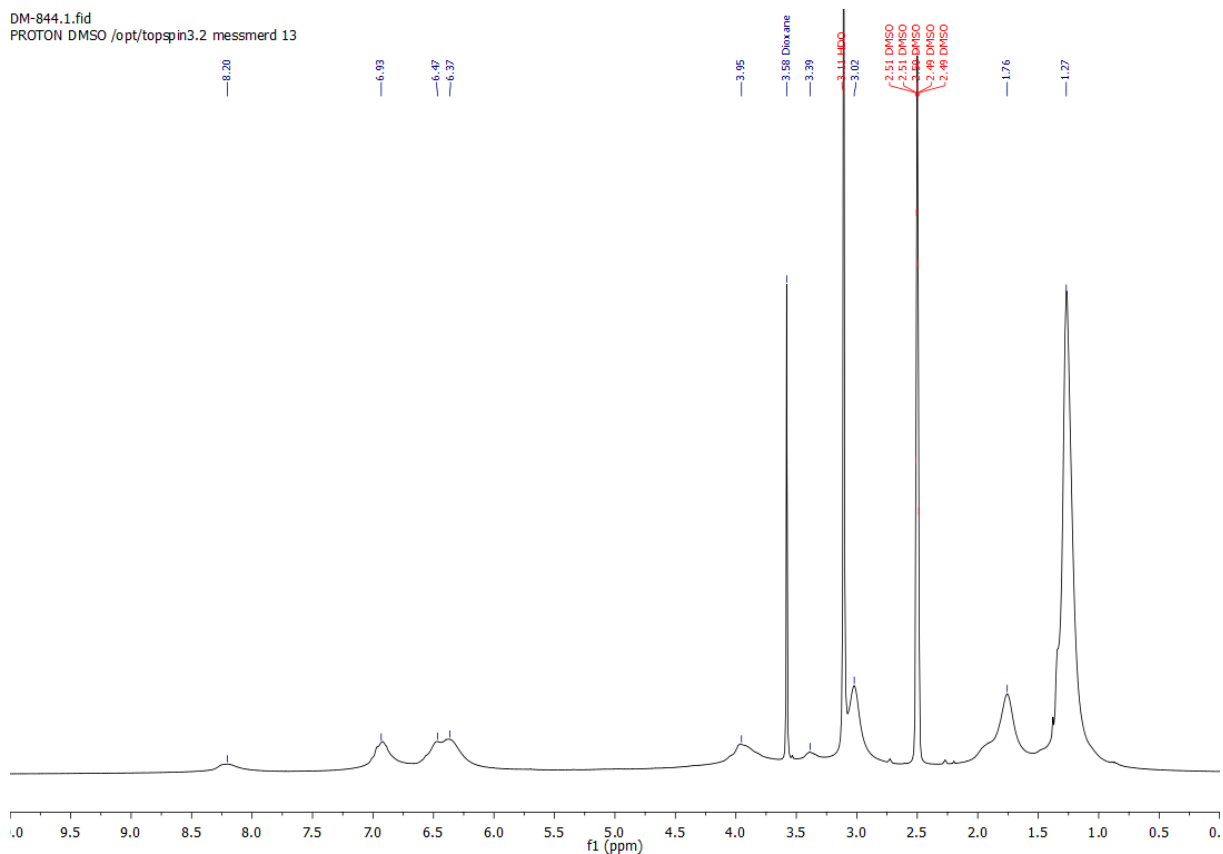


Figure A-47:  $^1\text{H-NMR}$  spectrum of  $\text{C-PG7}_{500}^{\text{NHBOC}}$  (**36**).

DM-918.1.fid  
DM-918 PG8-500  
PROTON DMSO /opt/topspin3.2 messmerd 8

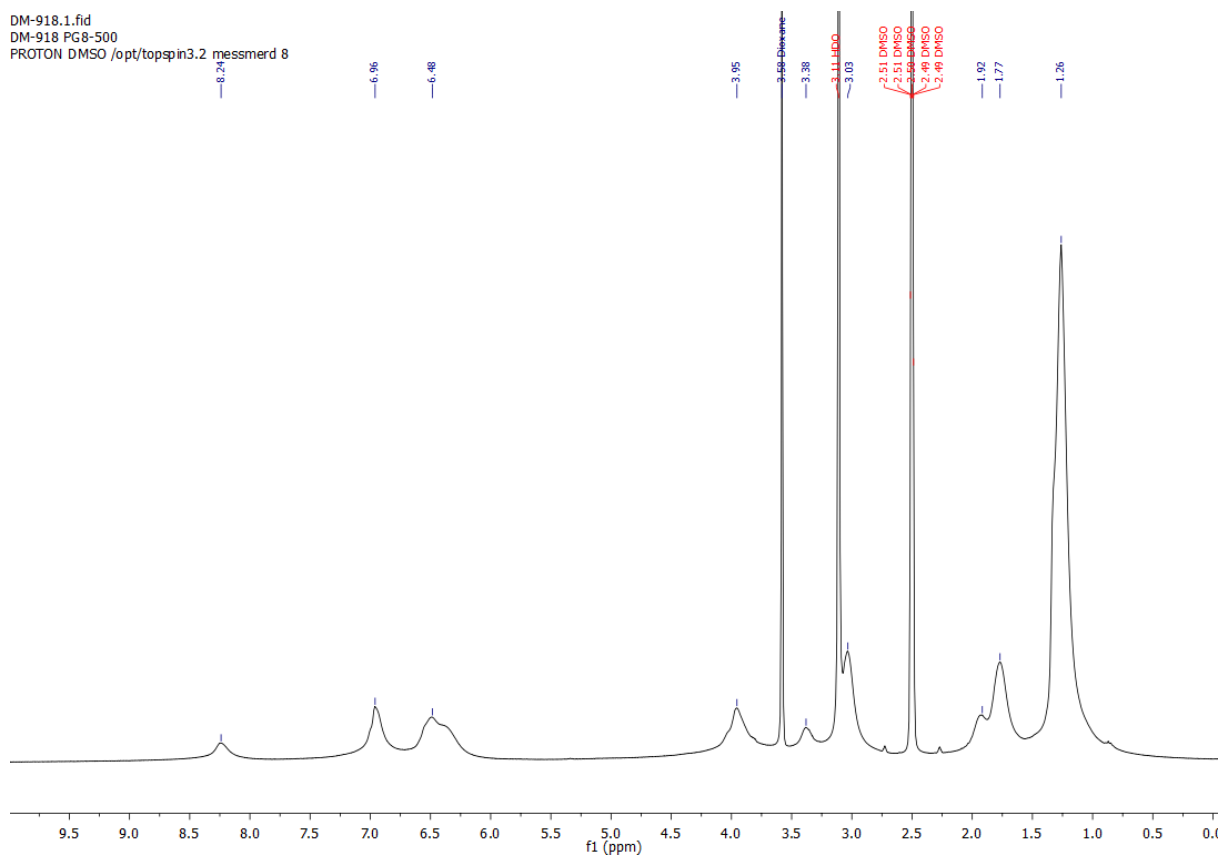
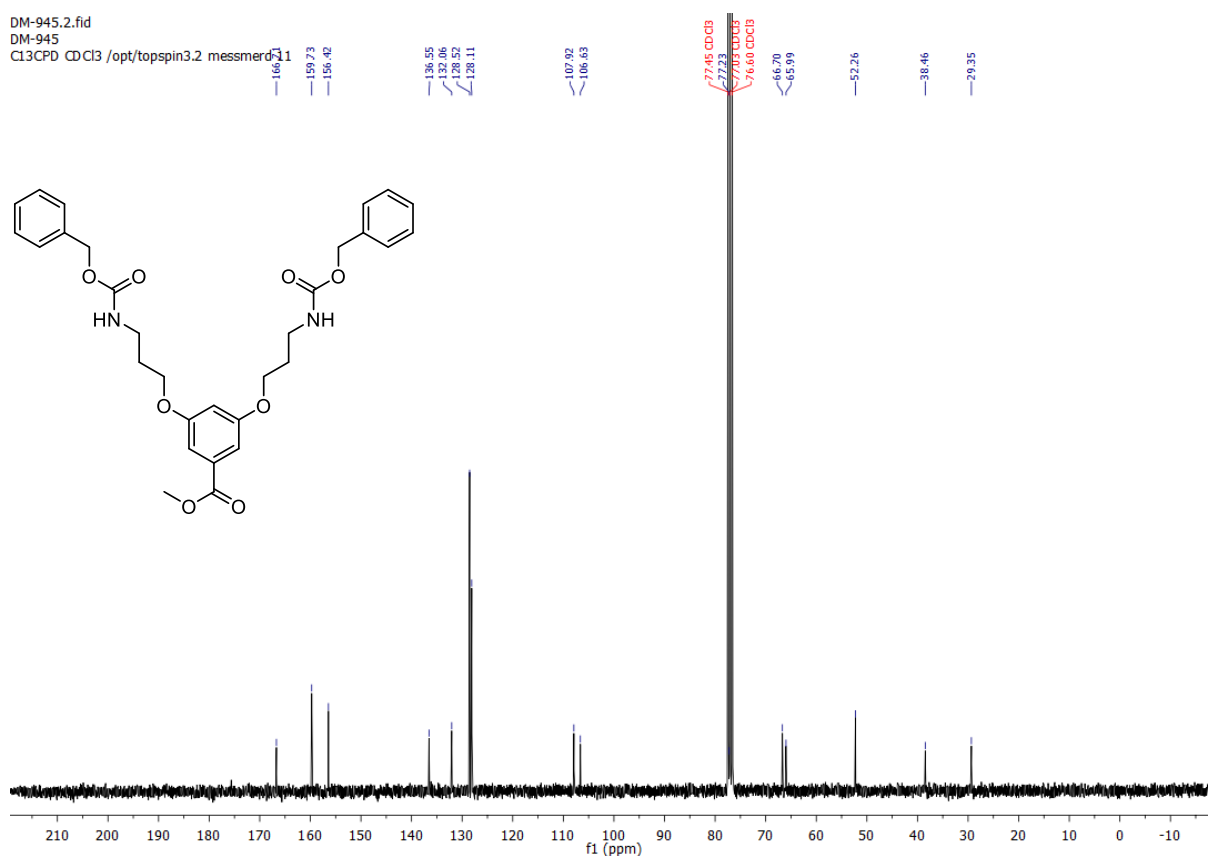
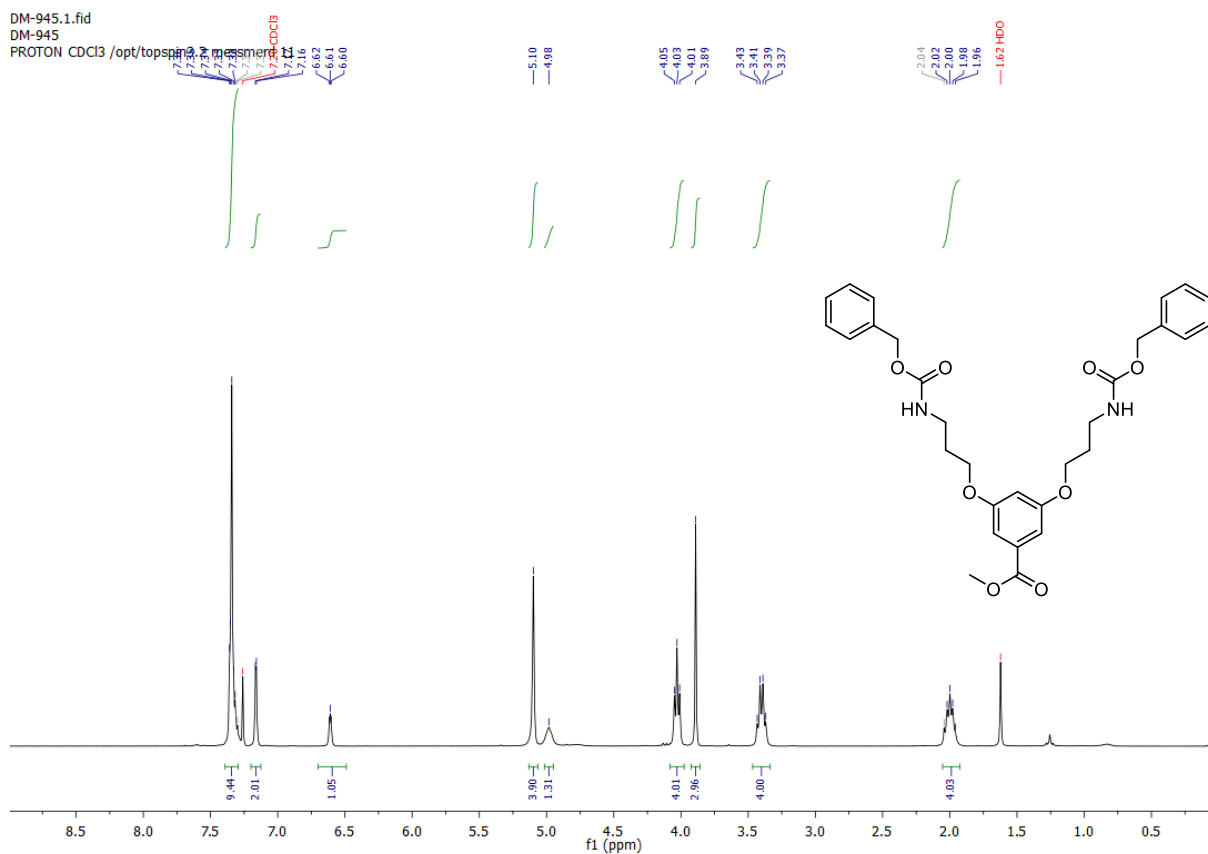


Figure A-48:  $^1\text{H-NMR}$  spectrum of  $\text{C-PG8}_{500}^{\text{NHBOC}}$ .



DM-947.2.fid  
 DM-947  
 PROTON DMSO /opt/topspin3.2 messmerd 56

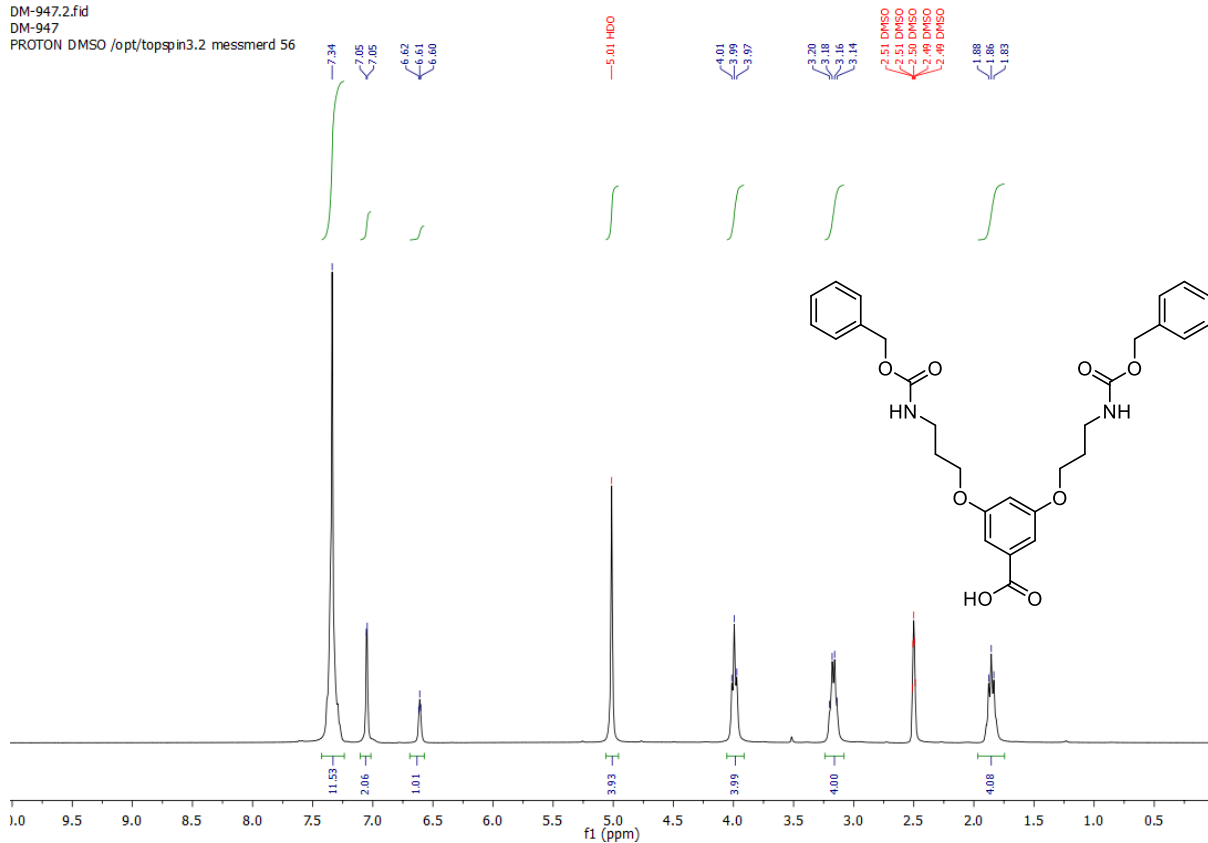


Figure A-51: <sup>1</sup>H-NMR spectrum of 101.

DM-947.5.fid  
 CL3CPD DMSO /opt/topspin3.2 messmerd 13

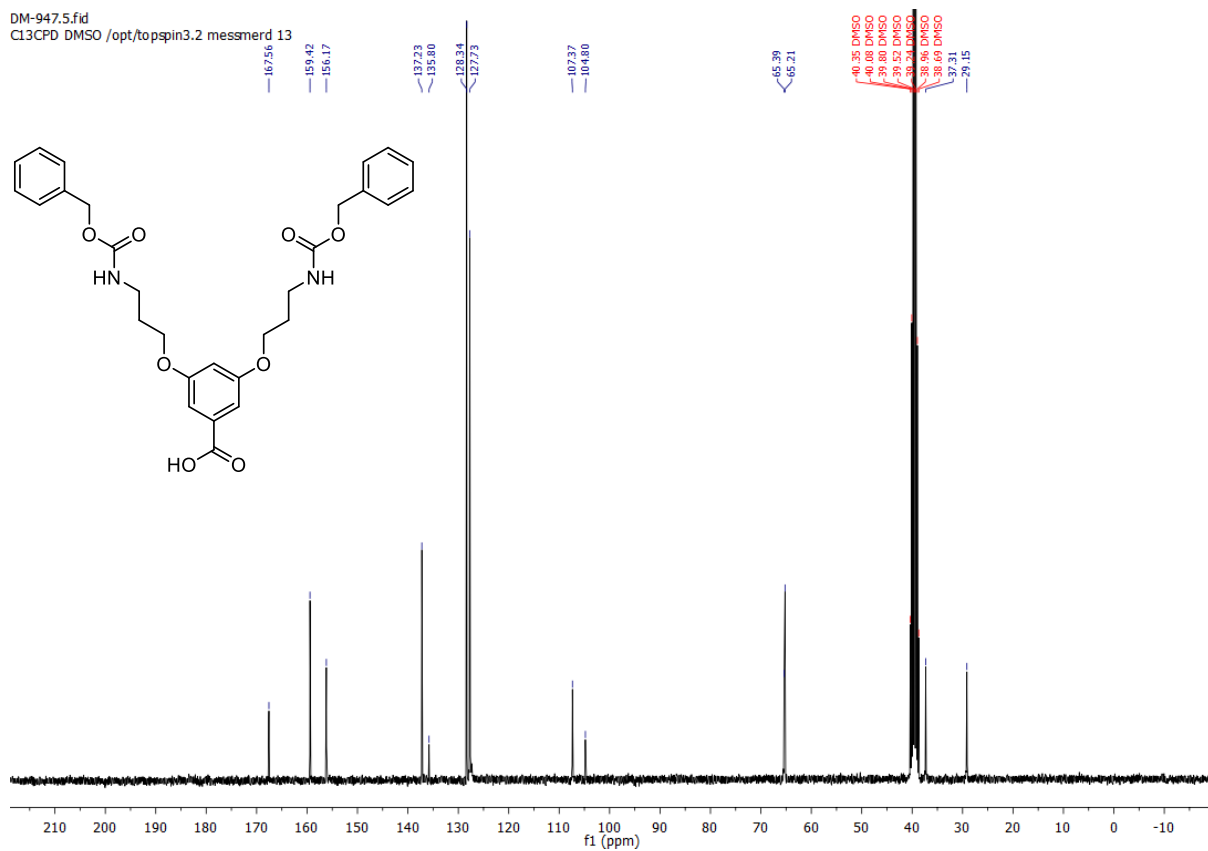
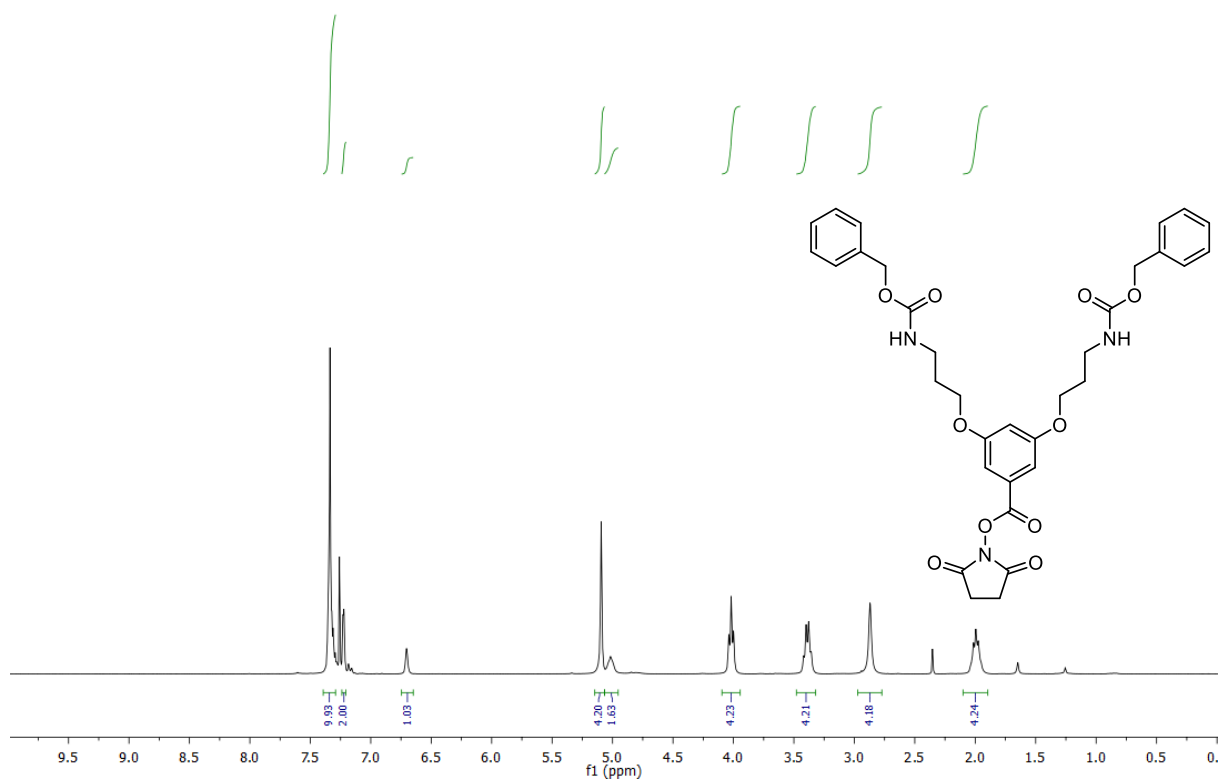
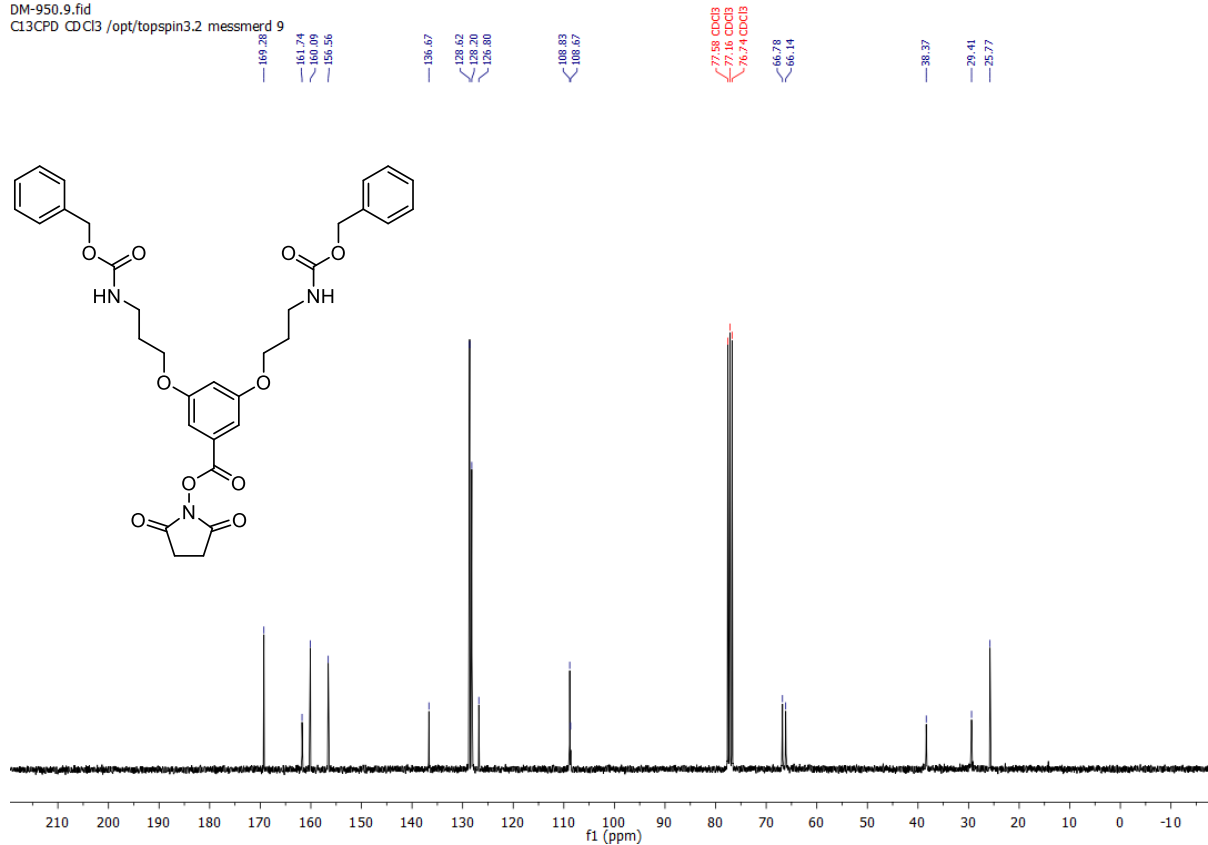


Figure A-52: <sup>13</sup>C-NMR spectrum of 101.

DM-950.4.fid  
PROTON CDCl3 /opt/topspin3.2 messmerd 7



DM-950.9.fid  
C13CPD CDCl3 /opt/topspin3.2 messmerd 9





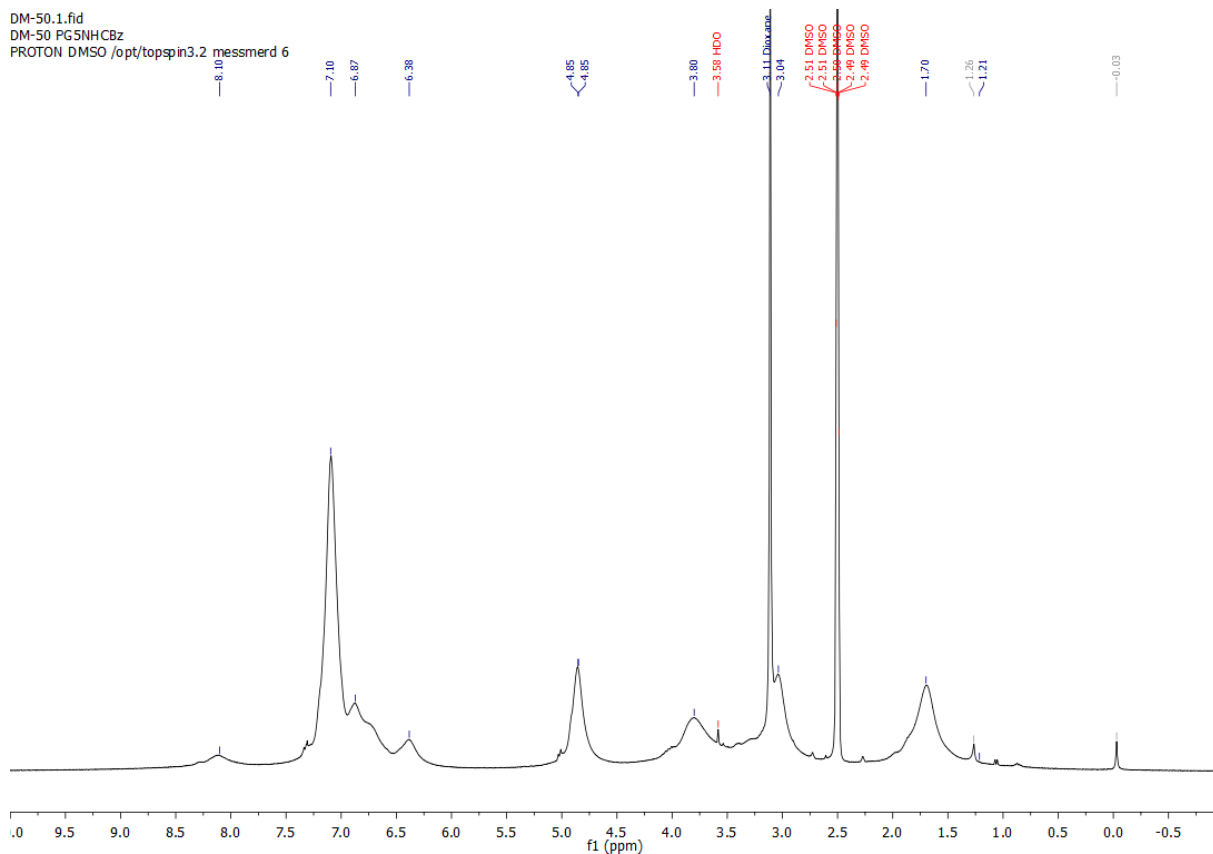


Figure A-55:  $^1\text{H-NMR}$  spectrum of  $\text{PG5}_{500}^{\text{NHCBz}}$  (**29**).

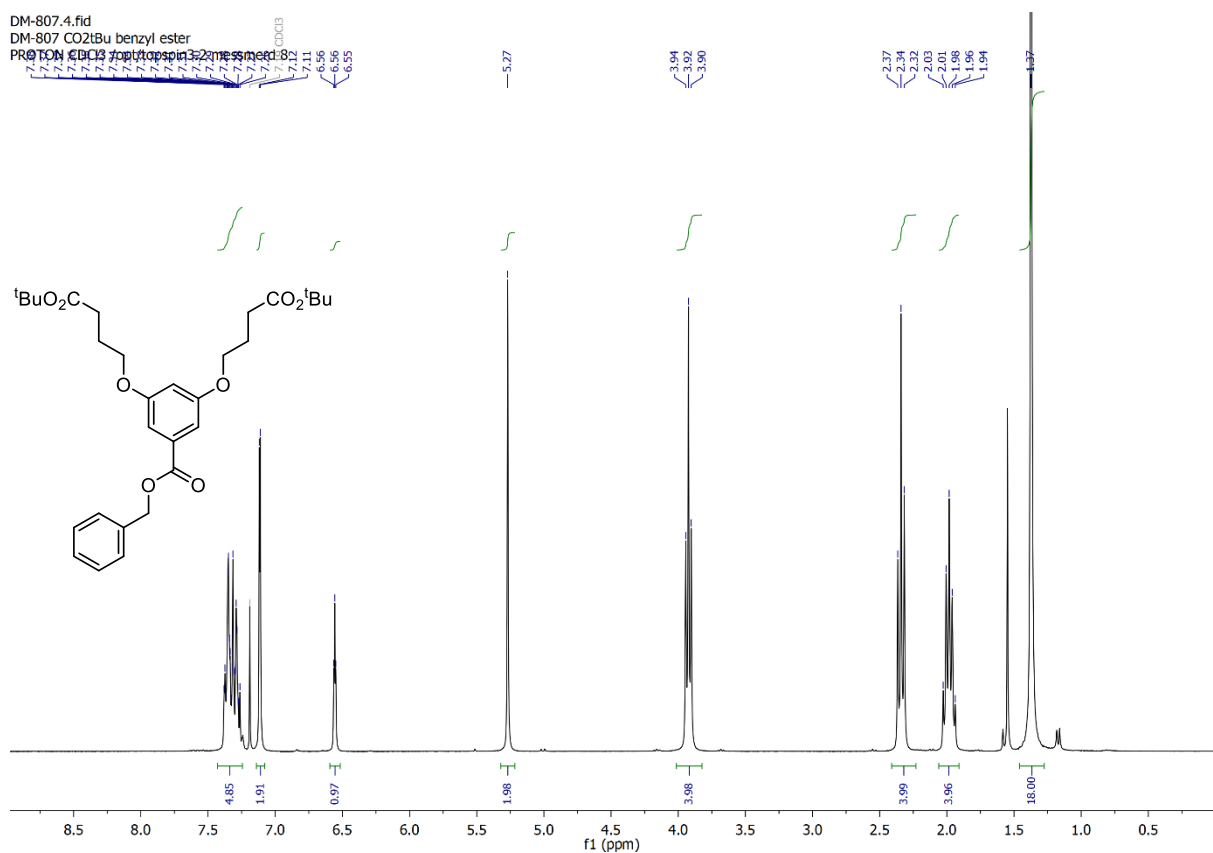
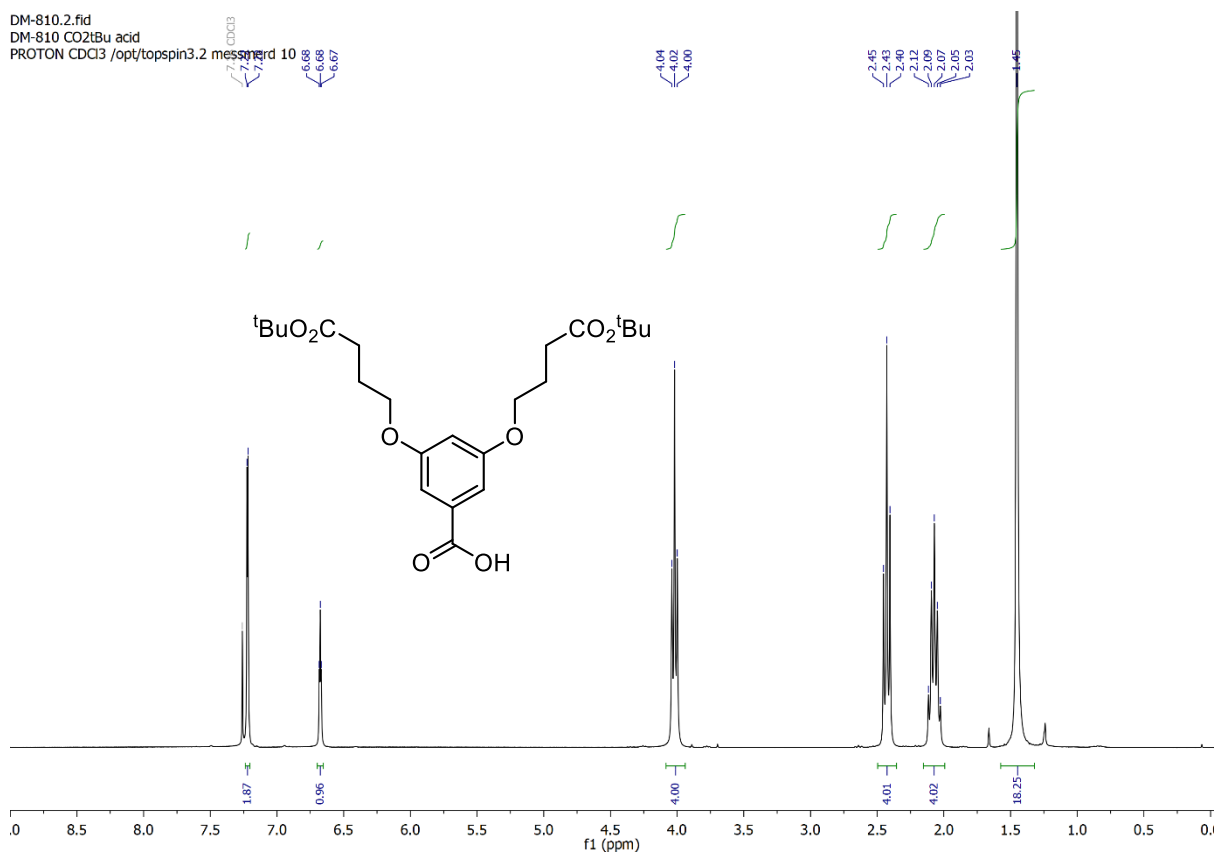
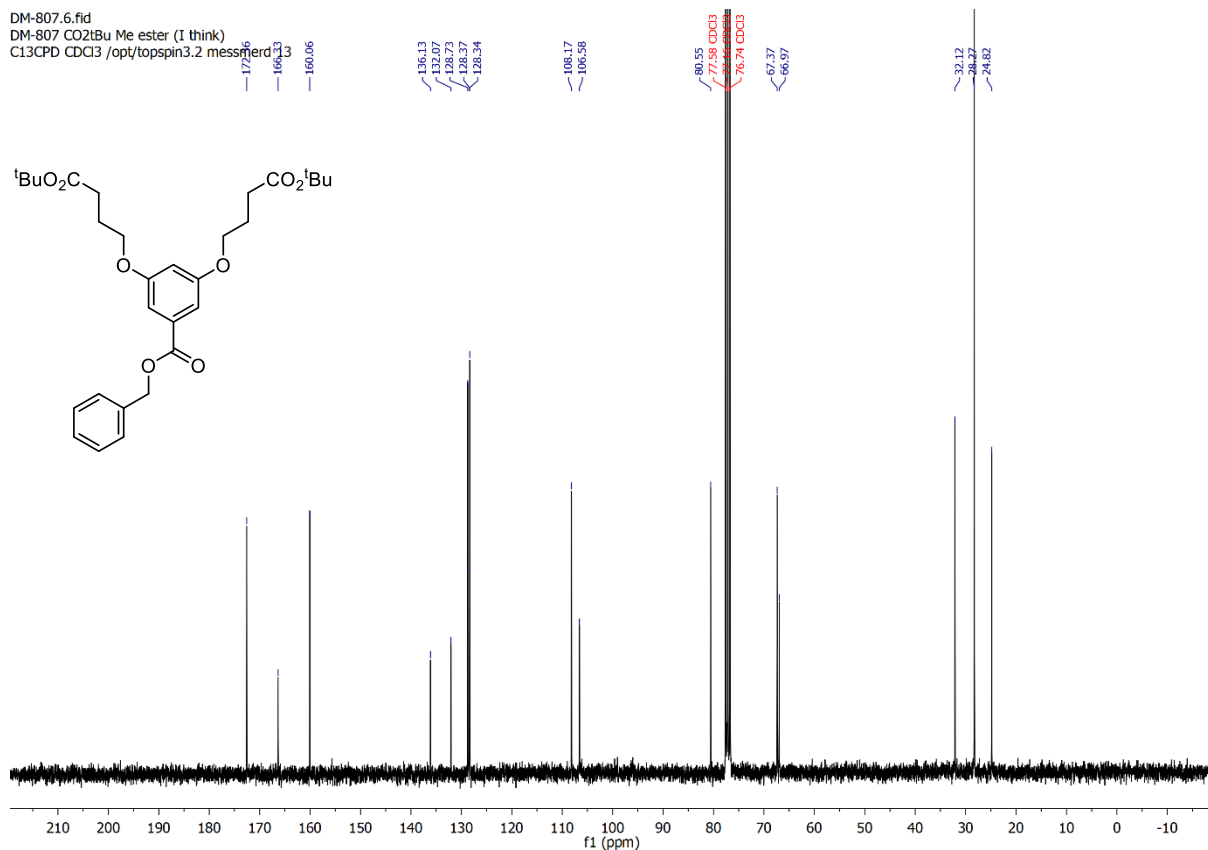
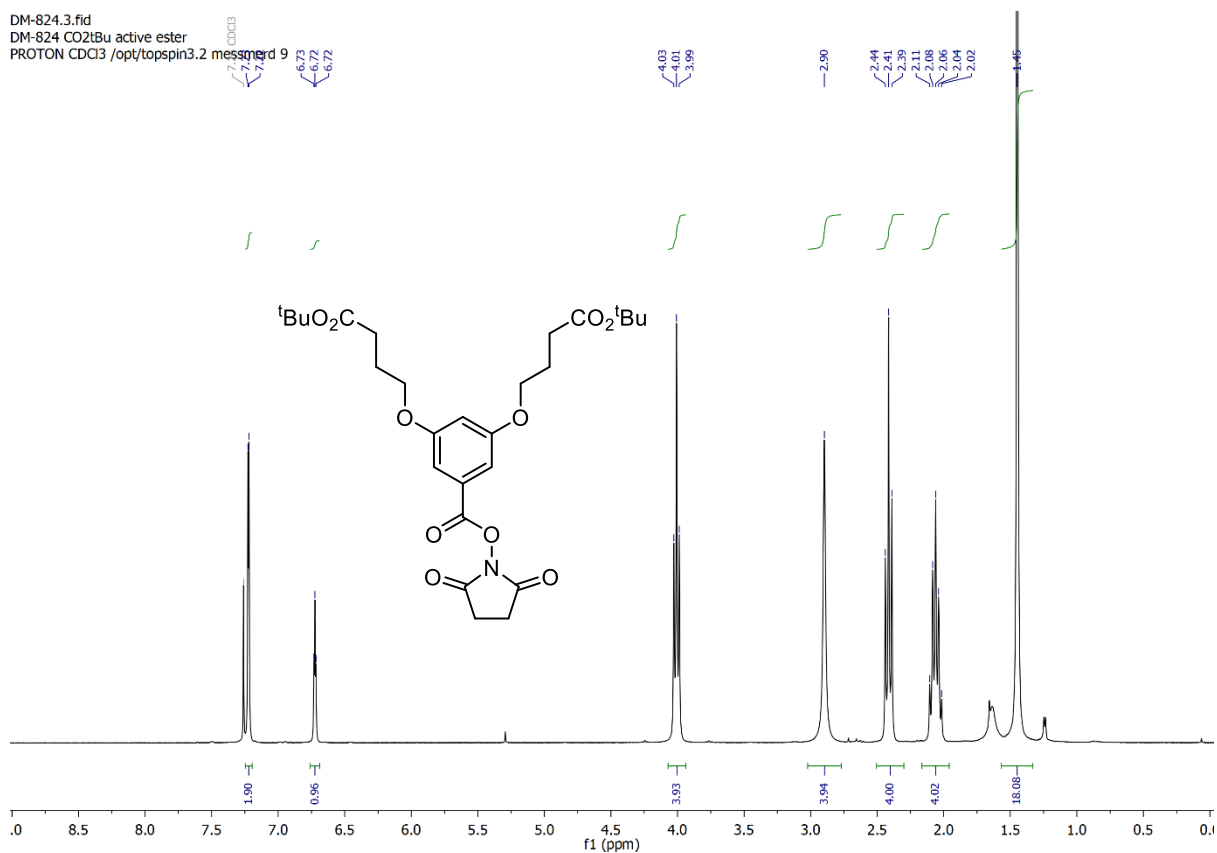
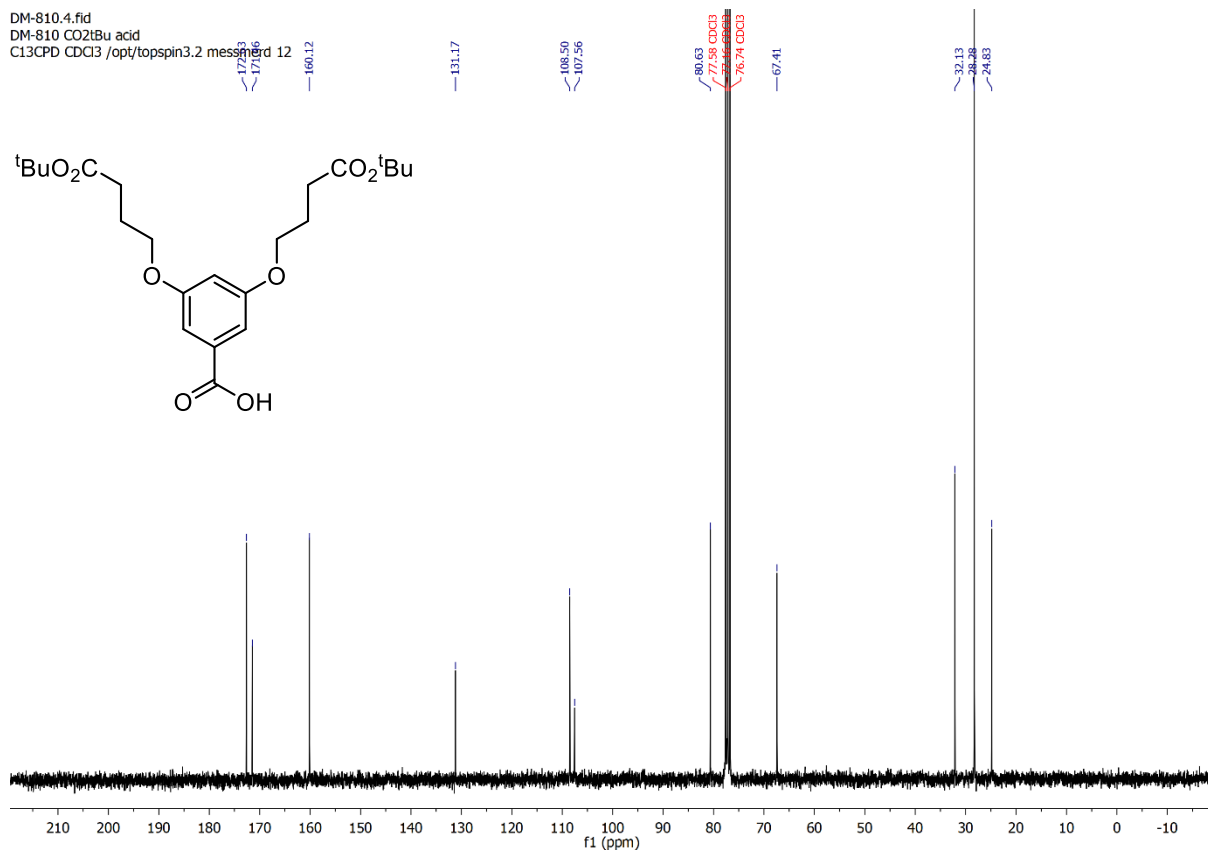
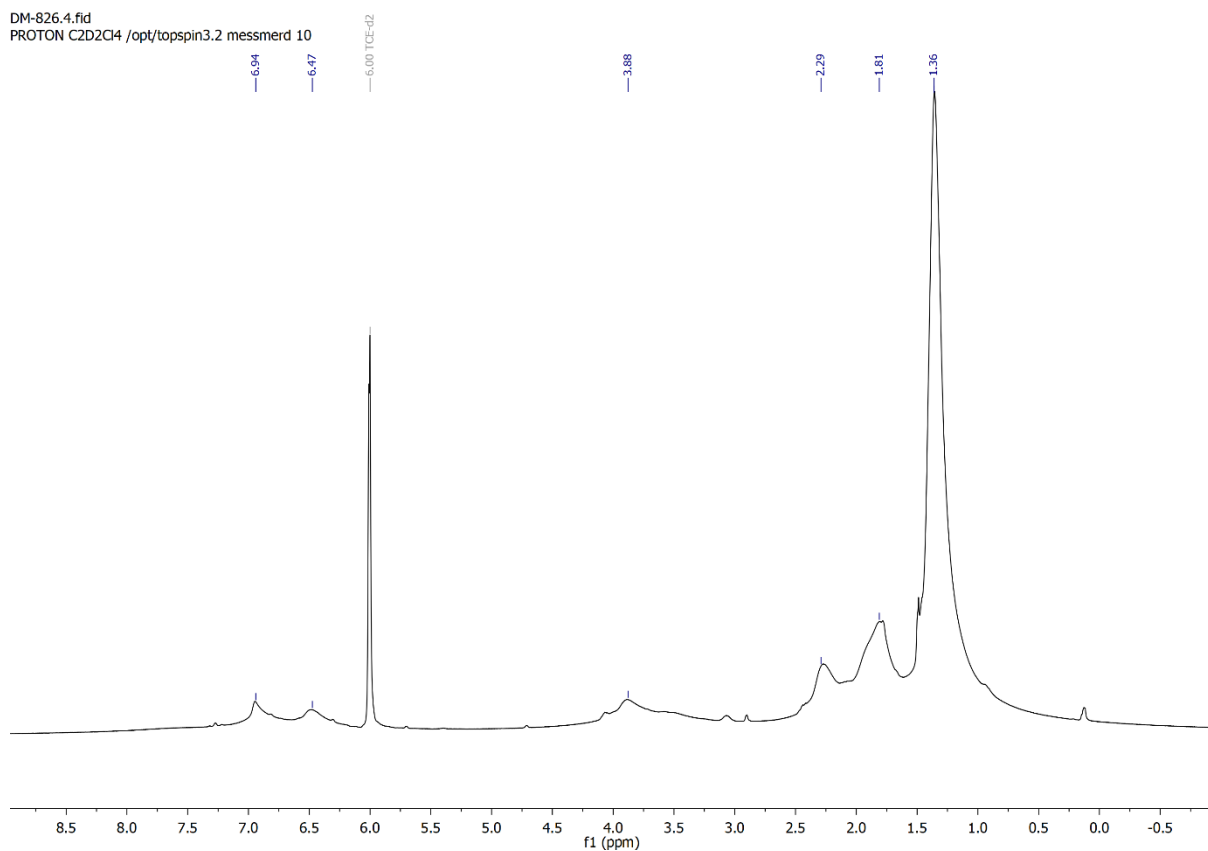
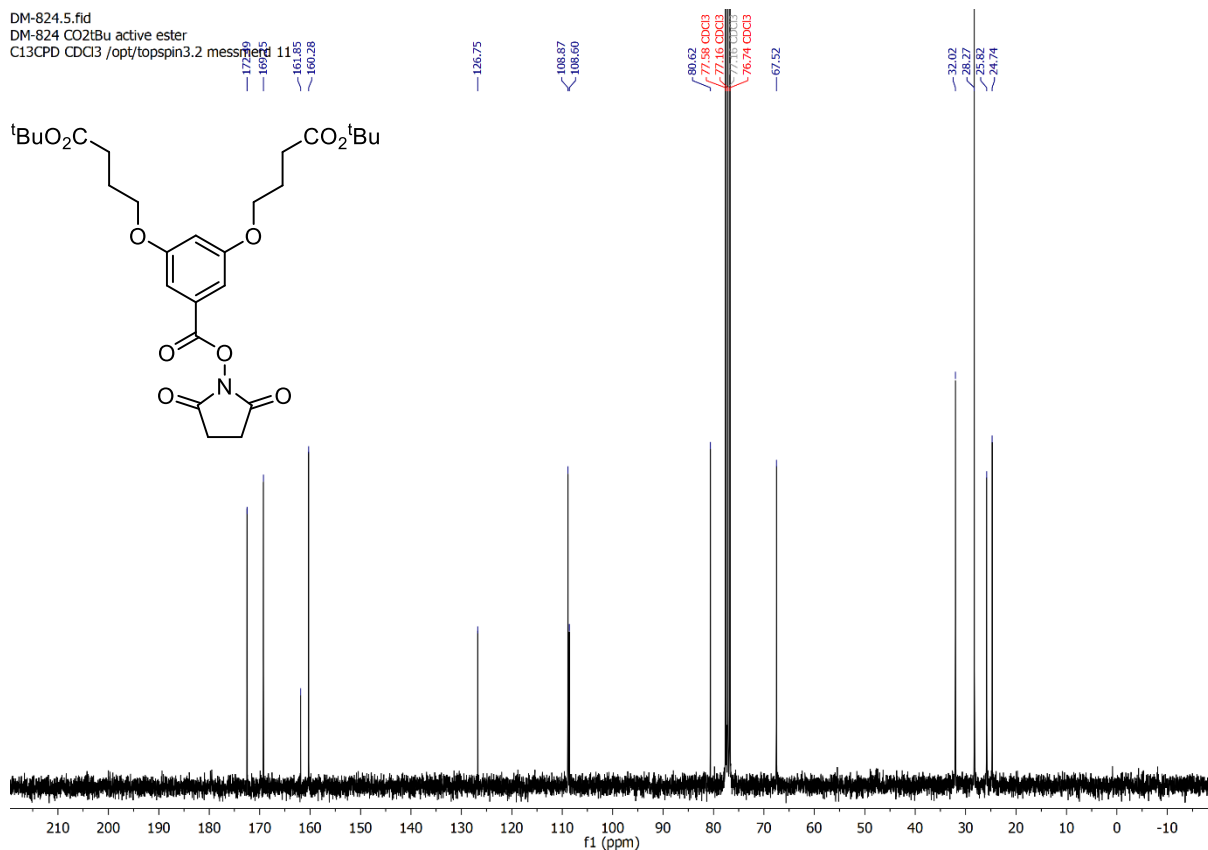


Figure A-56:  $^1\text{H-NMR}$  spectrum of **60**.







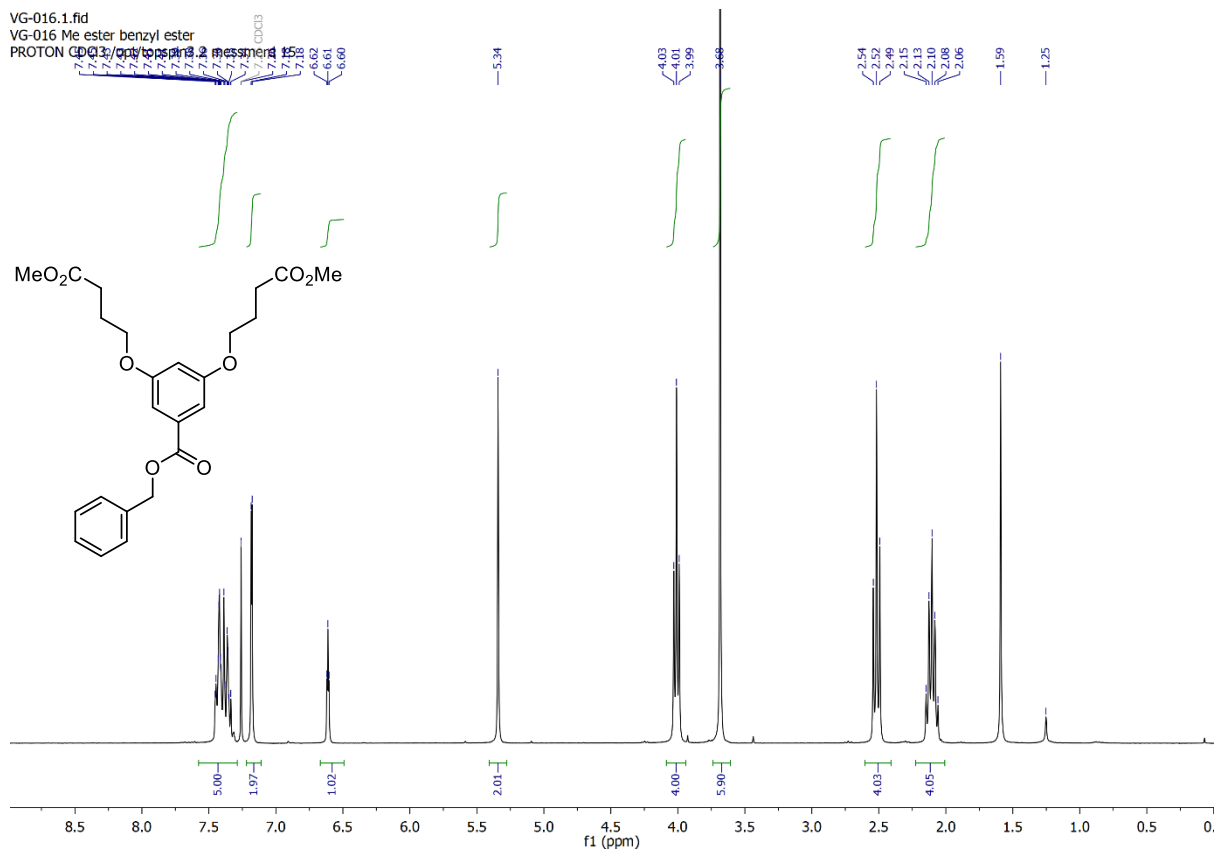


Figure A-63:  $^1\text{H-NMR}$  spectrum of 65.

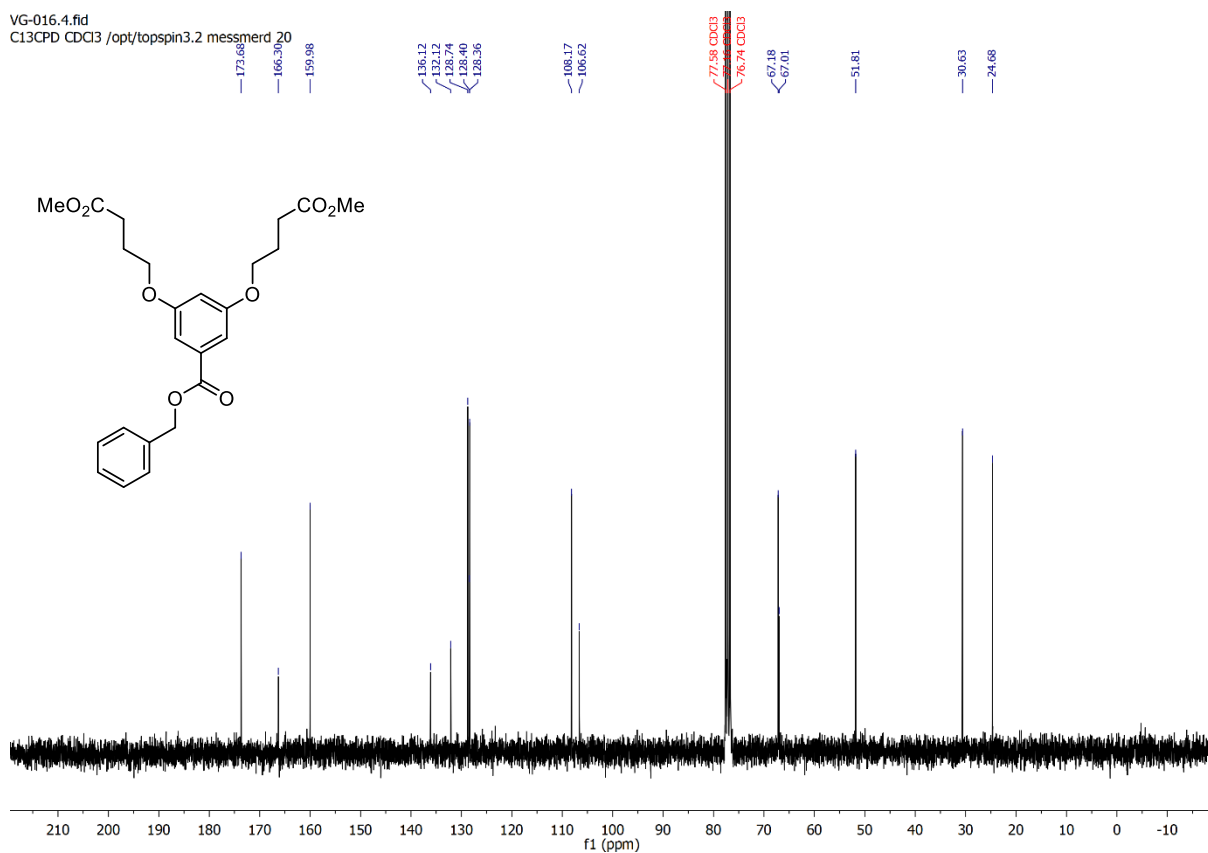


Figure A-64:  $^{13}\text{C-NMR}$  spectrum of 65.

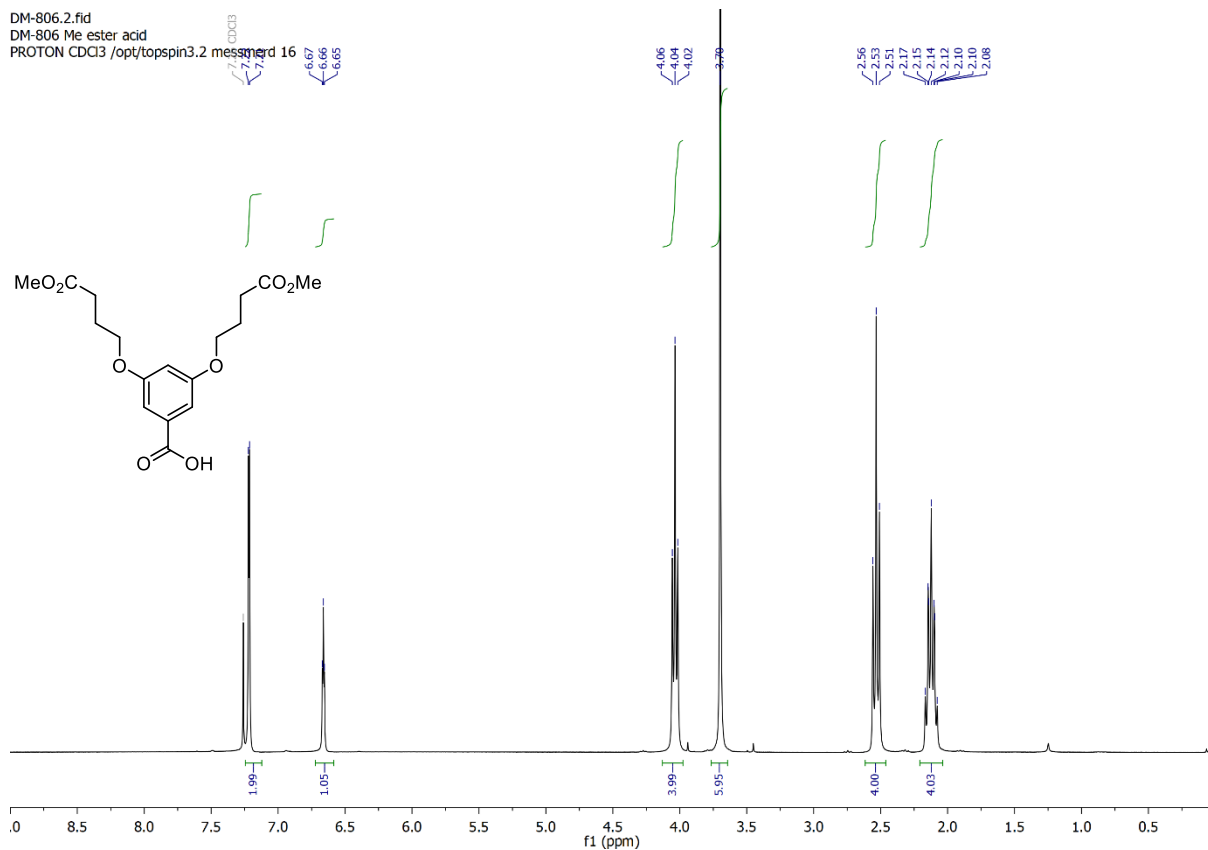


Figure A-65:  $^1\text{H-NMR}$  spectrum of 66.

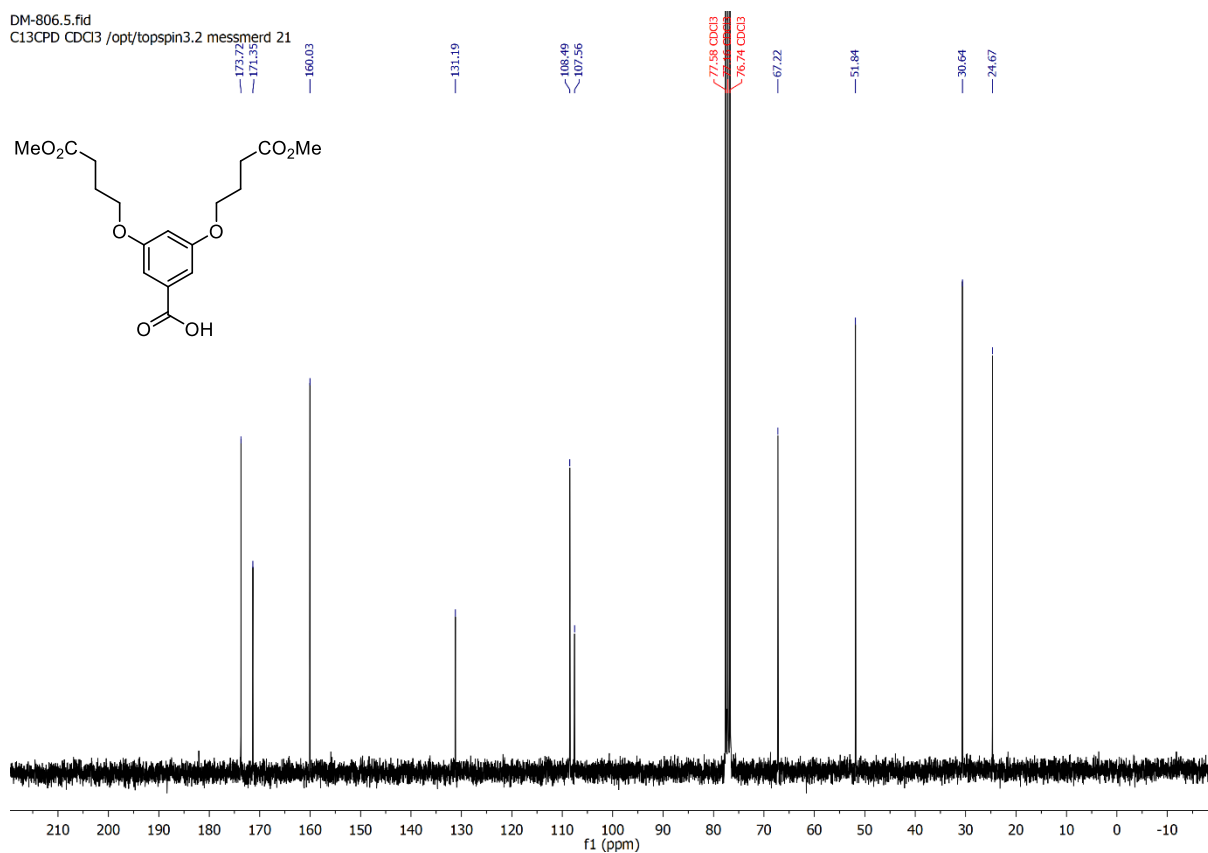


Figure A-66:  $^{13}\text{C-NMR}$  spectrum of 66.

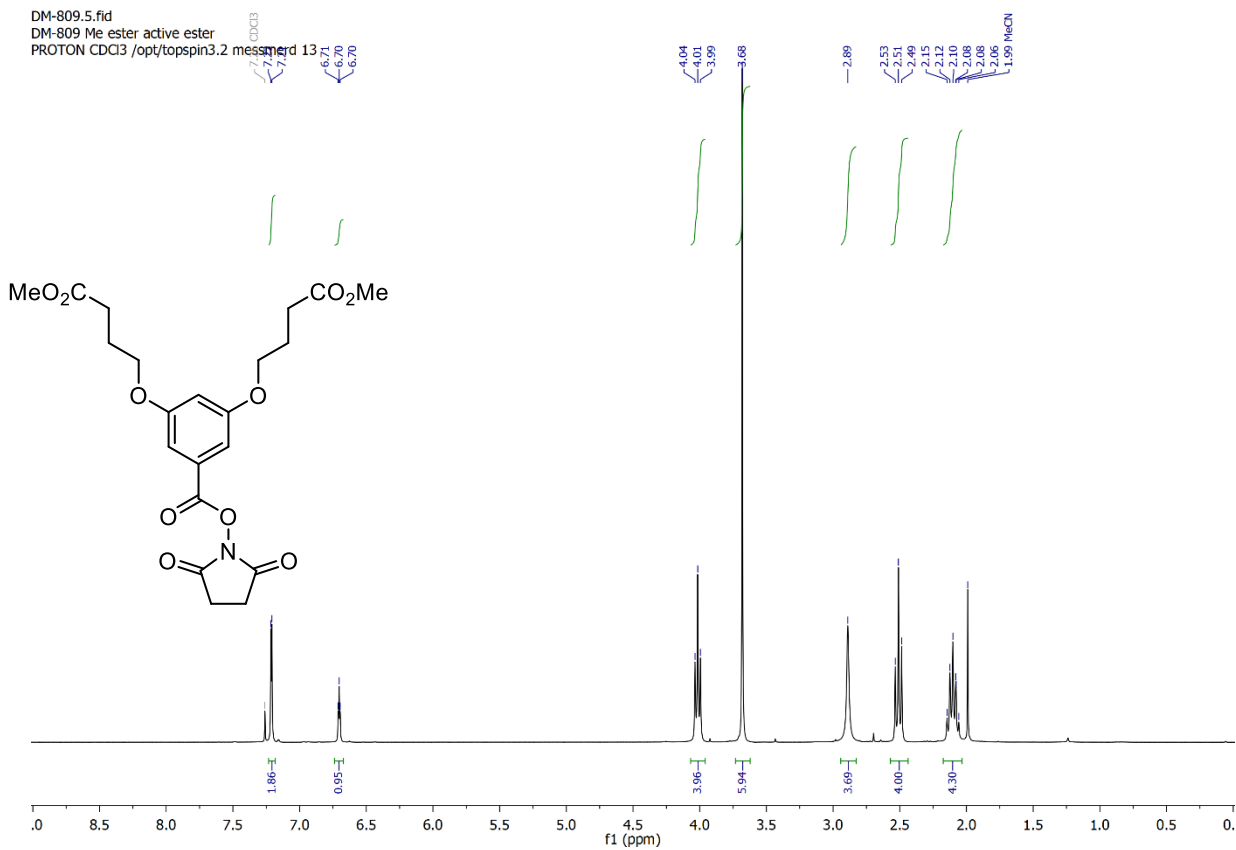


Figure A-67: <sup>1</sup>H-NMR spectrum of 67.

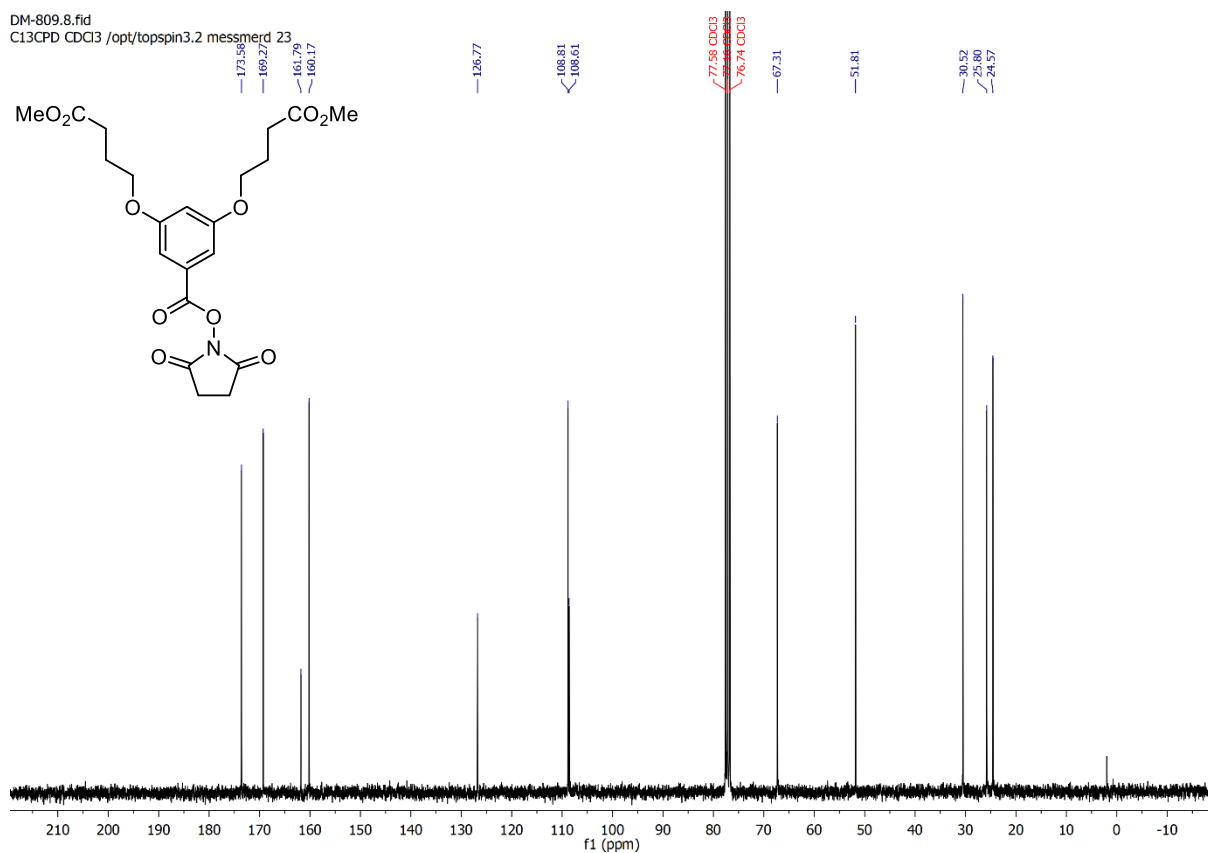


Figure A-68: <sup>13</sup>C-NMR spectrum of 67.

DM-916.1.fid  
DM-916 PG5 Me ester  
PROTON DMSO /opt/topspin3.2 messmerd 26

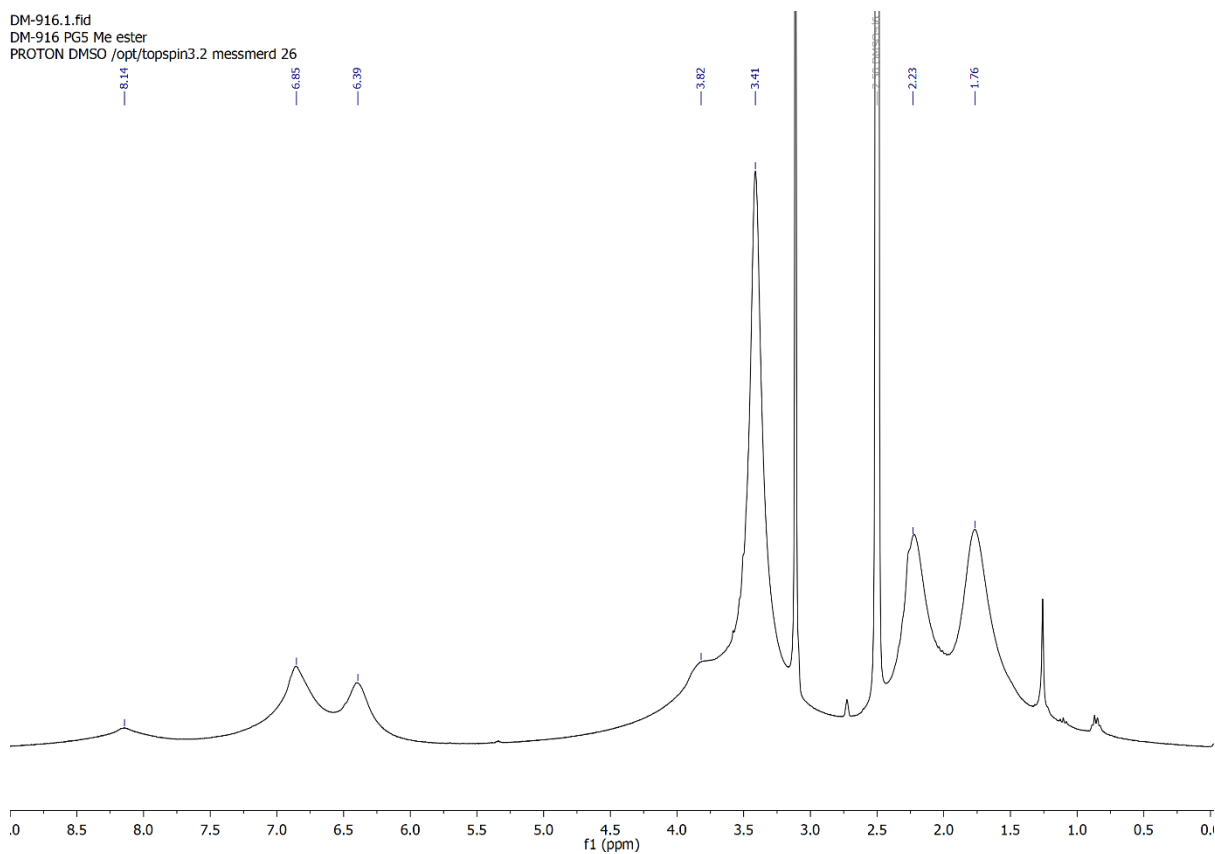


Figure A-69:  $^1\text{H-NMR}$  spectrum of  $\text{PG5}_{500}^{\text{CO}_2\text{Me}}$  **33**.

DM-953.1.fid  
PROTON DMSO /opt/topspin3.2 messmerd 32

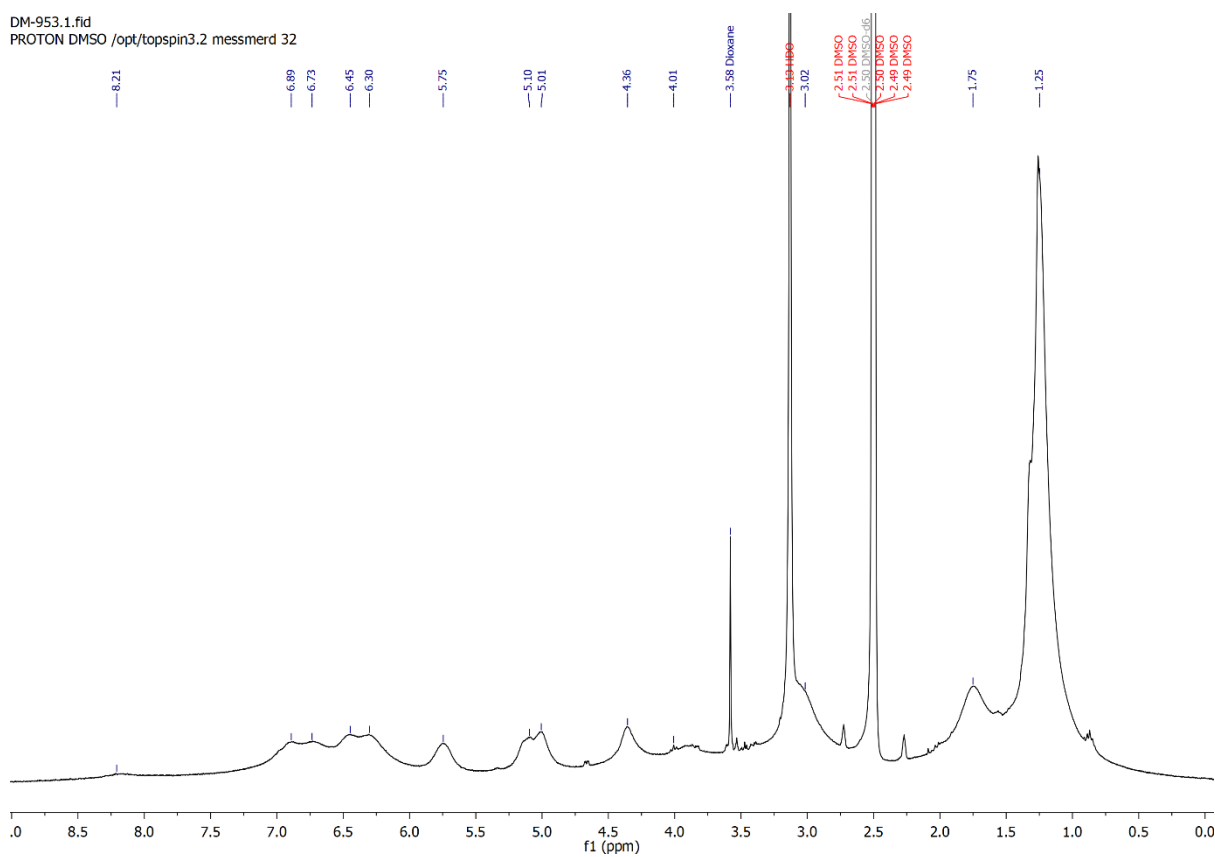


Figure A-70:  $^1\text{H-NMR}$  spectrum of  $\text{PG5}_{500}^{\text{Alloc36}}$ .



DM-954.1.fid  
PROTON DMSO /opt/topspin3.2 messmerd 33

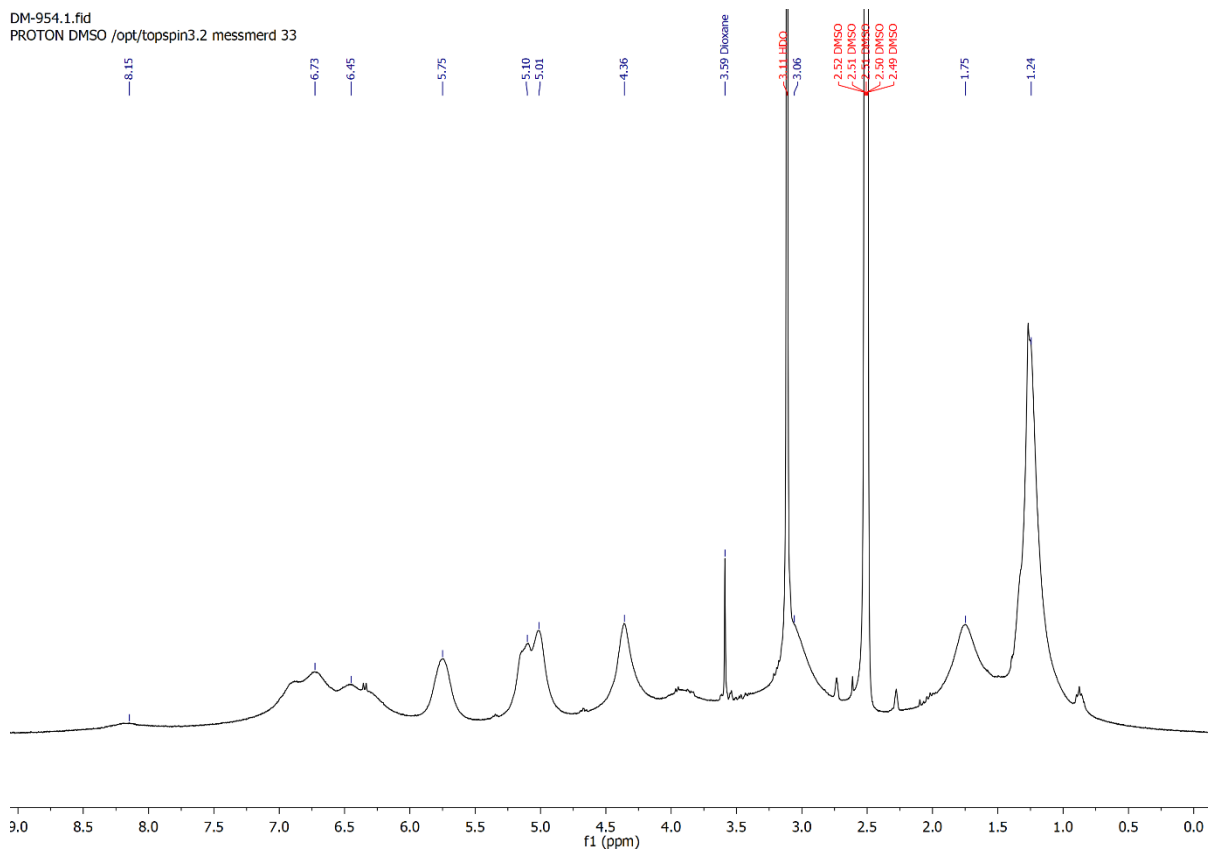


Figure A-71:  $^1\text{H-NMR}$  spectrum of  $\text{PG5}_{500}^{\text{Alloc57}}$ .

DM-955.1.fid  
PROTON DMSO /opt/topspin3.2 messmerd 34

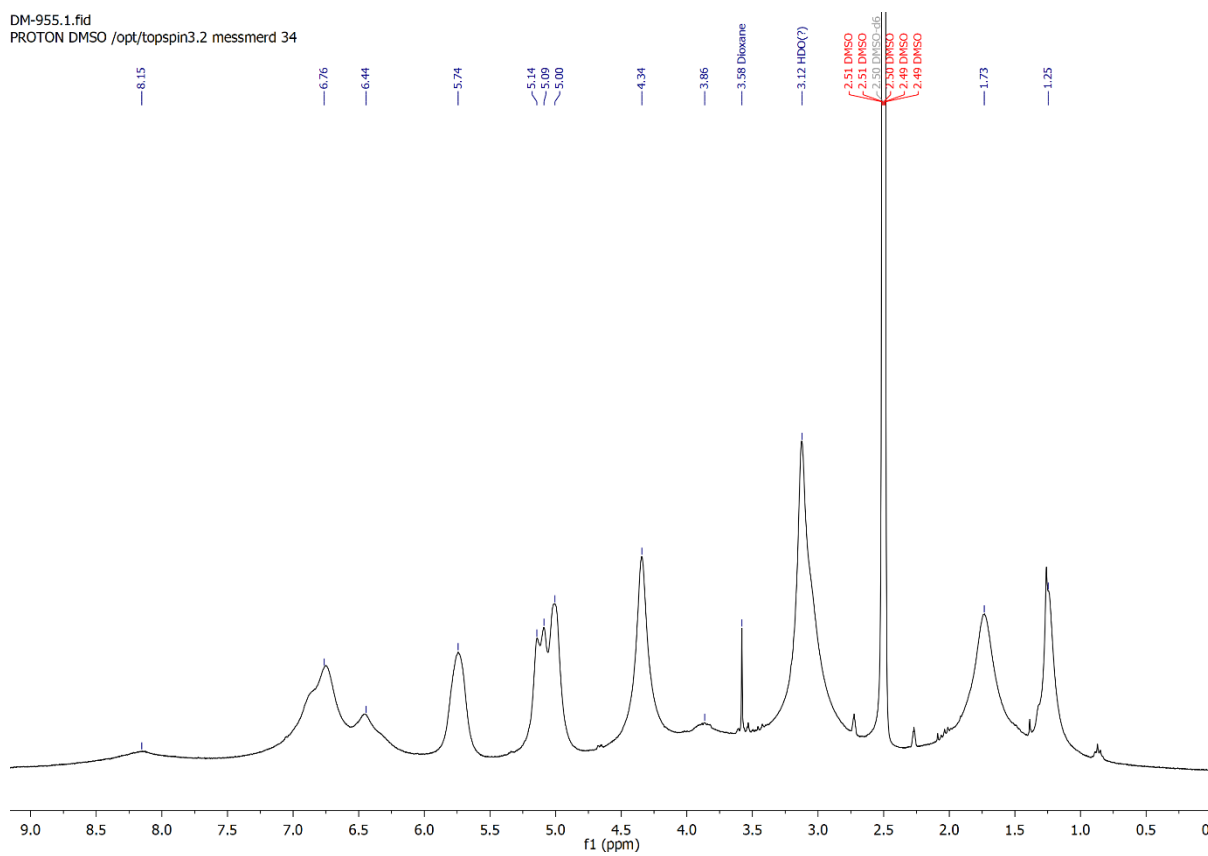


Figure A-72:  $^1\text{H-NMR}$  spectrum of  $\text{PG5}_{500}^{\text{Alloc80}}$ .

VG-010.1.fid  
PROTON DMSO /opt/topspin3.2 messmerd 18

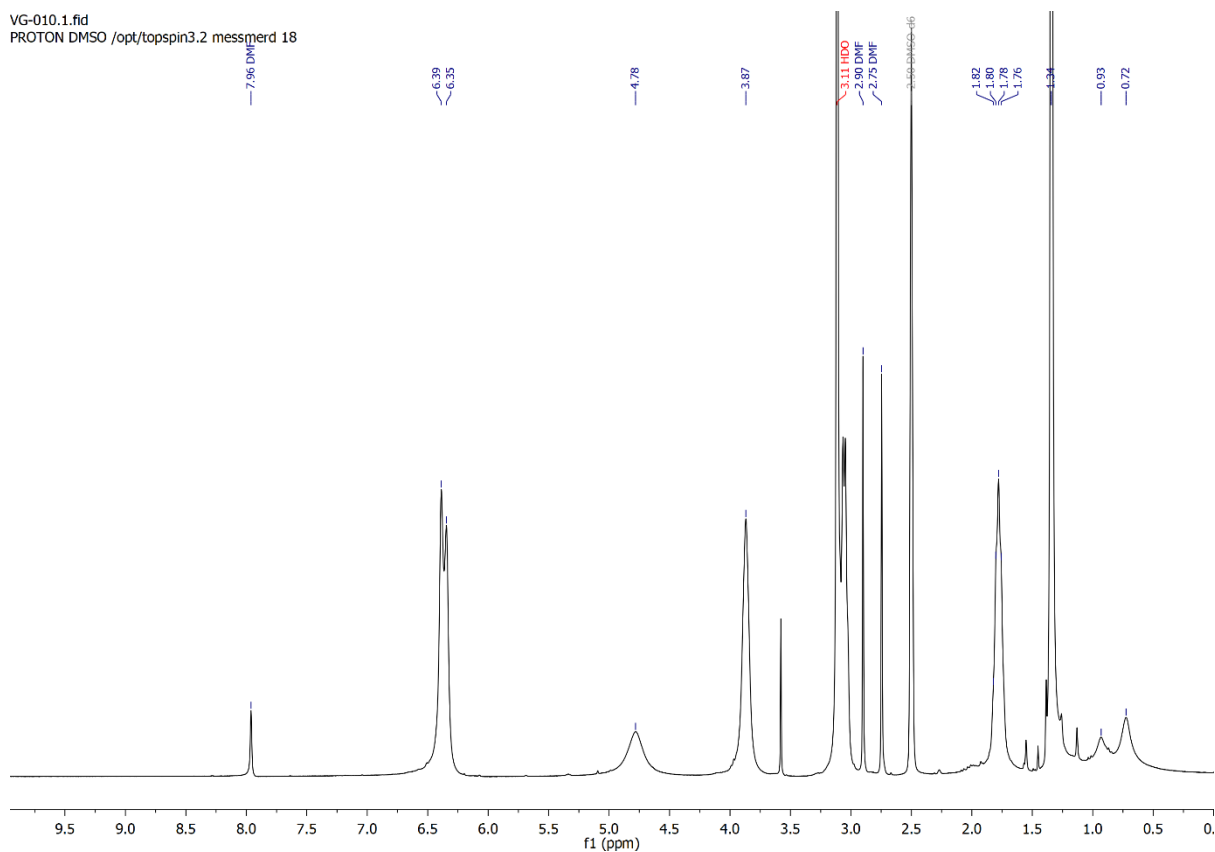


Figure A-73: <sup>1</sup>H-NMR spectrum of PG<sub>1</sub><sup>NHBOC</sup> (21).

DM-848.1.fid  
DM-848 PG2 > 10000  
PROTON DMSO /opt/topspin3.2 messmerd 44

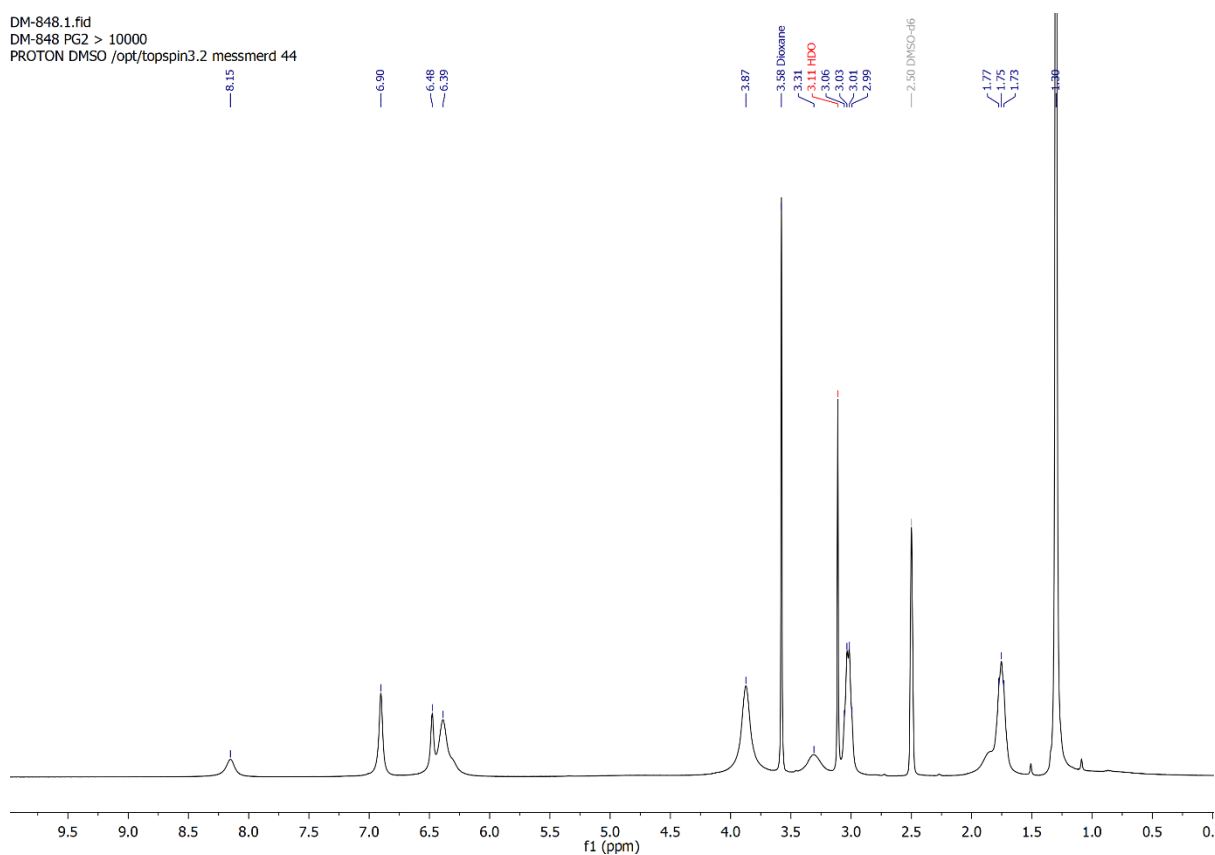


Figure A-74: <sup>1</sup>H-NMR spectrum of PG<sub>2</sub><sup>NHBOC</sup> (23).

DM-869.2.fid  
PROTON DMSO /opt/topspin3.2 messmerd 19

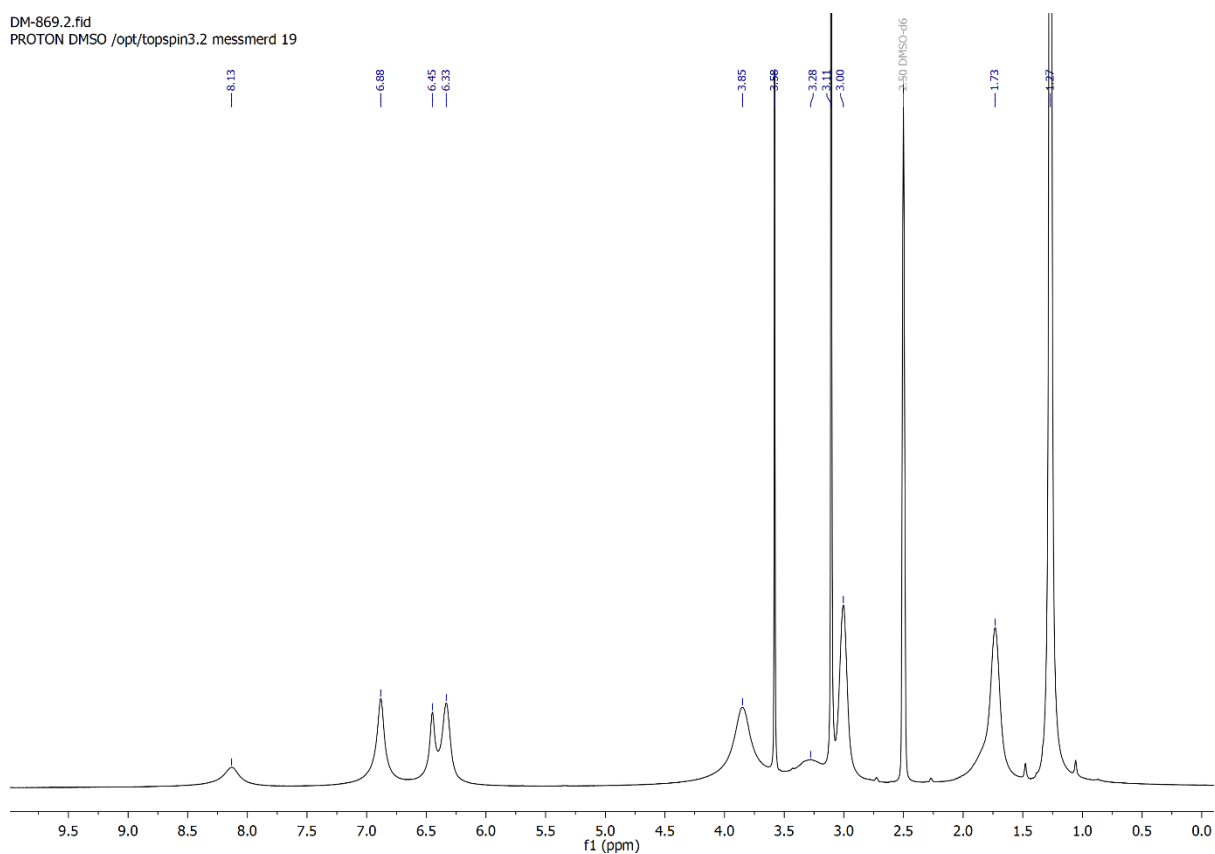


Figure A-75: <sup>1</sup>H-NMR spectrum of PG<sub>3</sub><sup>NHBOC</sup> (24).

DM-892.1.fid  
DM-892 PG4 long  
PROTON DMSO /opt/topspin3.2 messmerd 48

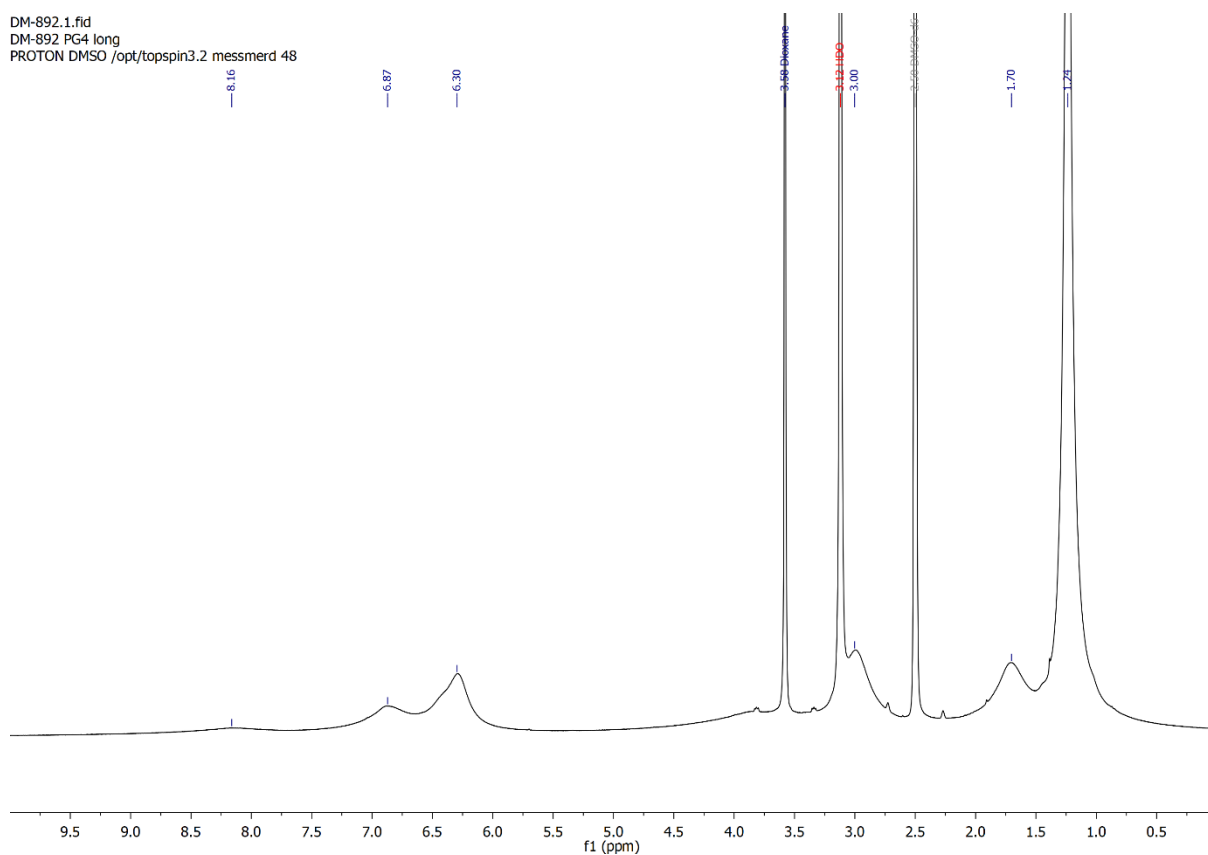


Figure A-76: <sup>1</sup>H-NMR spectrum of PG<sub>4</sub><sup>NHBOC</sup> (25).

DM-924.1.fid  
DM-924 lyophilizate  
PROTON DMSO /opt/topspin3.2 messmerd 8

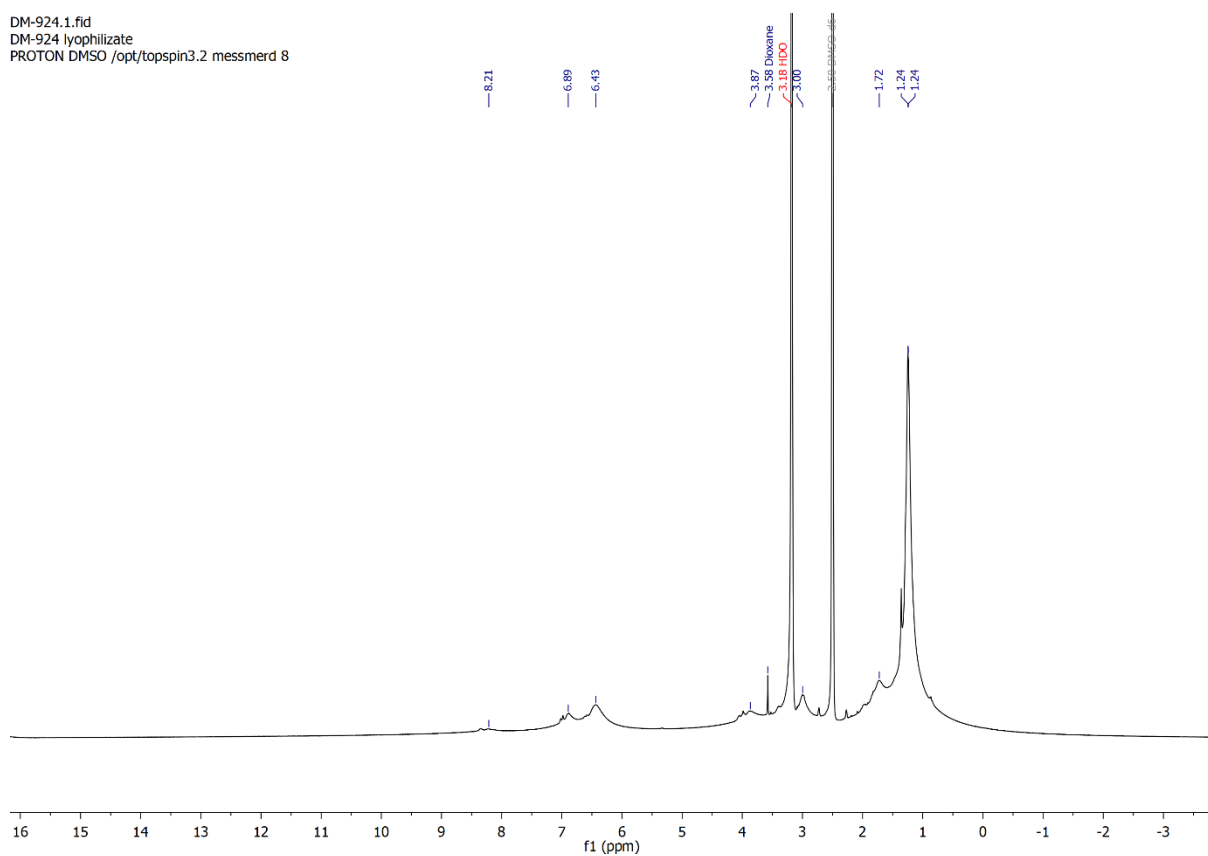


Figure A-77: <sup>1</sup>H-NMR spectrum of PG5<sup>NHBoc</sup> (26).

DM-931.1.fid  
DM-931 lyo  
PROTON DMSO /opt/topspin3.2 messmerd 9

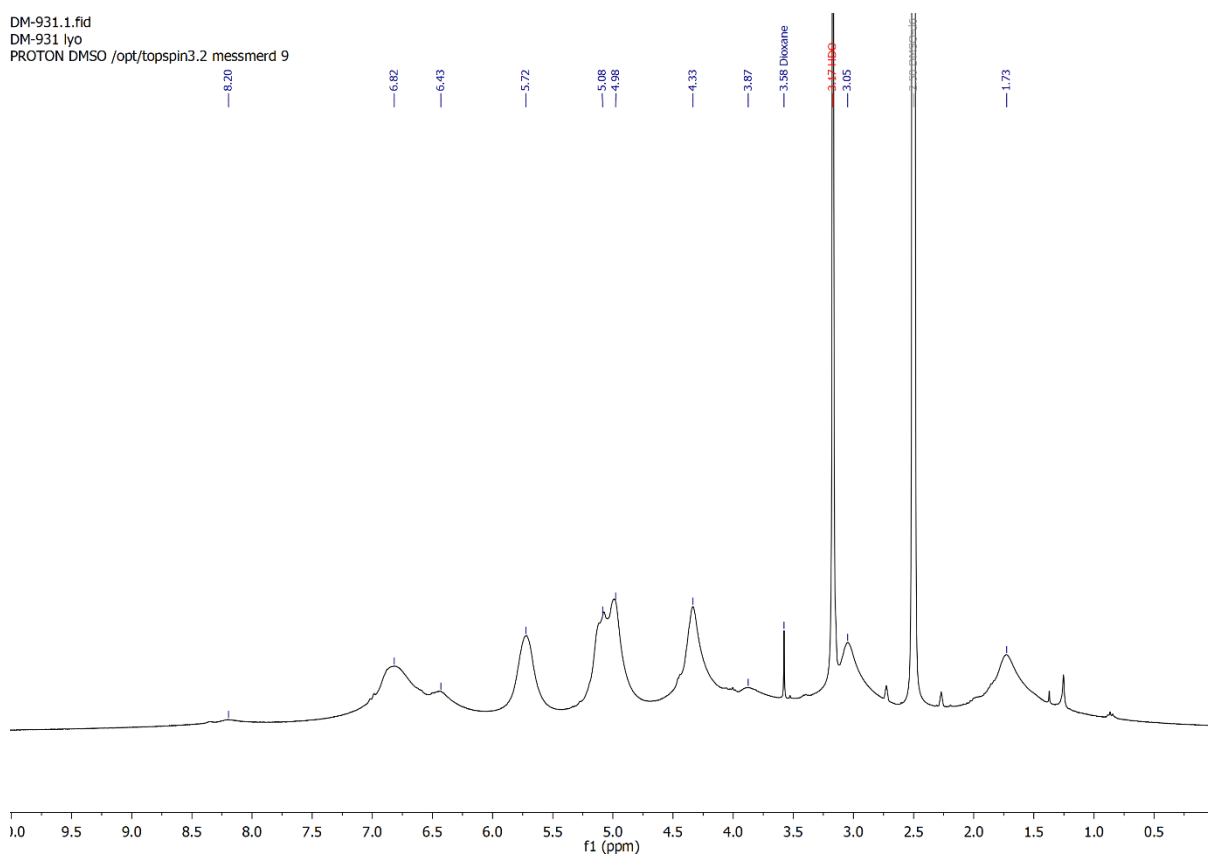


Figure A-78: <sup>1</sup>H-NMR spectrum of PG5<sup>NHAlloc</sup> (31).

DM-919.1.fid  
PROTON DMSO /opt/topspin3.2 messmerd 37

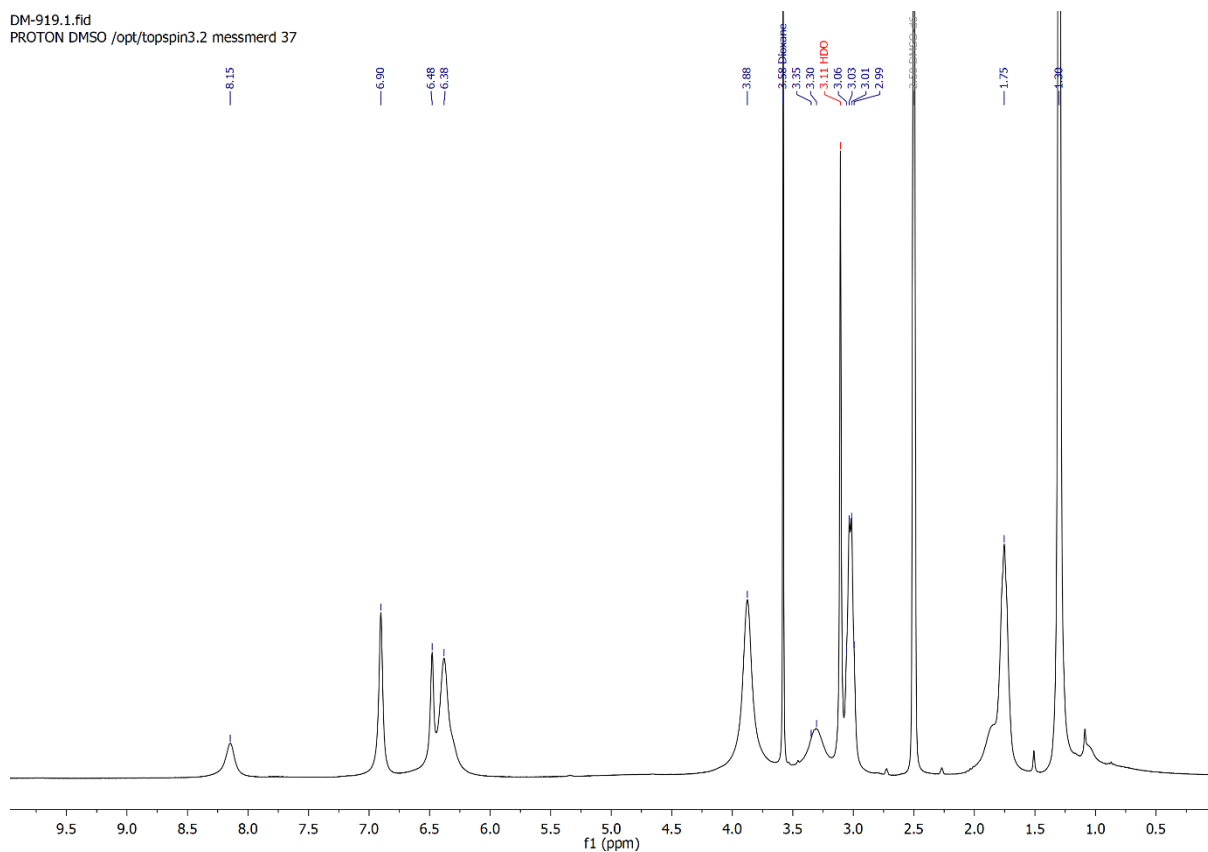


Figure A-79: <sup>1</sup>H-NMR spectrum of RhoB-PG2<sup>NHBOc</sup> (88).

DM-920.1.fid  
PROTON DMSO /opt/topspin3.2 messmerd 38

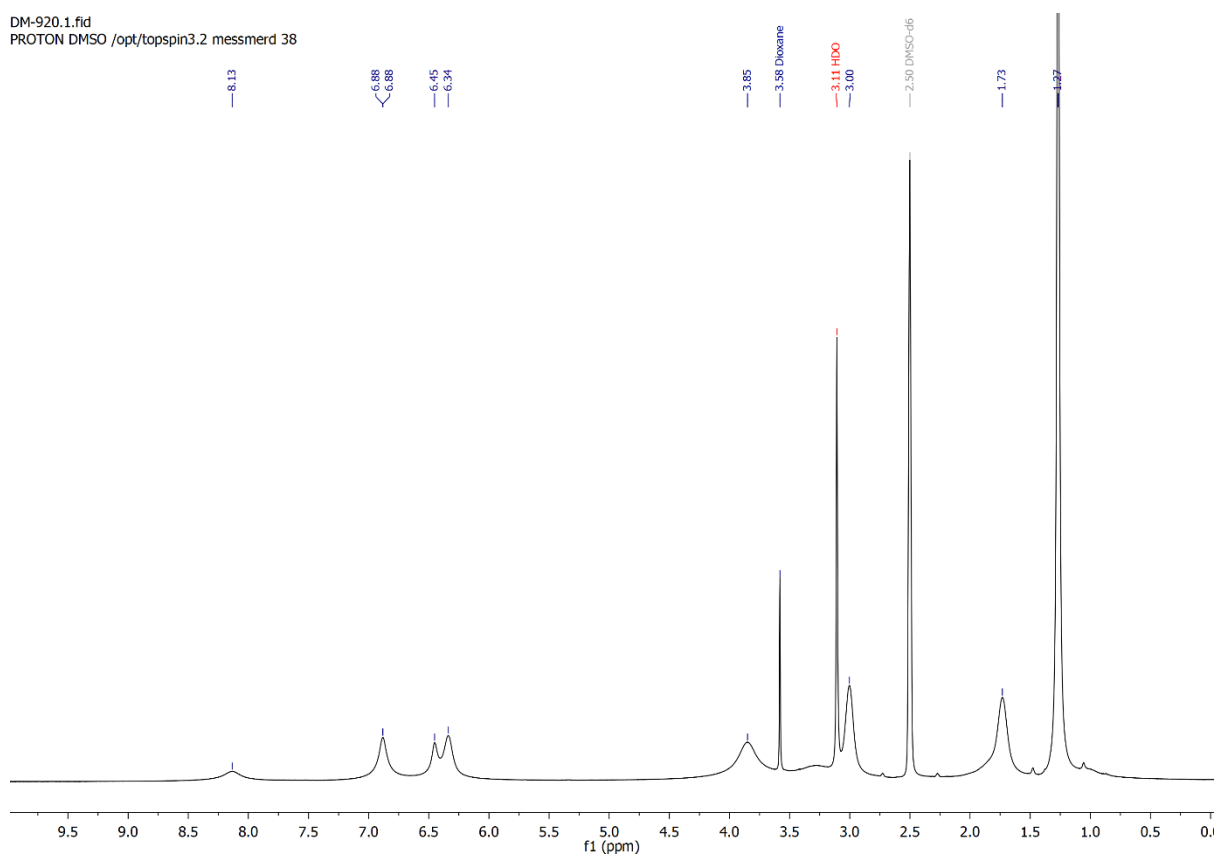


Figure A-80: <sup>1</sup>H-NMR spectrum of RhoB-PG3<sup>NHBOc</sup> (89).

DM-921.1.fid  
PROTON DMSO /opt/topspin3.2 messmerd 39

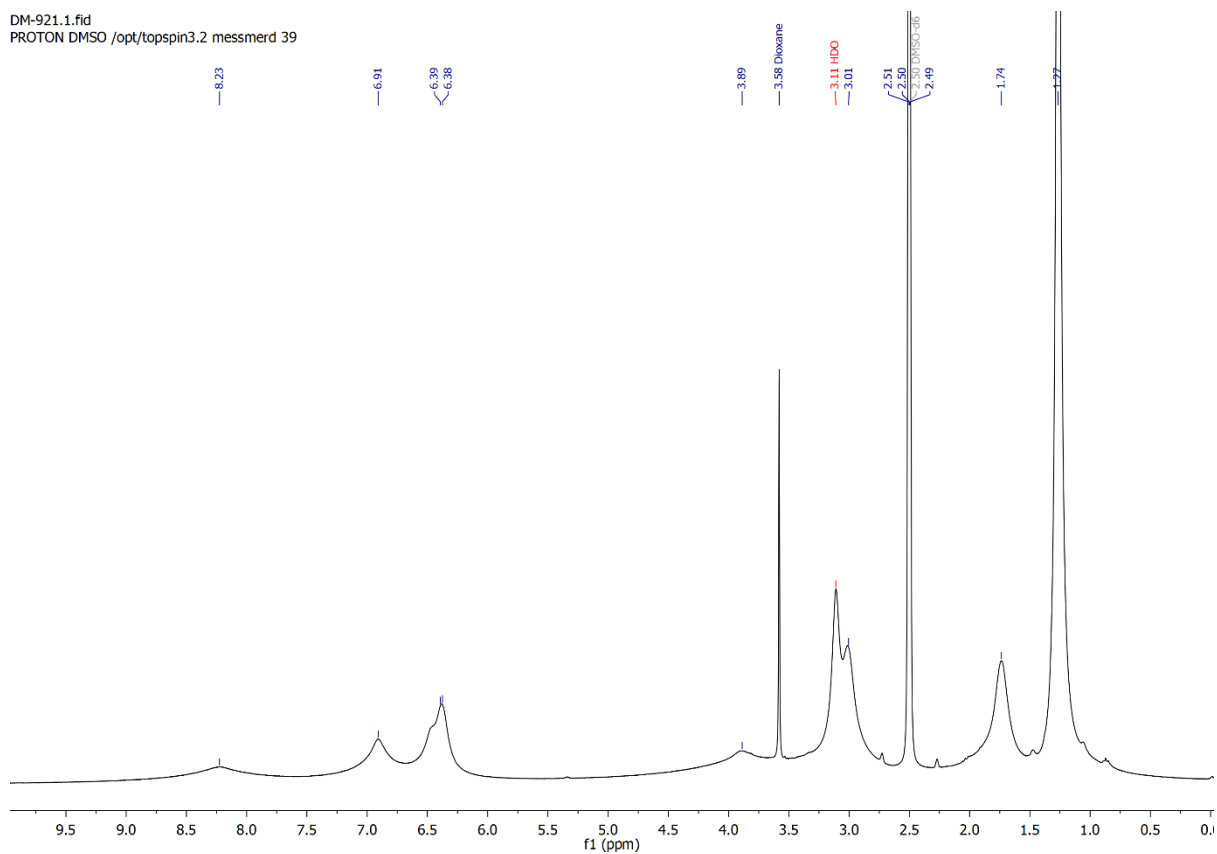


Figure A-81: <sup>1</sup>H-NMR spectrum of RhoB-PG4<sup>NHBOC</sup> (90).

DM-922.1.fid  
PROTON DMSO /opt/topspin3.2 messmerd 40

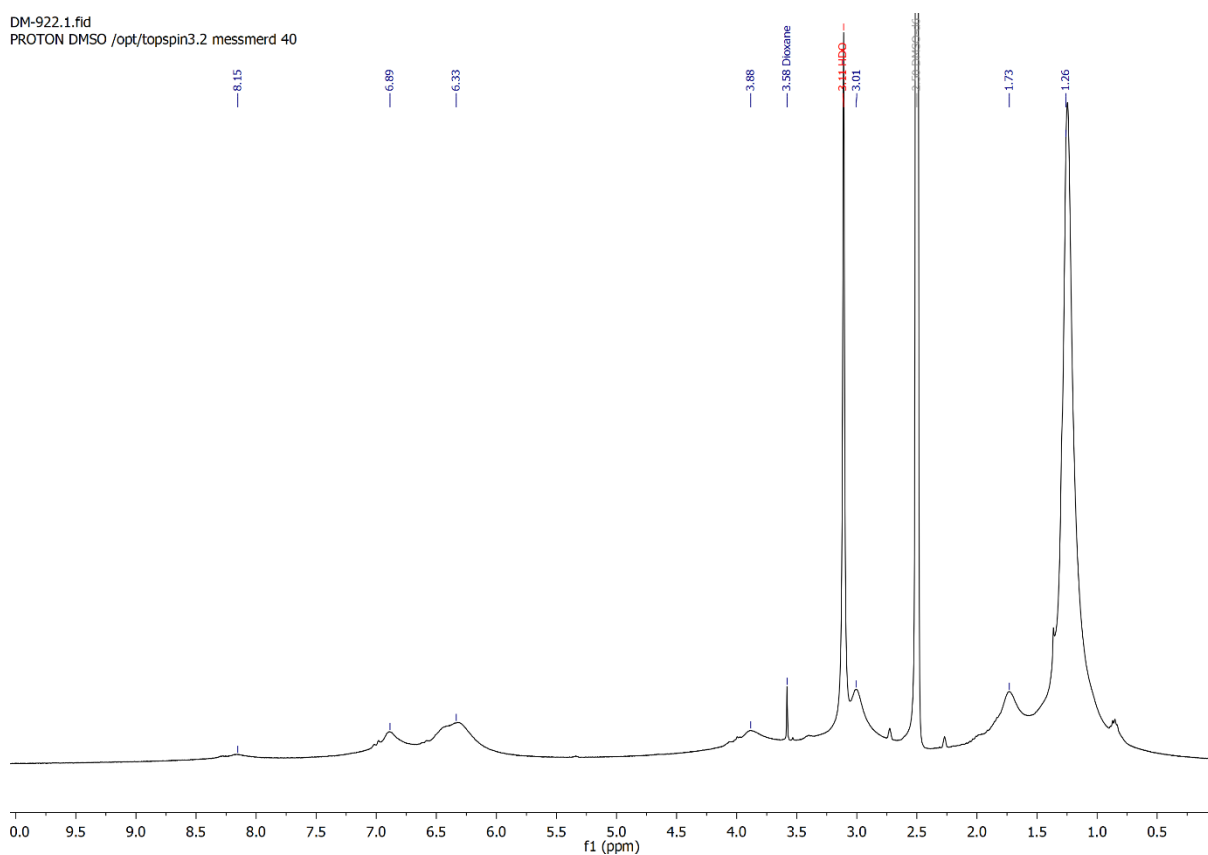


Figure A-82: <sup>1</sup>H-NMR spectrum of RhoB-PG5<sup>NHBOC</sup> (91).

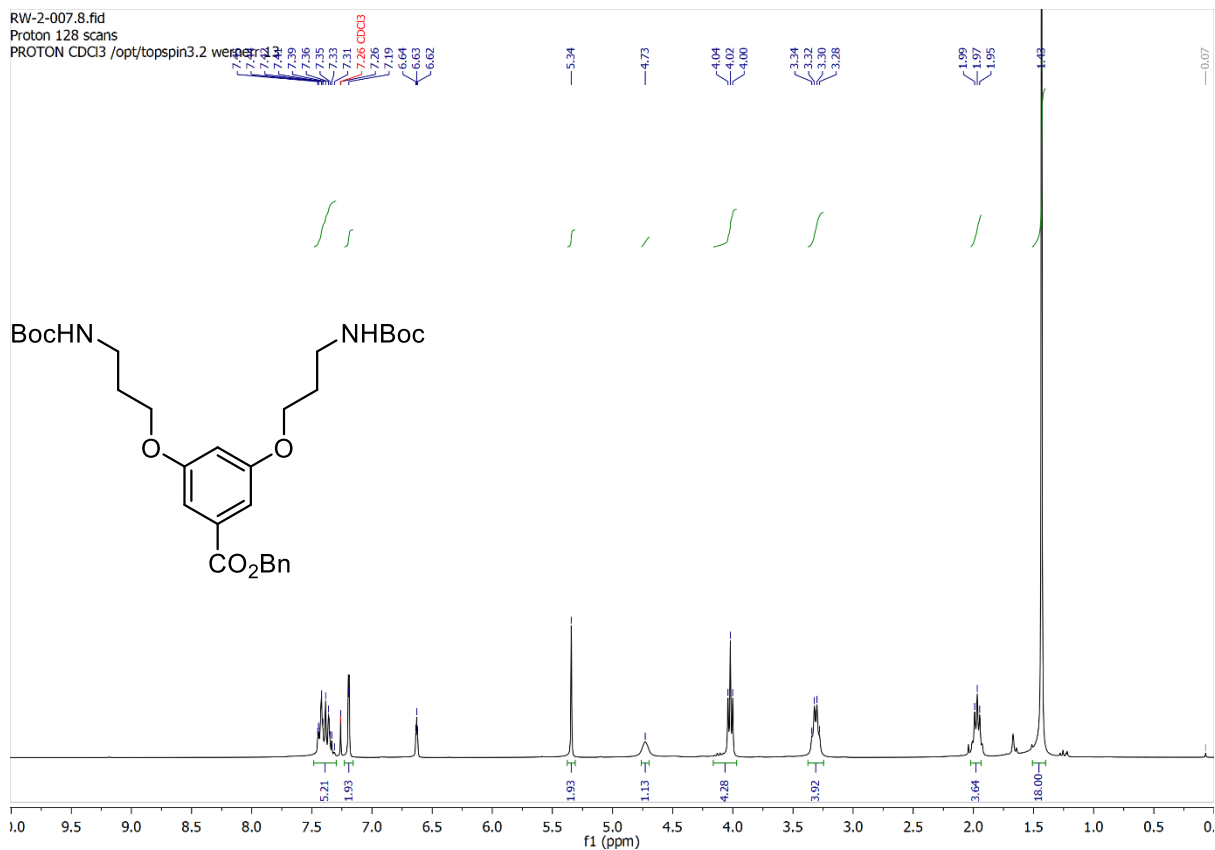


Figure A-83: <sup>1</sup>H-NMR spectrum of **92**.

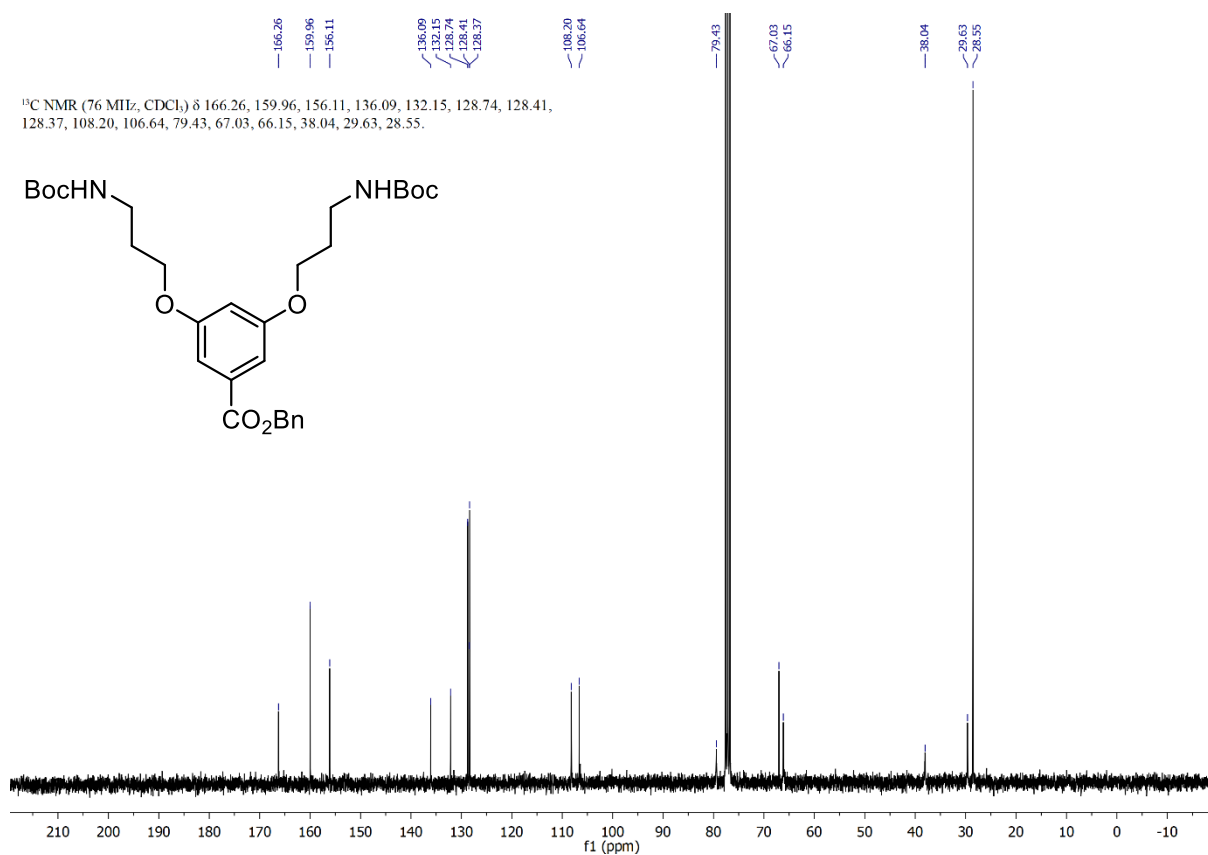


Figure A-84: <sup>13</sup>C-NMR spectrum of **92**.

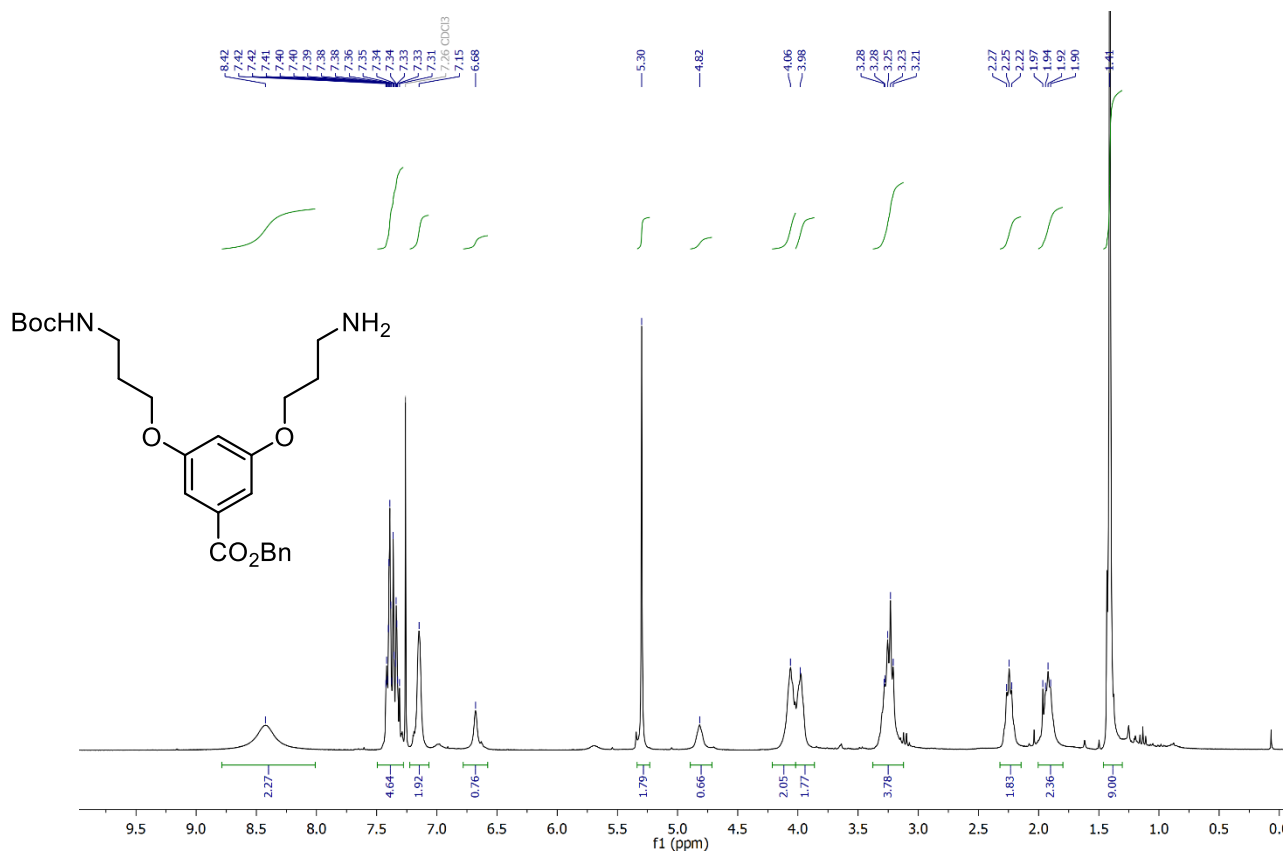


Figure A-85: <sup>1</sup>H-NMR spectrum of **93**.

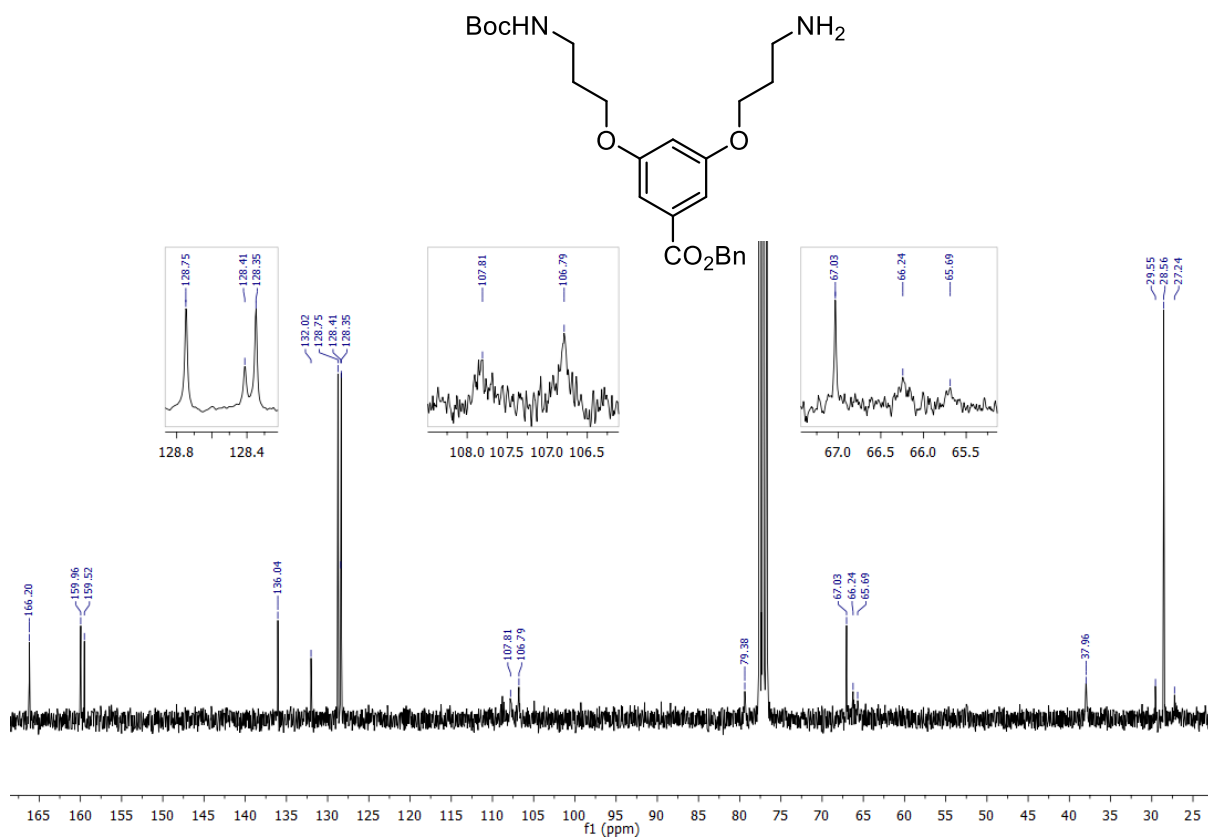


Figure A-86: <sup>13</sup>C-NMR spectrum of **93**.



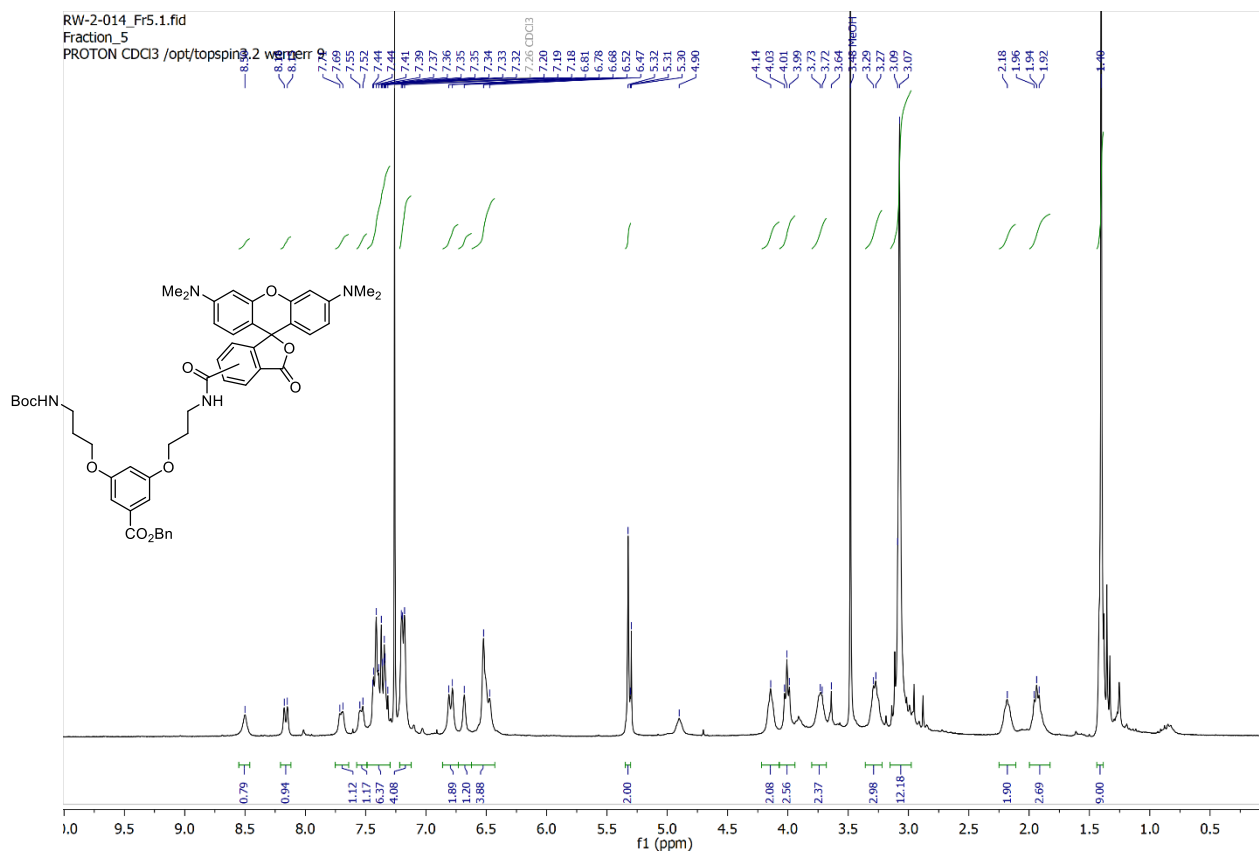


Figure A-87: <sup>1</sup>H-NMR spectrum of 94.

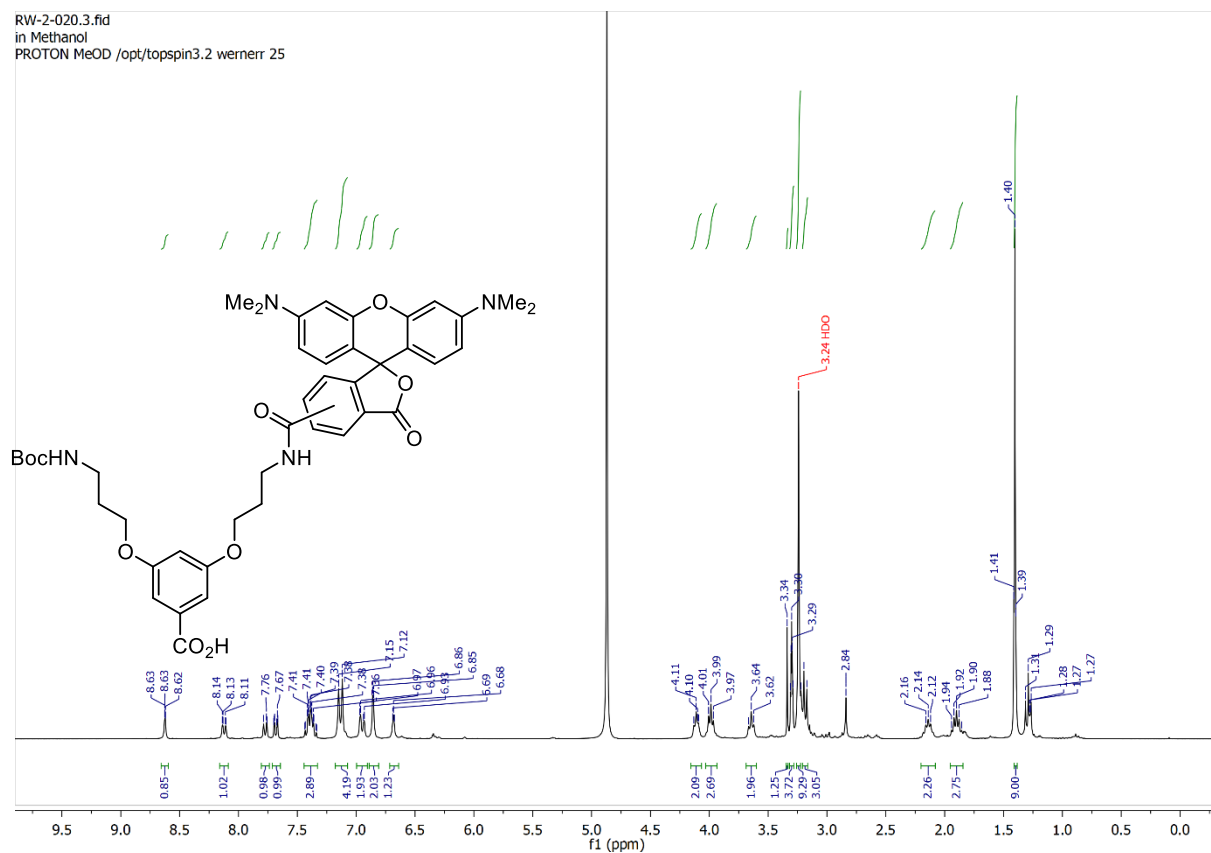


Figure A-88: <sup>1</sup>H-NMR spectrum of 95.

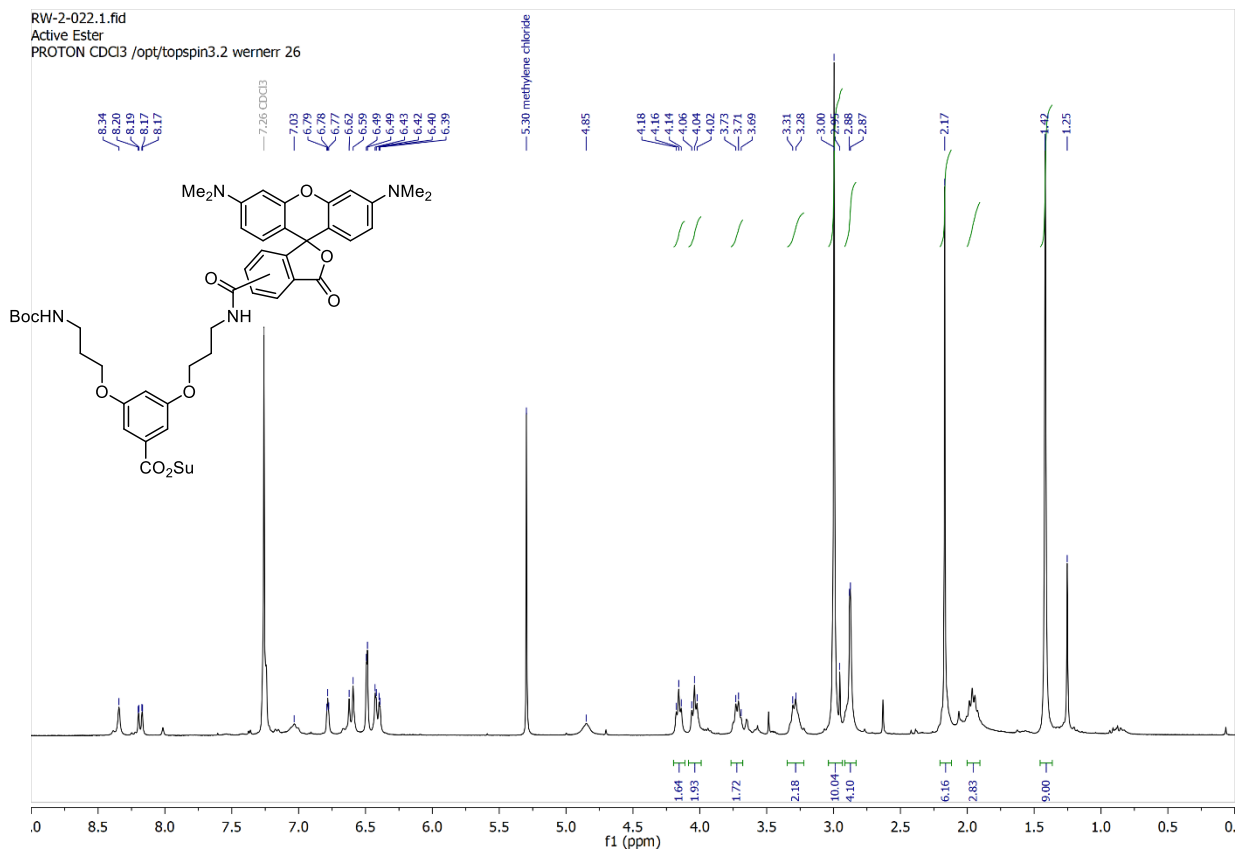


Figure A-89: <sup>1</sup>H-NMR spectrum of 96.

## Abbreviations

- <b>A-</b>	prefix indicating a DP was prepared by route <b>A</b> (Scheme 2-1)
- <b>A</b>	cross-sectional area [ $\text{m}^2$ , $\text{nm}^2$ , <i>etc.</i> ]
- AFM	atomic force microscopy
- Alloc	allyloxycarbonyl
- ATRP	atom transfer radical polymerization
- <b>B-</b>	prefix indicating a DP was prepared by route <b>B</b> (Scheme 2-1)
- Boc	<i>tert</i> -butoxycarbonyl
- Boc <sub>2</sub> O	di- <i>tert</i> -butyl dicarbonate (Boc anhydride)
- BODIPY	boron dipyrromethene (a class of dyes)
- <b>C-</b>	prefix indicating a DP was prepared by route <b>C</b> (Scheme 2-1)
- Cbz	benzyloxycarbonyl
- CDI	1,1'-carbonyldiimidazole
- cryo-ET	cryogenic (transmission) electron tomography
- $C(s)$	tangent-tangent correlation function
- CuAAC	copper(I)-catalyzed alkyne-azide cyclization
- <b>D</b>	dimensionality of a dendritic structure (D = 1: dendrimer; D = 2: DP; D = 3: dendritic forest)
- $\mathcal{D}$	polydispersity, molar mass distribution
- DBU	1,8-Diazabicyclo[5.4.0]undec-7-ene
- DCC	<i>N,N'</i> -dicyclohexylcarbodiimide
- dendron	group with a dendritic structure, <i>i.e.</i> comprising only dendritic and terminal repeat units, such that all terminal units are of the same remove from the focal point of the structure.
- DG <sup><i>g</i></sup> X	dendronization agent of dendritic generation <i>g</i> bearing peripheral groups X
- DIPEA	diisopropylethylamine; Hünig's base
- DLS	dynamic light scattering
- DMAc	<i>N,N</i> -dimethylacetamide
- DMAP	4-dimethylaminopyridine
- DMBA	<i>N,N'</i> -dimethylbarbituric acid
- DMF	<i>N,N</i> -dimethylformamide
- DMPU	<i>N,N'</i> -dimethylpropyleneurea (1,3-dimethyl-1,3-diazinan-2-one)
- DMPO	5,5-dimethyl-1-pyrroline <i>N</i> -oxide
- DMSO	dimethylsulfoxide
- DNA	deoxyribonucleic acid
- DP	dendronized polymer
- EDCI	<i>N</i> -(3-Dimethylaminopropyl)- <i>N'</i> -ethylcarbodiimide hydrochloride
- EtOH	ethanol
- EtOAc	ethyl acetate

- $f$	functionality of a branched monomer ( $\geq 3$ )
- Fmoc*	2,7-di- <i>tert</i> -butylfluorenylmethyloxycarbonyl
- FRP	free radical polymerization
- $g$	dendritic generation; number of branching points between the
- $g_{\max}$	maximum value of the dendritic generation $g$ up to which dendritic structures (dendrimers, DPs, surface-bound “forests” can theoretically be accessed without defects
- $g_J$	Landé $g$ -factor (EPR spectroscopy)
- GPC	gel permeation chromatography
- HDPE	high-density polyethylene
- HOPG	highly oriented pyrolytic graphite
- HOSu	<i>N</i> -hydroxysuccinimide
- ICP-OES	inductively coupled plasma optical emission spectroscopy
- $I_0$	incident beam intensity/electron flux
- $I_{\text{sca}}$	scattered beam intensity/electron flux
- iSIM	“instant” structured illumination microscopy
- $J$	NMR coupling constant [Hz]
- $L_c$	contour length, usually [nm]
- LDPE	low-density polyethylene
- $L_p$	persistence length, usually [nm] as defined in the WLC model ( <i>local flexibility</i> ).
- $\mathcal{L}_p$	<i>apparent</i> persistence length, usually [nm] as obtained from analysis of $R_g$
- $M$	molar mass [ $\text{g mol}^{-1}$ ]
- $m_a / \langle m \rangle$	atomic mass/weighted average atomic mass
- $\overline{M}_n$	number-average molar mass [Da]
- $\overline{M}_w$	weight-average molar mass [Da]
- MALDI-TOF-MS	matrix-assisted laser desorption/ionization time-of-flight mass spectrometry
- MD	molecular dynamics
- $M_{\text{exp}}$	molar mass calculated from $\chi$ [ $\text{g mol}^{-1}$ ]
- $\text{MG}g^x$	dendronized macromonomer polymer of dendritic generation $g$ , bearing peripheral groups X
- $M_L$	molar mass per length [ $\text{g mol}^{-1} \text{nm}^{-1}$ ]
- $M_{\max}$	theoretically accessible molar mass per repeat unit (depends on $g_{\max}$ [ $\text{g mol}^{-1}$ ])
- $M_{\text{RU}}$	molar mass of a perfect DP repeat unit [ $\text{g mol}^{-1}$ ]
- $M_{\text{voxel}}$	mass per scanned voxel (qSTEM)
- $n$	number of repeat units, used in structural formulae
- $n_D$	refractive index
- $\text{NEt}_3$	triethylamine
- NHAlloc	allyloxycarbonyl protected amino group (allyl carbamate)
- NHBoc	<i>tert</i> -butoxycarbonyl protected amino group ( <i>tert</i> -butyl carbamate)
- NHCbz	benzyloxycarbonyl protected amino group (benzyl carbamate)
- NHFmoc*	Fmoc* carbamate

- NMP	<i>N</i> -methylpyrrolidone
- MeCN	acetonitrile
- MeOH	methanol
- PAMAM	poly(amidoamide)
- PE	polyethylene
	periphery and the focal point of a dendron
- PEI	poly(ethyleneimine)
- PET	poly(ethylene terephthalate)
- PFMMA	poly(ferrocenylmethyl methacrylate)
- $PGg_n^X$	dendronized polymer of dendritic generation <i>g</i> and chain length <i>n</i> , Bearing peripheral groups X
- PMMA	poly(methyl methacrylate)
- $P_n$ , <i>n</i>	(number-average) degree of polymerization
- PP	polypropylene
- PS	polystyrene
- PTFE	poly(tetrafluoroethylene); Teflon
- PVC	poly(vinyl chloride)
- qSTEM	quantitative scanning transmission electron microscopy
- <i>R</i>	radius of a dendritic system (usually [nm])
- <i>R</i> , <i>R'</i> , ...	generic groups in chemical structures
- RAFT	reversible addition/fragmentation (polymerization)
- $R_f$	retention factor (chromatography)
- $R_g$	radius of gyration, usually [nm]
- RhoB-ITC	rhodamine B isothiocyanate
- $R_{max}$	radius [nm] of a dendritic system at its dendrons' maximum extension
- RNA	ribonucleic acid
- ROMP	ring-opening metathesis polymerization
- ROP	ring-opening polymerization
- $R_{packing}$	radius usually [nm] of a dendritic system in a densely packed state of $\rho = \rho_{packing}$
- RT	room temperature ( <i>ca.</i> 22 – 23 °C)
- RU	(constitutional) repeat(ing) unit
- RV	retention volume (GPC)
- $\sigma$	electron scattering cross-section
- SANS	small-angle neutron scattering
- SAW	self-avoiding walk
- SAXS	small-angle X-ray scattering
- SEM	scanning electron microscopy
- SLS	static light scattering
- STEM	scanning transmission electron microscopy
- TAMRA	(5,6)-tetramethylcarboxyrhodamine
- TBTU	2-(1 <i>H</i> -Benzotriazole-1-yl)-1,1,3,3-tetramethylammonium Tetrafluoroborate
- <sup>t</sup> BuOH	<i>tert</i> -butanol

- TCE 1,1,2,2-tetrachloroethane
- TEM transmission electron microscopy
- TFA trifluoroacetic acid
- UV/Vis ultraviolet/visible spectral range
- WLC worm-like chain (model)
- X generic peripheral group pendent to the propyloxy chain (dendron)
- $X$  core multiplicity of a dendron
- Y generic *N*-protecting group or other *N*-pendent group
- $\alpha$  measure of detected excess molar mass from defect labelling
- $\lambda$  wavelength (UV/Vis, X-ray, *etc.*)
- $\rho$  density [ $\text{g cm}^{-3}$ ]
- $\sigma / \langle \sigma \rangle$  (electron) scattering cross-section/weighted average
- $\chi$  functional group conversion [%] in a dendronization step, calculated using a recursive method

# Curriculum Vitae

Daniel Messmer  
Vladimir-Prelog-Weg 5  
8093 Zurich  
Email: daniel.messmer@mat.ethz.ch

## Personal Information

Date of Birth: May 8<sup>th</sup>, 1991  
Nationality: Swiss (place of origin: Dörflingen, SH)

## Education

Since March 2014: Doctoral studies in the group of Prof. Dr. A. Dieter Schlüter (Polymer Chemistry), Department of Materials, ETH Zurich.

September 2012 – February 2014: Master of Science in Chemistry, Department of Chemistry and Applied Biosciences, ETH Zurich, with a focus on organic and polymer chemistry (MSc Chemistry ETH Zurich awarded on Feb. 18<sup>th</sup>, 2014).

September 2009 – September 2012: Bachelor of Science in Chemistry, Department of Chemistry and Applied Biosciences, ETH Zurich (BSc Chemistry ETH Zurich awarded on Sept. 20<sup>th</sup>, 2012)

## Research Experience

Since March 2014: Doctoral research in the group of Prof. Dr. A. Dieter Schlüter: “Dendronized Polymers: Pushing Synthetic & Analytical Limits”. Successfully overcame synthetic obstacles which had prevented the synthesis of very high generation dendronized polymers previously; performed in-depth analyses of their properties, related mostly to the effects of endowing polymers with thickness.

February 2013 – January 2014: Research & MSc thesis projects in the group of Prof. Dr. A. Dieter Schlüter (Polymer Chemistry, Department of Materials, ETH Zurich) under the supervision of Drs. Hao Yu & Baozhong Zhang. Investigated the causes for chain degradation during dendronized polymer synthesis.

February 2012 – June 2012: Research project in the group of Prof. Dr. Antonio Togni (Laboratory of Inorganic Chemistry, Department of Chemistry and Applied Biosciences, ETH Zurich) under the supervision of Dr. Elisabeth Otth. Made first steps toward scorpionate Pd- and Pt-complexes hoped to be active in the trifluoromethylation of allylic substrates.

## Poster Presentations

February 2017: Macromolecular Colloquium, Freiburg, Germany: Messmer, D.; Tacke, S.; Sánchez-Ferrer, A.; Böttcher, C.; Kröger, M.; Mezzenga, R.; Halperin, A.; Schlüter, A. D. *High-Generation Dendronized Polymers: Synthesis and Electron Microscopic Investigations of Molecular Colloids*.

April 2017: ACS 253rd National Meeting, San Francisco, USA: Messmer, D.; Tacke, S.; Sánchez-Ferrer, A.; Böttcher, C.; Kröger, M.; Mezzenga, R.; Halperin, A.; Schlüter, A. D. *High-Generation Dendronized Polymers: Approaching  $g_{max}$  of Cylindrical Nano-Objects*.

## Scientific Talks

April 2017: ACS 253rd National Meeting, San Francisco, USA: *Synthesis of  $g > 5$  dendronized polymers with increased structural perfection: Approaching  $g_{max}$  of cylindrical nano-objects.*

## Publications

Maltar-Strmečki, N.; Yu, H.; **Messmer, D.**; Zhang, B.; Schlüter, A. D.; Hinderberger, D. *ChemPhysChem* **2016**, *17* (17), 2767-2772: *Exploring the Loading Capacity of Generation Six to Eight Dendronized Polymers in Aqueous Solution.*

Küchler, A.; **Messmer, D.**; Schlüter, A. D.; Walde, P. *Methods in Enzymology* **2017**, *590*, 445-474: *Preparation and Applications of Dendronized Polymer–Enzyme Conjugates.*

Spycher, P. R.; Amann, C. A.; Wehrmüller, J. E.; Hurwitz, D. R.; Kreis, O.; **Messmer, D.**; Ritler, A.; Küchler, A.; Blanc, A.; Béhé, M.; et al *ChemBioChem* **2017**, *18* (19), 1923–1927: *Dual, Site-Specific Modification of Antibodies by Using Solid-Phase Immobilized Microbial Transglutaminase.*

**Messmer, D.**; Kröger, M.; Schlüter, A. D. *Macromolecules* **2018**, *51* (14), 5420-5429: *Pushing Synthesis toward the Maximum Generation Range of Dendritic Macromolecules.*

**Messmer, D.**; Böttcher, C.; Yu, H.; Halperin, A.; Binder, K.; Kröger, M.; Schlüter, A. D. *Submitted*: Native 3D conformations of thick synthetic polymer chains observed by cryogenic electron microscopy

## Other activities

November 2012 – June 2014: Tutor in English, chemistry, and biology for Know-Now AG.

September 2014 – December 2017: Supervision of student laboratory courses (polymer synthesis & polymer analytics, courses organized by Dr. Martin Willeke, Department of Materials, ETH Zurich).

September 2014 – December 2017: Supervision of student research projects in the group of Prof. Dr. A. Dieter Schlüter (Polymer Chemistry, Department of Materials, ETH Zurich). Supervised 5 students (3 BSc Materials Science, 1 BSc Chemical Engineering (exchange student), 1 MSc Chemistry) for ca. 14 – 18 weeks each.



## Bibliography

- (1) Feringa, B. L. "We Must Be Able to Show How Science Is Beneficial to Society." *Chimia* **2009**, *63* (6), 352–356.
- (2) Braconnot, M. H. De La Transformation de Plusieurs Substances Végétales En Un Principe Nouveau. *Ann. Chim. Phys.* **1833**, *52*, 290–294.
- (3) Schützenberger, M. P. Action de l'Acide Acétique Anhydre Sur La Cellulose, l'Amidon, Les Sucres, La Mannite, et Ses Congénères. *Comptes Rendus Chim.* **1865**, *61*, 485–486.
- (4) Vaupel, E. Arthur Eichengrün—Tribute to a Forgotten Chemist, Entrepreneur, and German Jew. *Angew. Chem. Int. Ed.* **2005**, *44* (22), 3344–3355.
- (5) Baekeland, L. H. Condensation Product of Phenol and Formaldehyde and Method of Making the Same. US942700A, December 4, 1907.
- (6) *The Wiley Encyclopedia of Packaging Technology*; Yam, K. L., Ed.; John Wiley & Sons, Inc.: Hoboken, NJ, USA, 2009.
- (7) Simon, E. Ueber Den Flüssigen Storax (Styrax Liquidus). *Liebig's Ann. der Chemie* **1839**, *31* (3), 265–277.
- (8) Blyth, J.; Hofmann, A. W. Ueber Das Styrol Und Einige Seiner Zersetzungsproducte. *Liebig's Ann. der Chemie* **1845**, *53* (3), 289–329.
- (9) Baumann, E. Ueber Einige Vinylverbindungen. *Ann. der Chemie und Pharm.* **1872**, *163* (3), 308–322.
- (10) Scheirs, J. Historical Overview of Styrenic Polymers. In *Modern Styrenic Polymers: Polystyrenes and Styrenic Copolymers*; John Wiley & Sons, Ltd: Chichester, UK, 2003; pp 1–24.
- (11) Staudinger, H. Über Polymerisation. *Ber. dtsh. Chem. Ges.* **1920**, *53* (6), 1073–1085.
- (12) Mülhaupt, R. Hermann Staudinger and the Origin of Macromolecular Chemistry. *Angew. Chem. Int. Ed.* **2004**, *43* (9), 1054–1063.
- (13) *Nobel Lectures Chemistry 1942-1962: Including Presentation Speeches and Laureate's Biographies*; Elsevier, 1964.
- (14) Thiele, J. Zur Kenntniss Der Ungesättigten Verbindungen. Theorie Der Ungesättigten Und Aromatischen Verbindungen. *Liebig's Ann. der Chemie* **1899**, *306* (1–2), 87–142.
- (15) Brill, R. Über Seidenfibroin. I. *Liebig's Ann. der Chemie* **1923**, *434* (1), 204–217.
- (16) Staudinger, H.; Fritsch, J. Über Isopren Und Kautschuk. 5. Mitteilung. Über Die Hydrierung Des Kautschuks Und Über Seine Konstitution. *Helv. Chim. Acta* **1922**, *5* (5), 785–806.
- (17) PlasticsEurope. *Plastics – the Facts 2017*; 2017.
- (18) Jensen, W. B. The Origin of the Polymer Concept. *J. Chem. Educ.* **2008**, *85* (5), 624–625.
- (19) International Union of Pure and Applied Chemistry. *Compendium of Chemical Terminology (Gold Book)*; 2014.
- (20) Szwarc, M. 'Living' Polymers. *Nature* **1956**, *178*, 1168–1169.
- (21) Szwarc, M.; Levy, M.; Milkovich, R. Polymerization Initiated by Electron Transfer to Monomer. A New Method for Formation of Block Polymers. *J. Am. Chem. Soc.* **1956**, *78* (11), 2656–2657.
- (22) Bielawski, C. W.; Grubbs, R. H. Living Ring-Opening Metathesis Polymerization. In *Controlled and Living Polymerizations*; Wiley-VCH Verlag GmbH & Co. KGaA, 2009; pp 297–342.
- (23) Leitgeb, A.; Wappel, J.; Slugovc, C. The ROMP Toolbox Upgraded. *Polymer* **2010**, *51* (14), 2927–2946.

- (24) Matyjaszewski, K. General Concepts and History of Living Radical Polymerization. In *Handbook of Radical Polymerization*; Matyjaszewski, K., Davis, T. P., Eds.; Wiley-Blackwell, 2003; pp 361–406.
- (25) Matyjaszewski, K. Atom Transfer Radical Polymerization (ATRP): Current Status and Future Perspectives. *Macromolecules* **2012**, *45* (10), 4015–4039.
- (26) Perrier, S. RAFT Polymerization—A User Guide. *Macromolecules* **2017**, *50* (19), 7433–7447.
- (27) Brintzinger, H. H.; Fischer, D.; Mülhaupt, R.; Rieger, B.; Waymouth, R. M. Stereospecific Olefin Polymerization with Chiral Metallocene Catalysts. *Angew. Chem. Int. Ed.* **1995**, *34* (11), 1143–1170.
- (28) Matyjaszewski, K.; Ziegler, M. J.; Arehart, S. V.; Greszta, D.; Pakula, T. Gradient Copolymers by Atom Transfer Radical Copolymerization. *J. Phys. Org. Chem.* **2000**, *13* (12), 775–786.
- (29) Hadjichristidis, N.; Marinos Pitsikalis; Stergios Pispas, A.; Iatrou, H. Polymers with Complex Architecture by Living Anionic Polymerization. *Chem. Rev.* **2001**, *101* (12), 3747–3792.
- (30) Darling, S. B. Directing the Self-Assembly of Block Copolymers. *Prog. Polym. Sci.* **2007**, *32* (10), 1152–1204.
- (31) Mai, Y.; Eisenberg, A. Self-Assembly of Block Copolymers. *Chem. Soc. Rev.* **2012**, *41* (18), 5969.
- (32) Hailes, R. L. N.; Oliver, A. M.; Gwyther, J.; Whittell, G. R.; Manners, I. Polyferrocenylsilanes: Synthesis, Properties, and Applications. *Chem. Soc. Rev.* **2016**, *45* (19), 5358–5407.
- (33) Hudson, Z. M.; Boott, C. E.; Robinson, M. E.; Rupar, P. A.; Winnik, M. A.; Manners, I. Tailored Hierarchical Micelle Architectures Using Living Crystallization-Driven Self-Assembly in Two Dimensions. *Nat. Chem.* **2014**, *6* (10), 893–898.
- (34) Gao, Y.; Qiu, H.; Zhou, H.; Li, X.; Harniman, R.; Winnik, M. A.; Manners, I. Crystallization-Driven Solution Self-Assembly of Block Copolymers with a Photocleavable Junction. *J. Am. Chem. Soc.* **2015**, *137* (6), 2203–2206.
- (35) Lutz, J.-F.; Ouchi, M.; Liu, D. R.; Sawamoto, M.; Pinheiro, V. B. Sequence-Controlled Polymers Synthetic Genetic Polymers Capable of Heredity and Evolution. *Science* **2012**, *336* (339), 341–344.
- (36) Ouchi, M.; Sawamoto, M. Sequence-Controlled Polymers via Reversible-Deactivation Radical Polymerization. *Polym. J.* **2018**, *50* (1), 83–94.
- (37) Gutekunst, W. R.; Hawker, C. J. A General Approach to Sequence-Controlled Polymers Using Macrocyclic Ring Opening Metathesis Polymerization. *J. Am. Chem. Soc.* **2015**, *137* (25), 8038–8041.
- (38) Weiss, R. M.; Short, A. L.; Meyer, T. Y. Sequence-Controlled Copolymers Prepared via Entropy-Driven Ring-Opening Metathesis Polymerization. *ACS Macro Lett.* **2015**, *4* (9), 1039–1043.
- (39) Ziegler, K.; Holzkamp, E.; Breil, H.; Martin, H. Polymerisation von Äthylen Und Anderen Olefinen. *Angew. Chemie* **1955**, *67* (16), 426–426.
- (40) Natta, G.; Pasquon, I. The Kinetics of the Stereospecific Polymerization of  $\alpha$ -Olefins. *Adv. Catal.* **1959**, *11*, 1–66.
- (41) Cossee, P. Ziegler-Natta Catalysis I. Mechanism of Polymerization of  $\alpha$ -Olefins with Ziegler-Natta Catalysts. *J. Catal.* **1964**, *3* (1), 80–88.
- (42) Kaminsky, W. Highly Active Metallocene Catalysts for Olefin Polymerization. *J. Chem. Soc. Dalt. Trans.* **1998**, *0* (9), 1413–1418.
- (43) Baier, M. C.; Zuideveld, M. A.; Mecking, S. Post-Metallocenes in the Industrial Production of Polyolefins. *Angew. Chem. Int. Ed.* **2014**, *53* (37), 9722–9744.
- (44) George, W.; Tucker, P. Studies of Polyethylene Shish-Kebab Structures. *Polym. Eng. Sci.* **1975**, *15* (6), 451–459.
- (45) *Handbook of Industrial Polyethylene and Technology : Definitive Guide to Manufacturing, Properties,*

- Processing, Applications and Markets*; Spalding, M. A., Chatterjee, A. M., Eds.; John Wiley & Sons, Inc.: Hoboken, NJ, USA, 2017.
- (46) Zhang, B.; Grayson, S. M. The Ring-Closure Approach for Synthesizing Cyclic Polymers. In *Topological Polymer Chemistry*; Tezuka, Y., Ed.; World Scientific Publishing Co.: Singapore, 2013; pp 157–197.
- (47) Tezuka, Y. Metathesis Polymer Cyclization. In *Topological Polymer Chemistry*; Tezuka, Y., Ed.; World Scientific Publishing Co.: Singapore, 2013; pp 107–121.
- (48) Bunha, A.; Cao, P.-F.; Mangadlao, J. D.; Advincula, R. C. Cyclic Poly(Vinylcarbazole) via Ring-Expansion Polymerization-RAFT (REP-RAFT). *React. Funct. Polym.* **2014**, *80*, 33–39.
- (49) Boydston, A. J.; Holcombe, T. W.; Unruh, D. a; Fréchet, J. M. J.; Grubbs, R. H. A Direct Route to Cyclic Organic Nanostructures via Ring-Expansion Metathesis Polymerization of a Dendronized Macromonomer. *J. Am. Chem. Soc.* **2009**, *131* (15), 5388–5389.
- (50) Bielawski, C. W.; Benitez, D.; Grubbs, R. H. An “Endless” Route to Cyclic Polymers. *Science* **2002**, *297* (5589), 2041–2044.
- (51) Yamamoto, T.; Tezuka, Y. Topological Polymer Chemistry: A Cyclic Approach toward Novel Polymer Properties and Functions. *Polym. Chem.* **2011**, *2* (9), 1930.
- (52) Pérez-Camargo, R. A.; Mugica, A.; Zubitur, M.; Müller, A. J. Crystallization of Cyclic Polymers. In *Polymer Crystallization I From Chain Microstructure to Processing*; Auriemma, F., Alfonso, G. C., de Rosa, C., Eds.; Springer, Cham, 2015; pp 93–132.
- (53) Michieletto, D.; Turner, M. S. A Topologically Driven Glass in Ring Polymers. *Proc. Natl. Acad. Sci. USA* **2016**, *113* (19), 5195–5200.
- (54) Pasquino, R.; Vasilakopoulos, T. C.; Jeong, Y. C.; Lee, H.; Rogers, S.; Sakellariou, G.; Allgaier, J.; Takano, A.; Brás, A. R.; Chang, T.; et al. Viscosity of Ring Polymer Melts. *ACS Macro Lett.* **2013**, *2* (10), 874–878.
- (55) Kapnistos, M.; Lang, M.; Vlassopoulos, D.; Pyckhout-Hintzen, W.; Richter, D.; Cho, D.; Chang, T.; Rubinstein, M. Unexpected Power-Law Stress Relaxation of Entangled Ring Polymers. *Nat. Mater.* **2008**, *7* (12), 997–1002.
- (56) Roovers, J.; Toporowski, P. M. Synthesis of High Molecular Weight Ring Polystyrenes. *Macromolecules* **1983**, *16* (6), 843–849.
- (57) Schaefgen, J. R.; Flory, P. J. Synthesis of Multichain Polymers and Investigation of Their Viscosities. *J. Am. Chem. Soc.* **1948**, *70* (8), 2709–2718.
- (58) Ren, J. M.; McKenzie, T. G.; Fu, Q.; Wong, E. H. H.; Xu, J.; An, Z.; Shanmugam, S.; Davis, T. P.; Boyer, C.; Qiao, G. G. Star Polymers. *Chem. Rev.* **2016**, *116* (12), 6743–6836.
- (59) Barner-Kowollik, C.; Davis, T. P.; Stenzel, M. H. Synthesis of Star Polymers Using RAFT Polymerization: What Is Possible? *Aust. J. Chem.* **2006**, *59* (10), 719–727.
- (60) Khanna, K.; Varshney, S.; Kakkar, A. Miktoarm Star Polymers: Advances in Synthesis, Self-Assembly, and Applications. *Polym. Chem.* **2010**, *1* (8), 1171–1185.
- (61) Iatrou, H.; Avgeropoulos, A.; Sakellariou, G.; Pitsikalis, M.; Hadjichristidis, N. Miktoarm Star ( $\mu$ -Star) Polymers: A Successful Story. In *Miktoarm Star Polymers: From Basics of Branched Architecture to Synthesis, Self-assembly and Applications*; Kakkar, A., Ed.; Royal Society of Chemistry: Cambridge, UK, 2017; pp 1–30.
- (62) Mavroudis, A.; Hadjichristidis, N. Synthesis of Well-Defined 4-Miktoarm Star Quarterpolymers (4 $\mu$ -SIDV) with Four Incompatible Arms: Polystyrene (S), Polyisoprene-1,4 (I), Poly(Dimethylsiloxane) (D), and Poly(2-Vinylpyridine) (V). *Macromolecules* **2005**, *39* (2), 535–540.
- (63) Quirk, R. P.; Tsai, Y. Trifunctional Organolithium Initiator Based on 1,3,5-Tris(1-Phenylethenyl)Benzene. Synthesis of Functionalized, Three-Armed, Star-Branched Polystyrenes. *Macromolecules* **1998**, *31* (23), 8016–8025.

- (64) Erdogan, T.; Ozyurek, Z.; Hizal, G.; Tunca, U. Facile Synthesis of AB<sub>2</sub>-Type Miktoarm Star Polymers through the Combination of Atom Transfer Radical Polymerization and Ring-Opening Polymerization. *J. Polym. Sci. Part A Polym. Chem.* **2004**, *42* (10), 2313–2320.
- (65) Müllner, M.; Müller, A. H. E. Cylindrical Polymer Brushes – Anisotropic Building Blocks, Unimolecular Templates and Particulate Nanocarriers. *Polymer* **2016**, *98*, 389–401.
- (66) Sheiko, S. S.; Sumerlin, B. S.; Matyjaszewski, K. Cylindrical Molecular Brushes: Synthesis, Characterization, and Properties. *Prog. Polym. Sci.* **2008**, *33* (7), 759–785.
- (67) Tsukahara, Y.; Mizuno, K.; Segawa, A.; Yamashita, Y. Study on the Radical Polymerization Behavior of Macromonomers. *Macromolecules* **1989**, *22* (4), 1546–1552.
- (68) Tsukahara, Y.; Tsutsumi, K.; Yamashita, Y.; Shimada, S. Radical Polymerization Behavior of Macromonomers. 2. Comparison of Styrene Macromonomers Having a Methacryloyl End Group and a Vinylbenzyl End Group. *Macromolecules* **1990**, *23* (25), 5201–5208.
- (69) Kolb, H. C.; Finn, M. G.; Sharpless, K. B. Click Chemistry: Diverse Chemical Function from a Few Good Reactions. *Angew. Chem. Int. Ed.* **2001**, *40* (11), 2004–2021.
- (70) Gao, H.; Matyjaszewski, K. Synthesis of Molecular Brushes by “Grafting onto” Method: Combination of ATRP and Click Reactions. *J. Am. Chem. Soc.* **2007**, *129* (20), 6633–6639.
- (71) Wintermantel, M.; Gerle, M.; Fischer, K.; Schmidt, M.; Wataoka, I.; Urakawa, H.; Kajiwar, K.; Tsukahara, Y. Molecular Bottlebrushes. *Macromolecules* **1996**, *29* (3), 978–983.
- (72) Haugan, I. N.; Maher, M. J.; Chang, A. B.; Lin, T.-P.; Grubbs, R. H.; Hillmyer, M. A.; Bates, F. S. Consequences of Grafting Density on the Linear Viscoelastic Behavior of Graft Polymers. *ACS Macro Lett.* **2018**, 525–530.
- (73) Bolton, J.; Rzayev, J. Synthesis and Melt Self-Assembly of PS–PMMA–PLA Triblock Bottlebrush Copolymers. *Macromolecules* **2014**, *47* (9), 2864–2874.
- (74) Voit, B. Hyperbranched Polymers—All Problems Solved after 15 Years of Research? *J. Polym. Sci. Part A Polym. Chem.* **2005**, *43* (13), 2679–2699.
- (75) Lederer, A.; Burchard, W. *Hyperbranched Polymers*; Polymer Chemistry Series; Royal Society of Chemistry: Cambridge, 2015.
- (76) Gao, C.; Yan, D.; Frey, H. Promising Dendritic Materials: An Introduction to Hyperbranched Polymers. In *Hyperbranched Polymers*; John Wiley & Sons, Inc.: Hoboken, NJ, USA, 2011; pp 1–26.
- (77) Gao, C.; Yan, D. Hyperbranched Polymers: From Synthesis to Applications. *Prog. Polym. Sci.* **2004**, *29* (3), 183–275.
- (78) Jikei, M.; Chon, S.-H.; Kakimoto, M.; Kawauchi, S.; Imase, T.; Watanabe, J. Synthesis of Hyperbranched Aromatic Polyamide from Aromatic Diamines and Trimesic Acid. *Macromolecules* **1999**, *32* (6), 2061–2064.
- (79) Kim, Y. H.; Webster, O. W. Hyperbranched Polyphenylenes. *Macromolecules* **1992**, *25* (21), 5561–5572.
- (80) Vögtle, F.; Richardt, G.; Werner, N. *Dendrimer Chemistry*; Wiley-VCH, 2009.
- (81) Tomalia, D. A.; Christensen, J. B.; Boas, U. Synthetic Methodologies. In *Dendrimers, Dendrons, and Dendritic Polymers*; Cambridge University Press: Cambridge, 2012; pp 113–161.
- (82) Caminade, A.-M. *Dendrimers: Towards Catalytic, Material and Biomedical Uses*; Wiley, 2011.
- (83) Tomalia, D. A.; Baker, H.; Dewald, J.; Hall, M.; Kallos, G.; Martin, S.; Roeck, J.; Ryder, J.; Smith, P. A New Class of Polymers: Starburst-Dendritic Macromolecules. *Polym. J.* **1985**, *17* (1), 117–132.
- (84) Hawker, C.; Fréchet, J. M. J. A New Convergent Approach to Monodisperse Dendritic Macromolecules. *J. Chem. Soc. Chem. Commun.* **1990**, No. 15, 1010–1013.

- (85) Hawker, C. J.; Fréchet, J. M. J. Preparation of Polymers with Controlled Molecular Architecture. A New Convergent Approach to Dendritic Macromolecules. *J. Am. Chem. Soc.* **1990**, *112* (21), 7638–7647.
- (86) Guo, Y.; van Beek, J. D.; Zhang, B.; Colussi, M.; Walde, P.; Zhang, A.; Kröger, M.; Halperin, A.; Dieter Schlüter, A. Tuning Polymer Thickness: Synthesis and Scaling Theory of Homologous Series of Dendronized Polymers. *J. Am. Chem. Soc.* **2009**, *131* (33), 11841–11854.
- (87) Schlüter, A. D.; Halperin, A.; Kröger, M.; Vlassopoulos, D.; Wegner, G.; Zhang, B. Dendronized Polymers: Molecular Objects between Conventional Linear Polymers and Colloidal Particles. *ACS Macro Lett.* **2014**, *3* (10), 991–998.
- (88) Laurent, B. A.; Grayson, S. M. Synthesis of Cyclic Dendronized Polymers via Divergent “Graft-from” and Convergent Click “Graft-to” Routes: Preparation of Modular Toroidal Macromolecules. *J. Am. Chem. Soc.* **2011**, *133* (34), 13421–13429.
- (89) Xiong, X.; Chen, Y.; Feng, S.; Wang, W. Codendronized Polymers: Wormlike Molecular Objects with a Segmented Structure. *Macromolecules* **2007**, *40* (25), 9084–9093.
- (90) Rajaram, S.; Choi, T.-L.; Rolandi, M.; Fréchet, J. M. J. Synthesis of Dendronized Diblock Copolymers via Ring-Opening Metathesis Polymerization and Their Visualization Using Atomic Force Microscopy. *J. Am. Chem. Soc.* **2007**, *129* (31), 9619–9621.
- (91) Schlüter, A. D.; Rabe, J. P. Dendronized Polymers: Synthesis, Characterization, Assembly at Interfaces, and Manipulation. *Angew. Chem. Int. Ed.* **2000**, *39* (5), 864–883.
- (92) Frauenrath, H. Dendronized Polymers—building a New Bridge from Molecules to Nanoscopic Objects. *Prog. Polym. Sci.* **2005**, *30* (3–4), 325–384.
- (93) *Synthesis of Polymers: New Structures and Methods*; Schlüter, A.-D., Hawker, C. J., Sakamoto, J., Eds.; Wiley-VCH, 2012.
- (94) Feng, C.; Li, Y.; Yang, D.; Hu, J.; Zhang, X.; Huang, X. Well-Defined Graft Copolymers: From Controlled Synthesis to Multipurpose Applications. *Chem. Soc. Rev.* **2011**, *40* (3), 1282–1295.
- (95) Lartigue, M.-L.; Donnadiou, B.; Galliot, C.; Caminade, A.-M.; Majoral, J.-P.; Fayet, J.-P. Large Dipole Moments of Phosphorus-Containing Dendrimers. *Macromolecules* **1997**, *30* (23), 7335–7337.
- (96) Ruiz, J.; Lafuente, G.; Marcen, S.; Ornelas, C.; Lazare, S.; Cloutet, E.; Blais, J.-C.; Astruc, D. Construction of Giant Dendrimers Using a Tripodal Building Block. *J. Am. Chem. Soc.* **2003**, *125*, 7250–7257.
- (97) Lim, J.; Kostianen, M.; Maly, J.; da Costa, V. C. P.; Annunziata, O.; Pavan, G. M.; Simanek, E. E. Synthesis of Large Dendrimers with the Dimensions of Small Viruses. *J. Am. Chem. Soc.* **2013**, *135* (12), 4660–4663.
- (98) Gstrein, C.; Zhang, B.; Abdel-Rahman, M. A.; Bertran, O.; Alemán, C.; Wegner, G.; Schlüter, A. D.; Halperin, A.; Schlüter, A. D.; Talmon, Y.; et al. Solvatochromism of Dye-Labeled Dendronized Polymers of Generation Numbers 1–4: Comparison to Dendrimers. *Chem. Sci.* **2016**, *7* (7), 4644–4652.
- (99) Gstrein, C.; Walde, P.; Schlüter, A. D.; Nauser, T.; Besse, S.; Lindner, P.; King, B. T.; Sigel, R.; Schurtenberger, P.; Talmon, Y.; et al. Shielding Effects in Spacious Macromolecules: A Case Study with Dendronized Polymers. *Photochem. Photobiol. Sci.* **2016**, *15* (8), 964–968.
- (100) Yoshida, M.; Fresco, Z. M.; Ohnishi, S.; Fréchet, J. M. J. Efficient Divergent Synthesis of Dendronized Polymers with Extremely High Molecular Weight: Structural Characterization by SEC-MALLS and SFM and Novel Organic Gelation Behavior. *Macromolecules* **2004**, *38* (2), 334–344.
- (101) Zhang, B.; Wepf, R.; Fischer, K.; Schmidt, M.; Besse, S.; Lindner, P.; King, B. T.; Sigel, R.; Schurtenberger, P.; Talmon, Y.; et al. The Largest Synthetic Structure with Molecular Precision: Towards a Molecular Object. *Angew. Chem. Int. Ed.* **2011**, *50* (3), 737–740.
- (102) Yu, H.; Böttcher, C.; Maltar-Strmecki, N.; Hinderberger, D.; Zhang, B.; Kröger, M.; Wepf, R.; Schlüter, A. D. On the Size and Shape of 6th–8th Generation Dendronized Polymer Chains and the Loading Capacity of Their Peripherally Positively Charged Derivatives in Aqueous Medium. *In Preparation*.

- (103) Mynar, J. L.; Choi, T.-L.; Yoshida, M.; Kim, V.; Hawker, C. J.; Fréchet, J. M. J. Doubly-Dendronized Linear Polymers. *Chem. Commun.* **2005**, No. 41, 5169.
- (104) Schlüter, A. D. The Macromonomer Route to Dendronized Polymers. *Comptes Rendus Chim.* **2003**, *6* (8–10), 843–851.
- (105) Zhang, A. High-Molar-Mass, First and Second Generation L-Lysine Dendronized Polymethacrylates. *Macromol. Rapid Commun.* **2008**, *29* (10), 839–845.
- (106) Carlmark, A.; Malmström, E. E. ATRP of Dendronized Aliphatic Macromonomers of Generation One, Two, and Three. *Macromolecules* **2004**, *37* (20), 7491–7496.
- (107) Zhang, A.; Wei, L.; Schlüter, A. D. Narrowly Distributed Dendronized Polymethacrylates by Reversible Addition-Fragmentation Chain Transfer (RAFT) Polymerization. *Macromol. Rapid Commun.* **2004**, *25* (7), 799–803.
- (108) Zhu, B.; Han, Y.; Minghao, S.; Bo, Z. Water-Soluble Dendronized Polyfluorenes with an Extremely High Quantum Yield in Water. *Macromolecules* **2007**, *40* (13), 4494–4500.
- (109) Karakaya, B.; Claussen, W.; Gessler, K.; Saenger, W.; Schlüter, A. D. Toward Dendrimers with Cylindrical Shape in Solution. *J. Am. Chem. Soc.* **1997**, *119* (14), 3296–3301.
- (110) Lau, K.-N.; Chow, H.-F.; Chan, M.-C.; Wong, K.-W. Dendronized Polymer Organogels from Click Chemistry: A Remarkable Gelation Property Owing to Synergistic Functional-Group Binding and Dendritic Size Effects. *Angew. Chem. Int. Ed.* **2008**, *47* (36), 6912–6916.
- (111) Zhang, A.; Rodríguez-Ropero, F.; Zanuy, D.; Alemán, C.; Meijer, E. W.; Schlüter, A. D. A Rigid, Chiral, Dendronized Polymer with a Thermally Stable, Right-Handed Helical Conformation. *Chem. Eur. J.* **2008**, *14* (23), 6924–6934.
- (112) Zhang, A.; Zhang, B.; Wächtersbach, E.; Schmidt, M.; Schlüter, A. D. Efficient Synthesis of High Molar Mass, First- to Fourth-Generation Distributed Dendronized Polymers by the Macromonomer Approach. *Chem. Eur. J.* **2003**, *9* (24), 6083–6092.
- (113) Costa, L. I.; Kasëm, E.; Storti, G.; Morbidelli, M.; Walde, P.; Schlüter, A. D. Dendronized Polymers via Macromonomer Route in Supercritical Carbon Dioxide. *Macromol. Rapid Commun.* **2008**, *29* (19), 1609–1613.
- (114) Desai, A.; Atkinson, N.; Rivera, F.; Devonport, W.; Rees, I.; Branz, S. E.; Hawker, C. J. Hybrid Dendritic-Linear Graft Copolymers: Steric Considerations in Coupling to Approach. *J. Polym. Sci. Part A Polym. Chem.* **2000**, *38* (6), 1033–1044.
- (115) Zhuravel, M. A.; Davis, N. E.; Nguyen, S. T.; Koltover, I. Dendronized Protein Polymers: Synthesis and Self-Assembly of Monodisperse Cylindrical Macromolecules. *J. Am. Chem. Soc.* **2004**, *126* (32), 9882–9883.
- (116) Hassan, M. L.; Moorefield, C. N.; Newkome, G. R. Regioselective Dendritic Functionalization of Cellulose. *Macromol. Rapid Commun.* **2004**, *25* (24), 1999–2002.
- (117) Hassan, M. L.; Moorefield, C. N.; Kotta, K.; Newkome, G. R. Regioselective Combinatorial-Type Synthesis, Characterization, and Physical Properties of Dendronized Cellulose. *Polymer* **2005**, *46* (21), 8947–8955.
- (118) Kim, H.; Bang, K.-T.; Choi, I.; Lee, J.-K.; Choi, T.-L. Diversity-Oriented Polymerization: One-Shot Synthesis of Library of Graft and Dendronized Polymers by Cu-Catalyzed Multicomponent Polymerization. *J. Am. Chem. Soc.* **2016**, *138* (27), 8612–8622.
- (119) Helms, B.; Mynar, J. L.; Hawker, Craig, J.; Fréchet, J. M. J. Dendronized Linear Polymers via “Click Chemistry.” *J. Am. Chem. Soc.* **2004**, *126* (46), 15020–15021.
- (120) Ronda, J. C.; Reina, J. A.; Cádiz, V.; Giamberini, M.; Nicolais, L. Self-Organized Liquid-Crystalline Polyethers Obtained by Grafting Tapered Mesogenic Groups onto Poly(Epichlorohydrin): Toward Biomimetic Ion Channels. *J. Polym. Sci. Part A Polym. Chem.* **2003**, *41* (19), 2918–2929.

- (121) Girbasova, N.; Aseyev, V.; Saratovsky, S.; Moukhina, I.; Tenhu, H.; Bilibin, A. Conformations of Highly Charged Dendronized Polymers in Aqueous Solutions of Varying Ionic Strength. *Macromol. Chem. Phys.* **2003**, *204* (18), 2258–2264.
- (122) Yin, R.; Zhu, Y.; Tomalia, D. A.; Ibuki, H. Architectural Copolymers: Rod-Shaped, Cylindrical Dendrimers. *J. Am. Chem. Soc.* **1998**, *120* (11), 2678–2679.
- (123) Kim, C.; Kwark, K. Staff-Type Dendrimer: End Functionalization of the Dendronized Siloxane Polymer Me<sub>3</sub>SiO-(MeSiHO)<sub>n</sub>-SiMe<sub>3</sub>. *J. Polym. Sci. Part A Polym. Chem.* **2002**, *40* (8), 976–982.
- (124) Smitha, G.; Sinija, P. S.; Sherlymol, P. B.; Jisha, K. A.; Anjaly, K. J.; Sreekumar, K. Heterogeneous Dendronized Polymer with Peripheral Copper Moieties: From Synthesis to Catalysis and Comparison with Dendrigraft Polymer. *Polymer* **2017**, *120*, 100–110.
- (125) Suijkerbuijk, B. M. J. M.; Shu, L.; KleinGebink, R. J. M.; Schlüter, A. D.; van Koten, G. Single-Site Catalysts on a Cylindrical Support beyond Nanosize. *Organometallics* **2003**, *22* (21), 4175–4177.
- (126) Deng, G.-J.; Yi, B.; Huang, Y.-Y.; Tang, W.-J.; He, Y.-M.; Fan, Q.-H. Dendronized Poly(Ru-BINAP) Complexes: Highly Effective and Easily Recyclable Catalysts For Asymmetric Hydrogenation. *Adv. Synth. Catal.* **2004**, *346* (12), 1440–1444.
- (127) Huang, Y.-Y.; Yang, X.; Feng, Y.; Verpoort, F.; Fan, Q.-H. Chiral Ru/Ir Bimetallic Dendronized Polymer Catalysts Constructed through Sequential Metal Coordination and Applied in Asymmetric Hydrogenation of Quinaldine. *J. Mol. Catal. A Chem.* **2014**, *393*, 150–155.
- (128) Küchler, A.; Messmer, D.; Schlüter, A. D.; Walde, P. Preparation and Applications of Dendronized Polymer–Enzyme Conjugates. *Methods Enzymol.* **2017**, *590*, 445–474.
- (129) Küchler, A.; Adamcik, J.; Mezzenga, R.; Schlüter, A. D.; Walde, P. Enzyme Immobilization on Silicate Glass through Simple Adsorption of Dendronized Polymer–enzyme Conjugates for Localized Enzymatic Cascade Reactions. *RSC Adv.* **2015**, *5* (55), 44530–44544.
- (130) Spycher, P. R.; Amann, C. A.; Wehrmüller, J. E.; Hurwitz, D. R.; Kreis, O.; Messmer, D.; Ritler, A.; Küchler, A.; Blanc, A.; Béhé, M.; et al. Dual, Site-Specific Modification of Antibodies by Using Solid-Phase Immobilized Microbial Transglutaminase. *ChemBioChem* **2017**, *18* (19), 1923–1927.
- (131) Percec, V.; Ahn, C.-H.; Bera, T. K.; Ungar, G.; Yeardley, D. J. P. Coassembly of a Hexagonal Columnar Liquid Crystalline Superlattice from Polymer(s) Coated with a Three-Cylindrical Bundle Supramolecular Dendrimer. *Chem. Eur. J.* **1999**, *5* (3), 1070–1083.
- (132) Canilho, N.; Kasemi, E.; Schlüter, A. D.; Mezzenga, R. Comblike Liquid-Crystalline Polymers from Ionic Complexation of Dendronized Polymers and Lipids. *Macromolecules* **2007**, *40* (8), 2822–2830.
- (133) Prokhorova, S. A.; Sheiko, S. S.; Ahn, C.-H.; Percec, V.; Möller, M. Molecular Conformations of Monodendron-Jacketed Polymers by Scanning Force Microscopy. *Macromolecules* **1999**, *32* (8), 2653–2660.
- (134) Stocker, W.; Karakaya, B.; Schürmann, B. L.; Rabe, J. P.; Schlüter, A. D. Ordered Dendritic Nanorods with a Poly(p-Phenylene) Backbone. *J. Am. Chem. Soc.* **1998**, *120* (31), 7691–7695.
- (135) Kim, Y.; Mayer, M. F.; Zimmerman, S. C. A New Route to Organic Nanotubes from Porphyrin Dendrimers. *Angew. Chemie* **2003**, *115* (10), 1153–1158.
- (136) Buhleier, E.; Wehner, W.; Vögtle, F. “Cascade”- and “Nonskid-Chain-like” Syntheses of Molecular Cavity Topologies. *Synthesis* **1978**, *2* (155–158).
- (137) Denkwalter, R. G.; Kolc, J.; Lukasavage, W. J. Macromolecular Highly Branched Homogeneous Compound Based on Lysine Units. US4289872A, April 6, 1979.
- (138) de Gennes, P. G.; Herve, H. Statistics of “Starburst” Polymers. *J. Phys. Lettres* **1983**, *44* (3), 351–360.
- (139) Lescanec, R. L.; Muthukumar, M. Configurational Characteristics and Scaling Behavior of Starburst Molecules: A Computational Study. *Macromolecules* **1990**, *23* (8), 2280–2288.

- (140) Boris, D.; Rubinstein, M. A Self-Consistent Mean Field Model of a Starburst Dendrimer: Dense Core vs Dense Shell. *Macromolecules* **1996**, *29*, 7251–7260.
- (141) Ballauff, M.; Likos, C. N. Dendrimers in Solution: Insight from Theory and Simulation. *Angew. Chem. Int. Ed.* **2004**, *43* (23), 2998–3020.
- (142) Han, M.; Chen, P.; Yang, X. Molecular Dynamics Simulation of PAMAM Dendrimer in Aqueous Solution. *Polymer* **2005**, *46* (10), 3481–3488.
- (143) Carbone, P.; Müller-Plathe, F. Molecular Dynamics Simulations of Polyaminoamide (PAMAM) Dendrimer Aggregates: Molecular Shape, Hydrogen Bonds and Local Dynamics. *Soft Matter* **2009**, *5* (13), 2638–2647.
- (144) Bertran, O.; Zhang, B.; Schlüter, A. D.; Halperin, A.; Kröger, M.; Alemán, C.; Spellmeyer, D. C.; Fox, T.; Caldwell, J. W.; Kollman, P. A.; et al. Computer Simulation of Dendronized Polymers: Organization and Characterization at the Atomistic Level. *RSC Adv.* **2013**, *3* (1), 126–140.
- (145) Wiesler, U.-M.; Weil, T.; Müllen, K. Nanosized Polyphenylene Dendrimers. In *Topics in Current Chemistry*; Springer, Berlin, Heidelberg, 2001; pp 1–40.
- (146) Rubinstein, M.; Colby, R. H. *Polymer Physics*; Oxford University Press, 2003.
- (147) Tomalia, D. A.; Naylor, A. M.; Goddard, W. A. Starburst Dendrimers: Molecular-Level Control of Size, Shape, Surface Chemistry, Topology, and Flexibility from Atoms to Macroscopic Matter. *Angew. Chem. Int. Ed.* **1990**, *29* (2), 138–175.
- (148) Zhang, B.; Wepf, R.; Kröger, M.; Halperin, A.; Schlüter, A. D. Height and Width of Adsorbed Dendronized Polymers: Electron and Atomic Force Microscopy of Homologous Series. *Macromolecules* **2011**, *44* (17), 6785–6792.
- (149) Kröger, M.; Schlüter, A. D.; Halperin, A. Branching Defects in Dendritic Molecules: Coupling Efficiency and Congestion Effects. *Macromolecules* **2013**, *46* (18), 7550–7564.
- (150) Zhang, B.; Yu, H.; Schlüter, A. D.; Halperin, A.; Kröger, M. Synthetic Regimes Due to Packing Constraints in Dendritic Molecules Confirmed by Labelling Experiments. *Nat. Commun.* **2013**, *4*, 1993.
- (151) Advincula, R. C. The Analysis and Characterization of Polymer Brushes: From Flat Surfaces to Nanoparticles. In *Polymer Brushes*; Wiley-VCH: Weinheim, 2005; pp 187–212.
- (152) Wilms, D.; Stiriba, S.-E.; Frey, H. Hyperbranched Polyglycerols: From the Controlled Synthesis of Biocompatible Polyether Polyols to Multipurpose Applications. *Acc. Chem. Res.* **2010**, *43* (1), 129–141.
- (153) Lu, X.-Y.; Wu, D.-C.; Li, Z.-J.; Chen, G.-Q. Polymer Nanoparticles. *Prog. Mol. Biol. Transl. Sci.* **2011**, *104*, 299–323.
- (154) Caminade, A.-M.; Laurent, R.; Delavaux-Nicot, B.; Majoral, J.-P. “Janus” Dendrimers: Syntheses and Properties. *New J. Chem.* **2012**, *36* (2), 217–226.
- (155) Ruiz-Sanchez, A. J.; Mesa-Antunez, P.; Barbero, N.; Collado, D.; Vida, Y.; Najera, F.; Perez-Inestrosa, E. Synthesis of All-Aliphatic Polyamide Dendrimers Based on a 3,3'-Diaminopivalic Acid Scaffold. *Polym. Chem.* **2015**, *6* (16), 3031–3038.
- (156) Jishkariani, D.; Macdermaid, C. M.; Timsina, Y. N.; Grama, S.; Gillani, S. S.; Divar, M.; Yadavalli, S. S.; Moussodia, R.-O.; Leowanawat, P.; Berrios Camacho, A. M.; et al. Self-Interrupted Synthesis of Sterically Hindered Aliphatic Polyamide Dendrimers. *Proc. Natl. Acad. Sci. USA* **2017**, *114* (12), E2275–E2284.
- (157) Ihre, H.; Hult, A.; Fréchet, J. M. J.; Gitsov, I. Double-Stage Convergent Approach for the Synthesis of Functionalized Dendritic Aliphatic Polyesters Based on 2,2-Bis(Hydroxymethyl)Propionic Acid. *Macromolecules* **1998**, *31* (13), 4061–4068.
- (158) Malkoch, M. A.; Malmström, E.; Hult, A. Rapid and Efficient Synthesis of Aliphatic Ester Dendrons and Dendrimers. *Macromolecules* **2002**, *35* (22), 8307–8314.



- (159) Ihre, H.; Padilla De Jesus, O. L.; Fréchet, J. M. J. Fast and Convenient Divergent Synthesis of Aliphatic Ester Dendrimers by Anhydride Coupling. *J. Am. Chem. Soc.* **2001**, *123* (25), 5908–5917.
- (160) Dendritech, Inc. <http://www.dendritech.com/index.html> (accessed May 8, 2018).
- (161) van Dongen, M. A.; Desai, A.; Orr, B. G.; Baker, J. R.; Banaszak Holl, M. M. Quantitative Analysis of Generation and Branch Defects in G5 Poly(Amidoamine) Dendrimer. *Polymer* **2013**, *54* (16), 4126–4133.
- (162) Müller, R.; Laschober, C.; Szymanski, W. W.; Allmaier, G. Determination of Molecular Weight, Particle Size, and Density of High Number Generation PAMAM Dendrimers Using MALDI–TOF–MS and NES–GEMMA. *Macromolecules* **2007**, *40* (15), 5599–5605.
- (163) Blais, J.-C.; Turrin Cédric-Olivier; Caminade, A.-M.; Majoral, J.-P. MALDI TOF Mass Spectrometry for the Characterization of Phosphorus-Containing Dendrimers. Scope and Limitations. *Anal. Chem.* **2000**, *72* (20), 5097–5105.
- (164) de Brabander-van den Berg, E. M. M.; Meijer, E. W. Poly(Propylene Imine) Dendrimers: Large-Scale Synthesis by Heterogeneously Catalyzed Hydrogenations. *Angew. Chem. Int. Ed.* **1993**, *32* (9), 1308–1311.
- (165) Shu, L.; Schäfer, A.; Schlüter, A. D. Dendronized Polymers: Increasing of Dendron Generation by the Attach-to Approach. *Macromolecules* **2000**, *33* (12), 4321–4328.
- (166) Shu, L.; Schlüter, A. D.; Ecker, C.; Severin, N.; Rabe, J. P. Extremely Long Dendronized Polymers: Synthesis, Quantification of Structure Perfection, Individualization, and SFM Manipulation. *Angew. Chem. Int. Ed.* **2001**, *40* (24), 4666–4669.
- (167) Zhang, A.; Zhang, B.; Wächtersbach, E.; Schmidt, M.; Schlüter, A. D. Efficient Synthesis of High Molar Mass, First- to Fourth-Generation Distributed Dendronized Polymers by the Macromonomer Approach. *Chem. Eur. J.* **2003**, *9* (24), 6083–6092.
- (168) Canilho, N.; Kasemi, E.; Mezzenga, R.; Schlüter, A. D. Liquid-Crystalline Polymers from Cationic Dendronized Polymer-Anionic Lipid Complexes. *J. Am. Chem. Soc.* **2006**, *128* (43), 13998–13999.
- (169) Yu, H.; Schlüter, A. D.; Zhang, B. Main-Chain Scission of a Charged Fifth-Generation Dendronized Polymer. *Helv. Chim. Acta* **2012**, *95* (12), 2399–2410.
- (170) Erickson, B. W.; Merrifield, R. B. Solid-Phase Peptide Synthesis. In *The Proteins*; 1976; pp 255–527.
- (171) Shu, L.; Gössl, I.; Rabe, J. P.; Schlüter, A. D. Quantitative Aspects of the Dendronization of Dendronized Linear Polystyrenes. *Macromol. Chem. Phys.* **2002**, No. 203, 2540–2550.
- (172) Yu, H. Synthesis of Densely-Packed, Extremely High Generation Dendronized Polymers, ETH Zurich, 2015.
- (173) Kawaguchi, T.; Walker, K. L.; Wilkins, C. L.; Moore, J. S. Double Exponential Dendrimer Growth. *J. Am. Chem. Soc.* **1995**, *117*, 2159–2165.
- (174) Yu, H.; Schlüter, A. D.; Zhang, B. Synthesis of High Generation Dendronized Polymers and Quantification of Their Structure Perfection. *Macromolecules* **2014**, *47* (13), 4127–4135.
- (175) Rumble, J. R.; Lide, D. R.; Bruno, T. J. *CRC Handbook of Chemistry and Physics : A Ready-Reference Book of Chemical and Physical Data. Online Edition 2018*, 98th ed.; CRC Press.
- (176) Scherz, L. F. Dendronized Polymers with Tailored Intermolecular Interactions: Synthesis and Thermomechanical Characterization, ETH Zürich, 2017.
- (177) Canilho, N.; Kasemi, E.; Schlüter, A. D.; Ruokolainen, J.; Mezzenga, R. Functional Columnar Liquid Crystalline Phases From Ionic Complexes of Dendronized Polymers and Sulfate Alkyl Tails. *Macromol. Symp.* **2008**, *270* (1), 58–64.
- (178) Zhuang, W.; Kasemi, E.; Ding, Y.; Kröger, M.; Schlüter, A. D.; Rabe, J. P. Self-Folding of Charged Single

- Dendronized Polymers. *Adv. Mater.* **2008**, *20* (17), 3204–3210.
- (179) Scherz, L. F.; Costanzo, S.; Huang, Q.; Schlüter, A. D.; Vlassopoulos, D. Dendronized Polymers with Ureidopyrimidinone Groups: An Efficient Strategy To Tailor Intermolecular Interactions, Rheology, and Fracture. *Macromolecules* **2017**, *50* (13), 5176–5187.
- (180) Hawker, C. J.; Wooley, K. L.; Frechet, J. M. J. Solvatochromism as a Probe of the Microenvironment in Dendritic Polyethers: Transition from an Extended to a Globular Structure. *J. Am. Chem. Soc.* **1993**, *115* (10), 4375–4376.
- (181) Barner, J.; Al-Hellani, R.; Schlüter, A. D.; Rabe, J. P. Synthesis with Single Macromolecules: Covalent Connection between a Neutral Dendronized Polymer and Polyelectrolyte Chains as Well as Graphene Edges. *Macromol. Rapid Commun.* **2010**, *31* (4), 362–367.
- (182) Al-Hellani, R.; Barner, J.; Rabe, J. P.; Schlüter, A. D. Covalent Connection of Individualized, Neutral, Dendronized Polymers on a Solid Substrate Using a Scanning Force Microscope. *Chemistry* **2006**, *12* (25), 6542–6551.
- (183) Grebikova, L.; Maroni, P.; Muresan, L.; Zhang, B.; Schlüter, A. D.; Borkovec, M. Interactions between Individual Charged Dendronized Polymers and Surfaces. *Macromolecules* **2013**, *46* (9), 3603–3610.
- (184) Grebikova, L.; Maroni, P.; Zhang, B.; Schlüter, A. D.; Borkovec, M. Single-Molecule Force Measurements by Nano-Handling of Individual Dendronized Polymers. *ACS Nano* **2014**, *8* (3), 2237–2245.
- (185) Grebikova, L.; Kozuharov, S.; Maroni, P.; Mikhaylov, A.; Dietler, G.; Schlüter, A. D.; Ullner, M.; Borkovec, M. The Persistence Length of Adsorbed Dendronized Polymers. *Nanoscale* **2016**, *8*, 13498–13506.
- (186) Kröger, A.; Zhang, B.; Rosenauer, C.; Schlüter, A. D.; Wegner, G. Solvent Induced Phenomena in a Dendronized Linear Polymer. *Colloid Polym. Sci.* **2013**, *291* (12), 2879–2892.
- (187) Kurzbach, D.; Kattinig, D. R.; Zhang, B.; Schlüter, A. D.; Hinderberger, D. Loading and Release Capabilities of Charged Dendronized Polymers Revealed by EPR Spectroscopy. *Chem. Sci.* **2012**, *3* (8), 2550–2558.
- (188) Maltar-Strmečki, N.; Yu, H.; Messmer, D.; Zhang, B.; Schlüter, A. D.; Hinderberger, D. Exploring the Loading Capacity of Generation Six to Eight Dendronized Polymers in Aqueous Solution. *ChemPhysChem* **2016**, *17* (17), 2767–2772.
- (189) Yu, H.; Schlüter, A. D.; Zhang, B. Synthesis of Dendronized Polymers by a “n + 2” Approach. *Macromolecules* **2012**, *45* (21), 8555–8560.
- (190) Wuts, P. G. M.; Greene, T. W. *Greene’s Protective Groups in Organic Synthesis, Fourth Edition*, 4th ed.; John Wiley & Sons: Hoboken, New Jersey, 2006.
- (191) McOmie, J. F. W. *Protective Groups in Organic Chemistry*; Springer, 1976.
- (192) Isidro-Llobet, A.; Lvarez, M.; Albericio, F. Amino Acid-Protecting Groups. *Chem. Rev.* **2009**, *109*, 2455–2504.
- (193) Al-Hellani, R.; Schlüter, A. D. A Series of First- and Second-Generation Dendronized Polymers with Orthogonally Protected Amine Groups in the Periphery. *Macromolecules* **2006**, *39* (26), 8943–8951.
- (194) Rawal, V. H.; Cava, M. P. Thermolytic Removal of T-Butyloxycarbonyl (Boc) Protecting Group on Indoles and Pyrroles. *Tetrahedron Lett.* **1985**, *26* (50), 6141–6142.
- (195) Choy, J.; Jaime-Figueroa, S.; Jiang, L.; Wagner, P. Novel Practical Deprotection of N-Boc Compounds Using Fluorinated Alcohols. *Synth. Commun.* **2008**, *38* (21), 3840–3853.
- (196) Ashworth, I. W.; Cox, B. G.; Meyrick, B. Kinetics and Mechanism of N-Boc Cleavage: Evidence of a Second-Order Dependence upon Acid Concentration. *J. Org. Chem.* **2010**, *75*, 8117–8125.
- (197) Subhas Bose, D.; Kiran Kumar, K.; Narsimha Reddy, A. V. A New Protocol for Selective Deprotection of

- N-Tert -Butoxycarbonyl Protective Group (t -Boc) with Sn(OTf)<sub>2</sub>. *Synth. Commun.* **2003**, *33* (3), 445–450.
- (198) Evans, E. F.; Lewis, N. J.; Kapfer, I.; Macdonalda, G.; Taylor, R. J. K. A Tert-Cutoxycarbonyl (Boc) Deprotection Using Boron Trifluoride Etherate. *Synth. Commun.* **1997**, *27* (11), 1819–1825.
- (199) Olah, G. A.; Narang, S. C. Iodotrimethylsilane—A Versatile Synthetic Reagent. *Tetrahedron* **1982**, *38* (15), 2225–2277.
- (200) Jacquemard, U.; Bénétteau, V.; Lefoix, M.; Routier, S.; Mérour, J.-Y.; Coudert, G. Mild and Selective Deprotection of Carbamates with Bu<sub>4</sub>NF. *Tetrahedron* **2004**, *60* (44), 10039–10047.
- (201) Stigers, K. D.; Koutroulis, M. R.; Chung, D. M.; Nowick, J. S. Fmoc: A More Soluble Analogue of the 9-Fluorenylmethoxycarbonyl Protecting Group. *J. Org. Chem.* **2000**, *65* (12), 3858–3860.
- (202) Carpino, L. a. The 9-Fluorenylmethoxycarbonyl Family of Base-Sensitive Amino-Protecting Groups. *Acc. Chem. Res.* **1987**, *20* (11), 401–407.
- (203) Hoeg-Jensen, T.; Jakobsen, M. H.; Holm, A. A New Method for Rapid Solution Synthesis of Shorter Peptides by Use of PyBOP. *Tetrahedron Lett.* **1991**, *32* (44), 6387–6390.
- (204) Sheppeck, J. E.; Kar, H.; Hong, H. A Convenient and Scaleable Procedure for Removing the Fmoc Group in Solution. *Tetrahedron Lett.* **2000**, *41* (28), 5329–5333.
- (205) Larrivé-Aboussafy, C.; Jones, B. P.; Price, K. E.; Hardink, M. A.; Mclaughlin, R. W.; Lillie, B. M.; Hawkins, J. M.; Vaidyanathan, R. DBU Catalysis of N,N'-Carbonyldiimidazole-Mediated Amidations. *Org. Lett.* **2010**, *12* (2), 324–327.
- (206) Al-Hellani, R.; Schlüter, A. D. On the Synthesis and Selective Deprotection of Low-Generation Dendrons with Orthogonally Protected Peripheral Amine Groups and a Possible Impact of the Deprotection Conditions on the Stability of Dendronized Polymers' Skeletons. *Helv. Chim. Acta* **2006**, *89* (11), 2745–2763.
- (207) Paryzek, Z.; Koenig, H.; Tabaczka, B. Ammonium Formate/Palladium on Carbon: A Versatile System for Catalytic Hydrogen Transfer Reductions of Carbon-Carbon Double Bonds. *Synthesis* **2003**, *2003* (13), 2023–2026.
- (208) Gomez-Martinez, P.; Dessolin, M.; Guibé, F.; Albericio, F.; Loffet, A.; Bernard, J.-M.; Beyermann, M. N<sub>α</sub>-Alloc Temporary Protection in Solid-Phase Peptide Synthesis. The Use of Amine–borane Complexes as Allyl Group Scavengers. *J. Chem. Soc. Perkin Trans. 1* **1999**, *31* (20), 2871–2874.
- (209) Guibé, F. Allylic Protecting Groups and Their Use in a Complex Environment Part II: Allylic Protecting Groups and Their Removal through Catalytic Palladium π-Allyl Methodology. *Tetrahedron* **1998**, *54* (13), 2967–3042.
- (210) Lemaire-Audoire, S.; Savignac, M.; Blart, E.; Pourcelot, G.; Genêt, J. P.; Bernard, J.-M. Selective Deprotective Method Using Palladium-Water Soluble Catalysts. *Tetrahedron Lett.* **1994**, *35* (47), 8783–8786.
- (211) Corey, E. J.; Suggs, J. W. Cleavage of Allyloxycarbonyl Protecting Group from Oxygen and Nitrogen under Mild Conditions by Nickel Carbonyl. *J. Org. Chem.* **1973**, *38* (18), 3223–3224.
- (212) Thieriet, N.; Alsina, J.; Giralt, E.; Guibé, F.; Albericio, F. Use of Alloc-Amino Acids in Solid-Phase Peptide Synthesis. Tandem Deprotection-Coupling Reactions Using Neutral Conditions. *Tetrahedron Lett.* **1997**, *38* (41), 7275–7278.
- (213) Dangles, O.; Guibe, F.; Balavoine, G.; Lavielle, S.; Marquet, A. Selective Cleavage of the Allyl and (Allyloxy)Carbonyl Groups through Palladium-Catalyzed Hydrostannolysis with Tributyltin Hydride. Application to the Selective Protection-Deprotection of Amino Acid Derivatives and in Peptide Synthesis. *J. Org. Chem.* **1987**, *52* (22), 4984–4993.
- (214) Merzouk, A.; Guibé, F.; Loffet, A. On the Use of Silylated Nucleophiles in the Palladium Catalysed Deprotection of Allylic Carboxylates and Carbamates. *Tetrahedron Lett.* **1992**, *33* (4), 477–480.

- (215) Zorn, C.; Gnad, F.; Salmen, S.; Herpin, T.; Reiser, O. Deprotection of N-Alloc Amines by Pd(0)/DABCO— an Efficient Method for in Situ Peptide Coupling of Labile Amino Acids. *Tetrahedron Lett.* **2001**, *42* (40), 7049–7053.
- (216) Unverzagt, C.; Kunz, H. Synthesis of Glycopeptides and Neoglycoproteins Containing the Fucosylated Linkage Region of N-Glycoproteins. *Bioorg. Med. Chem.* **1994**, *2* (11), 1189–1201.
- (217) Neumann, D. M.; Cammarata, A.; Backes, G.; Palmer, G. E.; Jursic, B. S. Synthesis and Antifungal Activity of Substituted 2,4,6-Pyrimidinetrione Carbaldehyde Hydrazones. *Bioorg. Med. Chem.* **2014**, *22*, 813–826.
- (218) Garro-Helion, F.; Merzouk, A.; Guibe, F. Mild and Selective Palladium(0)-Catalyzed Deallylation of Allylic Amines. Allylamine and Diallylamine as Very Convenient Ammonia Equivalents for the Synthesis of Primary Amines. *J. Org. Chem.* **1993**, *58* (22), 6109–6113.
- (219) Allyl chloroformate 97% | Sigma-Aldrich  
[https://www.sigmaaldrich.com/catalog/product/aldrich/242306?lang=de&region=CH&gclid=Cj0KCQjw7Z3VBRC-ARIsAEQifZS3HBOytT-IN3PDWDyMfy7JVDwtgXGnQd6rVspREtMqr5txqwG024UaArd9EALw\\_wcB](https://www.sigmaaldrich.com/catalog/product/aldrich/242306?lang=de&region=CH&gclid=Cj0KCQjw7Z3VBRC-ARIsAEQifZS3HBOytT-IN3PDWDyMfy7JVDwtgXGnQd6rVspREtMqr5txqwG024UaArd9EALw_wcB) (accessed Mar 13, 2018).
- (220) Trost, B. M.; Xu, J. The O-Acylation of Ketone Enolates by Allyl 1H-Imidazole-1-Carboxylate Mediated with Boron Trifluoride Etherate A Convenient Procedure for the Synthesis of Substituted Allyl Enol Carbonates. *J. Org. Chem.* **2007**, *72* (24), 9372–9375.
- (221) Kunz, H.; Unverzagt, C. The Allyloxycarbonyl (Aloc) Moiety? Conversion of an Unsuitable into a Valuable Amino Protecting Group for Peptide Synthesis. *Angew. Chem. Int. Ed.* **1984**, *23* (6), 436–437.
- (222) Schlüter, A.-D.; Harnisch, H.; Harnisch, J.; Szeimies-Seebach, U.; Szeimies, G. Zur Chemie Einiger Verbrückter Bicyclo[1.1.0]but-1(3)-En-Derivate. *Chem. Ber.* **1985**, *118* (9), 3513–3528.
- (223) Hayakawa, Y.; Wakabayashi, S.; Kato, H.; Noyori, R. The Allylic Protection Method in Solid-Phase Oligonucleotide Synthesis. An Efficient Preparation of Solid-Anchored DNA Oligomers. *J. Am. Chem. Soc.* **1990**, *112*, 1691–1696.
- (224) Gallagher, W. P.; Vo, A. Dithiocarbamates: Reagents for the Removal of Transition Metals from Organic Reaction Media. *Org. Process Res. Dev.* **2015**, *19* (10), 1369–1373.
- (225) Nielsen, K. T.; Bechgaard, K.; Krebs, F. C. Removal of Palladium Nanoparticles from Polymer Materials. *Macromolecules* **2005**, *38*, 658–659.
- (226) Caruso, F.; Mantellato, S.; Palacios, M.; Flatt, R. J. ICP-OES Method for the Characterization of Cement Pore Solutions and Their Modification by Polycarboxylate-Based Superplasticizers. *Cem. Concr. Res.* **2017**, *91*, 52–60.
- (227) Messmer, D.; Kröger, M.; Schlüter, A. D. Pushing Synthesis towards the Maximum Generation Range of Dendritic Macromolecules. *Macromolecules* **2018**, *51* (14), 5420–5429.
- (228) Bertran, O.; Zhang, B.; Schlüter, A. D.; Kröger, M.; Alemán, C. Computer Simulation of Fifth Generation Dendronized Polymers: Impact of Charge on Internal Organization. *J. Phys. Chem. B* **2013**, *117* (19), 6007–6017.
- (229) Nadgorny, M.; Gentekos, D. T.; Xiao, Z.; Singleton, S. P.; Fors, B. P.; Connal, L. A. Manipulation of Molecular Weight Distribution Shape as a New Strategy to Control Processing Parameters. *Macromol. Rapid Commun.* **2017**, *38* (19), 1700352.
- (230) Wypych, G. *PVC Degradation and Stabilization*; Elsevier, 2015.
- (231) Ayre, W. N.; Denyer, S. P.; Evans, S. L. Ageing and Moisture Uptake in Polymethyl Methacrylate (PMMA) Bone Cements. *J. Mech. Behav. Biomed. Mater.* **2014**, *32*, 76–88.
- (232) Sakaguchi, M.; Sohma, J. ESR Evidence for Main-Chain Scission Produced by Mechanical Fracture of Polymers at Low Temperature. *J. Polym. Sci. Polym. Phys. Ed.* **1975**, *13*, 1233–1245.

- (233) Kawashima, T.; Shimada, S.; Kashiwabara, H.; Sohma, J. ESR Studies on the Molecular Mechanisms of Fracture of Polymers at Low Temperatures. *Polym. J.* **1973**, *5* (2), 135–143.
- (234) Campbell, D.; Peterlin, A. Free-Radical Formation in Uniaxially Stressed Nylon. *J. Polym. Sci. Part B Polym. Lett.* **1968**, *6* (7), 481–485.
- (235) Gol'dberg, V. M.; Zaikov, G. E. Kinetics of Mechanical Degradation in Melts under Model Conditions and during Processing of Polymers—A Review. *Polym. Degrad. Stab.* **1987**, *19* (3), 221–250.
- (236) Szalay, A. Die Zerstörung von Hochpolymeren Molekülen Mittels Ultraschallwellen. *Zeitschrift für Phys. Chemie* **1933**, *164A* (1), 234–240.
- (237) Tabata, M.; Miyazawa, T.; Kobayashi, O.; Sohma, J. Direct Evidence of Main-Chain Scissions Induced by Ultrasonic Irradiation of Benzene Solutions of Polymers. *Chem. Phys. Lett.* **1980**, *73* (1), 178–180.
- (238) Schaefer, M.; Icli, B.; Weder, C.; Lattuada, M.; Kilbinger, A. F. M.; Simon, Y. C. The Role of Mass and Length in the Sonochemistry of Polymers. *Macromolecules* **2016**, *49* (5), 1630–1636.
- (239) May, P. A.; Munaretto, N. F.; Hamoy, M. B.; Robb, M. J.; Moore, J. S. Is Molecular Weight or Degree of Polymerization a Better Descriptor of Ultrasound-Induced Mechanochemical Transduction? *ACS Macro Lett.* **2016**, *5* (2), 177–180.
- (240) Rånby, B.; Rabek, J. F. Photodegradation of Polymer Materials. In *Comprehensive Polymer Science and Supplements*; Elsevier, 1989; pp 253–283.
- (241) Verdu, J. Structural Changes Caused by Oxidation. In *Oxidative Ageing of Polymers*; John Wiley & Sons, Inc.: Hoboken, NJ, USA, 2013; pp 163–201.
- (242) Kaminsky, W.; Franck, J. Monomer Recovery by Pyrolysis of Poly(Methyl Methacrylate) (PMMA). *J. Anal. Appl. Pyrolysis* **1991**, *19*, 311–318.
- (243) Raudino, A.; Fragalà, M. E.; Compagnini, G.; Puglisi, O. Modeling of Low-Temperature Depolymerization of Poly (Methyl Methacrylate) Promoted by Ion Beam. *J. Chem. Phys.* **1999**, *111* (4), 1721.
- (244) Grassie, N.; Davidson, A. J. Thermal-, Photothermal- and Photodegradation of Copolymers of Methyl Methacrylate and Maleic Anhydride. *Polym. Degrad. Stab.* **1980**, *3* (1), 25–44.
- (245) Lewis, E. E.; Naylor, M. A. Pyrolysis of Polytetrafluoroethylene. *J. Am. Chem. Soc.* **1947**, *69* (8), 1968–1970.
- (246) Dal Nogare, S.; Punderson, O. J. Polyoxymethylene Carboxylates of Improved Thermal Stability. US2998409 (A), 1961.
- (247) Reichmanis, E.; Thompson, L. F. Polymer Materials for Microlithography. *Chem. Rev.* **1989**, *89*, 1273–1289.
- (248) Uhrich, K. E.; Cannizzaro, S. M.; Langer, R. S.; Shakesheff, K. M. Polymeric Systems for Controlled Drug Release. *Chem. Rev.* **1999**, *99*, 3181–3198.
- (249) Lundt, B. F.; Johansen, N. L.; Vølund, A.; Markussen, J. Removal of T-Butyl and t-Butocycarbonyl Protecting Groups with Trifluoroacetic Acid: Mechanisms, Diproduct Formation and Evaluation of Scavengers. *Int. J. Pept. Protein Res.* **1978**, *12* (5), 258–268.
- (250) Mehta, A.; Jaouhari, R.; Benson, T. J.; Douglas, K. T. Improved Efficiency and Selectivity in Peptide Synthesis: Use of Triethylsilane as a Carbocation Scavenger in Deprotection of t-Butyl Esters and t-Butoxycarbonyl-Protected Sites. *Tetrahedron Lett.* **1992**, *33* (37), 5441–5444.
- (251) Lebedeva, N. V.; Nese, A.; Sun, F. C.; Matyjaszewski, K.; Sheiko, S. S. Anti-Arrhenius Cleavage of Covalent Bonds in Bottlebrush Macromolecules on Substrate. *Proc. Natl. Acad. Sci. USA* **2012**, *109* (24), 9276–9280.
- (252) Korotkikh, N. I.; Cowley, A. H.; Moore, J. A.; Glinyanaya, N. V.; Panov, I. S.; Rayenko, G. F.; Pekhtereva,

- T. M.; Shvaika, O. P. Reaction of 1-Tert-Butyl-3,4-Diphenyl-1,2,4-Triazol-5-Ylidenes with a Malonic Ester. *Org. Biomol. Chem.* **2008**, *6* (1), 195–199.
- (253) Beugelmans, R.; Neuville, L.; Bois-Choussy, M.; Chastanet, J.; Zhu, J. Palladium Catalyzed Reductive Deprotection of Alloc: Transprotection and Peptide Bond Formation. *Tetrahedron Lett.* **1995**, *36* (18), 3129–3132.
- (254) Roos, E. C.; Bernabe, P.; Hiemstra, H.; Speckamp, W. N.; Kaptein, B.; Boesten, W. H. J. Palladium-Catalyzed Transprotection of Allyloxycarbonyl-Protected Amines: Efficient One-Pot Formation of Amides and Dipeptides. *J. Org. Chem.* **1995**, *60* (6), 1733–1740.
- (255) Kasemi, E.; Zhuang, W.; Rabe, J. P.; Fischer, K.; Schmidt, M.; Colussi, M.; Keul, H.; Yi, D.; Colfen, H.; Schlüter, A. D. Synthesis of an Anionically Chargeable, High-Molar-Mass, Second-Generation Dendronized Polymer and the Observation of Branching by Scanning Force Microscopy. *J. Am. Chem. Soc.* **2006**, *128* (15), 5091–5099.
- (256) Lou, X.; de Waal, B. F. M.; van Dongen, J. L. J.; Vekemans, J. A. J. M.; Meijer, E. W. A Pitfall of Using 2-[(2E)-3-(4-Tert-Butylphenyl)-2-Methylprop-2-Enylidene]Malononitrile as a Matrix in MALDI TOF MS: Chemical Adduction of Matrix to Analyte Amino Groups. *J. Mass Spectrom.* **2010**, *45* (10), 1195–1202.
- (257) Campbell, D. Electron Spin Resonance of Polymers. *J. Polym. Sci. Macromol. Rev.* **1970**, *4* (1), 91–181.
- (258) Manring, L. E. Thermal Degradation of Poly(Methyl Methacrylate). 4. Random Side-Group Scission. *Macromolecules* **1991**, *24*, 3304–3309.
- (259) Stoliarov, S. I.; Westmoreland, P. R.; Nyden, M. R.; Forney, G. P. A Reactive Molecular Dynamics Model of Thermal Decomposition in Polymers: I. Poly(Methyl Methacrylate). *Polymer* **2003**, *44* (3), 883–894.
- (260) Inaba, A.; Kashiwagi, T.; Brown, J. E. Effects of Initial Molecular Weight on Thermal Degradation of Poly(Methyl Methacrylate): Part 1—Model 1. *Polym. Degrad. Stab.* **1988**, *21* (1), 1–20.
- (261) Kashiwagi, T.; Inaba, A.; Hamins, A. Behavior of Primary Radicals during Thermal Degradation of Poly(Methyl Methacrylate). *Polym. Degrad. Stab.* **1989**, *26* (2), 161–184.
- (262) Wilkie, C. A. TGA/FTIR: An Extremely Useful Technique for Studying Polymer Degradation. *Polym. Degrad. Stab.* **1999**, *66* (3), 301–306.
- (263) Cornell, W. D.; Cieplak, P.; Bayly, C. I.; Gould, I. R.; Merz, K. M.; Ferguson, D. M.; Spellmeyer, D. C.; Fox, T.; Caldwell, J. W.; Kollman, P. A. A Second Generation Force Field for the Simulation of Proteins, Nucleic Acids, and Organic Molecules. *J. Am. Chem. Soc.* **1995**, *117* (19), 5179–5197.
- (264) Wang, J.; Wolf, R. M.; Caldwell, J. W.; Kollman, P. A.; Case, D. A. Development and Testing of a General Amber Force Field. *J. Comput. Chem.* **2004**, *25* (9), 1157–1174.
- (265) Dewick, P. M. *Essentials of Organic Chemistry : For Students of Pharmacy, Medicinal Chemistry and Biological Chemistry*; J. Wiley, 2006.
- (266) Tugulu, S.; Klok, A. Stability and Nonfouling Properties of Poly(Poly(Ethylene Glycol) Methacrylate) Brushes under Cell Culture Conditions.
- (267) Klok, A.; Genzer, J. Expanding the Polymer Mechanochemistry Toolbox through Surface-Initiated Polymerization. **2015**.
- (268) Sun, X.; Lindner, J.-P.; Bruchmann, B.; Schlüter, A. D. Synthesis of Neutral, Water-Soluble Oligo-Ethylene Glycol-Containing Dendronized Homo- and Copolymers of Generations 1, 1.5, 2, and 3. *Macromolecules* **2014**, *47* (21), 7337–7346.
- (269) Mantovani, J. G.; Allison, D. P.; Warmack, R. J.; Ferrell, T. L.; Ford, J. R.; Manos, R. E.; Thompson, J. R.; Reddick, B. B.; Jacobson, K. B. Scanning Tunneling Microscopy of Tobacco Mosaic Virus on Evaporated and Sputter-Coated Palladium/Gold Substrates. *J. Microsc.* **1990**, *158* (1), 109–116.
- (270) Zenhausern, F.; Adrian, M.; Emch, R.; Taborrelli, M.; Jobin, M.; Descouts, P. Scanning Force Microscopy and Cryo-Electron Microscopy of Tobacco Mosaic Virus as a Test Specimen. *Ultramicroscopy* **1992**, 42–

- 44, 1168–1172.
- (271) Drygin, Y. F.; Bordunova, O. A.; Gallyamov, M. O.; Yaminsky, I. V. Atomic Force Microscopy Examination of Tobacco Mosaic Virus and Virion RNA. *FEBS Lett.* **1998**, *425* (2), 217–221.
- (272) Käs, J.; Strey, H.; Sackmann, E. Direct Imaging of Reptation for Semiflexible Actin Filaments. *Nature* **1994**, *368*, 226–229.
- (273) Betzig, E.; Patterson, G. H.; Sougrat, R.; Lindwasser, O. W.; Olenych, S.; Bonifacino, J. S.; Davidson, M. W.; Lippincott-Schwartz, J.; Hess, H. F. Imaging Intracellular Fluorescent Proteins at Nanometer Resolution. *Science* **2006**, *313*, 1642–1645.
- (274) Urban, E.; Jacob, S.; Nemethova, M.; Resch, G. P.; Small, V. J. Electron Tomography Reveals Unbranched Networks of Actin Filaments in Lamellipodia. *Nat. Cell Biol.* **2010**, *12*, 429–435.
- (275) Gras, S. L.; Waddington, L. J.; Goldie, K. N. Transmission Electron Microscopy of Amyloid Fibrils; Humana Press, Totowa, NJ, 2011; pp 197–214.
- (276) Amzallag, A.; Vaillant, C. D.; Jacob, M.; Unser, M.; Bednar, J.; Kahn, J. D.; Dubochet, J.; Stasiak, A.; Maddocks, J. H. 3D Reconstruction and Comparison of Shapes of DNA Minicircles Observed by Cryo-Electron Microscopy. *Nucleic Acids Res.* **2006**, *34* (18), e125.
- (277) Dustin, I.; Furrer, P.; Stasiak, A.; Dubochet, J.; Langowski, J.; Egelman, E. Spatial Visualization of DNA in Solution. *J. Struct. Biol.* **1991**, *107* (1), 15–21.
- (278) Hansma, H. G.; Sinsheimer, R. L.; Li, M.-Q.; Hansma, P. K. Atomic Force Microscopy of Single-and Double-Stranded DNA. *Nucleic Acids Res.* **1992**, *20* (14), 3585–3590.
- (279) Hamon, L.; Pastre, D.; Dupaigne, P.; Breton, C. L.; Cam, E. L.; Pietrement, O. High-Resolution AFM Imaging of Single-Stranded DNA-Binding (SSB) Protein–DNA Complexes. *Nucleic Acids Res.* **2007**, *35* (8), e58–e58.
- (280) Sugihara, K.; Kumaki, J. Visualization of Two-Dimensional Single Chain Conformations Solubilized in a Miscible Polymer Blend Monolayer by Atomic Force Microscopy. **2012**.
- (281) Kumaki, J.; Hashimoto, T. Conformational Change in an Isolated Single Synthetic Polymer Chain on a Mica Surface Observed by Atomic Force Microscopy. **2003**.
- (282) Higgins, M. K.; Lea, S. M. On the State of Crystallography at the Dawn of the Electron Microscopy Revolution. *Curr. Opin. Struct. Biol.* **2017**, *46*, 95–101.
- (283) Fernandez-Leiro, R.; Scheres, S. H. W. Unravelling Biological Macromolecules with Cryo-Electron Microscopy. *Nature* **2016**, *537* (7620), 339–346.
- (284) Dubochet, J.; McDowell, A. W. Vitrification of Pure Water for Electron Microscopy. *J. Microsc.* **1981**, *124* (3), 3–4.
- (285) Adrian, M.; Dubochet, J.; Lepault, J.; McDowell, A. W. Cryo-Electron Microscopy of Viruses. *Nature* **1984**, *308* (5954), 32–36.
- (286) Frank, J. Single-Particle Reconstruction of Biological Molecules—Story in a Sample (Nobel Lecture). *Angew. Chem. Int. Ed.* **2018**, *57*, 2–18.
- (287) Patterson, J. P.; Xu, Y.; Moradi, M.-A.; Sommerdijk, N. A. J. M.; Friedrich, H. CryoTEM as an Advanced Analytical Tool for Materials Chemists. *Acc. Chem. Res.* **2017**, *50* (7), 1495–1501.
- (288) Ercius, P.; Alaidi, O.; Rames, M. J.; Ren, G. Electron Tomography: A Three-Dimensional Analytic Tool for Hard and Soft Materials Research. *Adv. Mater.* **2015**, *27* (38), 5638–5663.
- (289) Kirchenbuechler, I.; Guu, D.; Kurniawan, N. A.; Koenderink, G. H.; Lettinga, M. P. Direct Visualization of Flow-Induced Conformational Transitions of Single Actin Filaments in Entangled Solutions. *Nat. Commun.* **2014**, *5*, 5060.
- (290) Resch, G. P.; Goldie, K. N.; Krebs, A.; Hoenger, A.; Small, J. V. Visualisation of the Actin Cytoskeleton by

- Cryo-Electron Microscopy. *J. Cell Sci.* **2002**, *115* (9), 1877 LP-1882.
- (291) Yang, C.; Svitkina, T. Visualizing Branched Actin Filaments in Lamellipodia by Electron Tomography. *Nat. Cell Biol.* **2011**, *13* (9), 1012–1013.
- (292) Mueller, J.; Pfanzelter, J.; Winkler, C.; Narita, A.; Le Clairche, C.; Nemethova, M.; Carlier, M.-F.; Maeda, Y.; Welch, M. D.; Ohkawa, T.; et al. Electron Tomography and Simulation of Baculovirus Actin Comet Tails Support a Tethered Filament Model of Pathogen Propulsion. *PLoS Biol.* **2014**, *12* (1), e1001765.
- (293) Rohs, R.; Jin, X.; West, S. M.; Joshi, R.; Honig, B.; Mann, R. S. Origins of Specificity in Protein-DNA Recognition. *Annu. Rev. Biochem.* **2010**, *79* (1), 233–269.
- (294) Bednar, J.; Furrer, P.; Katritch, V.; Stasiak, A.; Dubochet, J.; Stasiak, A. Determination of DNA Persistence Length by Cryo-Electron Microscopy. Separation of the Static and Dynamic Contributions to the Apparent Persistence Length of DNA. *J. Mol. Biol.* **1995**, *254* (4), 579–594.
- (295) Lei, D.; Marras, A. E.; Liu, J.; Huang, C.-M.; Zhou, L.; Castro, C. E.; Su, H.-J.; Ren, G. Three-Dimensional Structural Dynamics of DNA Origami Bennett Linkages Using Individual-Particle Electron Tomography. *Nat. Commun.* **2018**, *9* (1), 592.
- (296) Xu, Y.; Bolisetty, S.; Drechsler, M.; Fang, B.; Yuan, J.; Ballauff, M.; Müller, A. H. E. PH and Salt Responsive Poly(N,N-Dimethylaminoethyl Methacrylate) Cylindrical Brushes and Their Quaternized Derivatives. *Polymer* **2008**, *49* (18), 3957–3964.
- (297) Wittemann, A.; Drechsler, M.; Talmon, Y.; Ballauff, M. High Elongation of Polyelectrolyte Chains in the Osmotic Limit of Spherical Polyelectrolyte Brushes: A Study by Cryogenic Transmission Electron Microscopy. *J. Am. Chem. Soc.* **2005**, *127* (27), 9688–9689.
- (298) Xu, Y.; Bolisetty, S.; Drechsler, M.; Fang, B.; Yuan, J.; Harnau, L.; Ballauff, M.; Müller, A. H. E. Manipulating Cylindrical Polyelectrolyte Brushes on the Nanoscale by Counterions: Collapse Transition to Helical Structures. *Soft Matter* **2009**, *5* (2), 379–384.
- (299) Natarajan, B.; Lachman, N.; Lam, T.; Jacobs, D.; Long, C.; Zhao, M.; Wardle, B. L.; Sharma, R.; Liddle, J. A. The Evolution of Carbon Nanotube Network Structure in Unidirectional Nanocomposites Resolved by Quantitative Electron Tomography. *ACS Nano* **2015**, *9* (6), 6050–6058.
- (300) Majoinen, J.; Haataja, J. S.; Appelhans, D.; Lederer, A.; Olszewska, A.; Seitsonen, J.; Aseyev, V.; Kontturi, E.; Rosilo, H.; Sterberg, M. O.; et al. Supracolloidal Multivalent Interactions and Wrapping of Dendronized Glycopolymers on Native Cellulose Nanocrystals. *J. Am. Chem. Soc.* **2014**, *136*, 47.
- (301) Wirix, M. J. M.; Bomans, P. H. H.; Friedrich, H.; Sommerdijk, N. A.; de With, G. Three-Dimensional Structure of P3HT Assemblies in Organic Solvents Revealed by Cryo-TEM. *Nano Lett.* **2014**, *14* (4), 2033–2038.
- (302) Berlepsch, H. v.; Thota, B. N. S.; Wyszogrodzka, M.; de Carlo, S.; Haag, R.; Böttcher, C. Controlled Self-Assembly of Stomatosomes by Use of Single-Component Fluorinated Dendritic Amphiphiles. *Soft Matter* **2018**, *14* (25), 5256–5269.
- (303) Parry, A. L.; Bomans, P. H. H.; Holder, S. J.; Sommerdijk, N. A.; Bigini, S. C. G. Cryo Electron Tomography Reveals Confined Complex Morphologies of Tripeptide-Containing Amphiphilic Double-Comb Diblock Copolymers. *Angew. Chem. Int. Ed.* **2008**, *120*, 8991–8994.
- (304) Barnhill, S. A.; Bell, N. C.; Patterson, J. P.; Olds, D. P.; Gianneschi, N. C. Phase Diagrams of Polynorbornene Amphiphilic Block Copolymers in Solution. *Macromolecules* **2015**, *48* (4), 1152–1161.
- (305) Danev, R.; Baumeister, W. Expanding the Boundaries of Cryo-EM with Phase Plates. *Curr. Opin. Struct. Biol.* **2017**, *46*, 87–94.
- (306) Kuijper, M.; van Hoften, G.; Janssen, B.; Geurink, R.; De Carlo, S.; Vos, M.; van Duinen, G.; van Haeringen, B.; Storms, M. FEI's Direct Electron Detector Developments: Embarking on a Revolution in Cryo-TEM. *J. Struct. Biol.* **2015**, *192* (2), 179–187.
- (307) Faruqi, A. R.; McMullan, G. Direct Imaging Detectors for Electron Microscopy. *Nucl. Instruments*



- Methods Phys. Res. Sect. A Accel. Spectrometers, Detect. Assoc. Equip.* **2018**, *878*, 180–190.
- (308) van Heel, M.; Frank, J. Use of Multivariate Statistics in Analysing the Images of Biological Macromolecules. *Ultramicroscopy* **1981**, *6* (2), 187–194.
- (309) Cheng, Y.; Grigorieff, N.; Penczek, P. A.; Walz, T. A Primer to Single-Particle Cryo-Electron Microscopy. *Cell* **2015**, *161* (3), 438–449.
- (310) Zhang, X.; Zhang, L.; Tong, H.; Peng, B.; Rames, M. J.; Zhang, S.; Ren, G. 3D Structural Fluctuation of IgG1 Antibody Revealed by Individual Particle Electron Tomography. *Sci. Rep.* **2015**, *5* (1), 9803.
- (311) Karuppasamy, M.; Karimi Nejadasl, F.; Vulovic, M.; Koster, A. J.; Ravelli, R. B. G.; IUCr. Radiation Damage in Single-Particle Cryo-Electron Microscopy: Effects of Dose and Dose Rate. *J. Synchrotron Radiat.* **2011**, *18* (3), 398–412.
- (312) Pedersen, J. S.; Cannavacciuolo, L.; Schurtenberger, P. Scattering from Wormlike Micelles. In *Giant Micelles*; Zana, R., Kaler, E. W., Eds.; Taylor & Francis Group, 2007; pp 179–220.
- (313) Rathgeber, S.; Pakula, T.; Wilk, A.; Matyjaszewski, K.; Beers, K. L. On the Shape of Bottle-Brush Macromolecules: Systematic Variation of Architectural Parameters. *J. Chem. Phys.* **2005**, *122* (12), 124904.
- (314) Hsu, H.-P.; Paul, W.; Rathgeber, S.; Binder, K. Characteristic Length Scales and Radial Monomer Density Profiles of Molecular Bottle-Brushes: Simulation and Experiment. *Macromolecules* **2010**, *43* (3), 1592–1601.
- (315) Hsu, H.-P.; Paul, W.; Binder, K. Standard Definitions of Persistence Length Do Not Describe the Local “Intrinsic” Stiffness of Real Polymer Chains. *Macromolecules* **2010**, *43* (6), 3094–3102.
- (316) Hsu, H.-P.; Paul, W.; Binder, K. Polymer Chain Stiffness vs. Excluded Volume: A Monte Carlo Study of the Crossover towards the Worm-like Chain Model. *Europhys. Lett.* **2010**, *92* (2), 28003.
- (317) Schäfer, L.; Ostendorf, A.; Hager, J. Scaling of the Correlations among Segment Directions of a Self-Repelling Polymer Chain. *J. Phys. A. Math. Gen.* **1999**, *32* (45), 7875–7899.
- (318) Zeitler, E.; Bahr, G. F. A Photometric Procedure for Weight Determination of Submicroscopic Particles Quantitative Electron Microscopy. *J. Appl. Phys.* **1962**, *33* (3), 847–853.
- (319) Tacke, S.; Messmer, D.; Nüsse, H.; Klingauf, J.; Schlüter, A. D.; Wepf, R. A. Single-Particle Cryo-QSTEM – a New Approach for Structure, Mass and Mass Density Correlation of Nano-Materials at High-Resolution. *In Preparation* **2018**.
- (320) Bedard, M.; Huber, H.; Myers, J. L.; Wright, G. F. The Crystalline Form of 1,3,5,7-Tetranitro-1,3,5,6-Tetrazacyclooctane (HMX). *Can. J. Chem.* **1962**, *40* (12), 2278–2299.
- (321) WS Hampshire Inc. Typical Properties of Teflon  
[http://catalog.wshampshire.com/Asset/psg\\_teflon\\_ptfe.pdf](http://catalog.wshampshire.com/Asset/psg_teflon_ptfe.pdf) (accessed Aug 23, 2018).
- (322) Mezzenga, R.; Ruokolainen, J.; Canilho, N.; Kasëmi, E.; Schlüter, A. D.; Lee, W. B. L.; Fredrickson, G. H. Frustrated Self-Assembly of Dendron and Dendrimer-Based Supramolecular Liquid Crystals. *Soft Matter* **2009**, *5* (1), 92–97.
- (323) Costanzo, S.; Scherz, L. F.; Schweizer, T.; Kröger, M.; Floudas, G.; Schlüter, A. D.; Vlassopoulos, D. Rheology and Packing of Dendronized Polymers. *Macromolecules* **2016**, *49* (18), 7054–7068.
- (324) Edwards, S. F. The Statistical Mechanics of Polymers with Excluded Volume. *Proceedings Phys. Soc.* **1965**, *85* (5), 613–624.
- (325) Doi, M.; Edwards, S. F. Dynamics of Concentrated Polymer Systems Part 1 .-Brownian Motion in the Equilibrium State. *J. Chem. Soc. Faraday Trans. 2* **1978**, *74*, 1789–1801.
- (326) De Gennes, P. G. Reptation of a Polymer Chain in the Presence of Fixed Obstacles. *J. Chem. Phys.* **1971**, *55* (2), 572–579.

- (327) Kantor, R. M.; Guo, X.-H.; Huff, E. J.; Schwartz, D. C. Dynamics of DNA Molecules in Gel Studied by Fluorescence Microscopy. *Biochem. Biophys. Res. Commun.* **1999**, *258* (1), 102–108.
- (328) Samor, P.; Ecker, C.; Gössl, I.; de Witte, P. A. J.; Cornelissen, J. J. M. L.; Metselaar, G. A.; Otten, M. B. J.; Rowan, A. E.; Nolte, R. J. M.; Rabe, J. P. High Shape Persistence in Single Polymer Chains Rigidified with Lateral Hydrogen Bonded Networks. **2002**.
- (329) Keshavarz, M.; Engelkamp, H.; Xu, J.; Braeken, E.; Otten, M. B. J.; Uji-i, H.; Schwartz, E.; Koepf, M.; Vananroye, A.; Vermant, J.; et al. Nanoscale Study of Polymer Dynamics. *ACS Nano* **2016**, *10* (1), 1434–1441.
- (330) Van Buul, A. M.; Schwartz, E.; Brocorens, P.; Koepf, M.; Beljonne, D.; Maan, J. C.; Christianen, P. C. M.; Kouwer, P. H. J.; Nolte, R. J. M.; Engelkamp, H.; et al. Stiffness versus Architecture of Single Helical Polyisocyanopeptides. *Chem. Sci.* **2013**, *4*, 2357–2363.
- (331) Schroeder, C. M. Single Polymer Dynamics for Molecular Rheology. *J. Rheol. (N. Y. N. Y.)* **2018**, *62* (1), 371–403.
- (332) Perkins, T. T.; Smith, D. E.; Chu, S. Single Polymer Dynamics in an Elongational Flow. *Science* **1997**, *276* (5321), 2016–2021.
- (333) Mai, D. J.; Saadat, A.; Khomami, B.; Schroeder, C. M. Stretching Dynamics of Single Comb Polymers in Extensional Flow. *Macromolecules* **2018**, *51* (4), 1507–1517.
- (334) Li, Y.; Hsiao, K.-W.; Brockman, C. A.; Yates, D. Y.; Robertson-Anderson, R. M.; Kornfield, J. A.; San Francisco, M. J.; Schroeder, C. M.; McKenna, G. B. When Ends Meet: Circular DNA Stretches Differently in Elongational Flows. *Macromolecules* **2015**, *48* (16), 5997–6001.
- (335) Hell, S. W. Far-Field Optical Nanoscopy. *Science* **2007**, *316* (5828), 1153–1158.
- (336) Hell, S. W.; Kroug, M. Ground-State-Depletion Fluorescence Microscopy: A Concept for Breaking the Diffraction Resolution Limit. *Appl. Phys. B Lasers Opt.* **1995**, *60* (5), 495–497.
- (337) Hell, S. W.; Wichmann, J. Stimulated-Emission-Depletion Fluorescence Microscopy. *Opt. Lett.* **1994**, *19* (11), 780–782.
- (338) Rust, M. J.; Bates, M.; Zhuang, X. Sub-Diffraction-Limit Imaging by Stochastic Optical Reconstruction Microscopy (STORM). *Nat. Methods* **2006**, *3* (10), 793–796.
- (339) Gustafsson, M. G. L.; Webb, W. Nonlinear Structured-Illumination Microscopy: Wide-Field Fluorescence Imaging with Theoretically Unlimited Resolution. *Proc. Natl. Acad. Sci. USA* **2005**, *102* (37), 13081–13086.
- (340) York, A. G.; Chandris, P.; Nogare, D. D.; Head, J.; Wawrzusin, P.; Fischer, R. S.; Chitnis, A.; Shroff, H. Instant Super-Resolution Imaging in Live Cells and Embryos via Analog Image Processing. *Nat. Methods* **2013**, *10* (11), 1122–1126.
- (341) Zhang, B.; Schlüter, A. D. Non-Charged, Water Soluble Dendronized Polymers. *New J. Chem.* **2012**, *36* (2), 414–418.
- (342) Fornera, S.; Bauer, T.; Schlüter, A. D.; Walde, P. Simple Enzyme Immobilization inside Glass Tubes for Enzymatic Cascade Reactions. *J. Mater. Chem.* **2012**, *22* (2), 502–511.
- (343) Grotzky, A.; Nauser, T.; Erdogan, H.; Schlüter, A. D.; Walde, P. A Fluorescently Labeled Dendronized Polymer–Enzyme Conjugate Carrying Multiple Copies of Two Different Types of Active Enzymes. *J. Am. Chem. Soc.* **2012**, *134* (28), 11392–11395.
- (344) Piao King, T.; Wei Zhao, S.; Lam, T. Preparation of Protein Conjugates via Intermolecular Hydrazone Linkage. *Biochemistry* **1986**, *25* (80), 5774–5779.
- (345) Schwartz, D. A. Hydrazine-Based and Carbonyl-Based Bifunctional Crosslinking Reagents. US 6,800,728, 2004.

- (346) Scientific, T. F. The Molecular Probes Handbook  
<https://www.thermofisher.com/ch/en/home/references/molecular-probes-the-handbook.html>  
(accessed Apr 9, 2018).
- (347) Gonçalves, M. S. T. Fluorescent Labeling of Biomolecules with Organic Probes. *Chem. Rev.* **2009**, *109* (1), 190–212.
- (348) Fülöp, L.; Penke, B.; Zarándi, M. Synthesis and Fluorescent Labeling of Beta-Amyloid Peptides. *J. Pept. Sci.* **2001**, *7* (8), 397–401.
- (349) Beija, M.; Afonso, C. A. M.; Martinho, J. M. G. Synthesis and Applications of Rhodamine Derivatives as Fluorescent Probes. *Chem. Soc. Rev.* **2009**, *38* (8), 2410–2433.
- (350) Kvach, M. V.; Ustinov, A. V.; Stepanova, I. A.; Malakhov, A. D.; Skorobogatyi, M. V.; Shmanai, V. V.; Korshun, V. A. A Convenient Synthesis of Cyanine Dyes: Reagents for the Labeling of Biomolecules. *Eur. J. Org. Chem.* **2008**, *2008* (12), 2107–2117.
- (351) Khalfan, H.; Abuknesha, R.; Rand-Weaver, M.; Price, R. G.; Robinson, D. Aminomethyl Coumarin Acetic Acid: A New Fluorescent Labelling Agent for Proteins. *Histochem. J.* **1986**, *18* (9), 497–499.
- (352) Peneva, K.; Mihov, G.; Nolde, F.; Rocha, S.; Hotta, J.; Braeckmans, K.; Hofkens, J.; Uji-i, H.; Herrmann, A.; Müllen, K. Water-Soluble Monofunctional Perylene and Terrylene Dyes: Powerful Labels for Single-Enzyme Tracking. *Angew. Chem. Int. Ed.* **2008**, *47* (18), 3372–3375.
- (353) Zhao, N.; Williams, T. M.; Zhou, Z.; Fronczek, F. R.; Sibrian-Vazquez, M.; Jois, S. D.; Vicente, M. G. H. Synthesis of BODIPY-Peptide Conjugates for Fluorescence Labeling of EGFR Overexpressing Cells. *Bioconjug. Chem.* **2017**, *28* (5), 1566–1579.
- (354) Zilles, A.; Arden-Jacob, J.; Drexhage, K.; Kemnitzer, N. U.; Hamers-Schneider, M. Sulfonamide Derivatives of Polycyclic Dyes Used for Analytical Applications. US9035042B2, July 2, 2004.
- (355) Khanna, P. L.; Ullman, E. F. 4',5'-Dimethoxy-6-Carboxyfluorescein: A Novel Dipole-Dipole Coupled Fluorescence Energy Transfer Acceptor Useful for Fluorescence Immunoassays. *Anal. Biochem.* **1980**, *108* (1), 156–161.
- (356) Loison, S.; Cottet, M.; Orcel, H.; Adihou, H.; Rahmeh, R.; Lamarque, L.; Trinquet, E.; Kellenberger, E.; Hibert, M.; Durroux, T.; et al. Selective Fluorescent Nonpeptidic Antagonists For Vasopressin V<sub>2</sub> GPCR: Application To Ligand Screening and Oligomerization Assays. *J. Med. Chem.* **2012**, *55* (20), 8588–8602.
- (357) Drumheller, P. D.; Hubbell, J. H. Surface Immobilization of Adhesion Ligands for Investigations of Cell-Substrate Interactions. In *The Biomedical Engineering Handbook*; Bronzino, J., Ed.; CRC Press, 1999; Vol. 2.
- (358) Arbeloa, F. L.; Ojeda, P. R.; Arbeloa, I. L. Fluorescence Self-Quenching of the Molecular Forms of Rhodamine B in Aqueous and Ethanolic Solutions. *J. Lumin.* **1989**, *44* (1–2), 105–112.
- (359) Rosenfarb, J.; Huffman, H. L.; Caruso, J. A. Dielectric Constants, Viscosities, and Related Physical Properties of Several Substituted Liquid Ureas at Various Temperatures. *J. Chem. Eng. Data* **1976**, *21* (2), 150–153.
- (360) Matsumoto, T.; Kawai, M.; Masuda, T. Influence of Chain Stiffness on the Gelation and Gel Structure of Alginate Aqueous Systems. *J. Chem. Soc. Faraday Trans.* **1992**, *88* (18), 2673.
- (361) Brouwer, A. J.; Mulders, S. J. E.; Liskamp, R. M. J. Convergent Synthesis and Diversity of Amino Acid Based Dendrimers. *Eur. J. Org. Chem.* **2001**, *2001* (10), 1903–1915.
- (362) Machida, S.; Usuba, K.; Blaskovich, M. A.; Yano, A.; Harada, K.; Sebti, S. M.; Kato, N.; Ohkanda, J. Module Assembly for Protein-Surface Recognition: Geranylgeranyltransferase I Bivalent Inhibitors for Simultaneous Targeting of Interior and Exterior Protein Surfaces. *Chem. Eur. J.* **2008**, *14* (5), 1392–1401.
- (363) Kasemi, E.; Schlüter, A. D. An Easy Accessible Homologous Set of First to Fifth Generation Dendritic Methacrylic Macromonomers and Their Polymerizations. *New J. Chem.* **2007**, *31* (7), 1313–1320.

- (364) Shu, L.; Gössl, I.; Rabe, J. P.; Schlüter, A. D. Quantitative Aspects of the Dendronization of Dendronized Linear Polystyrenes. *Macromol. Chem. Phys.* **2002**, *203* (18), 2540–2550.
- (365) Shu, L.; Schlüter, A. D. Synthesis and Polymerization of a Amine-Terminated Dendronized Styrene. *Macromol. Chem. Phys.* **2000**, *201* (2), 239–245.
- (366) Usov, I.; Mezzenga, R. FiberApp: An Open-Source Software for Tracking and Analyzing Polymers, Filaments, Biomacromolecules, and Fibrous Objects. *Macromolecules* **2015**, *48* (5), 1269–1280.
- (367) Schindelin, J.; Arganda-Carreras, I.; Frise, E.; Kaynig, V.; Longair, M.; Pietzsch, T.; Preibisch, S.; Rueden, C.; Saalfeld, S.; Schmid, B.; et al. Fiji: An Open-Source Platform for Biological-Image Analysis. *Nat. Methods* **2012**, *9* (7), 676–682.
- (368) Klopsch, R.; Koch, S.; Schlüter, A. D. Amino-Functionalized, Second-Generation Dendritic Building Blocks. *Eur J. Org. Chem.* **1998**, *1998* (7), 1275–1283.
- (369) Karakaya, B.; Claussen, W.; Gessler, K.; Saenger, W.; Schlüter, A. D. Toward Dendrimers with Cylindrical Shape in Solution. *J. Am. Chem. Soc.* **1997**, *119* (14), 3296–3301.
- (370) Sun, H.; Dimagno, S. G. Anhydrous Tetrabutylammonium Fluoride. *J. Am. Chem. Soc.* **2005**, *127*, 2050–2051.
- (371) Thompson, S.; Hamilton, A. D. Amphiphilic  $\alpha$ -Helix Mimetics Based on a Benzoylurea Scaffold. *Org. Biomol. Chem.* **2012**, *10* (30), 5780.
- (372) Patel, R. N.; Goswami, A.; Chu, L.; Donovan, M. J.; Nanduri, V.; Goldberg, S.; Johnston, R.; Siva, P. J.; Nielsen, B.; Fan, J.; et al. Enantioselective Microbial Reduction of Substituted Acetophenones. *Tetrahedron: Asymmetry* **2004**, *15* (8), 1247–1258.
- (373) Wolfe, S.; Wilson, M.-C.; Cheng, M.-H.; Shustov, G. V.; Akuche, C. I. Cyclic Hydroxamates, Especially Multiply Substituted [1,2]Oxazinan-3-Ones. *Can. J. Chem.* **2003**, *81* (8), 937–960.
- (374) Pasquino, R.; Zhang, B.; Sigel, R.; Yu, H.; Ottiger, M.; Bertran, O.; Aleman, C.; Schlüter, A. D.; Vlassopoulos, D. Linear Viscoelastic Response of Dendronized Polymers. *Macromolecules* **2012**, *45* (21), 8813–8823.
- (375) Bertran, O.; Zhang, B.; Schlüter, A. D.; Kröger, M.; Alemán, C. Modeling Nanosized Single Molecule Objects: Dendronized Polymers Adsorbed onto Mica. *J. Phys. Chem. C* **2015**, *119* (7), 3746–3753.
- (376) Cieplak, P.; Cornell, W. D.; Bayly, C.; Kollman, P. A. Application of the Multimolecule and Multiconformational RESP Methodology to Biopolymers: Charge Derivation for DNA, RNA, and Proteins. *J. Comput. Chem.* **2018**, *16* (11), 1357–1377.
- (377) Bai, L.; Li, S.-N.; Zhai, Q.-G.; Jiang, Y.-C.; Hu, M.-C. Density, Refractive Index, and Viscosity of Binary Systems Composed of Ionic Liquids ([Cnmim]Cl,  $n = 2, 4$ ) and Three Dipolar Aprotic Solvents at  $T = 288.15$ – $318.15$  K. *Chem. Pap.* **2015**, *69* (10), 1378–1388.
- (378) Berendsen, H. J. C.; Postma, J. P. M.; van Gunsteren, W. F.; DiNola, A.; Haak, J. R. Molecular Dynamics with Coupling to an External Bath. *J. Chem. Phys.* **1984**, *81* (8), 3684–3690.
- (379) Ryckaert, J.-P.; Ciccotti, G.; Berendsen, H. J. . Numerical Integration of the Cartesian Equations of Motion of a System with Constraints: Molecular Dynamics of  $n$ -Alkanes. *J. Comput. Phys.* **1977**, *23* (3), 327–341.
- (380) Ludtke, S. J.; Baldwin, P. R.; Chiu, W. EMAN: Semiautomated Software for High-Resolution Single-Particle Reconstructions. *J. Struct. Biol.* **1999**, *128* (1), 82–97.
- (381) van Heel, R.; Portugal, A.; Rohuo, C.; Linnemayr, C.; Bebeacqua, R.; Schmidt, T.; Schatz, M. Four-Dimensional Cryo Electron Microscopy at Quasi Atomic Resolution: "IMAGIC 4D". In *International Tables for Crystallography Volume F: Crystallography of biological macromolecules*; 2011; pp 624–628.
- (382) Schatz, M.; Orlova, E. V.; Dube, P.; Stark, H.; Zemlin, F.; van Heel, M. Angular Reconstitution in Three-Dimensional Electron Microscopy: Practical and Technical Aspects. *Scanning Microsc.* **1997**, *11*, 179–

- 193.
- (383) Nguema Edzang, R. W.; Lejars, M.; Brisset, H.; Raimundo, J.-M.; Bressy, C. RAFT-Synthesized Polymers Based on New Ferrocenyl Methacrylates and Electrochemical Properties. *RSC Adv.* **2015**, *5* (94), 77019–77026.
- (384) Bosscher, F.; Ten Brinke, G.; Eshuis, A.; Challa, G. Crystal Structure of Isotactic Poly(Methyl Methacrylate). *Macromolecules* **1982**, *15* (5), 1364–1368.
- (385) Kusanagi, H.; Chatani, Y.; Tadokoro, H. The Crystal Structure of Isotactic Poly(Methyl Methacrylate): Packing-Mode of Double Stranded Helices. *Polymer* **1994**, *35* (10), 2028–2039.
- (386) Micka, U.; Kremer, K. Persistence Length of the Debye-Hückel Model of Weakly Charged Flexible Polyelectrolyte Chains. *Phys. Rev. E* **1996**, *54* (3), 2653–2662.
- (387) Micka, U.; Kremer, K. Persistence Length of Weakly Charged Polyelectrolytes with Variable Intrinsic Stiffness. *Europhys. Lett.* **1997**, *38* (4), 279–284.
- (388) Tacke, S.; Krzyzaneck, V.; Nüsse, H.; Wepf, R. A.; Klingauf, J.; Reichelt, R. A Versatile High-Vacuum Cryo-Transfer System for Cryo-Microscopy and Analytics. *Biophys. J.* **2016**, *110* (4), 758–765.
- (389) Chang, C. J.; Lippert, A. R.; Lin, V. S. Fluorescent Probes for Reactive Sulfur Species. US2012329085, 2012.
- (390) Yang, H.; Vasudevan, S.; Oriakhi, C.; Shields, J.; Carter, R. Scalable Synthesis of Lissamine Rhodamine B Sulfonyl Chloride and Incorporation of Xanthene Derivatives onto Polymer Supports. *Synthesis* **2008**, *2008* (6), 957–961.
- (391) Hanwell, M. D.; Curtis, D. E.; Lonie, D. C.; Vandermeersch, T.; Zurek, E.; Hutchison, G. R. Avogadro: An Advanced Semantic Chemical Editor, Visualization, and Analysis Platform. *J. Cheminform.* **2012**, *4* (1), 17.
- (392) Halgren, T. A. Merck Molecular Force Field. I. Basis, Form, Scope, Parameterization, and Performance of MMFF94. *J. Comput. Chem.* **1996**, *17* (5–6), 490–519.
- (393) Uppuluri, S.; Dvornic, P. R.; Klimash, J. W.; Carver, P. I.; Tan, N. C. B. *The Properties of Dendritic Polymers I: Generation 5 Poly(Amidoamine) Dendrimers (ARL-TR-1606)*; 1998.
- (394) Fischer, H.; Polikarpov, I.; Craievich, A. F. Average Protein Density Is a Molecular-Weight-Dependent Function. *Protein Sci.* **2004**, *13* (10), 2825–2828.
- (395) Zhang, A.; Wei, L.; Schlüter, a. D. Narrowly Distributed Dendronized Polymethacrylates by Reversible Addition-Fragmentation Chain Transfer(RAFT) Polymerization. *Macromol. Rapid Commun.* **2004**, *25* (7), 799–803.